Stellar Mass Loss in Globular Clusters

Iain McDonald

Doctor of Philosophy

Research Institute for the Environment, Physical Sciences and Applied Mathematics,
University of Keele.

September 2009

Declaration

I certify that:

(a) I understand that the decision to submit this thesis is entirely my own decision;

(b) the thesis being submitted for examination is my own account of my own research;

(c) my research has been conducted ethically;

(d) the data and results presented are the genuine data and results actually obtained by me during the conduct of the research;

(e) where I have drawn on the work, ideas and results of others this has been appropriately acknowledged in the thesis;

(f) where any collaboration has taken place with one or more other researchers, I have included within an Acknowledgments section in the thesis a clear statement of their contributions, in line with the relevant statement in the Code of Practice;

(g) the greater portion of the work described in the thesis has been undertaken subsequent to my registration for the higher degree for which I am submitting for examination;

(h) where part of the work described in the thesis has previously been incorporated in another thesis submitted by me for a higher degree (if any), this has been identified and acknowledged in the thesis;

(i) the thesis submitted is within the required word limit as specified in the Regulations.

Total words in submitted thesis (including the text and footnotes, but excluding references and appendices): .....

Signature of candidate ..... Date .....

Cc: Lead Supervisor

Director of Postgraduate Research

Abstract

This work investigates stellar mass loss in globular clusters. It comprises of optical and infra-red photometric imaging and spectroscopy, plus radio interferometry observations.

I present mid-infrared spectroscopic observations of stars in the globular clusters 47 Tucanae and ω Centauri, finding 47 Tuc V1 (and possibly V18) and ω Cen V6 surrounded by circumstellar silicate dust. ω Cen V42 may also be surrounded by carbon-rich dust.

Much of this work is devoted to finding the threshold for dust production and the mass-loss rates from cluster stars with both chromospherically- and dust- or pulsation-driven winds. Using very-high-resolution optical photometry, I have identified the transition between the two driving regimes as being at earlier spectral types than in solar-metallicity stars, suggesting that pulsation and continuum-driving become the dominant wind drivers at around K5$\sim$M3, or $\sim$1500 $L_{\odot}$. Even at low metallicity, pulsation is seen to occur, as evidenced by our discovery of long-period variable stars at [Fe/H] ~ -2.3 in M15.

In a similar vein, I have modelled spectral energy distributions of stars in ω Centauri using new photometry from the *Spitzer Space Telescope* and literature photometry. The total mass-loss rate for the cluster is $\gtrsim 1.2^{0.6}_{0.5} \times 10^{-6}$ $M_{\odot}$ yr^{-1}, some 30% of which is from two stars — V6 and V42. This implies the cluster is being cleaned of gas and dust every $\lesssim 10^5$ years. Dust production appears to be efficient on both the red and asymptotic giant branches, even at the cluster's low metallicity ([Fe/H] = –1.62). I also derive a new distance to the cluster of 4850 $\pm$ 200 (statistical) $\pm$ 200 (systematic) pc with a reddening of $E(B-V) = 0.08 \pm 0.02 \pm 0.02$ mag and a differential reddening of $\Delta E(B-V) < 0.02$ mag.

Finally, we also present new observations of the high velocity hydrogen cloud in the vicinity of ω Centauri, finding that it is likely not associated with the cluster.

Acknowledgements

A thesis is impossible without the help of others. Most notably, that help came from my supervisor, Jacco van Loon (JvL), who gave backing to my findings, and who assisted with both scientific theory and practise. Similarly, thanks to my colleagues at Keele for all the minutiae: from shell scripting to coffee making, and allowing me to indulge in other fields of research in my supposed 'free time'.

In such a small discipline, it is necessary to look beyond one's own borders. I have been lucky to collaborate with the University of Minnesota's finest: Martha Boyer (MLB), Chick Woodward, Bob Gehrz, Andrea Dupree (AKD); also Leen Decin and the others with whom I have worked over the past few years. There are many others with whom I have correspondended and who have helped me, not least those upon whose work this thesis is based. Perhaps fitting is Newton's famous statement, ironically a quote itself from John of Salisbury's *Metalogicon*:

> *"Bernard of Chartres used to say that we are like dwarfs on the shoulders of giants, so that we can see more than they, and things at a greater distance, not by virtue of any sharpness on sight on our part, or any physical distinction, but because we are carried high and raised up by their great size."*

Finally, a PhD consumes one's life — it is only fair that it should give something back. I am eternally indebted to the amateur group who maintain Keele Observatory, for allowing me to indulge astronomy both as a science and a hobby, and for the chance to play with various technical gubbins. I am also indebted to the British taxpayer, without whom I would have had to face the 'real world' a few years early and would not have had been paid to travel to exotic locations. Thanks go to the observatory staff (and dog) at La Silla, Paranal and Narrabri for enjoyable visits. Thanks to Virgin Trains, for doing their best to stitch the two halves of my life together; to Genny, for being one of those halves, and reminding me why I am here; and to the Postgraduate Association, for helping me forget again. Finally, thanks to everyone else I cannot name due to the limits of what fits in one book — this thesis would have been impossible without you.

Contents

List of Figures

List of Tables

1 Introduction and review

> *"With every passing hour our solar system comes forty-three thousand miles*[1] *closer to [the] globular cluster M13 in the constellation Hercules, and still there are some misfits who continue to insist that there is no such thing as progress."*
>
> — Kurt Vonnegut, Jr., *The Sirens of Titan* (1959).

1.1 Motivation

Mass loss from giant stars is key to the ecology of the Galaxy. Matter from these stars replenishes the Galactic inter-stellar medium (ISM) and allows the creation of new stars and planets. By looking at mass loss from some of the oldest stars, we can see how mass loss varies over time, but also over stellar mass and composition. In globular clusters, we have a set of stars with known characteristics, such as distance, composition (metallicity), age, *etc.*, which allows us to make much more accurate comparisons between stars than would otherwise be possible.

An understanding of how mass loss works in these environments will help us learn how the Galaxy and its stars came to be in their present form, how material is cycled through the Galaxy, how the elements that make up $\gg$99% of the Earth were formed, and the eventual fate of our Sun.

1.2 Globular clusters

1.2.1 A brief history of globular clusters

1.2.1.1 Early observations

The study of globular clusters is almost as old as the telescope itself. Their discovery has been accredited to Johann Ihle in 1665 (Jones 1991), who described his discovery

[1] The actual value, based on the cluster's heliocentric radial velocity, is rather larger: 550 000 mph.

(later named M22) as a *"composite nebula between the head and the bow of the archer onto which a great number of faint stars was projected"* (cited in Schultz 1866). This discovery was followed by the announcement in 1677 of nebulosity in ω Centauri[2] by Edmund Halley (of comet fame), who also discovered another globular, later named M13 (Halley 1714). Meanwhile, Gotfried Kirch had discovered a 'nebulous star' in 1702, which was to become M5 (Dreyer 1898). This was probably followed by Chéseaux's discovery of M4 in *circa* 1745, who describes it as *"white, round and smaller [than ω Cen or M22]"* (Sawyer Hogg 1949), and Miraldi's observations of M15 and M2 (Maraldi 1746).

The number of known globular clusters increased dramatically between 1764 and 1782, as the astronomer Charles Messier (with help from Pierre Méchain) compiled his famous catalogue (Messier 1774, 1780, 1781), which lists 29 globular clusters in total; though all but M4 (a *"cluster of very small [faint] stars"*) were then classified as *"round nebulae"* (Jones 1991) as Messier and his contemporaries could not resolve them, their telescopes being poorly reflective and only a few inches across.

The task of identifying the nature of globular clusters as resolvable groups of stars was left to William Herschel, with his much larger 1.26m-diameter telescope. Herschel successfully resolved the globular clusters catalogued by Messier and others and, through his own discoveries, increased the number of known globular clusters to 70 (Herschel 1786, 1789, 1802). In his second catalogue of deep sky objects (Herschel 1789), he began to classify stellar clusters into different groups, including a group which he called 'globular'. He frequently applied the term '*an insultation*' to these clusters, due to their marked appearance compared to the background. In the same discussion he conjectured that the clusters were physically real, self-gravitating, spherical conglomerations of stars; though his theories on their distances and evolution, and the idea that *all* nebulae were composed of unresolved stars were later to be proven

[2] ω Centauri was first catalogued by Ptolemy (*c.* 130–170AD), but named as a star. At a visual magnitude of 3.7, it is one of the few naked-eye globular clusters.

incorrect. Nevertheless, the notion of a globular cluster was born.

The remainder of the 19$^{\text{th}}$ century brought with it the first large aperture, high-resolution telescopes. This allowed globular clusters to be resolved much better than with previous instruments. It also brought new discoveries: building on Herschel's *General Catalogue*, Dreyer (1888) brought out his *New General Catalogue* or 'NGC'. This contained 104 Galactic globular clusters, plus 16 extragalactic clusters (belonging to the Magellanic Clouds). His Index Catalogue (IC — Dreyer 1895, 1908) also included a further three Galactic globulars: IC1275, IC1276 and IC4499.

1.2.1.2 Putting clusters in context

Improving 19th Century technology brought with it high-resolution spectroscopy. The Doppler effect, first observed in light by Huggins (1868), could then be used to measure the radial velocity of clusters with respect to the Earth. This was first performed by Slipher (1918, 1922, 1924). Slipher's preliminary results showed that globular cluster systems have high (≈ 150 km s^{-1}) velocities when compared to local stars.

These results were rapidly picked up by Shapley, who had spent the previous few years using (primarily) RR Lyrae and Cepheid variables to measure the distances to clusters. (Shapley 1918a) used distances to known globular clusters to estimate the distance to the Galactic Centre. His value of around 20 kpc was overestimated due to interstellar extinction (see §1.4), but repeat studies (*e.g.*Harris (1980)) have shown that this is a viable technique which agrees with the modern distance estimate of around 8.0 $\pm$ 0.5 kpc (Reid 1993). The overestimate of the size of the Galaxy was undoubtedly a factor in Shapley and other's resistance to the idea of the existence of 'spiral nebulae' being other galaxies (*e.g.* Shapley 1919a, 1919b) — a resistance that fuelled astronomy's 'Great Debate' (Curtis 1921a & Curtis 1921b) and one he did not concede until Hubble's measurement of Cepheid variables in M31 (Hubble 1929).

Both the distance measurements of Shapley and his successors, and the radial velocity measurements of Slipher and others (notably Mayall 1946) showed that glob-

ular clusters orbit independently of the Galactic Disc. Instead they swarm around the Galactic Centre in randomly-inclined, often highly eccentric, and usually open orbits (*e.g.* Dinescu, Girard & van Altena 1999, Fig. 2). Using Galactic potential models, we can see that these orbits intersect the Galactic Plane roughly every 10^8 years, with profound implications for the cluster which will be discussed later, in §1.2.2.4.

In the last century, the number of known Galactic globular clusters has increased to 151 (Harris 1996)[3]. Globular clusters also appear in other galaxies: dozens of old globular clusters are now known in the Magellanic Clouds (*e.g.* Grocholski et al. 2006), and several hundred have been found orbiting both M31 and M33 (Mochejska et al. 1993; Fusi Pecci et al. 1993). Many other galaxies also host globular clusters. The distribution of clusters around the Galaxy is shown in Fig. 1.1.

1.2.2 The globular cluster environment

1.2.2.1 Observational properties

Most simply, globular clusters are conglomerations of roughly 10^4 to 10^6 stars (Benacquista 2002) which show a strong, but variable degree of central condensation. Their distribution on the sky is highly biased towards the Galactic Centre, as their Galactocentric radii are typically less than or near the Sun's.

Using multi-colour photometry or spectroscopy, we can build up either colour-magnitude diagrams or Hertzsprung-Russell (H-R) diagrams, respectively (see *e.g.* Fig. 1.2). Globulars are seen to comprise mostly of faint, red stars, which are spectroscopically identifiable as lying near the lower end of the Main Sequence. Visually, the most prominent stars tend to be red giants. M13 and M71, shown in Fig. 1.3, are visually fairly typical examples with differing degrees of central condensation.

[3]Updated catalogue at: http://physwww.physics.mcmaster.ca/%7Eharris/mwgc.dat

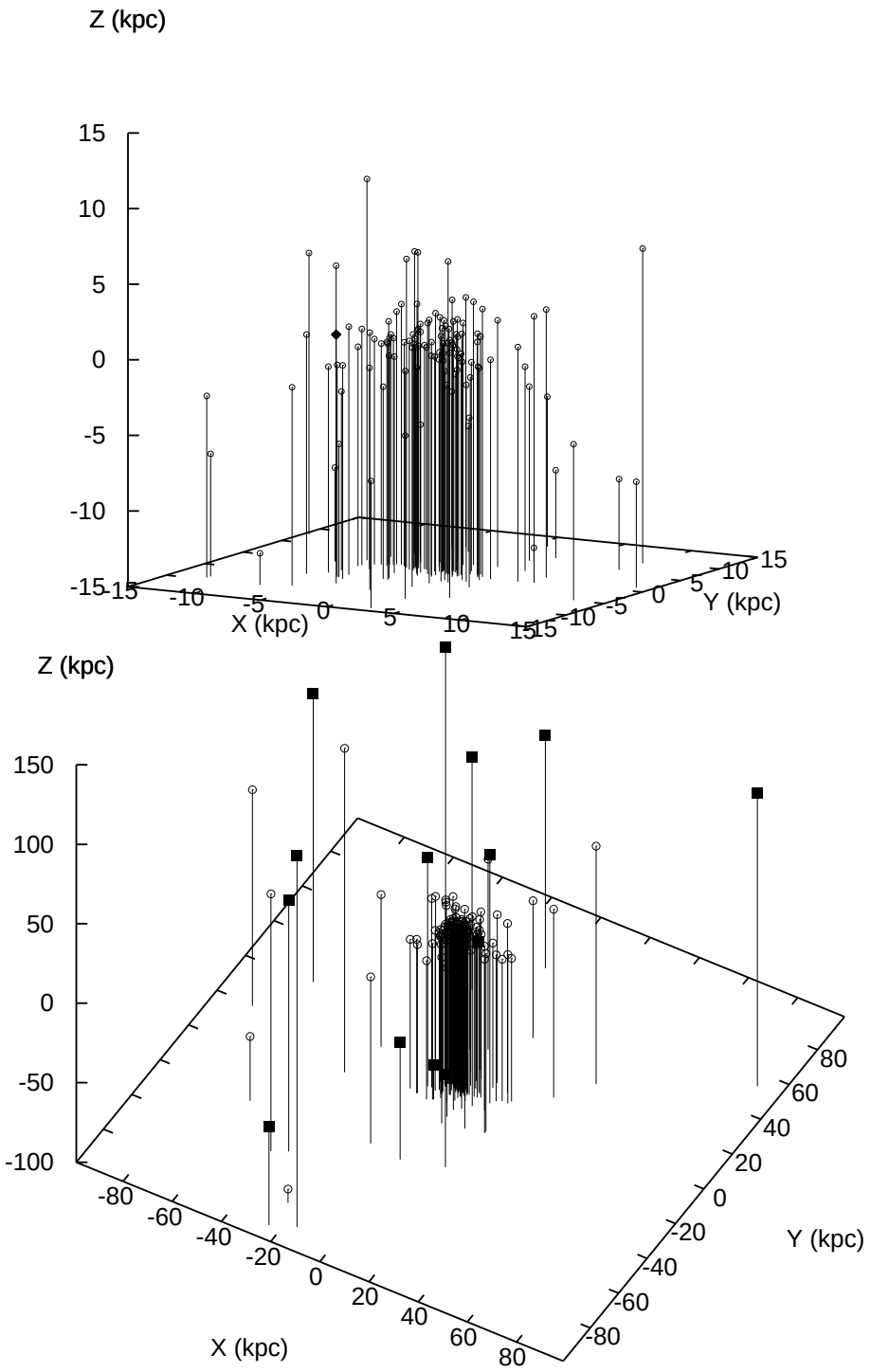

Figure 1.1: The distribution of Galactic globular clusters in galacto-centric co-ordinates from Harris (1996). Lines show projection onto the X-Y plane, squares denote some of the Milky Way's satellite dwarf galaxies (from Schwarzmeier 2007). The top panel shows the inner 30 kpc, with the Sun indicated by a diamond. Note that here there is not only a concentration toward the centre, but also the presence of a disc-like structure in the X-Y plane, matching that of the Galaxy itself.

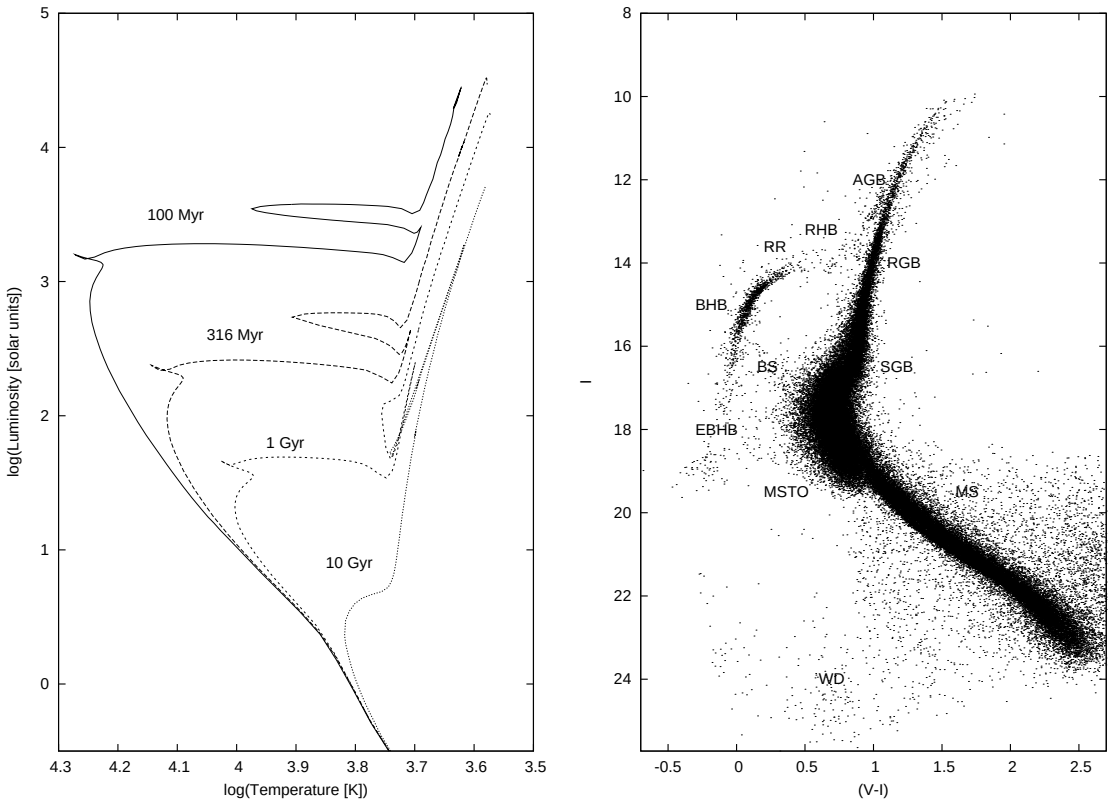

Figure 1.2: [Left Panel] Theoretical isochrones (lines on which all stars have identical ages) on a Hertzsprung-Russell diagram (data from Cioni et al. 2006a, 2006b). [Right Panel] Colour-magnitude diagram of ω Centauri, comprising two datasets (one for bright stars from Sollima et al. 2005a; one for faint stars from Sollima et al. 2007). The terms here are described later in the text. Abbreviations: AGB — Asymptotic Giant Branch, (E)BHB/RHB — (Extreme) Blue/Red Horizontal Branch), BS — Blue Stragglers, MS(TO) — Main-Sequence (Turn-Off), RGB — Red Giant Branch, RR — RR Lyrae Region, SGB — Sub-Giant Branch, WD — White Dwarfs.

Figure 1.3: [(Left) the Great or Hercules Cluster, M13, and (right) M71 as observed by the author with the Keele William Boulton Observatory 24" Thornton Telescope. The images are colour composites showing V, R and I bands. Note the bright red giants, which are distinct from the bluer main sequence stars, also note the central condensation of stars, which is much more apparent in M13 than M71.

1.2.2.2 Derived properties

The obvious factor that separates globular clusters from the rest of the Galactic population is their age. Using models of stellar evolution, the ages of globular clusters can be fit using isochrones — lines of constant age — on an H-R diagram (Fig. 1.2). The evidence strongly supports the idea that all stars within the majority of globular clusters have roughly the same age. Absolute ages are comparatively difficult to determine: estimated ages for Galactic globular clusters are typically 10–15 Gyr (Ashman & Zeph 1998; Jiménez 1998). As a result, the stars they contain are among the first stars to have formed in the Universe (which has an age of roughly 13.73 ± 0.12 Gyr — Hinshaw et al. 2009). Relative ages suggest the oldest, most-metal-poor clusters are roughly co-eval, forming well within 3 Gyr of the Big Bang, with the more metal-rich clusters forming over the following 3 Gyr (de Angeli et al. 2005).

Cluster stars are generally very metal-poor. Metallicities range from $[\mathrm{Fe/H}] = -2.3$ to solar metallicity, though typically $[\mathrm{Fe/H}] \approx -1.4 \pm 0.6$ (Harris 1996). Generally the population tends to be of roughly the same metallicity, typically within $\sim$10%, though again this is not always the case (Benacquista 2002).

It is perhaps not surprising that globular clusters are metal-poor, given their age, though it should be noted that their metallicity also depends on Galactocentric radius (Fig. 1.4). For comparison, the Galactic Bulge is of a similar age to many globulars, but contains some stars near solar metallicity.

These observations are in contrast with other galaxies. For example, in the Magellanic Clouds, many populous intermediate-age clusters exist that are 3–10 Gyr old (Bica, Dottori & Pastoriza 1986). Others, such as NGC 1984 and R 136, are as young as a few Myr (Santos et al. 1995). In galaxies further afield, globular clusters have a wide range of ages from $\approx$ 10–20 Gyr to only $\approx$ 10 Myr (*e.g.* Ma et al. 2006c [M31]; Schröder et al. 2002; Ma et al. 2006b [M81]) and are often seen to be forming in interacting galaxies (see §1.2.2.6). Globulars may therefore be better tracers of Galactic interaction, rather than peculiarities of a by-gone age.

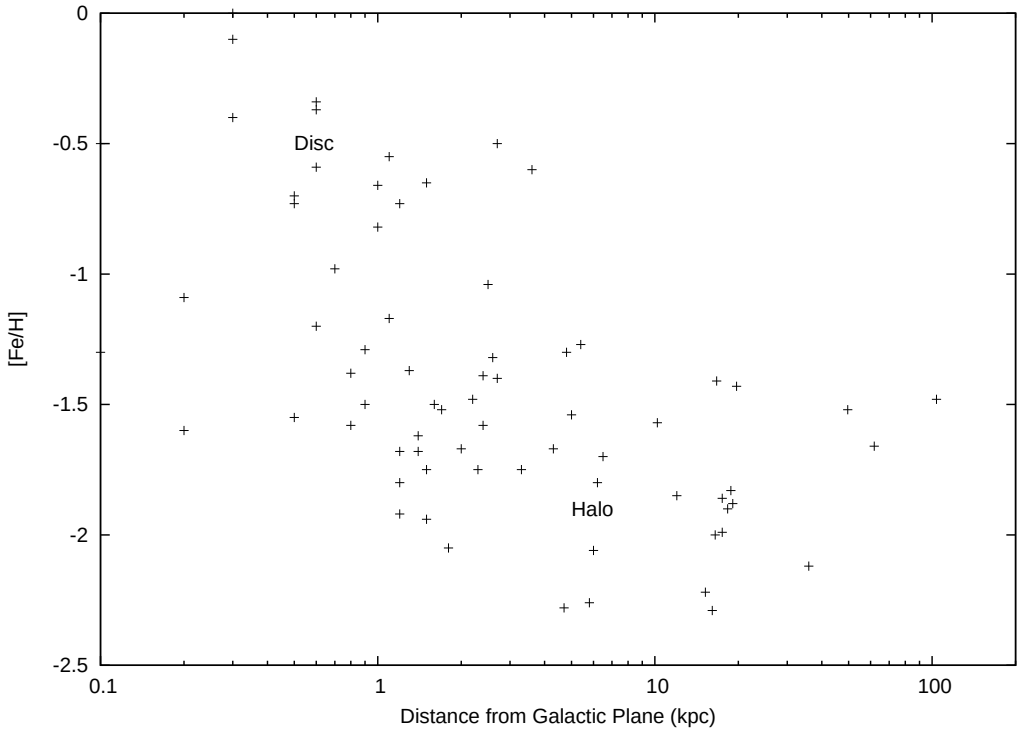

Figure 1.4: The correlation between distance from Galactic Plane and metallicity (data from Harris 1996). The Galactic globular cluster population can be split into two components: those near the Disc and those in the Halo.

Unusual globulars also occur in our own galaxy. Most famously ω Centauri contains more than one population, with a range in metallicity from 0.25% to 20% of solar (§C.6.4). Other clusters, such as NGC 2808, show abundance anomalies, most noticeably in helium (Piotto et al. 2007). NGC 6791 is also unusual, in being a very old (≈ 8 Gyr), metal-rich ([Z/H] ~ 0.05) *open* cluster, with many characteristics similar to globular clusters (van Loon, Boyer & McDonald 2008). This poses interesting questions concerning their formation and evolution.

1.2.2.3 Core collapse

Part of a cluster's evolution is certainly governed by gravitational dynamics. In the cluster cores, where densities are of order 10^4 $M_\odot$ pc^{-3} (Binney & Tremaine 1988), stellar encounters are frequent. This opens up the opportunity for stellar collisions, and the formation and destruction of binary or multiple star systems. More importantly,

due to exchange of orbital energies, stars can be flung out of the system by gravitational interactions. This process preferentially scatters low-mass stars, with the result that low-mass stars either achieve escape velocity and thus leave the cluster, or at least move to the outer regions of the cluster; meanwhile, high-mass and 'hard' (strongly-bound) binary stars gravitate towards the centre of the cluster. This process is known as 'mass segregation' and is well-documented in clusters and other bodies (White 1977; Spitzer 1987; Bonnell & Davies 1998; Khalisi, Amaro-Seoane & Spurzem 2007).

Mass segregation can lead to an increase in the density of the cluster's core. When the core density exceeds the mean density by a factor of around 710 (Bahcall 2004), this becomes a runaway process known as 'core collapse'.

As this process continues, dynamical interactions in the core serve to 'heat' the core, increasing the stellar velocities and resulting in 'core bounce', which reverses the collapse. Several clusters have been observed to be in this post-core collapse state (*e.g.* M 15, M 30, M 70 and possibly NGC 362 — Trager, King & Djorgovski 1995), and are thought to be undergoing repeated 'bounces' or 'gravitothermal oscillations'.

1.2.2.4 Tidal disruption

However, globular clusters are not truly isolated systems and, as mentioned previously, their periodic passages through the Galactic Disc have serious implications for their evolution. Stars which are only loosely bound to the cluster will come under the influence of the Galaxy's gravitational potential and will be stripped from the cluster. This will occur if the gravitational attraction of the galaxy is greater than that of the cluster. From Newtonian gravity (see also Binney & Tremaine 1988), this (instantaneous) tidal radius, $r_{\rm t}$, is given by:

$$r_{\rm t} = \sqrt{\frac{M_{\rm cl} R^2}{M_{\rm gal}}}, \tag{1.1}$$

where $M_{\rm cl}$ is the mass of the cluster, $M_{\rm gal}$ is the mass of the galaxy within the instantaneous orbital radius R of the cluster around the Galaxy.

The mass of a globular cluster within a certain radius can be estimated from the

dispersion of radial velocities of stars within that radius. Integrated masses of Galactic clusters are typically around 10^5 $M_\odot$ (Ashman & Zeph 1998), though ω Centauri weighs in at 2.5×10^6 $M_\odot$ (van de Ven et al. 2006).

The tidal radius varies significantly as the cluster moves through its orbit, being smallest when the cluster passes through the Galactic Disc (termed a Galactic plane crossing). The upshot of this is that a significant number of the outer stars are stripped from the globular cluster due to its repeated passages through the Galactic Plane. This eventually will result in the complete disruption of the cluster, on an evaporation timescale ($t_{\rm evap}$) given by (Bahcall 2004):

$$t_{\rm evap} = t_{\rm orbit} \frac{G M_{\rm cl} v_{\rm cl}^2}{20 g^2 r_{\rm h}^2}, \tag{1.2}$$

where $t_{\rm orbit}$ is the period between plane crossings (of order 100 Myr), $v_{\rm cl}$ is the cluster's velocity through the Disc, $r_{\rm h}$ is the cluster's half-mass radius and g is the gravitational acceleration from the Galaxy. Alternatively:

$$-\frac{dM}{dt} \propto \rho_{\rm h}^{1/2}, \tag{1.3}$$

for cluster half-mass density $\rho_{\rm h}$ (McLaughlin & Fall 2008). The evaporation time is typically equivalent to tens of gigayears, dependant on the cluster, resulting in a current evaporation rate of around five clusters per gigayear (Binney & Tremaine 1988). The evaporated stars will usually go on to lead or follow the cluster in a similar orbit around the Galaxy in tidal tails. Such processes have been seen in several Galactic globulars, most notably in Pal 5 (Odenkirchen et al. 2000; Koch et al. 2004), but also in other clusters, such as NGC 5466 (Belokurov et al. 2006; Grillmair & Johnson 2006).

1.2.2.5 Stellar remnants

Globular clusters also contain large numbers of stellar remnants: for almost every star that has 'died', there should be a stellar remnant of some sort (although whether it

remains bound to the cluster is another matter). On the whole these tend to be harder to observe due to their generally low emission, which varies according to their type: white dwarfs, neutron stars and black holes.

White dwarfs are obviously expected in populations of old stars, but due to their comparative faintness were not observed until relatively recently, when Richer (1978) found 61 in deep U- and B-band images of NGC 6752. With the deep photometry available from (primarily) the Hubble Space Telescope, many more white dwarfs have been found: 2000 are known in ω Cen alone (Monelli et al. 2005) and 27–37% of 47 Tuc's mass is thought to be made up of white dwarfs (Meylan 1988).

Neutron stars are the next most common remnants, with $\sim$1,000 in some of the richer globulars, though still making up $<$1% of the clusters' mass (Meylan 1988). The process of their formation can give them a high 'kick' velocity at birth, so they have the possibility of escaping the cluster potential. Apart from in the occasional interacting binary, we can usually only detect neutron stars as pulsars, of which there are 140 presently known in globular clusters[4], including $\sim$76 milli-second pulsars (Hessels et al. 2004) — neutron stars that are rotating with periods of a few milli-seconds due to accretion from a binary companion. Neutron stars may also have an important rôle to play in globular cluster plasma expulsion, which is touched upon in §1.5.2.2.

Black holes are also hypothesised to inhabit globular clusters, both in isolation and in X-ray binaries. Mass segregation causes high-mass objects (such as isolated black holes) to lose orbital energy and fall to the centre of the cluster's potential. This may give rise to merging intermediate-mass black holes in cluster centres. These have possible masses on the order of several hundred of solar masses (Kawakatu & Umemura 2005). The evidence for their existence in our Galaxy's globular clusters is debatable: M15 has the strongest evidence for an intermediate-mass black hole to date (Maccarone & Knigge 2007). However, black holes in the super-massive globular M31 G1 (Gebhardt, Rich & Ho 2002; Gebhardt, Rich & Ho 2005; Ulvestad, Greene & Ho

[4]A current list available from P. Freire: http://www.naic.edu/~pfreire/GCpsr.html

2007) and a globular in the elliptical galaxy NGC 4472 (Maccarone et al. 2007; Shih et al. 2008) appear to have been observed.

1.2.2.6 Formation scenarios

The origins of globular clusters are best described as uncertain and several possible scenarios exist. Indeed, Perez & Roy (2003) ask the question 'can we know how globular clusters form?' Despite much work being put into cataloguing and observing clusters and their component stars in the three centuries since their discovery, there appears to be very little early literature on the subject of their formation.

Originally, it was thought that globular clusters formed by fragmented collapse *in situ* (Eggen, Lynden-Bell & Sandage 1962; see also review: Chernoff 1993) as the Galactic Halo collapsed on a free-fall timescale. This was backed up by data (Fig. 1.4) showing the outer clusters, which orbit the Galaxy in a spherical halo, have a lower metallicity than those that orbit at smaller radii, which share kinematic properties with the Galactic Thick Disc.

This partition in metallicity is reflected in a related bimodality in integrated colour — a globular's integrated colour being a function of both metallicity and age. This bimodality has also been found in numerous other galaxies, where the peaks scale with parent galaxy luminosity (Puzia et al. 2002; Strader, Beasley & Brodie 2007 and references therein). This suggests the Milky Way is not unusual in having two different epochs and/or mechanisms of formation.

Debate on the existence, strength and relevance of these correlations took place during the early 1980s (*e.g.* Harris & Canterna 1979; Castellani, Maceroni & Tosi 1983; Pilachowski 1984), concluding with the evidence that clusters did not form separately to the Milky Way, but did participate in its general collapse to the Disc we see today.

While this may be globally true, another school of thought suggests that some of the Milky Way's globular clusters were captured from smaller galaxies that have either merged with, or passed by or through, the Milky Way (*e.g.* Searle & Zinn 1978;

Tsuchiya, Dinescu & Korchagin 2003). With the discovery of the Sagittarius Dwarf Elliptical Galaxy or 'SagDEG' (Ibata, Gilmore & Irwin 1994), it soon became clear that four globular clusters — M54, Arp 2, Terzan 7 and Terzan 8 — have roughly the same radial and proper motion velocities, distances and metallicities as the SagDEG (Sarajedini & Layden 1995; da Costa & Armandroff 1995; Ibata et al. 1997). It also appears (Dinescu et al. 2000) that the cluster Palomar 12 was accreted from the SagDEG around 1.7 Gyr ago. This hypothesis was further confirmed with the discovery of the Canis Major Dwarf Irregular Galaxy (Martin et al. 2004) and its association with four more globular clusters — M79, NGC 1851, NGC 2288 and NGC 2808. It has further been suggested by Yoon & Lee (2003) that the lowest metallicity clusters of the Milky Way have been tidally accreted from the LMC, due to their co-planar orbits.

A third possibility is that during this kind of process, where dwarf galaxies are integrated into the Milky Way, the outer regions of the galaxies have been stripped off, leaving a globular cluster as the galaxy core. This has been suggested as a formation mechanism for ω Cen, the Galaxy's most massive globular (§C.6.6), and for even more massive cluster G1 in M31 (Meylan et al. 2001b).

A final scenario argues that globular-sized clusters (along with dwarf galaxies) could be formed as a direct result of galactic mergers in tidal tails. This process is observed in several tidally-interacting galaxies, including the four classic 'Toomre Sequence' mergers: NGC 4038/4039 ('The Antennae'), NGC 3256, NGC 3921, and NGC 7252 ('Atoms for Peace') (Schweizer et al. 1996; Miller et al. 1997; Whitmore et al. 1997; Whitmore et al. 1999; Knierman et al. 2003). However, given the $\sim$3 Gyr timescale on which the Galactic globular cluster system appears to have formed, this cannot completely account for globular cluster formation in our own Galaxy.

1.2.2.7 Second parameter problem

A further interesting bimodality in the cluster population is the so-called 'Oosterhoff dichotomy'. This grouping of clusters is based on the mean periods of their regularly-

pulsating RR Lyrae stars (Oosterhoff 1939; Arp 1955), which can be markedly different for clusters of the same metallicity (*e.g.* Lee & Carney 1999).

Related to this, there is also what has become known as the 'Second Parameter Problem' or 'Second Parameter Effect'. This refers to the requirement of a second parameter, other than metallicity, to explain the temperature/colour distribution of stars in the Horizontal Branch (HB). A review of the second parameter effect can be found in Fusi Pecci & Bellazzini (1997). Various candidates have been proposed for the second parameter, most with the common denominator of RGB mass loss. These include the two leading contenders:

- Pre-HB (predominantly RGB) mass-loss, a leading contender (Catelan 2000);
- Cluster age: the second parameter effect depends strongly on Galactocentric distance; increased initial mass also leads to larger masses at the tip of the RGB, hence redder HBs (Zinn 1985; Catelan, Rood & Ferraro 2002; Catelan et al. 2002).

Other candidates seem to be needed as well (Stetson, VandenBerg & Bolte 1996; Richer et al. 1996; VandenBerg, Stetson & Bolte 1996). These include suggestions from, *e.g.*, Buonanno, Corsi & Fusi Pecci (1985); Yoon et al. (2008); and Moehler (2001), namely:

- stellar core rotation;
- stellar density;
- mixing at late evolutionary stages and/or varying helium content;
- metallicity spread;
- dynamical interactions.

These studies have also shown that the HB is often clumped and that there are significant complications from binarity. The determination of which factor(s) contribute to the second parameter remains as yet unsolved.

1.3 Mass loss

> *"We live in a changing universe, and few things are changing faster than our conception of it."*

— Timothy Ferris, *The Whole Shebang* (1997)

1.3.1 Introduction

1.3.1.1 History

As with many concepts in astronomy, when mass loss was observed, it was not uncovered for what it was. Chinese astronomers Shu & et al. (1044)[5] documented supernova SN1006, later identified with M1 — the Crab Nebula — and claimed it signalled good fortune for the state of Chêng (indeed they enjoyed relative prosperity for the following century). Brahe and Kepler later observed SN1572 and SN1604 (Brahe 1603a, 1603b; Kepler 1606). At the time, European opinion was that the heavens existed unchangingly and perpetually, but these discoveries helped start the scientific study of other types of variable star, notably including Mira[6] (see Fig. 1.5), whose brightness changes may have been noted for millenia (Muller & Hartwig 1918). All these stars are losing mass through one or more processes, and it is the Mira-like stars in which we are particularly interested here[7].

The science of mass loss is comparatively new. Willem Blaeu's discovery in 1600 of variability in P Cygni (Lamers & Cassinelli 1999) was not understood until early 19$^{\text{th}}$ century spectra showed very distinctive line profiles (see Fig. 1.6). Later, Wolf & Rayet (1867) discovered that a certain group of stars ("Wolf-Rayet stars") had similar features to novae and P Cygni profiles, but it wasn't until later that Campbell (1892) recognised that these features were due to Doppler-shifted light from moving stellar atmospheres. Two possibilities then existed: the stars either had a turbulent motion or they were expanding. Later photographs of novae shells confirmed the second hypothesis, thus confirming for the first time that stars lose mass.

[5]Translated and reprinted by Goldstein & Peng Yoke 1965.

[6]Variations in Mira (o Ceti) were discovered in 1596 by Fabricius and confirmed in 1609. Kepler, who disseminated the news, referred to this star as a candidate for the Star of Bethlehem (Kepler 1614), and it was christened by Hevelius (1662) as 'stella mira' or 'wonderful star'.

[7]Many of the stars discussed in this thesis are not true Miras (except 47 Tuc V1, V2, V3 and V8, and possibly ω Cen V42) yet are subject to the same mechanisms at low amplitude.

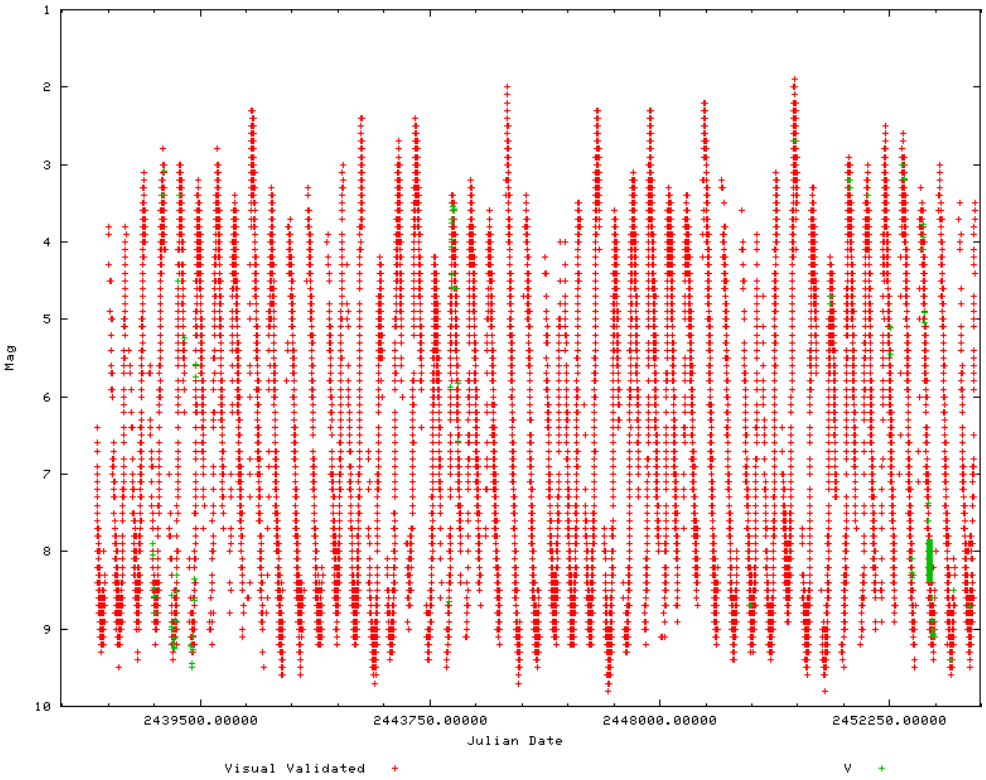

Figure 1.5: Light curve of Mira (omicron Ceti), courtesy of the AAVSO. Note the dramatic changes in brightness and the regular periodicity.

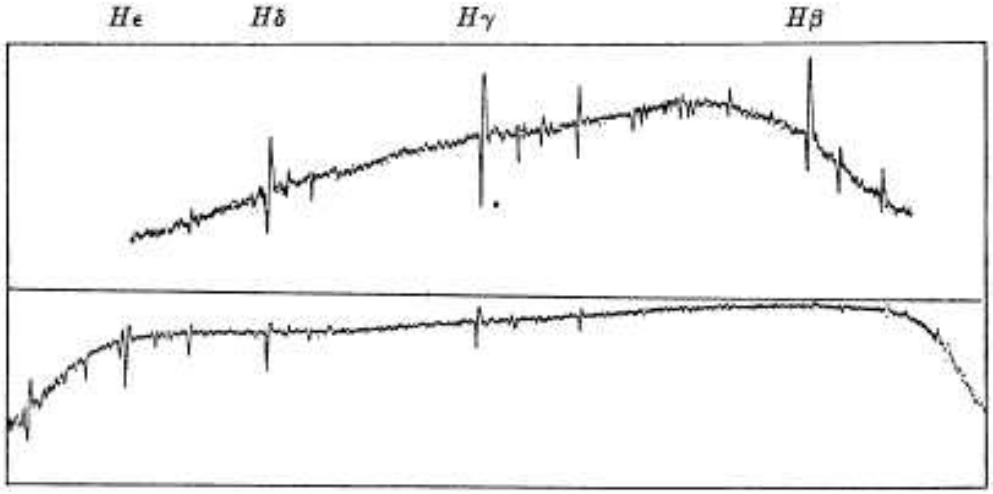

Figure 1.6: Early spectrum of P Cygni, originally published in Elvey (1928). The characteristic absorption-emission line profile can be seen in the hydrogen lines marked. Original caption: *"Density Curves of the spectrum of P Cygni. Above, March 21, 1928; below, April 27, 1928."*

However, all the above types of stars are either interacting binaries, or relatively short-lived, massive stars. Evidence for mass loss from single, less-massive stars (but still more massive than those present in Galactic globular clusters) was not to come until Adams & MacCormack (1935), who observed spectral line profiles of red supergiants, finding their atmospheres were expanding at $\sim$5 km s^{-1}. This is less than the stellar escape velocity and was thus thought to be due to a 'fountain' effect (Spitzer 1939).

The first observations of mass loss from low-mass stars came not from the stars themselves, but from the dust tails of comets. Biermann (1951) noticed that photon pressure alone was insufficient to describe the acceleration of cometary tails away from the Sun. Instead he surmised that particulate emission from the Sun was the driving force. This was later confirmed by the Mariner 2 probe (Neugebauer & Snyder 1962).

A few years before this confirmation, Deutsch (1956) made a crucial observation of the spectra of the M5II/G5V binary star α Herculis. Blueshifted spectral signatures from the primary were also visible on the secondary, meaning the star had to have an expanding circumstellar envelope. Deutsch calculated the mass-loss rate at around 3×10^{-8} M$_\odot$ yr^{-1}. With the discovery of other mass-losing stars during the late 1950s and early 1960s, he later went on to claim that mass loss occurred throughout the H-R diagram. Various attempts were made to determine a general parameterisation for the rate of mass-loss, notably Reimers (1975), though the variety of mechanisms by which stars lose mass now seem to preclude such generalisation.

1.3.1.2 Application to globular clusters

It is now well known that mass loss from stars enriches the ISM with gas and dust, which can then form new stars and planets; and that the mass loss from a star is governed by stellar evolution, and *vice versa*. Less well known is the precise rôle that mass, luminosity, temperature, metallicity, magnetic activity, rotation among other parameters have on how much mass is lost by a star, at which stages in its evolution this mass loss occurs and by which mechanisms.

Studies of mass loss in globular clusters may be able to help solve these problems as, while there is a large range in both age and metallicity among clusters, the stars in each cluster are typically of similar age and metallicity. Also, as the clusters periodically pass through the Galactic Plane (§1.2.2.4): plane crossing will remove any interstellar dust and gas in the cluster (Roberts 1986; Tayler & Wood 1975). Assuming this cleaning process is 100% efficient, the time-averaged amount of interstellar mass within a cluster, $M_{\rm is}$, can therefore be naïvely estimated (Roberts 1960) as:

$$M_{\rm is} = N_{\dot{M}} \frac{\Delta M}{\Delta t_{\dot{M}}} \frac{1}{2} t_{\rm p}, \tag{1.4}$$

where $N_{\dot{M}}$ is the number of stars losing mass in the cluster, ΔM is the amount of mass lost by an average star over a time $\Delta t_{\dot{M}}$ and $t_{\rm p}$ is the time between passages through the Galactic Plane.

1.3.2 Factors leading to mass loss

Research into mass loss has only properly come to the fore since the 1980s. We now recognise that several factors contribute to mass loss from stars, most notably stellar winds driven by radiation pressure, magnetic fields, pulsations or rotational excretion; mass loss in supernovae; and mass transfer in binary stars.

Stellar winds can be split into three categories according to their driving mechanism: radiation-driven winds (either line- or continuum-driven), magnetically-driven (chromospheric or coronal) winds, and acoustic- or pulsation-driven winds. Lamers & Cassinelli (1999) contains a comprehensive review of all three categories and forms the basis for this section, which describes the mechanisms at work in globular cluster stars.

1.3.2.1 Line-driven winds

Line-driven winds are the main method of mass loss in hot, luminous objects. In this scenario, radiation from the stellar core will scatter off or excite an ion (or atom) in

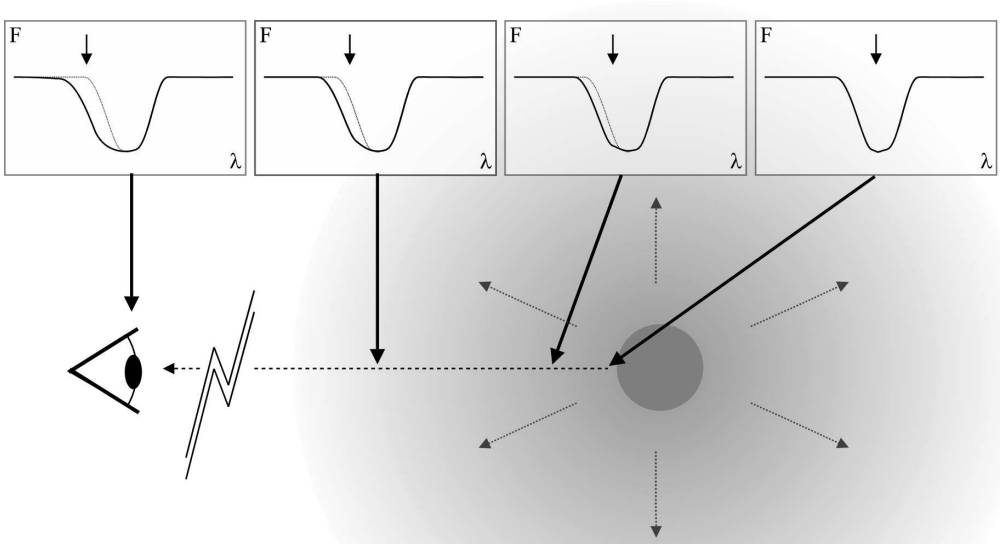

Figure 1.7: The formation of a blue-shifted absorption core in a line profile due to the transfer of energy from radiation to kinetic energy in the wind. The wind, as seen by the observer, becomes more blueshifted as it moves away from the star (vertical arrows in graphs), absorbing the wind at bluer wavelengths as it accelerates further and moves away from the star.

the atmosphere. The momentum transfer from a photon will accelerate the ion away from the star. If excited, the ion will (usually very quickly) relax towards the ground state and, in doing so, will emit one or more photons. As the emission is isotropic, this (on average) imparts a net outward force on the atom, increasing its momentum by $h\nu_0/c$, where ν_0 is the rest frequency of the line.

Of course, this process is only effective if there is a sufficient amount of exciting or ionising radiation being received. In a static system, all the radiation at the exciting frequency will be absorbed in the lower atmosphere. However, if there is a continual acceleration on ions, there will be a spread in velocity in the wind. In the ion's frame of reference, the light from the star will then be red-shifted, thus the rest frequency required to excite the ion will be slightly different, so a greater range of wavelengths (and therefore a greater amount of energy) is available to drive the wind. In hot stars, this has the potential to accelerate a wind of over 10^{-5} $M_\odot$ yr^{-1} to a speed of over 1000 km s^{-1}, creating a characteristic blue-shift in the core of the absorption line (Fig. 1.7).

In globular clusters, we observe line-driven winds primarily in less-evolved giant stars on both the AGB and RGB (*e.g.* Dupree, Hartmann & Avrett 1984; Mészáros, Dupree & Szalai 2009). These stars are magnetically active, with a hot chromosphere surrounding the cooler stellar photosphere (as evidenced by emission in line wings, particularly Hα and Ca II; §1.3.2.4, §3).

1.3.2.2 Continuum-driven winds

Cool, luminous objects, such as the more-evolved globular cluster giants probed in this work, lack the line opacity and UV-continuum photons of hotter stars. The temperature in the upper atmosphere of these stars is low enough ($\lesssim$ 1500 K) to allow dust formation, with the volume of dust being dependant on the temperature and density of the outflow. In carbon stars, dust grains have low albedo and large cross-sectional area. They absorb a wide range of frequencies, allowing them to be efficiently accelerated merely by the photon pressure of the light in the stellar continuum.

In this environment, the dust can collisionally couple with the gas. Here, collisions between rapidly-accelerated dust and slowly-accelerated gas can further accelerate the gas to a velocity comparable to the dust (*e.g.* Lewis 1989). Winds here are much slower — canonically $\sim$10 km s^{-1}. This is partly due to the slowing of the dust through collisional coupling, but also because the comparatively heavy dust grains require more momentum to accelerate. Nevertheless, the efficiency of continuum absorption means that mass-loss rates from these kind of objects can be even higher than those of line-driven winds (see below).

This process appears to be relatively well-understood in carbon stars. In oxygen-rich stars which host silicate-based winds, however, dust grain opacities are not high enough to generate the mass-loss rates observed via radiation pressure on these grains alone (Willson 2000; Woitke 2006b; Höfner 2007). Detailed time- and frequency-dependant modelling by Höfner & Andersen (2007) suggests that small amounts of carbon-based dust can still be formed in M-type (O-rich) giants if the equilibrium

chemistry is altered by pressure waves from stellar pulsations. The carbon-rich dust can thus drive the outflow, though the dominant chemistry remains silicate-based. However, this change in chemistry may be prevented if the free carbon quickly binds to sulphur atoms in the wind (Isabelle Cherchneff, private communication). The resolution of this issue may be particularly important in metal-poor globular cluster AGB stars, where there is very little carbon available to drive the wind.

1.3.2.3 Pulsations and their effect on mass loss

Many stars exhibit pulsations. The classical example of this are variables on the Instability Strip, such as Cepheid and RR Lyrae variables, due to the κ-mechanism. This is also the primary driver of pulsations in Mira-type variables (Ulmschneider 1998).

In the κ-mechanism, the ionisation zone of a particular species is unstable. Rising temperature and/or pressure allows the ionisation of a species, producing increased opacity in the atmosphere. The insulation caused by the opaque blanket results in an expansion of the atmosphere. The atmosphere then cools, the species recombines, and the opacity is lifted. The star then looses heat and shrinks, completing the pulsation cycle.

An alternative mechanism is the stochastic excitation of harmonic oscillation modes from convective motions. This is the primary driver of pulsations in stars such as the Sun, giving rise to its 3-minute pulsation period, but may also drive pulsations in semi-regular variables (Christensen-Dalsgaard, Kjeldsen & Mattei 2001).

Bowen (1988a) put forward that mass loss might be exacerbated by pulsation: in highly-evolved stars with low surface gravity, pulsation can provide extra energy to lift mass off the star. As the gravity of these stars is low ($v_{\rm esc} \sim 50$ km s^{-1}), so are the energies required. Pulsation amplitudes of $\sim$20 km s^{-1} have been recorded for the most evolved stars in 47 Tuc, meaning that pulsation can indeed provide a significant amount of the impetus required to levitate mass from the star (Lebzelter et al. 2005).

1.3.2.4 Convective-zone and magnetically-driven winds

In magnetically-active stars, convecting material can rise through the stellar atmosphere, forming an acoustic wave. These waves can transmit energy to the surface (Pijpers & Hearn 1989), though it seems unlikely that their energy is sufficient to provide the extra 'push' to levitate material from their surface (Koninx & Pijpers 1992).

The associated magnetic pressure wave (Alfvén wave), however, can travel into the upper stellar atmosphere (the chromosphere and corona), forming a magnetic loop. Magnetic reconnections in these loops generate heat, forming a temperature inversion. The hot, charged particles that form the loops can then escape on open field lines, driving mass loss.

Our Sun is the proto-typical example of a star losing mass by a coronal wind ($\dot{M} \approx 10^{-14}$ $M_\odot$ yr^{-1}), a discussion of which can be found in Brandt (1970). This is the primary mechanism by which most solar-type stars lose mass, with the subsequent loss of angular momentum substantially slowing the rotation speed of a star over its lifetime. It continues to be a mechanism for mass loss for as long as the rate of magnetic heating dominates over the cooling of outflowing gas, *i.e.* as long as the temperature inversion is sustained. This ratio of heating to cooling controls the existence and extent of the chromosphere and (if the ratio is high enough) a corona[8].

Chromospheric activity continues to dominate mass loss as a star evolves onto the giant branch. Here, it appears to provide the initial energy required to lift material from the stellar surface before line-driving becomes the dominant accelerative mechanism, further from the star. Observationally, chromospheres manifest themselves as 'wings' of emission seen on spectral lines, notably Hα, the calcium H and K lines (Deutsch 1970) and the rotational-vibrational transitions of CO (Heasley & Milkey 1976). These are caused by stimulated emission in the chromosphere and corona. The He I line, at

[8]The transition from chromosphere to corona is complicated, depending on several unrelated phenomena, including the dominance of magnetic forces, the ionisation of particular species and spectral line opacity. In this thesis, I will generically refer to observations as being of the stellar chromospheres, as the conditions for the existence of a corona are generally not met in the observations in this work — all the stars we investigate are above the canonical Haisch dividing line (Linsky & Haisch 1979).

1.083 μm, may also be present, but emission in this line requires a hot chromosphere $T \gtrsim 15000$ K.

Such activity has been observed in field giants for several decades (see review of Stencel 1981): Deutsch (1967) found that variability of α Tau and γ Aql was due to variable chromospheric activity and that this was heterogeneous among red giant stars for a given spectral type (Deutsch 1970). Lambert & Snell (1975) suggested that some of the infra-red excesses of cool giant stars (specifically Betelgeuse (α Ori) and W Hya) could be due to a chromosphere. In the specific case of Betelgeuse, heating and mass loss via pulsation shocks may also play a rôle (Newell & Hjellming 1982; Hebden, Eckart & Hege 1987; Cuntz 1992, 1997; Cuntz, Harper & Bennett 2001).

In more evolved giants, increased mass loss and decreased power in the ageing magnetic dynamo means that the temperature inversion caused by magnetic heating weakens (Wood 2004; Vlemmings, Diamond & Langevelde 2005). While a modest temperature inversion may still exist, the Hα emission observed is mostly due to photon scattering in the cooling, expanding, optically-thin circumstellar shell (Cohen 1976). Using the emission, a mass-loss rate can be calculated (Mallia & Pagel 1978; Cacciari & Freeman 1983; Gratton, Pilachowski & Sneden 1984; §3), though such theories have historically over-estimated the terminal velocities involved due to the complexities of modelling the superimposed photospheric absorption and chromospheric emission lines.

Dupree, Hartmann & Avrett (1984), investigating chromospheres in globular clusters, proved that the Hα emission could come from a static chromosphere, although an expanding chromosphere is needed to produce the asymmetries seen in the absorption line core (Fig. 1.7). Correlations have been made between UV (coronal) activity and rotation rates, photospheric temperature, stellar mass[9], and lithium abundance (though not metallicity as a whole); and an anti-correlation between activity and age, and activity and polarisation (molecular formation) (Dyck & Johnson 1969; Gray 1983;

[9]This is thought to hide several other relations (Pasquini, Brocato & Pallavicini 1990; Pasquini & Brocato 1992).

Cacciari & Freeman 1983; Steiman-Cameron, Johnson & Honeycutt 1985; Rutten & Pylyser 1988; Simon & Drake 1989; Pasquini, Brocato & Pallavicini 1990; Fekel & Balachandran 1994; Cuntz & Ulmschneider 1994; Dupree et al. 1994; Konstantinova-Antova 2001). It is therefore surprising that chromospheric activity increases along the red giant branch (Dupree, Hartmann & Smith 1990), given rotation rate, temperature and mass all decrease, while age increases.

Judge & Stencel (1991) also list some interesting results: warm (chromospheric) gas appears in dust-enshrouded stars, which appear to show similar mass-loss rates to dust-free stars; chromospheric heating is independent of a star's previous evolution and depends only on its current position in the H-R diagram; and there is no correlation between dust optical depth and computed mass loss. They also confirm that wind velocities are less than escape velocities (meaning an extra driving mechanism once material has been levitated from the star) and that velocities reach a minimum around spectral type M4.

This strongly suggests that at warmer temperatures, chromospheric mass-loss[10] dominates the mass loss budget; while at cooler temperatures, continuum-driving and pulsations are more important, masking the chromosphere's signature. This has also been observed by Eaton, Johnson & Cadmus (1990). The finding may be related to the period of the waves: short-period waves generate heating, while long-period waves are more efficient at driving mass loss (Judge & Stencel 1991).

Judge & Stencel (1991) further suggest that dust-to-gas coupling (see §1.3.2.1) is not necessarily very strong in chromospherically-active stars. They suggest mass-loss rates are determined by the stellar environment — specifically surface gravity — rather than the wind-driving process and dust-formation rate, and that mass loss occurs most likely due to acoustic wave dissipation, in contradiction to Koninx & Pijpers (1992). The dust formation process under chromospheric conditions is discussed in Beck et al.

[10] *i.e.* a wind accelerated from the chromospheric region through magnetic or acoustic effects, as opposed to a dust-driven wind, accelerated at a much greater radius.

(1992).

The M4 transition is investigated in Judge et al. (1993), who investigate three M4–M6 (P = 46–90 days) stars and find magnesium and calcium emission wings in all stars which appear to be chromospheric, not pulsation-shock induced, in nature. Their evidence (also Dupree et al. 1994) suggests that the chromospheres are steady, that pulsation-induced disturbances pass through them but do not disrupt them, and that there is little evidence of local (as opposed to global) heating.

With reference to this last point, modelling heating in giant star chromospheres has met with little success. Standard, solar-type models fail to reproduce observations, and some 'non-classical' effect (departure from hydrostatic equilibrium, shocks, inhomogeneities, unusual velocity fields) is required to explain them (Johnson, Luttermoser & Eaton 1994). The most modern studies (Cacciari et al. 2004; Mauas, Cacciari & Pasquini 2006) reproduce those of Dupree, Hartmann & Smith (1990) and Dupree, Hartmann & Avrett (1984) and find most stars, particularly near the RGB tip, exhibit chromospheric signatures, but with the need for an expanding chromosphere. Mauas et al.'s data suggest mass-loss rates of around 10^{-9} $M_\odot$ yr^{-1}, in correspondence with other estimates.

1.3.3 The effect of binarity and encounters

Binarity can also play a rôle in mass loss from stars. A review of binary stars and their effect on each other can be found in Hilditch (2001). This is particularly important in very tightly-bound ('hard') binaries, where the two stars are close together. Despite preferential retention (or even hardening) of these binaries in globulars, due to three-body encounters, many of these effects are not thought to be as significant in globular clusters: the binary fraction — some ∼50% in the field — is only a few percent in globulars (*e.g.* Davis et al. 2008).

In close binary systems, Roche Lobe Overflow (RLOF) leading to mass transfer between stars can dramatically affect the evolution of both stars. RLOF occurs when

an (initially separated) binary system evolves and its component stars expand. One star can then overflow the L_1 Lagrangian point between the two stars and mass can spill from one star onto the other.

A binary of nearly equal mass can evolve into a common envelope phase, where both stars expand to overflow the L_1 point. This is termed a contact binary. The stellar cores may then merge into a single star, which should exhibit unusual chemical signatures. This has been suggested as a mechanism for forming so-called 'blue stragglers' in globular clusters (*e.g.* Lanzoni et al. 2007; Sollima et al. 2008).

Additionally, binary systems hold a lot of a globular cluster's kinetic energy: encounters between binaries and single stars can lead to disruption of the binary system or ejection of the intervening body. There is possible observational evidence for these encounters (Dubath, Meylan & Mayor 1991; Meylan, Dubath & Mayor 1991), which are also an important source of 'heating' in the core bounce scenario described in §1.2.2.3.

Stellar encounters, although not true binary stars, are also important, as mass can be tidally stripped from a star passing very close to another, especially in a star with an extended atmosphere. Stellar collisions, while rare, also have the possibility to merge stars together. This has been suggested as an alternative method for forming blue stragglers, as the dense stellar environment found in globular clusters increases the potential for collisions to occur (*e.g.* Lombardi, Rasio & Shapiro 1996). Encounters with red giants can also spin up the red giant envelope to trigger rotational mixing and lead to mass transfer onto the passing MS star, leading to chemical peculiarities on the recipient (Yamada, Okazaki & Fujimoto 2008). Actual stellar collisions may also provide enough kinetic energy to remove material from within the cluster (Umbreit, Chatterjee & Rasio 2008).

1.3.4 Mass loss and stellar evolution

1.3.4.1 Introduction and methodology

Stellar evolution has thus far been described in a rather *ad hoc* fashion. Nevertheless, the evolutionary point at which a star is one of the main determinants of its mass-loss rate. Stellar evolution is perhaps best visualised on a Hertzsprung-Russell (H-R) or a colour-magnitude diagram. Figs. 1.8 & 1.9 show the evolutionary path of a typical, 0.85 solar-mass Galactic globular cluster giant branch star, which we will follow in this section. A review of the evolution of similar stars can be found in Habing & Olofsson (2003) and on-line[11].

1.3.4.2 Zero-age main sequence to the turn-off point

Despite the advanced age of most Galactic globular clusters, the vast proportion of their stars lie on the Main Sequence. Our example star will have taken ∼50 Myr to reach the Main Sequence, on which it spends most of its life.

Less massive stars spend longer in this phase of their lives, which is where we find them still today. Due to the stellar initial mass function (IMF), there will initially have been many more stars of low mass in the cluster. However, the present-day mass function of a globular cluster may be considerably different, due to mass segregation and tidal stripping (§1.2.2.3; Sollima, Ferraro & Bellazzini 2007).

The Main Sequence life of a star is characterised by hydrogen 'burning' via nuclear fusion in the stellar core. In our low-mass star, this takes place exclusively through the p-p chain, fusing hydrogen into helium. Chemically, the outer layers of the star will remain unchanged, as the convective zone does not extend down into the stellar core. Observationally, the stars will thus retain their primordial proportions of hydrogen, helium and most other elements.

While on the Main Sequence, the increase in molecular weight will cause the core

[11] *e.g.* http://www.maths.monash.edu.au/ johnl/StellarEvolnDemo/

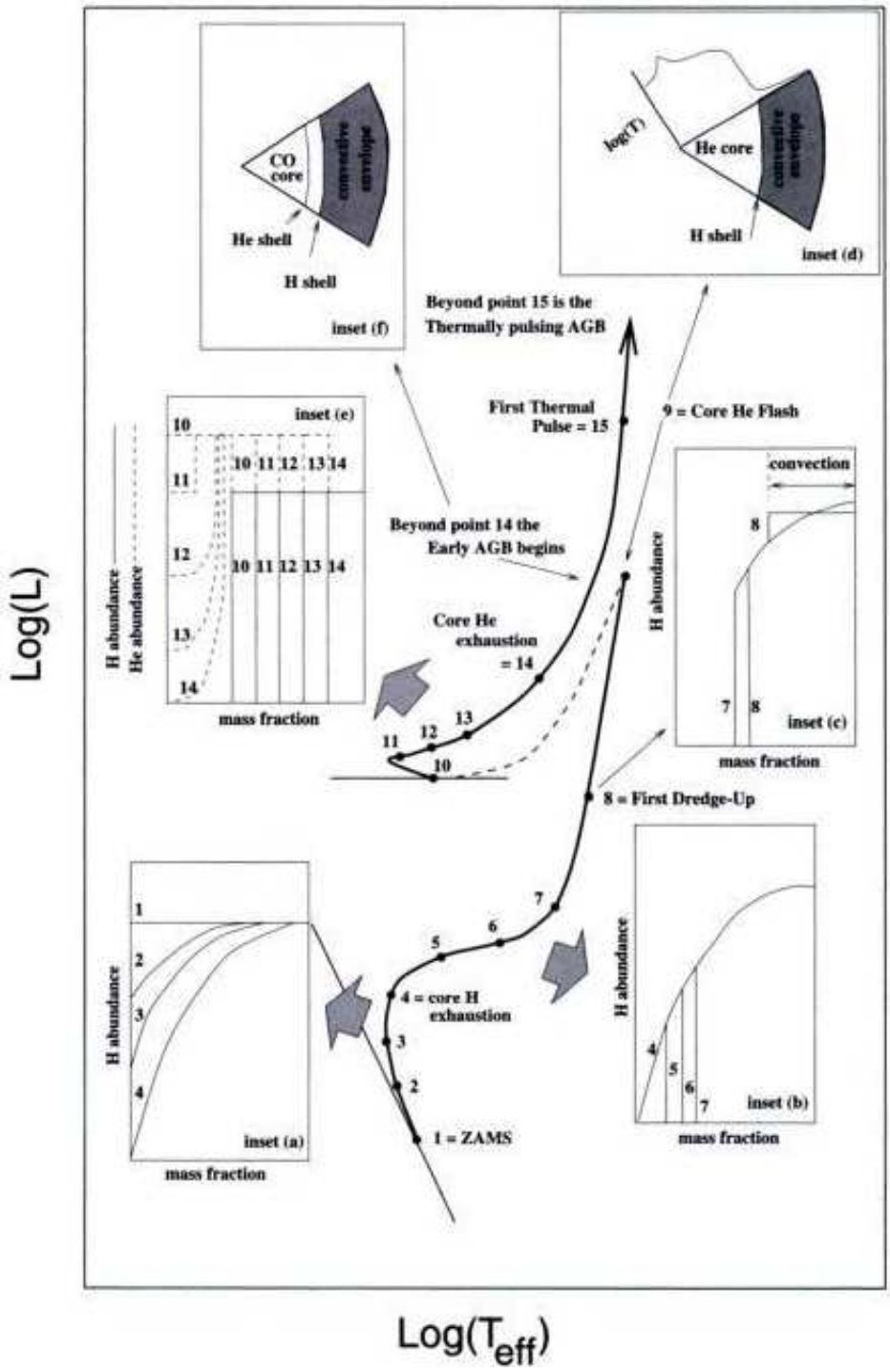

Figure 1.8: Schematic evolution on a Hertzsprung-Russell diagram of a solar-type star, originally from Habing & Olofsson (2003).

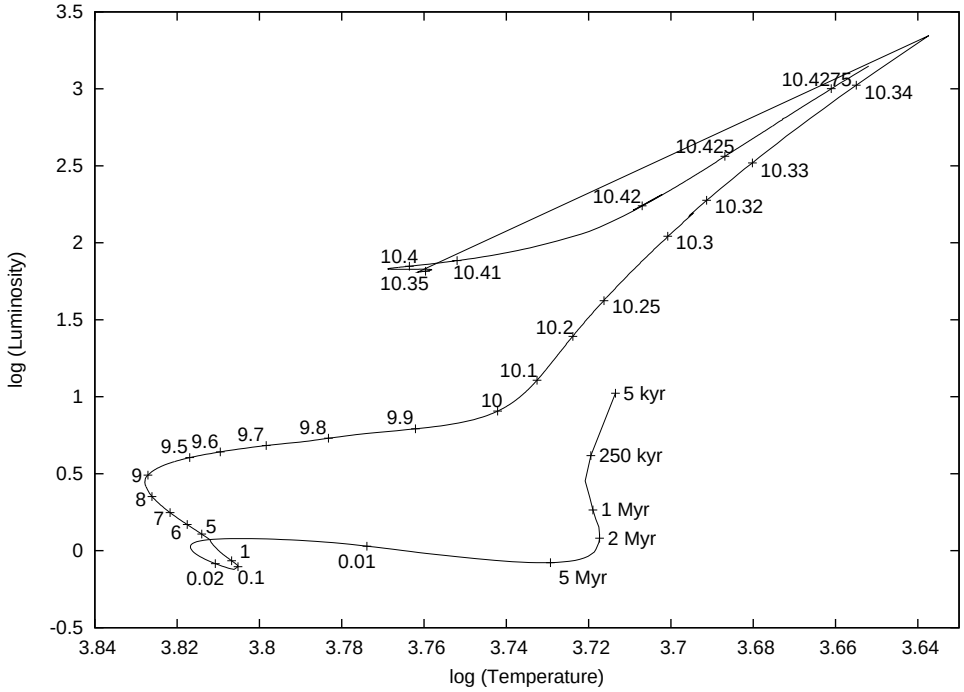

Figure 1.9: Calculated evolution on a Hertzsprung-Russell diagram of a 0.85 $M_\odot$ star with [Z/H] = −2, using data from Castellani et al. (2003) and Cariulo, Castellani & degl'Innocenti (2004), labelled with time since formation (in gigayears, unless otherwise stated). The evolutionary process is discussed in detail in the text.

density and temperature to rise. The star becomes slightly more luminous, causing its outer envelope to expand and cool slightly. For our example, this occurs towards age of ∼9 Gyr (point 4 in Fig. 1.8), and the position in the H-R diagram is referred to as the *turn-off point*. This turn-off point is a key feature for determining the age of a cluster.

Mass loss on the Main Sequence is usually through a coronal wind (see §1.3.2.4). Thus, each globular cluster star can expect to lose $\lesssim 10^{-14}$ $M_\odot$ yr^{-1}, or ∼0.03% of its mass, throughout its Main Sequence life.

1.3.4.3 Turn-off point to the red giant branch

Eventually, the fusion process in the core becomes choked by helium 'ash'. The core then contracts and heats up. This hotter, denser environment allows hydrogen burning to take place in a shell surrounding the core. The increased radiation from the core

can no longer be lost through the radiative atmosphere. This provokes a thermal expansion of the stellar atmosphere and a cooling of the surface. This decrease of effective temperature (points 5 to 7 in Fig. 1.8) is termed the *Hertzsprung Gap* due to its short timescale. In old clusters, this is somewhat of a misnomer, as crossing the gap (for our example star) takes the better part of a gigayear, since the p-p chain reaction is less temperature sensitive.

Once the stellar core has reached the pressure at which the helium becomes degenerate, the core ceases contracting and tries to cool radiatively, while a hydrogen-burning shell source continues to provide an increasing amount of luminosity for the star. The star then becomes a *Red Giant Branch* (RGB) star (points 7 to 9 in Fig. 1.8). In our example, this state sustains the star for another few hundred megayears.

A transition occurs during this phase, which is important to chemical analysis of RGB and more evolved stars. As the envelope expands and cools, its opacity increases. Convection then dominates over radiation as the dominant energy transport source, and the convective zone moves towards the core, encroaching on the region where hydrogen-burning has been occurring. The by-products of this burning (primarily helium in lower mass stars) are brought to the surface, increasing their fractional content in the stellar atmosphere. This stage is known as the *first dredge-up*.

An evolutionary curio during this phase is the presence of gaps in the H-R diagram — regions where there are no stars of a given temperature and luminosity. First noted in the giant branches of M15 by Sandage, Katem & Kristian (1968), these soon became identified in other clusters: 47 Tuc and M3 (Sandage 1971), M15 (Sandage, Katem & Kristian 1968), M5 (Simoda & Tanikawa 1970) and NGC 6752 (Cannon & Stobie 1973). Gaps in the sub-giant (Demarque & Armandroff 1984) and horizontal (Newell & Graham 1976; Bono, Fulle & Pulone 1990; Catelan et al. 1998) branches were also found. A definitive explanation has yet to be found, but theories include changes in chemistry due to mixing (Armandroff & Demarque 1984), changes in rotation periods (Behr et al. 2000), some other surface change, or as a result of merely stochastic effects.

In the late stages of RGB evolution towards the *RGB tip* (Fig. 1.8 point 9), stars undergo pulsations (§1.3.2.3). This change in the wind-driving mechanism (§1.3.2.4) apparently increases the mass-loss rate to typically 10^{-7} to 10^{-6} $M_{\odot}$ yr^{-1} (Origlia et al. 2002), leading to dust shells occurring around roughly 15% of RGB-tip stars (Origlia et al. 2002) and possibly creating the afore-mentioned gaps (Soker et al. 2001).

1.3.4.4 RGB tip and helium flash

In stars above $\sim$0.5 $M_{\odot}$, the core temperature reaches a critical point ($\sim 10^8$ K). The pressure and temperature in the degenerate helium gas become sufficient to ignite helium fusion via the triple-α process. In sub-solar-mass stars, this process spreads throughout the core within minutes (Seeds 2004) and is referred to as a 'helium flash'.

This sudden onset of helium burning in the stellar core causes an instantaneous (in evolutionary terms) expansion of the core. The core expansion also drives the hydrogen shell source outwards, making it far less efficient. Core helium-burning does not produce as much energy as the hydrogen shell, so the stellar luminosity drops, and the stellar atmosphere contracts. The star thus becomes hotter and bluer.

The star's evolution now becomes somewhat chaotic, and it takes a further two megayears or so (Sweigart 1994; Fig. 1.10) to stabilise. During this time, subsequent smaller flashes episodically promote convective pulses which disrupt hydrogen burning, while gradually lifting degeneracy from the remainder of the core.

The luminosity of the star now depends almost entirely on the mass of the helium core, though the effective temperature depends heavily on its mantle mass, which is determined by the star's initial mass and mass-loss history. While evidence exists that the mass-loss rates in RGB stars vary with initial metallicity, these effects are thought to be small (van Loon 2000a; 2006; van Loon et al. 2007). In general, metal-poor stars are from older systems, have less mantle mass, and thus become much bluer than metal-rich ones, and the terminology used for the two reflects this: metal-poor stars tend to lie on the *Horizontal Branch* (HB — Fig. 1.8 point 10), while metal-rich stars

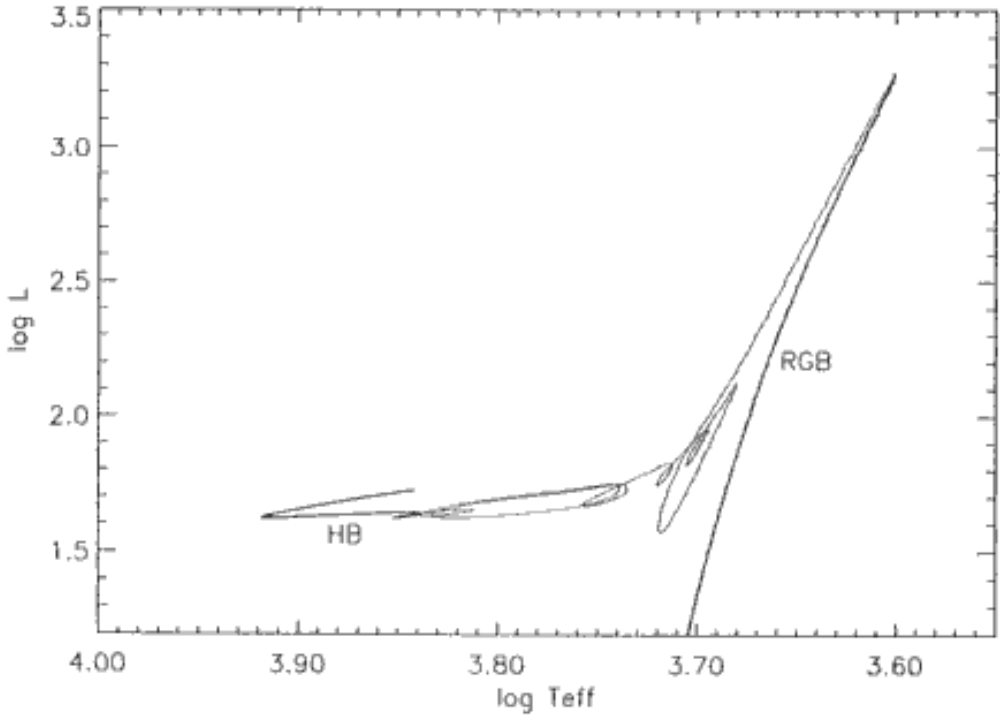

Figure 1.10: Illustration from Sweigart (1994), showing the evolutionary path through the helium flashes (see §1.3.4.4) not detailed in Fig. 1.8. Each of the loops is caused by a subsequent small flash.

lie in the *Red (Giant) Clump*. The HB itself was highlighted by Baade (1944) and is a peculiarity of old stellar systems: its shape may detail mass loss on the RGB and is a powerful tracer of both the cluster's mass-loss history and chemical peculiarities (§1.2.2.7).

Extended horizontal branches are found in ∼25% of clusters. These could be due to a He-enhanced second-generation sub-population, or stars exhibiting greater mass loss. These tend to be associated with the more massive clusters: *e.g.* ω Cen, NGC 6388 and M15 (Lee, Gim & Dinescu 2007).

Also noteworthy are "hot (He-)flashers": stars with high mass-loss rates that appear to leave the RGB early and settle towards the white-dwarf cooling track. Stars with too low a core mass to undergo the helium flash ("flash-manqué" stars) will stay on this track to become under-massive helium white dwarfs; whereas stars with sufficiently large helium core masses but very small mantle masses will undergo a helium flash at

much higher temperatures. They are now termed "blue hook" stars and become part of the *Extreme Horizontal Branch* (EHB). They will subsequently evolve to become "AGB-manqué stars" (Castellani & Castellani 1993; d'Cruz et al. 1996), as they do not reach the AGB (§1.3.4.6).

1.3.4.5 Horizontal branch evolution

Our globular cluster star now lies on the HB, with a helium-burning core and a hydrogen-burning shell source. The stellar core now undergoes a process known as *semi-convection*, the physics behind which is not relevant here. As a result, the stellar interior becomes composed of a convective core underlying a series of convective layers, separated by sharp boundaries. Convective mixing across these boundaries depends on the ratio of molecular to temperature diffusion. Descriptions of semi-convection can be found in Castellani, Giannone & Renzini (1970) and Spruit (1992).

Convective mixing sustains the helium fraction in the core, which is becoming carbon-oxygen rich. As the core helium is exhausted, the size of the convective core may increase in *core breathing pulses* (Sweigart & Demarque 1972, 1973; Castellani et al. 1985; Sweigart 1990; and references therein). Despite this possible pulsation, mass loss on the HB is much lower than near the RGB tip, at a rate of less than 10^{-9} $M_\odot$ yr^{-1} (Koopmann et al. 1994).

1.3.4.6 Early asymptotic giant branch evolution

After around 60—70 Myr on the HB (depending on its mass-loss history), our star's core helium is depleted to the point that core helium fusion cannot take place. The fusion site now moves out into a shell source. At this point (Fig. 1.8, point 14, inset f), the active star consists of a degenerate carbon-oxygen rich core, on top of which is a helium-burning shell, followed by a helium-rich radiative zone, and a hydrogen-burning shell. Lying on top of this is a thin radiative zone and a deep convective atmosphere, the latter of which will grow to a significant fraction of an AU across. The star is then

termed to be on the *(Early) Asymptotic Giant Branch* or (E−)AGB, so called because it approaches its previous track up the RGB asymptotically on the H-R diagram.

The helium shell produces a considerable amount of energy, causing the star to expand and cool. In more massive stars than our example, there can be a *second dredge-up* of material as the larger convective zone moves deeper into the star. The extended atmosphere and previous mass loss lead to a much lower surface gravity, making mass loss more efficient. However, mass-loss on the E-AGB is still likely to lie at $\sim 10^{-8}$ $M_{\odot}$ yr^{-1} or less (Wood, Bessell & Fox 1983; Wood et al. 1992).

1.3.4.7 Thermal pulses

Advance up the AGB is rapid, with the entire phase lasting only a few megayears. Here, the outward-moving shell sources exist in very close proximity to each other. As the triple-α hydrogen-burning process is highly temperature-dependant, this proximity causes the output of the helium shell to become locally and periodically unstable, leading to a dramatic increase in luminosity by a factor of up to 10^4 for ∼100 years, every few 10^5 years, leading to the term *thermal pulse* (Schwarzschild & Härm 1965; Weigert 1965; Blöcker 2001). The change in radiative output causes the thermal expansion and subsequent contraction of the envelope, resulting in the disruption of the hydrogen shell. The stellar luminosity does not change so drastically at first, but grows with subsequent pulses as the system becomes more unstable and the time between pulses decreases. The increase in luminosity during a thermal pulse should increase the mass-loss rate by a small factor, leading to the production of a cooling stellar shell (*e.g.* Wachter et al. 2008). The start of thermal pulsation marks a star's inception into the *thermally-pulsating AGB* (TP-AGB) (Fig. 1.8, point 15).

During the pulse event, convection can extend down into the *inter-shell region* between the H- and He-burning shells, allowing mixing to take place and a *third* dredge-up of heavy elements from the core to the surface. In more-massive stars (around 4—5 $M_{\odot}$ at solar metallicity and 2 $M_{\odot}$ at Z = 0) the process of hot bottom burning (HBB)

can occur. Here, fusion continues in the bottom of the convective envelope, resulting in an incomplete CNO cycle, thus burning of carbon to produce mostly nitrogen.

The third dredge-up phase lasts several decades, and can result in unusual surface abundances, particularly of lithium. Sufficient dredge-up may result in an over-abundance of carbon at the surface (unless HBB occurs), leading to an increased C/O ratio and hence the production of a *carbon star*, from which carbon-rich dust is produced. This dredge-up process means that, even in initially very metal-poor stars, the stellar wind contains metal ions. Note that, although carbon stars are formed in globular clusters, third dredge-up may not be particularly effective at low stellar masses ($\lesssim$1 $M_{\odot}$; van Loon et al. 2007). In less-massive stars, cool bottom burning (CBB) may be driven by a magnetic dynamo (Nordhaus et al. 2008).

TP-AGB stars are also very important for producing slow-neutron-capture (*s*-process) elements in the inter-shell region. The *s*-process creates about half the elements heavier than iron, as far as lead. The neutrons are liberated mainly by fusion of α particles with ^{13}C, or with ^{22}Ne during thermal pulses.

These neutrons are captured by iron 'seed' nuclei to assist the production of progressively heavier nuclei (Straniero, Gallino & Cristallo 2006; Bonačić Marinović et al. 2007). Over-abundances of *s*-process elements (*e.g* barium) in the stellar atmosphere can be taken as evidence of third dredge-up, or of 'pollution' by external sources.

1.3.4.8 Pulsation and mass loss

The star is also unstable to pulsation on shorter timescales (Fig. 1.5, §1.3.2.3). These increase in violence and regularity as the star evolves, with variations of several magnitudes in the visual being normal[12]. Their periods also increase, from a few weeks at the start of the AGB to a few years at the AGB tip, and in doing so the pulsations tend to become more stable.

[12]Stars with variations over 2.5 mag are termed *Miras*, after the proto-type star *o* Ceti.

The increase in pulsation period is well-correlated with the stellar luminosity. The pulsation period can lie on one of several harmonically-related period-luminosity relations (Menzies & Whitelock 1985). Recent work has focussed on cataloguing and understanding these relations (*e.g.* Menzies & Whitelock 1985; Wood et al. 1999; Wood 2000; Ita et al. 2004; Soszyński et al. 2004; Fraser et al. 2005; Derekas et al. 2006; Soszyński 2009). Fig. 1.11 shows these sequences for the LMC. Sequence C probably defines the fundamental mode of oscillation (Lebzelter & Wood 2005). Interestingly, there seems to be little or no relationship with metallicity (Whitelock, Feast & van Leeuwen 2008).

The origin of the long secondary periods (LSPs) in sequences D and E are not fully understood, though pulsation is likely to play a rôle (Hinkle et al. 2002; Munari et al. 2008). However, suggestions have been put forward that these are due to binary companions, possible matter accretion, non-radial pulsations, dust ejection and rotation scenarios (Wood, Olivier & Kawaler 2004; Soszyński et al. 2004; Derekas et al. 2006; Soszyński 2007). LSPs may also correlate with chromospheric activity and mass-loss rate (Wood, Olivier & Kawaler 2004). It has also been suggested that mass-loss rate and the loss of pulsation energy in the wind can affect the pulsation mode and/or its regularity (Pijpers 1993).

1.3.4.9 Stellar death and planetary nebulae

The mass-loss rates from low-mass AGB stars can reach 10^{-5} $M_{\odot}$ yr^{-1} as they approach the AGB tip (Wood et al. 1992), with a surprising range of complex molecules created in the wind (*e.g.* Agúndez et al. 2008). Naturally, a star cannot maintain this mass-loss rate for very long before its mantle evaporates. It is thought that, for solar-type stars, the TP-AGB lasts around 1–2 $\times 10^5$ years (Willson 2007).

The total mass lost on the AGB is considerable. During the final few pulse cycles, lasting $\sim 10^5$ yr (Tanabé et al. 1997), the stellar wind becomes strong enough to eject almost the entire convective hydrogen envelope from the star. This phase is known as

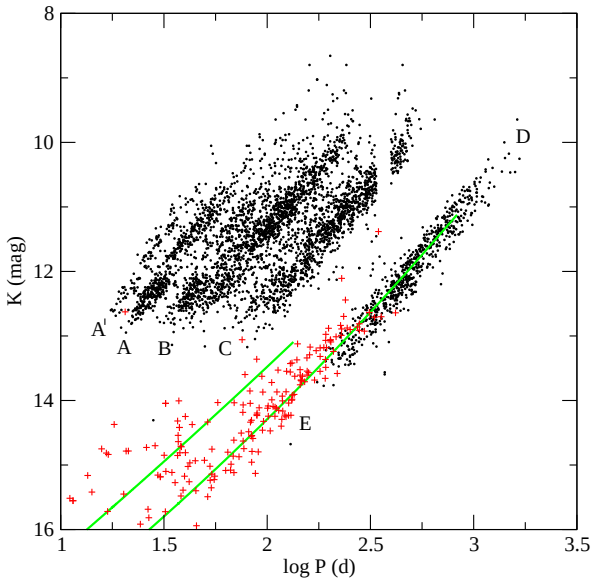

Figure 1.11: A period-luminosity (P-L) diagram for the LMC from Derekas et al. (2006), showing the different sequences which RGB/AGB stars tend to pulsate on. The gap at $\log(P) \approx 2.5$ is where stars have been removed to avoid confusion with the annual orbit of the Earth.

a *superwind*. The remainder of the atmosphere is then devoured by the hydrogen shell. The rate of this burning governs how long the star remains in this *post-AGB* phase, though typical timescales are $\sim 10^4$ yr (Hony 2002). Here, the ejected atmosphere moves away from the stellar core and disperses and cools. Once the shell has been completely burnt off, mass loss stops. Observationally, the stellar spectrum splits into two distinct components — a UV-bright central source and an IR-bright dust cloud. The stellar core is revealed as the atmosphere thins and becomes more transparent. The radiation ionises the ejected shell, which then re-emits in the optical, producing a *planetary nebula* (PN). The central object of the PN has now become a zero-age *white dwarf* (WD) and gradually cools down the white dwarf cooling track.

1.3.4.10 Total mass lost

The mass lost a given star can be considerable: a 0.8 $M_\odot$ star will typically lose 0.2 $M_\odot$ on the RGB (Schatzman, Praderie & King 1993), then 0.1 $M_\odot$ on the AGB (Chiosi

1998), leaving a 0.5 $M_\odot$ white dwarf. The remnant mass varies only weakly with initial mass: it reaches 1.4 $M_\odot$ by ∼9 $M_\odot$, meaning such stars lose ∼85% of their mass (Kalirai et al. 2008). The lost mass thus represents a significant proportion of the mass of the star, thus we naïvely expect to find a significant amount of gas and dust within the cluster.

To take a crude example, Guhathakurta et al. (1998) find that the 8×10^4 $M_\odot$, post-core collapse cluster M30 (NGC 7099) contains 1260 post-main-sequence stars, 713 of which are faint RGB stars, 98 of which are bright RGB/AGB stars, 98 of which are HB stars and 48 of which are blue stragglers[13] (Scarpa et al. 2007). Mass-loss rates from MS stars are unlikely to contribute more than 10^{-8} $M_\odot$ yr^{-1} to the ISM in total, the fainter RGB stars should contribute $\sim 10^{-5}$ $M_\odot$ yr^{-1} in total, the HB stars $\sim 10^{-7}$ $M_\odot$ yr^{-1} and the remaining bright RGB/AGB stars (excluding the brightest stars near the AGB tip) $\sim 10^{-6}$ $M_\odot$ yr^{-1} as well. The few TP-AGB objects that Guhathakurta et al. (1998) do not distinguish from the sample will contribute most to the mass loss, each producing up to 10^{-6} $M_\odot$ yr^{-1} per star.

The mass-loss rate from a cluster is therefore largely a function of the number of TP-AGB stars present, which usually number only a few. This means that the total mass loss from the cluster is likely to be $10^{-6} \sim 10^{-5}$ $M_\odot$ yr^{-1}, or $10^2 \sim 10^3$ $M_\odot$ between plane crossings. Cluster masses tend to be between $10^4 \sim 10^6$ $M_\odot$. Assuming the cleaning process is 100% efficient in removing gas and dust from the cluster, and in the absence of other methods of mass removal (discussed later) we expect to find $10 \sim 10^4$ $M_\odot$ of gas and dust in most of the massive clusters at any one time.

1.3.5 Variations in mass-loss rates

In analysing observations and in simulating mass-losing stars, a certain number of assumptions have to be made. Fully-descriptive models have quantities that are im-

[13]These should theoretically have mass-loss rates similar to that of main sequence stars

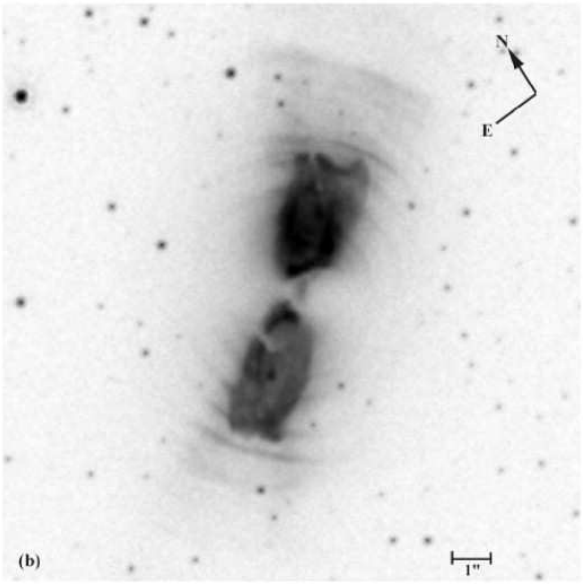

Figure 1.12: HST image from Kemper et al. (2003), showing scattered light from shells excerted from the evolved AGB star IRAS 17150–3224.

measurable, unknown, or would be too computer-intensive to feasibly run.

Perhaps the two most important standard assumptions are that the wind is spherically symmetric and temporally constant, which for pulsating AGB stars is certainly not observed (*e.g.* Decin et al. 2008). Modern modelling codes have recently started to include 3-D, time-dependant models, but analysis of observations currently lags behind.

1.3.5.1 Temporal variations

Temporal variations in mass loss show up in many nearby stars. Fig. 1.12 shows shells of lost mass surrounding the star IRAS 17150–3224. Kemper et al. (2003) measure the timescale between these shells to be 200–1000 years using reasonable distance and outflow velocity estimates. Similar values of several hundred to 2000 years have been found in other sources, notably IRC+10216 Mauron & Huggins (1999) and the Egg Nebula (CRL 2688) (Sahai et al. 1998). Observations also show the absence of warm dust around a number of AGB stars, which corresponds to a drop in mass loss ∼100 years before the observation. This backs up the hypothesis of episodic mass loss with a

timescale of hundreds of years — a timescale too long to attribute to radial pulsation and too short to be linked to thermal pulses.

Simis, Icke & Dominik (2001) suggest that these shells result from a partial or complete decoupling of the gas from the dust, giving rise to density enhancements with periods of 200–400 years, depending on the amount of decoupling. This has obvious implications for globular cluster AGB stars, where low metallicity means a higher gas-to-dust ratio, hence insufficient dust to drive a collisionally-coupled medium.

In globular cluster giants such pristine shells as in Fig. 1.12 may be disrupted by stellar encounters. Using the above values, the distance between shells around the above three stars is ~ 0.01 pc — similar to the typical separations for stars in globular cluster cores, although this value increases towards the periphery of the cluster.

1.3.5.2 Spatial variations

The spherical symmetry of the outflow can be modified by several processes, including convection, pulsation, rotation, magnetic fields, binarity and stellar encounters.

Convection in the stellar atmosphere can provide impetus for material to leave the star, particularly when coupled with a magnetic field. This can be observed in chromospheric mass loss (§1.3.2.4), but may also play a part in lifting material from the star during the TP-AGB. Here, convection (and possibly pulsation overtones) lead to *macroturbulence* and *microturbulence*[14] (Townsend 2007). Observationally, mass-loss rate indeed appears to be correlated with macroturbulence (Hagen, Stencel & Dickinson 1983), while the first observations are now coming through of clumping in AGB star atmospheres: IOTA measurements (Ragland et al. 2006) show that 29% of resolvable AGB stars show asymmetries in the H-band. Many planetary nebulae (PNe) are also bipolar in shape and have clumped structure, suggesting instabilities in AGB outflow can lead to a clumpy structure in the wind after only a few stellar radii (Woitke

[14]Observed in spectral lines, the difference between the two is merely the scale: macroturbulence being longer than the photon mean free path.

2006a).

The rotation of AGB stars is slow ($v_{\rm rot} \approx 1$–2 km s^{-1}), and small compared to the star's escape velocity ($\sim$50 km s^{-1}). However, it is a significant fraction of the $\sim$few km s^{-1} wind velocity and may provide enough energy to enhance equatorial mass loss. Dorfi & Höfner (1996) have shown that, for a slightly more massive star of 10^4 L$_\odot$ and $v_{\rm rot} = 1.7$ km s^{-1}, the mass loss from the equatorial and polar winds can differ by a factor of 1.3. In a "fast" rotator with $v_{\rm rot} = 6.9$ km s^{-1} this ratio can exceed 25.

Such a system can be produced from absorption of a binary component by the expanding stellar envelope (see also §1.3.3). Han, Podsiadlowski & Eggleton (1995) model that 30–40% of field AGB stars should have close enough companions to form such a merger, though it is not clear how this translates to globular clusters.

1.4 Dust

"We come spinning out of nothingness, scattering stars like dust"

— Jalal ad-Din Rumi, Persian Poet & Mystic (1207–1273).

1.4.1 History of dust research

Interstellar dust, which forms part of the ISM, has been observed for millennia. As far back as ancient Australian Aboriginal mythology, names such as 'the Emu' were given to the dark dust lanes in the Milky Way. Although Herschel noted the presence of a number of dark nebulae, his interest extended only as far as identifying the bright nebulae that often accompanied them (Marengo 2000), and it was only near the turn of the 20th Century that Edward Emerson Barnard started imaging these dark regions (Barnard 1919). Edwin Hubble's galaxy counts (Hubble 1926, 1934) and Robert Trumpler's extinction measurements (Trumpler 1940) then allowed the extent and depth of these obscuring clouds to be determined.

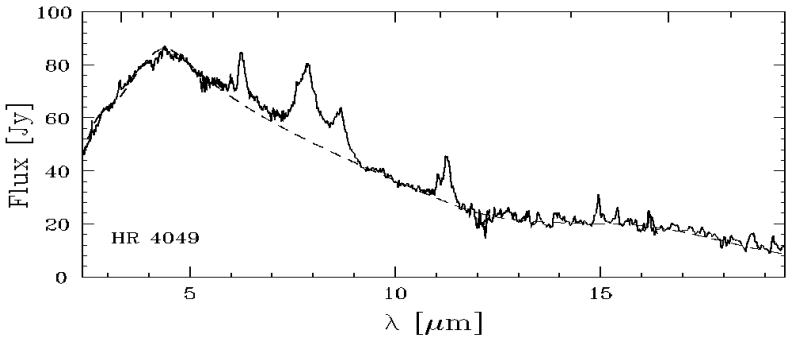

Figure 1.13: A spectrum of polycyclic aromatic hydrocarbons (PAHs) in the post-AGB star HR4049, reproduced from Beintema et al. (1996).

The composition of dust and its origins were surmised only relatively recently. Hoyle & Wickramasinghe (1969) compared extinction measurements with materials created in the laboratory, and found the dust in the ISM to be "*a mixture of graphite particles formed in carbon stars and of silicates in oxygen-rich giants.*" More recent discoveries in the field have not changed this statement: Gehrz (1989) estimates that 20% of interstellar dust comes from carbon stars and 35% from Miras, the majority of the rest coming from the more-massive, yet similarly-evolved radio-luminous stars (32%), M supergiants (4%) and supernovae (8%). Similarly, Sedlmayr (1994) estimates that 73% of Galactic dust is formed in TP-AGB stars, with 2.5% in other AGB stars and 7% in RGB stars, the remainder being formed primarily in (super-)novae.

1.4.2 Dust formation

The last few decades have seen major development in the field of complex interstellar chemistry. In particular, this is thanks to space-borne infra-red telescopes that can observe throughout the infra-red spectrum without the mitigating effect of obscuring water bands in the Earth's atmosphere. Peculiar spectral features were seen at 3–11 μm around a variety of objects — including post-AGB stars (Fig. 1.13) and PNe — leading Duley & Williams (1981) to suggest that they are caused by thermal excitation of polycyclic aromatic hydrocarbons (PAHs) or similar molecules. Earth science studies

on pollution show that PAHs are important in forming carbon particulates (Bittner & Howard 1981; Frenklach et al. 1984), and by inference they are thought of as likely 'seeds' around which astrophysical dust grains can grow. However, PAHs are typically not seen in environments with metallicities below [O/H] $\sim$ –0.6 (Engelbracht et al. 2005). In these conditions, silicate-rich dust tends to form around aluminium oxide (Al_2O_3) and titanium oxide (TiO) seeds. The process here, and in low-metallicity carbon-rich stars, is generally understood less well (Heras & Hony 2005).

The process of dust grain formation can be thought of as happening in three regions. In the first region, atoms, ions and simple molecules are ejected from the stellar photosphere, where they begin to cool.

In the second stage, the temperature becomes sufficiently low for dust formation to occur ($\sim$ 1500 K), and silicate- and carbon-rich material begins to condense onto the seed molecules. In general, the dominant chemistry depends on the ratio of carbon to oxygen in the star. The majority of both of these elements is bound up in molecules as carbon monoxide, with only the free carbon or oxygen available to create carbon- or silicate-rich (*i.e.* oxygen-rich) dust. These form the C-type and M-type spectral classes, with an additional S-type where the C/O ratio is approximately (but slightly less than) unity. The situation may be complicated, however, if out-of-equilibrium effects can produce carbon-rich dust in otherwise oxygen-rich stars (§1.3.2.1).

Finally, the stellar wind reaches a 'freeze-out' point, where the density is too low for dust formation to occur; the dust grains being accelerated away from the star due primarily to radiation pressure. This is summarised in Table 1.1. If densities remain high enough, ices can build up on the grain surfaces once they are far enough from the star. How radial acceleration works where oxygen-rich chemistry dominates remains unclear (Woitke 2006b) — the likely mechanisms are covered in §1.3.2.

Table 1.1: Circumstellar environment of carbon-rich (C) and oxygen-rich (M) giant stars, after Patzer, Köhler & Sedlmayr (1995).

	Increasing distance from star →			Primary dust-forming elements
M star	Lower-energy UV, ion line production, molecules, radicals	Ionic nuclei, constant growth	Heterogeneous dust grains	**O** H Si S Fe Mg C
C star	Little UV, ion line production, molecules, radicals	Carbon nuclei, PAH formation	Amorphous carbon grains, PAHs, PAH-ions	**C** H N S Si O

1.4.3 Observing of dust-enshrouded objects

Dust cools by re-radiating the optical and near-infrared light it receives, primarily via continuum emission in the mid-infrared, but also through de-excitation of the rotational and vibrational transitions of its molecular bonds. These emission spectra are peculiar to a particular dust species and temperature. Typically, it will be superimposed on the Rayleigh-Jeans tail of the star, leading to a *mid-infrared flux excess*. Observed from outside the extended dusty circumstellar envelope, the star will also appear optically redder due to the preferential absorption of blue radiation by the dust. In highly-evolved stars, the dust column may have sufficient optical depth to reprocess virtually all the star's optical emission, meaning the stars have no visible counterparts and are thus difficult to find in survey data.

Dust is thus most commonly identified through broadband photometry, where it will show up in infrared colour-magnitude diagrams (*e.g.* Gehrz & Woolf 1971) as a positive colour, or flux excess towards longer wavelengths. In the case of silicates, prominent features between 9 and 13 μm can be observed using N-band spectroscopy from the ground, while space-based missions such as *IRAS*, *Spitzer*, *AKARI* and the *JWST* have (had) filters in these or other spectral regions that can be used to detect warm dust. Colder dust (and larger or icy grains) are not particularly emissive in

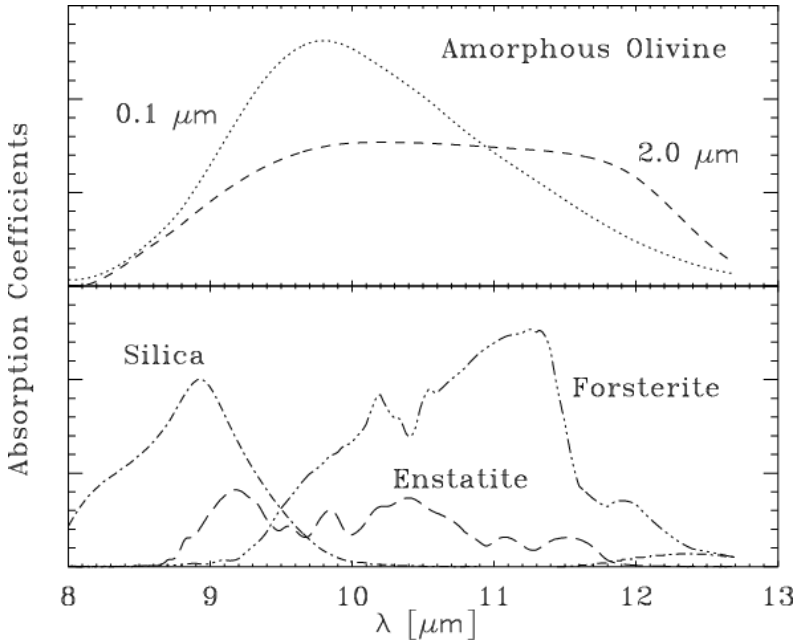

Figure 1.14: Absorption co-efficients for large and small amorphous olivine grains ($(Mg,Fe)_2SiO_4$ — top panel) and silica (SiO_2), crystalline forsterite (Mg_2SiO_4) and enstatite ($MgSiO_3$) grains from Schütz, Meeus & Sterzik (2005).

this region, though their thermal and ro-vibrational output can be detected at longer wavelengths by satellites such as *Herschel*, as well as ground-based facilities like the JCMT, APEX or ALMA.

Analysis of dust is very limited when only photometry is available: spectroscopy is the primary method of gaining information on dust and dust-enshrouded objects, revealing a great deal about the composition and temperature of the dust, and environment the dust is in. Low-resolution spectra are usually necessary to resolve the dust species present and the size of the grains (see Fig. 1.14).

A popular program for modelling spectra of dusty objects, used extensively throughout this work, is the DUSTY code (Nenkova, Ivezić & Elitzur 1999). This allows a set of blackbody sources or reference spectra to be modified by the effects of an intervening dusty medium, which can then be compared with an object's spectrum. In doing so, the properties of the dust (temperature, composition, amount, etc.) can be determined.

1.5 Survival of lost mass in clusters

"On a large enough time line, the survival rate for everyone drops to zero."

— Chuck Palahniuk, *Fight Club* (1996).

1.5.1 Observed excreta in clusters

Observational constraints can be placed on the mass of stellar excreta in clusters using diffuse atomic and molecular line emission, and using continuum emission from dust. Optical Hα (6563 Å) emission surveys allow the detection of hot, excited hydrogen, while H I (1.42 GHz, 21 cm) radio mapping traces neutral hydrogen. Radio CO emission (115, 230, 345 GHz) can trace cooler molecule formation and abundance in the interstellar and circumstellar environments. Finally, infra-red emission identifies dust in the cluster's direction, which is expected to be at 50∼80 K (Forte et al. 2002).

Suggestions have also been made that dark patches in globulars could be optically-thick clouds of ISM. These date back to the Earl of Rosse's observations (Rosse 1861) of M 13 and those of Holden (1891), Barnard (1931), Lindsay (1953) and Fitzgerald (1955), who all find dark clouds in M 13 and/or ω Centauri. Evidence is given by Roberts (1960) that these 'clouds' cannot be explained by statistical variations in stellar positions. Kanagy & Wyatt (1978) have measured extinction in dark regions in M 3, M 13 and M 15, and suggest that there is a 0.1–0.2 magnitude extinction in these areas, which are 0.1–0.3 parsecs across (if at the distance of these clusters), yielding an average dust mass of 0.003 $M_\odot$ per cloud. Forte & Mendéz (1989) give polarisation results that indicate that the purported clouds are likely part of the clusters. To date, further studies have hinted at dust clouds within clusters, but infrared surveys have repeatedly found no obvious dust near these dark patches (Boyer et al. 2006; §4).

Although theory predicts that there should be a large and very much measurable amount of gas present in globular clusters (§1.3.4.10), the observed masses are several orders of magnitude lower, or more frequently undetectable. This holds even in the

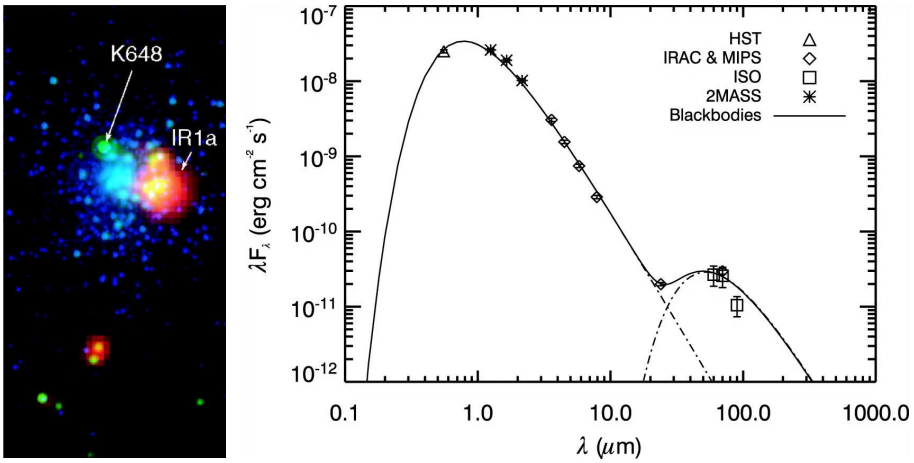

Figure 1.15: [Left Panel]: *Spitzer* image of M15 in 8, 24 and 70 μm. The PN K648 (Pease 1) and the main dust component (IR 1a) have been labelled. [Right Panel]: Broadband photometry of the dust component of M15, with theoretical blackbody curves, showing a hot stellar component, plus an obvious broadband emission feature with a temperature of around 70 K. Both images reproduced from Boyer et al. (2006).

clusters with the highest escape velocities (*e.g.* Smith et al. 1990).

Only in the last few years has equipment become sensitive enough and methods accurate enough to allow us to place reasonable limits on intra-cluster dust and gas mass. To date, the only definitive detection of intra-cluster medium (ICM) is in the metal-poor M15. First detected in 60–90 μm ISOPHOT data by Evans et al. (2003), Boyer et al. (2006) presented *Spitzer Space Telescope* 3.6–70 μm imagery showing an extended dust cloud of $(9 \pm 2) \times 10^{-4}$ $M_\odot$, offset from the cluster core (Fig. 1.15). This amount of dust is produced by the cluster about every 10^6 years — one tenth of the time since its last plane crossing — suggesting something else is removing the dust on timescales shorter than that its passage through the Galactic Plane. M15 is a very metal-poor cluster, so the presence of intra-cluster dust is all the more surprising. Although the dust is in the same line of sight and warm (70 K, compared to the line-of-sight interstellar temperature of ∼25 K), this does not necessarily associate it with the cluster. However, van Loon et al. (2006b) present 21 cm observations showing 0.3 $M_\odot$ of H I at a velocity identical to that of the cluster.

Faulkner et al. (1991) make an earlier possible detection of up to 200 $M_\odot$ of H I

in NGC 2808 using the Parkes receiver. However, Matsunaga et al. (2008) report no localised warm dust emission, and that the extended emission strongly suggests that this gas is merely foreground Galactic cirrus. Perhaps the most promising detection to date has been in 47 Tucanae by Freire et al. (2001). Using novel methods involving pulsar dispersion measures[15] they estimate the cluster's central electron density to be 0.067 ± 0.015 e^- cm^{-3}: a factor of 100 higher than the surrounding space. Assuming this plasma consists mostly of ionised hydrogen, this equates to roughly 0.025 $M_\odot$ pc^{-3}, or $\approx$0.2 $M_\odot$ over the cluster centre. Barmby et al. (2009) place an upper limit on the observed dust in the core of 47 Tuc of 1.2×10^{-5} $M_\odot$. Barmby et al. also present a tentative detection of dust in the metal-poor M92 (NGC 6341), though it may be that the discrete structures observed are either *circum*stellar dust or background sources.

1.5.2 Removal mechanisms

In light of the above observations, it is abundantly clear that some process must be clearing the gas from clusters on timescales of 10^5 years, rather than the 10^8 years between Galactic Plane crossings. Several processes may contribute towards the removal of gas and dust from the interstellar medium of the cluster, including the acceleration to escape velocity of stellar winds, either directly or through coupling with winds of other cluster stars; erosion and dissociation of dust, and acceleration out of the cluster by (beamed) radiation from compact objects within the cluster; accretion onto cluster objects; and ram-pressure stripping by hot halo gas as the cluster passes through the halo. A short review of these mechanisms is given in Roberts (1988).

1.5.2.1 Direct removal by stellar winds

Early estimates of globular cluster escape velocities were often overestimated. It is now known that they vary significantly, from around 2–3 km s^{-1} for the centre of many of

[15]The dispersion measure is a frequency-dependant delay in pulse arrival time due to interaction with intervening charged particles

the smaller clusters, up to 57 km s^{-1} for NGC 6440, 47 Tuc and NGC 2808, 60 km s^{-1} for NGC 6441 and 78 km s^{-1} for NGC 6388 (Webbink 1985). Objects further out in the cluster potential, however, will need a much lower escape velocity.

To escape, the wind not only has to achieve escape velocity from the star (the basic definition of a stellar wind), but also from the cluster. Several studies (*e.g.* Cacciari & Freeman 1983; Robinson, Carpenter & Brown 1998) based on Hα emission peaks, have suggested that chromospherically-driven winds expand with velocities of 50–80 km s^{-1}. More detailed modelling (*e.g.* §3) highlights that these are actually a superposition of emission and absorption features, so the real velocities are somewhat different. Dusty winds, particularly in low-metallicity environments, are thought to be much slower — typically estimated to be 10 km s^{-1} in solar-metallicity stars. Certain models (*e.g.* Bowen 1988a; Mattsson et al. 2008) suggest that pulsation shocks could increase this, but not to the escape velocity of the cluster.

1.5.2.2 Removal by compact objects

Evidence is growing that compact objects could influence removal of ICM. X-ray bright novae on accreting white dwarfs in binaries occur in a cluster every $\sim 10^3$ years and input energy into the ICM (Scott & Durisen 1978; Yokoo & Fukue 1992). This short timescale could lead to an effectively-constant driving mechanism for a cluster wind.

Spergel (1991) has also suggested that winds from fast-rotating neutron stars, spun up in binary systems, could provide enough energy to drive a wind. In this case, the energy comes from relativistic particles accelerated in the intense magnetic field of the neutron star. Winds from these objects, and other UV- and X-ray-bright objects, such as accreting white dwarfs, post-AGB-stars and EHB stars also have the potential to erode dust grains and dissociate molecules (Draine & Salpeter 1979).

1.5.2.3 Removal through accretion

Accretion of trapped cluster gas onto cluster objects has also been put forward as a method of removing lost mass from the ICM. Faulkner (1984) compares two scenarios in which gas collects in a central reservoir in the cluster and is accreted by a stellar-mass black hole and an MS star population. In a subsequent paper Faulkner & Coleman (1984) suggest that a ten solar-mass black hole could be formed by such accretion.

More recently, Thoul et al. (2001) have given a review on the accretion of cluster gas by stars. They investigate three methods: accretion from the AGB star wind (based on Smith 1996), accretion via close encounters with AGB stars (Ledent 2000), and accretion from a central reservoir. In the first case, the density is too low to accrete significant quantities. The second case does not provide a large amount of accretion unless the stars are on very similar orbits. However, in the final case, they find that significant accretion can occur (Thoul et al. 2000).

1.5.2.4 Removal by the Galactic Halo

A leading contender for the dominant removal mechanism is ram-pressure stripping (bow shocking) by Galactic Halo gas. Although the gas is very tenuous, the high temperatures present create a high-pressure environment. Clusters move through it with high speeds, reaching velocities of the order of several hundred km s^{-1}. The idea that this material could shock intra-cluster gas was suggested by Frank & Gisler (1976), who noted that the clusters most likely to contain this gas are associated with diffuse X-ray emission. The association between Halo gas and X-ray emission was later muted (Faulkner & Smith 1991b, 1991a), but recent observations show there is evidence that such bow shocks exist, provided the relative velocity of the cluster to the Halo is $\gtrsim 150$ km s^{-1} (Krockenberger & Grindlay 1995; Okada et al. 2007).

1.5.2.5 Removal by other mechanisms

Other ejection mechanisms include Smith's (1999) suggestion that the supersonic winds from main-sequence stars in the cluster could eject ICM, provided the cluster's velocity dispersion is $\sigma_{\rm v} < 22$ km s^{-1} and the winds are similar to our Sun's.

Umbreit, Chatterjee & Rasio (2008) propose a very different theory, however: that mass lost in stellar collisions could have enough momentum to remove gas and dust from the cluster. They estimate main-sequence - main-sequence star collisions to take place in M15 every 2–6 megayears, approximately the timescale required to clear the cluster. Unfortunately, this does not seem to happen on the even shorter timescales required to clear many of the clusters (Barmby et al. 2009; §5).

1.6 Direction of Research

"The important thing is not to stop questioning."

— Albert Einstein (1879–1955).

1.6.1 Open questions

The study of mass loss in globular clusters has the potential to answer some important questions in astrophysics, pertaining in particular to the fields of stellar evolution and the chemical evolution of the Universe.

The key understanding that needs to be made is to quantify the mass loss from these stars and uncover its relation to metallicity. Knowing this, we can then infer mass loss history in the early Universe. This has direct implications for a number of fields, including the enrichment of the ISM, the subsequent formation of molecular clouds, Population I star formation and associated (exo-)planetary formation, and the formation of the solar nebula.

Having a better quantitative estimate of the total mass lost in a cluster and its composition is also important for any discussion of mass retention by the cluster and

how lost mass is dissipated. Understanding the mechanism by which a cluster loses its ICM to the inter-galactic medium (IGM) or some other sink will inform us of the formation process and subsequent evolution of globular clusters, as well as present conditions in the Galactic Halo. This can then be used in efforts to model the evolution of the clusters and the Galaxy as a whole. The evolution of metal-poor globular stars can also be used to make inferences about the mass-loss history of Galactic stars that have helped form the Galactic ISM and IGM.

Quantifying the mass loss is particularly important to the late stages of stellar evolution and the formation of stellar remnants. Many AGB stars are expected to lose the majority of their mass during the late stages of evolution, but the fraction of mass lost at each evolutionary stage and the composition of the lost mass are largely unknown. These data have implications for the production and characteristics of white dwarfs in these systems.

Specific questions that remain to be better answered include the following:

- How much mass are stars of a given metallicity losing per unit time and at what speed?
- What precise mechanisms drive mass loss in evolved, oxygen-rich, low-mass stars?
- How do metal-poor stars produce substantial dust and does metallicity affect the dust-gas coupling?
- How much mass do they lose over the course of their evolution and in what stages?
- How much of this lost mass is present in the cluster and where has the remainder gone?
- How does mass loss vary with pulsation cycle and length?
- How have gas and dust that have been cleaned from the cluster escaped?

Obviously, all these questions cannot be adequately addressed in the scope of one PhD thesis. This work therefore focuses on investigating through observation how mass loss from individual stars proceeds in the hope of using statistical methods to answer

some of the above questions. In particular, we aim to address the relation between mass loss and metallicity.

1.6.2 Photometric approaches

Due to the comparatively large distances of globular clusters from the Earth, direct imaging of mass lost from individual stars is not possible. We therefore have to rely on photometric and spectroscopic techniques in order to further our understanding.

The applications of single-colour imaging and photometric studies are now somewhat limited. It is still used widely in stellar kinematics, such as *HST* proper motion studies (*e.g.* King & Anderson 2002; Anderson, King & Meylan 1998; Zoccali et al. 2001). Its uses in quantifying globular cluster mass loss are predominantly in identifying variable Mira-like stars and other long-period pulsators. Advances are being made using nearby Miras: in imaging such as that in Fig. 1.12, in monitoring of short-period variations (*e.g.* de Laverny et al. 1998), and in interferometry (*e.g.* Perrin et al. 2004).

Single-colour photometry is very useful at detecting stellar pulsations and other variations and while most clusters have been systematically surveyed for variable stars, many surveys have ignored longer-period stars. Long Secondary Periods are also ill-defined, primarily due to a lack of a long-timebase survey. Wide-angle surveys, such as the WASP project, are of limited use in clusters, since they do not have sufficient angular resolution to probe the cores. Higher-resolution surveys, such as those from the Large Synoptic Survey Telescope (LSST) (first light scheduled for 2013) should have sufficient angular resolution and may have a significant impact on AGB research, particularly if narrow-band TiO and CN filters are used (Ivezić 2007).

Results from Dehaes et al. (2007) suggest that (sub-)millimetre studies can also reflect molecular line variability in AGB stars of the order of tens of percent. Sub-millimetre and radio imaging also have the potential to find and/or map clouds of excreted gas within and nearby clusters.

Multi-colour photometry is also a useful tool in observing clusters. Primarily, it

can be used to construct colour-magnitude diagrams. These are useful for obtaining a first estimate of the stellar temperatures, metallicities and ages of cluster members and in finding any ranges in metallicity. It can also be used for estimating stellar masses from evolutionary models, from which local and global mass functions can be derived; useful for charting the interaction history of the cluster with the Galaxy (*e.g.* de Marchi, Pulone & Paresce 2009).

Broadband photometry can also be used for "quick-and-dirty" spectroscopy. This is particularly important in the infrared, where we can use infrared excesses to search for dust-enshrouded objects in clusters (see Chapter 2), and construct spectral energy distributions (SEDs) to model mass-loss rates and estimate the temperatures and radii of the dust envelope (see Chapter 5).

1.6.3 Spectroscopic approaches

Our main techniques, however, lie in spectroscopy. Generally speaking, spectroscopy can be used to better define metallicities, abundances, effective temperature and gravity. These can be used to infer other properties of individual stars and used globally to produce colour-magnitude or H-R diagrams that can be used in more accurate determinations of age, distance, *etc.*

Specific wavelengths can also be used to investigate different effects that occur at different heights (therefore temperatures) above the star. For example, UV emission lines (particularly in Lyman-α) can provide evidence of chromospheric activity, although use of the UV in globulars is mainly concerned with cataclysmic variables.

Visible spectroscopy is useful for identifying outflows from the stars. Balmer-α, -β, -γ (*etc.*) emission is also useful for measuring outflows, and identifying chromospheric activity (*e.g.* Dupree, Hartmann & Avrett 1984; Liller & Alcaíno 1987). Blue-shifted absorption in the same line can be used as evidence of outflow. This can be modelled using several existing computer codes, such as the SEI (Sobolev approximation with Exact Integration) method (Lamers, Cerruti-Sola & Perinotto 1987) in hotter stars, or

the CF (Comoving Frame) method (Keady 1982) (see also Chapter 3). Mass motions may also be detectable in the mid-infrared calcium triplet lines. Optical spectroscopy is also very useful for modelling abundances and other parameters with more sophisticated models, such as the PANDORA, PHOENIX and MARCS codes (Avrett & Löser 1992; Hauschildt & Baron 1999; Gustafsson et al. 2008).

Nowadays, the bulk of mass-loss science comes from infra-red wavelengths. Infra-red observation has only come to the fore in the last few years: early infra-red detectors were limited in their longer-wavelength sensitivities by background thermal noise. In the 1950s, the first lead-sulphide detectors were made, allowing observations to 3 μm, while the first truly long-wavelength bolometers, sensitive to mid- and far-infrared wavelengths, were only created in the early 1960s, and flown on balloons and rockets to observe above the worst of the atmospheric absorption.

Arguably the biggest advancement of modern times has been the advent of rapid scanning and infra-red array detectors in the 1980s, allowing far faster and better imaging and spectroscopy. The launch of the *IRAS* satellite in 1983, provided coarse, but high-quality mid- and far-infra-red datasets of the entire sky (Neugebauer et al. 1984). Further advancements have come with the surveys, including DENIS, and the launch of satellites, including *IRTS*, *ISO*, *MSX*, and *NICMOS* aboard the *HST*. The 2MASS survey, begun in 1997, has provided a very valuable high-resolution near-infra-red photometry dataset (Skrutskie et al. 2006). More recently, the launch in 2003 of the *Spitzer* Space Telescope, which has allowed infra-red imaging and spectroscopy over 3.6–160 μm in unprecedented detail. The all-sky survey data release from the *AKARI* satellite, due in 2009, will provide much improvement over the old *IRAS* measurements, and other upcoming satellites like *Herschel* and the *James Webb Space Telescope* will allow much more precise photometry and spectroscopy to be taken.

Infra-red spectroscopy can be used to search for warm dust around stars. Dust forms at temperatures below around 1500 K (Salpeter 1977; Draine 1981; Kozasa, Hasegawa & Seki 1984; Danchi et al. 1994; Tuthill et al. 2000; Gauba & Parthasarathy

2004), which corresponds to a blackbody peak at around 2 μm. By searching for broadband features at wavelengths > 2 μm, we can identify emission from dust grains such as silicates and absorption from carbon-rich molecules such as HCN, C_2H_2 and oxygen-rich molecules such as H_2O and SiO. Again, codes exist to enable measurement of temperatures and mass-loss rates, such as the DUSTY model (Nenkova, Ivezić & Elitzur 1999). Work with this code is presented in Chapters 2 & 5.

Infra-red spectroscopy has its advantage over visible wavelengths when dealing with substantially variable giant stars. In these cases, the optical brightnesses may change by several magnitudes, whereas the infra-red variations are substantially less. By using infra-red spectroscopy, we can observe more subtle changes that can occur during the pulsation cycle (*e.g.* (Ohnaka et al. 2007)).

Finally, radio velocity data can be used to search for vibrational, rotational and spin transitions in atoms and molecules. This is usually done to search for cold gas within a cluster, such as in the studies described above. The vibrational CO transition and the 21-cm spin transition for hydrogen give good indicators as to the presence of both of these chemicals. CO transitions in the near-infra-red can also be used as a reliable mass-loss indicator (Ramstedt et al. 2008). Relative signal strengths can then be used to get a quantitative answer of amounts of mass present.

1.6.4 Methods used in this work

In this thesis, several of the above techniques are used to determine mass-loss rates from stars and clusters, each with their own (dis)advantages. Namely, these techniques are: estimating dusty mass loss through infra-red spectroscopy or (spectro)photometry using the DUSTY code (Nenkova, Ivezić & Elitzur 1999); estimating gas mass-loss rate through optical line profiles of neutral hydrogen; and observing mid-infrared dust continuum and radio (H I emission in search of intra-cluster or circum-cluster media.

1.6.4.1 DUSTY

The DUSTY code is the most extensively used software in this thesis. As seen above (§1.4.3, §1.6.3), mid-IR emission results from re-radiated light from circumstellar dust, the spectral output of which yields the parameters of the outflowing wind. From the shape of the spectrum, the temperature of the inner edge of the dust envelope and the chemical species in the wind can be identified; from the amplitude of the spectrum and properties of the star, a ratio of mass-loss rate to wind velocity can be calculated.

To calculate an appropriate mass-loss rate with DUSTY, one must make several assumptions about the nature of the wind. These can often be either estimated, or derived logically or from empirical observation. The primary assumptions one needs to make are listed in the manual accompanying DUSTY[16], but can be summarised as follows:

- A stellar luminosity and temperature — these are usually determined fairly accurately from photometry or spectroscopy.
- The type of grain being formed in the wind. Pure 'astronomical' silicates are assumed for the stars herein, which are typical for stars with C/O < 1. Sometimes mid-IR spectroscopy will give us reason to choose other grain types and mixtures, as in §5. Altering grain types can change the mass-loss rate by a factor of 2–3.
- The grain density — typically unknown, but usually assumed to be about 3 g cm^{-3}. This has a linear effect on the wind velocity and thus the implied mass-loss rate, but the range of likely grain densities means that this is a negligible factor.
- The grain size distribution and the radial dependance of their number density — again typically unknown. The distributions used here are for a purely

[16]http://www.pa.uky.edu/∼moshe/dusty/manual.html

radiatively driven wind. This results in a "Catch 22" situation, as this method is performed for a final wind velocity, $v_\infty > 5$ km s^{-1}, however the wind may not necessarily be this fast in our comparatively low-luminosity, metal-poor stars. Conversely, if the winds *are* this fast, they will not be purely radiatively driven. Wind velocities are discussed later in this section. The uncertainty caused by this situation remains unquantified, but will likely be smaller than that introduced by the velocity.

- A law relating wind velocity, and hence mass-loss rate, to stellar parameters such as luminosity and metallicity. The choice of law is discussed below. This is likely the single largest source of uncertainty in the measurement of mass-loss rate. It is expected that errors in this law will provide a mainly systematic offset to the mass-loss rates herein, meaning comparative estimates of mass-loss rates will still be valid. It will not affect the ability to identify where dusty mass loss is taking place.

This last assumption — that of a law relating luminosity and metallicity to outflow velocity and mass-loss rate — is prescribed in DUSTY itself. Conservation of momentum dictates that the final wind velocity is given by $v \propto L^{1/4}(\psi\rho_\mathrm{s})^{-1/2}$, where L is the stellar luminosity, ψ is the gas-to-dust ratio and ρ_s is the grain density (Nenkova, Ivezić & Elitzur 1999). Assuming there is negligible bias for a particular element or molecule to be ejected from the stellar surface, ψ must be directly related to the metallicity of the wind (and thus, it is presumed, the star) by $\psi \propto 10^{-[Fe/H]}$. DUSTY assumes $\psi = 200$ for solar metallicity. For high ψ, the gas and dust may become partially decoupled in the wind, adding considerable uncertainty to wind calculations.

The dust mass-loss rate is related to the wind velocity by $\dot{M}_\mathrm{dust} \propto vL^{1/2}$ (the latter due to momentum imparted). The total mass-loss rate then being $\dot{M}_\mathrm{total} = \dot{M}_\mathrm{dust}(\psi\rho_\mathrm{s})$. Thus:

$$\dot{M}_\mathrm{total} = \dot{M}_\mathrm{DUSTY} L^{3/4}(\psi\rho_\mathrm{s})^{1/2}. \tag{1.5}$$

This formulism introduces an additional uncertainty of ∼30%, as DUSTY does not have any knowledge of the stellar gravity. The uncertainty comes from the undetermined ratio of radiation pressure to gravitational attraction. For high values of ψ, it may increase to >30% as the pressure-to-gravity ratio approaches unity, slowing the wind velocity to zero.

At this point, other energy sources become important and can increase the wind velocity by several times its original value. These include energy from pulsation or magneto-acoustic sources (§1.3.2).

Wind velocities remain to be widely measured in low-metallicity stars, although it is anticipated that they will be constrained by new measurements that were not yet analysed at the time of writing. Such measurements will be able to substantially reduce uncertainties in mass-loss rates derived from the above assumptions.

To summarise, DUSTY allows an accurate description of dusty stellar outflows, including determination of grain chemistry and temperature. While user input can be substantially varied to include energy sources other than radiation pressure, they require substantial editing of the inputs to include new radial density profiles — these can be very difficult, or impossible, to determine accurately. DUSTY cannot estimate mass loss from dustless winds.

1.6.4.2 Hα modelling

In Chapter §3, we use another technique to determine mass-loss rates from dustless stars. This involves constructing a model to determine the wind parameters from Hα absoprtion in the wind. The details are given in §3.6.

While our model is not unique in estimating mass-loss rate, it is among the simplest and more robust. The main difficulty with any approach to determining mass-loss rate via this process is the over-parameterisation of the model compared to the data. Many parameters (*e.g.* mass-loss rate, wind velocity and temperature) have some correlation among them to the point that even substantial changes in parameters may not yield a

significant change in the final spectrum. Nevertheless, it allows a dustless wind to be parameterised with a rudimentary level of accuracy.

1.6.4.3 Direct imaging

The final method used to observe mass loss in this thesis is direct imaging. This is done in Chapter §4 using mid-infrared dust emission maps and Chapter §6 using H I (21 cm) radio mapping. The aim of this is to identify mass that has left the circumstellar environment and entered the intra-cluster or circum-cluster medium.

The main advantage of this combination of dust and hydrogen mapping is that it allows a detailed (2-D) structural and kinematic (radial velocity) map of the target area. In principle, the resolution of this technique can be very good, with sub-arcsecond-sized details being visible, however this depends on the telescope setup(s) used. The main disadvantage of this technique is that it can rarely probe with sufficient depth to identify gas and dust in the vicinity of the cluster.

1.6.5 Overview of this work

The remainder of this work details the contributions I have made during my PhD to this field. Chapter 2 presents the detection of dust around giant stars in 47 Tucanae using mid-infrared observations with the TIMMI-2 spectrograph on the ESO 3.6 metre telescope at La Silla. Chapter 3 details work investigating the outflow from giant stars using high-resolution optical spectroscopy taken with the UVES spectrograph on the VLT. Chapter 4 describes the production of a mid-infrared atlas of ω Centauri using data taken with the *Spitzer* Space Telescope. Chapter 5 details spectral energy distribution modelling of the aforementioned *Spitzer* data, as well as new Gemini N-band spectra of ω Cen V6 and V42. Chapter 6 explains the analysis of ATCA 21cm imaging of a high-velocity cloud near ω Centauri. In Chapter 7 the findings of the previous chapters are discussed and in Chapter 8 I summarise my conclusions.

2 Silicate dust in mid-infrared spectra of giant stars in 47 Tuc

"You throw the sand against the wind
And the wind blows it back again."

— William Blake, *Poems from the note-book* (1800–1803)

Results from this chapter were published as van Loon, McDonald, Oliveira et al., A&A, 450, 339.

Contribution: *as second author on this work, significant proportions of the work were carried out by my colleagues, as initialled throughout the text. My contribution here was to assist in the organisation, execution and reduction of the observations; to produce some the included figures for the final publication; and to help explore the implications of our findings. Some additional work on V18, not published in the above article, is included in light of later observations.*

2.1 Incentive

This chapter describes the analysis of the first mid-infrared spectra of globular cluster red giants. The main impetus behind these observations was to explore the relationship between mass loss (both rate and dust composition) and metallicity.

47 Tucanae was selected as previous studies had suggested that mass-loss was taking place in several of the variable stars identified in the cluster. Three papers have provided the basis for our analysis: Ramdani & Jorissen (2001), hereafter RJ01; Origlia et al. (2002), hereafter OFFR02; and Lebzelter & Wood (2005), hereafter LW05 (from which variable numbers beginning LW are taken, the variables beginning V being taken from Sawyer Hogg (1973)). An overview of the cluster can be found in §C.3.

Table 2.1: List of targets, in order of increasing right ascension (J2000). Their photometric periods and 2.2 μm magnitudes are from Lebzelter & Wood (2005) and are derived from averages of literature maxima and minima, thus better representing average magnitudes. The 8.6 μm magnitudes are derived from our spectra: errors on the [2.2] − [8.6] colour can be taken as the errors in the 8.6 μm magnitude. Colons denote uncertain values.

Name	α ($^{\rm h}$ $^{\rm m}$ $^{\rm s}$)	δ ($^\circ$ $'$ $''$)	P (d)	[2.2]	[8.6]	[2.2]−[8.6]
LW10	00 24 02.6	–72 05 07	121:	6.40	6.37 ± 0.25	0.03
V26	00 24 07.9	–72 04 32	65:	6.25†	6.11 ± 0.22	0.14
V8	00 24 08.3	–72 03 54	155	6.70	5.56 ± 0.21	1.14
V1	00 24 12.4	–72 06 39	221	6.21	5.19 ± 0.26	1.02
V2	00 24 18.4	–72 07 59	203	6.29	5.45 ± 0.16	0.76
V18	00 25 09.2	–72 02 39	83:	7.47	7.01 ± 0.48	0.46
V11	00 25 09.0	–72 02 17	160:	6.71	6.67 ± 0.29	0.04
V3	00 25 15.9	–72 03 54	192	6.27	5.72 ± 0.18	0.55

† Blend in 2MASS; Origlia et al. (2002) list $K = 6.55$ for V26.

2.2 Observations

2.2.1 Target selection

Table 2.1 lists the properties of the observed stars. Our target list was selected from the stars in RJ01 and OFFR02 on the basis of 12-μm infra-red excess. We also included V1 and V2 — the most extreme objects listed in Frogel & Elias (1988). The brightest sources from this list were observed, along with V11, as it could be placed in the slit along with V18. LW19 was not observed list as the source could not readily be identified from *ISO* data. V8 and LW10 are also discussed in Chapter 3. Fig. 2.1 shows a period-luminosity relation for the program stars and a CMD.

Below is a brief summary of each target:

LW10 — Discovery reported in LW05. A secondary period is clearly present at twice the original period, giving a total amplitude for pulsation of approximately $\delta V = 1.4$ mag. This can be equated with Origlia et al's star #1 in OFFR02, who report a mass-loss rate of 2.5 $\times 10^{-7}$ $M_\odot$ yr^{-1}.

V26 — Also identified as A13, discovery reported in Lloyd Evans & Menzies (1973).

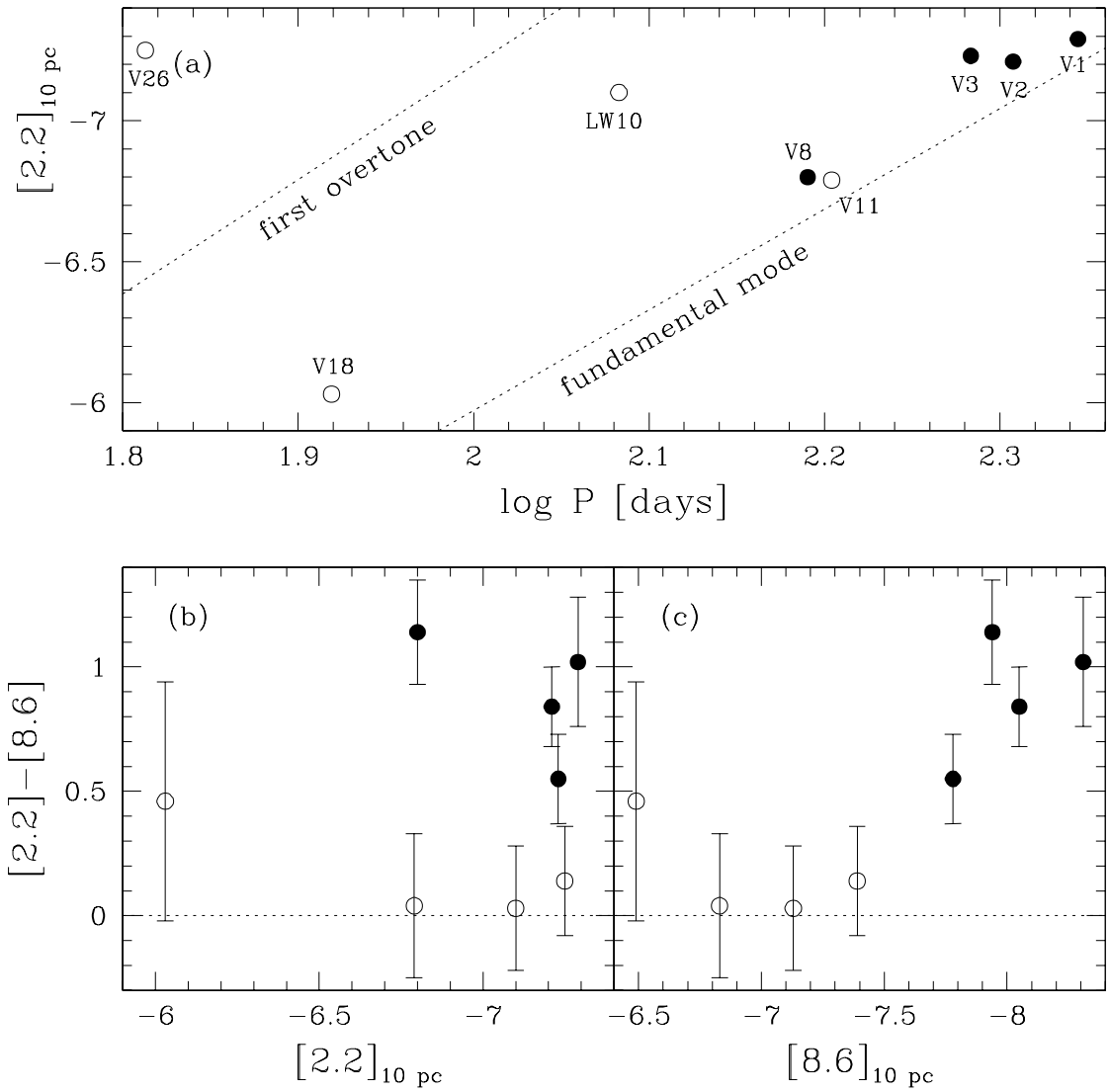

Figure 2.1: Period-luminosity and colour-magnitude diagrams for 47 Tuc, on the basis of 2MASS colours and TIMMI2 8.6 μm brightnesses. Filled symbols denote stars with [2.2]−[8.6] $\gtrsim$ 0.5. (a) Absolute 2.2 μm magnitude versus pulsation period from LW05, with pulsation modes from Ita et al. (2004). Lower panel: [2.2]−[8.6] colour versus absolute magnitude in (b) 2.2 μm and (c) 8.6 μm. The colour is clearly much better correlated with the 8.6 (rather than 2.2) μm magnitude.

Located near the edge of the cluster's core, it is identified with a strong [J–K] colour excess which can be attributed to circumstellar dust (Montegriffo et al. 1995). OFFR02 report a mass-loss rate of 3.4 $\times 10^{-7}$ $M_\odot$ yr^{-1}.

V8 — Present in the Sawyer Hogg's first catalogue of variable stars (Sawyer Hogg 1939). Also has a strong [J–K] colour excess. Forte et al. (2002) (hereafter FBV+02) report a 0.47% V-band polarisation, presumed due to circumstellar material. OFFR02 gives $\dot{M} = 4.8 \times 10^{-7}$ $M_\odot$ yr^{-1}.

V1 — Originally included in Pickering (1894). FVB+02 reports a 0.36% V-band polarisation. Bellazzini et al. (2004) place this object well above the RGB tip, and thus likely on the AGB.

V2 — Also recorded in Pickering (1894). FVB+02 finds this star is likely unpolarised.

V18 — Discovery reported in Lloyd Evans & Menzies (1973). An effective temperature of 3500−3800 K is given by Fox (1982). This star currently falls between pulsation sequences (Fig. 2.1 (a)), and may only show intermittent variability in the long term (RJ01). It has also been suggested that this star has recently undergone a thermal pulse (Lebzelter et al. 2005).

V11 — Present in Sawyer Hogg (1939); also identified as W12. FVB+02 gives 0.47% V-band polarisation. Quoted as having an effective temperature of 3360−3530 K by Fox (1982), who give periods of 52 ± 12 and 100 days and find a relatively strong [J–K] excess. RJ01 report that the dominant period may have changed between 1974 and 1984, suggesting it has recently switched pulsation modes.

V3 — Also first recorded in Pickering (1894). FVB+02 gives 0.42% polarisation in V-band. Fox (1982) give $T_{\rm eff} = 3470 - 3530$ K.

2.2.2 The observations

2.2.2.1 Instrument setup

Our observations were carried out on 19–21 October 2005 using the Thermal Infrared MultiMode Instrument (Timmi2) on the 3.6m telescope at the European Southern Observatory (ESO) at La Silla, Chile. The Timmi2 instrument, later decommissioned during P78, was placed at the Cassegrain focus of the telescope in the image plane of the f/35 chopping secondary. For our N-band observations, this gave a plate scale of 0.2″/pix. The system has a flux limit for longslit spectroscopy of 50 mJy at 10.6 μm to S/N=10 in one hour, and a resolution in N-band (8–13 μm) of $R_{\rm s} = 160$. The 1.2″ slit was used in all cases except for the observations of V11 and V18, which were observed simultaneously in the 3″ slit. Present during the observations were the author and JvL.

Target acquisition images were taken in addition to our spectra, using the $N1$ filter (central wavelength: 8.6 μm, half-intensity range: 8.0–9.2 μm, see Fig. 2.2). This range can include a SiO absorption feature, continuum dust emission and the blue wing of the 10-μm silicate dust emission feature. For comparison, the *Spitzer* IRAC4 band covers roughly 6.4–9.3 μm. Weather conditions during the observations were good, with 30–50% humidity, an air temperature of 10–12°C and an optical seeing of 0.3–1.1″. Atmospheric scintillation tends to decrease towards the infrared, so our observations were always diffraction limited by the apparatus ($\theta_{\rm D} = 0.6''$ at 10 μm).

2.2.2.2 Image reduction

To remove the sky background, which is high in the mid-infrared, the conventional techniques of chopping and nodding were utilised. For Timmi2, the chop frequency is 1.5 Hz for spectroscopy and 6 Hz for N-band imaging. Nodding is done every 1–3 minutes, depending on telescope position and atmospheric stability. Our throw (distance between the on- and off-source pointings) was 8–15″, depending on any likely sources of confusion. Integration times were one hour per target, except in the case of V2, which was only integrated for 10 minutes due to time constraints.

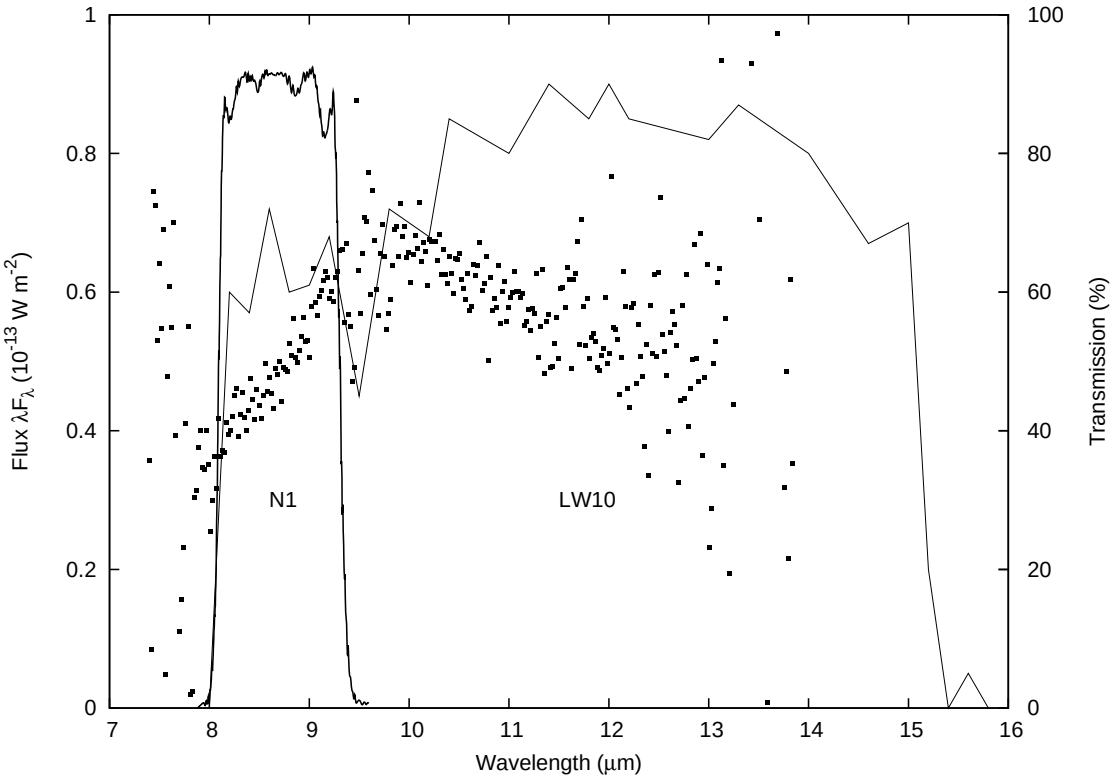

Figure 2.2: The transmission of the 8.6 μm $N1$ filter on TIMMI2 and the ISOCAM LW10 filter, against the observed spectrum of V1.

The raw images were reduced by JvL using the TIMMI2 pipeline in ESO's MIDAS software, using the long-slit spectrograph procedures. The remaining sky background was subtracted using a polynomial fit in the cross-dispersion direction. The spectra were then extracted using a weighted addition, based on the signal strength in each detector row in the dispersion direction.

The 8.6 μm magnitudes listed in Table 2.1 were computed in MIDAS using aperture photometry, with an aperture diameter of 2.4″. A zero point of 57.8 Jy was adopted (van der Bliek, Manfroid & Bouchet 1996), and differential magnitudes taken from standard stars from van der Bliek, Manfroid & Bouchet (1996) and Cohen et al. (1999).

Table 2.2: Parameters of the best-fit DUSTY model for 47 Tuc V1.

Parameter	Value
Luminosity	$7300\,L_\odot$
Optical depth in wind	0.15 at 0.55 μm
Inner envelope temperature	700 K
Terminal wind speed	$5\,km\ s^{-1}$
Mass-loss rate	$1 \times 10^{-6}\,M_\odot\ yr^{-1}$

2.3 Analysis of the spectra

2.3.1 V1

V1, the reddest, most luminous variable in the cluster, shows the strongest evidence for dust emission among our sample. Our observed spectrum is presented in Fig. 2.3.

Although many features can be seen on the spectrum, they appear to be Poissonian noise — none could be readily identified with known lines to any degree of certainty. The general structure, however, indicates a broad peak at $\sim$9.5 μm, commensurate with typical silicate emission features seen in other stars (see also Chapter 5).

Using the DUSTY code, a model spectrum was computed by JvL. Using an effective stellar temperature of 3400 K, from LW05, a grain bulk density of 3 g cm^{-3} and a standard MRN (Mathis, Rumpl & Nordsieck 1977) grain size distribution, with grain properties from Draine & Lee (1984) and a radiation-driven dust wind formalism (Ivezić & Elitzur 1995) as described in §1.3.2.1. Also assumed were a gas-to-dust ratio, ψ, which scales linearly with metallicity and that $\psi_\odot = 200$. The parameters for the best model fit are listed in Table 2.2. It is difficult to quantify errors for these parameters, though they are expected to be comparable to those determined for ω Cen V6 and V42 using similar methods in Chapter 5, *i.e.* of order a factor of two in wind velocity and mass-loss rate, and somewhat less in optical depth and inner envelope temperature.

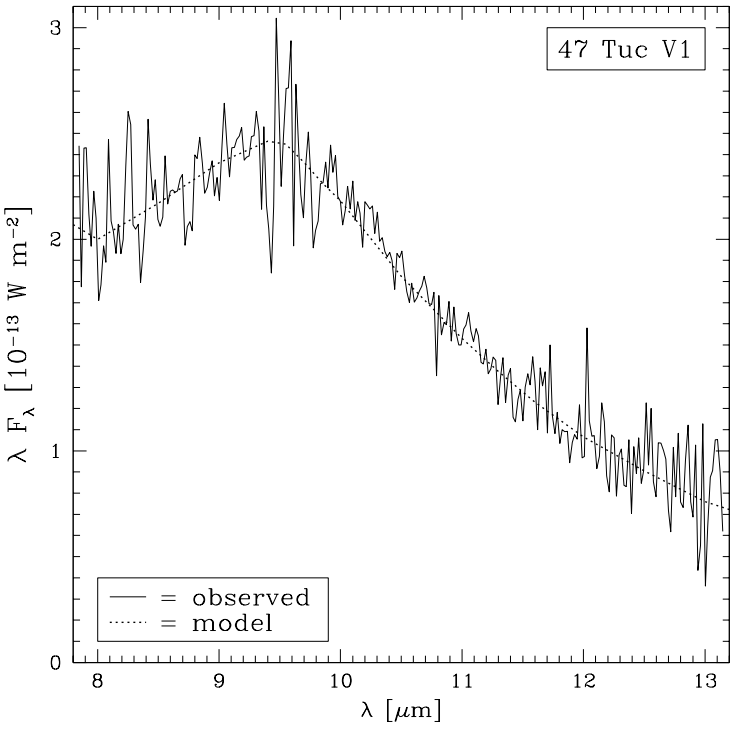

Figure 2.3: The observed N-band spectrum of 47 Tuc V1 (solid line), overlaid with a DUSTY model spectrum. Broad emission from amorphous silicate grains can be seen around 9.5 μm.

Table 2.3: Parameters of the DUSTY model for 47 Tuc V18 shown in Fig. 2.4.

Parameter	Value
Optical depth in wind	0.25 at 0.55 μm
Inner envelope temperature	300 K
Terminal wind speed	8 km s^{-1}
Mass-loss rate	2×10^{-7} M$_\odot$ yr^{-1}

2.3.2 V18

V18 shows a broad emission feature above the photospheric continuum (see Figs. 2.4 and 2.5). It is tempting to suggest that this also comes from silicate emission, though the emission peak is unclear and the stellar flux remains very low. It is difficult to determine any quantitative details about the star.

Using the DUSTY inputs already given for 47 Tuc V1, and assuming a stellar

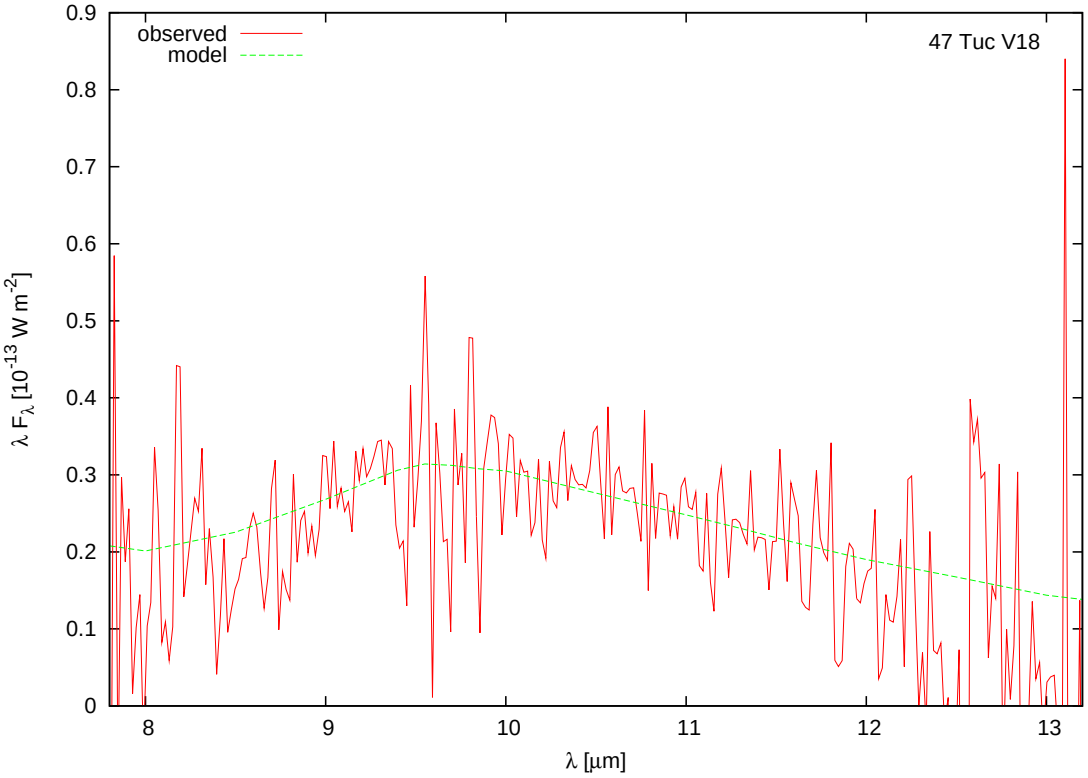

Figure 2.4: The observed N-band spectrum of 47 Tuc V18 (solid red line), overlaid with a DUSTY model spectrum. Broad emission can be seen, although the peak cannot readily be identified.

temperature of 3650 K and luminosity of 1175 $L_\odot$ (Fox 1982), the author has *a postori* computed a DUSTY model spectrum to fit the data to a first approximation, shown in Fig. 2.4. The parameters for this fit are shown in Table 2.3. Note that the inner envelope temperature is considerably lower than in the case of 47 Tuc V1 — most likely greater than the (undertermined) error involved in the temperature determination. Taking into account the sparsity of signal, if this is to be believed, it could be variant with pulsation cycle phase: dust may not be created close to the star during particular pulsation phases, but older dust could remain at larger distances during these times.

This mass-loss rate is an order of magnitude larger than that found by RJ01. Their suggestion that this star is intrinsically variable on timescales of decades could account for this. Such variability could come from the effect of period changes on dust production and/or episodic ejection of dust shells.

2.3.3 Other stars

Our other observed targets (as well as V18) are shown in Fig. 2.5. The dotted lines represent the spectrum of the apparently dust-free star γ Crux ($[2.2]_{2MASS} - [8.6] = -0.02$ mag), scaled in luminosity to match the 2.2 μm fluxes of the target stars: this can be thought of as an approximation to a pure photospheric spectrum.

The spectra of V11, LW10 and V26 appear to follow the photospheric spectrum exactly. Any spectral features visible are attributable to noise, particularly in the ozone band between 9.5 and 10 μm. The brighter objects in our sample — V3, V8 and V2 — show clear excesses in the observed wavelengths. However, they do not show any evidence for a 9.5 μm emission peak, thus we cannot tell the kind nor amount of dust they possess by this method. It is possible that these stars were observed near the peak of their pulsation cycle, thus were over-luminous in [8.6] at the time of observation.

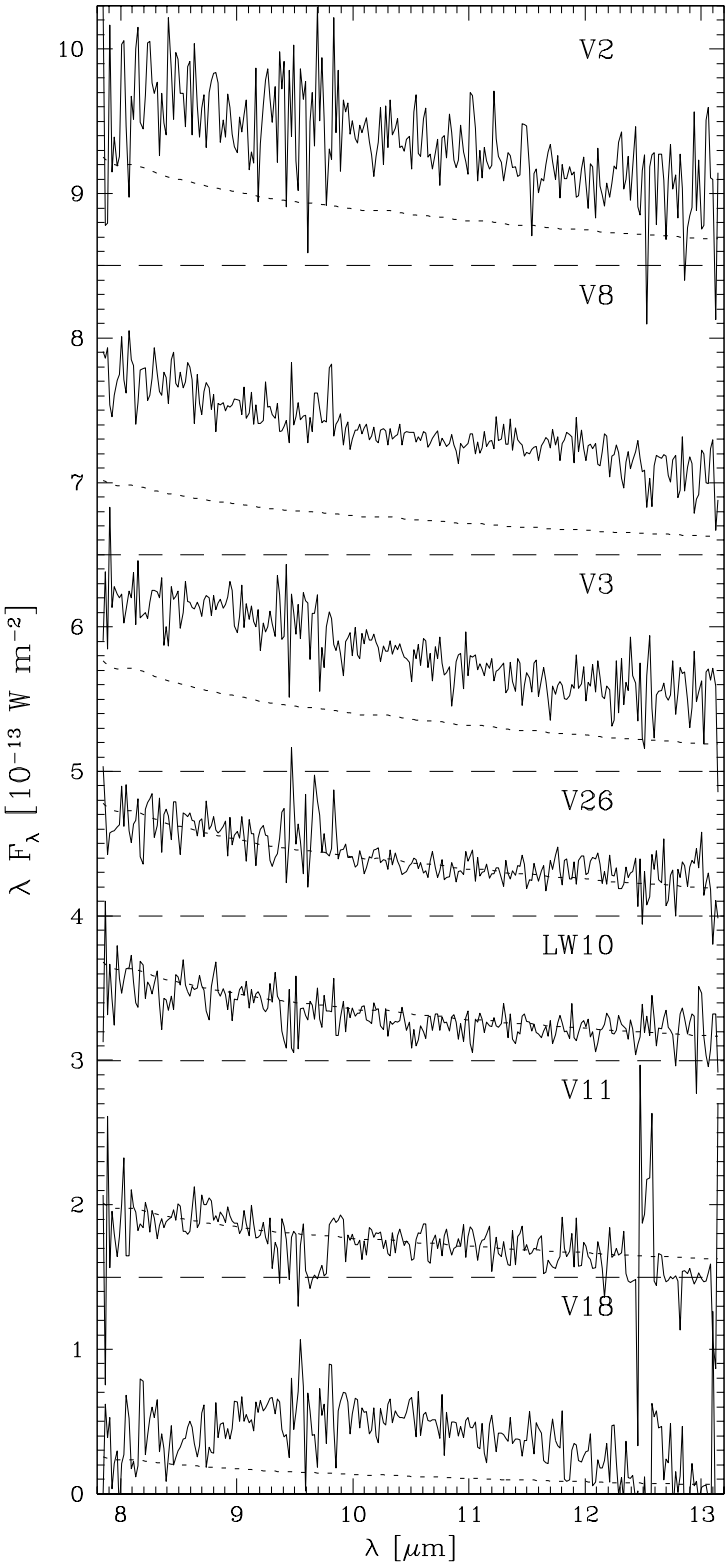

Figure 2.5: The observed N-band spectrum of our other DUSTY targets (solid line). The dotted line shows the template spectrum of the M3.5V star γ Crux, scaled to match the 2.2 μm flux density of each star. Note the possible 9.5 μm peak in V18.

2.4 Discussion

2.4.1 Infrared excess

Perhaps unsurprisingly, stars with the longest pulsation periods and highest luminosities show the reddest [2.2]−[8.6] colours. Fig. 2.1 (a) shows that the excessive stars mostly lie close to the fundamental mode. The two stars with no infra-red excess (V26 and LW10) appear to pulsate with higher modes. As noted earlier, the mid-infrared-colourless V11 shows good evidence that it is now a first overtone pulsator as well, strengthening this correlation. The four stars with the greatest excess — V1, V2, V3 and V8 — are all Mira-type variables, with large amplitude variations in luminosity and velocity, and well-defined, regular pulsations (Clement 1997).

The derived [2.2]−[8.6] colour appears to correlate more strongly with the 8.6 μm magnitude than the 2.2 μm. The photometry is not co-incident, so it is possible that pulsation could have affected the colour. Generally, pulsation should affect the 8.6 μm magnitude less than the 2.2 μm magnitude, where we expect that $\Delta[2.2] \lesssim 0.5$ magnitudes, being greater for the brighter, more dramatic variables (Frogel & Elias 1988; le Bertre 1993). This could theoretically affect the colour by a few tenths of a magnitude, though this is not thought to be the case, as we do not see any negative [2.2]−[8.6] colours. For comparison, the TIMMI2 standards (which are mostly K-type giants) have a [2.2]−[8.6] colour (again based on 2MASS) of −0.2 to +0.1 mag.

It is not immediately clear whether the highly-positive colours of our redder targets are due to excess emission from dust grains around the star, or whether it is from a cool photosphere. A zero colour is achieved for a pure blackbody at infinite temperature (or the temperature of the zero point calibrator of the photometric system — *e.g.* Vega). Cooler stars produce redder colours. It is unlikely, however, that severely excessive colours ([2.2]−[8.6] $\gtrsim$ 0.5 mag) come from a cool photosphere as the temperatures required to do this are much lower than those expected from other studies (see §2.2.1).

Table 2.4 compares our derived colours with those of RJ01 and OFFR02. Notably,

Table 2.4: List of targets, with colour comparisons from the literature. Errors on the [2.2]–[8.6] colours are approximate. No error values are given for the literature [2.2]−[12] colours.

Name	[2.2]−[8.6]	[2.2]−[12]	
	This work	RJ01	OFFR02
LW10	0.03 ± 0.25		1.20
V26	0.14 ± 0.22		1.16
V8	1.14 ± 0.21		1.64
V18	0.46 ± 0.48	1.37	
V11	0.04 ± 0.29	0.51	
V3	0.55 ± 0.18	0.64−1.13	

all stars show a much greater [2.2]–[12] colour than a [2.2]–[8.6] colour. This may be to be expected as the $N1$ filter mostly misses the dust feature. More-positive [2.2]–[8.6] colours may reflect warmer dust, or different compositions of dust, rather than the overall presence of dust itself, which is better-indicated by the [2.2]–[12] colour (Fig. 2.2).

Overall, a correlation does exist between the two colours, though it is not very strong. The OFFR02 result for V8 compares well with our moderate excess, while their other two stars — V26 and LW10 — do not appear to exhibit the excess emission that Origlia et al. have shown. Nevertheless, the values quotes by both our work and OFFR02 are still consistent with pure photospheric emission. It is also possible that some of the ISO data suffer from confusion from blending.

2.4.2 Winds

It is clear from the mid-infrared spectra that the best evidence for circumstellar dust comes from V1. Having the longest pulsation period, greatest pulsation amplitude, coolest photosphere and highest luminosity of the sample, this is probably not surprising.

A sequence for dust grain minerology in oxygen-rich stars has been suggested by

Dijkstra et al. (2005). At low mass-loss rates (typically corresponing to less-evolved stars), the stellar spectrum is dominated by emission from amorphous alumina (Al_2O_3) grains at 11−13 μm, which condense first at ∼1500 K (Speck et al. 2000). The bluer 9.5 μm broadband emission from amorphous silicates (especially olivine — $(Mg,Fe)_2SiO_4$) becomes visible at higher mass-loss rates as silicate grains condense on the alumina seeds, removing the spectral contribution of the alumina in dense winds (Tielens 1990).

Although Dijkstra et al. and others have shown the alumina feature to be present in massive AGB stars in the LMC up to the 10^{-6} $M_\odot$ yr^{-1} mass-loss rate of 47 Tuc V1, there is no evidence for alumina in V1's spectrum. It may be possible that, given the lower luminosity and metallicity of the star and the presumably slower, more compact wind it drives, there is less opportunity for bare alumina particles to exist.

Using bolometric corrections from Levesque et al. (2005), we find that 47 Tuc V1 should be around $M_{\rm bol} = -4.1$ mag or slightly brighter (Levesque et al. 2006). As noted earlier, this star is brighter than the RGB tip (Bellazzini et al. 2004). This makes it both the cluster's most-luminous and most-evolved star, and the only star we can reliably say is on the AGB. Comparing the mass-loss rate derived for V1 with that of dust-enshrouded, intermediate-mass, moderately-subsolar-metallicity stars in the LMC (van Loon et al. 1999), we find that the mass-loss rate lies well below the empirical maximum of around 4×10^{-5} $M_\odot$ yr^{-1}, but is still typical of stars of that luminosity and is still sufficient to drive a wind through radiation pressure on dust grains (Winters et al. 2000).

Like their intermediate-mass counterparts (van Loon, Marshall & Zijlstra 2005), metal-poor, low-mass AGB stars in this phase appear to have a primarily dust-driven wind. Due to the brevity of this phase, very few (if any) objects are thought to be present in any given globular cluster at a given time. The total amount of gas and dust lost by 47 Tuc V1 over its evolution is similar to that in the ICM of the massive, very-metal-poor globular M15 (Evans et al. 2003; van Loon et al. 2006b; Boyer et al. 2006). It is tempting to suggest that the reason ICM is not seen in most clusters is

that it is highly episodic, co-inciding with the death of one or more of its AGB stars, and is rapidly cleared from the cluster core by some process; thus we only see ICM shortly after a stellar death (see also §5).

2.5 Subsequent work

Following the publication of this chapter as a paper, Lebzelter et al. (2006) observed several of our targets with the Spitzer's IRS spectrograph. Observing between 7.5 and 22 μm, this provided a longer wavelength baseline for their observations. They find clear 9.5 μm dust emission from V1, V2, V4 and V18; and 11.5 and 13 μm dust emission from V4, V8 and V21 (and possibly 11.5 μm dust emission from V18). The signal-to-noise ratio of their data are much improved on ours.

Comparing the above observations to our own, we find that the emission from V1 is qualitatively very similar, although their emission is roughly 150% above the continuum, where as ours is approximately 50%. Their observation of $\sim$50% of continuum emission from V2 should have been detectable in our observations, but it is difficult to say whether or not this is the case. Their V18 observations also confirm the presence of dust emission in that star.

A striking difference is present between the two observations of V8, which clearly shows emission in Lebzelter et al., which is certainly not present in our data. Lebzelter et al's reasoning for the variation between our spectra and theirs is due to phase-dependance of the contrast between the feature and the photospheric continuum, although the K-band variation of V8 was too weak for a phase to be calculated. This theory is explored further in Chapter 5.

The following year, Ita et al. (2007) published mid-infrared photometry on 47 Tucanae and NGC 362. They found all of our stars to have excess [K]–[11] colour, with the exception of V11 and V18 (outside the field-of-view) and V26 (closely blended). They also find V1–4 and V8 to have substantial [7]–[24] colour excess. They also

present a spectral energy distribution of V1, showing features commensurate with the silicate feature described above. They find results consistent with Lebzelter et al.'s observations of a probable 11.5-, 13- and 20-μm Al_2O_3 feature in V13.

Origlia et al. (2007) also released a paper around the same time regarding dust production in 47 Tucanae. They attempted to create an empirical mass-loss law for the cluster (and by proxy all low-metallicity stars). They confirm excess in the *Spitzer* 8-μm band for V1 and V8 (also V4 and V6), and a number of other giant branch stars. Their resultant mass-loss law is also discussed in Chapter 5.

2.6 Conclusions

In this chapter, we have presented the first mid-infrared spectra of globular cluster red giant stars. We have shown that the most evolved object, 47 Tuc V1, is losing mass to the cluster at a rate of around 10^{-6} $M_\odot$ yr^{-1} facilitated by a dust-driven wind of amorphous silicate. Subsequent studies have backed this up, and have highlighted a possible variable nature to the mass loss in the case of V8.

3 Dust, pulsation, chromospheres: mass loss from red giants in globular clusters

"Twinkle, twinkle little star,
I don't wonder what you are;
From your spectroscopic ken,
I know you are hydrogen;
Twinkle, twinkle little star,
I don't wonder what you are."

— Lewis Fry Richardson or Ian D. Bush, after Jane Taylor (1806).

This chapter was published as McDonald & van Loon, 2007, A&A, 476, 1261.

3.1 Rationale

By studying stars losing mass at various stages of evolution and at various metallicities, it becomes possible to determine how mass-loss rate — and the mechanisms which determine it — vary with metallicity. Determining mass-loss rates, however, is notoriously difficult, especially if one is not sure about the gas-to-dust ratio, or in environments where that ratio is very high.

This chapter describes the observation and analysis of the highest-resolution spectra yet taken of globular cluster red giants. Here, we use asymmetries in the cores of absorption lines to model outflow from the central star. While this technique is not new (*c.f.* §1.3.2.4), we use a novel theoretical method to deduce not only the mass-loss rate, but also the wind velocity.

3.2 Instrumentation & observations

UVES — the Ultraviolet and Visual Echelle Spectrograph — is an instrument designed to provide high-spectral-resolution coverage over the entire optical spectrum, from the

300-nm atmospheric cutoff to the 1100 nm CCD detector limit. It is located at the Nasmyth B focus of the UT2 telescope, part of the Very Large Telescope on Cerro Paranal, Chile. The instrument contains two 'arms', for blue and red wavelengths, and operates at a maximum spectral resolution of $R = 110\,000$ (in the red arm).

The observations were co-ordinated and undertaken by JvL. The observation run took place during the nights of 22–23 and 23–24 July 2003. The red arm was selected with cross-disperser #4, resulting in a wavelength range of 6100–9900 Å, with a gap of ∼80 Å around 8000 Å due to the split between the two CCDs. Conditions during the observation run were extremely favourable: seeing was ∼0.3″ during the first 1.5 nights, increasing to 0.6″ for the remainder, wind speeds were between 5–10 m/s and humidity was ∼10%. This allowed the use of the 0.3″ slit and provided excellent data quality. Thus, the spectra are at the highest resolution the instrument is capable of ($R = 110\,000$), and are believed to represent the highest resolution spectral data of any globular cluster red giants. Data were reduced using the UVES package for MIDAS.

Targets were selected from bright, red objects in the vicinity of Galactic globular clusters and split into two categories based on the ISOCAM photometry of OFFR02: those with infra-red (IR) excess, $(K - [12]_0) \geq 0.65$ mag, are referred to here by the 'x' designator; and those without, $(K - [12]_0) < 0.65$, referred to by the 'o' designator. The latter were selected from the 2MASS catalogue. A per-cluster summary of these objects can be found in Table 3.1, and a list of individual objects in Table 3.2. Radial velocities taken from the spectra show all the stars to be likely cluster members, with the exception of the star observed in M54. The target selection is biased towards stars near the tip of the RGB and AGB, i.e. the most luminous red giant stars in the clusters, although we show that they do comprise an order of magnitude range in bolometric luminosity. Variability could have resulted in a bias towards stars in the bright maximum of their pulsation cycle, but the IR amplitudes are only of order a tenth of a magnitude and well within the spread of the magnitudes. The inclusion of stars with known IR excess could in principle also bias the sample towards stars with

higher mass-loss rates, but our analysis shows that stars without IR excess appear to experience similar mass-loss rates.

Two objects in NGC 362 — 2MASS J01031724−7050497 (B1) and 2MASS J01031474−7050589 (B2) — the 2MASS data were not sufficient to determine which star was our target. In these cases, all possible counterparts (namely: o05a and o05b; and x02a, x02b and x02c, respectively) were also observed. Comparing the UVES acquisition and 2MASS images, we can see that B1 is a blend comprising of two stars of similar magnitudes. We have assigned a flux based on Origlia et al.'s unpublished (J–K) data, split between the two stars on the basis of the comparative brightness in the acquisition images. The two stars have similar temperatures (see Table 3.2), so we can expect them to have roughly similar (J–K) colours. B2 is a more complex blend of three bright stars (x02a, x02b and x02c) and two faint (unobserved) stars. The star x02c is more detached from the blend and has its own identifier (#11) in Valenti, Ferraro & Origlia (2004): we do not consider it to contribute significant flux to the 2MASS blend. We thus assume that the majority of the flux observed in the 2MASS object is from the stars x02a and x02b and split the flux as before. Again, these stars were found to have similar temperatures. It thus appears likely that the 2MASS/ISOCAM identifiers are better associated with o05b and x02a, respectively. We show later that both sources appear to have higher mass-loss rates than their companions.

3.3 Stellar parameters

3.3.1 Radial velocity

The temperatures and radial velocities of our target stars were estimated using ATLAS9 model spectra (Kurucz 1993). A grid of models was created using a temperature range of 3500–6000 K, in 250 K steps; metallicity [Z/H] of −2.0 to −0.5, in steps of 0.5; and $\log(g)$ from 0 to 1.5, in steps of 0.5 dex. Titanium oxide bands (Kurucz 1999) were included, in addition to the normal atomic line lists, to better replicate cooler spectra.

A spectral type was assigned visually from standard reference spectra (Pickles 1998), and an ATLAS9 template spectrum was chosen from the above grid that best replicated the temperature expected for that spectral type, the host cluster metallicity, and an estimated gravity (based on Cioni et al. 2006a; 2006b; 2006c). Radial velocities were found by cross-correlating the ATLAS9 spectrum with the stellar spectrum in regions rich in atomic or molecular lines and clear of sky lines (avoiding the Hα and near-IR Ca II triplet lines). No significant difference between the velocities derived from the atomic- and molecular-line-rich regions was found. Spectra normalised in flux were also created using a running 1000-point (18–24 Å) wide boxcar filter, chosen to minimise smoothing of molecular bands while maximising the removal of residual fringes that affect these red spectra.

The hotter objects yielded radial velocities accurate to $\lesssim$0.3 km s^{-1}. The cooler stars, where the strong molecular bands were not covered by the ATLAS9 models, have much larger radial velocity errors. In particular, those of 47 Tuc x08, NGC 6388 o12 and ω Cen x01 are over 10 km s^{-1} (see Table 3.3). Comparison to other data (van Loon et al. 2007) shows that the velocity for ω Cen x01 appears correct to within a few km s^{-1}. This suggests that the formal errors we have calculated may be too large.

The only object with a radial velocity not co-incident with its host cluster is that of M 54 x01, suggesting it is either a field star or in a compact binary with a relatively massive companion. The calculated luminosity for the distance of the cluster is not unreasonable for a red giant, and the spectrum appears to be that of a low gravity star. This suggests it may be in a binary system. However, attempts to cross-correlate the spectrum with the ATLAS9 models to find a binary component with a different radial velocity were unsuccessful and its velocity suggests that it is most likely a field star, possibly in the Galactic Bulge (M 54 is at $l = 5.6°, b = -14.1°$).

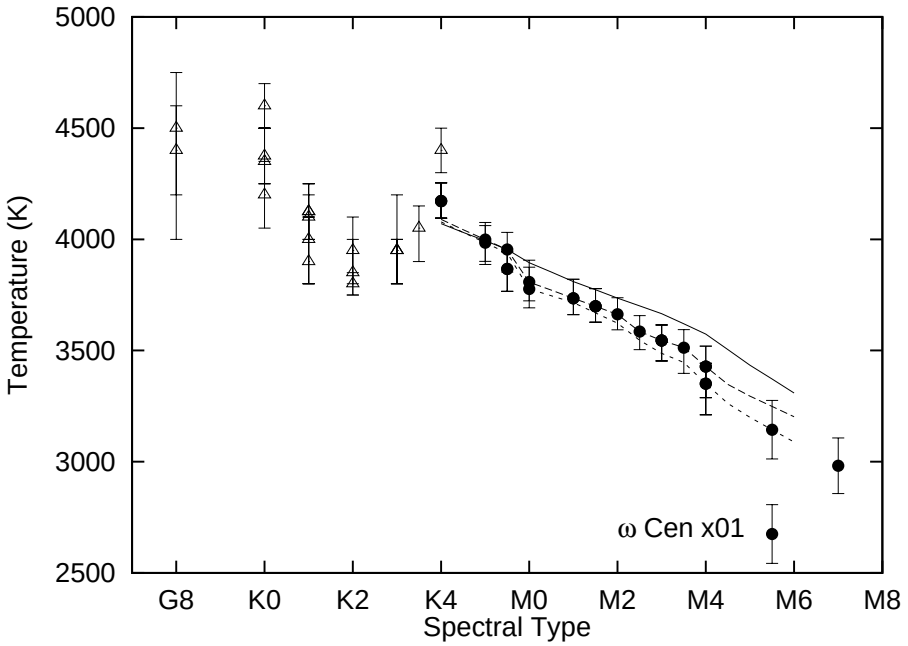

Figure 3.1: Comparison of temperature determinations between two methods: open triangles represent temperatures derived from Kurucz's ATLAS 9 model fitting, filled circles represent 'corrected' temperatures (see text) derived from (Fluks et al. 1994) and (Levesque et al. 2006). The lines show the corrections applied. The solid line represents Fluks et al.'s data for solar metallicity, the dashed line represents the correction to [Fe/H] = −0.6 (NGC 6388) and the dotted line to [Fe/H] = −0.76 (47 Tuc). The data for NGC 362 at [Fe/H] = −1.16 have not been shown for clarity, as the correction is negligible in the observed range (bluewards of K5.5). The M5.5 outlier is ω Cen x01, the fitting method for which is described in the text.

3.3.2 Stellar temperature

Stellar temperatures were calculated for the hotter objects via chi-squared minimisation using the ATLAS9 models, again using the host cluster metallicity and estimated gravity. This proved unsuitable for the cooler objects due to limitations of the ATLAS9 models. For these objects (which typically have spectral class K4 or cooler), temperature was estimated from their spectral type using the temperature-spectral type correlation from Fluks et al. (1994). These correspond to the 'uncorrected temperatures' in Table 3.3.

The Fluks et al. relations are valid for solar metallicity stars. As metallicity affects the effective temperature determined for a given spectral type, the cool objects' temperatures were corrected for the substantially sub-solar metallicities of the clusters.

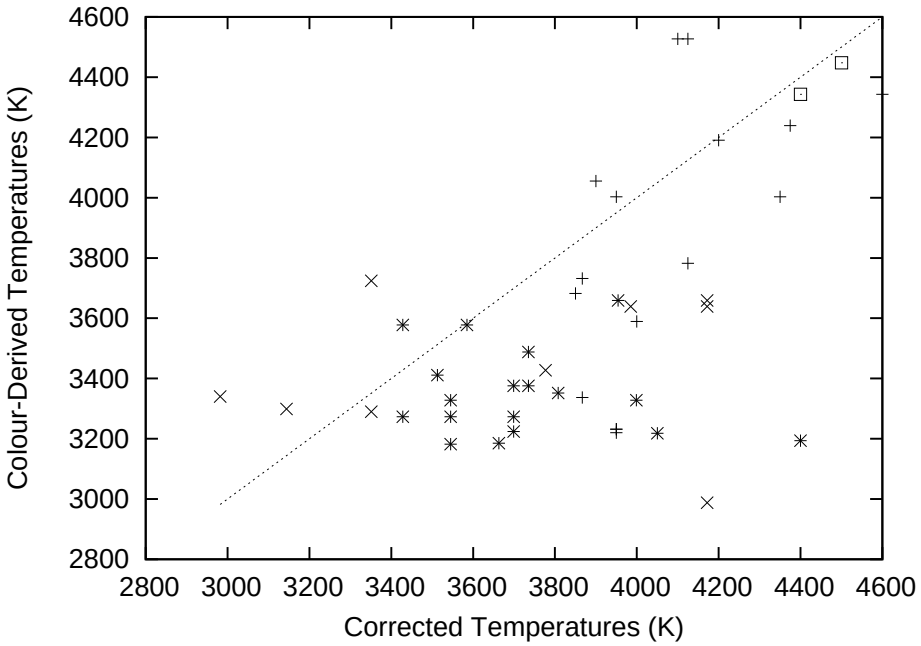

Figure 3.2: 'Corrected' temperatures from spectral typing or ATLAS9 model fitting versus temperatures determined from (J–K) colour using Houdashelt, Bell & Sweigart (2000). The two methods appear poorly correlated, as discussed in the text. Key: NGC 362: plus-signs, 47 Tuc: crosses, NGC 6388: asterisks, M 15: open squares, ω Cen: filled square.

To do this, we used a similar relation for LMC, SMC and Galactic red supergiants from Levesque et al. (2006) and interpolation the metallicity dependence at each spectral sub-type to our clusters' metallicities using a second-order polynomial. We assumed $[\mathrm{Z/H}]_{\mathrm{LMC}} = -0.3$ and $[\mathrm{Z/H}]_{\mathrm{SMC}} = -0.6$ (Russell & Dopita 1990), and $[\mathrm{Z/H}]_{\mathrm{MWG}} = 0$, and used a linear interpolation between sub-types where necessary. Overall, this has the effect of lowering the temperature of the stars by around 100–200 K.

This approach was satisfactory in all cases except the M-giant in ω Cen (V42), for which this method would yield a temperature of 2000 K. Here, a linear extrapolation using the Milky Way and SMC data at spectral type M2 (the last datapoint in the Levesque et al. data) was used instead of a parabola. We suggest that the temperature we find is still rather low, due to uncertainties in this correction process. Were this star part of the metal-rich sub-population, its temperature would be significantly higher (up to 3250 K, at $[\mathrm{Z/H}] = -0.6$). We have, however, no evidence to support this theory,

and van Loon et al. (2007) find that the M-type stars in ω Cen may have metallicities similar to the cluster average. We later (Chapter 5) derive the temperature of this star from its spectral energy distribution to be $3565 \pm^{385}_{281}$ K.

As the Levesque et al. data are for supergiants and not for the less massive and less luminous giants, we have to make a further correction. This crude correction, uses the offset between the temperatures of Levesque et al.'s supergiant Galactic sample and Fluks et al.'s red giant (Galactic) data. For each particular subtype, we subtract the difference from our result; again we interpolate where necessary. This has an effect of lowering the effective temperatures of types M0–M3 by ∼100 K, but little difference outside this range. These values correspond to the 'corrected temperatures' in Table 3.3. They are plotted alongside the ATLAS9 model fits in Fig. 3.1.

A comparison between the two methods for deriving temperature shows that the ATLAS9 models are still consistently around 200 K cooler than the corrected temperatures from spectral typing (Fig. 3.1), suggesting our corrections have been too small. This may be due to the uncertainty in extrapolating the empirical corrections to low metallicities. One would presume this offset still exists at cooler temperatures where the ATLAS9 models have not made a fit, however as this is uncertain we have not made any further corrections for this in our results. This suggests that metal-poor spectra may correspond to even lower temperatures (around the lower error values) than calculated here.

Comparisons were made with the colour-temperature tables in Houdashelt, Bell & Sweigart (2000), using (J–K) colour to estimate a temperature. The temperatures derived using this method are plotted against the temperatures found using the above methods (after corrections) in Fig. 3.2. The Houdashelt et al. relations are calibrated only for temperatures $\geq$ 4000 K, thus it is not surprising that we observe a poor correlation between the two methods.

3.3.3 Physical parameters

Physical parameters of the stars have also been calculated (Table 3.3). Luminosities were found from K-band magnitudes and using bolometric corrections made from Montegriffo et al. (1998) using a linear interpolation for metallicity. Radii were then computed using the 'corrected temperatures' described above and, using these, escape velocities were also computed. A mass of 0.8 $M_{\odot}$ was assumed for all stars, though some stars near the AGB tip may have lost up to ∼30% of this, which would lower their escape velocities by up to ∼17%.

3.3.4 Analysis

We display a Hertzsprung-Russell diagram in Figs. 3.3 & 3.4, including isochrones at 12.6 Gyr (Cioni et al. 2006a, 2006b). There is significant scatter in the plots, likely due to the uncertainty in temperature of the stars, though the stars of metal-rich and metal-poor clusters clearly match the metal-rich and metal-poor isochrones, respectively. The position of the RGB tip, at around 2000 $L_{\odot}$, does not change appreciably with metallicity nor within the likely range of ages. Assuming that the distances to the clusters are correct, we expect that the stars above the RGB tip are on the AGB (below the tip stars may be on the RGB or AGB) suggesting more than half of the sample are AGB stars. Note that, due to their intrinsic variability, the stars will naturally display a range in both luminosity and temperature: a 0.5 (bolometric) magnitude variability would change the luminosity by a factor of 1.58, and the temperature by about 130 K (assuming the net flux at the surface is roughly constant).

A period-magnitude diagram is shown in Fig. 3.5, using periodicity data from the Updated Third Catalogue of Variable Stars in Globular Clusters (Clement 1997) and from Matsunaga (2007), Ita et al. (2007) and Matsunaga (private communication). Frequency modes from Ita et al. (2004) have also been shown. These relations are for the LMC, so we expect our more metal-poor sample to be slightly brighter for a

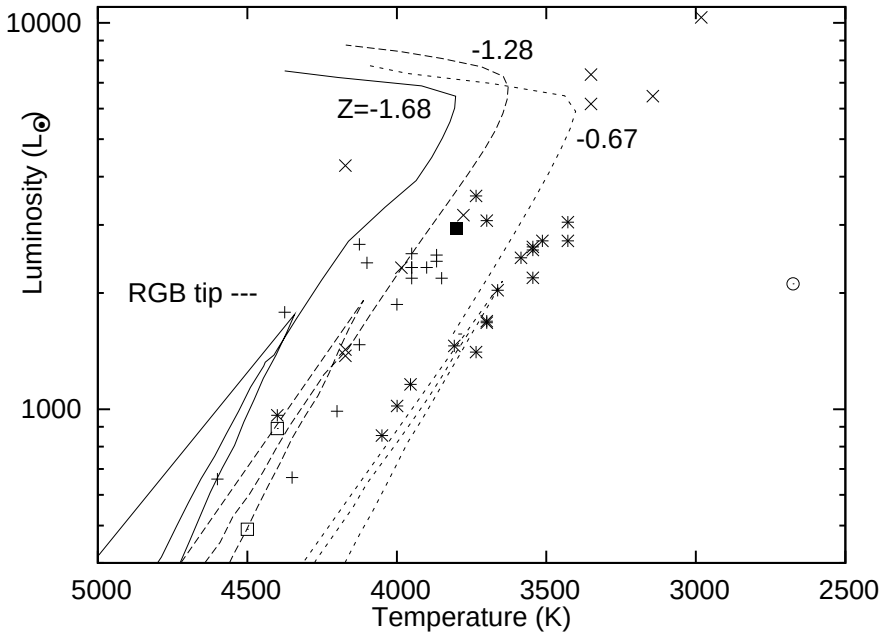

Figure 3.3: Hertzsprung-Russell diagrams of our targets. Top panel: stars identified by cluster: NGC 362 – plus signs, 47 Tuc – crosses, NGC 6388 – asterisks, M 15 – boxes, M 54 – filled box, ω Cen – circle. The temperature for our ω Cen target has probably been underestimated. Also shown are isochrones for [Z/H] = –0.67, –1.28 and –1.68 (labelled on top panel) from the models of Cioni et al. (2006a, 2006b) at an age of 12.6 Gyr.

given period (Wood 1990). It is notable that very few stars in our sample have known variability data, and we discuss this in §3.7.1.

3.4 Hα and Ca II profiles

In an effort to find mass-losing stars, we investigated the Hα (6562.8 Å) and calcium IR triplet lines (8498, 8542 and 8662 Å) for evidence of asymmetry and velocity shift. These lines are shown in Fig. 3.6. To accomplish this, we calculated line bisectors by interpolating the line profiles to uniform steps in flux. At each given flux, the two points at either side of the line centre (as determined by the line's rest wavelength with respect to the calculated radial velocity) were averaged.

Examination of the calcium triplet line bisectors shows most to be fairly symmet-

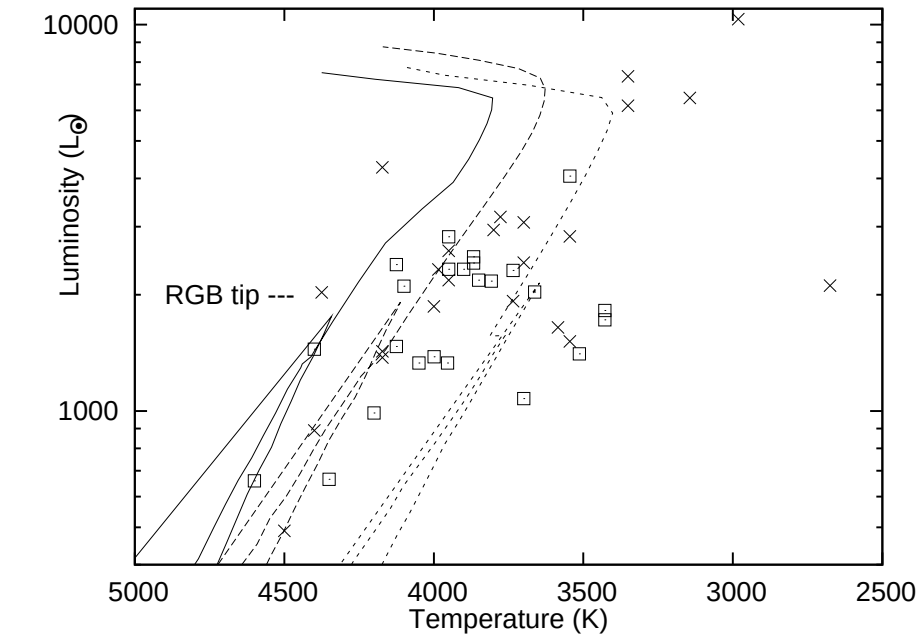

Figure 3.4: As Fig. 3.3, showing IR excessive stars (crosses) and non-excessive stars (boxes). The temperature for our ω Cen target has probably been underestimated. Also shown are isochrones for [Z/H] = –0.67, –1.28 and –1.68 (labelled on top panel) from the models of Cioni et al. (2006a, 2006b) at an age of 12.6 Gyr.

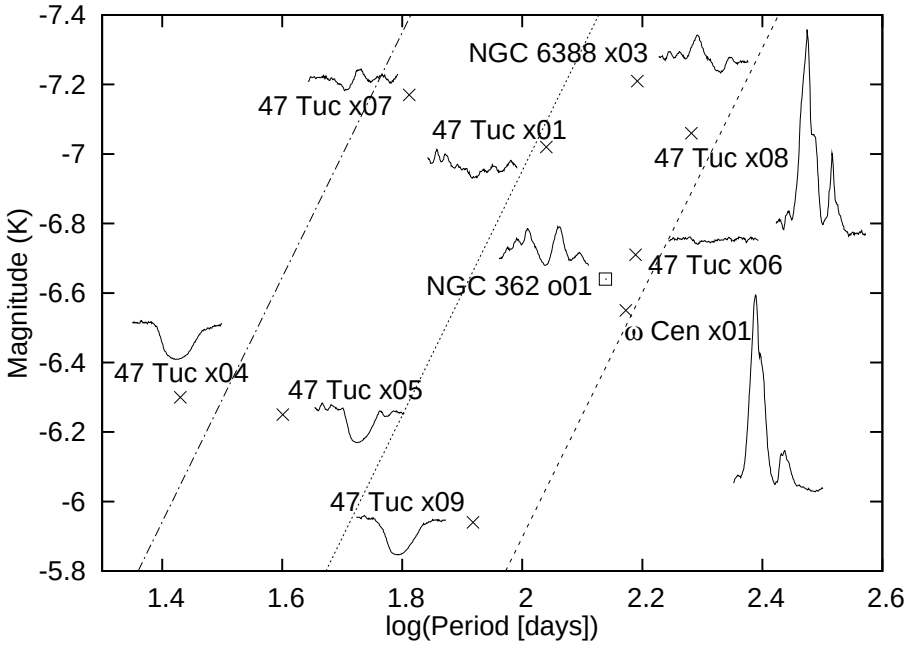

Figure 3.5: Period-magnitude diagram for stars with variability data. The lines show the fundamental mode (longest period), and first and second overtone (harmonic) periods, using the relations for the LMC given by Ita et al. (2004). The corresponding Hα profiles are plotted near the positions of the stars. Clearly, Hα emission is strongest in the fundamental mode and is therefore most likely linked to shocks in the pulsating atmosphere.

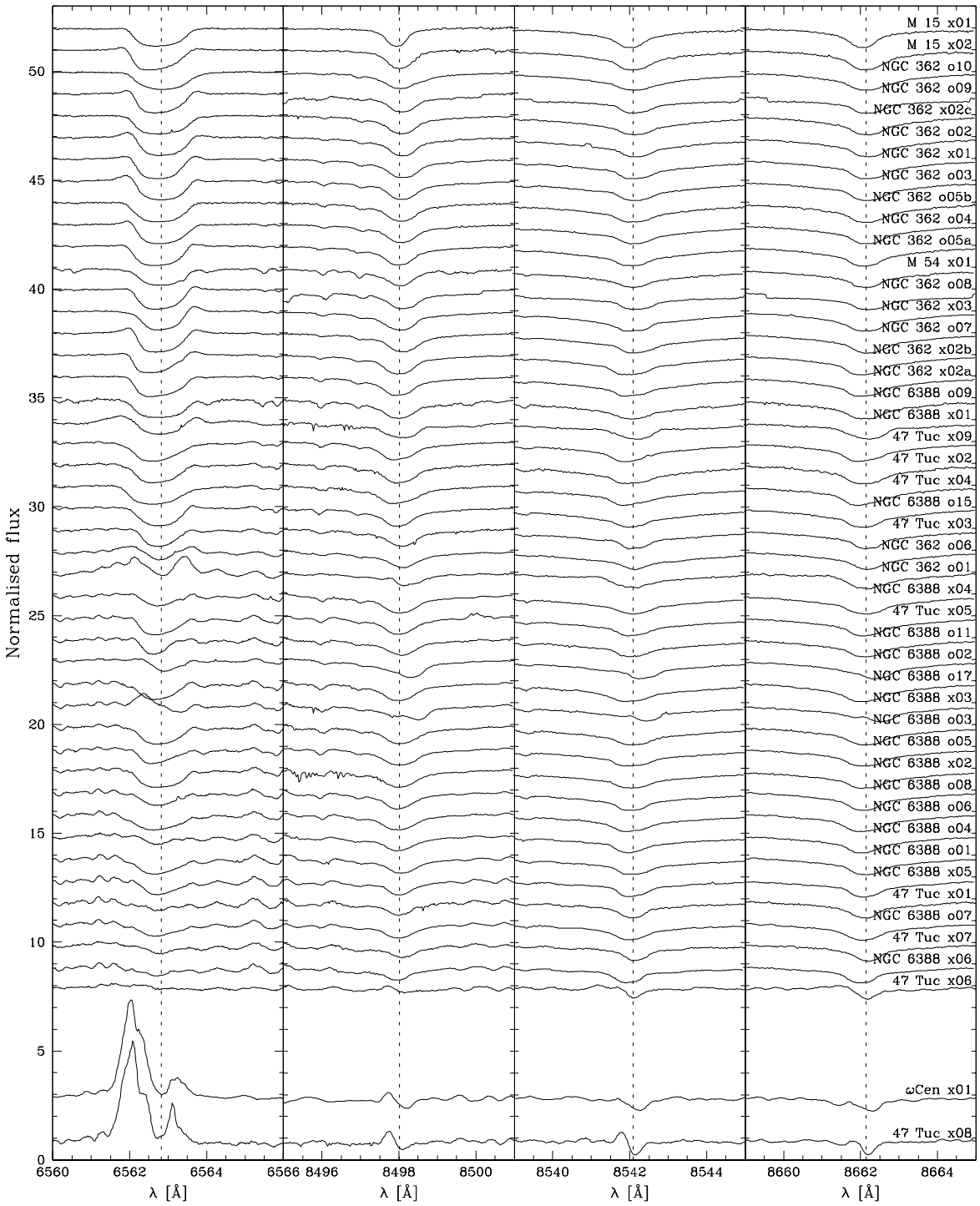

Figure 3.6: Hα and near-IR calcium triplet line profiles of the target stars, sorted by spectral type as in Fig. 5.13 and normalised to their continuum fluxes at the wavelengths of the respective lines. The spectra have also been shifted to laboratory wavelengths. Note the variety of asymmetric emission and absorption in the lines, especially in Hα. We consider the strong Hα emission from the two latest-type objects to be shock emission from pulsation. The similarity of the profiles is remarkable, despite very different metallicities.

rical. Some show slight blue- or red-shifted cores of the order 1–3 km s^{-1}, but these are not usually visible in all three lines and can probably be attributed to statistical noise, rather than as certain indicators of mass loss or pulsation (the exceptions being 47 Tuc x04 and x09, which show 4–5 km s^{-1} blue-shifted cores in all three lines). We visually estimate that the uncertainty on the shifts is of the order of 0.5–2 km s^{-1}, depending on the signal-to-noise of the data and effects of intruding metal lines. This is similar to, or less than, the radial velocity uncertainties. The Hα line shows similar features in some cases, but overall shows much more prominent emission and more significantly blue-shifted absorption at velocities of 2–12 km s^{-1}. The Hα lines also tend to be very deep, with over 90% absorption in the core in some cases.

In both elements, the lines were predominantly found to be 'banana-shaped', with a reddened kink at approximately 30–50% of the peak absorption depth. As such, the profiles are not well suited to the usual method of finding a 'velocity shift'; thus, we calculated the radial velocities of these 'kink' points and of the line cores (negating anything appearing to be statistical scatter due to Poisson noise) with respect to the stellar velocities described above. The results are included in Table 3.4.

Notable exceptions to these features appear in generally more luminous and cooler objects. Strong emission is clearly present in 47 Tuc x08 and ω Cen x01 in Hα and (to a lesser extent) in Ca II. Lesser versions of this can also be seen in NGC 362 o01 and to some extent in NGC 6388 x03 (Fig. 3.5). These four stars show a much larger K-band variability (hence much stronger pulsations) than the remainder of the objects for which we have variability data (see Table 3.2). This emission is therefore almost certainly due to heating by shock waves caused by pulsations. NGC 362 o01 and ω Cen x01 have also been shown to have variable Balmer line emission (Lloyd Evans 1983d, 1983a), further suggesting this is pulsation related. 47 Tuc x09 also shows variable Hα absorption (Lloyd Evans 1984).

Furthermore, it is interesting to note that the two most extreme objects show qualitatively very similar profiles in Hα and to a lesser extent in the calcium triplet.

This is particularly interesting given their clearly different metallicities: 47 Tuc x08 is estimated to be at 3–8 times of the metallicity of ω Cen x01, which is visibly manifest in the other, stronger spectral lines of the former in Fig. 3.6. This has obvious implications for the variance (or otherwise) of mass-loss rate with metallicity.

Weaker emission is also apparent in warmer stars. This has been noted for many giant stars in the literature and two related explanations have been put forward to model this. Cohen (1976) assumes a cooling circumstellar envelope surrounding the star at $\sim$2 R_*. Another theory, by Dupree, Hartmann & Avrett (1984), states that Hα emission could arise from chromospheric emission from a similar, hot shell source. Cacciari et al. (2004) have suggested that active chromospheres are the dominant producer of line emission in these stars. Mauas, Cacciari & Pasquini (2006) then used these chromospheric lines to model RGB mass loss in good agreement with evolutionary theory and previous estimates (Dupree et al. 1990, 1994) — notably they find the need for an outward velocity field in the chromosphere, which we also find (§3.7).

It is an obvious suggestion, backed up by more detailed modelling by Dupree et al. and Mauas et al., that blue-shifted absorption cores are evidence of outflow from the stars. The fact that we see red-shifted cores in only two cases (two of the pulsation-shocked objects) suggests that there is little or no inflow to the stars, or that this only occurs at very particular phases of the pulsation cycle. We assume that there is therefore a net mass loss from the sample.

3.5 SEI method

Our first attempt to quantify the mass-loss rate used a modification of the SEI (Sobolev method with Exact Integration) code (Lamers, Cerruti-Sola & Perinotto 1987). Based on the Sobolev approximation (Sobolev 1960; Castor 1970; Rybicki & Hummer 1978), it allows a simplified solution to the radiative transfer equation in media with high velocity gradients. This code was originally produced to study resonance lines in the

extended atmospheres of hot stars. It relies on the source function being a photospheric spectrum modified by a Gaussian turbulence parameter. As described in the previous section, we are assuming here that we have an emissive shell source (which may be a chromosphere) in many of our stars, overlayed by an extended, possibly dusty outer atmosphere. To successfully model this, we used the original SEI code to model the 'chromosphere' by treating it as a hot wind with a radially-increasing temperature. We then ran the code again, using the output spectrum from the first iteration as a replacement for the photospheric line spectrum, and solved again for the wind.

There are a number of problems inherent in this approach. Firstly, the calculated turbulences are high, which may invalidate the Sobolev approximation. Secondly, the absorption cores of the Hα lines are very deep (>90%). Although none appear saturated, a saturation at any point in the outflow (which may be partially filled-in by emission from the outflow) would invalidate the SEI method. Thirdly, the atmospheres may depart significantly from local thermodynamic equilibrium (LTE), which the SEI code requires, though this is less important in the warmer stars. Finally, there is considerable degeneracy between a large number of parameters — 12 for the initial fit, nine for the final fit, plus three global parameters — which cannot readily be broken. We therefore stress that the parameters fitted here are only given as indications and caution should be used in their interpretation. They have not been calculated for the cooler stars due to further complications from strong molecular lines.

We present the results in Table 3.5, listing the individual parameters for the fits. The first column contains the star ID, the next 13 columns contain the parameters used in the program, and the last two columns contain a goodness-of-fit parameter (χ^2/σ^2 — the units can be considered arbitrary) and the radius of the model chromosphere (as defined by the cut-off velocity). The parameters used in the program are as follows: the photospheric line is defined as a Gaussian of optical depth $a_{\rm p}$ and width $w_{\rm p}$ (all velocities are with respect to the terminal velocity, v_∞). The velocity law of the wind is defined as: $w(x) = w_0 + (1 - w_0)(1 - 1/x)^\gamma$ in the range $w_0 \leq w \leq w_1$, where x is the

radius in stellar radii. The chromosphere and/or wind properties (depending on the iteration) are modified by the optical depth of the wind, $\tau_{\rm tot}$; the ionisation parameters α_1 and α_2, which describe the run of opacity or ion density with velocity; the collisional term of the source-functions, ϵ_0; the Planck function in the wind, normalised to the continuum intensity, $(B_\nu/I_{\rm c})_0$, and the variation in temperature of the wind, $a_{\rm T}$, where $B_\nu/I_{\rm c} = (B_\nu/I_{\rm c})_0 \exp(-a_{\rm T}(w - w_0))$. We have also listed the terminal velocity, v_∞. Full details on these parameters can be found in Lamers, Cerruti-Sola & Perinotto (1987). $R_{\rm chrom}$ is defined as the radius at which $w(x) = w_1$.

Fig. 3.7 shows typical results, including the intermediate 'chromospheric' profile. The 'chromosphere' was predominantly fit using the red side of the line as this is not changed much in the final fit. The wind contribution was then calculated and both sets of parameters altered to provide as close a fit as possible to the observed spectrum. As noted, the strong correlations between the parameters make the values obtained rather uncertain, though some are more so than others. In particular, we consider the photospheric width ($w_{\rm p}$), turbulent velocity ($w_{\rm g}$) and final velocity (v_∞) to be accurate to within about 10%, subject to the validation conditions listed above.

Very little can be made of trends in the parameters, though we do find a low value for γ, the velocity law exponent. A low value of γ means a rapidly accelerating wind: if $\gamma = 0.2$, for example, the wind accelerates to $0.87v_\infty$ within a stellar radius of the surface. Additionally, the escape velocity is typically less than the final wind velocity ($v_{\rm esc} = 30 \sim 70$ km s^{-1}; $v_\infty \sim 60$ km s^{-1}). The difference between these two figures is greater than the typical velocities imparted by pulsation ($v_{\rm puls} < 10$ km s^{-1} — Barbier et al. 1988), and would imply that there *must* be some driving force accelerating material away from the star after it has left the surface.

On the basis of the limitations of the above approach, we conclude that the SEI method is not the most appropriate way of investigating the winds of these stars. Therefore, the conclusions above are somewhat less certain in the face of the limitations of this method.

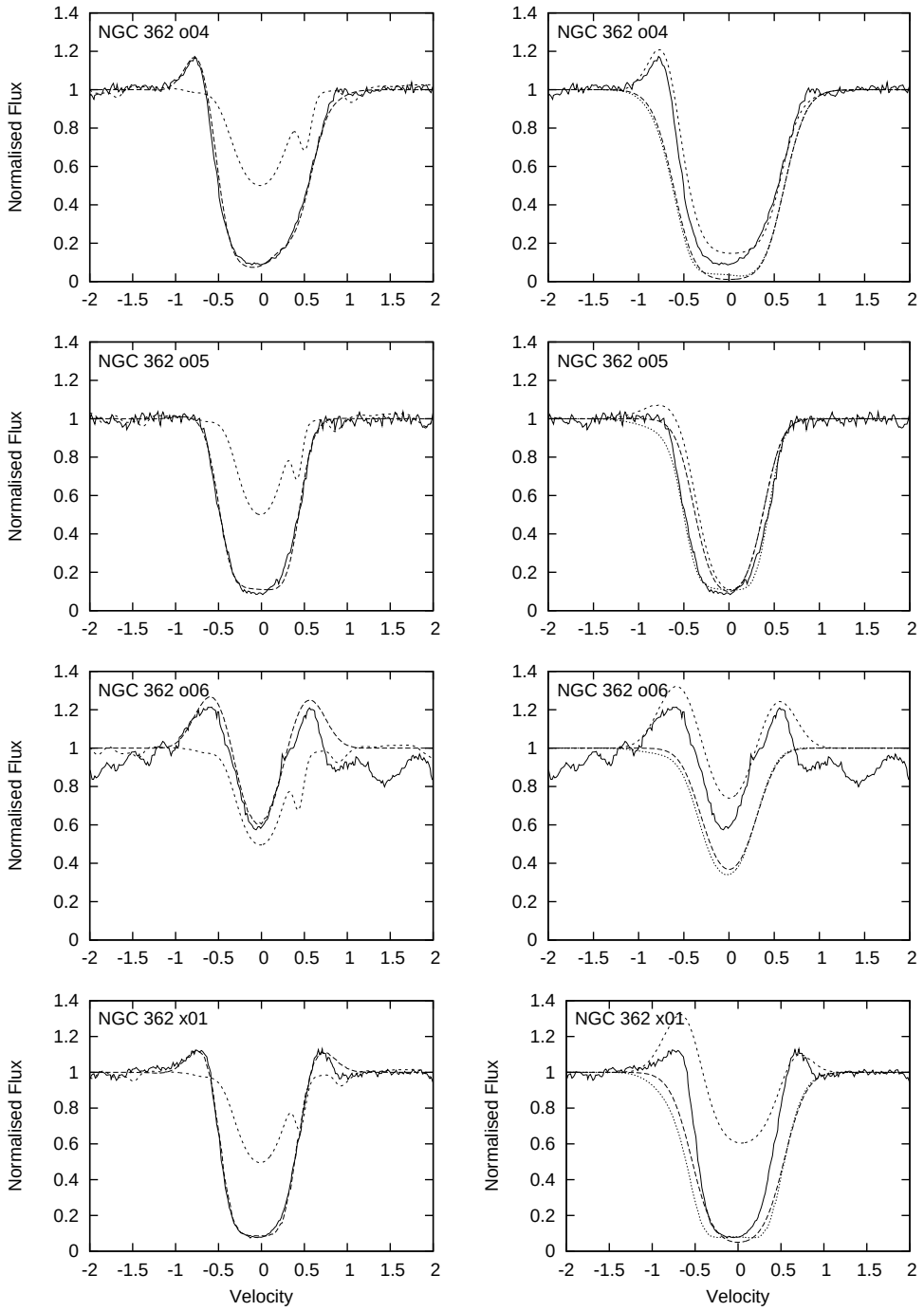

Figure 3.7: Examples of SEI fitting for (from top to bottom) NGC362 o04, o05, o06 and x01. The solid line in both panels represents the observed spectrum, normalised to the continuum flux. On the left panel, the long-dashed line represents the final fit and the short-dashed line represents the best-fit ATLAS9 model (the prominent line at normalised velocity $\sim$0.5 within the hydrogen profile is a cobalt line). On the right panel, the long-dashed line represents the photospheric line, the short-dashed line represents the first fit to the chromosphere without the wind, and the dotted line represents the fit to the wind without the chromosphere. The velocity scale is in terms of v_∞, which is shown in Table 3.3. Note the strong depth of the photospheric line compared to the ATLAS9 model.

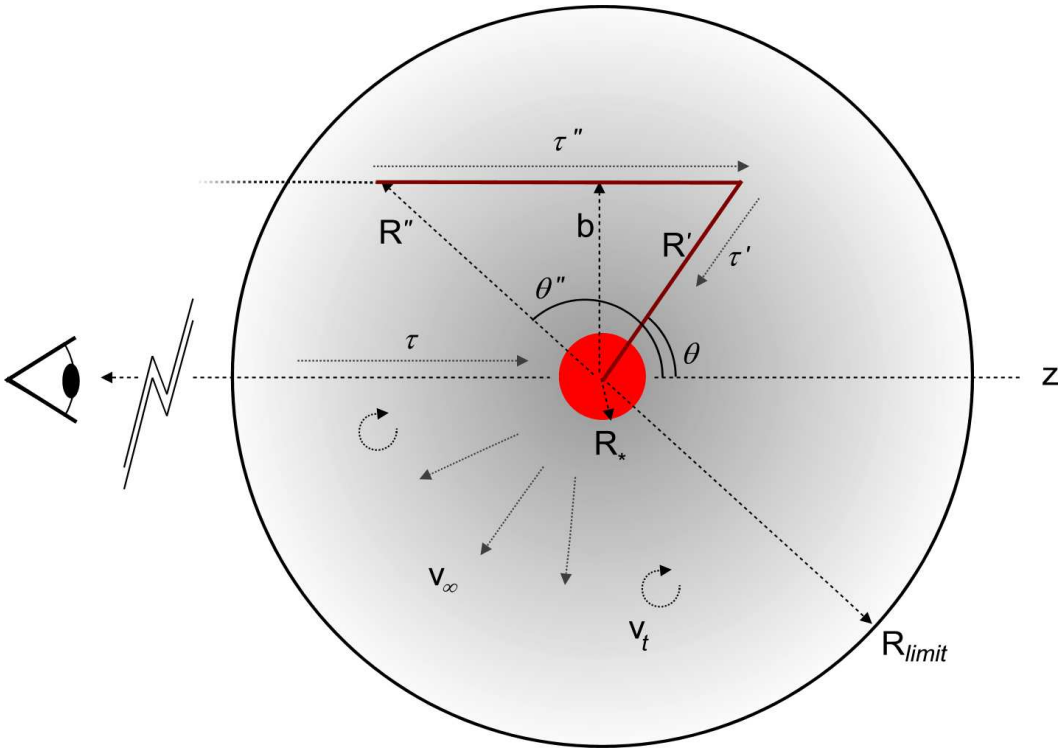

Figure 3.8: Illustration of our wind model, defining the symbols used in the text.

3.6 A simple model for estimating mass loss

3.6.1 The model

3.6.1.1 General form

In our attempt to quantify mass-loss rates from our sample of stars, we have created a simplistic model, based on some crude approximations, which we use to model the Hα line profile. Estimations of mass-loss rates based solely on line profiles are known to be notoriously uncertain, in part due to their inherent degeneracy in parameters such as velocity and turbulence (see *e.g.* Hagen 1978; Hagen, Stencel & Dickinson 1983). We address these problems in §3.6.2.

As illustrated in Fig. 3.8, we assume a spherically-symmetric wind expanding with constant speed v_∞, emanating from a non-rotating star. We assume that the emission from the surface of the star in the region of the Hα line can be simplified to a flat continuum, modified by a Gaussian-shaped absorption line, centred on Hα. This line

profile is then modified by the stellar wind and finally convolved with a Kurucz stellar model with the same metallicity, temperature and gravity as the star, broadened by a macroturbulence parameter $v_{\rm turb}$, but without any hydrogen lines. Calculating the model in this way, rather than starting with the ATLAS9 model as the output from the photosphere allows an analytical representation of the photospheric emission which greatly improves calculation speed.

The width of the photospheric Hα line is given by:

$$w \;= \sqrt{v_{\rm rms}^2 + v_{\rm turb}^2} \;= \sqrt{\frac{3kT_{\rm ph}}{\mu_{\rm H}} + v_{\rm turb}^2(r = R_*)}, \tag{3.1}$$

where k is Boltzmann's constant, $T_{\rm ph}$ is the effective temperature of the photosphere, $\mu_{\rm H}$ is the (reduced) atomic weight of hydrogen and $v_{\rm rms}$ is the root mean square velocity due to thermal motions (additional contributions to motion in the photosphere are covered by the 'turbulence' term, $v_{\rm turb}$). Thus, the flux subtracted from the continuum by the photosphere, in terms of the continuum flux, can be described as simply:

$$\left(\frac{A_{\rm ph}}{F_{\rm ctm}}\right)_{\rm v} = \left(1 - e^{-\tau_{\rm ph}}\right) \exp\left(\frac{-v^2}{2w^2}\right), \tag{3.2}$$

where v is the radial velocity relative to Hα and $\tau_{\rm ph}$ is the optical depth of the photospheric absorption in the line centre.

When calculating the wind contribution, we only consider the absorption and emission from bound-bound transitions for simplicity — unless there is a chromosphere or other temperature enhancement (discussed later in this section), the temperatures in cool giant winds are never high enough to create sufficient amounts of free electrons that other contributions to opacity and line broadening become important. Thus, the observed flux from the star in velocity interval dv can be modelled as:

$$\frac{F(v)dv}{F_{\rm ctm}dv} = 1 - \frac{A_{\rm ph}(v)dv}{F_{\rm ctm}dv} + \frac{E_{\rm wind}(v)dv}{F_{\rm ctm}dv} - \frac{A_{\rm wind}(v)dv}{F_{\rm ctm}dv}, \tag{3.3}$$

where $F_{\rm ctm}$ is the continuum emission near Hα; $E_{\rm wind}$ is the emission component of the wind, due to photons emitted by spontaneous emission directed *into* the line of sight; and $A_{\rm wind}$ is the absorption component of the wind, due to photons absorbed *from* the line of sight radiation from the stellar surface.

3.6.1.2 The absorption term

The absorption from the column in front of the star cannot be adequately modelled by a simple column of absorbing material, but must take into account the spherical nature of the star. Thus, we define an impact parameter, b, which represents the physical distance in the plane of the sky from the centre of the star.

We define the number density of absorbers (i.e. hydrogen atoms in the $n = 2$ level for Balmer α) at a given point in the wind as being $n_2(r)$. This can be found in local thermodynamic equilibrium (LTE) through the Saha-Boltzmann equations (the validity of an LTE environment is discussed later). Using this, we can calculate the optical depth *integrated over all velocities* in a particular radius bin dr as being $d\tau(r) = n_2(r)\sigma dr$ for the velocity-integrated absorption cross-section σ. Here, we use:

$$\sigma = \frac{\pi e^2}{mc^2} f, \tag{3.4}$$

giving a value of 6.537×10^{-12} m^2 using Gray (1992).

Integrating in annuli (b) over the observed stellar surface and outwards in radii, we can define the integrated optical depth of the absorption column at velocity v as:

$$\tau(v) = \int_{r=R_*}^{\infty} \int_{b=0}^{R_*} \frac{1}{\sqrt{2\pi} w(r)} \exp\left(\frac{-(v + v_\infty R_*/b)^2}{2w^2(r)}\right) \times \frac{2\pi b db}{\pi R_*^2} d\tau(r) dr, \tag{3.5}$$

with $v_\infty R_*/b$ being the projected velocity of the wind into our line of sight. We can

thus define the absorption component in the column in front of the star as:

$$\left(\frac{A_{\rm wind}}{F_{\rm ctm}}\right)_v = \left(1 - \frac{A_{\rm ph}(v)}{F_{\rm ctm}}\right)\left(1 - e^{-\tau(v)}\right). \tag{3.6}$$

3.6.1.3 The emission term

Assuming that emission in the Hα line comes entirely from spontaneous emission, thus presently neglecting any chromosphere, we can describe the emission contribution at a particular velocity as:

$$\left(\frac{E_{\rm wind}}{F_{\rm ctm}}\right)_v = \frac{\int_{r=R_*}^{\infty} p_{\rm spon} f_{\rm spon} dr}{P_{\rm ctm}}, \tag{3.7}$$

where $p_{\rm spon}$ is the power emitted from a shell of unit thickness *integrated over all velocities*, $f_{\rm spon}$ is the fraction of that shell at observed radial velocity v and $P_{\rm ctm}$ is the power emitted from the stellar continuum (for normalisation). This latter term is approximated as a blackbody, thus $P_{\rm ctm}$ is given by the familiar:

$$P_{\rm ctm} \approx \frac{2h\nu^3}{c^2}\frac{1}{\exp\left(\frac{h\nu}{kT_{\rm ph}}\right) - 1} \times 2\pi \times 4\pi R_*^2 d\nu, \tag{3.8}$$

and the power $p_{\rm spon}$ is given as:

$$p_{\rm spon} = 4\pi r^2 \; h\nu n_3(r) A_{32}, \tag{3.9}$$

where A_{32} is the Einstein co-efficient for the Hα de-excitation (4.39×10^7 s^{-1} — Menzel & Pekeris 1935).

The fraction $f_{\rm spon}$ is slightly more complex, as the wind cannot be considered to be optically thin in all cases. We must account for the absorption of the emitted light by the wind between the point of emission and the observer, and it is computationally convenient to merge this with the $f_{\rm spon}$ term. We thus consider annuli of constant observed radial velocity (which in a non-rotating star also have a common depth in the

wind from the observer's point of view), giving:

$$f_{\rm spon} = \int_{\theta=\theta_*}^{\pi} \frac{1}{\sqrt{2\pi}w(r)} \exp\left(\frac{-(v - v_\infty \cos\theta)^2}{2w^2(r)}\right) dv e^{-\tau_r''} \frac{2\pi r^2 \sin\theta}{4\pi r^2} d\theta, \tag{3.10}$$

where the Gaussian terms describe the fraction of atoms travelling in velocity dv, and the final term describes the fraction of the shell in that annulus. The lower integration limit (set to exclude flux emitted behind the star) is given as $\theta_* = \tan^{-1}(r/R_*)$. The term $e^{-\tau_r''}$ describes the subsequent absorption of this emission, as mentioned above. Defining an optical path, z, from the emitting region towards the observer, we can calculate τ_r'' (see Fig. 3.8):

$$\tau_r'' = \int_{z=0}^{\infty} n_2(r'') g_v'' \sigma dz, \tag{3.11}$$

where the distance from the stellar centre, r'' is given as:

$$r'' = \sqrt{(z - r'\cos\theta)^2 + (r'\sin\theta)^2}, \tag{3.12}$$

where r' is the distance from the stellar centre to the emitting material. The function g_v'' selects the appropriate fraction of atoms in dz at that velocity, namely:

$$g_v'' = \frac{1}{\sqrt{2\pi}w(r'')} \exp\left(\frac{-v''^2}{2w^2(r'')}\right), \tag{3.13}$$

with v'' defined as:

$$v'' = v\cos\theta - v_\infty \cos\theta'', \tag{3.14}$$

where the angle θ'' is given by:

$$r'' sin\theta'' = r\sin\theta. \tag{3.15}$$

Using the above formulae, we can formulate a model where the only inputs are v_∞, $T_{\rm ph}$, $\dot{M}$, R_*, $\tau_{\rm ph}$, $v_{\rm turb}(r = R_*)$, and the radial dependences of temperature, density and

(optionally) turbulence. The radial dependence of temperature can be considered to be constant for an isothermal wind and proportional to r^{-2} for an adiabatic, iso-kinetic wind. The radial dependence of density must be proportional to r^{-2} for a constant outflow velocity, from conservation of mass. R_* and $T_{\rm ph}$ have been determined earlier from photometry and spectroscopy (Table 3.3).

3.6.2 Limitations

Our model suffers from several limitations. The model assumes an LTE approximation, whilst non-LTE effects may be anticipated due to strong shocks and/or hot chromospheres. Attempts were made to model chromospheric heating in LTE using a wide range of temperature profiles up to $T \approx 7000$ K, but the model was unable to reproduce the emission seen in many of the line profiles. Also, free-bound recombinations were not taken into account, which would alter the $n = 2$ and $n = 3$ level populations. Although this is not significant at temperatures up to T $\sim$ 5500 K, it will play a rôle at higher temperatures where the plasma is ionised to a greater degree and is photo-electrically controlled (*c.f.* Thomas (1957); Dupree, Hartmann & Avrett (1984)). We thus *do not expect the model to accurately reproduce the emission seen in the line wings.*

Furthermore, although it contains some turbulence, our model assumes that the wind is isotropic. There is good evidence from both theory and observation (*e.g.* Asida & Tuchman 1995; Tuthill, Monnier & Danchi 1999) that red giant winds should not be isotropic. Magnetic effects in the warmer stars, and pulsation and shocking effects in the cooler stars will mean that density enhancements are likely to exist in the wind as well, which may play an important part in shaping the observed line profile.

Additionally, there are numerical limitations to consider: a limiting radius, $R_{\rm lim}$ must be taken for integration and a suitable step size must be chosen for dv, dr, dz, $d\theta$ and db. In our implementation, we use a constant step-size in all three parameters, for ease of computation. In terms of $R_{\rm lim}$, we recover the approximate true mass loss (assuming an inverse-square law for density and an isothermal, constant-velocity wind)

by taking:

$$\begin{aligned} \dot{M}_{\rm true} &= \frac{4}{3}\dot{M}_{\rm computed} \int_{r=R_*}^{R_{\rm lim}} r^{-2} dr \Bigg/ \int_{r=R_*}^{\infty} r^{-2} dr \\ &= \frac{4}{3}\dot{M}_{\rm computed} \frac{(R_{\rm lim}/R_*) - 1}{R_{\rm lim}/R_*}, \end{aligned} \tag{3.16}$$

where the factor $\frac{4}{3}$ comes from the correction from a hydrogen mass-loss rate to a total mass-loss rate, assuming the wind is 75% atomic hydrogen by mass. This last value is subject to error, given possible helium enrichment and/or molecular hydrogen.

We must also consider errors in the determination of the input values $T_{\rm ph}$ and R_*. Varying the temperature by 100 K can alter the mass-loss rate by approximately a factor of two, due to the sensitive variation of the excited populations with temperature — the effects of a chromosphere are discussed later in this section. Similarly, the mass-loss rates we list are dependent on column densities in front of the star, thus they vary with the square of the stellar radius, and this then adds a $\sim$20% uncertainty.

Finally, there is also considerable degeneracy among the parameters in the model, particularly between $\dot{M}$ and v_∞, with a range of models able to produce similar spectra. Thus we conclude that our mass-loss rates are only reliable to an order of magnitude, and our wind and macroturbulence velocities ($v_{\rm turb}$) to within a few km s^{-1}. Errors could be derived from Monte-Carlo analysis of the modelling procedure, but this is prohibitively computationally expensive. Using this model, we cannot claim to correctly determine mass-loss rates below about 10^{-8} M$_\odot$ yr^{-1}, depending predominantly on the stellar temperature (high temperatures have higher populations in $n = 2$ and 3).

3.6.3 The fitting method and results

The observed spectrum of Hα is also affected by lines of other elements, notably the neutral cobalt line at 6563.403 Å and the singly-ionised hafnium line at 6563.860 Å. Thus, we took the best-fit Kurucz spectrum (as described in §3.3), convolved it with

a macroturbulent velocity (the value of this velocity is discussed later) and resampled it to the wavelengths of the model bins. The data were also resampled to the model wavelengths, re-normalised in flux using the velocity ranges between 55 and 70 km s^{-1} either side of the Hα rest wavelength for some stars (denoted *a* in Table 3.6), or re-normalised by setting the integrated flux of the model and normalised data to be equal (denoted *b*). A goodness-of-fit parameter was then calculated. To better fit the core of the line profiles, in which blue-shifted absorption is the most reliable tracer of mass loss, we decided upon a chi-squared statistic, with a weight proportional to the inverse square of the observed flux. Method *b* produces better fits to the Hα profiles of stars with moderately-strong molecular lines, though we chose to accept the model with the minimum value of the chi-squared statistic.

Bearing in mind the above limitations, we have fitted models to all our targets, except those with the most extreme emission. This was done using a downhill-simplex search in four dimensions, using the parameters $\log(\dot{M})$, $\log(v_\infty)$, $\log(\tau_{\rm ph})$ and $\log(v_{\rm turb})$. The first vertex of the initial simplex had values of -6.5, 1, 0 and 0.5, respectively; the other four vertices had these parameters changed in turn to –5.5, 1.33, –0.2 and 1.0, respectively, with the other parameters left at the original values. We also set $dv = 4$ km s^{-1}, $R_{\rm lim} = 4R_*$, $dr = 0.035R_*$, $dz = 0.07R_*$, $d\theta = \pi/25$ and $db = R_*/25$. Fits were also attempted using the following parameters, which have smaller step sizes: $dv = 2$ km s^{-1}, $R_{\rm lim} = 8R_*$, $dr = 0.02R_*$, $dz = 0.04R_*$, $d\theta = \pi/40$ and $db = R_*/25$, and a larger value for $R_{\rm lim}$, but they could not reproduce the observations as well in the majority of cases. We suspect that this is due to the poorly-modelled cobalt line, which does not appear in most cases to be as strong as the Kurucz spectrum would suggest, even when plausible forms of line broadening are taken into account. A few individual cases required special starting conditions in order to reproduce a good fit to the data, notably NGC 362 o10, which appears to have a net inflow.

In all cases, we chose an isothermal wind. The mass-loss rates required by winds with radially-decreasing temperatures were unreasonably high if the winds cooled by

much more than ∼1000 K by 4 R_*. The macroturbulent velocity was not varied throughout the wind.

Fig. 3.9 and Table 3.6 show the results of the model fitting. Several of the cooler stars could not be fit due to strong interference from molecular lines, though the wind signature is often seen in their Hα line profiles. Additionally, NGC 362 o01 and o06, 47 Tuc x08, NGC 6388 x03 and ω Cen x01 were not correctly modelled due to their strong emission.

In general, the absorption profiles otherwise match the observations reasonably well. The exception being the strength of the other lines in the profiles. In particular, the cobalt and hafnium lines (at +27 and +48 km s^{-1} with respect to Hα) are weaker in all the observed profiles (except the M 15 stars) than the ATLAS9 model predicts. Furthermore, it is interesting to note the variations in the observed line strengths when compared to the ATLAS9 model in NGC 6388. While much of this is likely attributable to our relatively coarse temperature grid (250 K spacing), it is also possible that some temperatures have been inaccurately determined, or that the stars have substantially non-solar relative abundances.

Two cases are worth highlighting here. All of the stars for which we have computed profiles show a significant amount of mass loss, with the exception of NGC 362 o10 and M 15 x01. NGC 362 o10 cannot be modelled with an expanding wind, and has a Hα line core that is red-shifted beyond any error in radial velocity. We find it to be accreting material at a substantial rate. It is not known to pulsate strongly, nor does it exhibit a significantly red (J–K) colour, but it may be that it has only recently started to pulsate and we observe it in the contracting phase of its pulsation cycle where mass may have the ability to flow inwards. Material ejected at a velocity of ∼10 km s^{-1} during half of the pulsation cycle will reach a height of < 10 R$_*$. The escape velocity of NGC 362 o10 is one of the highest in our sample, and will drop to < 10 km s^{-1} only at a distance of ∼76 R$_*$. If the driving mechanism responsible for removing the ejected material from the system is too weak in this star, then the ejected material is bound

to fall back. Indeed, pulsation-related radial velocity variations of this order have been seen both in field giants (Lebzelter 1999) and globular cluster giants (Lebzelter et al. 2005), with wind models suggesting that inflowing material in the wind is also possible (Lebzelter et al. 2002). However, it remains a possibility that some of the blue wing of the Hα line is filled in by emission, moving the absorption core redwards. A similar phenomenon may also be present in NGC 6388 o02, if the emission in this object is due to a chromosphere. However, given the high luminosity and low temperature of this object, it seems more likely that the emission seen here is due to pulsation.

Conversely, M 15 x01 appears to have both very little emission and very little (though still clearly non-zero) mass loss. It perhaps represents the most quiescent of our sample, which, given its low metallicity, is interesting. M 15 x02, on the other hand, displays both emission wings and a strong blue-shifted outflow signature, so the metallicity dependence is far from clear-cut.

3.6.4 The influence of chromospheres on the spectral line profiles

As noted, our simple model does not include all the physics necessary for high-energy plasmas. Thus, we cannot expect to accurately model a chromosphere and reproduce the observed line profile. However, we have experimented with the introduction of a layer in the wind with variable temperature, density and outflow velocity. By inserting a near-stationary layer with the temperature and density enhanced relative to the wind, we can mimic a chromosphere and use it to qualitatively explore its effects.

The observed emission wings seen in several profiles cannot be reproduced by a localised density enhancement (with the corresponding change in velocity). We find that, in order to reproduce the emission wings, there needs to be a significant fraction of gas at a temperature well above that of the photosphere ($T \gtrsim 7000K$), meaning it will be largely ionised — i.e. a chromosphere. We find it is likely restricted to radii

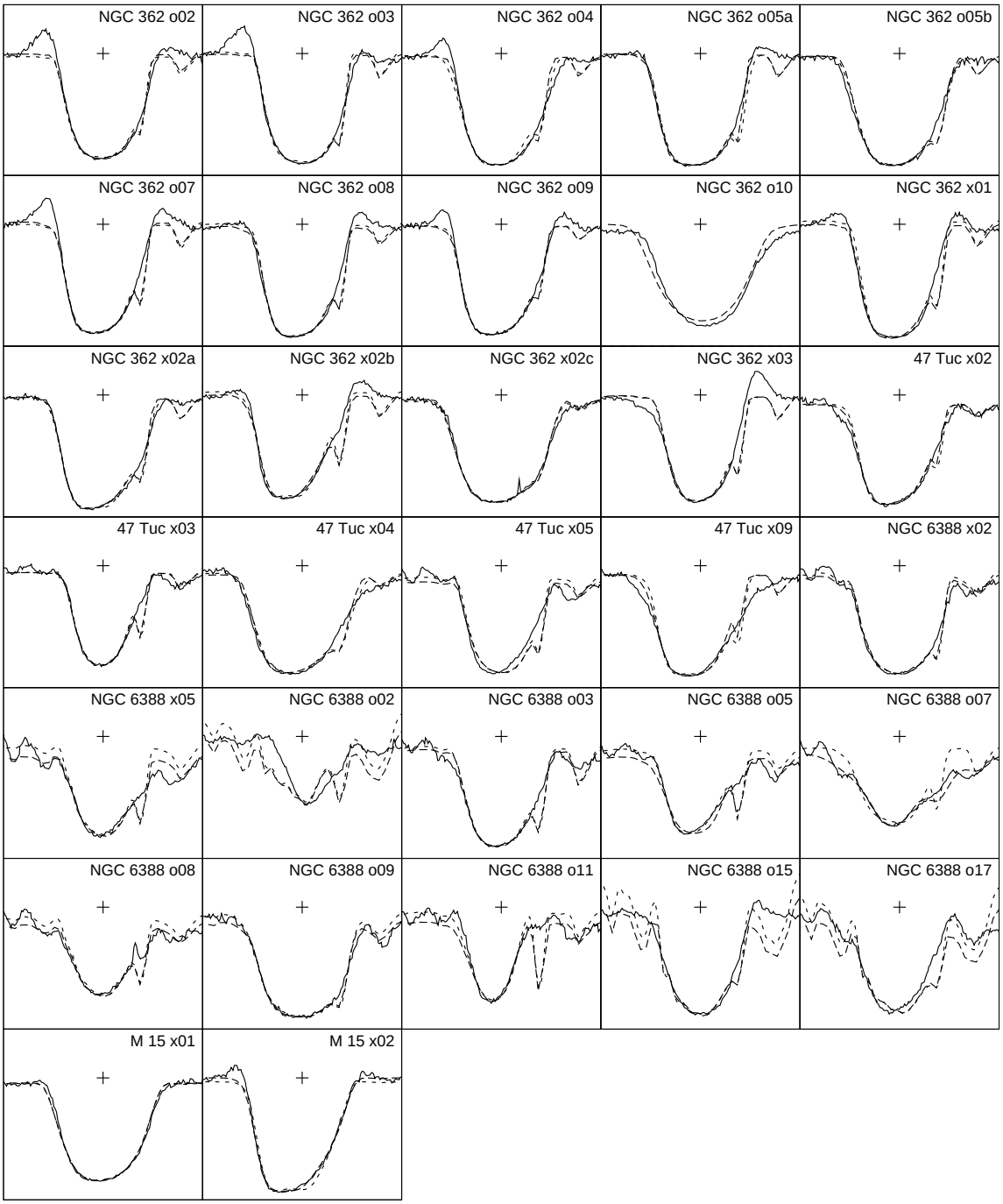

Figure 3.9: Results of model fitting to the Hα lines. X-axis is velocity from –70 to +70 km s^{-1}, y-axis is normalised flux from zero to 1.4 times the continuum. The solid lines show the UVES spectrum; the long-dashed lines show the model fit using method (a); and the short-dashed lines show method (b). For NGC 362 o10, only method (a) was calculated, and this was done for an *inflowing* wind. The cross represents zero velocity and the continuum flux level. The profiles are discussed in the text.

of $\lesssim 2R_*$ for stars showing only a blue emission wing, as this is likely a result of the red wing being blocked by the stellar disk; whereas stars showing both red and blue emission wings are likely to also have a large amount of material at radii $\gtrsim 1.5R_*$. It seems further likely that stars showing only a red emission wing, or P-Cygni-type profile, have the blue wing re-absorbed by the material in front of the emitting region.

The existence of a chromosphere can mean that the true (instantaneous) mass-loss rates differ significantly from those calculated above. Emission wings create two competing effects: firstly, the temperature enhancement increases the fraction of atoms in the $n = 2$ level, leading us to overestimate the mass-loss rate; secondly, the infilling of the blue-shifted absorption core leads us to underestimate both the mass-loss rate and expansion velocity. In general our modelling suggests that the former term dominates, and in the stars showing the strongest wings, the mass-loss rate may be overestimated by up to a factor of roughly ten and the velocity underestimated by up to 10 km s^{-1}. Weaker emission wings will cause less of an effect. The affected mass-loss rates are listed as uncertain, and the velocities as lower limits, in Table 3.6.

3.7 Discussion

3.7.1 Spectroscopic correlations with infrared excess

One of our original aims was to identify differences between the populations with and without mid-IR excess, with the expectation that the excesses were likely due to dust-rich winds. We present some statistical properties of our sample in Tables 3.7 & 3.8 (47 Tuc has not been included for comparison due to its small sample size, and the strong molecular bands and effects of shocking in its cooler stars).

It appears as though there is little, if any, statistical difference between IR-normal and IR-excessive stars whatsoever. If we consider the entire sample, the temperature of the IR-excessive stars is slightly lower, but this appears to be due to selection effects when making up the original sample and disappears when we only consider the

clusters where we have both excessive and non-excessive objects (as in Tables 3.7 & 3.8). Interestingly, the temperatures of the two sets of stars are also identical, contrary to the expectation the IR-excessive stars should be cooler due to their advanced evolution (which leads to dust production and IR-excess).

One possibility for this is that the intrinsic brightness variability of the stars, due to their pulsation, is causing some objects to appear to have an IR excess when they do not. As the photometry used to assign stars with an excess is not strictly co-temporal, this suggests that it is normal variability, rather than dust, which separates our 'IR excessive' stars from the rest of the sample. As such, we would expect there to be little or no difference between the parameters, as is the case. However, the IR excesses listed in OFFR02 are of order of a magnitude, while the K-band amplitudes found for these stars (Table 3.2) are ≤ 0.6 magnitudes, suggesting this cannot be the only reason. Hagen, Stencel & Dickinson (1983) find little correlation between mass-loss rate and dust-to-gas ratio, thus we should perhaps not expect any differences in the IR-excessive stars, which presumably contain more dust.

It should be noted that the objects with excess show higher variances in velocity offsets and ranges, particularly in the core velocity. Considering the period-magnitude diagram (Fig. 3.5) we find that the objects with longer periods are the objects with stronger pulsations (Table 3.2, *c.f.* §2.4.1). All the objects for which we have variability information are (barring NGC 362 o01) identified as IR-excessive in the ISOCAM photometry, as are the few most luminous and coolest stars (see Figs. 3.3 & 3.4).

The chromospheric activity appears more pronounced in IR-normal stars, but this bias is most likely due to selection effects, since the stars in NGC 362 (which contains most stars showing chromospheric activity) are hotter and more luminous, therefore are more likely to have chromosphere-driven winds, rather than pulsation-driven winds. However, if IR excess is linked with dust formation, then it would not be surprising that dust formation is inhibited while the hot chromosphere is still in place.

These factors suggest that those objects labelled IR-excessive stars are, by and

large, more active objects with greater variability — hence more evolved objects. Further evidence for this comes from Figs. 3.3 & 3.4, which shows that the most luminous, coolest objects are all IR-excessive. We do not find any significant correlation between period and temperature, nor between core asymmetry and luminosity, nor core asymmetry and temperature. It is important to realise that the stars are within a factor $\sim$4 of the RGB tip: stars lower on the RGB are likely to pulsate less, and dust formation at lower luminosities may be more stochastic and a by-product of outflows, rather than an integral part of driving a wind.

Also in Tables 3.7 & 3.8, we compare the two clusters, which are at significantly different metallicities (Table 3.1). Given our relatively small sample size, there are no statistically significant variations between the clusters in the Hα line, despite the clear difference in stellar temperature. This suggests that temperature is not a strong influence on the outflow velocity.

3.7.2 Line core velocities

Fig. 3.10 shows the variation of Hα versus Ca II core velocities, with respect to the stellar rest velocity and the 'kink' velocity described previously. Clearly a correlation exists in both cases, although the calcium lines are only perturbed by around 30% of the velocity of the hydrogen lines. This suggests that the lower layers of the atmosphere, where the calcium lines form, have not yet been accelerated to the terminal velocity. The two outliers showing redshifted Hα cores in the lower panel of Fig. 3.10 are NGC 362 o01 and NGC 6388 x03, both of which show strong emission in Hα.

Though their results are mostly for the Na D lines rather than Hα and Ca II, Bates, Kemp & Montgomery (1993) find that low-luminosity stars show only small core velocity shifts, though these increase beyond a luminosity of $\approx$ 1000 $L_\odot$ and become more scattered. Most of our sample is above 1000 $L_\odot$, thus we cannot verify this claim. We do see considerable scatter, but do not find any correlation between line core velocity and luminosity within the luminosity range of our sample.

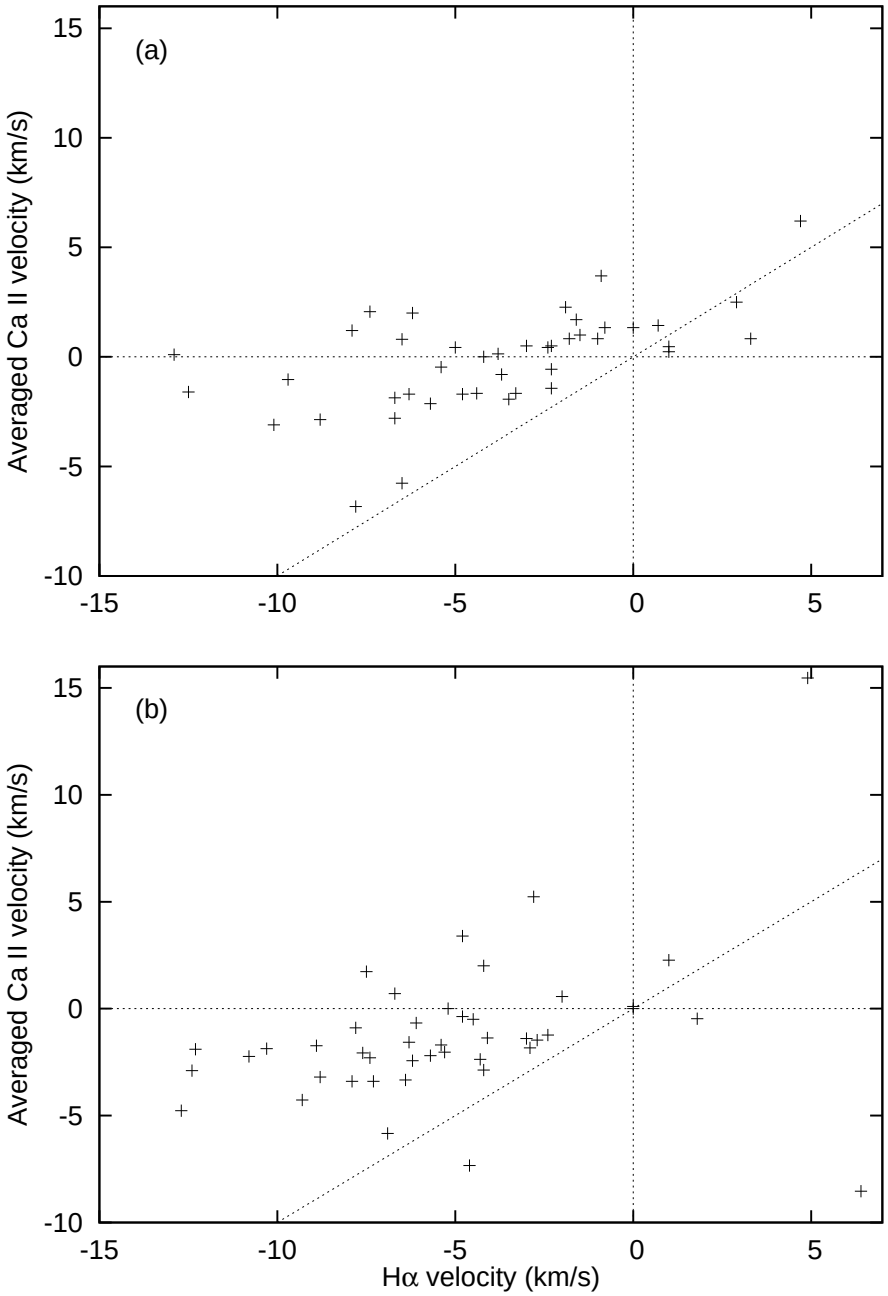

Figure 3.10: Plots of Hα core velocity against calcium triplet core velocity (averaged over the three lines). Velocity is taken with respect to (a) the stellar radial velocity and (b) with respect to the line 'kink'; see §3.4 for details. The dotted lines indicate zero and equal velocities for both the Hα and Ca II lines.

3.7.3 Line profile shapes

Fig. 3.6 clearly shows unusually deep line profiles. To investigate this, and the other line profile features already noted, the ATLAS9 model at the corresponding stellar temperature and metallicity was subtracted from the Hα profile. Interpolations were made to more accurately model the correct metallicity. The results are shown in Figs. 3.11 & 3.12.

Two things are immediately apparent from these figures: firstly, that the absorption components are indeed much deeper than the ATLAS9 modelling would suggest; and secondly, that emission in both red and blue components persists. We have discussed a chromospheric model for producing the emission. The deep absorption could arguably be produced by the same phenomenon: from an optically thick chromosphere.

Another facet of Figs. 3.11 & 3.12 is the progression of emission and line asymmetry with spectral type and metallicity. In the figures, the emission spike present in most stars in NGC 6388 (and possibly 47 Tuc) at 6563.4 Å co-incides with a Co I line. This line has been grossly over-subtracted, suggesting that there may be a cobalt deficiency in these objects, or an error in our temperature calculations for intermediate ($\sim$4000 K) temperatures. However, examination of the original data (Fig. 3.6) suggests that at least some part of this emission may be still associated with the Hα line.

Looking within clusters, blue asymmetry and line depth appear to increase as luminosity increases towards 2400 $L_\odot$ (or as temperature decreases towards $\sim$3900 K). As luminosity continues to increase and temperature decrease, profiles become more variable. Similarly, broad emission wings only appear in stars below $\approx$ 2400 $L_\odot$ (above $\sim$3900 K), and in cool stars is only present if they show high photometric variability and pulsation shocks. The emission wings are only seen clearly in NGC 362 and M 15, the low-metallicity clusters (and possibly NGC 6388 o02, though at this luminosity and temperature this could be due to pulsation), with little or no emission seen in the higher-metallicity NGC 6388 and 47 Tuc. While our low-metallicity sample are generally warmer stars where chromospheres may be expected, and where there are

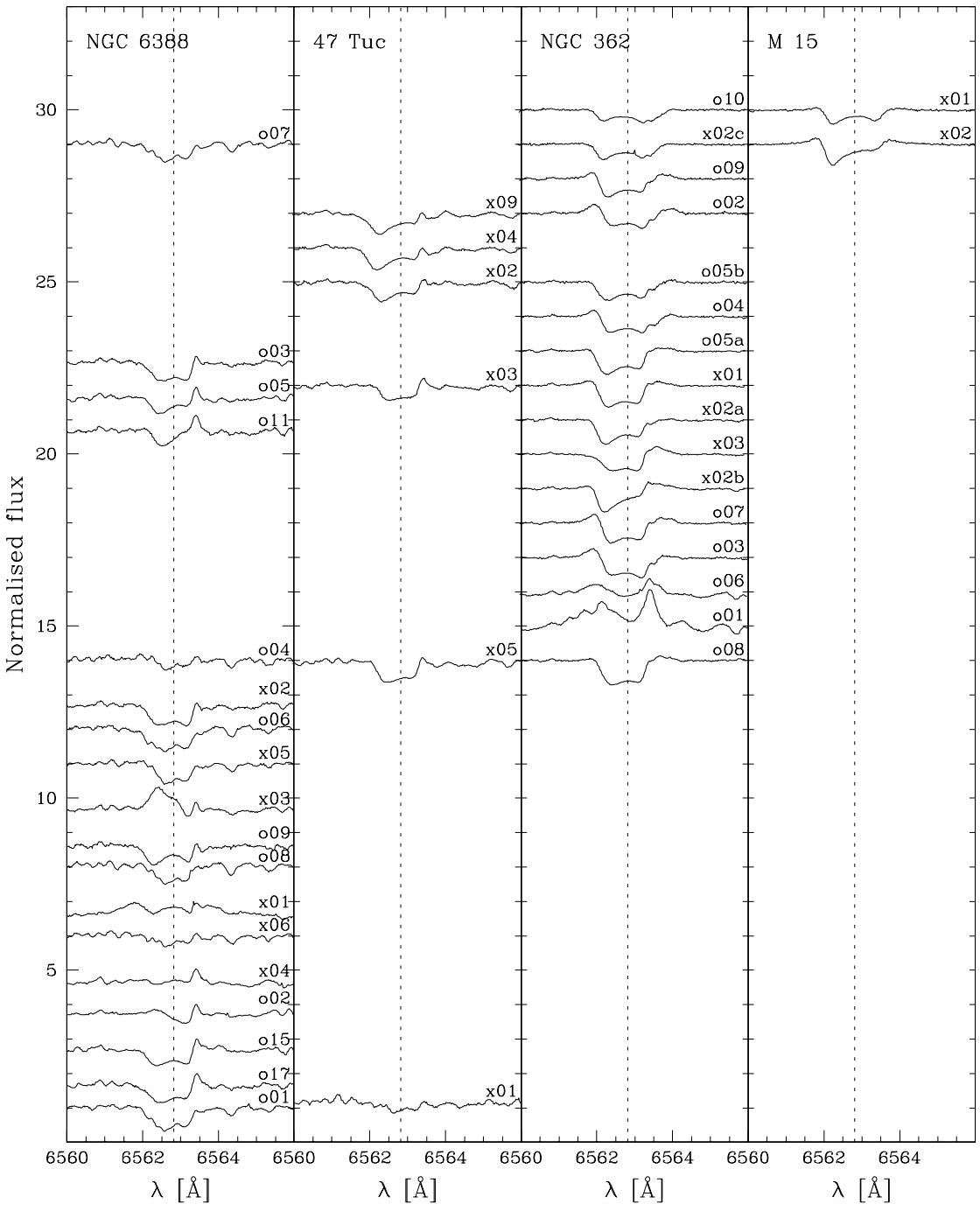

Figure 3.11: Hα line profiles of the target stars, sorted by temperature (temperature increases upwards), with the appropriate ATLAS9 model spectrum subtracted. Spectra have been normalised to their continuum fluxes as in Figs. 5.13 & 3.6 and shifted to laboratory wavelengths. Spectra for 47 Tuc x06, x07 and x08, and ω Cen x01 have not been shown, as they are too cool to be accurately matched to an ATLAS9 model. The four panels show objects in different clusters, with metallicity decreasing from left to right. A Co I line at 6563.4 Å appears to have been over-subtracted in NGC 6388, giving the false impression of red-shifted emission.

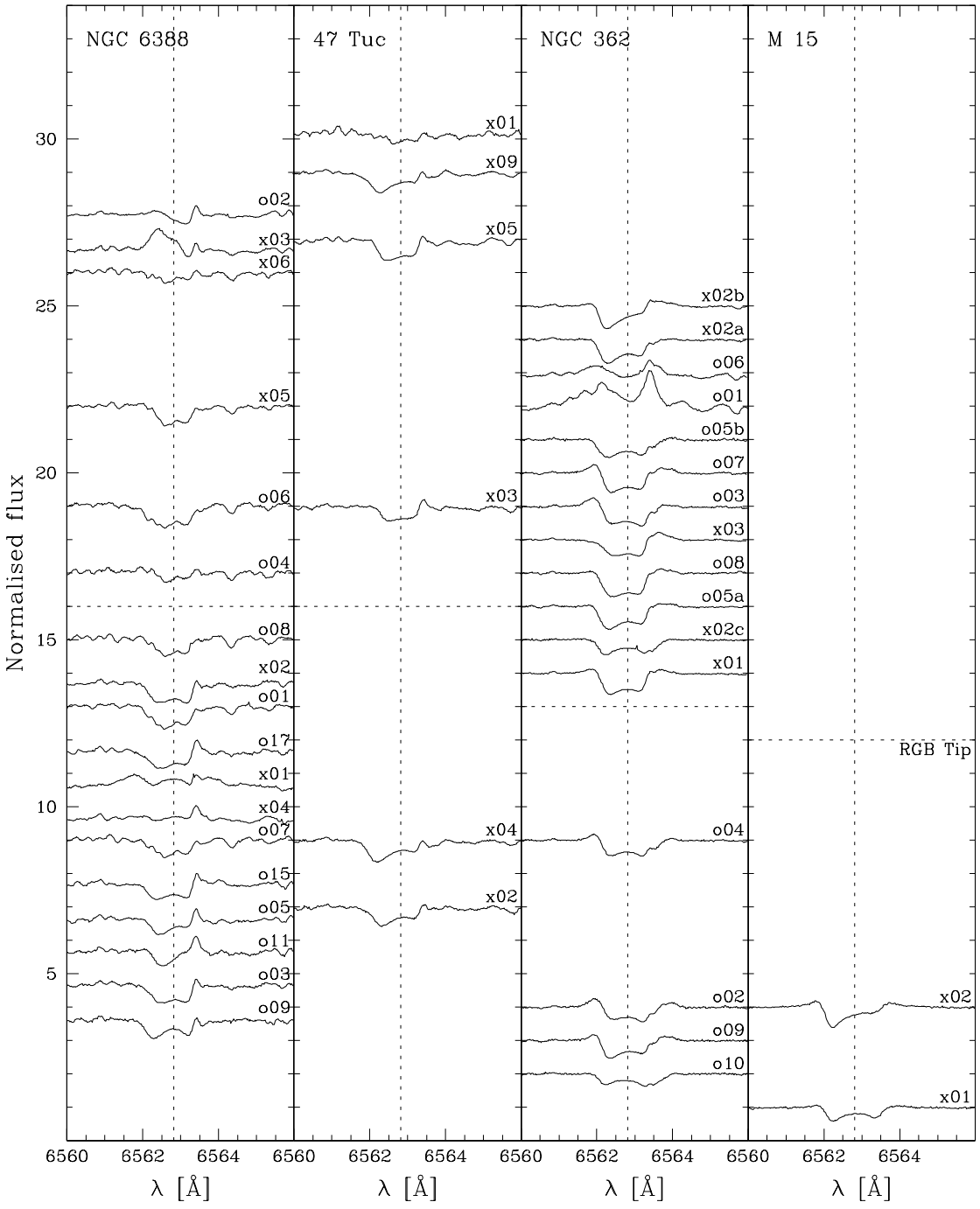

Figure 3.12: As Fig. 3.11 but with spectra sorted by luminosity (most luminous at top).

fewer strong spectral lines to mask their signature, the complete lack of apparent line wing emission in the high-metallicity stars is striking. This may mean that mass loss from metal-poor stars is dominated by their chromospheres longer in the evolution of the star. Note that the deep Hα line, blue asymmetry and emission appear to disappear for the cool stars (which are *not* the most luminous) in NGC 6388. We remind the reader that we cannot readily differentiate whether stars below ≈2400 $L_\odot$ are on the RGB or AGB, which could confuse these results.

3.7.4 Mass-loss rates and wind velocities

The calculated mass-loss rates can be found in Table 3.9, which also includes the following semi-empirically-determined mass-loss rates from Reimers (1975), SC05 and Nieuwenhuijzen & de Jager (1990, hereafter NdJ90), respectively (in $M_\odot$ yr^{-1}):

$$\dot{M}_{\rm R75} = 4 \times 10^{-13} \eta \frac{LR}{M} \tag{3.17}$$

$$\dot{M}_{\rm SC05} = 8 \times 10^{-14} \frac{LR}{M} \left(\frac{T_{\rm eff}}{4000{\rm K}} \right)^{3.5} \left(1 + \frac{g_\odot}{4300 g_*} \right) \tag{3.18}$$

$$\dot{M}_{\rm NdJ90} = 9.631 \times 10^{-15} L^{1.42} M^{0.16} R^{0.81}, \tag{3.19}$$

for luminosity L, radius R, mass M in solar units and stellar and solar gravities g_* and $g_\odot$ (see Table 3.3, where $M = 0.8$ $M_\odot$ has been adopted); and a semi-empirically determined constant η, which is usually in the range $0.4 < \eta < 3$ (Stancliffe & Jeffery 2007), with $\eta \sim 0.5$ being most favoured (SC05). Although values up to $\eta = 10$ have been used effectively in specific cases (*e.g.* Straniero et al. (1997) in modelling for intermediate-mass field stars), whereas SC05 express η in terms of $T_{\rm eff}$ and g, based on a heuristic model for the chromospheric driving of mass-loss. In this work, we assume $\eta = 1$, as it provides a closer match to the SC05 results. We also compare our results to those of OFFR02, who determine mass-loss rates near-independently (save for identical photometry with which we have calculated the stellar parameters) and Gratton (1983),

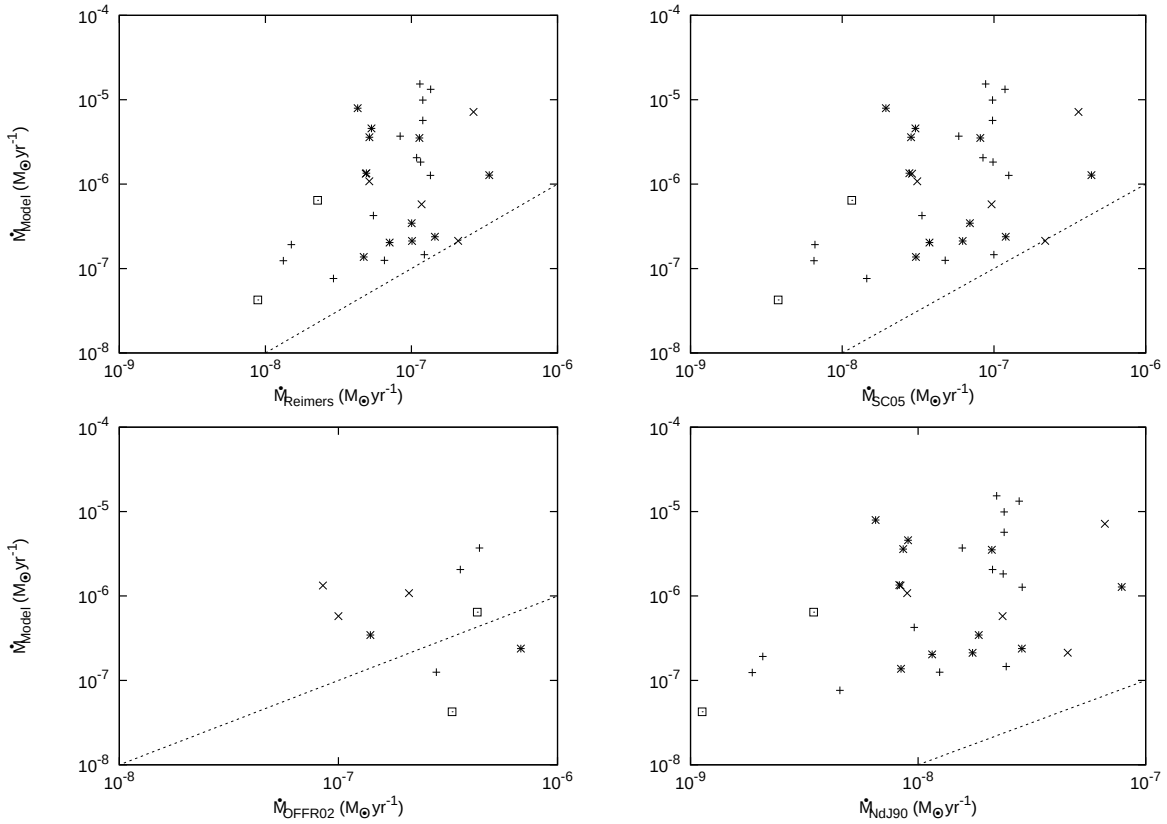

Figure 3.13: Comparison of estimated mass-loss rates from our modelling, Reimers (1975), OFFR02, SC05 and NdJ90. Key: NGC 362: plus-signs, 47 Tuc: crosses, NGC 6388: asterisks, M 15: open squares. The dashed lines indicate a one-to-one correlation. Our mass-loss rates are very weakly correlated with, but significantly higher than those predicted by Reimers, SC05 and NdJ90, but in reasonable agreement with those observationally determined by OFFR02, which are determined through measured dust masses and dust temperatures.

which is discussed later in this section. OFFR02 use dust masses inferred from infrared colours and scale them to estimate the total mass loss, via a gas-to-dust ratio, for which they adopt:

$$M_{\rm gas}/M_{\rm dust} = 200 \times 10^{-([{\rm Fe/H}]+0.76)}. \tag{3.20}$$

Fig. 3.13 shows a comparison between the first five methods in Table 3.9. Although they weakly follow the predicted correlation with stellar parameters, all our targets clearly lie above the mass-loss rate predicted by all three semi-empirical relations. However, our mass-loss rates agree well with those determined by OFFR02 — the observed scatter is concordant with our expected errors. As the OFFR02 results are

derived independently from ours, it seems probable that our mass-loss rates — at least for the IR-excessive stars — are roughly correct.

The reason behind the lack of agreement with the semi-empirical relations is unclear, but could be influenced by several factors. Though Reimers' formula focussed on giants, the mass-loss rates for all three semi-empirical relations are mainly derived from, on average, more massive, more luminous and hotter stars than we see here. The Reimers and SC05 models also do not make allowances for winds influenced by dust or pulsation, which are undoubtedly important in some of our sample. It has also been suggested that the NdJ90 models use an unphysical prescription based on a mix of mass-loss rates from dust-driven and non-dust-driven sources (Schröder & Cuntz 2007). Furthermore, the models make no account of individual variations between stars outside of the parameters they use, such as pulsation phase and composition; they are also calibrated using only Galactic stars, and relations for stars at near-solar metallicities may not necessarily hold for low-metallicity environments such as these. Origlia et al.'s values, however, are calculated for each star individually using the DUSTY model (Nenkova, Ivezić & Elitzur 1999). The systematically higher mass-loss rates that we find with respect to the predictions from semi-empirical relations cannot be accounted for merely by a bias in the target selection procedure (§3.2), and it suggests instead that the efficiency of mass loss for low-mass, metal-poor red giants at the tip of the RGB and AGB is underestimated by the semi-empirical relations.

We find little correlation among our mass-loss rates, velocities and the other stellar parameters investigated. Perhaps the strongest correlation is between mass-loss rate and luminosity (Fig. 3.14), which shows a general increase in mass-loss rate with luminosity (hence evolution), in a similar fashion as is seen in more massive dust-enshrouded AGB stars in the Magellanic Clouds (*e.g.* van Loon, Marshall & Zijlstra 2005). Note that the coolest and most luminous stars which show the strongest emission have not been modelled, but are expected to have mass-loss rates near the top of this distribution, which would further enhance this correlation.

We also present the relationships between modelled wind velocity and computed escape velocity (Fig. 3.15) and wind momentum versus effective temperature (Fig. 3.16) after JS91. In the first instance, like JS91, we do not find any correlation between the two parameters, but we do find similiar average velocities around 10 km s^{-1}. Our wind momenta follow roughly the relation they suggest, but the momentum we derive appears to be several times lower for a given temperature. We suggest that this is due to the fact that our stars are less massive (likely $\sim$0.5–0.8 $M_{\odot}$, depending mostly on mass-loss history), wheras some of their sample could be up to 4 $M_{\odot}$. We do not find that wind velocity decreases with later spectral type (*c.f.* point four in JS91's conclusions). We also cannot support the claim that wind velocity increases with luminosity, as Cahn & Wyatt (1978) suggest for field stars. It is also noteworthy that the velocities we find are significantly lower than the escape velocity of the star. Given our results are most sensitive to the material within the first few stellar radii, this suggests that the material *must* receive an accelerating force long after it leaves the stellar surface. Once again, with their strong pulsations the coolest (unmodelled) stars are likely to have large wind momenta and thus contribute to the correlation observed. We do not find any correlation between metallicity and wind velocity, nor turbulent velocity (*c.f.* Gratton, Pilachowski & Sneden 1984).

Both Figs. 3.14 & 3.15 show broad scatter, the former particularly towards higher luminosities. The scatter is greater than typical errors, which can be estimated as around half an order of magnitude in $\dot{M}$ and 30–50% in v_{∞} (the errors in luminosity and escape velocity are comparatively negligible). This could possibly represent variation of mass-loss rate with pulsation phase or differences between the RGB and AGB. In both figures there are hints of a bimodality in both NGC 362 and NGC 6388 individually, and in the sample as a whole. A histogram in Fig. 3.17 shows that the distribution is indeed slightly bimodal, avoiding the mass-loss region of $\sim 10^{-6}$ $M_{\odot}$ yr^{-1}, though the strength of this bimodality depends sensitively on the size of the bins.

The cause of this bimodality is unclear. It may correspond to a 'on' and 'off' phases

of mass loss as the star expands and contracts, or may be related to chromospheric instability. The poor correlation with luminosity suggests it is not a product of different evolutionary phases, though considering there is only one star *clearly* above the RGB tip that shows low mass-loss, the bimodality may reflect a difference in mass-loss on the RGB and AGB. Were this the case, the Reimers and SC05 mass-loss laws would still hold for the weaker RGB winds, where dust and pulsation may not be important, though they would not apply to the stronger, dusty and/or pulsation-driven winds of the AGB stars.

It does, however, become difficult to explain the high mass-loss rates derived for these temperatures unless all the stars for which we have calculated a mass-loss rate are in a brief phase of particularly high mass loss. Using Cioni et al.'s models, we find that an (initially) 0.8 $M_\odot$ star loses 0.13 $M_\odot$ on the portion of the AGB above the luminosity of the RGB tip ($\approx$ 1900–2200 $L_\odot$, depending on metallicity) over a period of around 2.5 Myr, placing a limit on the *average* mass-loss rate of 5.2 $\times 10^{-7}$ $M_\odot$ yr^{-1} during that phase. Our average value from modelling is 4.2 $\times 10^{-6}$ $M_\odot$ yr^{-1}, and may be larger, depending on the mass-loss rates of the unmodelled, most luminous stars. Also, our highest mass-loss rates ($\gtrsim 4 \times 10^{-6}$ $M_\odot$ yr^{-1}) are among stars without IR excess or observed pulsation (except 47 Tuc x09), but also without strong evidence of chromospheric activity (line wing emission) in all but NGC 362 o07 and x01. These stars are mostly around spectra types K1–K3 and may have derived temperatures which are too low for their spectral type (see Fig. 3.1); the later type stars this applies to are all in the metal-rich NGC 6388 and the Hα line may be significantly affected by molecular lines that were not correctly modelled.

If we assume the presence of a chromosphere, we can reduce our derived mass-loss rates to lie more in line with theory. However, this may mean that the results given by OFFR02 are also too high. This could be due to incorrect assumptions on their part, particularly in the assumed gas-to-dust ratio (although that would require near-solar values even in metal-poor stars). We find no significant deviation between our mass-

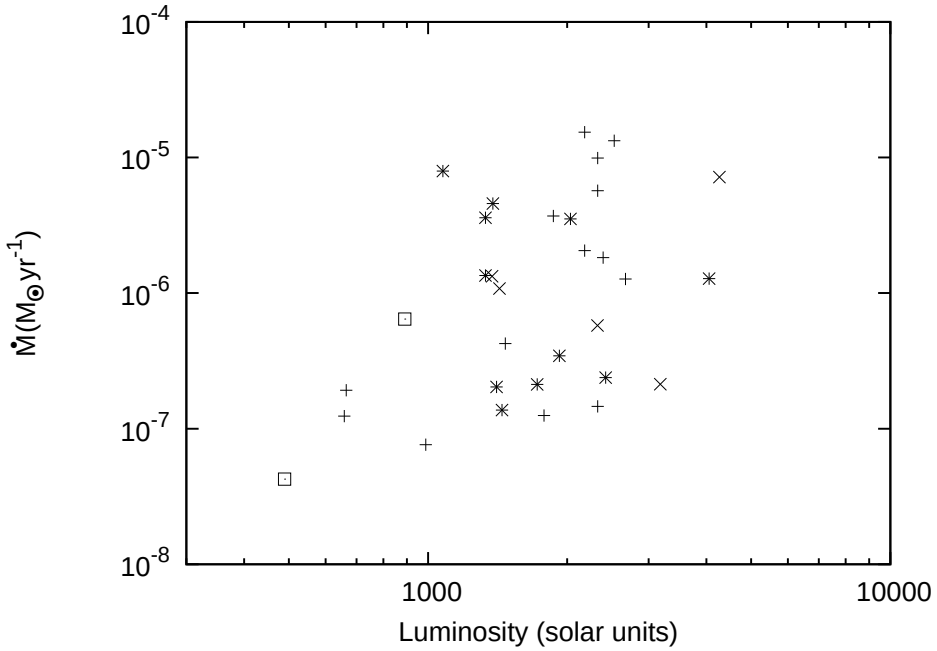

Figure 3.14: Variation of mass-loss rate with luminosity. Key is as in Fig. 3.13.

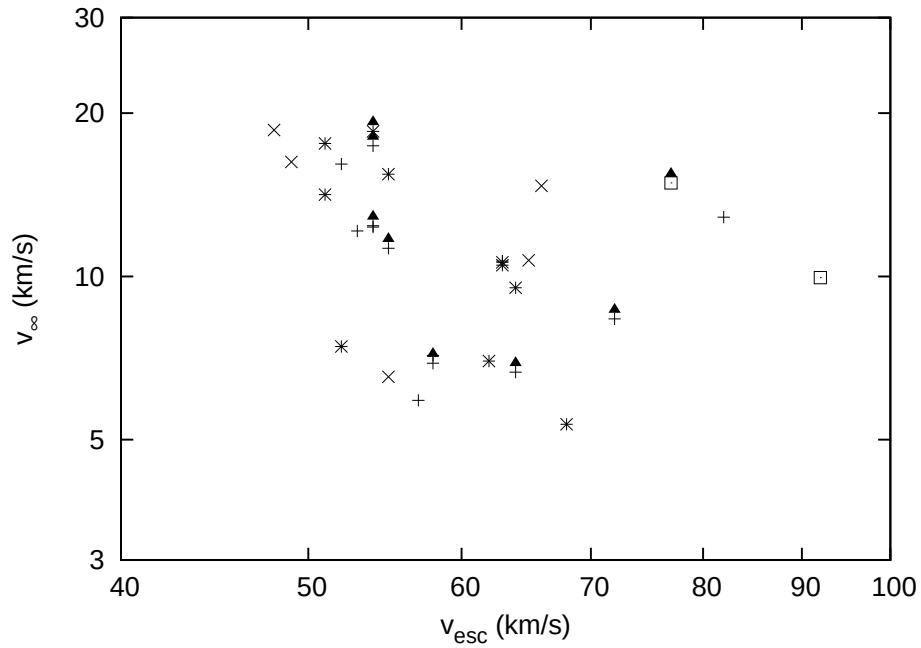

Figure 3.15: Variation of wind velocity with escape velocity. Key is as in Fig. 3.13. Attached triangles denote lower limits.

loss rates and those of Origlia et al. among the clusters, suggesting that their scaling of gas-to-dust with metallicity may be correct.

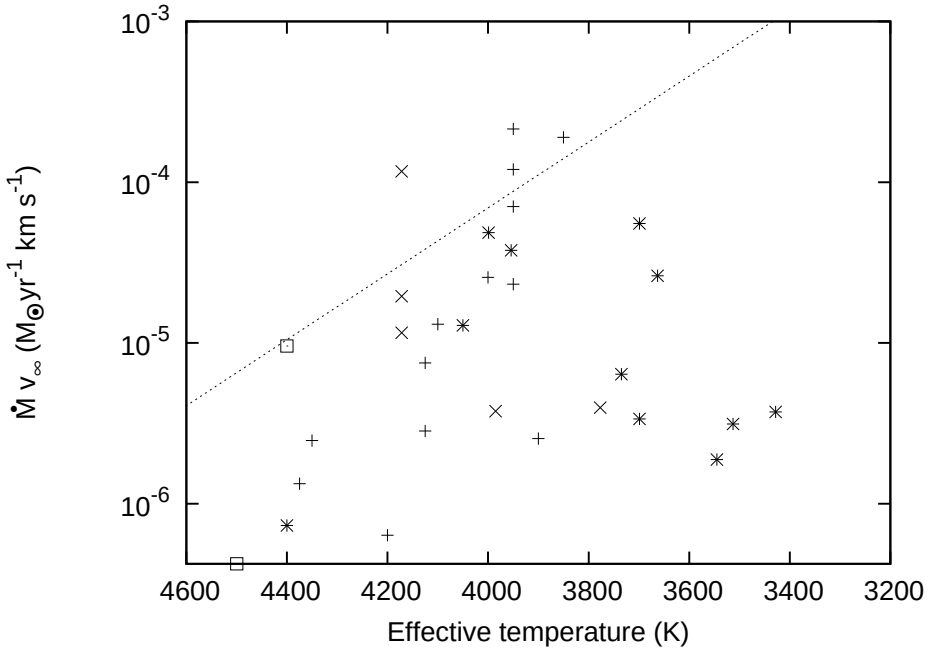

Figure 3.16: Variation of wind momentum with stellar effective temperature. Key is as in Fig. 3.13. The dotted line represents the fit by Judge & Stencel (1991) for field giants.

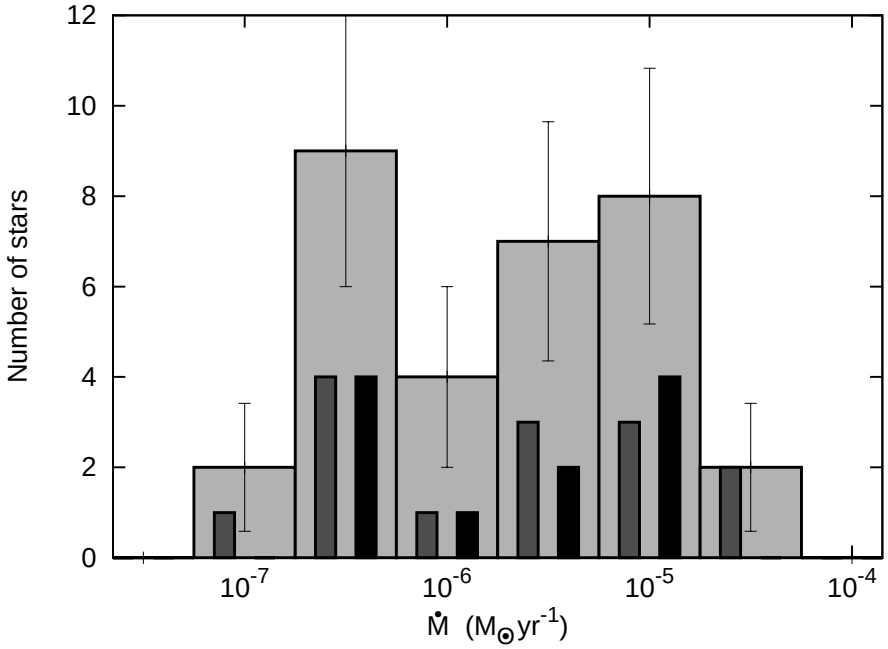

Figure 3.17: Histogram of mass-loss rate. The entire sample is represented in light grey, with the corresponding Poissonian errors; NGC 362 is shown on the left of each bin in dark grey and NGC 6388 is shown in black on the right of each bin. Note the bimodality seen both in each cluster and the sample as a whole.

3.7.5 Shell temperatures and chromospheres

In order to further explore the properties of the chromosphere and outflow, we also compute mass-loss rates from the Hα emission wings using the formula modified from Cohen (1976):

$$\dot{M} = \frac{4}{3}\eta v_\infty R_* (R_s W_\lambda)^{0.5} e^{-1.1/T_4}, \tag{3.21}$$

(in $M_\odot$ yr^{-1}) where R_s is the radius of the shell in stellar radii (assumed to be around $2R_*$, though this value is not critical when compared to the uncertainty in the other parameters), W_λ is the equivalent width (in Å) of the emission line (see Table 3.9), and T_4 is the temperature of the shell in units of 10^4 K. The constant η has been given as 6.6×10^{-10} by Gratton 1983), which we adopt here; and as 2.4×10^{-11} by Cacciari & Freeman (1983) (both derived using G & K stars). The origin of the difference between these two values is unclear. The factor $\frac{4}{3}$ arises from the conversion from hydrogen mass-loss rate to total mass-loss rate (ignoring molecular hydrogen).

It should be noted that Cohen's model (used by Gratton and Cacciari & Freeman) bases the outflow velocity on the peak of the emission wing. These velocities are typically a factor ∼4 larger than the velocities we obtain from modelling the absorption profile. We follow their procedure and estimate the velocity from the emission wings, which are listed in Table 3.10. Gratton (1983) calculates T_4 as:

$$T_4 = 10^{-4} \frac{T_*}{1 + (T_*/2.2 \times 10^4) \ln[R_s^2/W_\lambda]}, \tag{3.22}$$

produces temperatures of typically around 2400–2550 K for all stars due to the terms in the denominator. It is difficult to see how a shell at this temperature could produce the substantial amount of emission seen. On the contrary, exploration of our model suggests that the shell temperatures must be $\gtrsim 6000$ K in order to produce the observed line profiles, though we cannot determine this accurately using only the physics we have incorporated into the model. This latter figure would be in better agreement with other predictions, such as those of Falceta-Gonçalves, Vidotto & Jatenco-Pereira (2006). We

assume a shell temperature of 8500 K (following Dupree, Hartmann & Avrett (1984)). The mass-loss rates thus computed with Eq. (3.21) are listed in Table 3.9 and plotted in Fig. 3.18 where we compare them with the mass-loss rates from our model. There is a fair correlation and agreement between Gratton's and our models, except that our model suggests an order of magnitude higher rates for some of the more extreme stars.

The velocities we list in Table 3.10 are from the line wing emission peaks, for consistency with the previous works. They are identical within the ∼5–10% error to those velocities found from measuring the peak of the residual spectrum after subtraction of our model. Interestingly, these velocities are comparable to the escape velocity found at around ∼3 R_*. Assuming the shell is at roughly this radius from the star (both Gratton and Cacciari & Freeman assume 2 R_*), this weakens the need for a mechanism to drive the wind beyond this radius, thus allowing a situation where mass-loss can occur solely through the chromosphere. In the case of NGC 6388 o02, pulsation may already be strong enough to eject matter from the surface.

Additionally, an anti-correlation exists between escape velocity and wind velocity as measured by our model (Fig. 3.15); though it does not exist in the sample as a whole, the anti-correlation may be weakly seen on a per-cluster basis. This would suggest that gravity inhibits the wind acceleration.

3.7.6 Chromospheric disruption and the metallicity dependence of mass loss

Our observations suggest that, as luminosity increases and the stellar surface cools, the dominance of chromospheric activity is replaced by radial pulsation. Unless by coincidence the chromosphere switches off at the point where significant pulsation begins, it seems likely that pulsation may play a more active rôle in diminishing the chromospheric control on atmospheric behaviour. Either pulsation disrupts the mechanism responsible for heating the chromosphere, or the pulsation-induced shocks overrun the

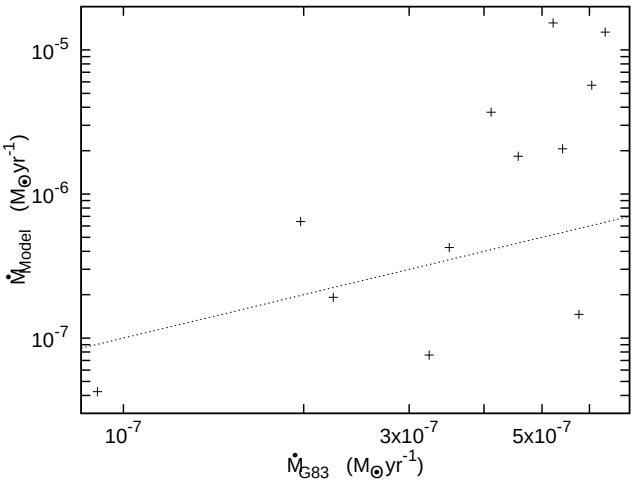

Figure 3.18: Comparison of mass-loss rates between the model of Gratton (1983) and our model. The dotted line indicates a one-to-one correlation. The expansion velocities used in the calculation of the Gratton mass-loss rate are taken from the emission peak, in keeping with their analysis.

chromosphere and displace the hot gas to further out in the wind where the shocks dissipate, turning the expanding column in front of the star (which provides absorption and hence blue asymmetry in the profile) into an emitting column of material. This leads to a weakening of the line core and the onset of the type of profiles seen in NGC 362 o01 and NGC 6388 x03, and then those seen in 47 Tuc x08 and ω Cen x01.

The transition from chromospheric activity to pulsation-related activity is not absolute, and the wide variety of profiles may represent either pulsation or a chromosphere dominating activity, depending on the phase of the pulsation cycle. This transition appears to happen around spectral type K3–K5.5 in NGC 362, with pulsation-related shocking becoming noticable at around spectral types M1–M2 in NGC 6388. This is much earlier than the ∼M5 spectral type for field stars found by JS91, which is highly suggestive of a metallicity relation among the three. This corresponds to temperatures of ∼3500 K in the field stars, ∼3700 K in NGC 6388 and ∼3800–4000 K in NGC 362 (see Fig. 3.1). As can be seen from Figs. 3.11 & 3.12, it is not clear from our sample whether the transition is more dependent on temperature or luminosity, though these temperatures would all roughly correspond to the RGB tip (see Figs. 3.3 & 3.4). It is

possible that our lack of differentiation between the RGB and AGB could be influencing our conclusions, though pulsation-induced shocks are only visible above the RGB tip. Interestingly, these temperatures also mark the divergence of the temperature vs. spectral type relations of Levesque et al. (Fig. 3.1), though it is not obvious why the two phenomena should be linked.

The fractional occurence of Hα emission was investigated by Gratton, Pilachowski & Sneden (1984), who find that 70% of stars above 500 $L_\odot$ (with no metallicity variation) and $\sim$80% of stars above 2000 $L_\odot$ show Hα emission in some form, though they did not differentiate between chromospheric-like emission and pulsation-related emission. Our data show 37% and 42%, respectively, for the same statistics. We have only one star (M 15 x01) below 500 $L_\odot$ and, of the remainder, ten (22%) are presumed to have chromosphere-induced emission and seven (15%) exhibit pulsation-induced emission (on the assumption NGC 6388 o02 exhibits pulsation-induced emission), with a strong metallicity bias towards the presence of emission in the two most metal-poor clusters. Clearly the results are disparate. This may be a result of a higher average metallicity of our sample (Gratton et al.'s sample averages [Fe/H] = -1.35 whereas ours averages [Fe/H] = -0.91), which in turn could affect the visibility of Hα emission through masking by stronger atomic or molecular lines due to higher abundances and lower temperatures. Their sample only contains two stars from 47 Tuc and none from NGC 362 or 6388, so we cannot perform a comparative study on individual clusters.

The mass-loss rates appear to be no different for stars in metal-poor and metal-rich clusters with similar properties, (Fig. 3.13) such as luminosity (Fig. 3.14). This correlates with the statement made by JS91, that mass-loss rate in this phase of evolution does not strongly depend on the driving process.

3.7.7 Subsequent work

Two recent studies have explored similar phenomenon to those described here, namely Mészáros, Dupree & Szentgyörgyi (2008) and Mészáros, Dupree & Szalai (2009). They

also refer to the similar study in NGC 2808 of Cacciari et al. (2004).

These three papers analyse high-resolution spectra of 370 stars in NGC 2808, M15, and M13 and M92. All three papers find that emission wings become prevalent on giants with $L \gtrsim 500\mathrm{L}_{\odot}$, $T \lesssim 4500$ K, and $R \gtrsim 30\ \mathrm{R}_{\odot}$. Their line bisector analysis suggests that outflow also appears to start at this point. Comparison to the Ca II K lines also shows that the outflow accelerates as it passes through the chromosphere. Velocities in the outflows increase with stellar luminosity, and do not appear to depend on metallicity. Where the stars are identifiable as being on the RGB or AGB, it also appears that AGB stars (with lower surface gravity and higher temperatures) show increased wind speeds.

There appears little evidence that the amount of chromospheric emission decreases in the most evolved stars in the metal-poor M15 and M92. However, the coolest stars of M13 do appear to show 'little or no outflow' in the Hα bisector (we presume they do still have significant mass loss via a slower, dusty wind).

3.8 Conclusions

In this study, we have presented VLT/UVES data of a set of giant branch stars in globular clusters, which are among the highest resolution, high signal-to-noise spectra of their kind. We use these to characterise and quantify the outflow from their atmospheres.

We have used Kurucz's ATLAS9 models to determine stellar temperature and, from this, we have calculated basic stellar parameters, which appear typical for red and asymptotic giant branch stars.

Many of the stars we have investigated show clear emission in Hα, most spectacularly when strong pulsation is present, which is seen to occur at luminosities above the RGB tip. It is also noted that many of the stars show strongly blue-shifted absorption cores, suggesting bulk outflow from the stellar surface. This is also mirrored in some

cases in the near-infrared calcium triplet line profiles.

In an effort to quantify this outflow, we have constructed a simple model for the warmer and more metal-poor stars. We have calculated terminal velocities for the winds which are of order 10 km s^{-1} — much lower than the escape velocity of the stars — and mass-loss rates of $\approx 10^{-7}$ to 10^{-5} $M_{\odot}$ yr^{-1}, which lie well above theoretical expectations, but are consistent with the mass-loss rates derived from IR emission from circumstellar dust. These models also suggest that an emissive shell exists close to the stellar surface in many stars, with the wind probably being largely isothermal beyond it. Outflow velocities of the emission are of order 40 km s^{-1}, and mass-loss rates derived from this emission are similar to the ones we obtain from modelling the absorption profile. In the most extreme cases we may have either over-estimated the mass-loss rate from our model, or under-estimated the temperature of the emitting shell. Mass-loss rates correlate weakly with luminosity, but stars showing strong IR excesses (linked with dust production) do not necessarily exhibit higher gas mass-loss rates. We find no correlation between mass-loss rate and metallicity.

We suggest that the emission and mass-loss in early-type ($\lesssim$ K3–K5) giants are dominated by a warm chromospheric region, as suggested by some studies, though late-type ($\gtrsim$ M3) giants have mass loss dominated by pulsation. It seems likely that the spectral type of the transition between the two regimes is metallicity-dependent, occurring at later spectral types for higher metallicities. The outward velocity of the warm emissive shells associated with the chromospheres is similar to the escape velocity at their anticipated radius (2 to 3 R_{*}), allowing the chromosphere to be the sole driver of mass loss in these stars.

Table 3.1: List of clusters observed.

NGC Number	[Fe/H]	Heliocentric Radial Velocity (km s^{-1})	Velocity Dispersion (km s^{-1})	Distance (kpc)	Absolute Visual Magnitude	Stars with(out) IR Excess			References
						With	Without	Unknown	
104 (47 Tuc)	–0.76	–18.7	11.5	4.5	–9.42	9	0	0	1
362	–1.16	223.5	7.5	8.5	–8.41	3	11	2	2
5139 (ω Cen)	–1.62†	232.2	19.6	5.3	–10.29	1	0	0	1
6388	–0.60	81.2	18.9	10.0	–9.42	6	12	0	3
6715 (M 54)	–1.58	141.9	14.2	26.8	–10.01	0	0	1	2
7078 (M 15)	–2.26	–107.0	11.0	10.3	–9.17	2	0	0	1

Metallicity, radial velocity and distance values from Harris (1996). Other references: 1 – Paturel & Garnier (1992); 2 – McLaughlin & van der Marel (2005); 3 – Gebhardt et al. (1997). †Metal-rich ([Fe/H] $\sim$ –0.6) and metal-intermediate (–1.3 < [Fe/H] < –1.0) populations are also believed to be present (Norris & da Costa 1995; Pancino et al. 2000; Sollima et al. 2005a).

Table 3.2: List of objects observed with positions, photometry and ancillary data.

Our ID	RA (J2000.0)	Dec (J2000.0)	J Mag	K Mag	IR Excess?	Other Names	Period (days)	Amplitude (K-band)	Notes
				NGC 362					
o01	01 03 15.1	–70 50 32	9.93	8.78	N	V16	138	0.5	7
o02	01 03 13.6	–70 50 59	10.27	9.51	N				
o03	01 03 13.8	–70 51 09	9.60	8.79	N				
o04	01 03 12.6	–70 50 38	10.05	9.13	N				
o05a	01 03 17.1	–70 50 50	9.91:	9.19:	N				2, 5
o05b	01 03 17.3	–70 50 50	9.95:	9.27:	N				2, 5
o06	01 03 13.6	–70 50 37	9.68	8.74	N			0.15:	7
o07	01 03 20.1	–70 50 55	9.58	8.75	N				
o08	01 03 10.7	–70 50 54	9.85	8.89	N				
o09	01 03 10.9	–70 50 59	10.66	9.83	N				
o10	01 03 14.7	–70 51 15	10.38	9.67	N				
x01	01 03 19.0	–70 50 52	9.96	8.96	Y				
x02a	01 03 14.7	–70 50 59	9.64:	8.27:	Y?				2
x02b	01 03 14.9	–70 51 00	9.82:	8.45:	Y?				2, 5
x02c	01 03 14.5	–70 50 59	10.45	9.64	Y				3, 5
x03	01 03 13.7	–70 51 14	10.10	8.82	Y				
				47 Tuc					
x01	00 24 02.6	–72 05 07	7.73	6.75	Y	LW10	110		
x02	00 24 07.8	–72 05 09	8.80	7.79	Y				
x03	00 24 09.4	–72 04 49	8.37	7.35	Y			0.15:	7
x04	00 23 57.7	–72 05 30	8.77	7.75	Y	LW8	27	0.15:	7
x05	00 24 23.2	–72 04 23	8.30	7.16	Y	LW19	40		
x06	00 24 08.6	–72 03 55	8.09	6.84	Y	V8?	155	0.3	7
x07	00 24 07.9	–72 04 32	7.82	6.56	Y	LW13	65		

Continued on next page

Table 3.2 – continued from previous page

Our ID	RA (J2000.0)	Dec (J2000.0)	J Mag	K Mag	IR Excess?	Other Names	Period (days)	Amplitude (K-band)	Notes
x08	00 25 16.0	–72 03 55	7.66	6.45	Y	V3	192	0.6	1, 7, 8
x09	00 25 09.2	–72 02 40	8.67	6.56	Y	V18	83		1
				NGC 6388					
o01	17 36 14.9	–44 43 12	10.73	9.31	N	V9			
o02	17 36 11.4	–44 44 08	10.02	8.80	N	V12		0.25:	7
o03	17 36 20.2	–44 44 32	11.01	9.65	N				
o04	17 36 17.6	–44 43 46	10.49	9.29	N				
o05	17 36 16.7	–44 43 28	10.86	9.64	N				
o06	17 36 17.7	–44 44 22	10.37	9.27	N				1
o07	17 36 15.5	–44 44 26	10.72	9.31	N				
o08	17 36 15.3	–44 44 31	10.91	9.47	N				
o09	17 36 18.9	–44 44 14	11.31	10.13	N				
o10	17 36 16.0	–44 43 49	10.73	9.72	N				
o11	17 36 20.4	–44 44 16	11.12	9.97	N				
o12	17 36 18.9	–44 44 04	11.09	9.81	N				
x01	17 36 18.1	–44 43 25	10.80	9.75	Y	V8?		0.4	7
x02	17 36 13.1	–44 43 05	10.65	9.47	Y				
x03	17 36 15.1	–44 43 33	10.27	8.99	Y	V3	156	0.3	7
x04	17 36 21.4	–44 43 42	11.15	9.87	Y				
x05	17 36 18.8	–44 43 46	10.60	9.25	Y				
x06	17 36 16.0	–44 44 36	10.64	9.19	Y				
				M 15					
x01	21 29 58.9	+12 10 18	11.1810.50	YAC761					
x02	21 29 58.2	+12 09 47	10.639.92	YAC414			9		
				M 54					
x01	18 55 04.5	–30 29 35	11.74	11.12	Y				

Continued on next page

Table 3.2 – continued from previous page

Our ID	RA (J2000.0)	Dec (J2000.0)	J Mag	K Mag	IR Excess?	Other Names	Period (days)	Amplitude (K-band)	Notes
				ω Cen					
x01	13 26 46.4	–47 29 30	9.70	8.75	Y	V42	149	0.5	7, 8

Notes: Astrometry/photometry from OFFR02 or their unpublished data unless noted otherwise. Photometry sources: (1) 2MASS (corrected to the photometric system of OFFR02); (2) UVES acquisition images (see text); (3) VFO04. Colons denote uncertain values. Astrometry sources: (4) 2MASS; (5) UVES acquisition images (see text); (6) VFO04. Variability sources: LW indicates variables from Lebzelter & Wood (2005). (7) Matsunaga (2007), Ita et al. (2007) or Matsunaga (private communication); (8) Feast, Whitelock & Menzies (2002). (9) Identified with 2MASS J21295815+1209466, which is bright at 24μm (M_{24} =1.66 – Boyer et al. 2006). AC identifiers are for (non-variable) sources from Aurière & Cordoni (1981).

Table 3.3: Stellar parameters derived from spectral typing and comparisons to model atmospheres.

ID	Spectral Type	*	Uncorrected Temperature (K)	Corrected Temperature (K)	Colour-Derived Temperature (K)	Radial Velocity (km s^{-1})	Luminosity ($L_\odot$)	Radius ($R_\odot$)	Escape Velocity (km s^{-1})
				NGC 362					
o01	K5.5	F	3954^{+77}_{-101}	3867^{+77}_{-101}	3337	2.5 ± 4.3	2415 ± 102	109 ± 5	53 ± 6
o02	K0	K	4200^{+250}_{-250}	4200^{+250}_{-250}	4191	9.3 ± 1.0	988 ± 86	59 ± 6	72 ± 10
o03	K1	K	3900^{+250}_{-250}	3900^{+250}_{-250}	4055	-16.7 ± 1.0	2327 ± 226	105 ± 12	54 ± 8
o04	K1	K	4125^{+250}_{-250}	4125^{+250}_{-250}	3782	-4.2 ± 0.3	1468 ± 131	75 ± 8	64 ± 9
o05a	K1	K	4100^{+250}_{-250}	4100^{+250}_{-250}	4527	-6.8 ± 0.3	2103 ± 189	91 ± 10	58 ± 9
o05b	K1	K	4125^{+250}_{-250}	4125^{+250}_{-250}	4527	-5.8 ± 0.3	2392 ± 213	95 ± 10	57 ± 8
o06	K5.5	F	3954^{+77}_{-101}	3867^{+77}_{-101}	3732	0.7 ± 2.7	2505 ± 105	111 ± 6	52 ± 6
o07	K3	K	3950^{+250}_{-250}	3950^{+250}_{-250}	4003	-8.6 ± 0.3	2327 ± 222	103 ± 12	54 ± 8
o08	K2	K	3850^{+250}_{-250}	3850^{+250}_{-250}	3682	7.3 ± 0.3	2182 ± 215	105 ± 12	54 ± 8
o09	K0	K	4350^{+250}_{-250}	4350^{+250}_{-250}	4003	10.3 ± 0.3	665 ± 54	45 ± 5	82 ± 12
o10	K0	K	4600^{+250}_{-250}	4600^{+250}_{-250}	4343	1.7 ± 0.4	659 ± 48	40 ± 4	87 ± 12
x01	K1	K	4000^{+250}_{-250}	4000^{+250}_{-250}	3589	-1.6 ± 0.3	1866 ± 175	90 ± 10	58 ± 9
x02a	K3	K	3950^{+250}_{-250}	3950^{+250}_{-250}	3232	-1.4 ± 0.3	2599 ± 248	109 ± 12	53 ± 8
x02b	K3	K	3950^{+250}_{-250}	3950^{+250}_{-250}	3232	6.2 ± 0.4	2824 ± 269	113 ± 13	52 ± 8
x02c	K0	K	4375^{+250}_{-250}	4375^{+250}_{-250}	4239	0.9 ± 0.3	2027 ± 164	78 ± 8	62 ± 9
x03	K2	K	3950^{+250}_{-250}	3950^{+250}_{-250}	3220	-4.1 ± 0.3	2182 ± 208	99 ± 11	55 ± 8
				47 Tuc					
x01	M4	F	3574^{+92}_{-140}	3351^{+92}_{-140}	3724	-7.4 ± 6.4	6172 ± 427	232 ± 19	36 ± 5
x02	K4	F	4147^{+82}_{-77}	4172^{+82}_{-77}	3659	7.2 ± 2.4	1375 ± 51	71 ± 3	66 ± 7
x03	K5	F	3993^{+77}_{-98}	3985^{+77}_{-98}	3639	-10.5 ± 0.6	2325 ± 103	101 ± 5	55 ± 6
x04	K4	F	4147^{+82}_{-77}	4172^{+82}_{-77}	3639	-5.6 ± 3.1	1427 ± 53	72 ± 3	65 ± 7
x05	M0	F	3895^{+98}_{-85}	3777^{+98}_{-85}	3427	10.4 ± 3.0	3180 ± 135	131 ± 6	48 ± 5

Continued on next page

Table 3.3 – continued from previous page

ID	Spectral Type	*	Uncorrected Temperature (K)	Corrected Temperature (K)	Colour-Derived Temperature (K)	Radial Velocity (km s^{-1})	Luminosity ($L_\odot$)	Radius ($R_\odot$)	Escape Velocity (km s^{-1})
x06	M5.5	F	3371^{+132}_{-132}	3144^{+132}_{-132}	3299	-2.7 ± 7.3	6463 ± 448	270 ± 22	34 ± 4
x07	M4	F	3574^{+92}_{-140}	3351^{+92}_{-140}	3290	4.5 ± 6.4	7352 ± 509	254 ± 21	35 ± 4
x08	M7	F	3188^{+125}_{-125}	2982^{+125}_{-125}	3340	-6.5 ± 11.7	10338 ± 711	380 ± 31	28 ± 4
x09	K4	F	4147^{+82}_{-77}	4172^{+82}_{-77}	2988	10.8 ± 2.6	4270 ± 158	125 ± 5	49 ± 5
					NGC 6388				
o01	M4	F	3574^{+92}_{-140}	3428^{+92}_{-140}	3578	4.4 ± 4.1	1820 ± 117	121 ± 9	50 ± 6
o02	M3	F	3666^{+70}_{-92}	3545^{+70}_{-92}	3328	-16.0 ± 4.0	4055 ± 171	168 ± 8	43 ± 5
o03	K3	K	4050^{+250}_{-250}	4050^{+250}_{-250}	3218	23.8 ± 0.3	1331 ± 122	74 ± 8	64 ± 10
o04	M0	F	3895^{+98}_{-85}	3808^{+98}_{-85}	3352	31.7 ± 3.0	2168 ± 79	107 ± 5	53 ± 6
o05	K5	F	3993^{+77}_{-98}	3999^{+77}_{-98}	3328	3.4 ± 3.1	1380 ± 54	77 ± 3	63 ± 7
o06	M1	F	3810^{+85}_{-74}	3735^{+85}_{-74}	3488	3.1 ± 2.5	2312 ± 77	115 ± 4	52 ± 6
o07	K4	K	4400^{+250}_{-250}	4400^{+250}_{-250}	3194	7.2 ± 0.8	1445 ± 115	65 ± 6	68 ± 10
o08	M2	F	3736^{+74}_{-70}	3663^{+74}_{-70}	3185	-19.5 ± 3.8	2032 ± 66	112 ± 4	52 ± 6
o09	M1.5	F	3773^{+79}_{-72}	3699^{+79}_{-72}	3376	5.9 ± 3.0	1077 ± 35	80 ± 3	62 ± 7
o10	K5.5	F	3954^{+77}_{-101}	3954^{+77}_{-101}	3659	-16.4 ± 2.6	1331 ± 54	78 ± 4	63 ± 7
o11	M3.5	F	3620^{+81}_{-116}	3513^{+81}_{-116}	3411	0.1 ± 8.4	1406 ± 74	101 ± 6	55 ± 6
o12	M4	F	3574^{+92}_{-140}	3428^{+92}_{-140}	3273	-12.5 ± 11.3	1722 ± 111	117 ± 9	51 ± 6
x01	M3.5	F	3701^{+72}_{-81}	3585^{+72}_{-81}	3578	-0.1 ± 4.4	1644 ± 61	105 ± 5	54 ± 6
x02	M1	F	3810^{+85}_{-74}	3735^{+85}_{-74}	3376	-5.7 ± 2.4	1923 ± 64	104 ± 4	54 ± 6
x03	M1.5	F	3773^{+79}_{-72}	3699^{+79}_{-72}	3273	-19.6 ± 3.4	3076 ± 101	135 ± 5	48 ± 5
x04	M3	F	3666^{+70}_{-92}	3545^{+70}_{-92}	3273	26.4 ± 4.0	1514 ± 64	103 ± 5	54 ± 6
x05	M1.5	F	3773^{+79}_{-72}	3699^{+79}_{-72}	3224	7.9 ± 2.4	2421 ± 79	119 ± 5	51 ± 5
x06	M3	F	3666^{+70}_{-92}	3545^{+70}_{-92}	3182	9.2 ± 3.6	2831 ± 119	141 ± 7	47 ± 5
					M 15				
x01	G8	K	4500^{+250}_{-250}	4500^{+250}_{-250}	4448	-14.7 ± 7.7	489 ± 37	36 ± 3	92 ± 13

Continued on next page

Table 3.3 – continued from previous page

ID	Spectral Type	*	Uncorrected Temperature (K)	Corrected Temperature (K)	Colour-Derived Temperature (K)	Radial Velocity (km s^{-1})	Luminosity ($L_\odot$)	Radius ($R_\odot$)	Escape Velocity (km s^{-1})
x02	G8	K	4400^{+250}_{-250}	4400^{+250}_{-250}	4343	10.3 ± 5.1	891 ± 71	51 ± 5	77 ± 11
					M 54				
x01	K2	K	3800^{+250}_{-250}	3800^{+250}_{-250}		-182.9 ± 0.2			
					ω Cen				
x01	M5.5	F	3371^{+132}_{-132}	2675^{+132}_{-132}	3707	44.3 ± 26.2	2111 ± 161	213 ± 19	38 ± 5

Notes: Column 3: F – from spectral typing, using Fluks et al. (1994); K – derived from Kurucz's ATLAS9 models (see §3.3). The colour-derived temperature is from (J–K) colours, from Houdashelt, Bell & Sweigart (2000) (see text). Radial velocity is relative to the mean motion for the cluster from Harris (1996), listed in Table 3.1. See text for details on M54 x01 and ω Cen x01. Formal errors have been assigned on the basis of a 0.1 dex uncertainty in metallicity, a 100 pc uncertainty in distance and a 0.1 $M_\odot$ error in mass.

Table 3.4: Radial velocities of the Hα and Ca II lines.

ID	Hα profile appearance	Hα velocity 6563 Å		Ca II velocity 8498 Å		Ca II velocity 8542 Å		Ca II velocity 8662 Å	
		Core	Kink	Core	Kink	Core	Kink	Core	Kink
				NGC 362					
o01	MOL, BE, RE	3.3[c]	–3.1[ca]	4.0	10.5	–0.9	10.9	–0.6	6.7
o02	PHOT, be	–1.9:	4.8[a]	2.7[d]	0.6[d]	2.2[b]	2.2[b]	1.9[b]	1.9[b]
o03	PHOT, be	0.7	5.0[a]	1.7	3.5	1.3	4.0	1.3	3.9
o04	PHOT, be	–2.4:	6.5[a]	0.5	1.7	0.7	2.7	0.1	2.1
o05a	PHOT, re?	–6.5	–0.4	1.5[b]	1.5[b]	0.9[b]	0.9[b]	0.0	2.0
o05b	PHOT, wide	–1.8:	0.9[a]	2.0[b]	2.0[b]	0.0	2.0	0.5	2.9
o06	phot, BE, RE	–1.6:	2.5[a]	2.8[b]	2.8[b]	1.0	2.2	1.3	4.2
o07	PHOT, be, re	–6.2	4.1[a]	3.5[b]	3.5[b]	–0.8	4.8	3.3[b]	3.3[b]
o08	PHOT, re	–7.9:	–0.1	1.3	1.8	0.8	2.0	1.5	2.5
o09	PHOT, be, re	–5.4:	2.0[a]	–0.5	1.4	–1.9	2.6	1.0	1.5
o10	PHOT	2.9	9.3[a]	2.1	5.1	2.9	6.0	2.5	6.4
x01	PHOT, be?, re	–3.8:	0.4[a]	2.0[b]	2.0[b]	–2.0	2.9	0.4	4.1
x02a	PHOT, asy	–10.1	2.6[a]	–1.8	1.5	–5.4	1.3	–2.1	2.2
x02b	PHOT, asy, re	–12.5	–1.7	1.0[b]	1.0[b]	–4.3	–0.0	–1.5	0.9
x02c	PHOT	–1.5:	–3.3[a]	1.5[b]	1.5[b]	0.9[b]	0.9[b]	0.6	2.0
x03	PHOT, RE	–3.5	1.0	1.4[d]	–2.1[d]	–7.2	–0.1	0.0	–2.1
				47 Tuc					
x01	MOL	.....	0.7:	2.8	0.8:[b]	0.8:[b]	2.0:	0.0:	
x02	PHOT, asy	–8.8	–0.9	–0.9:	1.2:	–6.7	–0.1[a]	–1.0:	0.5:
x03	PHOT, narrow	–1.0	4.4	4.4[d]	0.4[d]	–1.9	4.2	0.0:	3.0:
x04	PHOT, asy	–6.5:	–1.9[a]	–4.1	1.5	–6.2	2.7	–7.0:	0.5:
x05	PHOT, mol	–4.8	4.0[a]	–1.0	1.7	–2.6	1.8	–1.5:	1.0:
x06	Noisy continuum	.....	.....	–0.5:	1.0:[a]	0.0:	1.0:[a]		

Continued on next page

Table 3.4 – continued from previous page

ID	Hα profile appearance	Hα velocity 6563 Å		Ca II velocity 8498 Å		Ca II velocity 8542 Å		Ca II velocity 8662 Å	
		Core	Kink	Core	Kink	Core	Kink	Core	Kink
x07	Noisy continuum	.....	6.0:[d]	0.1:[d]	4.7[b]	4.7[b]	–1.0:	1.0:[a]	
x08	BE, RE	–5.0:	–2.0:[a]	1.0:	3.0:[a]	0.0	1.5:[a]	0.3	1.0:[a]
x09	PHOT, asy	–7.8	–0.9[a]	–4.6	–0.3	–7.9	–1.2	–8.0:	–1.5:[a]
				NGC 6388					
o01	PHOT, mol	–6.7	0.6	–0.4	1.6	–3.9	1.6[a]	–1.3	1.4
o02	phot	4.7	9.5	8.5[d]	–0.4:[d]	3.1	7.4	7.0	1.4:[d]
o03	PHOT	–4.4	0.9	–1.7	1.2	–0.6[b]	–0.6[b]	–2.7	0.5
o04	phot	–2.3:	0.1	0.1[b]	0.1[b]	–2.8	–0.6[a]	–1.6	–0.1
o05	PHOT, asy	–9.7	2.6[a]	1.0[b]	1.0[b]	–2.3	0.6	–1.8	1.0
o06	PHOT, mol	–6.7	–0.5	–0.1[b]	–0.1[b]	–5.0	–0.3[a]	–3.3	–0.7
o07	phot, mol, asy	–5.7	1.9	–0.6	1.0	–3.5	–0.9	–2.3	–0.3:
o08	phot, mol	–2.3	0.6	–0.5	1.8	–1.0	0.8	–0.2	1.2
o09	PHOT, wide	–0.0:	2.0	1.7[d]	–0.1[d]	1.1[b]	1.1[b]	1.2[b]	1.3[b]
o10	PHOT, asy	–7.4	–2.6[a]	4.5[d]	2.1:[d]	–0.2	3.3	1.9[b]	1.9[b]
o11	PHOT, be?	1.0[b]	1.0[b]	0.7[b]	0.7[b]	–0.1[b]	–0.1[b]	0.8[b]	0.8[b]
o12	PHOT, mol	–6.3	–0.6	0.0	1.6	–2.6:	–0.8[a]	–2.5	0.7
x01	phot, BE, RE	–0.9	1.9	4.1[d]	0.4:[d]	3.7[d]	–3.4[d]	3.3	–1.6[d]
x02	PHOT	–3.7	2.6	0.2[b]	0.2[b]	–1.8	0.9	–0.8	1.2
x03	BE	24.3[c]	19.4[c]	17.0[d]	1.9:[d]	11.7[d]	–4.7:[d]	14.7[d]	–0.2:[d]
x04	phot, mol	–2.3:	2.9	0.4[b]	0.4[b]	0.5[b]	0.5[b]	0.6[b]	0.6[b]
x05	PHOT, mol, asy	–3.3	6.0[a]	–0.5	2.8	–3.3	1.7	–1.2	3.3
x06	MOL	1.0:[b]	1.0:[b]	2.8:[d]	–0.4:[d]	–2.6	0.3	0.5[b]	0.5[b]
				M 15					
x01	PHOT	–4.2	3.3[a]	0.1[d]	–1.7[d]	0.0[d]	–3.6[d]	–0.1[b]	0.1[b]
x02	PHOT, be, re?	–12.9	–0.5[a]	1.2	2.7	0.8	2.4	–1.7	3.9

Continued on next page

Table 3.4 – continued from previous page

ID		Hα profile appearance	Hα velocity 6563 Å		Ca II velocity 8498 Å		Ca II velocity 8542 Å		Ca II velocity 8662 Å	
			Core	Kink	Core	Kink	Core	Kink	Core	Kink
					ω Cen					
x01	BE, re		–3.0[c]	–4.0[c]	+1.0[c]	+0.5[c]	+0.5[c]	–1.8[c]	0.0[c]	–4.0[c]

Positive values denote red-shifts (in km s^{-1}). Colons denote ill-defined values due to noise. Abbreviations: phot – photospheric profile visible; asy – asymmetric; mol – molecular bands; be/re – blue/red emission wing; capitalisation indicates strong features. Notes: [a] kink not present, value given near continuum level; [b] no significant velocity shift in bisector, approximate average given; [c] core at a greater red-shift than kink or no kink, due to an emission line or ([d]) unusual profile.

Table 3.5: List of the parameters used in the SEI model fits.

ID	Photospheric			Chromospheric (top) & Wind (bottom)									Other		
	a_p	w_p	w_g	w_0	γ	τ_{tot}	α_1	α_2	w_1	ϵ_0	$\frac{B_v}{I_c}$	a_T	v_∞ (km s^{-1})	χ^2/σ^2	R_{chrom} (R$_*$)
NGC 362															
o02	8.00	0.32	0.23	0.70	0.14	0.04	0.0	–1.0	0.95	2.0	2.2	–8.5	59	1.9 $\times10^{-3}$	1.40
				0.01	0.20	0.30	0.0	0.0	1.00	1.0	1.0	3.0			
o03	5.20	0.38	0.19	0.78	0.05	0.35	0.0	0.0	0.98	2.0	1.0	–4.5	57	0.6 $\times10^{-3}$	1.20
				0.01	0.10	0.06	–1.0	0.0	1.00	1.0	0.5	3.0			
o04	4.50	0.45	0.17	0.78	0.05	0.30	0.0	0.0	0.98	2.0	1.0	–4.5	52	0.5 $\times10^{-3}$	1.20
				0.01	0.12	0.35	–1.0	0.0	1.00	1.1	0.5	3.0			
o05	2.30	0.34	0.30	0.70	0.02	0.30	0.0	0.0	0.97	1.0	1.5	–1.0	64	0.6 $\times10^{-3}$	1.01
				0.01	0.30	1.40	–1.5	0.0	1.00	0.0	0.0	0.0			
o06	1.00	0.34	0.23	0.70	0.20	0.22	0.0	0.0	0.90	3.0	1.0	–4.0	62	3.8 $\times10^{-3}$	1.15
				0.01	0.50	0.15	–1.0	0.0	1.00	1.0	0.1	3.0			
o07	9.00	0.34	0.21	0.70	0.18	0.14	0.0	0.0	0.92	1.0	1.3	–9.0	59	0.8 $\times10^{-3}$	1.20
				0.01	0.20	0.80	–1.3	0.0	1.00	1.0	1.3	3.0			
o08	9.50	0.35	0.28	0.70	0.22	0.28	0.0	0.0	0.90	1.0	1.0	–6.0	55	0.3 $\times10^{-3}$	1.20
				0.01	0.30	1.60	–1.3	0.0	1.00	1.0	0.3	3.0			
o09	9.00	0.34	0.21	0.70	0.19	0.11	0.0	0.0	0.92	1.0	1.3	–9.0	59	0.8 $\times10^{-3}$	1.25
				0.01	0.20	1.00	–1.2	0.0	1.00	1.0	1.3	3.0			
ob2	4.00	0.37	0.22	0.70	0.20	0.35	0.0	0.0	0.90	1.0	1.0	–5.0	62	0.4 $\times10^{-3}$	1.15
				0.13	0.70	1.90	–3.1	0.0	1.00	1.0	0.1	3.0			
oa5	5.50	0.38	0.28	0.70	0.20	0.26	0.0	0.0	0.90	1.0	1.0	–6.0	57	0.4 $\times10^{-3}$	1.15
				0.01	0.30	2.30	–1.5	0.0	1.00	1.0	0.3	3.0			
x01	3.00	0.44	0.26	0.70	0.20	0.32	0.0	0.0	0.90	1.0	1.0	–7.0	59	0.6 $\times10^{-3}$	1.15
				0.01	1.00	2.20	–1.5	0.0	1.00	0.0	0.0	0.0			
x02	6.00	0.28	0.21	0.40	0.12	0.17	0.0	0.0	0.90	1.0	1.0	–3.0	80	2.0 $\times10^{-3}$	1.30

Continued on next page

Table 3.5 – continued from previous page

ID	Photospheric			Chromospheric (top) & Wind (bottom)									Other		
	a_p	w_p	w_g	w_0	γ	τ_{tot}	α_1	α_2	w_1	ϵ_0	$\frac{B_v}{I_c}$	a_T	v_∞ (km s^{-1})	χ^2/σ^2	R_{chrom} (R$_*$)
				0.01	0.12	0.04	–2.0	0.0	1.00	1.0	1.0	2.0			
xa2	4.00	0.38	0.12	0.70	0.20	0.10	0.0	0.0	0.90	1.0	1.5	–4.0	64	0.6 $\times 10^{-3}$	1.15
				0.01	0.12	0.20	–1.5	0.0	1.00	0.3	0.5	+0.0			
								M 15							
x01	3.50	0.39	0.05	0.70	0.20	0.08	0.0	0.0	0.90	1.0	1.0	–4.0	64	0.6 $\times 10^{-3}$	1.15
				0.01	0.12	0.03	–1.0	0.0	1.00	0.3	0.5	0.0			
x02	3.50	0.39	0.15	0.70	0.20	0.20	0.0	0.0	0.90	1.0	1.5	–4.0	64	1.6 $\times 10^{-3}$	1.15
				0.01	0.10	0.67	–2.0	0.0	1.00	0.3	0.5	0.0			

Table 3.6: Fitted Hα line profiles using the wind model described in §3.6.

Cluster	ID	$\dot{M}$ ($M_\odot$ yr^{-1})	v_∞ (km s^{-1})	τ_{ph}	v_{turb} (km s^{-1})	χ^2_r	*
NGC 362	o02	7.6×10^{-8}:	> 8.4	1.93	9.2	240	a
	o03	1.5×10^{-7}:	>17.4	2.38	7.8	432	a
	o04	4.3×10^{-7}:	> 6.7	1.96	10.3	386	a
	o05a	1.8×10^{-6}	7.2	1.60	13.0	604	b
	o05b	1.3×10^{-6}	5.9	1.53	15.2	495	b
	o07	5.7×10^{-6}:	>12.4	1.78	8.0	427	a
	o08	1.5×10^{-5}	12.3	1.94	7.8	507	a
	o09	1.9×10^{-7}:	>12.9	1.74	9.1	233	a
	o10	-1.2×10^{-7}	-5.9	1.12	19.3	167	c
	x01	3.7×10^{-6}:	> 6.9	1.60	9.7	660	b
	x02a	9.9×10^{-6}	12.1	1.63	11.4	373	a
	x02b	1.3×10^{-5}	16.1	0.84	11.5	350	a
	x02c	1.3×10^{-7}	10.7	1.71	14.6	93	a
	x03	2.1×10^{-6}:	>11.3	1.89	7.1	499	a
47 Tuc	x02	1.3×10^{-6}	14.7	1.58	8.2	277	a
	x03	5.8×10^{-7}	6.5	1.39	7.2	165	a
	x04	1.1×10^{-6}	10.7	1.22	18.9	478	b
	x05	2.1×10^{-7}	18.6	1.90	8.0	938	a
	x09	7.2×10^{-6}	16.3	1.68	6.0	504	a
NGC 6388	x02	3.5×10^{-7}	18.5	2.04	10.1	412	b
	x05	2.4×10^{-7}	14.2	1.38	8.3	446	a
	o02	1.3×10^{-6}:	$\gtrsim$1.5	0.37	14.3	420	b
	o03	1.4×10^{-6}	9.5	1.72	8.5	598	a
	o05	4.6×10^{-6}	10.6	0.55	12.6	293	b
	o07	1.4×10^{-7}	5.3	0.01	34.0	92	a
	o08	3.5×10^{-6}	7.4	0.84	10.7	190	a
	o09	7.9×10^{-6}	7.0	1.99	12.3	407	a
	o10	3.6×10^{-6}	10.5	0.41	0.7	489	b
	o11	2.0×10^{-7}:	15.4:	1.81	8.6	1066	a
	o12	2.1×10^{-7}:	17.6:	1.70	11.1	1112	b
M 15	x01	4.3×10^{-8}	10.0	1.60	14.0	45	a
	x02	6.4×10^{-7}:	>14.9	1.24	13.6	175	a

Notes: Fits are to an isothermal, isovelocital wind, without a chromosphere. The value χ^2_r is a *relative* goodness-of-fit parameter. The coolest stars are not included due to strong interference from molecular bands (see text). Errors are discussed in §3.6.2. Values denoted ':' are uncertain: see §3.6.4. *(a) normalised using a continuum taken at ± (55–70) km s^{-1} from Hα; (b) at −70 to +70 km s^{-1}; (c) normalised as (a), but uses an inflowing wind (see text).

Table 3.7: Properties of stars with and without IR excess in clusters NGC 362 and NGC 6388.

Property	Objects with:	
	No excess (24)	Excess (23)
Effective Temp. (K)	3886 ± 280 ± 57	3893 ± 327 ± 103
	Hα	
Core offset	–3.5 ± 4.3 ± 0.9	–0.4 ± 9.1 ± 2.9
Kink offset	1.9 ± 3.3 ± 0.7	3.5 ± 6.1 ± 1.9
Velocity range	–5.4 ± 3.9 ± 0.8	–3.8 ± 5.2 ± 1.6
	Ca II 8498 Å	
Core offset	1.5 ± 2.2 ± 0.4	2.7 ± 5.3 ± 1.7
Kink offset	1.9 ± 2.2 ± 0.5	0.8 ± 1.4 ± 0.4
Velocity range	–0.4 ± 2.7 ± 0.6	1.9 ± 5.3 ± 1.7
	Ca II 8542 Å	
Core offset	–0.7 ± 2.2 ± 0.5	–0.6 ± 5.3 ± 1.7
Kink offset	2.2 ± 2.9 ± 0.6	0.0 ± 2.3 ± 0.7
Velocity range	–2.8 ± 2.6 ± 0.5	–0.6 ± 7.3 ± 2.3
	Ca II 8662 Å	
Core offset	0.3 ± 2.3 ± 0.5	1.6 ± 4.8 ± 1.5
Kink offset	2.0 ± 1.9 ± 0.4	1.0 ± 2.0 ± 0.6
Velocity range	–1.7 ± 2.3 ± 0.5	0.6 ± 5.8 ± 1.8
	Ca II Average	
Core offset	0.4 ± 2.0 ± 0.4	1.3 ± 5.0 ± 1.6
Kink offset	2.0 ± 2.1 ± 0.4	0.6 ± 1.6 ± 0.5
Velocity range	–1.6 ± 2.1 ± 0.4	0.6 ± 5.9 ± 1.9

c.f. Table 3.8.

Table 3.8: Properties of all stars in clusters NGC 362 and NGC 6388.

	All objects in:	
	NGC 362 (12)	NGC 6388 (18)
Effective Temp. (K)	4221 ± 186 ± 46	3713 ± 219 ± 52
	Hα	
Core offset	–3.3 ± 4.6 ± 1.3	–1.7 ± 7.4 ± 1.8
Kink offset	2.5 ± 3.6 ± 1.0	2.7 ± 4.9 ± 1.2
Velocity range	–5.8 ± 4.5 ± 1.3	–4.4 ± 3.9 ± 0.9
	Ca II 8498 Å	
Core offset	1.9 ± 1.3 ± 0.4	2.1 ± 4.5 ± 1.0
Kink offset	3.0 ± 2.7 ± 0.8	0.9 ± 0.9 ± 0.2
Velocity range	–1.1 ± 2.1 ± 0.6	1.2 ± 4.5 ± 1.1
	Ca II 8542 Å	
Core offset	0.2 ± 1.9 ± 0.6	–0.5 ± 3.8 ± 0.9
Kink offset	3.4 ± 2.9 ± 0.8	0.4 ± 2.5 ± 0.6
Velocity range	–3.2 ± 3.2 ± 0.9	–0.9 ± 5.2 ± 1.2
	Ca II 8662 Å	
Core offset	0.9 ± 1.3 ± 0.4	0.7 ± 4.3 ± 1.0
Kink offset	3.2 ± 1.8 ± 0.5	0.7 ± 1.1 ± 0.3
Velocity range	–2.3 ± 2.0 ± 0.6	0.0 ± 4.6 ± 1.1
	Ca II Average	
Core offset	1.0 ± 1.2 ± 0.3	0.7 ± 4.1 ± 1.0
Kink offset	3.2 ± 2.4 ± 0.7	0.7 ± 1.2 ± 0.3
Velocity range	–2.2 ± 2.2 ± 0.7	0.1 ± 4.5 ± 1.1

Notes: The other clusters have been excluded to reduce selection effects. The first error column gives the standard deviation from the mean of the sample, the second error is the error in the mean. Velocity range is defined by kink velocity (or redmost velocity when the kink is not present) minus core velocity. Units are km s^{-1}, except where noted.

Table 3.9: Estimated mass-loss rates and equivalent widths (EW) of the Hα line profile emission contribution.

ID		EW	$\dot{M}$ (10^{-7}M$_\odot$yr^{-1})					
		(Å)	(a)	(b)	(c)	(d)	(e)	(f)
NGC 362	o01			1.3	1.1	0.26		
	o02	0.14	0.8	0.3	0.15	0.05		3.2
	o03	0.14	1.5	1.2	1.0	0.24		5.8
	o04	0.10	4.3	0.6	0.34	0.10		3.5
	o05a	0.11	18	1.0	1.3	0.19		4.6
	o05b		13	1.4	0.99	0.29		
	o06			1.4	1.2	0.28		
	o07	0.18	57	1.2	0.98	0.24		6.1
	o08	0.13	154	1.1	0.88	0.22		5.2
	o09	0.11	1.9	0.15	0.07	0.02		2.2
	o10		–1.2	0.13	0.07	0.02		
	x01	0.10	37	0.8	0.59	0.16	4.4	4.1
	x02a		99	1.4	0.98	0.29		
	x02b	0.16	133	1.6	1.2	0.34		6.4
	x02c		1.3	0.8	0.48	0.16	2.8	
	x03	0.16	21	1.1	0.85	0.21	3.6	5.4
47 Tuc	x01			7.2	13.8	1.85	2.5	
	x02		14	0.5	0.29	0.08	0.9	
	x03		5.8	1.2	0.96	0.24	1.0	
	x04		11	0.5	0.31	0.09	2.1	
	x05		2.1	2.1	2.2	0.45	11	
	x06			8.7	17.8	2.23	4.8	
	x07			9.3	21.1	2.55	3.4	
	x08			19.6	64.5	5.73	46$^{(g)}$	
	x09		72	2.7	3.6	0.66		
NGC 6388	o01			1.1	0.71	0.19		
	o02	0.34	13	3.4	4.4	0.78		20.1
	o03		14	0.5	0.28	0.08		
	o04			1.2	0.88	0.22		
	o05		46	0.5	0.30	0.09		
	o06			1.3	1.1	0.26		
	o07		1.4	0.5	0.31	0.08		
	o08		35	1.1	0.81	0.21		
	o09		79	0.4	0.19	0.07		
	o10		36	0.5	0.28	0.09		
	o11		2.0	0.7	0.38	0.12		
	o12		2.1	1.0	0.62	0.17		
	x01			0.9	0.52	0.15	1.4	
	x02		3.5	1.0	0.69	0.18	1.4	

Continued on next page

Table 3.9 – continued from previous page

ID		EW	$\dot{M}$ (10^{-7}M$_\odot$yr^{-1})					
		(Å)	(a)	(b)	(c)	(d)	(e)	(f)
	x03			2.1	2.09	0.44	2.2	
	x04			0.8	0.44	0.13	1.2	
	x05		2.4	1.4	1.20	0.29	6.8	
	x06			2.0	1.87	0.41	2.3	
M 15	x01	0.03	0.4	0.09	0.04	0.01	3.3	0.9
	x02	0.06	6.4	0.23	0.12	0.03	4.3	2.0
ω Cen	x01			2.3	1.67	0.38		

Equivalent widths are determined using residuals from the model fits. Mass-loss rates determined using or quoted from: (a) our model (§3.6); (b) Reimers (1975), (c) Schröder & Cuntz (2005); (d) Nieuwenhuijzen & de Jager (1990); (e) Origlia et al. (2002); (f) Gratton (1983), assuming a shell temperature of 8500 K and using the peak of the emission wing as v_∞; (g) rate for 47 Tuc x08 from Frogel & Elias (1988), using similar methods to Origlia et al. The errors on these values are large and discussed in the text.

Table 3.10: Comparison of wind velocities and escape velocities.

ID		Velocity (km s^{-1})				
		v_∞			$v_{\rm esc}$	
		Core	Model	Wing	R$_*$	3 R$_*$
		(a)	(b)	(c)	(d)	(e)
NGC 362	o02	1.9	8.4	43.5	72	41
	o03	–0.7	17.4	43	54	31
	o04	2.4	6.7	44.5	64	37
	o05a	6.5	7.2	41	56	32
	o07	6.2	12.4	40.5	54	31
	o08	7.9	12.3	41	54	31
	o09	5.4	12.9	43	82	47
	x01	3.8	6.9	42.5	58	34
	x02b	12.5	16.1	43.5	53	31
	x03	3.5	11.3	40	55	32
NGC 6388	o02	–4.7	1.5	60	43	25
M 15	x01	4.2	10.0	44.5	92	53
	x02	12.9	14.9	47	77	45

Velocities: (a) blueshifted Hα line core velocity; (b) v_∞ from our model; (c) line wing emission velocity (averaged where both wings show emission); (d) escape velocity at surface; (e) escape velocity at 3 R$_*$. The emission in NGC 6388 o02 may be due to pulsation, but it is included here for completeness.

4 A *Spitzer* atlas of ω Centauri

"The true harvest of my life is intangible — a little star dust caught, a portion of the rainbow I have clutched"

— Henry David Thoreau (1817–1862)

This chapter is a summary of Boyer, McDonald, van Loon, Woodward, Gehrz, Evans, & Dupree, AJ, 135, 1395, 2008.

Contribution: *as second author on this work, significant proportions of the work were carried out by my colleagues, as initialled throughout the text. Here, I contributed to the testing and refinement of the final photometric catalogue. I was also heavily involved in analysing our findings for the discussion used in the above article.*

4.1 Incentive

By creating a complete infra-red census of all evolved stars in a globular cluster, one can determine the fraction of stars that are dust-producing at any given evolutionary stage and the rates at which they lose mass. Through this, one can determine the total mass lost by the cluster and the evolutionary stages at which dust production is important. This is not only important for the very final stages of dust production, but also to the 'second parameter problem' (see §1.2.2.6). The following two chapters deal with the collection, reduction, and subsequent analysis of *Spitzer Space Telescope* observations of ω Centauri; and the analysis the dust producing stars and the calculation of their mass-loss rates.

4.2 Observations & photometry

Observations were led by JvL (*Spitzer* PID 20648). Image tiles (441 tiles of $5' \times 5' \times 10.4$ seconds) were taken with the Infrared Array Camera (IRAC) in all four filters (3.6, 4.5, 5.8 & 8 μm) on 26 March 2006. Correction of saturated targets was performed

using identical 0.4 second images. The imagery is limited by *Spitzer*'s size to 1.6–1.8″ resolution, with sensitivities giving 90% completeness down to between magnitudes 14.3 and 15.9 (8 and 3.6 μm, respectively).

Scan maps were also taken with Multiband Imaging Photometer (MIPS) (Fazio et al. 2004; Rieke et al. 2004) at 24 and 70 μm. In each filter, 4620 images were taken over seven scans. These images were taken on 22 February and 02 March 2006. The 24-μm images are limited to 5.3″ × 5.6″ resolution and a 90% completeness depth of magnitude 11.6. The 70-μm images do not have complete coverage over either the 35′ × 35′ IRAC or 35′ × 55′ MIPS fields as half of the 70-μm array was not working during the observations.

The tile maps were centred at $13^h\ 26^m45\overset{s}{.}9\ -47°28'37\overset{''}{.}0$ [J2000.0], and extended to at least 3.2× the cluster radius ($r_{\rm hm} = 4.8'$ — Harris 1996).

The IRAC and MIPS scan maps were mosaiced (Fig. 4.1) and photometry extracted and combined using DAOphot by MLB. Point-source extraction was performed using PSF-fitting. Extraction of artificially-inserted stars was performed to determine completeness limits. Fluxes were colour-corrected as described in the *Spitzer* Data Handbooks[1] using a 5000-K blackbody, representative of a typical RGB star, and converted to magnitudes using the Handbooks.

These observations were, for the first time, able to resolve the individual stars in the cluster at mid-infrared wavelengths several magnitudes below the RGB tip (*c.f.* previous ground- and space-based data in Origlia, Ferraro & Fusi Pecci 1995). The resulting *Spitzer* point source catalogue contains over 40 000 objects.

Objects were cross-identified among the wavebands using DAOphot and with Leiden Identifiers (LEIDs) from van Leeuwen et al. (2000). This catalogue was also used to identify the probability of cluster membership, unless a radial velocity was available from van Loon et al. (2007). In these cases, probability was set to 100% or 0%, depending on whether the star matched the cluster's radial velocity. In total, 7613

[1] http://ssc.spitzer.caltech.edu/irac/dh/

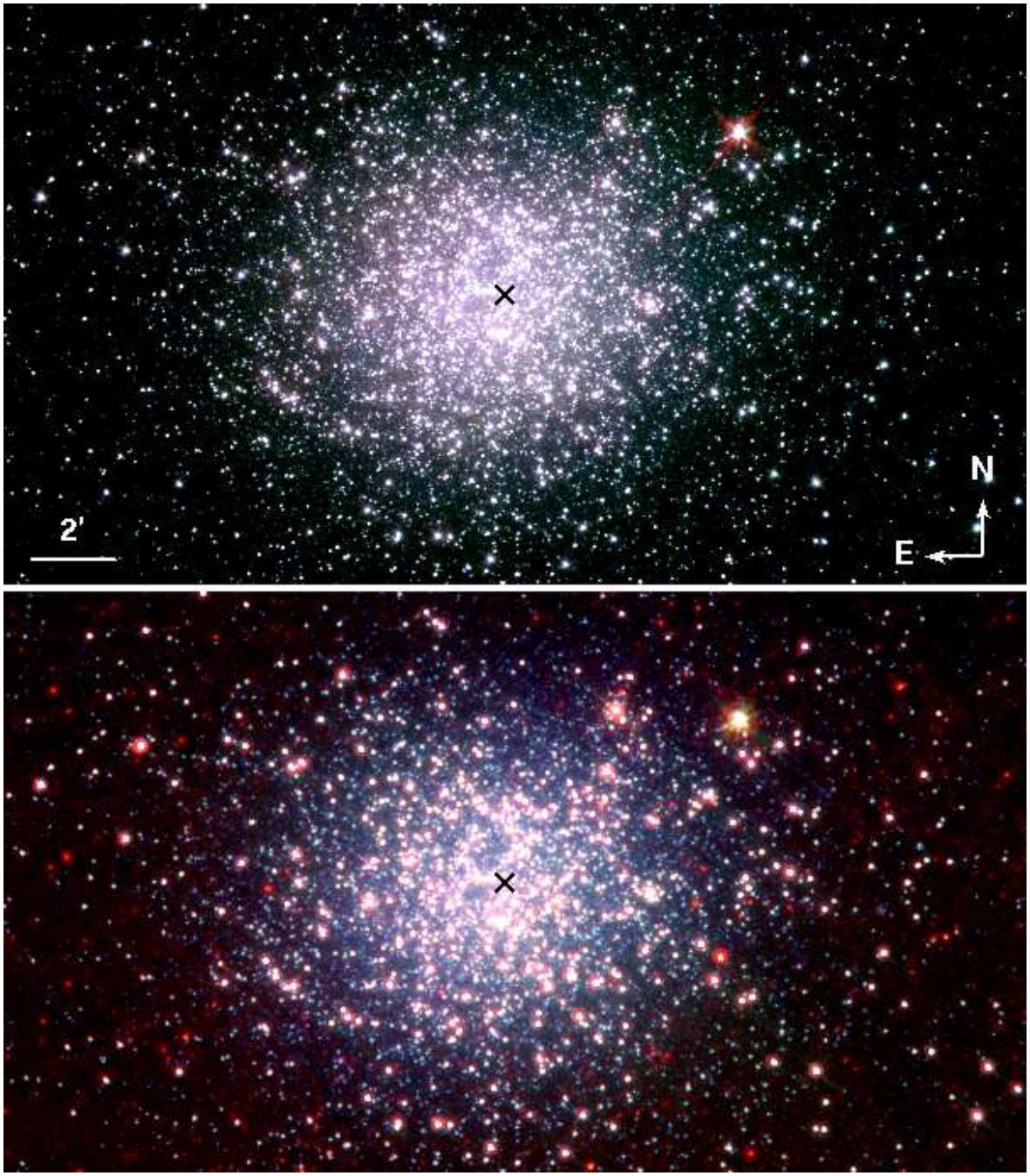

Figure 4.1: Upper panel: Blue is 3.6 μm, green is 4.5 μm and red is 5.8 μm. Lower Panel: Blue is 3.6 μm, green is 8 μm and red is 24 μm. The black X marks the cluster center. Faint, red objects in the lower panel are background galaxies that become more emissive at longer wavelengths. No obvious intra-cluster dust is visible.

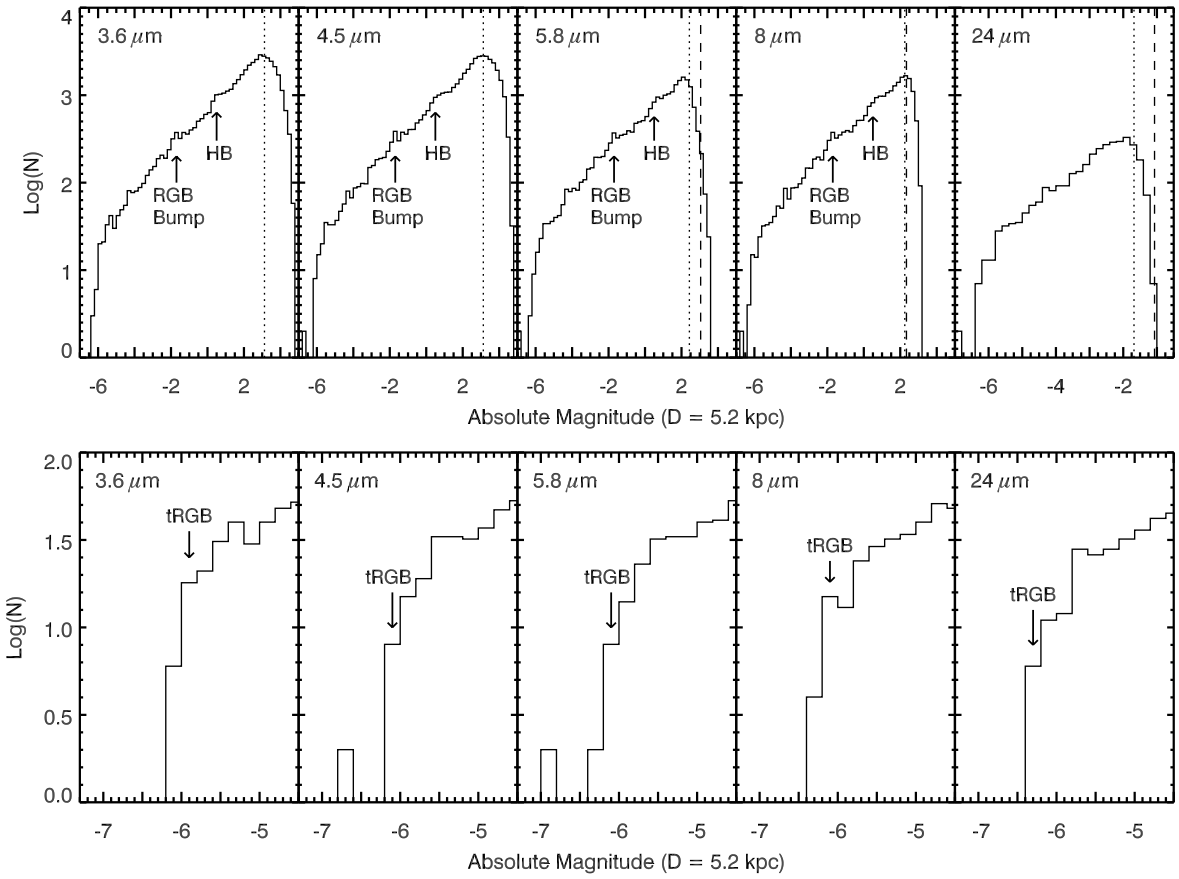

Figure 4.2: Luminosity histograms of point sources extracted from *Spitzer* observations of ω Cen. The horizontal branch and RGB bump and tip are denoted, as is the 50% completeness limit (dotted line). The upper panel shows all sources, the lower panel only those confirmed as cluster members through proper motion selection from van Leeuwen et al. (2000).

objects were found with LEIDs, 6579 of which were proper motion or radial velocity cluster members.

Blending was assessed by convolving the 8-μm image with the 24-μm PSF. Sources with significantly higher 8-μm fluxes in the convolved image were flagged as blended objects at 24 μm.

4.3 Results

4.3.1 Luminosity functions

Luminosity functions were also determined by MLB, and are shown in Fig. 4.2. In these, the RGB tip can be identified at absolute magnitudes of –5.9 ± 0.2 at 3.6 μm; –6.1 ± 0.2 at 4.5, 5.8 and 8 μm; and –6.3 ± 0.2 at 24 μm. This is comparable with the observed K-band RGB tip magnitude of –6.04 ± 0.16 (Bellazzini et al. 2004) and the RGB tip at [3.6] = –6.4 for similarly-aged LMC clusters (van Loon, Marshall & Zijlstra 2005).

The RGB bump and horizontal branch can also clearly be identified from the luminosity functions, at absolute magnitudes of ~ -2 and 0, respectively; as can the completeness limits at magnitudes of ~ -2 for the IRAC bands and $\sim +1.75$ for MIPS 24μm.

4.3.2 Colour-magnitude diagrams

Colour-magnitude diagrams (CMDs) for the cluster are shown in Fig. 4.3 and Fig. 4.4, which also includes the optical and near-IR observations from van Leeuwen et al. (2000) and the 2MASS catalogue (Skrutskie et al. 2006), used extensively in the next chapter.

Due to the close proximity of the colours and luminosities of RGB and AGB stars, the two giant branches are not well-separated in any of the colour-magnitude diagrams. This is exacerbated both by errors in computed magnitudes, which are typically 4–5%, and intrinsic variation within the cluster's stars. No differences are seen between the main RGB population and RGB-a, apart from perhaps a slight negative [3.6]–[4.5] colour for the RGB-a, possibly due to increased molecular absorption at 4.5 μm.

A population of background galaxies can be clearly identified in the [8]–[24] vs. [24] CMD. These objects are very faint at shorter wavelengths — most of them are not observed at all. Their position in the CMD clearly shows that they are apparently faint

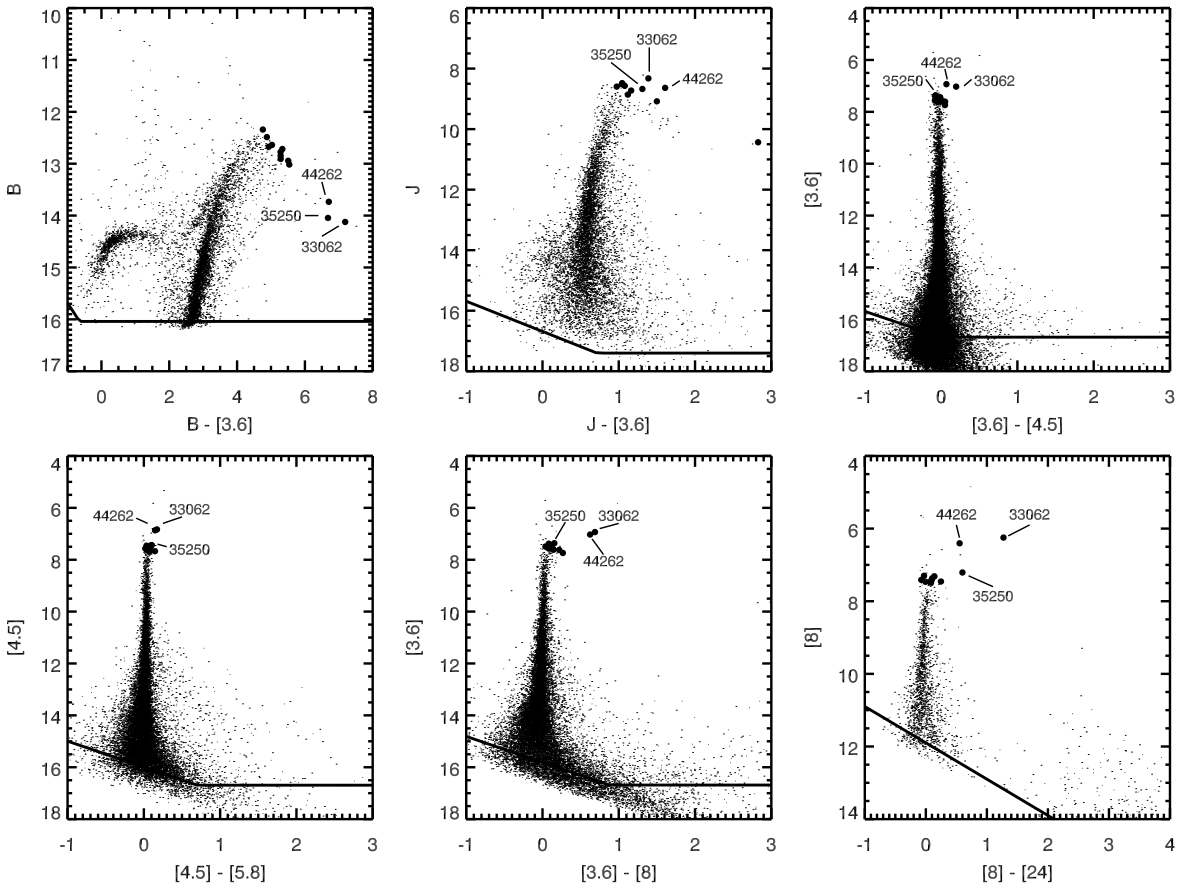

Figure 4.3: Colour-magnitude diagrams of ω Centauri, showing fluxes corrected for reddening (using $E(B-V) = 0.11$ mag; Lub 2002). B magnitudes are from van Leeuwen et al. (2000); J magnitudes from Sollima et al. (2004). The solid lines mark the detection limits in the optical/near-IR data. The three most extreme stars (V6 = LEID 33062, V42 = LEID 44262, V17 = LEID 35250) are marked. The large circles denote the brightest cluster members at 3.6 to 8.0 μm.

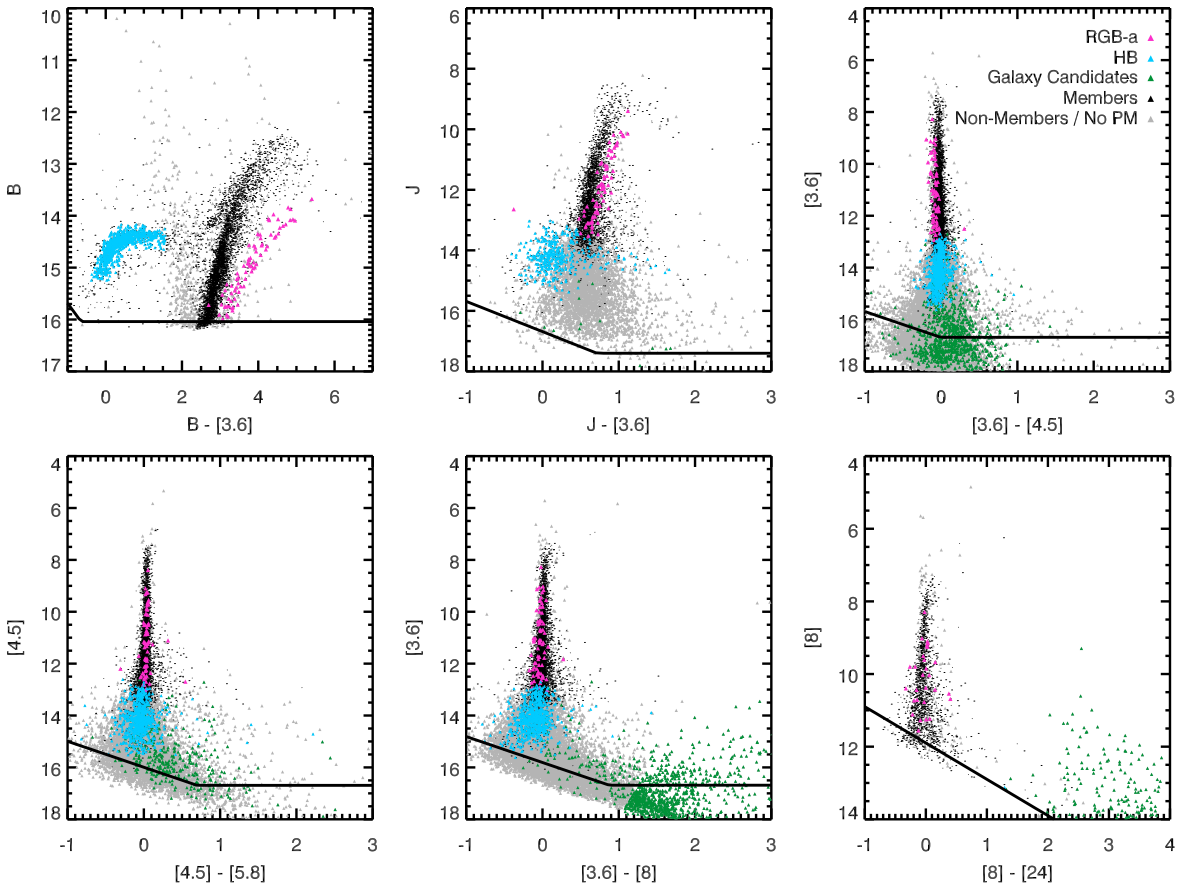

Figure 4.4: As Fig. 4.3, but showing evolutionary groups, including anomalous-RGB stars (RGB-a) and horizontal branch stars (HB).

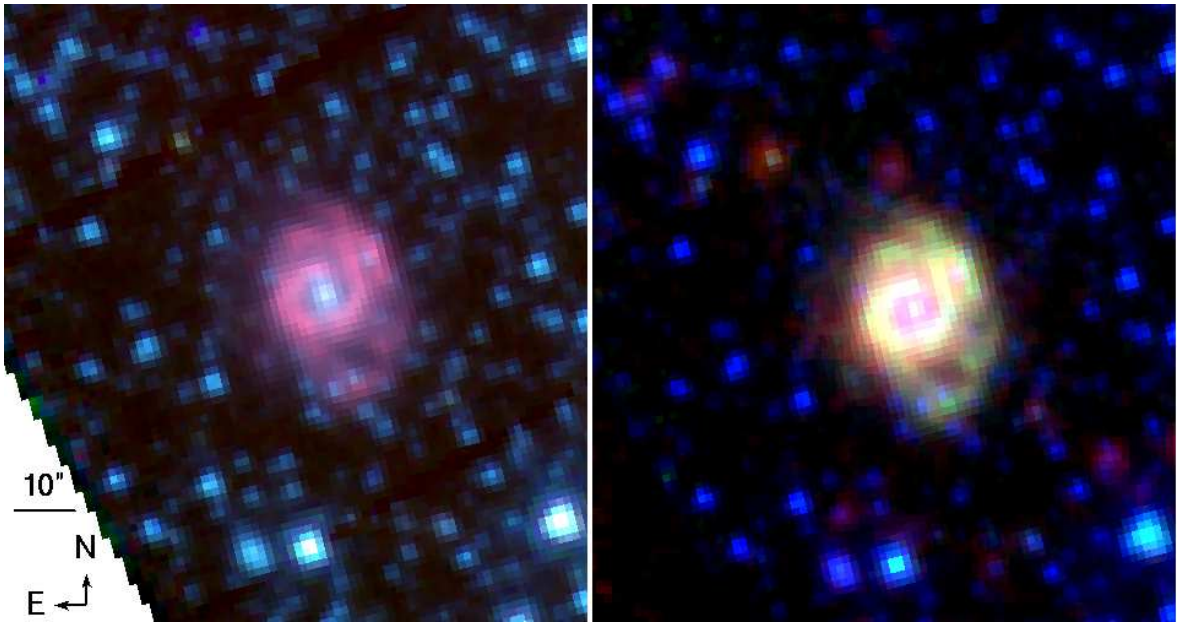

Figure 4.5: Three-colour images of the galaxy 2MASS J13272621–4746042, at 3.6, 4.5 and 5.8 μm (left) and 3.6, 8 and 24 μm (right).

and contain a very large, yet comparatively cold, dust component. Their identification as non-cluster sources can be determined from their ubiquity in the raster maps (they are not centrally condensed towards the cluster centre — Fig. 4.6). This is further corroborated by their colours, which match those of 2MASS J13272621–4746042 (Fig. 4.5), spectroscopically-confirmed to be a resolved background galaxy by AKD.

Nine sources are also observed in the incomplete 70-μm images (Fig. 4.7). These include the above galaxy (Fig. 4.5) and another source with no optical identification. Two of these objects were cross-identified by MLB with cluster members in van Loon et al. (2007): LEID 27094, otherwise normal RGB star with strong CH lines; and LEID 46055, which shows strong CH, CN and Ba lines, suggesting it is an AGB star that has undergone third dredge-up. All objects, including the confirmed members and background galaxy, show an apparent blackbody at 49–68 K. The temperatures of the two cluster stars were determined by blackbody fitting to be 4664 $\pm$ 19 K and 4329 $\pm$ 16 K, respectively. All other objects, with the exception of one star not covered in the original catalogue (Boyer et al. source 8) have blackbody-fitted temperatures too

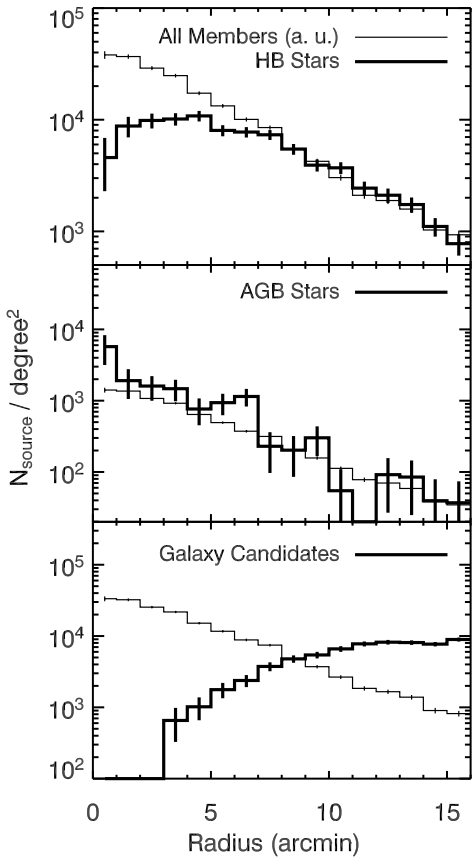

Figure 4.6: Radial source density profiles for all cluster members (arbitrary units), horizontal branch stars, AGB stars and galaxy candidates. Note that the galaxy candidates are distributed near-evenly at large radii, decreasing toward the core due to source confusion in the dense central regions. This may also explain the slight downturn in horizontal branch stars in the very centre.

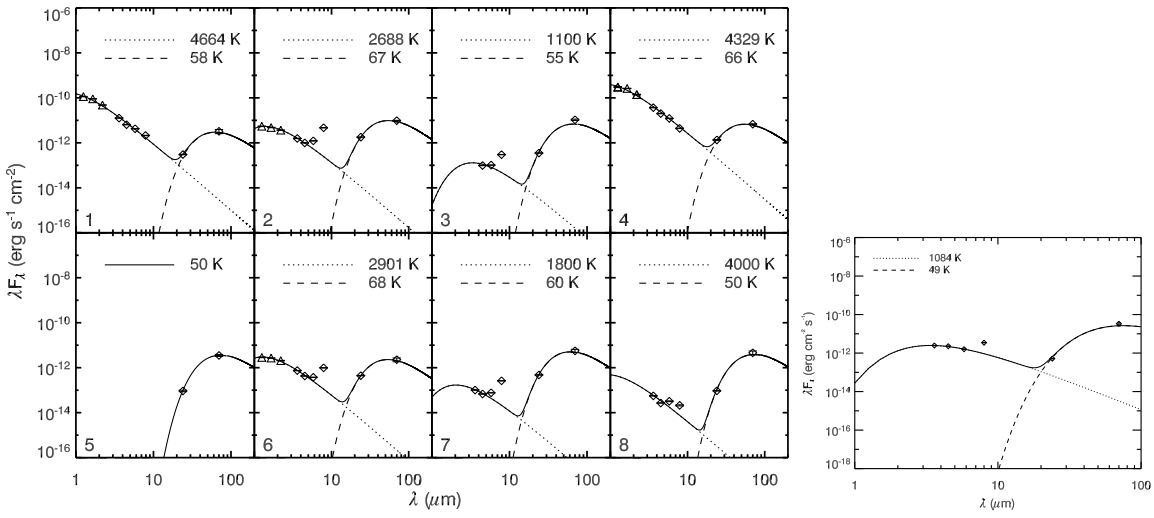

Figure 4.7: Spectral energy distributions of sources present in the 70-μm maps, showing fluxes corrected for a reddening of $E(B-V) = 0.11$ mag (Lub 2002). The right-most SED is of the resolved galaxy 2MASS J13272621–4746042.

low to be stars, unless they are surrounded by highly-attenuating dust envelopes with optical depths greater than those of the most-evolved stars. This is not thought to be the case, as though their [8]–[24] colours would suggest the presence of dust, their [24] magnitudes place them in the region containing numerous background galaxies. They also show excess emission at 5.8 and 8 μm , which could be attributable to PAH emission.

The expected number of stellar blends can be estimated from the galaxy candidate density at large radii, which is $\sim$9000 deg^{-2} (Fig. 4.6). Within a 6″-diameter MIPS 24-μm annulus, one can therefore expect to find $\sim$0.02 galaxies. With 1627 cluster members identified at 24 μm, one therefore expects $\sim$32 cluster members blended with galaxies. Such blending with galaxies (and nearby stars) was addressed (§4.2). However, there is a limit to how rigorously blending can be identified, set by the difference in magnitude between the blended stars and the photometric accuracy of the observations. We may here have identified the six galaxy blends with the brightest galaxies (plus the resolved galaxy). With a full 70-μm map we may have expected a further six or seven. This is still far less than the $\sim$32 we might expect, thus we may still expect a very small proportion of the fainter stars to suffer blending with galaxies.

4.3.3 Mass loss

Within the colour-magnitude diagrams, $\approx$140 stars were identified as having positive [8]–[24] colours (Fig. 4.8), suggesting they are surrounded by a dusty envelope. Non-members were discounted from this list using the proper motion membership criterion from van Leeuwen et al. (2000). [8]–[24] colours were converted to an equivalent mass-loss rate for a standard star ($\dot{M}_{\rm G}$) using tabulated data from Groenewegen (2006). Groenewegen's standard star is a 3000 L$_\odot$, solar metallicity star, with a 10 km s^{-1} wind. To calculate the final mass-loss rates, we the following formula (*c.f.* §1.6.4.1):

$$\dot{M} = \dot{M}_{\rm G} \left(\frac{v}{10 \text{ kms}^{-1}} \right) \left(\frac{200}{\psi} \right) \left(\frac{L}{3000 \text{ L}_\odot} \right)^{1/2}, \tag{4.1}$$

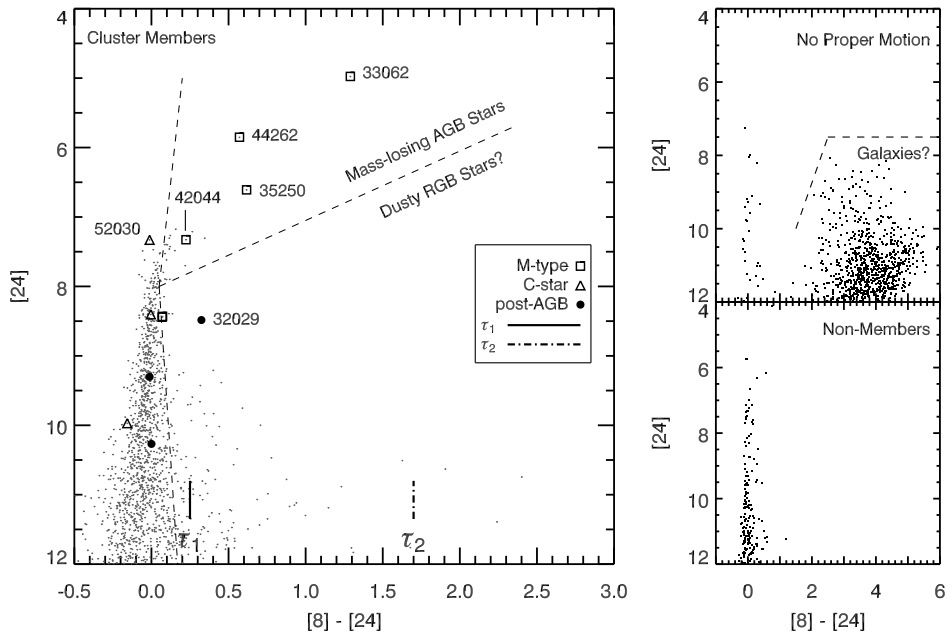

Figure 4.8: Colour-magnitude diagrams for ω Cen. Left panel: identification of mass-losing stars, including the likely divide of mass-losing RGB from AGB stars, but excluding possible 24-μm blends. The values τ_1 and τ_2 show colours for dust-enshrouded stars at optical depths of 0.26 and 1.70. Objects without proper-motion identifiers are shown in the upper-right to display probable background sources, and proper-motion non-members (mostly foreground objects) are shown in the bottom-right panel.

where v is the outflow velocity, ψ is the gas-to-dust ratio and L is the stellar luminosity. We here assume, after van Loon (2000b) and Marshall et al. (2004), that:

$$v = 10 \text{ kms}^{-1} \left(\frac{\psi}{200}\right)^{-1/2} \left(\frac{L}{10\,000 \text{ L}_\odot}\right)^{1/4}, \tag{4.2}$$

and:

$$\psi = \frac{\psi_\odot}{10^{[Fe/H]}}. \tag{4.3}$$

Luminosities at this stage were derived by MLB by fitting blackbodies to spectral energy distributions and assuming a distance to the cluster of 5.2 kpc. As we will see in the next Chapter, where we refine the values of mass-loss rate and temperature, this may result in some inaccuracies.

It is found that, for silicate dust around a star with a photospheric temperature

of 3850 K, the mass-loss rates of the three largest dust producers — LEIDs 33062, 44262 and 35250 (V42, V6 and V17) — are, respectively, 13, 2.8 and 1.8 $\times 10^{-7}$ $M_\odot$ yr^{-1}. This means that these three stars produce around 2/3 of the cluster's estimated 2.9×10^{-6} $M_\odot$ yr^{-1} of mass lost from dusty stars. As noted in §1.6.4.1, the errors on these absolute values are large, but the errors on relative values are small. While unquantified, more detailed modelling and results in Chapter 5 suggest that they may be correct to within about a factor of two.

It is also apparent from the colour-magnitude diagrams that the fraction of dusty stars decreases from $\sim 100\%$ at magnitudes brighter than $[24] \sim 7$, to $< 20\%$ at fainter magnitudes (Fig. 4.9). The transition region covers less than a magnitude. This is in direct contrast to the finding of Origlia et al. (2007), who find red objects in 47 Tucanae to be consistently present at all magnitudes as far down as the horizontal branch. The same objects are apparent in ω Cen, but here they are clearly identified with stars that are blended at 24 μm.

The cluster is approaching the Galactic plane, and will intercept it in a few megayears, suggesting that it has been $\sim$50 Myr since the last place crossing (Tayler & Wood 1975; Leon, Meylan & Combes 2000). Using the above mass-loss rates as a lower limit (mass will also be lost through chromospherically-driven winds), this suggests $\gtrsim$10 $M_\odot$ of lost gas will have built up within the cluster, along with (assuming $\psi \sim 10^4$) over 10^{-3} $M_\odot$ of dust. This is somewhat lower than the canonical ~ 100 $M_\odot$ predicted from stellar evolution and is a figure revised in the next chapter.

4.3.4 The intra-cluster medium

Despite obvious mass loss taking place within the cluster, there is no evidence of any gas or dust in the ICM of ω Cen. Eq. (4.2) predicts that the wind velocities are $\lesssim 1$ km s^{-1}, compared to the cluster's escape velocity of 44 km s^{-1} (Gnedin et al. 2002). The wind velocity may be greater, however, if dust and gas are not well coupled or if forces other than radiation pressure are also driving the wind. Although typically $<$15 km s^{-1},

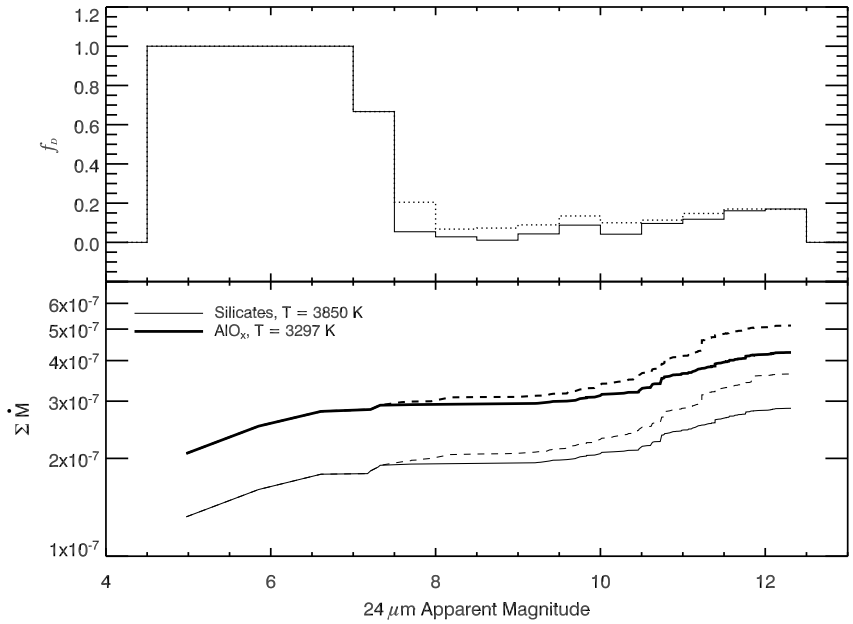

Figure 4.9: The fraction of dusty stars (top panel) and cumulative mass-loss rate (bottom panel) above a given luminosity in ω Cen. The solid lines exclude potential 24-μm blends, while the dotted lines include them. Mass-loss rates are plotted assuming pure aluminium oxide (AlO_x) and silicate grains. The increase between magnitudes 9 and 12 is not likely to be real, and probably due to increased photometric scatter in fainter stars and faint, unresolved blends with galaxies and other cluster stars (§4.3.2).

some systems losing mass through chromospheric activity may have velocities exceeding the escape velocity (Dupree, Sasselov & Lester 1992; Smith, Dupree & Strader 2004). However, the momentum from these systems is still unlikely to clear the cluster of all ICM.

The estimated limit to the sensitivity of the 24-μm maps is ≈ 25 kJy str^{-1}. An estimated sensitivity to intra-cluster dust ($M_{\rm dust}$) was placed (by MLB) using the following equation from Evans et al. (2003):

$$\frac{M_{\rm dust}}{\rm M_\odot} = 4.79 \times 10^{-17} f_\nu \frac{D^2}{\kappa_\nu B(\nu, T_{\rm d})}, \tag{4.4}$$

where f_ν is the flux received in mJy, D is the distance in kpc, κ_ν is the dust absorption co-efficient (cm^2 g^{-1}), and $B(\nu, T_{\rm d})$ is the Planck function (cgs units) for a dust temperature of $T_{\rm d}$ Kelvin. A standard Mathis-Rumpl-Nordsieck distribution (Mathis,

Rumpl & Nordsieck 1977) at 70 K yields a limit to the mass of intra-cluster dust of $1-2\times10^{-4}$ $M_\odot$, if the cloud is centrally condensed within the cluster, and at ≈70 K, as in M15. This corresponds to $\lesssim$4 Myr of dust production, if the cumulative mass-loss rate is $\lesssim5\ \times10^{-7}$ $M_\odot$ $yr^{-}1$ (Fig. 4.9) and the gas-to-dust ratio is ∼10 000, meaning that the cluster is cleared of dust via some mechanism within this timescale.

Extensive dust emission is seen outside the cluster (Fig. 4.10). This emission, and its association with the cluster and other objects, is further discussed in Chapter 6.

4.4 Conclusions

Our point-source catalogue provides the most complete atlas at mid- and far-infra-red wavelengths of any globular cluster to date. Little structure is seen in the colour-magnitude diagrams, which show mainly colourless stars and several hundred background galaxies.

Excess at [8]–[24] is found in ∼140 stars, particularly the known variables V6, V42 and V17. They produce the majority of the cluster's dusty mass loss, suggesting that $1-2\times10^{-3}$ $M_\odot$ of dust has been produced since the last Galactic Plane crossing. Similar limits can be placed on the amount of ICM observed within the cluster, suggesting intra-Plane-crossing clearing may be occurring. While ICM is not observed within the cluster, foreground medium is observed outside the cluster (see also Chapter 6).

4.5 Subsequent work

A subsequent study with the AKARI satellite (Matsunaga et al. 2008) revealed two far-infrared sources visible at 24, 65 and 90 μm. The colour of these objects in both the *Spitzer* and AKARI data suggests that they are unresolved background galaxies. No stellar sources were identified by the AKARI team.

Matsunaga et al. also place upper limits on the dust mass within the globular

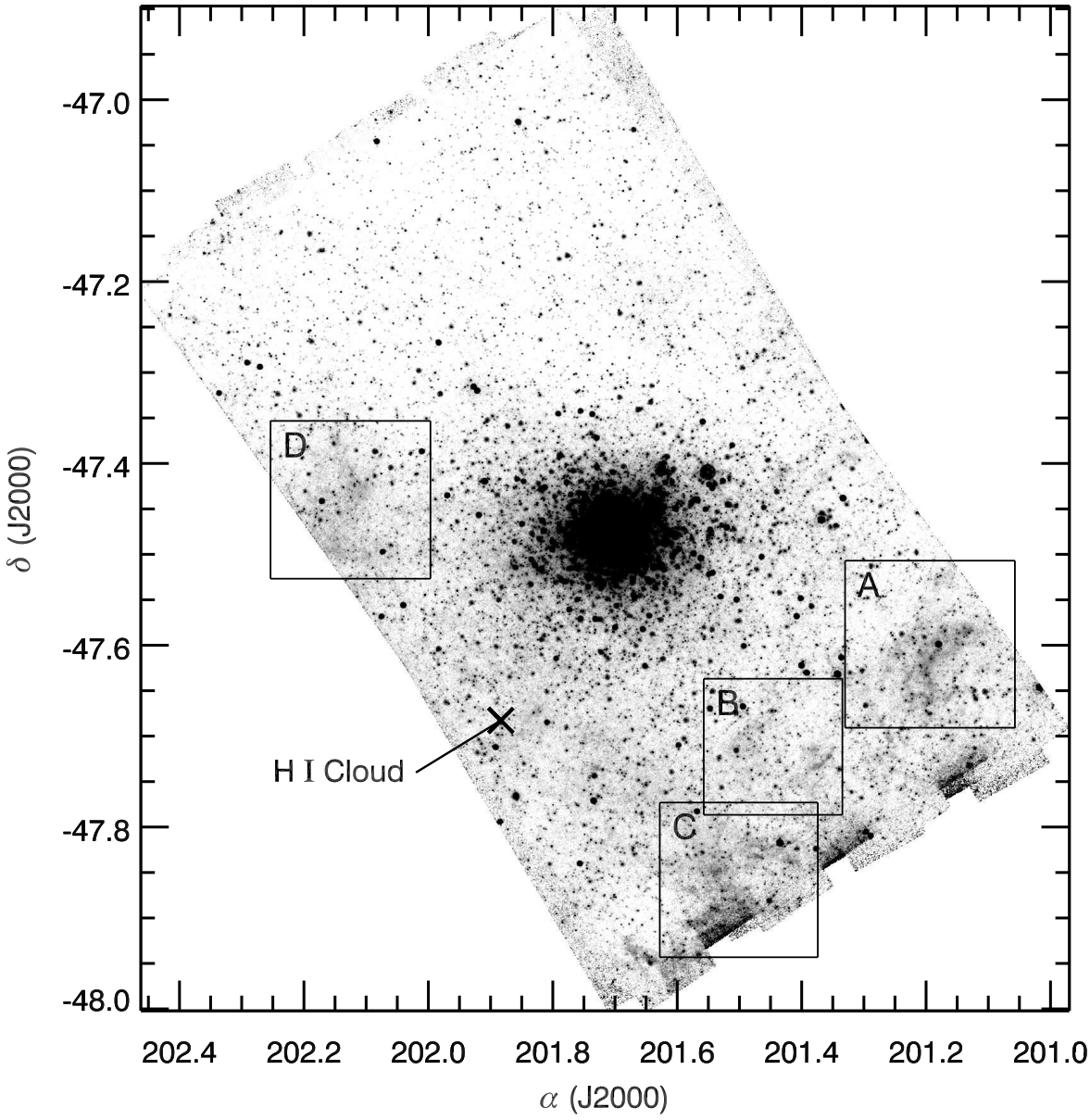

Figure 4.10: Dust emission in the line of sight of ω Cen, showing the four dusty regions identified in the paper that accompanies this Chapter and the HIPASS H I cloud. These are discussed further in Chapter 6.

cluster of 7.2×10^{-4} and 6.7×10^{-5} $M_\odot$ of dust, if the dust is at 35 or 70 K, respectively, giving clearing times of 0.3–3 Myr.

Barmby et al. (2009) provides a further interesting comparison. This study uses *Spitzer* MIPS 24- and 70-μm maps to find upper limits to intra-cluster dust volumes contained in several globular clusters: 47 Tuc, M3, M5, M13, M92, NGC 362, NGC 1851 and NGC 6752. Their upper limits are typically 10^{-4} $M_\odot$ of dust in the cluster and $1 - 2 \times 10^{-5}$ $M_\odot$ in the cluster core. They estimate clearing timescales for ICM, using a similar method to that described above. Their estimated upper limits on timescales range from 30–210 Myr for eight different clusters.

5 The globular cluster ω Centauri: distance and dust production

"Destroying is a necessary function in life. Everything has its season, and all things eventually lose their effectiveness and die."

— Margaret J. Wheatley & Geoff Crinean, *"Solving, not Attacking, Complex Problems: A Five-State Approach Based on an Ancient Practice"* (2004)

This chapter has been published as McDonald, van Loon, Decin,* et al., *2009, MNRAS, 394, 831.

5.1 Introduction

The work presented in this Chapter provides a major, in-depth analysis of the infra-red atlas of ω Centauri presented in the preceding Chapter. Here, we construct spectral energy distribution models of all the stars (6875) for which we have obtained reliable, multi-wavelength photometry. Having calculated the temperatures and luminosities of the stars from these, we go on to re-determine the distance and inter-stellar reddening toward the cluster, and estimate mass-loss rates for its constituent stars.

5.2 The input datasets

5.2.1 Literature photometry and variability data

Our input list of objects was derived from the optical photometry of van Leeuwen et al. (2000, hereafter vL+00). We have selected from this catalogue those stars that have at least one detection in the mid-IR *Spitzer* IRAC (3.6, 4.5, 5.8 and 8 μm) and MIPS (24 μm) imaging published in Boyer et al. (2008, §4, hereafter B+08). We have combined these data with photometry from 2MASS (Skrutskie et al. 2006). Of the resultant list

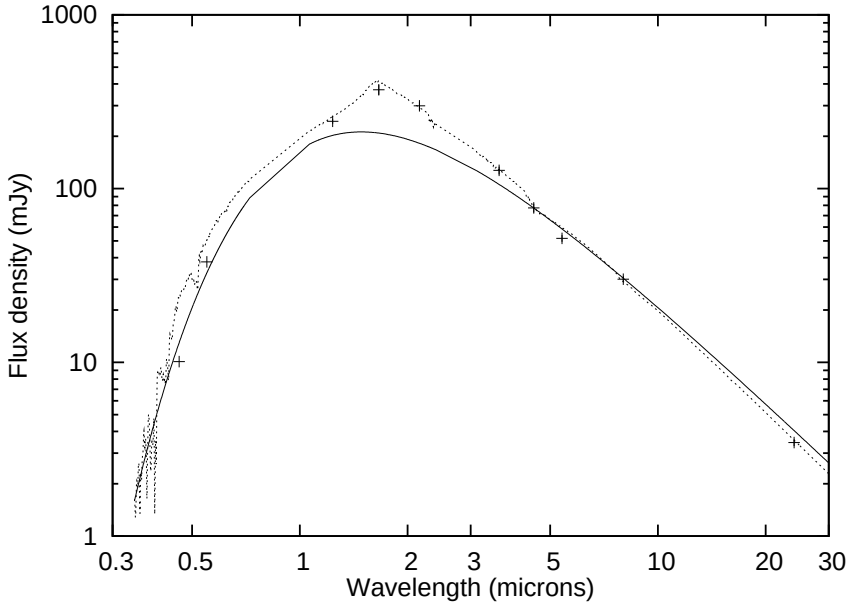

Figure 5.1: Spectral energy distribution for the star LEID 43265 (crosses). Also shown is a MARCS model at $g = 1.5$ and $T = 4000$ K (dotted line), corrected for interstellar reddening as described in the text. A comparative blackbody at 3650 K, similarly corrected, is shown as a solid line. The artifact short of 1 μm is an artifact of interpolation to the filter passbands. Note how the excess flux between $\sim$1.0 and 4.5 μm is not covered by the blackbody.

of 6875 stars, 6018 are proper motion members, 1145 are radial velocity members in van Loon et al. (2007, hereafter vL+07), and 1701 have photometry at both 8 and 24 μm.

5.2.2 The model spectra

As evident from Figs. 5.1 and 5.2, many of our stars — particularly the cooler objects — depart significantly from a blackbody spectrum. We have used model spectra to derive the stellar parameters. A grid of spectra were created using the Model Atmosphere in Radiative and Convective Scheme (MARCS) code (Gustafsson et al. 1975, 2008). MARCS uses atomic and molecular data to create synthetic model atmospheres, similar to the Kurucz models used in Chapter §3, but with a much more comprehensive molecular database. The latest edition of MARCS also samples opacity at different

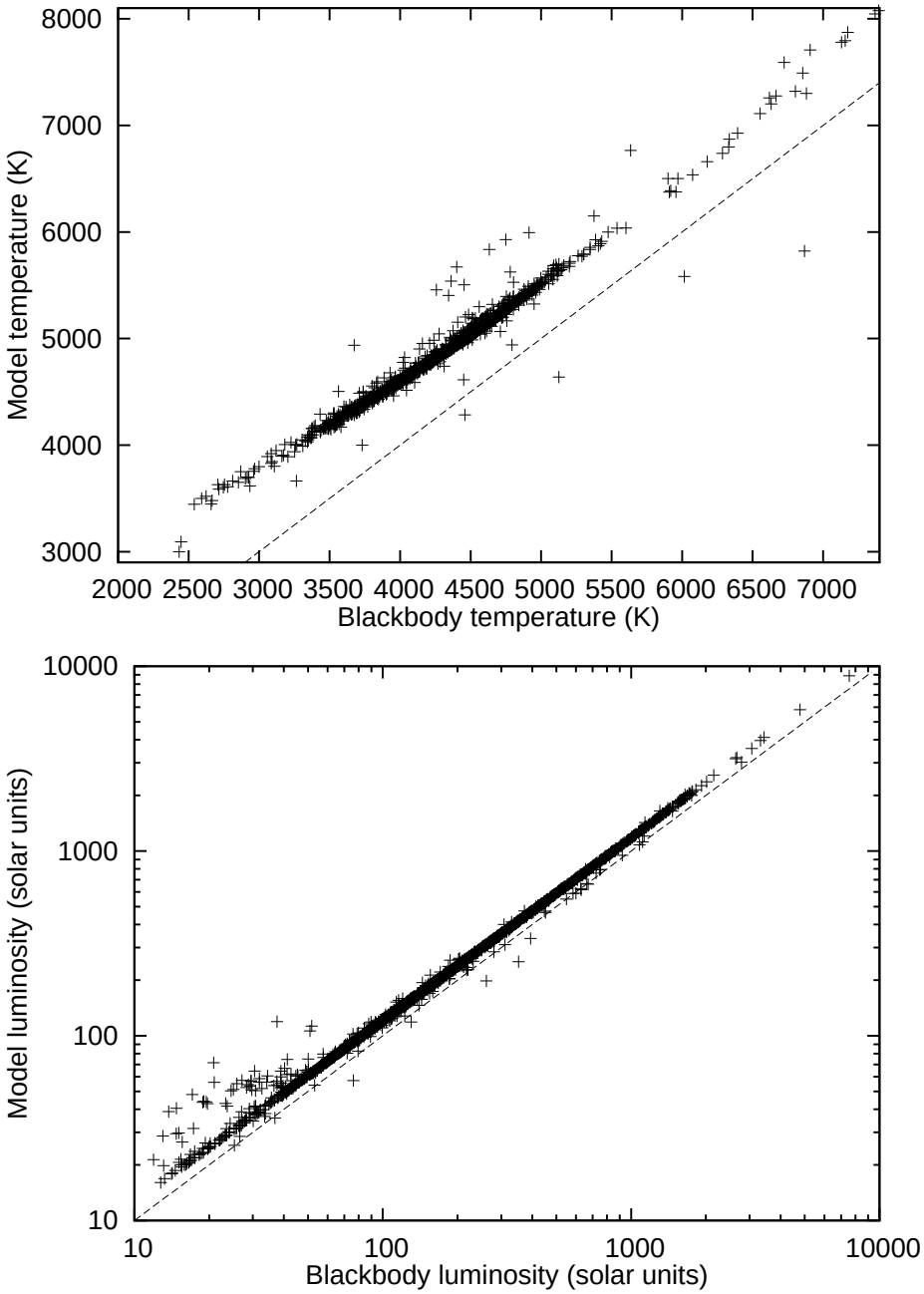

Figure 5.2: Comparison between blackbody and final MARCS model fits to stellar temperature and luminosity. Cluster non-members are also included. The dashed line shows a one-to-one correlation. Note that the scatter from the main relation is largely due to remaining blending issues and poor photometry in low luminosity stars (see bottom panel).

depths, following Peytremann (1974) and Sneden, Johnson & Krupp (1976). This provides a better match between models and spectra where molecules contribute opacity at different wavelengths, depending on their height in the atmosphere (*e.g.* carbon stars).

Certain limitations present in the models have the potential to affect the accuracy and validity of our derived stellar parameters. Notably, the model assumes a stratified atmosphere and LTE conditions in its opacity calculations, which may not be entirely valid for very evolved stars with high-amplitude pulsations. However, the optical variability of the stars, and thus the error in measured fluxes, is much greater than the deviations caused by the MARCS code's limitations.

The model grid spans from 4000 K to 6500 K in steps of 250 K, with an additional dataset at 3500 K; gravities were sampled from $\log(g) = 0.0$ to 3.5 in steps of 0.5. At each grid point, a further dimension in metallicity was sampled at [Z/H] = 0.0 with solar abundances; at [Z/H] = –1.0 with $[\alpha/\mathrm{Fe}] = +0.3$; and at [Z/H] = −1.5 and −2.0, with $[\alpha/\mathrm{Fe}] = +0.4$. For each grid point, a synthetic spectrum was created with $R = 20\,000$ over the range 0.13 to 20 μm. Some models did not converge; these were replaced with a neighbouring convergent model that had the same temperature and the closest available combination of metallicity and gravity.

The spectra were extrapolated beyond 20 μm using a Rayleigh-Jeans tail fit to the range 18–20 μm. This was used in preference to the normally more-appropriate Engelke function (Engelke 1992; Decin & Eriksson 2007) as the Engelke function overestimated the flux we observe by up to 20–40%, while the over-estimation from a Rayleigh-Jeans tail is only around 10–20%. Both a Rayleigh-Jeans tail or Engelke function are expected to *under*-estimate the flux we observe at 24 μm for our cooler stars, though the reverse may be true in warmer giants. The immediate reasons behind the apparent *over*-estimation these functions provide when compared to our data are not clear and we make an empirical correction in §5.5.3.1.

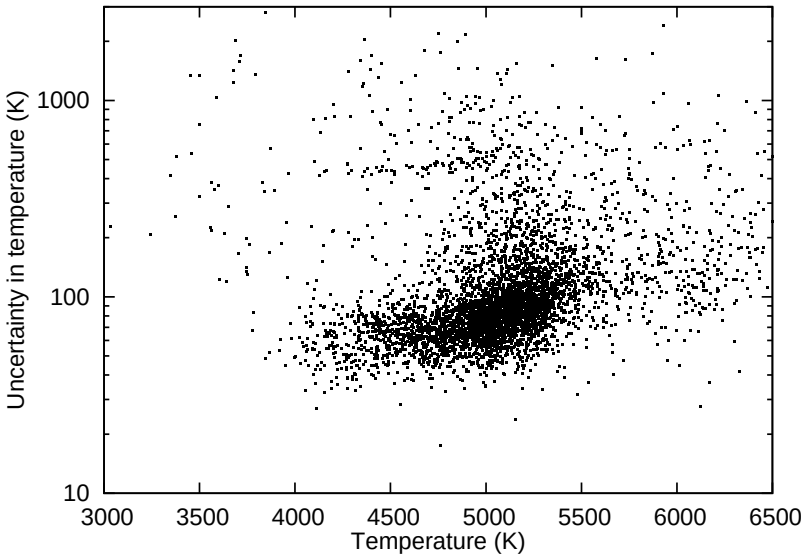

Figure 5.3: Distribution of internal errors in temperature over the giant branch stars. Errors increase to typically ± ∼1000 K for stars not covered by our hottest models (> 6500 K).

5.3 Spectral energy distributions

Firstly, the literature photometry and model spectra were converted into F_ν (Janskys) using the zero points in Table B.2, including the 1.5% addition to IRAC 4 from Rieke et al. (2008). The models were then degraded in resolution by a factor of 100 to $R = 200$ to save on computing time and, using a cubic spline, interpolated in wavelength onto filter transmission data in the relevant filters. Comparing the photometric flux from the original spectrum and the interpolated spectrum, we find the differences to be $\ll 1\%$ in all cases except B-band, where the lower-resolution sampling of strong spectral lines lead to the systematic over-estimation of the flux by up to ∼3% for the cooler stars. These are comparable to the errors present in the photometry, and much less than the observed photometric variation of our mass-losing candidates, thus we do not consider it to be a major source of error in our analysis. An additional source of systematic error comes from uncertainties in the filter and imaging device responses, and instrumental photometric zero points. Though difficult to quantify, we expect these effects to affect our photometry at the level of 3% or less and correspondingly systematically alter our

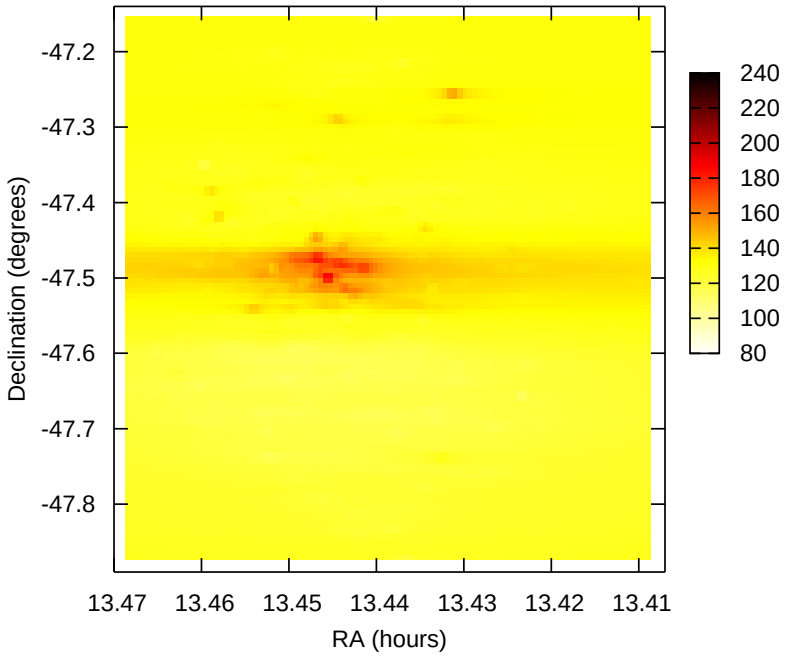

Figure 5.4: Distribution of internal errors in temperature over the cluster, containing only stars on the giant branches (here defined at $T < 5500$ K). Errors increase towards the cluster centre due to blending. The horizontal smearing is an interpolation artefact.

temperature and luminosities by $\lesssim$1%, as the errors will tend to average out among the different filters.

A blackbody was fitted to the observed photometry to provide a first-order estimate of temperature and luminosity. From this we derive an initial value for $\log(g)$, using the standard:

$$\log(g) = -10.6113 + \log(M) + 4\log(T_{\rm eff}) - \log(L) \tag{5.1}$$

for luminosity L and mass M in solar units, and temperature $T_{\rm eff}$ in Kelvin. We here assume a mass of 0.8 $M_\odot$ for all stars, but note that $\log(g)$ could be reduced by as much as 0.2 in a 0.5 $M_\odot$ AGB star near the end of its life.

An initial grid of MARCS models was set up to coarsely define the temperature. For computing purposes, the grid was chosen to be between 4096 and 6144 K, in steps of 512 ($= 2^8$) K. For stars falling outside this range (as determined by the following fitting procedure), the grid was extended — to 3072 K in the case of cooler stars, and to 18 442 K for warmer stars. The step size was chosen to provide the computationally-fastest determination of temperature, while ensuring the true best-fit temperature is reached. For each of these temperatures, a spectrum was produced from the closest two model grid temperatures by linearly interpolating in [Fe/H] and $\log(g)$. These two spectra were then combined into a single spectrum ($F_{\rm final}$).

Simply averaging the spectra, would not fully take into account the changes in the underlying blackbody distribution. Instead, the spectra (F_1 and F_2) were normalised by dividing by blackbodies of the corresponding temperatures ($B_\nu(T_1)$ and $B_\nu(T_2)$). Multiplying by the final required temperature (T) then maps the spectral features from temperatures F_1 and F_2 to temperature T, producing two new spectra, F_1' and

F'_2, thus:

$$\begin{aligned} F'_1 &= F_1 \frac{B_\nu(T)}{B_\nu(T_1)}, \\ F'_2 &= F_2 \frac{B_\nu(T)}{B_\nu(T_2)}, \end{aligned} \tag{5.2}$$

The final spectrum can then be linearly interpolated between the two spectra, as follows:

$$F_{final} = \frac{T - T_2}{T_2 - T_1} F'_1 + \frac{T - T_1}{T_2 - T_1} F'_2. \tag{5.3}$$

This method is much more accurate at replicating spectra, especially at shorter wavelengths.

By comparing the interpolated spectrum with the original, we calculate that our interpolation method can accurately reproduce a model value for a photometric band at any temperature above 4000 K, with any gravity and metallicity within our model grid to within 1%. For stars below 4000 K, a lack of converging models at 3750 K and $<$ 3500 K means that the models will tend to over-estimate the photometric flux at short wavelengths (B- and V-band) by perhaps 3–5% for the very coolest stars we sample, which is still (much) less than the expected stellar variability, differential interstellar reddening or (in some cases) photometric uncertainty in this regime.

Since ω Cen exhibits moderate but noticeable interstellar reddening, it was necessary to redden the model spectrum appropriately. Estimates of the reddening towards the cluster vary considerably from $E(B-V) = 0.09$ to 0.15 mag (Djorgovski 1993; Harris 1996; Kovács 2002). A differential reddening across the cluster of $\Delta E(B-V) \lesssim 0.04$ mag has also been inferred (Norris & Bessell 1975; Calamida et al. 2005; vL+07). For our analysis, we adopted a reddening of $E(B-V) = 0.08$ mag across the entire cluster to better fit the evolutionary isochrones (see §5.4). Assuming $A_{\rm V}/E(B-V) \approx 3.05$ (Whittet 1992), this yields an extinction of $A_{\rm V} \approx 0.24$ mag.

To compute the reddening as a function of wavelength, we have used the relationship from Draine (1989), with an empirical correction for wavelengths of < 1 μm based

on Draine's Figure 1. Using $E(J-K) = 0.52E(B-V)$ (after Whittet 1992), this becomes:

$$\frac{A_\lambda}{E(B-V)} = \begin{cases} 1.248\lambda^{-1.75-(\lambda-1)/1.3} & \text{for } \lambda \leq 1\ \mu\text{m} \\ 1.248\lambda^{-1.75} & \text{for } \lambda \geq 1\ \mu\text{m} \end{cases} . \tag{5.4}$$

By examining the effective temperature and luminosity at different reddening factors on a subset of stars, we can deduce the size of this correction. We find that the corresponding temperature and luminosity, T' and L' (in Kelvin and solar luminosities), are well approximated (for an arbitrary $E(B-V)$, denoted e) by:

$$T' = T + \frac{e-0.08}{0.13}\left(\left(\frac{T-3000}{45}\right)^{1.5} - 50\right), \tag{5.5}$$

$$L' = L\left(1 + \frac{e-0.08}{0.13}\left(\frac{L}{13200} - 0.155\right)\right)\left(\frac{d}{5300}\right)^2, \tag{5.6}$$

where L and T are the luminosity and temperature for $E(B-V) = 0.08$ mag and d is the distance in parsecs.

Draine estimates a 10% error in his relationship, which would alter our corresponding corrections by a similar amount. Our composite relation described above differs in individual filters by up to $10-15\%$ compared to Whittet (1992), suggesting a similar inherent uncertainty in our reddening correction. The uncertainty in $E(B-V)$ affects the shorter wavelengths the most, and is typically greater than that produced by our filter convolution and interpolation above. Differential reddening *across* the cluster thus leads to a scatter of up to $\pm 50-100$ K in temperature and $\pm 1-4\%$ in luminosity. Uncertainty in the *average* extinction to the cluster, which is of the same order, is the largest systematic error in our temperature and luminosity estimates.

We do not consider circumstellar reddening here, as it only becomes significant in individual stars for the most extreme cases, where the effect is dwarfed (by a factor of $\sim$10) by the variability due to pulsation at any particular wavelength. This will not significantly affect our determination of distance or extinction to the cluster, but may lead to a slight under-estimation of the temperature and luminosity of the most

enshrouded stars.

Once appropriately reddened, the spectrum was convolved with the filter responses to obtain the expected flux density received in that filter. The 24-μm data were not included in this calculation as we aim to fit the underlying photosphere, not the photosphere plus the wind's dust component.

A true error estimate was impossible due to incomplete error information. We thus construct a relative error estimate (denoted σ), calculated as:

$$\sigma = \sum_{i=1}^{N} \left(\log(F_{\rm o,i}) - \log(F_{\rm m,i})\right)^2 , \tag{5.7}$$

where $F_{\rm o,i}$ and $F_{\rm m,i}$ are the observed and model fluxes in passband i.

The process was repeated for each of the points in the one-dimensional temperature grid and the best-fit model, corresponding the minimum value of σ ($\sigma_{\rm min}$), was identified. The value of $\log(g)$ was re-determined for the temperature of the best-fit model ($T_{\rm min}$). Values of σ was re-determined at half the grid spacing, $T_{\rm min} \pm 256$ K, and a σ minimum re-defined. This process was iteratively carried out to refine the temperature to a *precision* of 1 K. The resulting distribution of stellar temperatures (§5.4.2) suggests that the internal *accuracy* is typically better than $\pm$70 K, but increases towards lower luminosities and higher temperatures. Note that while colour-$T_{\rm eff}$ transformations often give more precise values for $T_{\rm eff}$, our procedure yields the most consistent values for $T_{\rm eff}$ *and* luminosity, taking into account the full observed SED.

Relative temperature errors are plotted in Fig. 5.3. These are calculated using a parabolic fit to the σ results at differing temperatures, and estimated the point at which the $\sigma = 2\sigma_{\rm min}$. This value approximates the maximum likely error determined from the data (§5.4.2). Luminosity errors have been estimated from the relation $L \propto T_{\rm eff}^4$, thus $\Delta L/L = 4\Delta T_{\rm eff}/T_{\rm eff}$.

In Table 5.1, we list the average and standard deviation of the difference between the MARCS modelled flux and the observed flux in each photometric band. We have

limited this to stars with $T_{\rm eff} < 6500$ K, due to our lack of models at higher temperatures. We find a systematic offset from the model photometry in most bands, though it remains unclear whether this is due to inaccuracies in the photometric zero points or the MARCS models. In particular, the models appear to systematically over-estimate the H-band brightening around the H^- opacity minimum. Note also that the accuracy of our temperatures is mostly determined by the accuracy of our B and V-band flux.

We include an interpolated map of the temperature errors in Fig. 5.4, showing they increase toward the cluster centre. The giant-branch stars with larger temperature errors ($\gtrsim$200 K) are caused by errant photometry, particularly in the B- and V-bands, due to source blending in the dense cluster core. As a guide, this affects roughly 25% of stars between 100 $L_\odot$ and 500 $L_\odot$ in the inner 12′. As illustrated in Fig. 5.3, there is only a very weak dependence between the magnitude of the error and the stellar temperature (and thus luminosity if the star is on the giant branch). The frequency of errors due to blending does increase as one heads to lower temperatures and luminosities. Crucially, however, the very presence of these errors allows us to determine which stars suffer from blending. We find that, on the upper giant branch, where mass loss is taking place, the only stars to suffer from substantial errors (130–330 K) are known variables (specifically V42, V6, V152 and V148), whose temperatures are expected to be uncertain due to their inherent variability.

Literature distance estimates vary from 4.8 kpc (vL+00) to 5.52±0.13 kpc (del Principe et al. 2006), with 5.3 kpc being the median (Peterson 1993; Harris 1996; Thompson & Kałużny, J. and Pych, W. and Burley, G. and Krzemiński, W. and Paczyński, B. and Persson, S. E. and Preston, G. W.). This introduces some error (see §5.5.2.1, §5.6.2). We adopted 5.0 kpc as an initial estimate, based on evolutionary isochrones (§5.4). Assuming this distance, a luminosity was calculated by integrating the final model spectrum. Due to the limits of integration (>130 nm) determined by the model spectra, we note that the luminosities of stars with considerable flux at $\lambda < 130$ nm (i.e. stars with $T \gg 8000$ K) will likely be more luminous than we have

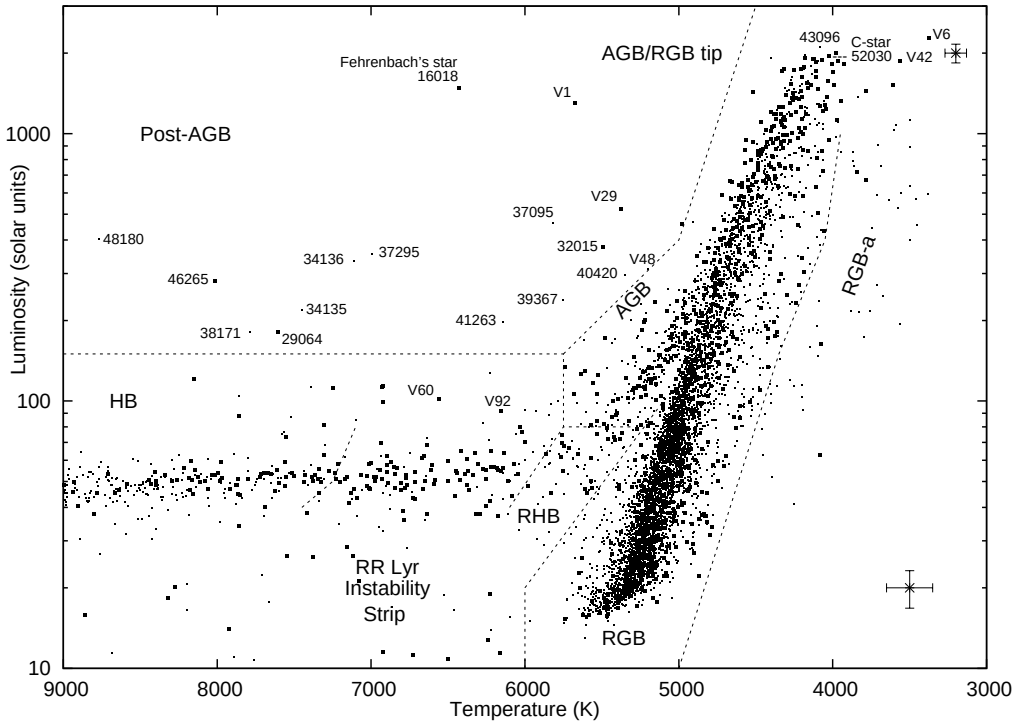

Figure 5.5: A physical HRD for the giant branch of ω Cen. Dots show proper motion members (>50% probability); squares show objects that are (also) confirmed radial velocity members ($v_{\rm LSR} > 100$ km s^{-1}). Representative statistical errors for individual objects are shown in the lower- and upper-right corners. The limits to the RR Lyrae instability strip are taken from Bono, Caputo & Marconi (1995).

Table 5.1: Average differences between modelled and observed fluxes, and standard deviations of those differences, for stars below 6500 K.

Band	Number of stars	Average difference	Standard deviation
B	5867	+5.1%	9.9%
V	5861	–6.9%	9.9%
J	5645	+0.9%	7.2%
H	5598	–2.2%	6.7%
K	5585	+4.2%	8.8%
3.6μm	5463	+2.6%	8.4%
4.5μm	5673	–0.6%	8.3%
5.8μm	5319	+0.4%	14.5%
8.0μm	5759	–1.3%	12.6%

listed here, though this is not certain as our stellar models become progressively less reliable beyond 6500 K. The final stellar parameters are listed in Table 5.2.

A physical Hertzsprung-Russell diagram (HRD) is shown in Fig. 5.5. The RGB and AGB can clearly be distinguished up to ∼150 $L_{\odot}$, with the Horizontal Branch (HB) extending towards high temperatures at ∼50 $L_{\odot}$. The expected errors suggest the majority of the spread in the diagram is real. The cooler giant branches should therefore represent the more metal-rich objects. Post-AGB stars are present at higher luminosities towards the warm side of the giant branch. The RGB-a stars are visible to the right of the main RGB. Interestingly, they do not appear to extend to the RGB tip, but as they are so few in number, this could merely be a stochastic effect.

5.4 Comparisons with stellar isochrones

With an HRD of this quality, a comparison with stellar evolution models can yield accurate determinations of the cluster's parameters, such as distance and reddening

Table 5.2: Sample of derived stellar parameters ordered in decreasing luminosity, assuming $E(B-V) = 0.08$ mag and a distance of 5.0 kpc, including Leiden Identifier and proper motion (PM) percentage likelihood of membership from vL+00, and radial velocity from vL+07, where available.

LEID	T (K)	L ($L_\odot$)	Gravity log(cm s^{-2})	PM Mem %	$v_{\rm LSR}$ km s^{-1}
33062	$3375 \pm^{257}_{204}$	$2278 \pm^{695}_{550}$	0.10	100	221
43096	$4082 \pm^{90}_{108}$	$2117 \pm^{186}_{223}$	0.46	99	
43099	$3980 \pm^{61}_{82}$	$2012 \pm^{123}_{167}$	0.44	100	210
45232	$4183 \pm^{103}_{124}$	$1964 \pm^{193}_{233}$	0.54	100	
52030	$4022 \pm^{89}_{121}$	$1944 \pm^{171}_{233}$	0.47	99	204
48060	$4181 \pm^{65}_{76}$	$1923 \pm^{120}_{139}$	0.54	100	190
47226	$4402 \pm^{106}_{123}$	$1912 \pm^{185}_{213}$	0.64	100	
52017	$4120 \pm^{45}_{51}$	$1903 \pm^{83}_{95}$	0.52	100	206
26025	$4129 \pm^{52}_{62}$	$1900 \pm^{96}_{113}$	0.53	100	229
61015	$4067 \pm^{62}_{74}$	$1881 \pm^{114}_{138}$	0.51	99	218
44277	$3963 \pm^{125}_{164}$	$1873 \pm^{236}_{310}$	0.46	100	211
46062	$4094 \pm^{73}_{84}$	$1869 \pm^{133}_{154}$	0.52	100	
44262	$3565 \pm^{385}_{281}$	$1862 \pm^{803}_{587}$	0.28	100	261
...	...	...	...	...	...

(we assume a fixed age of ≈12 Gyr as this is better estimated using the main-sequence turnoff). These parameters can be re-derived using the empirical corrections in Eq. (5.5) & (5.6). Distance and reddening are important for both calibrating our luminosities and estimating mass-loss rates from individual stars. Evolutionary tracks and, in particular, the rate of stellar evolution, can already yield some constraint on mass loss on the RGB.

5.4.1 Padova isochrones

Fig. 5.6 shows Padova stellar isochrones from Marigo et al. (2008). The isochrones are for zero extinction, containing the dust solutions from Bressan, Granato & Silva (1998), with a log-normal initial mass function from Chabrier (2001). They are shown for the metallicities and ages suggested by Origlia et al. (2003) and Hilker et al. (2004), namely: 12.1 Gyr at [Fe/H] = –1.6 for the metal-rich population, 10.5 Gyr at [Fe/H]

= –1.2 for the metal-intermediate population and 9.4 Gyr at [Fe/H] = –0.7 for the metal-rich population. Using these isochrones, we fitted the extinction and distance as $E(B-V) = 0.09 \pm 0.01$ mag and 4800 ± 150 pc, respectively.

We stress that these two parameters are somewhat correlated, and the errors given are based on single-parameter errors only. In this case, the distance is fitted primarily by the location of the zero-age horizontal branch (ZAHB), and the isochrones are then matched to the data by the correct reddening. While we have not undertaken a full quantitative analysis, comparing the two panels in Fig. 5.6, we can see that a fit with a distance of 5000 pc and $E(B-V)$ of 0.08 mag also falls within visually plausible errors, however this does not reproduce the early-AGB and early-RGB so well.

Despite efforts to fit the distance and reddening, the Padova isochrones still do not provide a good fit to the slope of the RGB or AGB. We suggest that this is inherent in the models for three reasons:

- on the basis of our above analysis, circumstellar dust starts reddening the stars at lower luminosities than their models predict, at around 1000 $L_{\odot}$ (*c.f.* Fig. 5.19) — this occurs both on the RGB and AGB;

- RGB mass loss is not included in the Padova models (the accumulated mass loss is assumed to happen 'instantaneously' at the RGB tip): stars which have lost mass will have larger radii and thus be cooler than the models predict;

- the [α/Fe] enhancement in the models is incorrect (Marigo et al. currently do not provide a mechanism with which to alter this) — increased [α/Fe] will make the stars cooler than the models.

It also appears that the mass-loss rates from Marigo et al. (2008) for the RGB are not high enough for a large number of stars, as they do not reproduce the blueward extent of the HB that results from low mantle masses. We can therefore assume that mass loss on the RGB is higher than that predicted by the Padova isochrones, which

assume an initial mass of 0.843 $M_\odot$, and 0.117 $M_\odot$ of mass loss on the RGB for a 12.1 Gyr, [Fe/H] = –1.6 model.

5.4.2 Dartmouth isochrones and ZAHB models

Fig. 5.7 shows a similar plot, but for isochrones from the Dartmouth database (Dotter et al. 2008). In the top panel, we take a 12.1 Gyr model at [Fe/H] = –1.62, a standard helium abundance of $Y = 0.245 + 1.5Z$ and an [α/Fe] ratio scaled to solar abundances. We also include a HB model at $M = 0.70$ $M_\odot$, implying again that ∼0.11 $M_\odot$ is lost on the giant branch (the RGB tip corresponds to an initial stellar mass of 0.81 $M_\odot$ in this model).

By applying a reddening correction to $E(B-V) = 0.08 \pm 0.01$ mag and a distance of 4900 ± 100 pc, we can yield a good match to the isochrones: the RGB is matched nearly exactly, as is the AGB. The HB morphology is not well fit by solar-scaled helium abundance and [α/Fe]. In the middle panel of Fig. 5.7, we show the effect of varying mantle mass at solar [α/Fe] with $Y = 0.33$. In the bottom panel, we show the effect of fixed stellar mass with varying [α/Fe]: this affects the mass of the stellar core which, for fixed stellar mass, has the reverse effect on the mantle mass. We note that the errors given above are in that parameter only, however we can rule out a fit at $E(B-V) = 0.07$ mag and $d = 5100$ pc, or at $E(B-V) = 0.11$ mag and $d = 4500$ pc by examining the locations of the start of the AGB and the tip of the RGB.

It seems clear that variation of the mantle mass can account for the observed spread in the HB of ω Cen. This arises from a combination of varying core mass due to intrinsic metallicity and abundance differences. It can also arise from different efficiencies of mass loss on the RGB, which could well be due to the original metallicity and abundance differences themselves. At first sight, it is not clear whether varying mass loss or varying core mass is the primary factor. However, the spread of the early AGB is very narrow (∼10–15% in luminosity at a fixed temperature, 50–90 K in temperature at a fixed luminosity), most of this is likely due to temperature and

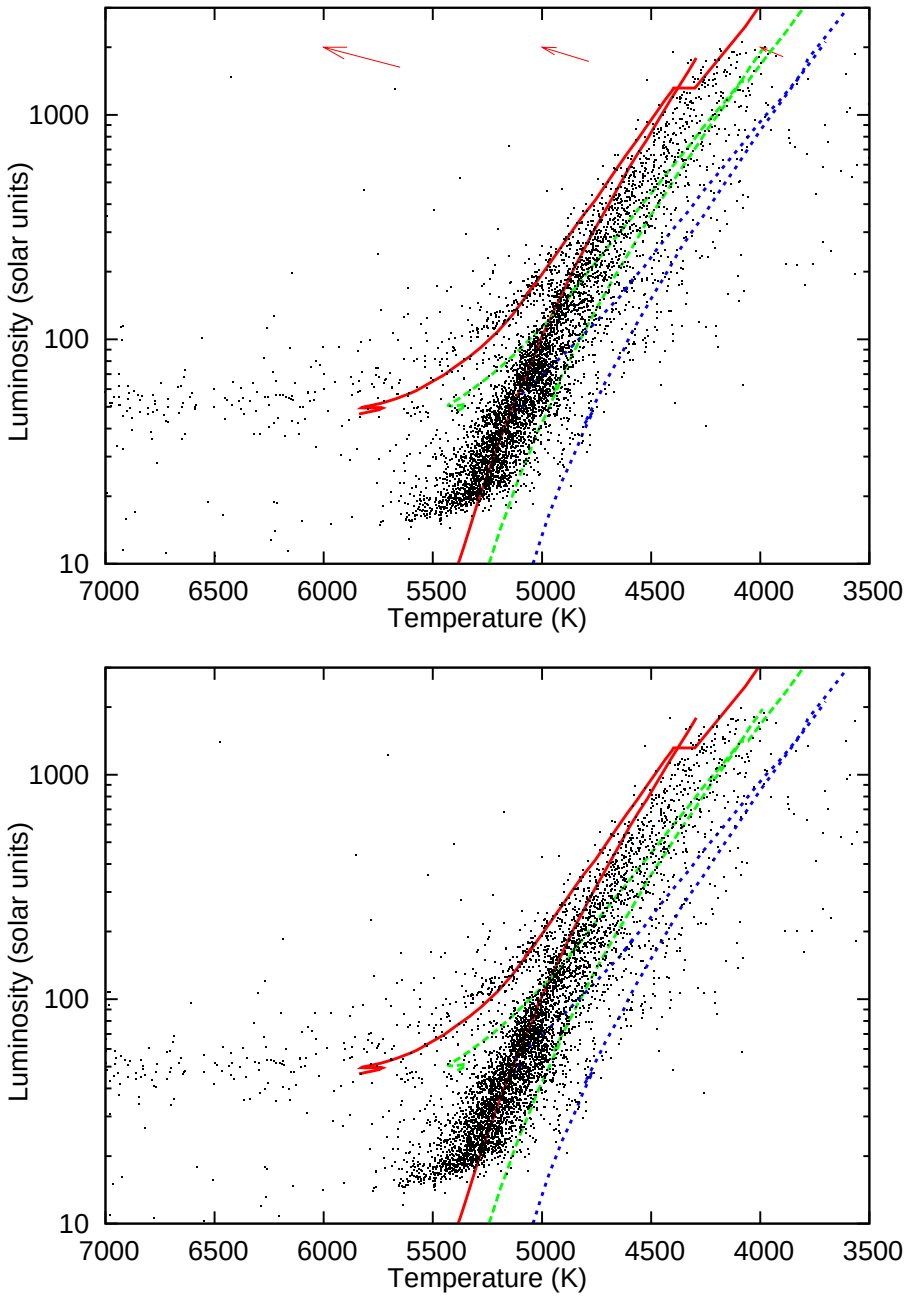

Figure 5.6: HRD of cluster members, including isochrones from Marigo et al. (2008). The top panel shows isochrones for metallicities of [Fe/H] = –1.6, –1.2 and –0.7 (from left to right), assuming a distance of 5000 pc. The arrows show the approximate reddening correction (taking $E(B-V) = 0.08$ mag) for that temperature. The bottom panel shows the same diagram, but with an *approximate* correction to $E(B-V) = 0.09$ mag and a distance of 4800 pc. The isochrones are described in the text, with metallicity increasing from left to right.

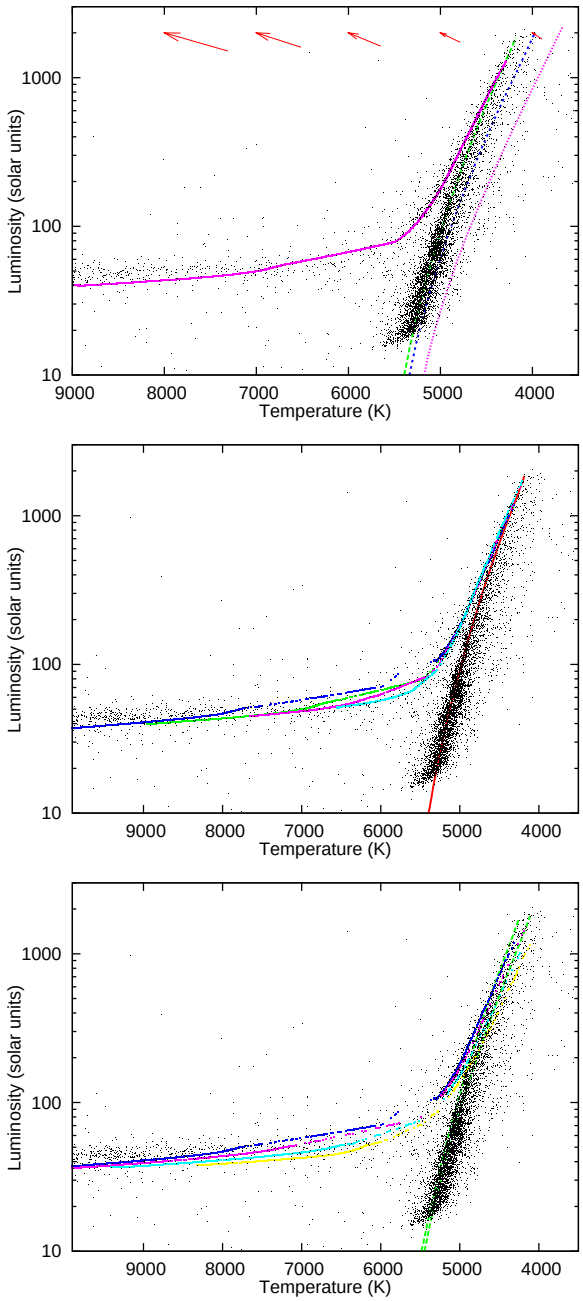

Figure 5.7: As Fig. 5.6, using RGB isochrones and HB models generated using the Dartmouth database (Dotter et al. 2008). The top panel shows the same three RGB isochrones as Fig. 5.6, with a solar-abundance-scaled HB track at 0.70 $M_{\odot}$. The middle panel shows the same diagram, using only the 12.1 Gyr isochrone, but with an *approximate* correction to $E(B-V) = 0.08$ mag and a distance of 4900 pc, with HB models at (top to bottom) 0.65, 0.70, 0.75 and 0.81 $M_{\odot}$. The bottom panel is as the middle panel, showing the HB track at 0.65 $M_{\odot}$, but with [α/Fe] enhancements of (bottom to top) 0.0, +0.2, +0.4 and +0.6; the RGB isochrones are shown for [α/Fe] = 0.0 (left) and [α/Fe] = +0.4 (right), both have helium abundances of $Y = 0.33$.

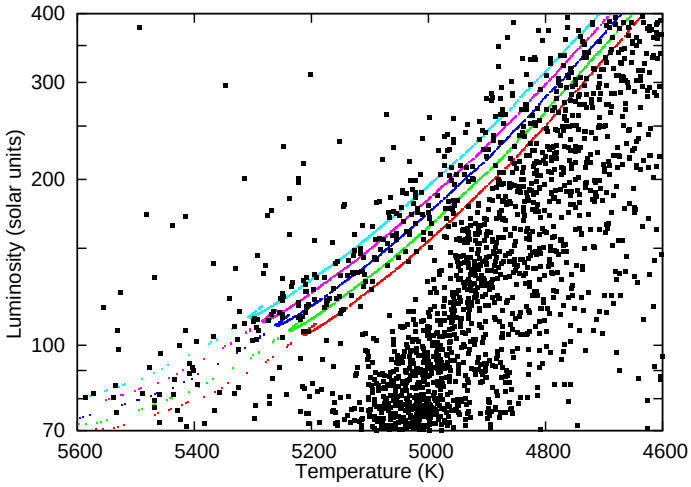

Figure 5.8: As Fig. 5.7, middle panel, showing a Dartmouth model covering the early AGB for a stellar mass of 0.65 $M_\odot$, at [Fe/H] = –1.62 and [α/Fe] = +0.2, with reddening (from left to right) of $E(B-V) = 0.11$, 0.10, 0.09, 0.08 and 0.07 mag. The data are shown at $E(B-V) = 0.08$ mag and $d = 4900$ pc.

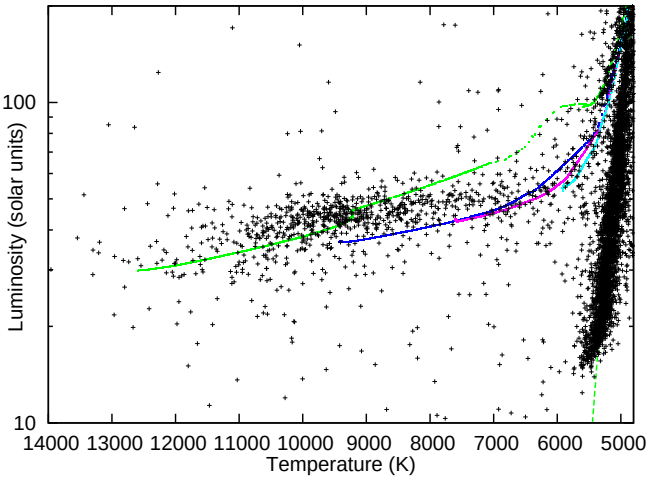

Figure 5.9: As Fig. 5.7, middle panel, showing the HB for stellar masses of (top to bottom) 0.60, 0.65, 0.70 and 0.81 $M_\odot$, at [Fe/H] = –1.62 and [α/Fe] = +0.4.

luminosity errors, with small contributions from differential reddening across the cluster (implying, from Eq. (5.5), $\Delta E(B-V) \lesssim 0.02$ mag) and varying distance within the cluster. It would therefore seem that we need a range of models that produce almost zero spread in the early AGB, a condition satisfied by changing the stellar mass, rather than [α/Fe].

We can further estimate the maximum value of $\Delta E(B-V)$ across the cluster. Fig.

5.8 shows the effect of different values of $E(B-V)$ on the early AGB. In the absence of other variations leading to the dispersion of the AGB (which include photometric errors, and [α/Fe], metallicity and distance variation), we can assume that the variation of $E(B-V)$ across the cluster, $\Delta E(B-V)$, is < 0.04 mag.

By examining the HB (Fig. 5.9), we can approximate the mass loss on the RGB. It would appear that the majority of the HB stars lie between the 0.60 and 0.65 $M_{\odot}$ models in both temperature and luminosity, but with some more closely following the higher-mass models. We must stress that our models do not cover the HB: while we expect temperatures to be broadly correct (within a few hundred to a thousand Kelvin), luminosities may be too low. We may also not cover the blue extent of the HB in its entirety, as bluer HB stars will be fainter at *Spitzer*'s IR wavelengths than their redder counterparts.

A stellar mass of around 0.62–0.64 $M_{\odot}$ suggests that 0.18–0.20 $M_{\odot}$ is lost on the RGB, which is in keeping with Dotter (2008), who suggests that the total mass lost on the RGB does not greatly depend on metallicity above [Fe/H] $\sim$ –2.

Globular cluster white dwarf masses (*e.g.* Moehler et al. 2004) suggest that $\sim$0.3 $M_{\odot}$ must be lost on the RGB and AGB combined (the core mass in this case is 0.49 $M_{\odot}$), implying that around two thirds of the mass loss occurs on the RGB in ω Cen. Interestingly, we also expect about a third of the mass loss from the cluster to be in the form of chromospheric winds (see §5.6.5.2), implying at least half the dusty mass loss occurs on the RGB.

Some concerns have been raised that the HB models from the Dartmouth models may be marginally too warm for low-metallicity stars (A. Dotter, private communication). Nevertheless, given the much more precise fit to the data, we would advocate the Dartmouth model values over those derived from Marigo et al. (2008).

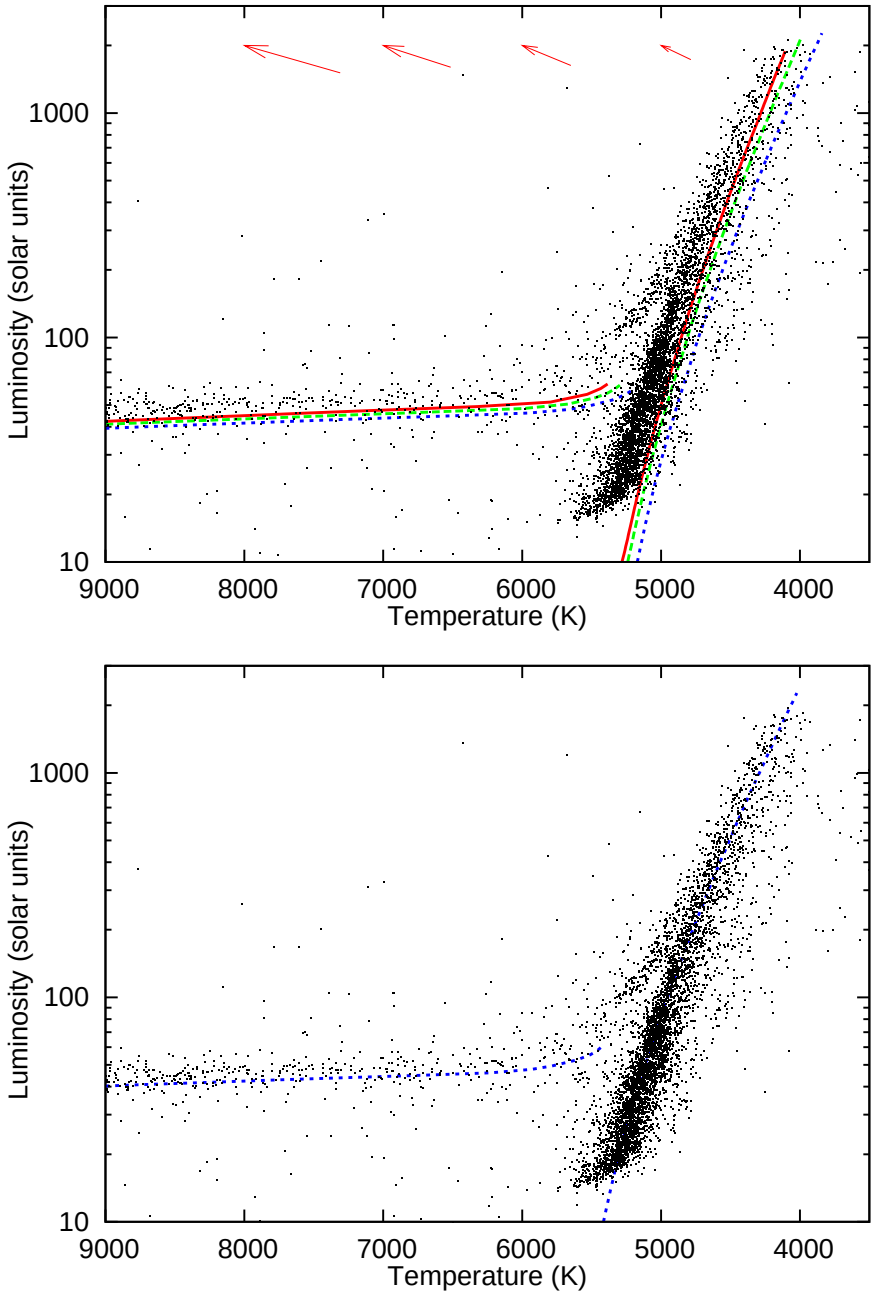

Figure 5.10: As Fig. 5.6, using Victoria-Regina isochrones and ZAHB models from VandenBerg, Bergbusch & Dowler (2006). The top panel shows a 12 Gyr isochrone and ZAHB model for [Fe/H] = –1.61, with [α/Fe] = +0.0 (solid line), +0.2 (dashed line) and +0.4 (dotted line). The bottom panel shows the fitted model at [α/Fe] = +0.4, still at 12 Gyr, with E(B–V) = 0.09 mag and d = 4800 pc, with the model temperatures increased by 4.7% (0.02 dex).

5.4.3 Victoria-Regina isochrones and ZAHB models

We have performed a similar analysis using the Victoria-Regina (VR) isochrone and ZAHB models of VandenBerg, Bergbusch & Dowler (2006), which we show in Fig. 5.10. Here, we take the models at [α/Fe] = +0.0, +0.2, +0.4 for [Fe/H] = –1.61 at 12 Gyr. No values of reddening or distance, nor any sensible value of age can accurately match the VR isochrone on the RGB to our data for any value of [α/Fe]. In order to achieve a fit, we must either increase the temperature of the VR model, or decrease the temperatures of our stellar data, by around 0.01 dex (2.3%) in the case of [α/Fe] $\sim$ 0 or 0.02 dex (4.7%) in the case of [α/Fe] $\sim$ +0.4. The value of [α/Fe] is suggested to be around +0.3 for cluster stars with [Fe/H] $\lesssim -1$ (Pancino 2003). Under this assumption, we find a reddening of around $E(B-V) = 0.08$ mag and a distance of 4800 ± 100 pc.

On the assumption that the ZAHB location for the majority of metal-poor stars is well-represented by the clump around 8500–11 000 K, and that [α/Fe] $\approx$ +0.3, we find that most stars have a ZAHB mass of around 0.61 ± 0.02 M$_\odot$ (Fig. 5.11). Obviously, this issue is clouded by HB evolution and lack of fully accurate measurements of temperatures and luminosities in this area, but the figure is broadly consistent with that from the Dartmouth models above, predicting only a slightly lower stellar mass. The 12 Gyr VR model predicts that the initial mass of RGB tip stars is 0.85 M$_\odot$ and that the core mass is 0.49 M$_\odot$ at $\alpha = +0.3$. This suggests that $\approx$0.24 M$_\odot$ is lost on the RGB and $\sim$0.12 M$_\odot$ on the AGB, if the entire envelope is ejected. This ratio of 2:1 is consistent with that derived from the Dartmouth models.

5.4.4 BaSTI isochrones

We show a fit using the BaSTI models ('A bag of stellar tracks and isochrones'; Pietrinferni et al. 2006) in Fig. 5.12 (top panel). As before, we take a 12 Gyr model at [Fe/H] = –1.62 at a helium content of $Y = 0.246$. We use the α-element enhanced models with

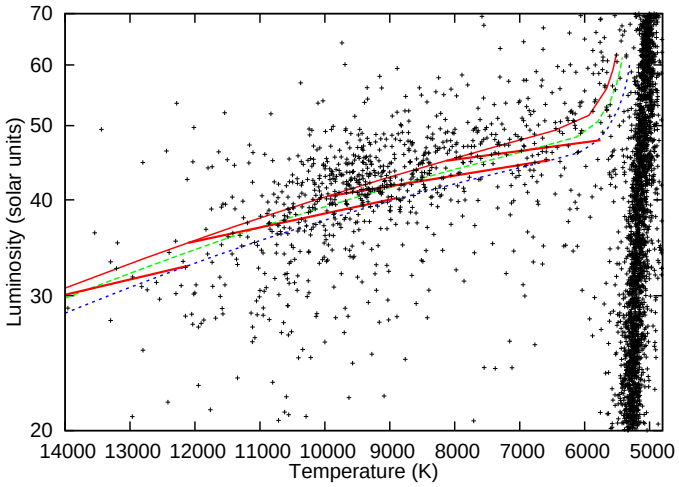

Figure 5.11: As Fig. 5.9, with $d = 4750$ pc and $E(B-V) = 0.08$ mag, showing the ZAHB models from the Victoria-Regina models, at [Fe/H] = –1.61 and [α/Fe] = +0.0, +0.2 and +0.4 (as in Fig. 5.10). Thicker lines show the stellar masses on the ZAHB at 0.575, 0.600, 0.625 and 0.650 $M_\odot$.

$\eta = 0.2$ and 0.4 (Reimers 1975), incorporating BaSTI's synthetic AGB evolutionary tracks from Iben & Truran (1978).

We note that, although the synthetic HB and AGB data fit the empirical cluster data well, the RGB is significantly cooler and under-luminous in the BaSTI model. The only way we can find to rectify the large gap between the early AGB and RGB is by assuming the cluster is much younger than has previously been calculated, at an age of $\lesssim 9.5$ Gyr. Taking models at this age, we found the reddening to be only $E(B-V) = 0.06$ mag and $d = 4900$ pc.

The young age of the fitted model is at odds not only with the luminosities of the RGB and AGB tips, but with previous age estimations of typically 11–14 Gyr, derived using a variety of data and methods including isochrone fitting to colour-magnitude diagrams including stars down to ~ 0.15 $M_\odot$ (Thompson & Kałużny, J. and Pych, W. and Burley, G. and Krzemiński, W. and Paczyński, B. and Persson, S. E. and Preston, G. W. ; Kałużny, J. and Thompson, I. and Krzemiński, W. and Olech, A. and Pych, W. and Mochejska, B. ; Chaboyer & Krauss 2002; Pancino 2003; Platais et al. 2003; Hilker et al. 2004). BaSTI models this old do not have the narrow separation between

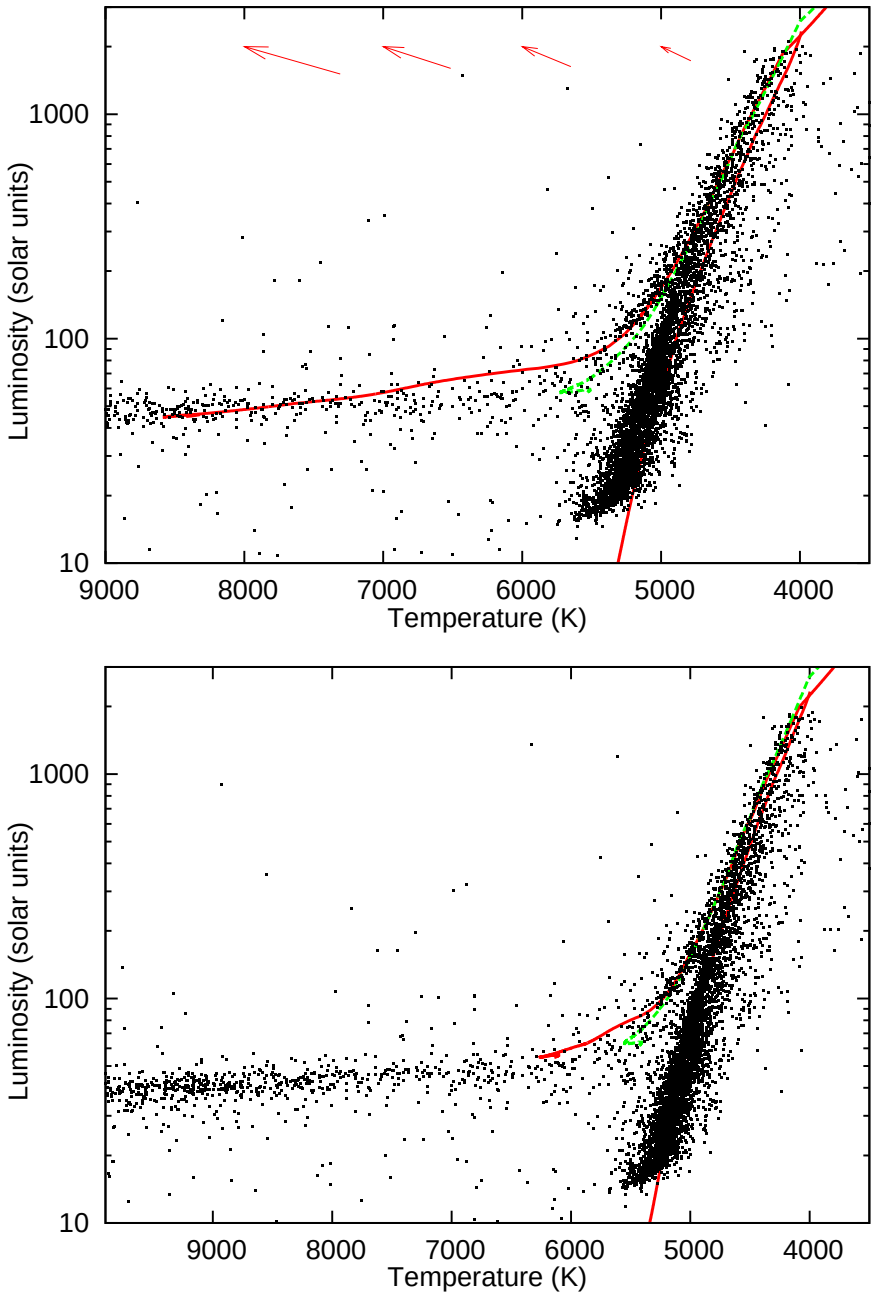

Figure 5.12: As Fig. 5.6, using BaSTI isochrones. The top panel shows the same three RGB isochrones as Fig. 5.6, with the α-enhanced AGB-extended BaSTI model for $Z = 0.001$ ([Fe/H] = –1.62), at 12 Gyr. The bottom panel shows the fitted model, at 9.5 Gyr, with E(B–V) = 0.06 mag and $d = 4900$ pc. The solid lines assume Reimers' $\eta = 0.4$; the dotted lines show the AGB for $\eta = 0.2$.

the RGB and AGB. Another implication of this is that mass-loss efficiency must range from $\eta \approx 0.2$ to $\eta \gg 0.4$ (probably ≈ 0.7 to 0.8 and perhaps higher for the Extreme HB, which we do not model). This level of mass-loss efficiency is not considered to be impossible, and very similar values have been suggested for ω Cen in the past (d'Cruz et al. 1995).

5.4.5 Summary of isochrone fitting

In summary, we find that the Dartmouth models provide the best fit to our data, although the models of Marigo et al. (2008) may provide a similarly good fit if the mass-loss efficiency could be increased. The BaSTI models provide too small a temperature difference between the early RGB and AGB, which would appear unlikely to be due to a systematic error in our data, and can consequently only fit our data with a significantly decreased age. The Victoria-Regina models have an effective temperature which clearly differs from our data by up to 5% in both the isochrones and the ZAHB models.

Taken in combination, the models consistently suggest a distance to the cluster of around 4850±200 pc, and an average reddening to the cluster of $E(B-V) = 0.08 \pm 0.02$ mag. These values are both at the lower limit of those derived in the literature, which roughly span the ranges of 5160±360 pc and $E(B-V) = 0.12 \pm 0.03$ mag (see §5.3 for references). The distance is very close to the 4740±160 pc in vL+00, whose data we use here. However, we note that this was derived using velocity dispersion data, not the photometry we use here, and is thus nearly independent. We cannot entirely rule out a distance of 5000 pc, though this fits the start of the early AGB less well, and requires a reddening of only $E(B-V) = 0.05$ mag. Conversely, a reddening of $E(B-V) = 0.12$ mag would suggest a distance of ∼4600 pc.

The potential for systematic error in our temperatures and luminosities (§5.3) is relatively small for stars within the range 4000–6500 K, and increases as one moves away from this region. We estimate that, excluding uncertainties in distance, and average and differential reddening, systematic differences on the RGB and AGB can

be limited in temperature to $< 1\%$ and in luminosity to $\lesssim 5\%$. Very red stars and HB stars have the potential for higher systematic errors due to the lack of MARCS models covering these temperature ranges. This has the potential to make a systematic offset to our distance of up to ± 120 pc and of up to ± 0.015 mag in $E(B-V)$. The 10–15% discrepancy in our reddening correction found in §5.3 and the assumption that the foreground ISM follows the approximation $A_{\rm V}/E(B-V) \approx 3.05$ probably inflates the systematic error in $E(B-V)$ to 0.020 mag. Treatment of convection by the stellar evolution models may also cause a systematic offset in the distance and reddening we determine to the cluster. However, all four models include physics describing convective core overshoot. The exact physics employed does not appear to have made a significiant difference to our results, as the distance we estimate to the cluster is roughly the same with all four models.

As interstellar extinction has a larger effect at bluer wavelengths, the alteration of $E(B-V)$ does not much affect the values we derive for our mass-losing stars, which are typically cooler than the giant branch, although a distance of 4850 pc would mean that their luminosities would still decrease by 6% due to the distance correction. The net effect would be a decrease in our total mass-loss rates by 4.5%, though this is included in the errors we list in §5.5.2 & §5.6.2.

From arguments stemming from the location of evolutionary sequences on the HRD, we conclude that most of a cluster star's mass loss must occur near the tip of the RGB, rather than on the AGB. The HB morphology of the cluster requires that typically 0.20–0.25 $M_\odot$ of stellar atmosphere is lost from the (initially) 0.85 $M_\odot$ stars on the RGB. Stars then attempt to lose a further 0.05 $M_\odot$ or more on the AGB, but many may have insufficient atmospheric mass to lose and thus become post-early-AGB stars or even AGB-*manqué* stars ('failed' AGB stars — see, *e.g.* O'Connell 1999, §6.2). That mass loss can work this efficiently at metallicities as low as [Fe/H] ~ -1.6 suggests that metallicity and mass loss have only a weak dependence in this metallicity regime.

5.5 Deriving mass-loss rates

5.5.1 Mid-IR spectra and additional data of V6 and V42

Spectra were taken of the two most extreme red giants in the cluster: V6 (LEID 33062, ROA 162) and V42 (LEID 44262, ROA 90). Taken with the T-ReCS spectrograph on the Gemini South Telescope (de Buizer & Fisher 2005), the data are between 8 and 13 μm and have a resolving power of $\Delta\lambda/\lambda = 300 - 600$, along with N'-band (11 μm) acquisition images, on each of the nights of 2007 August 16 & 18, for V6; and on 2007 August 27 & 28, for V42. Two spectra of 2.5 hours integration were taken each night, using the low resolution 10-μm grating, along with the 0.72″ slit. The full width at half maximum of the standard star — the K0 giant θ Cen — was $\sim$0.44″ in the N'-band acquisition images.

The spectra were reduced using the IRAF package[1] designed for T-ReCS using the default settings. No wavelength offsets were observed, and differences among the spectra were small, so a flux-density-weighted average was taken to provide a single, high-signal-to-noise spectrum for each target. An absolute flux density for each target was estimated by comparing the acquisition images of the target stars and θ Cen using aperture photometry. Assuming an N'-band flux density of 45.4 Jy for θ Cen[2], a flux density of 203$\pm$12 mJy was calculated for V6 and 91$\pm$16 mJy for V42. The acquisition field for V42 also included the mid-M-type irregularly-variable red giant star V152 (LEID 44277), which is a confirmed cluster member (vL+00, vL+07). By comparison to V42, we estimate its N'-band flux density is 36$\pm$8 mJy. Comparison with the 8- and 24-μm *Spitzer* data shows this value to be consistent with a mid-infrared excess, but the error on the *Gemini* photometry is too large to constrain whether a 10-μm silicate feature is present in V42.

The flux-density-calibrated spectra for both stars are shown in Fig. 5.13. Clear

[1] IRAF is distributed by the National Optical Astronomy Observatories (NOAO), which is operated by the Association of Universities for Research in Astronomy, Inc., under co-operative agreement with the National Science Foundation.

[2] Extrapolated from http://www.gemini.edu/sciops/instruments/miri/T-ReCSBrightStan.txt

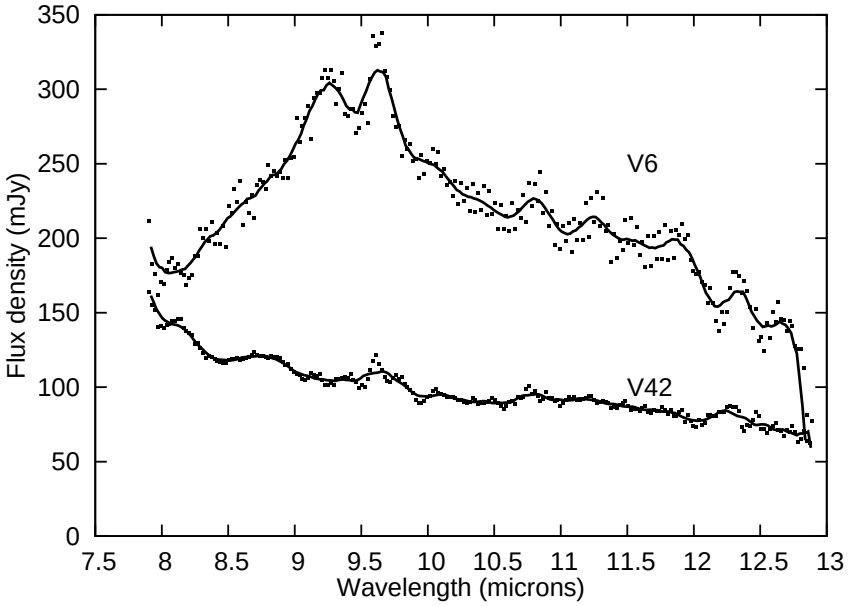

Figure 5.13: Flux-density-calibrated Gemini T-ReCS spectra of the two extreme red giant stars ω Cen V6 and V42, overlaid with a running boxcar average of 10 pixels.

fringing in the spectrum of V6 can be seen. Attempts to correct for this by moving each spectrum by an integer number of pixels failed to improve this. We note that many of the 'features' in the spectra are also the result of imperfect atmospheric correction. The most notable of these, the double-peaked 9.5-μm emission, is associated with ozone in the Earth's atmosphere. The underlying, broadband emission, however, is intrinsic to V6.

In the case of V6, additional optical photometry was available from Cannon & Stobie (1973), Lloyd Evans (1983c), and Clement (1997). Near-IR data from Persson et al. (1980) were also used. Of particular use were the works by Dickens et al. (1972), and Glass & Feast (1973, 1977), which not only provide flux densities, but variability amplitudes, allowing us to see the temperature and luminosity changes in the star from U- to L-band. We have previously obtained a 2dF optical spectrum for this star (published in vL+07), where it was determined to have a temperature of $\sim$3500 K (the lowest-temperature model).

For V42, the same papers provided information on flux densities and variability.

Additional data were available from the DENIS survey (Deep Near Infrared Survey of the Southern Sky; Fouqué et al. 2000); Menzies & Whitelock (1985), which includes variability information; and 9.6-, 10- and 12-μm photometric data points (Origlia, Ferraro & Fusi Pecci 1995; Origlia et al. 2002, hereafter O+02). In addition to a 2dF spectrum, we also have an optical VLT/UVES spectrum for V42 (Chapter §3), though our previous temperature estimates have not been particularly reliable as a result of veiling by emission dissipated in the pulsation shock. The resulting SEDs for V6 and V42 are shown in Fig. 5.14.

5.5.2 Deriving a mass-loss rate for V6 and V42

5.5.2.1 Mass loss of V6 from Gemini spectroscopy

Estimates of the mass-loss rate for the two stars V6 and V42 were determined using the DUSTY modelling code (Nenkova, Ivezić & Elitzur 1999). Our Gemini T-ReCS spectrum of V6 (Fig. 5.13) shows clear emission from silicate dust grains around 10 μm, typical of well-developed dusty winds seen around AGB Mira variables in the Solar Neighbourhood (*e.g.* Speck et al. 2000). The spectrum is not well fit by the classic 'astronomical' silicates alone (Draine & Lee 1984), especially the 9.5-μm peak, regardless of the dust properties used. Our best fit was for 65% (by number of grains) 'astronomical' silicates (Draine & Lee 1984), 15% compact Al_2O_3 (optical constants from Jena database[3]), and 10% each of glassy and crystalline silicates (Jäger et al. 1994) (Fig. 5.14). Although we have used these to produce the best fit, we do not claim that these are necessarily the particular species of silicates involved, nor that they are present in these proportions. We assume a radiatively-driven wind and a standard MRN grain size distribution (Mathis, Rumpl & Nordsieck 1977), where the number of grains of size a is given by $n(a) = a^{-q}$, where we here take $q = 3.5$ over the range $a = 0.005 - 0.05$ μm. We derive an inner edge to the dust envelope at a

[3]http://www.astro.uni-jena.de/Users/database/entry.html

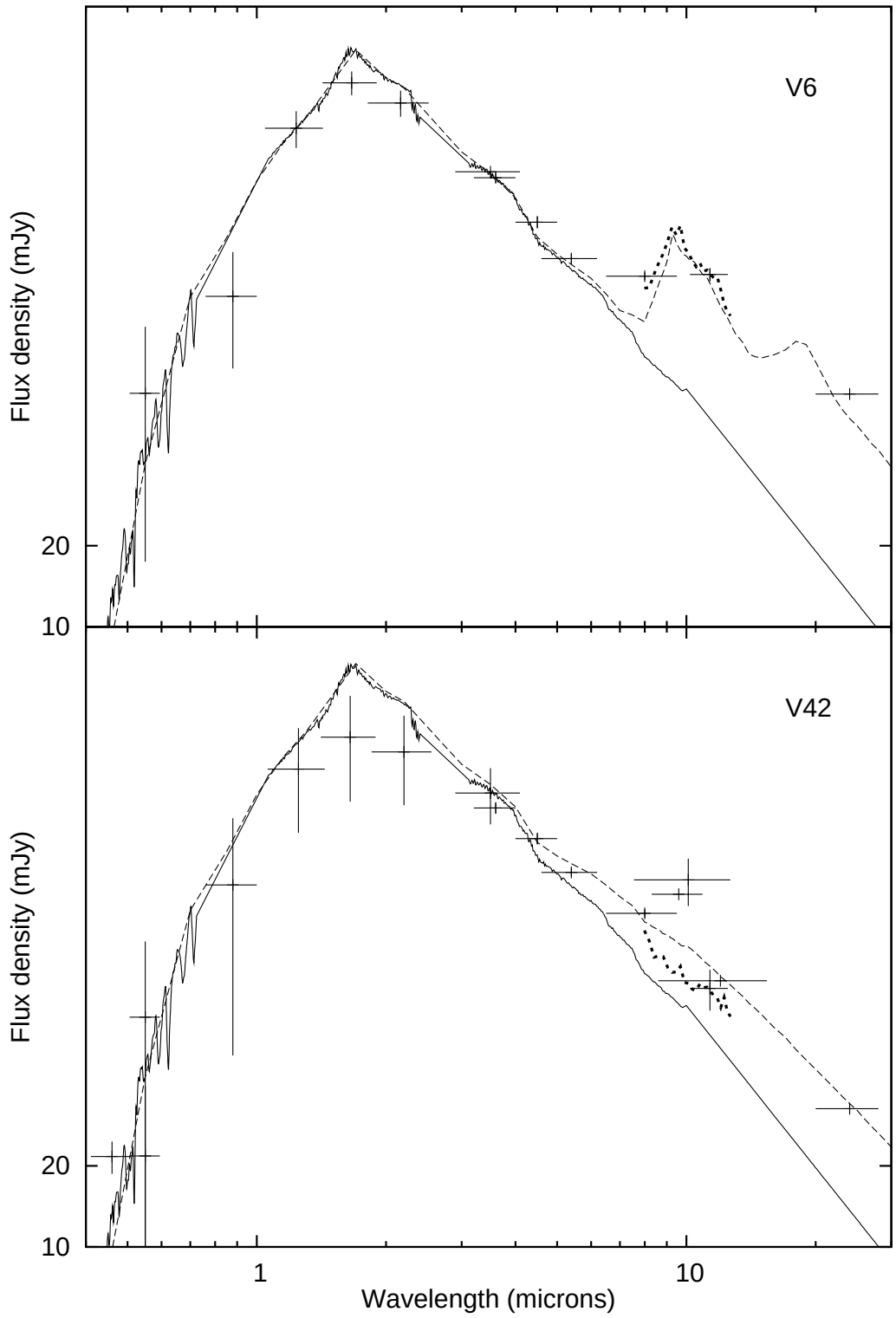

Figure 5.14: SED models of V6 (top) and V42 (bottom), showing MARCS models smoothed to $R = 200$ (solid lines), smoothed Gemini T-ReCS spectra (dotted lines) and literature photometry (crosses with error bars). The error bars in the latter reflect either the photometric variability or the measurement error (see text for details). The dashed curve shows the corresponding DUSTY model, fitted to the Gemini spectrum and 24-μm *Spitzer* datum in the case of V6 and the literature photometry, including *Spitzer* data, in the case of V42.

temperature of 650 K, and a V-band optical depth of $\tau_{\rm V} = 0.08$ for V6. This dust temperature is relatively cool, and could potentially be related to mid-IR variability, which we discuss in §5.5.2.2. An increase in the dust temperature to a more typical 1000 K would decrease the mass-loss rate by a factor of nearly two (§5.5.3.2).

The maximum grain size also has a weak effect on the dust mass-loss rate. Here, we have chosen 0.05 μm, which we believe is representative of this metal-poor environment, which may be subject to substantial UV flux from other cluster members. This also provides a marginally better fit to the region around 11 μm in our V6 spectrum (*c.f.* Voshchinnikov & Henning 2008, Fig. 1). Our value is, however, less than the usual value of 0.1 μm, or higher, assumed in the literature (*e.g.* Papoular & Pégourié 1983). Increasing the maximum grain size to 0.1 μm would decrease the mass-loss rate by $\sim$20%, a factor that does not change much as one further increases the parameter. While theoretically possible to measure, it is very difficult to constrain the grain sizes involved purely from the SED alone (Carciofi, Bjorkman & Magalhães 2004).

The dust mass-loss rate and total mass-loss rate from a star are related to the DUSTY output by the following equations (Nenkova, Ivezić & Elitzur 1999; §1.6.4.1):

$$\dot{M}_{\rm dust} = \frac{\dot{M}_{\rm DUSTY}}{200} \left(\frac{L}{10^4}\right)^{3/4} \left(\frac{\psi}{200}\right)^{-1/2} \left(\frac{\rho_{\rm s}}{3}\right)^{1/2}, \tag{5.8}$$

$$\dot{M} = \dot{M}_{\rm dust}\psi, \tag{5.9}$$

where L is the luminosity in solar units, ψ is the gas-to-dust ratio and $\rho_{\rm s}$ is the bulk grain density in g cm^{-3} (we assume it to be 3 g cm^{-3} for silicates; *e.g.* Suh 1999).

Eq. (5.9) holds when condensation into grains occurs efficiently. We expect much of the condensible material to form silicate grains: the higher condensation of iron oxides mean they will typically form "seed" inclusions, rather than competing with silicon. We therefore expect silicate grain growth to scale inversely linearly with the metallicity, and specifically the abundance of silicon. Eq. (5.9) may not extend to stars where chromospheric mass-loss is important and dust production is not efficient, where

the dust-to-gas ratio is expected to follow a square-law dependence on metallicity (van Loon 2000a, 2006). We assume here that $\psi = 200$ for solar composition stars, which for V6 we take as [Fe/H] $= -1.19$ (Zinn & West 1984; Norris & da Costa 1995; Vanture, Wallerstein & Suntzeff 2002).

These mass-loss rates are uncertain due to:

- 30% uncertainty in the dust mass-loss rate from internal errors in DUSTY, due to an uncertain (and unspecifiable) stellar gravity (see §1.6.4.1);
- $\lesssim 30\%$ uncertainty in the dust mass-loss rate due to uncertain dust chemistry, temperature and grain size;
- 11% and 6% uncertainty in the photometric *excess* above the SED at 8 and 24 μm, respectively;
- $\sim 3\%$ uncertainty in the dust mass-loss rate due to inaccuracies in the stellar temperature;
- $\lesssim 5\%$ uncertainty due to error in the integrated flux density from the SED;
- 22% uncertainty due to error in luminosity;
- $\sim 5\%$ uncertainty due to error in the reddening;
- $\sim 12\%$ uncertainty due to error in the distance.

When added in quadrature, this gives a total error of $\lesssim 52\%$ in the *dust* mass-loss rate from V6, and is also based on the following assumptions:

- that the mid-IR spectrum V6 has not varied substantially between the 8- and 24-μm exposures;
- that $\psi \propto 10^{-[\mathrm{Fe/H}]}$ (see §1.6.4.1);
- that the wind velocity scales as prescribed in the DUSTY code: $v \propto L^{1/4}\psi^{-1/2}$, (also discussed in §1.6.4.1);
- that the dust is coupled to the gas.

We discuss these assumptions in §5.5.2.2 & §5.6.3. As we presently cannot quantify whether these assumptions are valid, their effect on the total uncertainty remains unknown. Departure from the first two assumptions is likely to be small, however

departure from the final two assumptions could (respectively) increase and decrease the total mass-loss rate by a factor of several.

We thus find that for V6, if the above assumptions are valid, $\dot{M}_{\rm dust} = 3.8 \pm^{2.0}_{1.3} \times 10^{-10}$ M$_\odot$ yr^{-1} and $\dot{M}_{\rm total} = 1.1 \pm^{0.6}_{0.4} \times 10^{-6}$ M$_\odot$ yr^{-1}.

This total mass-loss rate for V6 is comparable to our earlier measurements in 47 Tuc (van Loon et al. 2006a), though it is generally higher than more metal-rich, solar-mass Mira variables in the Solar Neighbourhood (Jura & Kleinmann 1992), probably due to its proximity to the RGB/AGB tip. It is also slightly inflated from those derived in B+08 purely on the basis of the *Spitzer* data and the models of Groenewegen (2006). We note that the above values and quoted errors depend on the invariance of V6 between the acquisition times of the *Spitzer* IRAC and MIPS photometry, and of the Gemini T-ReCS spectrum.

5.5.2.2 Mass loss of V42 from Gemini spectroscopy

The mass-loss rate of V42 is more complicated to derive, as there are considerable variations in the mid-IR spectrum, plus the metallicity of the star is unknown. The literature data on V42 (see Table 5.3) appear to show a clear silicate feature, which we have fitted using DUSTY. We have set the dust envelope's inner edge to be at 1200 K, near the temperature limit for SiO condensation under normal circumstances (Nuth & Ferguson 2006). The fitted model has an optical depth of $\tau_{\rm V} = 0.25$, with the remaining input parameters staying the same as the model for V6. Assuming a metallicity of [Fe/H] = –1.62, this yields rates of $\dot{M}_{\rm dust} = 8.6 \times 10^{-11}$ M$_\odot$ yr^{-1} and $\dot{M}_{\rm total} = 7.2 \times 10^{-7}$ M$_\odot$ yr^{-1}.

The Gemini spectrum shows excess above the Rayleigh-Jeans tail that could be attributable to dust. The rise towards 8 μm could represent the SiO fundamental band in emission, but this is near the edge of the atmospheric window and thus uncertain. The absence of a silicate feature in the spectrum is puzzling, given the clear feature apparently present in the literature broadband photometry (see Table 5.3 & Fig. 5.14).

Table 5.3: Mid-IR photometry of ω Cen V42.

Phase[1]	Date	Ref.[2]	Telescope/Instrument	λ (μm)[3]	Flux[4]
0.00	02 Jun 94	a	ESO 3.6m/TIMMI	10	3.1
	Feb/Aug 97	b	*ISO*/ISOCAM	9.6	2.5
	Feb/Aug 97	b	*ISO*/ISOCAM	12	1.8
29.87	02 Mar 06	c	*Spitzer*/MIPS	24	1.9
30.03	26 Mar 06	c	*Spitzer*/IRAC	8	1.6
30.87	29 Jul 07	d	*Spitzer*/IRS	5–37	2.3
31.07	27 Aug 07	e	Gemini/T-ReCS	8–13	1.3

Notes: (1) Phase in pulsation periods from I-band maximum, taken to be MJD 49506 after Dickens, Feast & Lloyd Evans (1972), with $P = 148.64$ days (vL+00); (2) References: a — Origlia, Ferraro & Fusi Pecci (1995); b — O+02; c — B+08; d — G. Sloan, private communication; e — this work; (3) Ranges denote spectra; (4) Flux as a multiple of the photospheric contribution, extrapolated from spectral models; flux calculated using a $F \propto \lambda^{-1.7}$ approximation for photometric observations that are not at 10 μm.

These historical estimates for the mid-IR brightness of V42 have been high. Previous estimates of its mass loss have suggested a mass-loss rate of 7–10 $\times$ 10^{-7} $M_\odot$ yr^{-1}, with a 200–350 K dust envelope, and it has been suggested that this is associated with a period of dust ejection around 1925, possibly linked to a thermal pulse event (Origlia et al. 1995; O+02). This is similar, though cooler than, the mass-loss rate estimated from the DUSTY fit to our *Spitzer* and Gemini data. However, what is obvious from Table 5.3 is the factor of 2.4 range in the 10-μm flux received from V42 since 1994. The obvious solution would be that this is connected with a periodic phenomenon linked to the pulsation cycle. There is no obvious link with pulsation cycle phase, though all observations were taken close to zero phase. The amplitude of variation is also somewhat larger than the factor of 1.6 change in the L-band flux observed by Dickens et al. 1972. Note that all flux values in Table 5.3 show mid-IR excesses, strongly suggesting the presence of circumstellar dust.

Surprisingly for this M-type star, the emission from the *Spitzer* photometry and

Gemini spectrum are well-fit by an *amorphous carbon* wind (following Hanner 1988) with a constant temperature of 600 K and a mass-loss rate of between 1.7–4.3 $\times$ 10^{-10} $M_{\odot}$ yr^{-1} in dust and 1.4–3.6 $\times$ 10^{-6} $M_{\odot}$ yr^{-1} in total. The variance here comes from the uncertainty in the absolute flux calibration of the spectrum. Note that this figure is some 2–4 times greater than that derived from fitting *silicate* dust to the literature photometry. The implied carbonaceous nature of the wind is puzzling, as this is not a *bone fide* carbon star (vL+07).

This carbon-rich model also holds for a recent *Spitzer* IRS spectrum of V42, taken four weeks prior, covering the range 5–37 μm (G. Sloan, private communication). This spectrum shows an essentially 'naked' star with no silicate feature, but with considerable flux excess, particularly at longer wavelengths.

It is clear that neither of the recent spectra show silicate emission. What is interesting is that, although the spectrum does not change appreciably between the two epochs, the *flux* received from V42 decreases considerably, mirroring the wide range in the historic photometry measurements. We discuss possible reasons for this in §5.6.5.4.

The key consequence of the mid-IR variability observed in V42 is that it now becomes virtually impossible to accurately pin down a mass-loss rate to better than a factor of $\sim$2 without simultaneous observations of the flux at $\lesssim$ 4 μm, where the dust component does not dominate, to define the stellar temperature and luminosity.

With respect to the rest of our data, it would appear that the accuracy of the mass-loss rates of other stars may depend on their optical variability, plus the optical properties of their circumstellar dust. This is a potential source of error in our analysis, but given that V6 and V42 are by far the most extreme pulsators, it would appear that V6 is the only other likely candidate for significant mid-IR variability. Our only comparison here is between the *Spitzer* photometric data and the Gemini spectrum, but would appear to limit the effect to a level much less than the known errors present in our mass-loss analysis.

5.5.3 Derivation of mass-loss rates for other stars

5.5.3.1 Correction of systematic differences between *Spitzer* photometry and model atmospheres

Fig. 5.15 shows the distributions of excess above the model at 8 and 24 μm, respectively. Clearly, V6 and V42 are the most excessive stars, although there are a few others exhibiting excesses at both 8 and 24 μm. Those objects with flux excesses at low luminosities are likely background galaxies or mis-identifications.

There is an observable offset between the model atmospheres provided by MARCS and the 8- and 24-μm photometry data for the warmer, less luminous stars (the giant branch is offset from unity towards the bottom of Fig. 5.15). This effect is only $\sim$1% for the brightest stars, but increases to $\sim$4% and $\sim$10% for the fainter stars at 8 and 24 μm, respectively. The reason behind this is unclear, as from a modelling perspective one would assume that the Rayleigh-Jeans tail that has been used in extending the model atmospheres out to the limit of the 24-μm filter would be more accurate in a warmer atmosphere. A silicate absorption feature caused by interstellar material (*c.f.* Evans et al. 2002) can also be ruled out, as it is only expected to affect our 8- and 24-μm photometry by about 0.5% in each case, based on a 100 K interstellar medium at $A_{\rm V} = 0.4$ mag. A combination of SiO and H_2O absorption in the region of the 24-μm filter bandpass may affect the cooler giants. It may be that this under-luminosity in the fainter stars is a result of imperfect data reduction of the *Spitzer* MIPS data near the sensitivity limit of the instrument.

While this correction is not significant on the level of individual stars, it is important when considering the cluster as a whole: without a correction for this effect, the total mass-loss rate for the cluster would be grossly incorrect. In order to minimise the effects of statistical scatter in the photometry, we have assumed that stars with less-than-expected 8- and 24-μm fluxes have negative mass-loss rates. This is unphysical, but by making this assumption we can examine stars with low mass-loss rates in a statistical manner, with a minimum bias from random uncertainty in the photometry.

To calculate the correction, we have assumed that the average star produces negligible dust, therefore will have no flux excess. The rapid drop-off of flux excess to a constant fraction at around $\sim L_\odot$ (Fig. 5.15) suggests the amount of dust production below this luminosity is small. This may also be expected as stars become progressively more solar-like in appearance and mass-loss mechanism as one heads down the RGB (§3). Furthermore, the amount of dust produced for a given excess is proportional to $L^{1/4}$ (Nenkova, Ivezić & Elitzur 1999), meaning the observable limit of dusty mass-loss rates (gradually) decreases with luminosity also.

There are then two situations where this assumption could be untrue: (1) that every star produces a small, constant, near-identical amount of dust — this has not been observed and would require some explanation; or (2) that some stars of these stars produce an amount of dust too small to be observed. In the latter case, we estimate this cannot exceed an average of 2×10^{-12} $M_\odot$ yr-1 for the brighter stars, or 10^{-9} $M_\odot$ yr$^-1$ in total.

Under the above assumption, the data is then split into luminosity bins of 0.1 dex, and for each, calculate the average offset. These form a tight correlation, except at the lower and upper limits, where poor-quality data and significantly dusty atmospheres (respectively) deviate the median. Taking the intermediate points (representing 21 bins, containing 1624 stars at 8 μm and 1207 stars at 24 μm), we have computed a best-fit line and removed this from the data. These corrections are:

$$\left(\frac{F_{\rm obs}}{F_{\rm exp}}\right)'_{8\mu{\rm m}} = \left(\frac{F_{\rm obs}}{F_{\rm exp}}\right)_{8\mu{\rm m}} + 0.01\log(L) - 0.035, \tag{5.10}$$

$$\left(\frac{F_{\rm obs}}{F_{\rm exp}}\right)'_{24\mu{\rm m}} = \left(\frac{F_{\rm obs}}{F_{\rm exp}}\right)_{24\mu{\rm m}} + 0.025\log(L) - 0.27. \tag{5.11}$$

5.5.3.2 Dust temperatures

For the remainder of the stars we examine, we have only the 8- and 24-μm data from which we derive a mass-loss rate. At this point, we are forced to make some assumptions

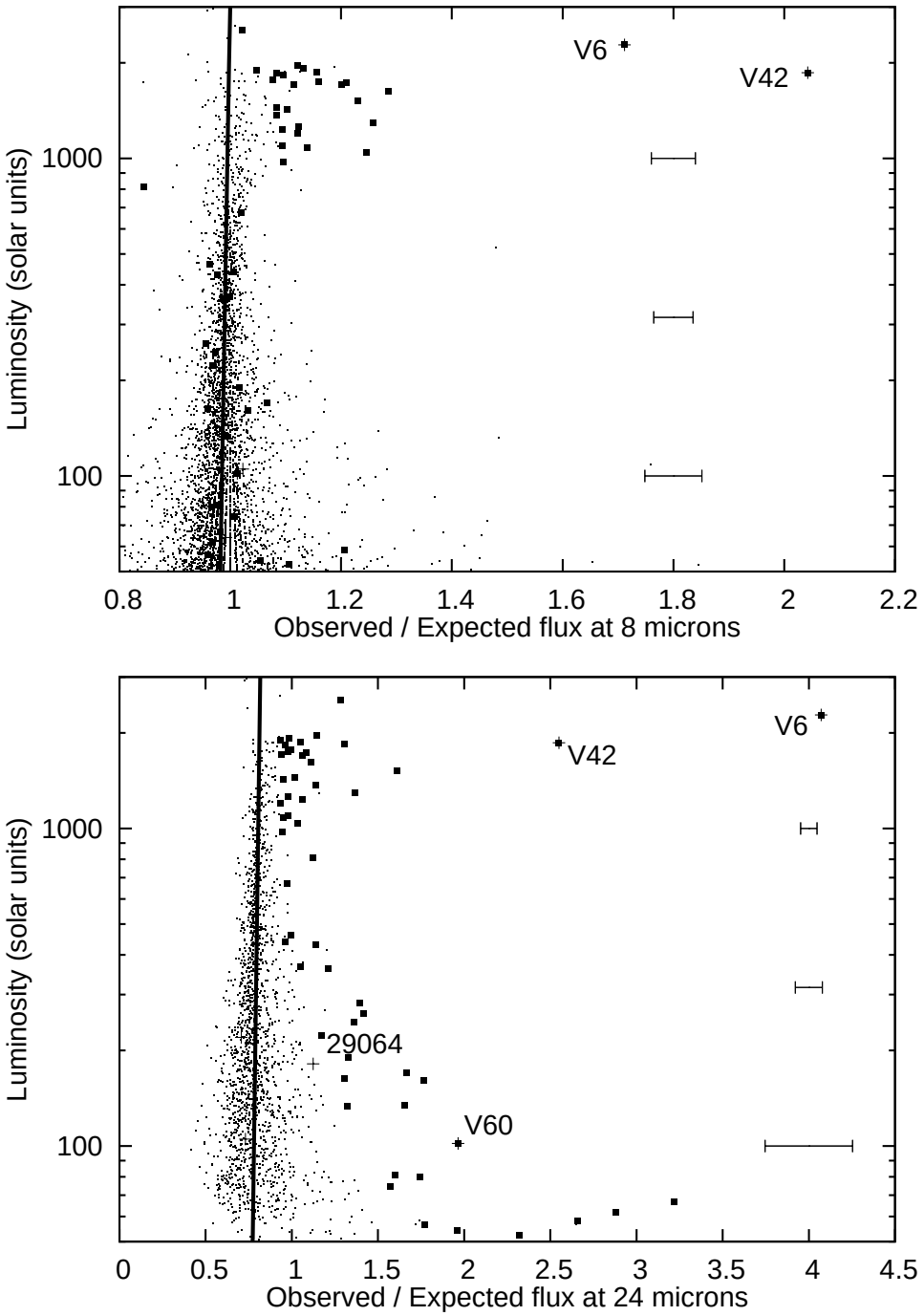

Figure 5.15: Observed mid-IR excess (attributable to dust) at 8 and 24 μm, derived from fitting to model atmospheres. Over-plotted is the line we have taken marking 'zero' dust mass loss from Eqs. (5.10) and (5.11). Representative 1σ error bars are shown to the right of the plots — stars which have mid-IR excess above the 3σ level at 24 μm are marked by large squares.

about the mineralogy of the dust. We assume here for simplicity that all stars show 'astronomical' silicate dust, following Draine & Lee (1984). This thus means that our dust mass-loss rates will tend to under-estimate the total mass-loss rate of the star, as our wavelength coverage misses the 12-μm Al_2O_3 and 13-μm $MgAl_2O_4$ bands seen at the start of the proposed dust condensation sequence (Lebzelter et al. 2006). Carbon-rich dust is also not considered for the majority of stars: if it is present, the assumption of silicate dust alone will again lead to an under-estimation of total mass-loss rate, as in the case of V42, by a factor of two to four.

Our first priority was to derive an estimated dust temperature for the stars as, for a given optical depth, mass loss can vary significantly with dust temperature. In order to do this, we constructed a grid of DUSTY models at 4000 K, with similar dust properties as those used for V6, but with a pure 'astronomical' silicate dust component and $\tau_V = 0.02$ and a standard MRN distribution. The temperature of the inner edge of the dust envelope was varied from 200 to 1500 K, in steps of 100 K.

The dependence of the calculated mass-loss rate on the assumed photospheric temperature of the star is relatively weak: for a constant IR excess and stellar luminosity, a comparison of DUSTY models shows that $\dot{M}$ scales roughly as $T^{1.25}$ in the region of 4000–4500 K, providing a reasonable (within 10%) fit to photospheric temperatures up to 6000 K. This factor takes into account the increase in wind velocity (from increased radiation pressure) that DUSTY calculates for higher-temperature stars. A velocity scaling relation of $v_\infty \propto T^{1/3}$ can be shown to match the output from DUSTY to within 2% over temperatures from 3500 to 6000 K. We make these corrections in our final rates, but they do not add a considerable effect over the range of temperatures at which stars appear to be losing mass by dust-driven winds.

Errors in the stellar temperature will have an impact here, though their primary influence is on the inferred luminosity of the star, since our dust mass-loss rates use photometry taken from the Rayleigh-Jeans tail of the stellar spectra. This will add a 10% error in the mass-loss rates of the most-luminous non-variable stars, and up

to 30% in the mass-loss rates of the most-luminous variable stars, due to their higher temperature uncertainties. Due to the stochastic nature of these errors, the effect on the sample as a whole will be greatly reduced from this.

We can then derive the temperature of the dust, under the assumption that the underlying photospheric spectrum follows a Rayleigh-Jeans tail. The [8]–[24] colour *of the excess emission from the dust* will then be directly indicative of the dust temperature, provided the chemical make-up of the dust does not change. For each model, we derive the [8]–[24] colour we would observe by convolving the DUSTY model spectrum with the *Spitzer* filter responses and taking the ratio of the resulting fluxes. We then compare our observed [8]–[24] colour with the models and linearly interpolate between them to find the dust temperature.

Unfortunately, the excess flux from the dust component is typically of order of the errors within the photometry or less: only 30 stars — 27 cluster members and three non-members — show excess flux above the model SED at 24 μm with a significance of over three standard deviations (for comparison, only four stars show a similar flux deficit, all of which are under five standard deviations). The dust temperature is also *very* sensitive to the zero points of the photometry: the additional factor of 1.015 in IRAC 4 (8 μm) from Rieke et al. (2008) raises the temperature of the warmest dust surrounding V6 by 110 K and V42 by 340 K and raises the dust temperatures of all other stars even more significantly. We were therefore only able to obtain dust temperature estimates for these two stars, plus a handful of others, listed in Table 5.4. LEID 40220 is omitted as, despite showing clear mid-IR excess, its photometric errors are still too large for a temperature to be determined.

For many of these 30 stars, the [8]–[24] colour of the excess emission is sufficiently high or low that it is outside the bounds of our test range (100–1500 K). We would not expect significant amounts of circumstellar dust hotter than 1500 K, and we would expect the inner edge of the dust envelope to exceed 100 K unless the star had recently completed a period of mass loss and was now in (mass-losing) quiescence. The stars

with very cool dust are all low-luminosity objects, suggesting they are blends with dust-containing background galaxies (see §5.6.1.3). Stars with warm dust may have emission in the IRAC 8-μm band. Several of the stars with evidence for warm dust are known variables. It is quite possible that, in the cases of V152, V138, V148 and V161, changes in the stellar luminosity may impact our derivation of mid-IR excess and thus dust temperature. It therefore appears that most of the cluster's mass-losing stars have warm circumstellar dust, with the most evolved, most IR-excessive stars (V6, V42 and possibly V17) showing probably slightly colder dust.

It is noteworthy that we find much colder dust around V6 using only the *Spitzer* data points than we do when we also consider the Gemini T-ReCS spectrum. This is due primarily to the marginally different dust chemistry, which has a substantial effect on the derived dust temperature, but may be related to low-level variability of the star between the 24- and 8-μm observations, or the presence of an additional, lower-temperature dust component.

For the remainder of this analysis, we have assumed that the temperature of the inner edge of the dust envelope is the typical 1000 K (Habing 1996) in all stars other than V1, V6, V17, V42, and LEIDs 39105 and 45232, where we take the temperatures or lower limits as given in Table 5.4. In terms of mass-loss rates, this represents a roughly average value out of the possible range, with a possible variation of $\pm$80% between the coldest dust likely based on Table 5.4 and the hottest dust likely to form ($\lesssim$ 1500 K, based on interferometric observations and condensation temperatures — Salpeter 1977; Draine 1981; Kozasa, Hasegawa & Seki 1984; Danchi et al. 1994; Tuthill et al. 2000; Gauba & Parthasarathy 2004).

5.5.3.3 Calculating the mass-loss rates along the RGB/AGB

Using these assumed temperatures, we can derive the expected excess flux at 8 μm by taking the ratio of the 8-μm flux from each DUSTY model and dividing it by the flux

Table 5.4: Dust temperatures (based on pure 'astronomical' silicate dust) for stars with the highest computed dust mass-loss rates. Errors are on the basis of *Spitzer* photometry only and do not include the comparatively small uncertainties in estimating stellar luminosity. Variable numbers are from Clement (1997).

LEID	Variable number	Maximum Dust temperature (K)	Inner radius of dust envelope (R_*)	(AU)	Notes
55114		>1400			4
44277	V152	>1400			4
49123	V138	>1400			4
41455	V148	>1400			4
39105		>801	<23	<8.8	
32029	V1	>685	<50	<8.8	1
47153	V161	>595	<26	<8.4	
45232		>556	<27	<10.7	
44262	V42	$937\ ^{+207}_{-143}$	$15\ ^{+6}_{-5}$	$7.6\ ^{+3.0}_{-2.5}$	6
34041	V2	$715\ ^{+109}_{-88}$	$22\ ^{+6}_{-6}$		2
35250	V17	$509\ ^{+177}_{-138}$	$50\ ^{+44}_{-24}$	$23.2\ ^{+20.5}_{-10.7}$	
33062	V6	$320\ ^{+48}_{-48}$	$111\ ^{+43}_{-27}$	$72.6\ ^{+27.9}_{-17.7}$	
37098		<706			3
45169		<371			5
47135		<328			5
40015		<240			5
31159		<186			5
44457		<100			5
54135		<100			5
51019		<100			5

Notes: (1) Post-AGB, proper motion membership probability 3%, radial velocity 188 km s^{-1}; (2) proper motion and radial velocity non-member V825 Cen; (3) proper motion membership probability 0%, no radial velocity data, variable identified in vL+00 with $P = 1.0253$ days; (4) suspected SiO or other emission near 8 μm; (5) faint stars, suspected blends with background galaxies; (6) for silicate dust.

from a similar DUSTY model with no dust. This is repeated for the 24-μm excess. Our mass-loss rate then scales similarly to Eqs. (5.8) and (5.9), with:

$$\dot{M}_{\rm dust} = \frac{\dot{M}_{\rm DUSTY}}{200} \left(\frac{\psi}{200}\right)^{-1/2} \left(\frac{L}{10^4}\right)^{3/4} R_{\rm E}, \tag{5.12}$$

where $R_{\rm E}$ is the ratio of the observed excess flux at 8 and 24 μm, to the comparative excess flux predicted by DUSTY at those wavelengths:

$$R_{\rm E} = \frac{F_{\rm e}^{\rm o}(8) + F_{\rm e}^{\rm o}(24) - 2}{F_{\rm e}^{\rm d}(8) + F_{\rm e}^{\rm d}(24) - 2}, \tag{5.13}$$

where $F_{\rm e}^{\rm o}$ is the flux observed above the Rayleigh-Jeans tail in our SED fit at 8 and 24 μm, and $F_{\rm e}^{\rm d}$ is a similar value, calculated for our DUSTY model at the relevant dust envelope temperature and scaled to the star's luminosity. The constant (-2) comes from the need to subtract the photospheric contribution at both 8 and 24 μm in both cases, leaving only the excess flux. The factor of 200 in Eq. (5.12) comes from the conversion from the DUSTY *total* mass-loss rate, which assumes a gas-to-dust ratio of 200, to a mass-loss rate purely for the dust component.

Our computed mass-loss rates are listed in Table 5.5, which excludes those stars identified as blends at 24 μm in B+08. The correlation between mass-loss rate and luminosity is shown in Fig. 5.16, which confirms that it is the most luminous objects that are losing observable quantities of dust, and that most of the dust mass loss is indeed coming from V6 and V42. We also note that V6 and V42 have very similar mass-loss rates in our analysis here, which only contains the *Spitzer* data, as in our analysis in §5.5.3.2, which also includes our Gemini spectra and other data. This is despite the assumed dust temperatures being considerably different in both cases.

Also noteworthy are the stars with apparent significant dust mass-loss rates at *low* luminosities ($L \lesssim 500$ L$_\odot$, $\dot{M}_{\rm dust} \sim 10^{-11}$ M$_\odot$yr^{-1}) in Fig. 5.16. Close inspection of these targets shows that they are mostly warm stars (some on the HB) with very little or no 8-μm excess, but considerable 24-μm excess. It appears most likely that these

Table 5.5: List of mass-loss rates from corrected IR excesses, in order of decreasing total mass loss, excluding stars with known blending issues from B+08, stars with 24-μm excesses of $< 3\sigma$ and stars dimmer than 500 $L_\odot$. Variable numbers are from Clement (1997).

LEID	$\dot{M}_{\rm dust}$ ($10^{-10}\,M_\odot\,{\rm yr}^{-1}$)	$\dot{M}_{\rm total}$ ($10^{-7}\,M_\odot\,{\rm yr}^{-1}$)	[Fe/H]	Notes
44262	0.88	7.34	–1.62	1, 3, 6, V42
32029	0.50	5.87	–1.77	2, 3, V1
33062	1.96	6.02	–1.19	1, 3, V6
35250	0.35	2.88	–1.62	3, 6, V17
45232	0.34	2.80	–1.62	6
49123	0.23	1.91	–1.62	3, 6, V138
48060	0.10	1.90	–1.97	3
56087	0.11	1.82	–1.92	3
55114	0.19	1.67	–1.64	3
44277	0.18	1.54	–1.62	3, 6, V152
41455	0.37	1.46	–1.29	3, V148
32138	0.09	1.38	–1.87	
37110	0.15	1.22	–1.62	3, 6
25062	0.09	1.16	–1.83	
47153	0.12	1.02	–1.62	6, V161
48150	0.11	0.92	–1.62	6
43351	0.11	0.91	–1.62	6
42044	0.11	0.88	–1.62	6, V184
42302	0.10	0.83	–1.62	6
39165	0.09	0.78	–1.62	6
36036	0.03	0.78	–2.05	4
42205	0.09	0.77	–1.62	6
26025	0.08	0.75	–1.68	
52030	0.26	0.67	–1.10	4, 5
39105	0.46	0.65	–0.85	
52111	0.07	0.57	–1.62	6

Notes: (1) Values based solely on *Spitzer* photometry; (2) post-AGB star; (3) also shows significant ($> 3\sigma$) excess at 8 μm; (4) shows 24-μm excess *below* 3σ, but shows 8-μm excess above 3σ; (5) carbon star, see §5.6.1.2; (6) no metallicity known, we have used the cluster average, [Fe/H] = –1.62.

are cluster stars blended with background galaxies (see §5.6.1.3).

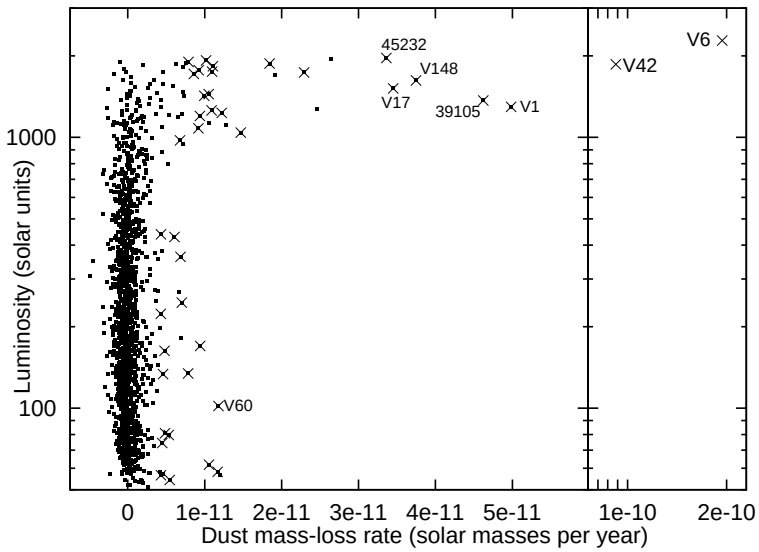

Figure 5.16: Correlation between mass-loss rate and luminosity for confirmed proper-motion cluster members. Objects with 24-μm excess over 3σ are marked by crosses.

5.6 Discussion

5.6.1 Notable objects besides V6 and V42

5.6.1.1 Post-AGB objects

The cluster contains two confirmed post-AGB objects: Fehrenbach's Star (LEID 16018) and V1 (LEID 32029). It is notable that, while Fehrenbach's Star does not appear to show a dusty circumstellar envelope, V1 does. From the spectra of vL+07, Fehrenbach's Star also has very weak emission lines, but those of V1 are strong.

It is difficult to reconcile the similarities between the dust shells in V1 and the mass-losing AGB/RGB-tip stars (see Table 5.4), given that V1 has evolved off the AGB tip. It is worth noting that V1 is up to twenty times more metal poor[4], so we may not necessarily expect the historic wind from V1 to be the same as in V6. The proximity of V1's dust shell to the star does raise the interesting possibility that the dust shell in V1 is relatively stationary, supporting the low velocity given by DUSTY's

[4]([Fe/H]$_{V1}$ = –2.6, –2.4, respectively, from Moehler et al. 1998; and Thompson et al. 2007), though note that iron depletion in the post-AGB V1 will mean that the global metallicity, [Z/H], will likely be higher.

scaling of $v \propto \psi^{-1/2}$.

For Fehrenbach's Star, we can surmise that the absence of dust is due to either the dust having dispersed and become too cold to detect with our *Spitzer* data, or the dust having been destroyed. It does not appear to be present at any significant level in the longer-wavelength *AKARI* data from Matsunaga et al. (2008).

Several other potential post-AGB stars have been highlighted in our HRD (Fig. 5.5). These are listed in Table 5.6. Of these, several show bad cross-identifications or poor quality 2MASS data. As we expect such objects to scatter excessively in the HRD, this should not be surprising, and we anticipate these are the exceptions, rather than the standard in our dataset. In particular, LEID 34135 is identified as an RGB-a star, LEID 40240 is a known blend in our 24-μm data. The exact status of LEID 38171 remains unresolved: it shows a mid-IR deficit in our *Spitzer* 5.8- and 8-μm data, though it may be an early-AGB star with poor 2MASS photometry. The remainder have SEDs visually consistent with their ascribed temperature and luminosities, although we note that, of these, only LEIDs 29064, 30020, 32015, 43105, 46054 and 46265 have radial velocity measurements that confirm their cluster membership. These could potentially be post-early-AGB stars, which have left the AGB sequence before reaching the thermally-pulsating stages. None show a mid-IR excess at 24 μm above the photometric errors.

5.6.1.2 Carbon stars

Of the known carbon stars in the cluster (LEIDs 52030, 41071, 32059, 14043, and 53019; see vL+07), only the most luminous of these, LEID 52030, shows significant dust mass loss, and even this is only a 4σ detection. The values we quote here are for silicate dust. Carbonaceous dust reproduces the observed 8-μm excess marginally better than silicate dust. However, any analysis of this star is uncertain as our photospheric models are for *oxygen*-rich stars.

Table 5.6: List of post-AGB candidates identified from the HRD (Fig. 5.5), showing luminosities, temperatures, proper motion membership percentage probabilities (PM Mem.) from vL+00, radial velocities from vL+07 and individual notes.

LEID	T (K)	L ($L_\odot$)	PM % Mem.	RV ($km\,s^{-1}$)	Notes
46162	5201	310	98		V148, 1, 4
40420	5347	296	72		5
43105	5376	524	100	212	V29
32015	5493	378	100	205	
32029	5675	1297	3	188	V1, 6
39367	5750	239	99		2, 9
37095	5817	464	72		
41263	6145	197	100		
16018	6427	1480	18	225	6, 7
37295	6993	356	100		
34136	7109	335	76		
34135	7450	219	99		2, 9
29064	7604	181	100	206	
38171	7784	182	100		8
46265	8014	282	100	224	
48180	8769	405	100		2, 9
43188	9166	1017	97		2, RGB
50182	10 051	157	100		3, HB?
46054	11 106	178	100	226	
30020	11 438	335	100	207	
30120	>18 953		100		
32163	>18 953		100		3, HB?
41457	>18 953		100		1, HB?
56071	>18 953		100		1, HB?

Notes: (1) Poor or no 2MASS data; (2) blend in 2MASS; (3) bad cross-identification in 2MASS; (4) $L \sim 190$ $L_\odot$, probable early-AGB star with low mantle mass; (5) young post-early-AGB or very bright early-AGB star; (6) confirmed post-AGB star; (7) Fehrenbach's Star; (8) isolated object with very steep spectrum, nature unresolved; (9) likely early-RGB/AGB object.

We estimate that the mass-loss rate for amorphous carbon dust with the same grain parameters as our silicate dust model is roughly 50% higher, at $\sim 4 \times 10^{-11}$ $M_{\odot}$ yr^{-1}, though the error in the mass-loss rate itself is over 50%. It would appear at first sight that these stars are no more effective at producing dust than their M-type counterparts.

5.6.1.3 Low-luminosity giant stars

We find a number of stars below 500 $L_{\odot}$, both on the giant branches and the HB, which have significant IR excess. As they appear to occur with roughly equal prevalence across the HRD, we suggest that these are merely blends with background galaxies (*c.f.* §5.5.3.2). Fig. 5.17 shows that the mid-IR-excessive stars nicely bifurcate into these two colour groups: we expect large 24-μm excesses but little 8-μm excess ('cold dust') to most likely be blends with background galaxies (*c.f.* 2MASX J13272621–4746042 in B+08), while we expect fairly comparable 8- and 24-μm excesses for stars with circumstellar dust. Note that V6 and V42 lie off the diagram to the right, as does the low-luminosity RGB star LEID 31159, which lies just below the 600 K line. The low-luminosity stars with mid-IR excess also spatially follow the distribution of *all* stars, not just cluster members, and show no concentration towards the centre of the cluster, ruling out crowding in the cluster core as a primary factor for generating these detections.

In total, 37 stars with luminosities below 500 $L_{\odot}$ show significant ($> 3\sigma$) excess at 24 μm. Of these, however, 34 have little or no excess at 8 μm. While we have made every effort to remove 24-μm blends from our sample, the glare from nearby stars up to 150 times brighter may prevent an accurate 24-μm flux measurement being made in these cases. The remaining three stars are: LEID 31159, an 18 $L_{\odot}$ RGB star; LEID 44457, a 49 $L_{\odot}$ RGB star; and LEID 47135, an early-AGB star. We have no reason, *a priori*, to assume that any of these is likely to harbour circumstellar dust.

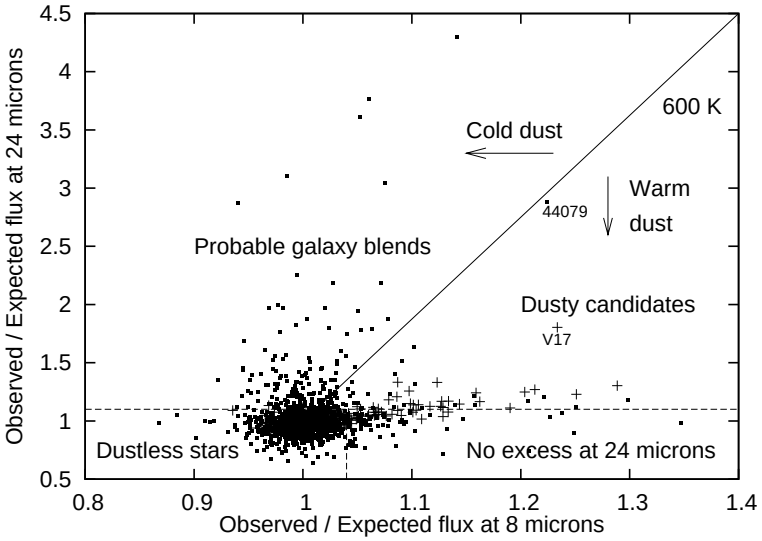

Figure 5.17: Observed mid-IR excess (attributable to dust) at 8 versus 24 μm, which corresponds (for given dust properties) to the inner temperature of the dust envelope. Potentially dusty stars and probable blends with background galaxies can be split by a line corresponding to a 600 K silicate dust envelope. Stars above 500 $L_\odot$ are shown as crosses, stars below 500 $L_\odot$ as dots.

5.6.1.4 Non-members

Our SED modelling also includes a number of stars that have been confirmed as non-members, either by proper motion or radial velocity measurement. These include V2 (V825 Cen, LEID 34041), an emission-line M-giant with a fitted temperature of 3346 K and a strong IR excess. It was identified as a radial velocity non-member by Feast (1965) and has a period of 236 days (Kałużny, J. and , M. and Szymański, M. and Udalski, A. and Krzemiński, W. and Mateo, M.).

A fit to the IR excess in V2 is shown in Fig. 5.18, with a 850 K blackbody. The temperature of this blackbody is comparable to the $715\pm^{109}_{88}$ K we find in §5.5.3.2. This blackbody has a flux density scaling constant (L/R^2) that is ten times that of the underlying photosphere; though without a good distance measure, we cannot estimate its mass-loss rate. We cannot attain a good fit to the spectrum using oxygen-rich dust, due to the high flux in the IRAC 4.5- and 5.8-μm bands and the absence of any silicate-like feature (which would show up at 8 and 24 μm). Carbon-rich dust could provide

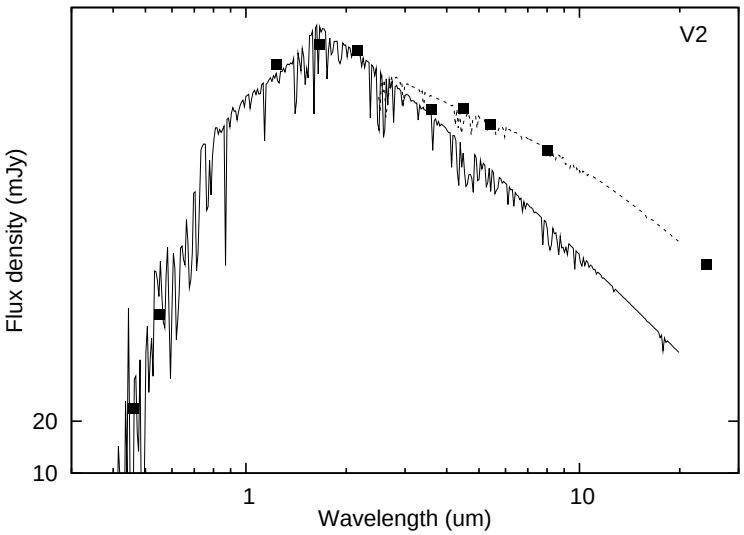

Figure 5.18: The SED for the radial velocity non-member V2 (filled squares). Overplotted is a 3500 K spectral model (solid line) and the same model with a 850 K blackbody (dashed line).

a fit, though without a mid-IR spectrum of the star, we have no reason to believe it harbours such dust.

The star LEID 37098 (VLR O-123) was identified in vL+00 as a variable star with a period of around a day. It exhibits little excess at 8 μm, but considerable excess at 24 μm. We estimate the mass-loss rate at 1.4×10^{-8} $(d/\mathrm{kpc})^{-1.5}$ $\mathrm{M}_\odot$ yr^{-1}, though the absence of 8-μm emission suggests that the star is most likely blended with a background galaxy.

5.6.2 Total mass-loss rate of ω Centauri

Our calculation of the total mass-loss rate for ω Cen is subject to broadly similar errors as discussed in §5.5.2:

- 30% uncertainty in the dust mass-loss rate from internal errors in DUSTY;
- $\lesssim$ 30% uncertainty in the dust mass-loss rate due to uncertain dust chemistry and grain size;
- negligible uncertainty in the cluster's metallicity, which would affect the gas-to-dust ratio (the cluster's overall metallicity is well-constrained, and most dusty stars — aside from V42 — have measured metallicities);

- $\lesssim$ 10% uncertainty due to errors in scaling the mass-loss rate of the stars to the photospheric temperature (see §5.5.3.2);
- $\lesssim$ 5% uncertainty due to error in the integrated flux density of the stars from fitting the SED, including errors in stellar temperature;
- $\sim$ 10% uncertainty due to error in the interstellar reddening;
- $\sim$ 20% uncertainty due to error in the distance;
- errors due to the corrections we have made to the photometric excesses above. Though difficult to discern analytically, we have altered the parameters of the constants in Eqs. (5.10) and (5.11), and obtained a visual estimate of the error involved, finding it to be at most 30%;
- uncertainty in the dust envelope temperature, although we do not expect the associated error in mass-loss rate to be as high as the 80% error in individual stars (§5.5.3.2), as this arises from (random) photon noise. However, since we do not have any sensible upper limits on dust temperature, bar the maximum dust condensation temperature around 1500 K, the error involved may still be as high as $\sim$30%.

Added in quadrature, this gives a total error of 65%.

For the remainder of this analysis, we have removed any objects thought to be 24-μm blends on the basis of B+08. We include V1, which is listed as a proper-motion non-member in vL+00 (at a membership probability of 3%), but a radial velocity member in vL+07. We do not include mass-loss rates from stars with $L < 500$ L$_\odot$, as these appear not to be losing mass (§5.6.1.3). We also include the mass-loss rates derived from our Gemini spectra for V6 and V42, in preference to those found from *Spitzer* data alone. Integrating the mass-loss rates of the remaining cluster members, we find the total stellar dust mass-loss rate within ω Cen, under the same assumptions listed in §5.5.2, to be:

$$\dot{M}_{\rm dust} = 1.3 \pm^{0.8}_{0.5} \times 10^{-9}\ {\rm M}_\odot\ {\rm yr}^{-1}. \tag{5.14}$$

Due to the incompleteness of our knowledge on precise dust composition, detailed in §5.5.3.2, we suggest that, in reality, this is a lower limit. It is notable that, of this value, V6 and V42 therefore presently produce around half of the dust produced by

the entire cluster, with V6 being the marginally larger contributor due to its higher metallicity. Also, the cluster's entire dust mass loss appears to come entirely from stars within a magnitude of the giant branch tip. This is in contrast to the case of 47 Tuc, where O+07 find that most of the dust mass loss occurs in the more numerous stars much further down the giant branch. Even the shallow exposure of M15 (Boyer et al. 2006) revealed dusty giants at least 1.5 magnitudes below the tip of the RGB. It is possible that O+07's result was affected by blending at longer wavelengths in this visually more compact cluster, which would produce apparent excesses at these wavelengths. Observations of other clusters are needed to confirm the extent of the dust mass loss.

In our analysis, we have not considered gas mass loss by methods other than a dust-driven wind. The most important of these is chromospheric mass loss. There is weak evidence (Smith & Dupree 1988; Mauas, Cacciari & Pasquini 2006; McDonald & van Loon 2007) that the dust-driven wind begins following the extension of the stellar chromosphere by pulsation, although the exact sequence of events is yet to be fully explained. For this reason, as well as those described in §5.5.3.2, we here derive only a lower limit to the total mass-loss rate from the cluster. Multiplying the dust mass-loss rate for each star by its gas-to-dust ratio (see §5.5.2.1), we can again integrate the total mass-loss rate of all the dusty cluster stars, finding it to be: $\dot{M}_{\rm total} \gtrsim 8 \pm^{5}_{3} \times 10^{-6}$ M$_{\odot}$ yr^{-1}. If we include the contribution from dustless (chromospherically-driven) winds, by integrating the mass-loss rates prescribed by Schröder & Cuntz (2005) (see later, Eq. (5.16)) over all 'dustless' stars, this lower limit rises to around $\dot{M}_{\rm total} \gtrsim 1.2 \pm^{0.6}_{0.5} \times 10^{-5}$ M$_{\odot}$ yr^{-1}, depending on the point at which chromospheric mass loss is replaced by dust-driven and/or pulsation-induced mass loss.

It is interesting to note here that the fraction of the *total* mass loss provided by V6 and V42 is somewhat less, due to the higher metallicity (hence presumed gas-to-dust ratio) of V6 and the inclusion of dustless winds. V42 now produces around 20% of the gas produced by dust-producing stars (not including mass loss from giants with

chromospheres), but V6 is reduced to around 9% of this total.

5.6.3 Mass loss along the giant branch

5.6.3.1 The onset and evolution of dust formation

While we have no clear measure in the data presented here of mass loss by means other than a dusty wind, we can place constraints on when dust production starts to become efficient and explore the parameters upon which it depends. Fig. 5.19 shows the variation of mass-loss rate with gravity, luminosity and stellar effective temperature. It is difficult to say what happens in denser, fainter, warmer stars due to lack of sensitivity in the photometry. Despite this, the fact that extreme dust mass loss occurs towards minimum gravity and maximum luminosity is obvious, although it is not clear which parameter is *physically* responsible. There are arguments for mass loss to be linked to any or all of these parameters.

Surface gravity is a measure of escape velocity and of the ease with which dust grains can be accelerated away and lost from the star. It has previously been suggested that this is the primary determining parameter of mass loss (Judge & Stencel 1991), and we do indeed observe a smooth trend in Fig. 5.19.

Radiation pressure on the dust grains increases with increasing stellar luminosity (and likely temperature, depending on the grain opacities). Stars evolving along the giant branch increase monotonically in luminosity, but at the same time their photospheres cool as their radii increase, also in a monotonic fashion. As the stars in GCs have very similar masses, the differences in surface gravity amongst stars along the giant branch essentially depend on the radius. Therefore, it is not surprising that if a correlation is found with any of the three parameters luminosity, temperature and surface gravity, that a similar correlation is found with the remaining parameters. We do observe an increasing trend in mass-loss rate with luminosity. The post-AGB star V1 fits the luminosity relation better, possibly since its mass-loss rate was determined

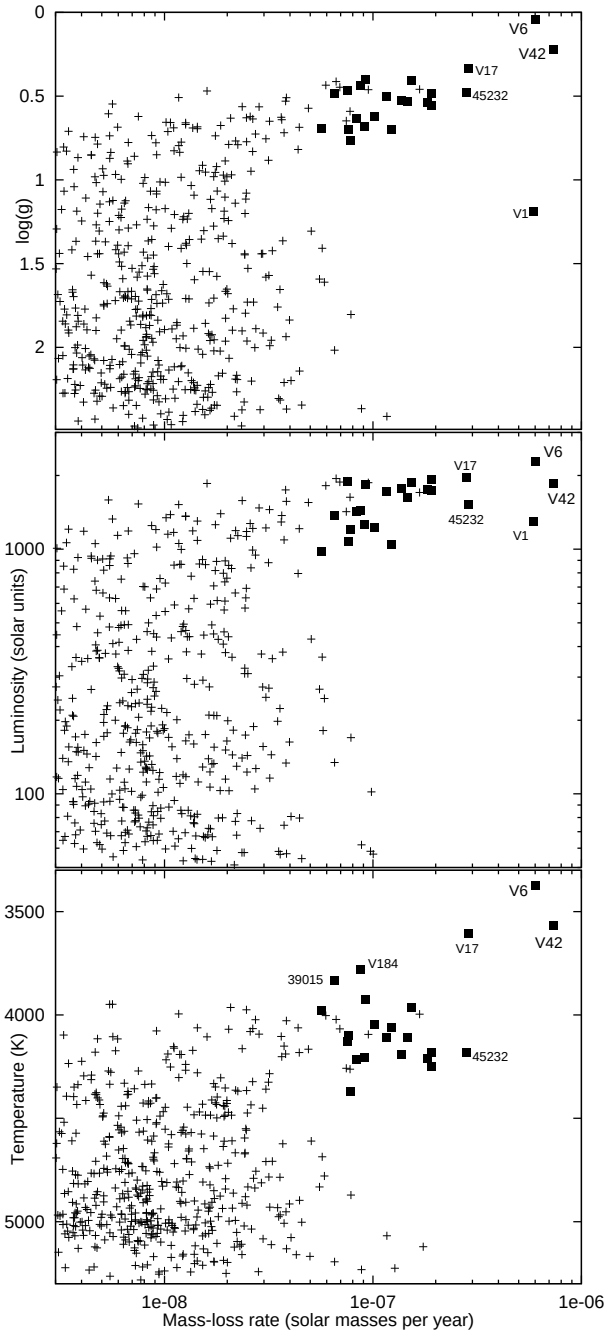

Figure 5.19: Computed total mass-loss rates and their dependence on $\log(g)$ (top panel), luminosity (middle panel) and stellar effective temperature (bottom panel). Large squares denote stars above $L > 500$ $L_{\odot}$ with individually statistically-significant mass loss, based on a 3σ cut on 24-μm excess.

while it was still on the AGB at a similar luminosity, but very different surface gravity.

Dust formation requires a sufficiently low temperature at still a sufficiently high pressure — a condition most easily met in the atmospheres of the coolest stars. At warmer temperatures, we see that no stars with $T_{\rm eff} \gtrsim 4500$ K are producing dust significantly. Following the trend to cooler temperatures, however, we find that there is a clear transition to statistically-significant dust mass-loss rates for around half the stars below ∼4300 K. By 3900 K, all stars seem to be producing dust at a substantial rate. The onset of dusty winds in ω Cen therefore seems to occur at a somewhat cooler and more luminous threshold than found in the more metal-poor M15 (Mészáros et al. 2008).

The sudden transition at ∼4400 K could correspond to a sudden transition to allow significant dust production to occur in dense environments, as Wachter et al. (2008) suggest occurs in carbon-rich stars. This may be a particularly important factor if the temperature gradient is small and pressure (*i.e.* density) gradient is high in these metal-poor stars, as suggested by Mattsson et al. (2008). The fact that there is a regime where some stars show significant mass-loss rates, while others show insignificant mass-loss rates could be due to episodic mass loss, where stars produce dust for increasing periods of time until they reach ∼4000 K, at which point the continuous dust production may take place. The fraction of dust-producing stars at a given temperature would then yield the relative duration of the dust-producing phase. It may also be possible that the AGB stars (which typically have a lower surface gravity at a given surface temperature) can maintain a significant dusty wind already at higher surface temperatures than their RGB counterparts. The gas-to-dust ratio may also play a rôle: it is possible to have higher mass-loss rates at higher temperatures, but in winds containing fractionally less dust.

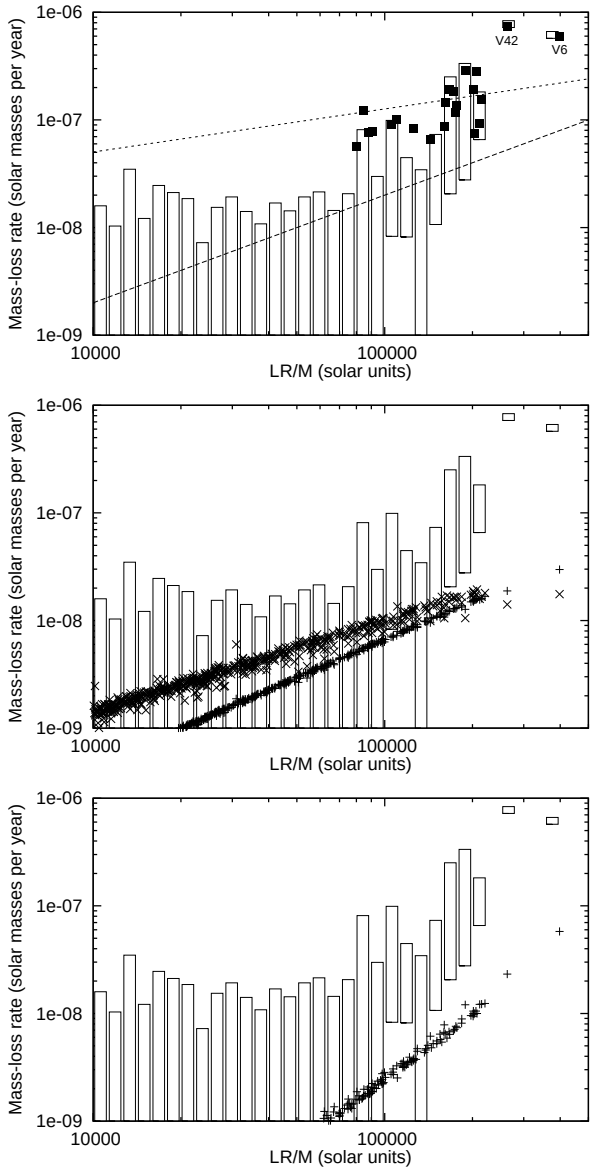

Figure 5.20: Comparison of our estimated total mass-loss rates to literature relations. Our data have been binned in units of $0.05\log(LR/M)$ and are shown as boxes with heights of $\pm 1\sigma$. Individual stars with statistically-significant mass-loss rates have been shown in the top panel as filled squares. Comparisons: Reimers (1975) — top panel, dashed line; Origlia et al. (2007) — middle panel, dotted line; Schröder & Cuntz (2005) — bottom panel, crosses; Nieuwenhuijzen & de Jager (1990) — middle panel, plus signs; Wachter et al. (2008) — bottom panel, crosses.

5.6.3.2 Comparison with literature relations

In reality, the main drivers behind mass loss are likely to be determined by a combination of surface gravity, luminosity, pulsation behaviours, *etc.* Such has been the supposition of previous empirical determinations of mass-loss laws, such as those of Reimers (1975), Nieuwenhuijzen & de Jager (1990), Schröder & Cuntz (2005), and O+07.

Reimers' law is based on the following simple parameterisation for chromospheric mass-loss:

$$\dot{M} = 10^{-13}\eta_{\rm R}\frac{L_*R_*}{M_*}\ {\rm M}_\odot\ {\rm yr}^{-1}, \tag{5.15}$$

where L_*, R_* and M_* are the luminosity, radius and mass of the star in solar units, and $\eta_{\rm R}$ is a constant, generally assumed to be in the range 0.4 to 3 (Stancliffe & Jeffery 2007), but most commonly 0.5 (Schröder & Cuntz 2005), which we assume here. The modified relation given by Schröder & Cuntz (2005) is based on the energetics of momentum transfer in a chromospheric outflow, namely:

$$\dot{M} = \eta_{\rm S}\frac{L_*R_*}{M_*}\left(\frac{T_{\rm eff}}{4000{\rm K}}\right)^{3.5}\left(1+\frac{g_\odot}{4300g_*}\right), \tag{5.16}$$

where $\eta_{\rm S}$ is suggested to be $(0.8\pm0.1)\times10^{-13}$ ${\rm M}_\odot$ ${\rm yr}^{-1}$. Nieuwenhuijzen & de Jager (1990) give a parameterisation similar to that of Reimers, but fitted to the entire HRD:

$$\dot{M} = \eta_{\rm N}L_*^{1.42}R_*^{0.81}M_*^{0.16}, \tag{5.17}$$

where $\eta_{\rm N} = 9.63\times10^{-15}$ ${\rm M}_\odot$ ${\rm yr}^{-1}$. O+07 base their relationship on a similar method to ours, using (K–[8]) colour excess to attribute dust mass-loss rates, and fit the following parameterisation:

$$\dot{M} = 4\times10^{-10}C\left(\frac{L_*}{g_*R_*}\right)_\odot^{0.4}\ {\rm M}_\odot\ {\rm yr}^{-1}, \tag{5.18}$$

where:

$$C = (\psi/200)^{0.5}(v_\infty/10)(\rho_{\rm s}/3), \tag{5.19}$$

with gravity (g_*) and radius (R_*) in solar units. As ψ and v_∞ vary among our stars, we here take $C = 1$.

We compare the expected relations from these laws to our data in Fig. 5.20. In this figure, we have assumed $M = 0.8$ M$_\odot$. For the O+07 relation, we used $\psi = 2000$, on the basis that ω Cen is an order of magnitude less metal-rich than 47 Tuc, where O+07 assumed $\psi = 200$. The other relations have no dependence on ψ. We also compare the carbon-star relation of Wachter et al. (2008) for the SMC (at [Fe/H] ~ -0.7), namely:

$$\dot{M} = C' \left(\frac{L_*}{L}\right)^{2.84} \left(\frac{T_*}{2600\mathrm{K}}\right)^{-6.81} M_*^{-3.01}. \tag{5.20}$$

Though Wachter et al. use $C' = 2.34 \times 10^{-5}$ M$_\odot$ yr^{-1} as their constant for the SMC, based on their modelled scaling with metallicity, we would expect C' to be roughly 1×10^{-5} M$_\odot$ yr^{-1} for ω Cen. This can be derived from our assumed weak scaling of mass-loss rate with metallicity ($\dot{M} \propto \sqrt{\psi}$), which is similar to the scaling Wachter et al. find in their comparison with their Milky Way relations (Wachter et al. 2002). which we use in the following comparison of the aforementioned relations.

We can scale our mass-loss rates to match the above relations given our assumption that $\dot{M} \propto \sqrt{\psi}$, with the solar-metallicity value being 200. This places V6 at $\psi = 2600$ and the majority of the cluster (probably including V42) at $\psi = 8300$. We do not expect the gas-to-dust ratio to attain solar-metallicity values (*i.e.* $\psi \sim 200$) in these stars, simply due to the lack of condensable material which can form dust (van Loon 2008).

Fig. 5.20 shows the relation from O+07 successfully reproduces the distribution of our dusty stars in the range $7.5 \times 10^5 \lesssim LR/M \lesssim 2.5 \times 10^6$ times the solar value, suggesting that $\dot{M} \propto \sqrt{\psi}$ does hold between 47 Tuc and ω Cen. However, the quality of the fit decreases dramatically once we include the dust-free stars and stars where we have a marginal detection of dust. The gas-to-dust ratios we require for V6 and V42 to be consistent with O+07 are $\psi \approx 800$ and 500, respectively. This may not be

unreasonable, if V42 is part of the cluster's most metal-rich sub-population, though Origlia et al. themselves find several stars showing dusty emission above their own model, suggesting the relation does not describe these more unusual objects very accurately. We also note that our data do not reproduce the high mass-loss rates seen in O+07 below $LR/M \approx 7.5 \times 10^5$ times solar.

The classic Reimers' relation is meant to describe mass loss in solar-metallicity environments where a chromosphere, *not* dust, is the primary wind driver. We should therefore not be especially surprised that it does not fit the upper giant branch of this metal-poor cluster well, where we expect the chromospheres to be disrupted and a dust-driven wind to be present. That it over-predicts the dusty mass-loss rate below $LR/M \approx 7.5 \times 10^5$ times solar suggests that chromospheric mass loss may dominate here, while its under-estimate of mass-loss for greater values of LR/M confirms that a dusty wind is the primary mass-losing mechanism here. The formula from Schröder & Cuntz (2005) is essentially a downward revision of Reimers' law, derived for similar environments. This provides a similar conclusion, although the over-prediction around $LR/M \approx 2$ to 7.5×10^5 times solar is less severe.

The Nieuwenhuijzen & de Jager (1990) relation provides a slightly better match to the slope of the relation than the other laws, but grossly under-estimates the mass loss, requiring $\psi \sim 100 - 500$ for the dustiest stars but $\psi < 100$ for V6 and V42. It is, however, in agreement with the upper limits further down the giant branch. The values of ψ required near the giant branch tip are unphysical, but perhaps this should not be surprising, given that Nieuwenhuijzen & de Jager themselves state that the relation does not work well for dusty stars.

Empirical literature relations therefore do not seem to be able to reproduce the mass-loss rates we find. Without data on the gas-to-dust ratios in the wind, we cannot tell whether it is truly the mass-loss rate which changes, or merely the gas-to-dust ratio, which in turn influences our derived mass-loss rates. In Fig. 5.21, we show two

fits to the data, given by:

$$\dot{M} = 3.3 \times 10^{-22} \left(\frac{L_*}{g_* R_*} \right)_\odot^{8/3} \ \mathrm{M}_\odot \ \mathrm{yr}^{-1}, \tag{5.21}$$

and:

$$\dot{M} = 4.5 \times 10^{-14} \left(\frac{L_*}{g_* R_*} \right)_\odot^{5/4} \ \mathrm{M}_\odot \ \mathrm{yr}^{-1}. \tag{5.22}$$

These two fits show, respectively, the fit to all stars with $LR/M > 80\,000$ and the fit to only those stars with significant mass-loss rates (defined, as above, by a $> 3\sigma$ flux excess at 24 μm). These two fits are markedly different, and highlight the necessity to treat all stars, not just those which are observed to lose mass, when creating relationships between mass loss and other parameters.

We stress that Eq. (5.21) is not a replacement for the theoretical relations examined above, but simply a parametric fit to our data. Taking $T \propto R^{-2}$, it is in relatively good agreement with the model of Wachter et al. (2008), aside from a factor of $\sim$10 in the constant, despite the fact that their relation is modelled on carbon-rich dust producers and not the oxygen-rich dust we have in the majority of ω Cen's stars. If we assume their almost-linear scaling of mass-loss rate with metallicity, our models have a product of ψv_∞ that is about ten times too high. If we assume the scaling from DUSTY, the same is true for the product $\sqrt{\psi} v_\infty$. A decrease in outflow velocity would be surprising, given how low the observed outflow velocities we calculate are (see §5.6.3.3). A decrease to the value of ψ by a factor of 10 would be more promising, though a factor of 100 would again bring ψ to sub-solar values.

5.6.3.3 Wind velocity

DUSTY prescribes by simple argument that the wind velocity (if the dust and gas are coupled) must scale as $L^{1/4}(\psi \rho_\mathrm{s})^{-1/2}$, and also comes with the proviso that the mass-loss rates provided are only valid if the calculated wind velocity exceeds 5 km s^{-1}. The main reason for this is that the turbulence in the wind is expected to be of order 1–2

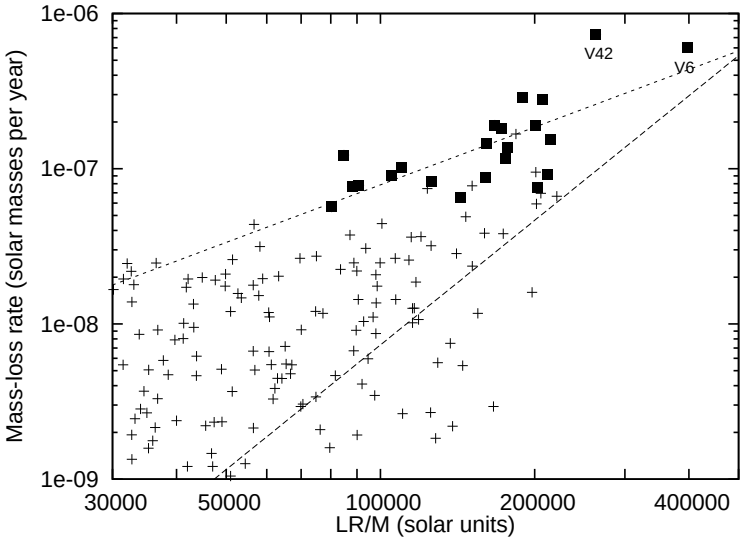

Figure 5.21: Correlation between total mass-loss rate and physical stellar parameters. The dashed line denotes the fit to the entire data above $LR/M = 80\,000$, described in Eq. (5.21); the dotted line fits only the stars with significant mass loss, described in Eq. (5.22). Individual stars with statistically-significant mass-loss rates have been shown as filled squares.

km s^{-1} (*e.g.* Schöier et al. 2004), suggesting a wind that is highly fractal in nature, as large-scale turbulence causes some parts of the wind to sink back towards the star (*c.f.* Icke, Frank & Heske 1992).

From our DUSTY models, we find the calculated velocities for V6 and V42 are only 1.16 and 0.76 km s^{-1}, respectively (assuming $[\mathrm{Fe/H}]_{\mathrm{V42}} = -1.62$). A typical RGB-tip star, with $L \sim 2000$ L$_\odot$ and [Fe/H] = –1.62, then has a wind velocity of ∼1 km s^{-1}. Clearly this is much less than DUSTY's minimum valid wind velocity, and gives us some cause for concern. Observationally, very similar very-low-velocity winds have been suggested in Galactic halo carbon stars (Mauron 2008), as well as the likely more metal-rich Galactic M5–M6 IIIe star L$_2$ Pup and the M8 IIIv star EP Aqr, which show hints of some asphericity or inhomogeneity in their outflows (Jura, Chen & Plavchan 2002; Winters et al. 2007).

Rotation and magnetic activity could also play a rôle in modifying mass loss. Perhaps the largest effect, however, is present in the stars near the AGB tip. Here,

pulsation-induced shocks could increase the wind velocity considerably beyond that which DUSTY predicts (*c.f.* Bowen 1988b). Depending on the strength of the shocks, controlled by the piston amplitude of the pulsation, a wind speed of 10 km s^{-1} could theoretically be obtained. This is similar to the situations in Mattsson et al. (2008), where the kinetic energy input (along with the amount of condensable carbon) controls the wind outflow: this is corroborated by observational evidence (van Loon et al. 2008). Shocks could facilitate dust formation, which would only occur when the pulsation becomes strong enough to cause shocks capable of accelerating the wind. Given the highest mass-loss rates we find are in LPVs, this is perhaps not surprising. A side-effect of this is that, since mass-loss rate depends linearly on velocity, the mass-loss rates observed for these stars would be significantly higher than the above values.

5.6.3.4 Evolutionary status of dusty stars

A comparison of the relative abundance of stars on the RGB and AGB can provide evidence of the evolutionary stage of our dusty stars. To compute this ratio, we have used the relative evolutionary rates ($\mathrm{d}t/\mathrm{d}L$, proportional to the number of stars in a given luminosity interval — $\mathrm{d}N/\mathrm{d}L$) along the Padova and BaSTI RGB and AGB isochrones:

$$F_{\mathrm{AGB}}(L) = \frac{(\mathrm{d}N/\mathrm{d}L)_{\mathrm{AGB}}}{(\mathrm{d}N/\mathrm{d}L)_{\mathrm{AGB}} + (\mathrm{d}N/\mathrm{d}L)_{\mathrm{RGB}}}, \quad (5.23)$$

$$R_{\mathrm{A/R}}(L) = \frac{(\mathrm{d}N/\mathrm{d}L)_{\mathrm{AGB}}}{(\mathrm{d}N/\mathrm{d}L)_{\mathrm{RGB}}}. \quad (5.24)$$

These ratios define, respectively, the fraction of stars on the AGB, and the ratio between AGB and RGB stars, at a given luminosity on the giant branch. In practice, these values are upper limits, signifying the fact that some stars may evolve off the AGB as a post-early-AGB or AGB-*manqué* star before reaching the model's canonical AGB-tip (defined here by the last thermal pulse). The Padova isochrones suggest F_{AGB} declines from 30% to 20% between 100 and 2000 $\mathrm{L}_{\odot}$, while the BaSTI isochrones suggest the

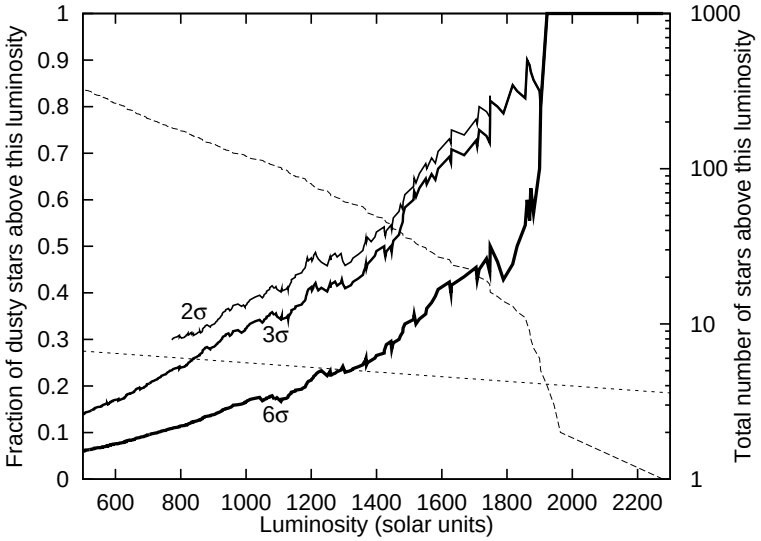

Figure 5.22: The fraction of dusty stars in the most evolved regions of the RGB+AGB, as a function of luminosity. The solid lines show the fraction of objects, above a given luminosity, with combined 8 + 24-μm excesses of at least one, two, three and six times the photometric errors, in order of increasing thickness. The dashed line (right axis) shows the total number of stars above that luminosity. The dotted line (left axis) demarcates the maximum likely fraction on the AGB: $\int_L^\infty F_{AGB}\mathrm{d}L$. Dusty stars above this line therefore imply dust production on the RGB.

decline is from ∼19% to ∼13%. We note that this percentage depends on the physics of convection used in the models, but that empirical constraints on convection mean that the physics used is unlikely to lead to significant alteration of our conclusions (Vandenberg et al. 2006).

We have used the Padova isochrones as an upper limit for $F_{\rm AGB}$ in Fig. 5.22, where we present the fraction of dusty stars as a function of statistical significance. Here, we can afford to relax our criteria for significance from our previous value of 3σ, as we are dealing with a statistical sample, rather than individual stars, thus we expect errant data due to random noise will average out.

This figure suggests that even from the start of measurable dust mass loss ($\sim$ 1300 $\mathrm{L}_\odot$), at least some stars on the RGB must be producing dust, at a confidence level of $\sim 6\sigma$. It also suggests that all stars which reach the RGB tip become dust producers.

Both the Padova and BaSTI isochrones imply a reduction in $\mathrm{d}N/\mathrm{d}L$ by a factor

of 2–7 for luminosities above the RGB tip, suggesting we might see 9–30 stars in the 1000 $L_\odot$ above the RGB tip. In fact, we see none, with the possible exception of the metal-rich V6. This includes all post-AGB objects, both confirmed and unconfirmed, which further suggests that the majority of AGB stars do not regain the luminosity of the RGB tip in ω Cen.

We can see how this may occur if we consider the implied mass-loss efficiency on the RGB. Our isochrone fitting (particularly using the Dartmouth models) suggests that RGB/AGB stars initially have masses of 0.85 $M_\odot$, that *typically* 0.20–0.25 $M_\odot$ of that is lost on the RGB and around half that value on the AGB, leaving a remnant of around 0.5 $M_\odot$. A significantly larger spread of RGB mass loss than this is required to explain the entire HB distribution. If mass loss on the AGB occurs at the same rate as on the RGB for a given luminosity, we can estimate that the AGB mass loss is given simply by the RGB mass loss, divided by the comparative rate of evolution (and hence $\mathrm{d}N/\mathrm{d}L$) between the RGB and AGB, thus:

$$\dot{M}_{\mathrm{AGB}}(L) = \frac{\dot{M}_{\mathrm{RGB}}(L)}{R_{\mathrm{A/R}}(L)}. \tag{5.25}$$

The value of $R_{\mathrm{A/R}}(L)$ is 0.20–0.25 near the tip, where most mass loss takes place, implying a mass loss of 0.04–0.06 $M_\odot$ on the AGB. In practise, the mass loss on the AGB is likely to be more than this, as it is easier to levitate mass off AGB stars as their mass (hence gravity) is less. This would suggest that many (perhaps most) stars either do not reach the AGB (AGB-*manqué* stars) or 'peel off' the AGB before they reach the tip. This further corroborates with the large number of low-luminosity post-early-AGB candidates we find in §5.6.1.1, though these may also be very-low-mantle-mass horizontal-branch stars on the transition to the AGB. This in turn again suggests that most dusty cluster members are actually *RGB*-tip rather than *AGB*-tip stars.

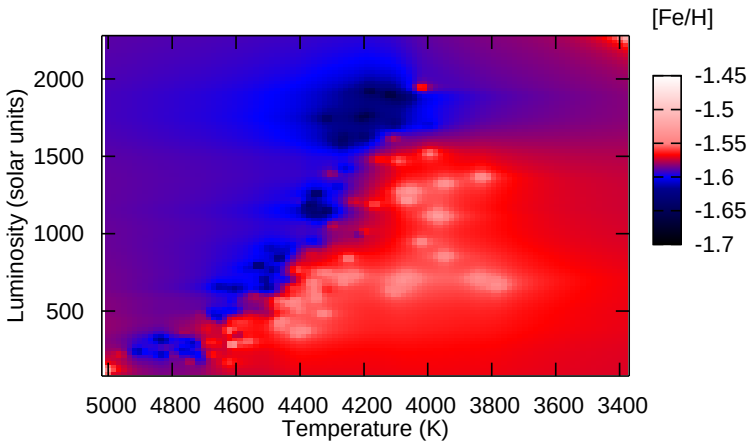

Figure 5.23: HRD, using our luminosity and temperature values, but showing interpolated literature spectroscopic metallicities from Cayrel de Strobel, Soubiran & Ralite (2001) and Johnson et al. (2008).

5.6.4 Comparisons between stellar groups

We have taken the metallicity data available on ω Cen giants from Cayrel de Strobel, Soubiran & Ralite (2001) and Johnson et al. (2008) and super-imposed them onto a HRD of our data. These are displayed in Fig. 5.23. In Fig. 5.24, we show a similar diagram, identifying those stars measured as CN- or Ba-rich in vL+07.

As expected, the stars determined to be metal-rich occupy a region much further to the cooler side of the giant branch. Of the stars with measured line strengths, the CN-rich stars do not appear to cluster to any one region more so than the CN-poor stars. This confirms that CN enrichment is primordial and not a result of the stars' evolution themselves. The absence of CN-rich stars at the hottest and coolest temperatures can be linked to the break-up of the molecule at high temperatures, and the masking by other molecular bands at low temperatures. The Ba-rich stars are more likely to be found towards the cool side of the sequence, down to luminosities below the HB, suggesting that these stars are probably metal-rich, and not associated with the AGB (*c.f.* vL+07). The strong temperature-dependence of the Ba λ4554 line used

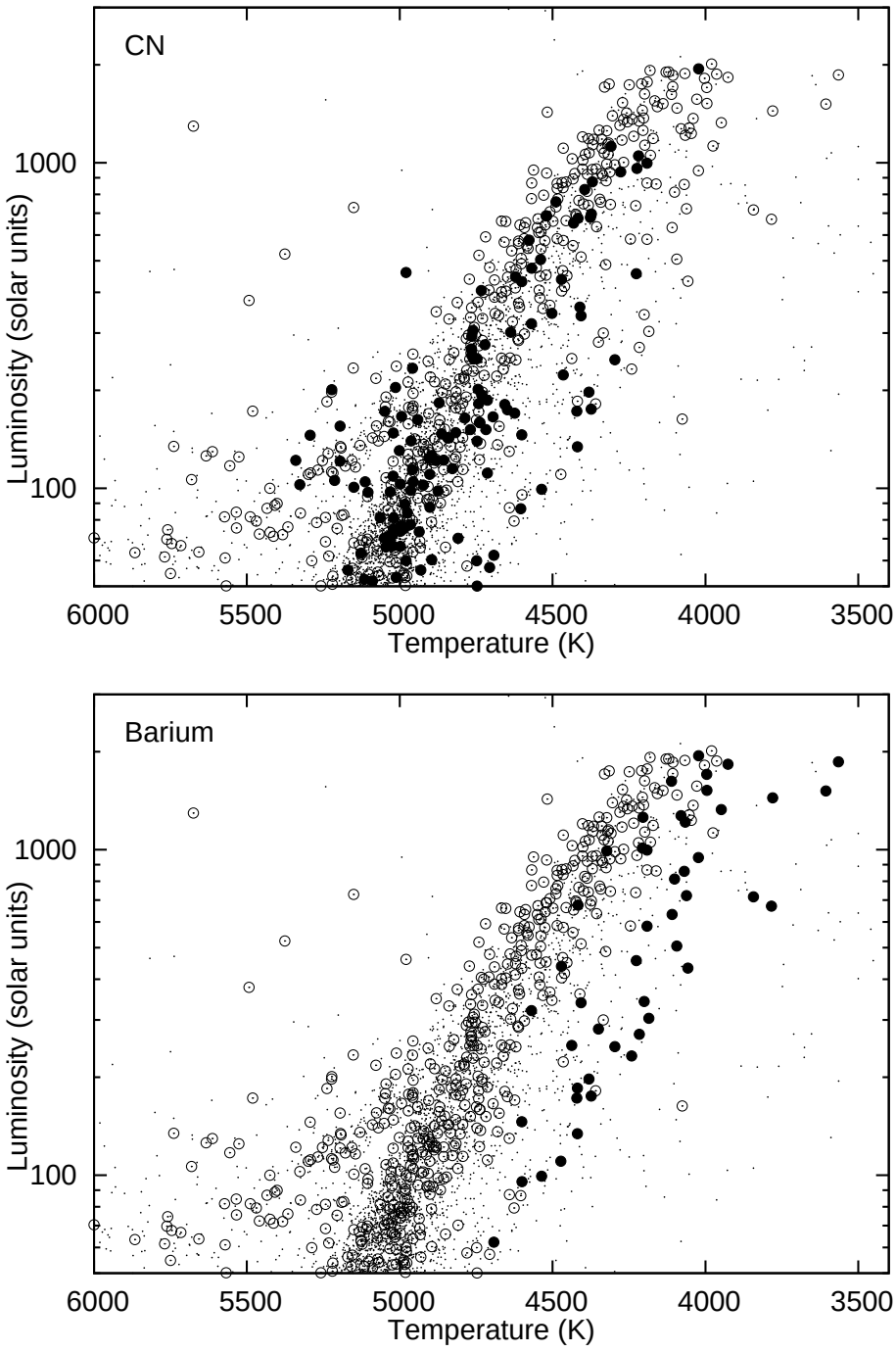

Figure 5.24: HRD, showing stars with measured CN (top) and barium (bottom) line strengths from vL+07. Small points show stars with no measurements, circles show stars with measured line strengths, CN- and Ba-rich stars are shown as filled circles.

to determine barium richness also suggests that the strong lines in the Ba-rich stars are due to the stars' low temperatures and higher metallicities, and that the relative abundances do not differ as much as is apparent in vL+07.

Fig. 5.25 shows the variation of the same indices with dust mass-loss rate. Here we define two indices to measure the richness of CN and barium. These are taken relative to the demarcations for richness marked in Figs. 13 and 20(f) of vL+07, and are described thus:

$$\alpha = \mathrm{S3839} - 2.2(\mathrm{CH4300} - 0.1), \tag{5.26}$$

$$\kappa = \mathrm{Ba4554} - 0.127(\mathrm{S3839} + 1.26), \tag{5.27}$$

where S3839, CH4300 and Ba4554 are the line indices as described in vL+07. The values of α and κ are positive for CN- and Ba-rich stars, respectively. Interestingly, there does not appear to be any significant variation of mass-loss rate with measured [Fe/H] values, unless one takes only those stars with highly significant excesses. However, there does appear to be a strong relation with barium-richness. This correlation is strengthened if we remove the special case of V1 — the dusty post-AGB star. We also note that then, the four most-mass-losing stars are metal-rich, suggesting a weak correlation may still be present. The barium may simply trace the coolest and metal-richest subpopulations in ω Cen, which one would expect to be the most prolific dust producers.

Using the above criteria, and setting a cut at 500 $L_\odot$, there is no obvious dependence of dust production on CN-richness: of the cluster members with observable mass loss ($\gtrsim 10^{-12}$ $M_\odot$ yr^{-1}), four are CN-rich, and 53 CN-poor. This is comparable to the figures of 12 and 95 in the non-dusty sample. The only CN-rich star losing large amounts of mass is, perhaps unsurprisingly, the carbon star LEID 52030. The lack of CN-rich M-type giants has been noted in vL+07.

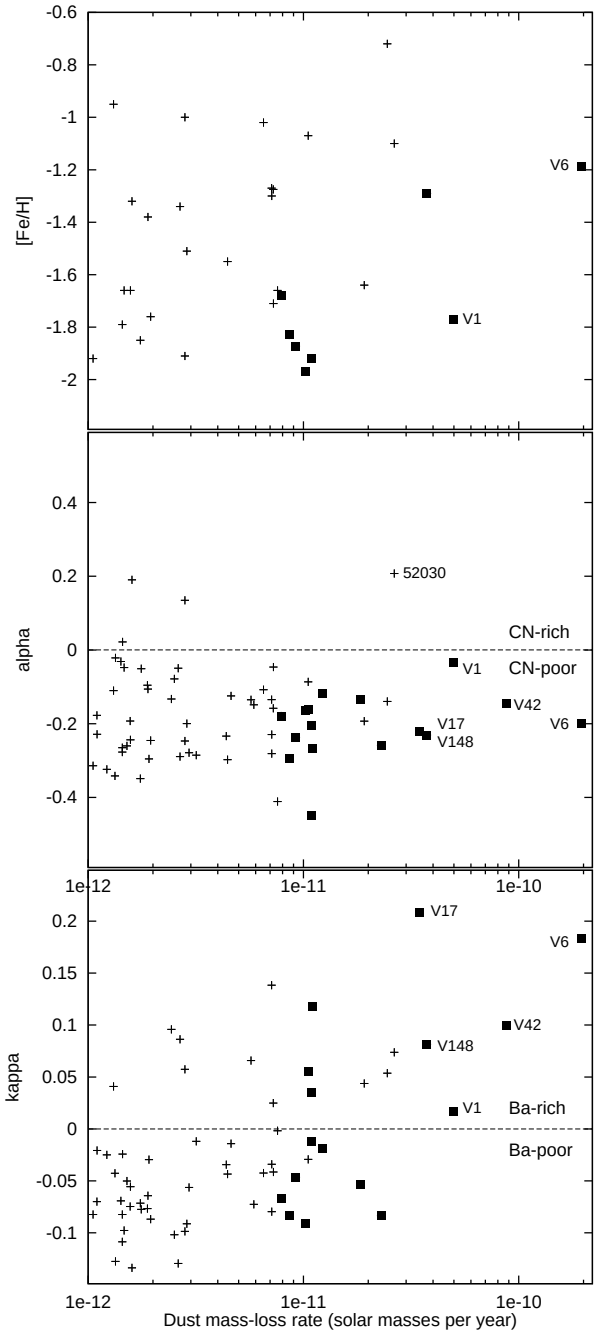

Figure 5.25: Dust mass-loss rates for stars with $L > 500$ $L_{\odot}$ and their dependence on [Fe/H] (top panel), and the CN (middle panel) and barium (lower panel) richness indicators α and κ (see text). Large squares show stars with individually statistically-significant ($> 3\sigma$) mid-IR excesses.

5.6.5 Implications and further work

5.6.5.1 Mass-loss rate and variability of metal-poor giants

There are several implications that result from our analysis.

- Mid-infrared excess, thus the inferred amount of dust, appears highly variable in pulsating stars on timescales of a month or less, much shorter than thought possible. Actual mass-loss rates may thus be considerably different from literature values. The true mass-loss rate may not be attainable without mid-IR photometry and spectroscopy throughout the pulsation cycle.

- An accurate measure of dust and gas mass loss requires knowing: how the gas-to-dust ratio varies both with evolution and metallicity, whether gas is coupled to dust, and how low the outflow velocity can reasonably be to support strong mass loss.

- Lack of correlation between our results and literature relations and studies (§5.6.3.2 & §5.6.3.3) highlights the difficulty in obtaining empirical relations between mass loss and other stellar parameters in an inhomogeneous sample of stars. From our analysis of V42 (§5.5.2.2) and other stars (Chapter 3), it seems more likely that other non-LTE effects, such as shocks and chromospheres, are significantly modifying the winds.

- Our mid-IR spectrum and critical evaluation of other data of V42 suggest that the analysis of Höfner & Andersen (2007) may be at least partially correct in assuming that some C-rich mass loss can occur in conditions that depart from LTE, though there remain issues with preventing that carbon reacting with sulphur. This may provide the opacity source required to drive O-rich dust-driven winds (Woitke 2006b).

5.6.5.2 The fate of ω Cen's lost mass

The fate of the lost mass is also interesting. The mass loss from the cluster must be stochastic at some level if it is being fed by only a very small number of stars, as these stars do not maintain a constant dust production throughout their evolution. Based on our observations, the current mass loss from the cluster should be around 1.2×10^{-5} $M_\odot$ yr^{-1} or more, depending on the contribution from chromospherically-driven winds, the gas-to-dust ratio in winds, and the gas-to-dust coupling efficiency.

With this total mass-loss rate and assuming 48 Myr since the last Galactic plane crossing (when tidal friction is expected to strip away intra-cluster material) based on the proper motions from vL+00, we might expect $\gtrsim 290$ $M_\odot$ of gas and $\sim$0.05 $M_\odot$ of dust to have built up within the cluster. Our *Spitzer* observations (B+08) suggest the amount of dust in the cluster is $< 10^{-4}$ $M_\odot$ (*c.f.* Boyer et al. 2006, who detect 9×10^{-4} $M_\odot$ of dust in M15), and data in the literature imply that < 2.8 $M_\odot$ of neutral gas can be present (Smith et al. 1990). The possibility remains that the intra-cluster medium (ICM) in ω Cen is in a hot, ionised state — the ICM in 47 Tuc contains at least 5% ionised gas (Smith et al. 1990; Freire et al. 2001). The fact that cold ICM in both gas and dust phase is observed in M15 suggests that neutral ICM is likely an existing phase in many GCs.

On this basis, it would seem likely that *neutral* gas is being processed or removed from the cluster environment on timescales of $\lesssim 3 \times 10^5$ years, and dust within 1×10^5 years. With a tidal radius of around 85 pc (Harris 1996), it would take a wind 8 Myr to escape the cluster if it were escaping at 10 km s^{-1}, or 1.2 Myr if swept clean as a result of ram pressure by the hot Galactic Halo (ω Cen has a space velocity of 69.1$\pm$5.6 km s^{-1} with respect to the Halo; Okada et al. 2007).

Another possibility is that the dust mass-loss rates (and thus also the gas mass-loss rates) we derive are too high due to their intrinsic variability, however we would expect this to average out through addition of errors in quadrature so that our value is only affected by this at the $\sim$15% level, which mostly comes from the error in the

mass loss of V42. Without knowing the long-term trend of this mass loss it is difficult to tell, but we can argue based on the sustainability of the mass-loss rate of V6, given the total mass loss we expect over its RGB or AGB evolution. Based on the total mass-loss rate we derive in §5.5.2, we find that, at the current rate, the star would lose the $\sim$0.1 $M_\odot$ required by evolutionary theory in 90 000 years. Given its position at the top of the giant branch, this does not appear too unreasonable, so we can assume our global rates are relatively sound.

We can also consider the dynamical effect of lost mass on the cluster. If a mass-loss rate of 1.2×10^{-5} $M_\odot$ yr^{-1} is indeed representative, this equates to some $\sim$0.46% of the cluster's mass per gigayear (Merritt, Meylan & Mayor 1997; van de Ven et al. 2006). If assumed constant in the past, the cluster will thus have lost 5–7% of its initial mass, with only small dynamical consequences. However, more massive stars lose a much larger fraction of their mass, and thus the cluster mass loss will have been more significant in the past — even when the cluster was already a Gyr old and intermediate-mass AGB stars were the main contributors to this mass loss. Cluster mass loss is therefore not a phenomenon limited exclusively to the first 10 Myr or so when exploding massive stars assured significant mass loss from the cluster's gravitational potential.

5.6.5.3 Are globular clusters only producing dust episodically?

Our analysis appears to show that the total mass loss from GCs is highly episodic. In ω Cen, V6 and V42 appear to be producing most of the dust mass loss in the cluster, and the total mass loss from the cluster appears dominated by a small number of stars.

Mass loss in ω Cen would seem to be stochastically variable. The high number of low-luminosity post-(early)-AGB stars and candidates suggests many stars may leave the AGB early, and that there may be a considerable number of AGB-*manqué* stars, leaving a significantly depleted fraction of stars actually reaching the AGB tip. By implication, the mass loss from other GCs of similar metallicity would have even more stochastically-variable mass-loss rates, as they are less populous and therefore have

(numerically) even fewer stars exhibiting high mass-loss rates.

Mass loss from a cluster may increase dramatically in the event that a single star undergoes the ejection of a planetary nebula. Several of these have now been observed in GCs: notably Pease 1 (K648) in M15 (Pease 1928), but also IRAS 18333–2357 (GJJC1) in M22 (Gillett et al. 1989), JaFu1 in Pal6, and JaFu2 in NGC 6441 (Jacoby et al. 1997). The fact that, out of all the clusters observed to date, only M15 shows convincing evidence of hosting an observable intra-cluster medium (Boyer et al. 2006; Barmby et al. 2009), could be due to a random effect, rather than due to M15's particularly low metallicity. This implies that the diffuse matter seen in M15 could merely be a diffusing planetary nebula that was ejected $\gtrsim 10^4$ years ago, however its large mass ($\gtrsim 0.3$ $M_\odot$; van Loon et al. 2006b) would suggest that a single such event is unlikely to be the sole producer of this much material. Potentially this free gas and dust could also be the results of a stellar collision, which by their nature are also episodic. Simulations in GCs fail to reproduce this level of mass loss in the case of colliding main-sequence stars (Lombardi, Rasio & Shapiro 1996), however a collision between a red giant and a neutron star may have the potential to eject the entire $\sim$ 0.3 $M_\odot$ stellar mantle (Rasio & Shapiro 1991). Such collisions have been suggested as a method of clearing GCs of ISM (Umbreit, Chatterjee & Rasio 2008). The true fate of the lost mass, and the precise origin of the cloud in M15, remains at this time unknown.

5.6.5.4 The nature of V42's mass loss

It is clear from §5.5.2.2 that V42, with its mass-loss rate of 1.4–3.6 $\times 10^{-6}$ $M_\odot$ yr^{-1}, stands out from the rest of the group. One possibility for this is that this represents a 'superwind' phase akin to that seen in more-massive long-period variables (*e.g.* van Loon et al. 1999; Schröder, Winters & Sedlmayr 1999). Here, the mass loss increases dramatically shortly before the star makes the transition from AGB-tip star to post-AGB star. If this were the case, we would expect V42 to denote the AGB-tip in Fig.

5.5. As we are unable to separate the RGB from the AGB, we are unable to tell whether this is the case, as the RGB tip may be more luminous. V42 is also clearly less luminous than V6 both in the data we have used to determine its luminosity, and the variability studies of Dickens et al. (1972). We should also note that the luminosity of V42 is likely variable on timescales significantly longer than the pulsation timescale — it is possible that V42 has recently experienced a thermal pulse, as suggested by Origlia et al. (1995), and that it is currently in an associated luminosity minimum.

The position of V42 on the HRD (Fig. 5.5) also suggests a second possibility — that the star is part of one of the metal-rich sub-populations, like V6. If it is 0.5 dex more metal-rich, this would decrease the calculated outflow velocity of its wind and hence its dust mass-loss rate by 0.25 dex and decrease its gas mass-loss rate by 0.75 dex to better match V6 in Fig. 5.20.

The possible presence of carbon-rich dust highlighted in §5.5.2.2 is surprising, given the oxygen-rich nature of the star. We put forward three suggestions to explain this behaviour: firstly, that a large variation in dust production is producing significant variations in the amount of dust in the wind; secondly, that luminosity changes in the star are altering the amount of light reprocessed by the dusty wind; or finally, that the grain size varies sufficiently that the silicate feature disappears periodically. In the first case, it can be argued that the criteria for dust formation to occur are only met during part of the pulsation cycle, leading to episodic dust formation under non-LTE conditions (*e.g.* Höfner & Andersen 2007). This may lead to carbon-rich dust at some epochs, with oxygen-rich dust forming at others, which we propose as a possible solution to the disparity between the mid-IR spectra (suggesting carbon-rich dust) and accumulated literature photometry (suggesting oxygen-rich dust). It has been put forward, however, that sulphur atoms would likely immediately bond with any free carbon, removing it from the wind and preventing the formation of carbon-rich dust under these conditions (Isabelle Cherchneff, private communication). Whether this remains true over all likely conditions, particularly those that depart substantially

from LTE, remains untested.

Under the second scenario, the rapid, large-scale changes seen in the mid-IR amplitude of V42 are due to the variation of light from the pulsation cycle: during periods when the star is warm, there is more optical emission to be re-processed by the dusty wind, which is much more opaque at these wavelengths. During periods when the star is cool, the optical emission is suppressed, the re-processing of optical radiation is decreased, and the mid-IR emission drops accordingly.

It would, at face value, appear unlikely that the grain size in V42 could become sufficient (*i.e.* a few tens of microns) to completely mask the silicate feature, due to the low metallicity and thus the infrequency of particle collisions that would lead to the aggregation of large grains. However, we note that it is not presently possible to observationally distinguish between these three scenarios.

Episodic and/or variable mass loss near the RGB/AGB tip is not a new concept: previous studies, including O+02 and Mészáros, Dupree & Szentgyörgyi (2008), have argued on observationally-based grounds that episodic mass loss is occuring. Applying this principle to other stars, the consequences of this could be quite far ranging: historical mass-loss rates have been assumed to be accurate probes of the mass lost over many years, yet many observed stars have very strong optical variations. It is thus important that, when calculating dusty mass-loss rates from such stars, that investigators have a good estimation of the stellar luminosity and temperature *at the time of measurement*.

5.7 Conclusions

We have here presented stellar parameters derived from spectral energy distribution fitting to stars over two orders of magnitudes in luminosity down the RGB and AGB of ω Centauri, creating a physical HRD of luminosity versus temperature, outlining the RGB, HB and AGB in great detail and accuracy, and identifying several new post-AGB

star candidates. From isochrone and spectral energy distribution fitting, we estimate the following parameters for the cluster:

- Distance: $d = 4850 \pm 200$ (statistical) ± 120 (systematic) pc;
- Reddening: $E(B-V) = 0.08 \pm 0.02$ mag (statistical) ± 0.02 mag (systematic) ± 0.02 mag (differential);
- Total dust mass loss: $\dot{M}_{\rm dust} = 9 \pm^{6}_{4} \times 10^{-10}$ M$_\odot$ yr^{-1};
- Total gas mass loss: $\dot{M}_{\rm gas} \sim 1.2 \times 10^{-5}$ M$_\odot$ yr^{-1} ($\sim 2/3$ from dusty winds, $\sim 1/3$ from chromospheric mass-loss);
- Timescale to clear the intra-cluster medium from cluster: $\lesssim 10^5$ yr;

under the following assumptions:

- gas-to-dust ratio, $\psi \propto 10^{-[{\rm Fe/H}]}$;
- wind velocity, $v \propto L^{1/4}\psi^{-1/2}$;
- absence of substantial mid-IR variability;
- constant dust chemistry along the giant branch;
- inner dust envelope temperature of 1000 K;
- our low wind velocities (~ 1 km s^{-1}) are accurate and still produce an accurate mass-loss rate.

We derive inner dust envelope temperatures for a handful of stars (including V6 and V42), suggesting they are typically $\gtrsim 600$ K.

We show that V6 and V42 contribute $\sim$25% of the cluster's dust production. V42 may be variable at mid-infared wavelengths on timescales of as little as a few weeks, suggesting equally variable dust production, meaning a single estimate of mass-loss rate and wind conditions may not accurately reflect the long-term conditions in this and similar stars. V42, an oxygen-rich star, may also be producing carbon-rich dust.

Dusty mass loss appears to start suddenly at a threshold of $\sim$4400 K, or ~ 1000 L$_\odot$, for a significant fraction of stars. There appear to be additional star-to-star differences, suggesting that other factors also influence the mass-loss rate. Empirical literature relations do not accurately reflect the dust production rates we measure in ω Cen.

By comparing our stellar parameters with optical line strengths, we have deduced that the Ba-rich stars in ω Cen belong to the more metal-rich populations and not to the AGB. These stars are characterised by dustier winds.

Mass loss along the RGB appears quite efficient with typically 0.20–0.25 $M_{\odot}$ lost on the RGB and $\gtrsim$0.05 $M_{\odot}$ on the AGB, possibly leading to large numbers of AGB-*manqué* and post-early-AGB stars. Dust production in ω Cen appears not confined to the AGB, with most dust producing stars in the cluster near the RGB-tip. This analysis unequivocally demonstrates that efficient mass loss is not exclusively a feature of metal-rich stellar populations.

6 The 21 cm emission towards ω Centauri

"Not all chemicals are bad. Without chemicals such as hydrogen and oxygen, for example, there would be no way to make water, a vital ingredient in beer."

— Dave Barry (1947–)

Contribution: *although I have been lead author in this continuing work, significant proportions of the work were carried out by my supervisor, as initialled throughout the text. The work below is my own creation, though the initial proposal and final data reduction are the creation of my supervisor (JvL), who was also present during the observations and has had naturally had significant input into the analysis of our data. My primary contributions are thus my rôle in taking the observations, and the discussion of the final maps included below.*

6.1 Introduction

The existence of a high-velocity cloud (HVC) in the direction of the globular cluster ω Centauri (NGC 5139) has been known since the work of Smith et al. (1990). Their H I Parkes survey found its radial velocity as some 48 km s^{-1} less than the cluster's 232 km s^{-1} (van de Ven et al. 2006) and it has a full width at half maximum (FWHM) of around 35 km s^{-1}. The HIPASS survey (Barnes et al. 2001; Putman et al. 2002) locates the source of the H I cloud (HVC 309.2+14.7+184, $\alpha_{2000} = 13^{\rm h}27^{\rm m}\dot{6}, \delta_{2000} =$ –47°43$^{\rm m}$) to some 16′ to the south-east of the cluster ($\alpha_{2000} = 13^{\rm h}26^{\rm m}46^{\rm s}, \delta_{2000} =$ –47°28$^{\rm m}$37$^{\rm s}$, $l = 309.10, b = 14.97$), with a total flux of 27.2 Jy km s^{-1}.

The true nature of this source remains unknown: it may be part of the leading arm of the Magellanic System, which towards ω Centauri contains other HIPASS HVCs at typically 200–400 km s^{-1} (Brüns et al. 2005), but its location and velocity also raise the possibility that it is material in the process of being lost from the cluster (Smith et al. 1990). This would be an important detection, as it has become evident that some mechanism is clearing interstellar medium (ISM) from globular clusters over a timescale of 10^6 years or less (see, *e.g.*, Chapter 5): presently, M 15 remains the only

Galactic globular cluster for which we have a secure detection of intra-cluster medium (ICM; Evans et al. 2003; Boyer et al. 2006; van Loon et al. 2006b), and stringent upper limits have been placed on both intracluster H I and dust in other clusters (*e.g.* van Loon et al. 2006b; van Loon et al. 2009; Barmby et al. 2009). van Loon et al. (2009) also report a similar detection of a resolved H I cloud near the cluster Pal 4, which would suggest that this is not an isolated co-incidence.

Further detections of diffuse emission toward the cluster have been made at various wavelengths. The *Einstein* satellite also reputedly found diffuse X-ray emission to the south of the cluster (Hartwick, Grindlay & Cowley 1982), but this was not found in later *UIT* imaging (Whitney et al. 1994). Origlia et al. (1997) detect CO (1–0) emission at 115.27 GHz near the cluster centre and to the west, crucially this detection is at roughly the same velocity (190∼200 km s^{-1}) as the H I cloud. More recently, our *Spitzer* images (Chapter 4) detect diffuse emission at 24 μm that shares some morphological features with diffuse nebular emission found by Cannon (1980a) and warm dust emission mapped by *IRAS* (Beichmann, Helou & Walker 1988). Given these correlations, it was considered prudent to obtain higher-resolution 21cm maps of the region.

6.2 Observations & results

6.2.1 Observations

Observations were undertaken with the CSIRO Australia Telescope Compact Array (ATCA) at Narrabri on 29–30 September 2007. The most-compact configuration (H75) was used, giving baselines between 31–89 m. This yielded a synthesised beam FWHM of 7.45′ and a primary beam FWHM of 33.6′ using baselines from the five mobile dishes in the array. The data from the more-distant, sixth, static dish was discounted as it could not be successfully matched to the rest of the map.

Two pointings were taken. The first, on the location of the HVC in the HIPASS

survey ($\alpha = 13^{\rm h}27^{\rm m}50^{\rm s}, \delta = -47°38'$), was tracked for 12 hours. The second, overlapping pointing was on the location of diffuse emission detected with *Spitzer* (cloud 'A' in Boyer et al. 2008; $\alpha = 13^{\rm h}25^{\rm m}20^{\rm s}, \delta = -47°40'$), tracked for nine hours. The FULL_8_512-128 correlator configuration was used, giving 512 channels over an 8 MHz bandwidth (providing a resolution of 3.3 km s^{-1} channel^{-1} at 1420 MHz) and two orthogonal polarisations for line spectroscopy. The correlator also produces a simultaneous 128-MHz, 32-channel continuum output, with all four Stokes polarisation parameters, centred at 1384 MHz. The primary calibrators 1934−638 (15 Jy) and 0407−658, though more frequently the secondary calibrator 1421−490, were measured and used to calibrate the gain and bandpass.

6.2.2 Reduction

The datacubes were reduced by JvL using the standard procedures within the MIRIAD software package. First, poor-quality channels in each baseline (due to interference, antenna shadowing, *etc.*) were flagged as bad. This was carried out partly manually using *blflag* and partly automatically. An image was produced from the visibilities by Fourier inversion, using a compromise between natural and uniform weighting. The images were then mapped onto $1' \times 1'$ pixels over a $1° \times 1°$ field. The beam was cleaned of sidelobes, resulting in a Gaussian with a FWHM of $476'' \times 294''$ at a position angle of $-84.4°$ for the first pointing, and a FWHM of $427'' \times 287''$ at a position angle of $-81.9°$ for the second pointing. The image was then convolved with the cleaned beam, following Högbom (1974). The line data were mapped onto a Local Standard of Rest velocity scale from −200 to +400 km s^{-1} in steps of 1 km s^{-1}, adopting a rest frequency for H I of 1.4204058 MHz. The final maps are shown in Fig. 6.1.

Our observations show four distinct bright continuum sources, labelled ATCA-1 through -4. The HVC itself appears as an extended object, concentrated near ATCA-2, but not directly superimposed. It exhibits a head-tail structure, with the tail extending some $20'$ to the south-west towards ATCA-3. These sources are listed in Table 6.4,

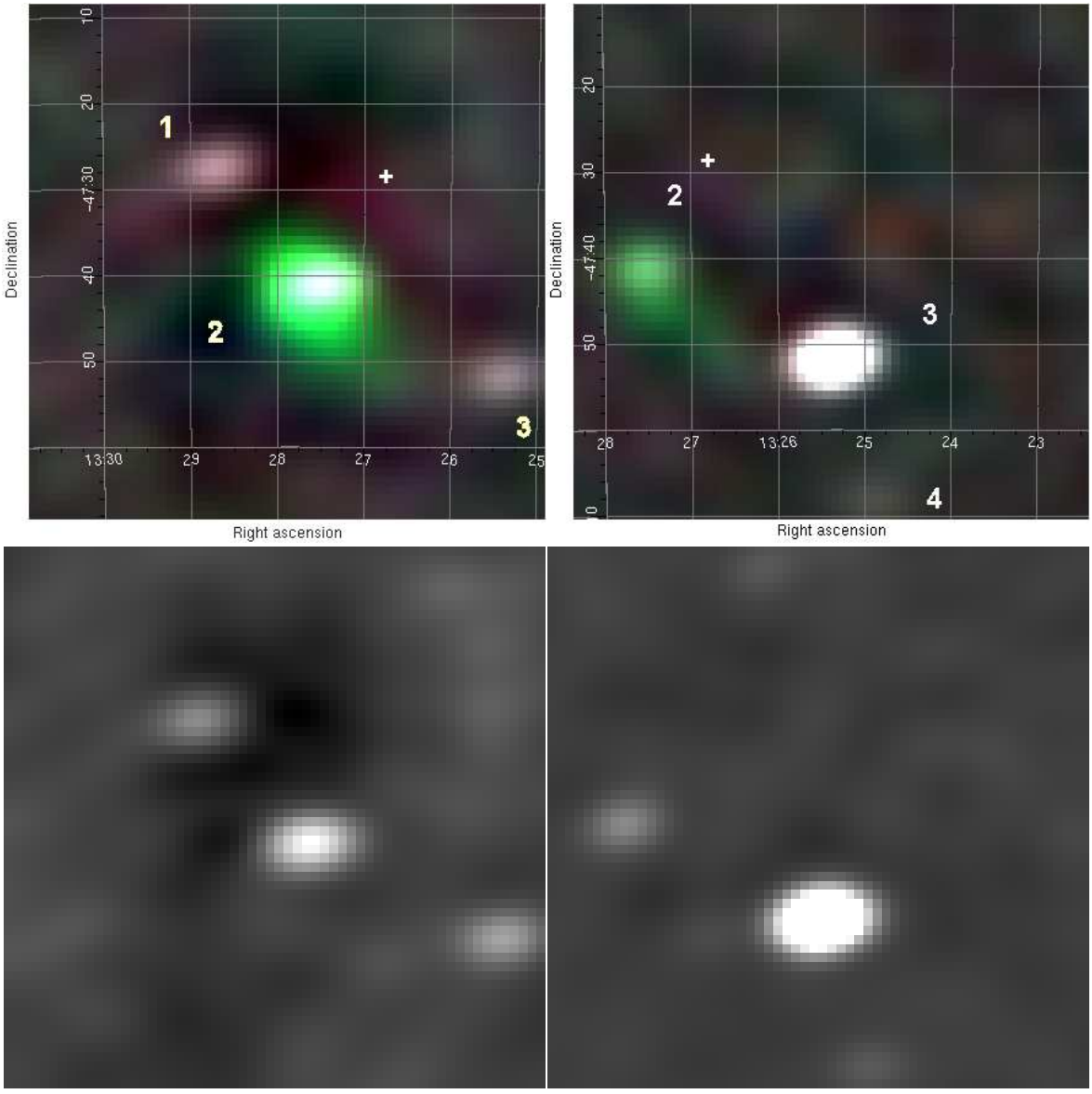

Figure 6.1: Radio maps obtained from our ATCA observations. Source details are listed in Table 1. Top panel: line map; colours: red = –200 to +165 km s^{-1} (Galactic foreground), green = 165 to 200 km s^{-1} (HVC) and blue = 200 to 260 km s^{-1} (cluster); images scaled to –20 to 100 mJy $beam^{-1}$ km^{-1} s; the cross marks the centre of ω Centauri. Bottom panel: continuum map covering the same area; images scaled to –26 to 85 mJy $beam^{-1}$.

where the ATCA position errors have been assigned as the standard deviation of the positions over the velocity range –200 to –50 km s^{-1} in 10 km s^{-1} bins.

Flux measurements of the sources (also listed in Table 6.4) have been calculated under the assumption of point sources, where the flux is simply equal to the peak in the flux distribution. As we will later see, ATCA-2 and -3 are multiple sources. The effect of this on our flux measurements is not thought to be large, as the individual sources are well within the synthesised beam of the interferometer, and the ratio between the fluxes is sufficiently large that the brighter source dominates.

An adjustment was applied to the observed flux measurements ($F_{\rm obs}$) to correct for the attenuation towards the edges of the receivers' primary beams:

$$F_{\rm actual} = F_{\rm obs} \exp\left(-\frac{r^2}{2\sigma^2}\right), \tag{6.1}$$

where r (in arcminutes) is the distance from the beam centre, and σ is given by:

$$\sigma = \frac{\rm FWHM}{2\sqrt{2\ln 2}}, \tag{6.2}$$

the FWHM being 33.6′, making $\sigma = 14.3'$.

6.3 Discussion

6.3.1 The continuum sources

6.3.1.1 Catalogues used in comparisons

In this section, we compare our observations with several images and data catalogues from other sources. These include:

- the 843 MHz Sydney University Molonglo Sky Survey (SUMSS; Mauch et al. 2003) — this high-resolution interferometric mosaic contains several point sources that match with our ATCA continuum sources (Table 6.4);

- the 4.85 GHz Parkes-MIT-NRAO survey (PMN; Gregory et al. 1994) — at a resolution of 5′, this is only marginally better-resolved than our data and contains several faint continuum sources (Table 6.4);

- *Spitzer* IRAC/MIPS 3.6–24 μm photometry and MIPS 24 μm imaging (Boyer et al. 2008, §4; Table 6.4);

- the optical/IR catalogues from the United States Naval Observatory B (USNO-B; Monet et al. 2003), *Hubble Space Telescope* Guide Star Catalogue (GSC; Space Telescope Science Institute & Osservatorio Astronomico di Torino 2007), 2MASS (Cutri et al. 2003) and Optical Gravitational Lensing Experiment (OGLE; Kałużny, J. and , M. and Szymański, M. and Udalski, A. and Krzemiński, W. and Mateo, M.).

Each object is identified on a high-resolution Sloan Digital Sky Survey optical image (Fig. 6.2), along with the locations of objects in the above catalogues (also Table 6.4).

6.3.1.2 ATCA-1

This source is probably the easiest to identify in the other catalogues. Its position is commensurate with a known radio continuum source, present in the SUMSS and PMN catalogues. This is offset slightly to the north-east from a source in the *Spitzer* catalogue, which is co-incident with a 2MASS and optical sources. This source is apparently seen through a relatively-dense region of the Galactic ISM (labelled Cloud D in Boyer et al. 2008; see Fig. 6.3).

While the optical photometry is sometimes unclear due to source confusion, the spectrum from J-band (1.25 μm) to 843 MHz (35 cm) exhibits a continuum slope of $F_\nu \propto \nu^{-0.45}$, suggesting a synchrotron source. The associated *Spitzer* source has been labelled as a candidate 'background galaxy' in Boyer et al. (2008). It shows no obvious association with the foreground ISM. The obvious spectral slope at all wavelengths, and lack of an apparent stellar component, suggests that the radio source is beyond

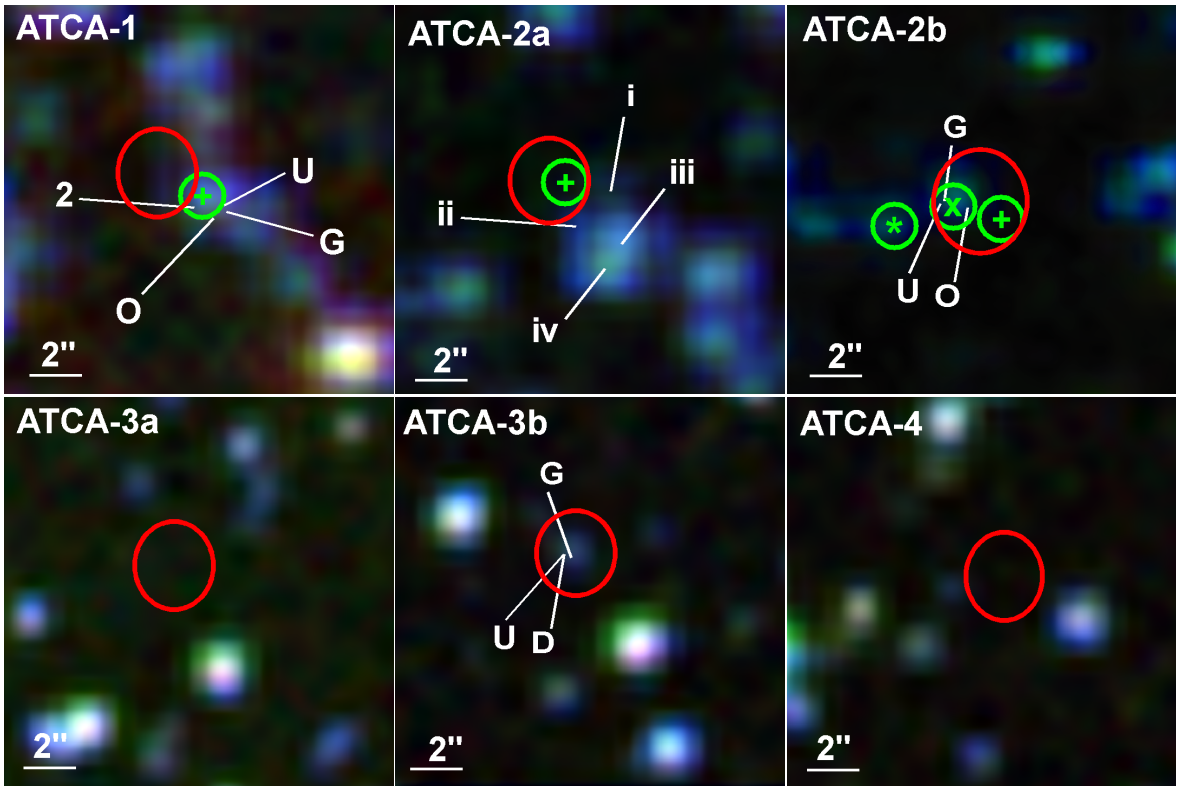

Figure 6.2: Digitised Sky Survey POSS2 maps (Adelman-McCarthy et al. 2008), with blue, red and infrared mapped to blue, green and red, respectively. The red circles represent the SUMSS error ellipses for the individual sources. The green symbols ($+$, $\times$ and $*$) mark the location of the *Spitzer* sources with the surrounding circle representing the IRAC1 3.6 μm point spread function FWHM. The remaining white symbols are discussed in the text.

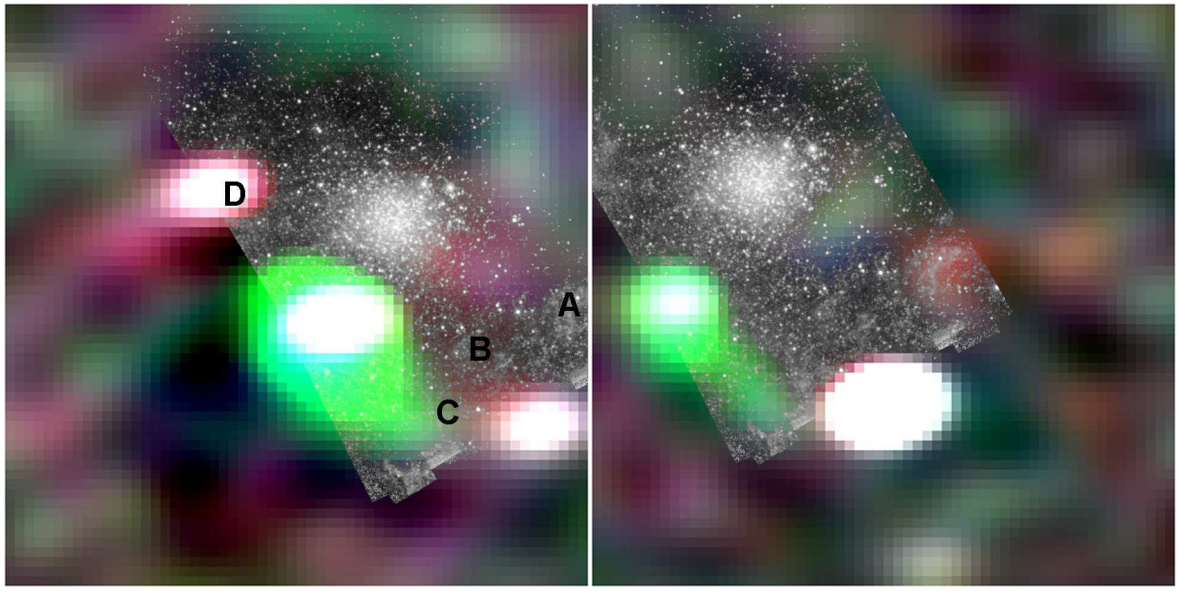

Figure 6.3: Comparison between the ATCA radio maps and *Spitzer*/MIPS 24 μm imaging, from Boyer et al. (2008). Colours as in Fig. 6.1, scaled between –10 and +30 mJy beam^{-1} km^{-1} s. The four *Spitzer* clouds have been labelled A–D, after Boyer et al. (2008).

the Galactic Disc and indeed an active galactic nucleus.

6.3.1.3 ATCA-2

The continuum source ATCA-2 is superimposed with the HVC, though is probably located slightly to the west of the main part of the cloud. While the source is not listed in the PMN radio catalogue, there are two sources in the SUMSS catalogue that lie within the ATCA position error circle. ATCA-2 appears to be a blend of the two sources, here labelled ATCA-2a and ATCA-2b.

The brighter SUMSS source, ATCA-2a, has a co-incident *Spitzer* detection. Several nearby objects (labelled i–iv in Fig. 6.2 & Table 6.4) are identified in the optical OGLE database, though they are sufficiently distant from the SUMSS/*Spitzer* source that they are probably not associated. These optical sources also appear in the USNO and GSC catalogues. The flux distribution from this source appears to peak slightly short of 3.6 μm, but clearly does not follow a blackbody-like distribution in the mid-

infrared (3.6–8.0 μm). The flux distribution suggests that this is also an active galaxy, though one where the starlight represents a larger component, compared to the galactic nucleus.

The fainter SUMSS source, ATCA-2b, has a further two *Spitzer* sources falling within its error circle. Of these, the eastern source (Fig. 6.2; labelled $\times$) has a detection in the optical USNO, GSC and OGLE databases. It shows a stellar-like optical spectral energy distribution, with a temperature of $\sim$4000 K, with considerable infra-red flux excess. The western source (+) has similar infra-red colours and no optical counterpart. A third *Spitzer* source ($*$), identified as a candidate galaxy in Boyer et al. (2008), lies outside the SUMSS error circle. The nature of ATCA-2b is difficult to determine. The infrared colours of the three *Spitzer* sources suggest this is an unresolved galaxy group. The radio source may therefore be another background galaxy, possibly with a superimposed foreground star.

6.3.1.4 ATCA-3

This source is the strongest on our maps. It is also identified with a comparatively strong source in the PMN catalogue. The SUMSS catalogue lists this as a composite object, comprising of two continuum sources, which we name ATCA-3a and ATCA-3b.

Sadly, the field was not covered by the *Spitzer* maps. There is no other detection for ATCA-3a, suggesting that the object is probably non-stellar, though its identification remains unknown. The object ATCA-3b is a perfect match for an apparently unremarkable point source with $(B - R)$ colours recorded in several catalogues between 0.7 and 1.1 mag. These colours are similar to those of many stars, but also of AGN (Cutri et al. 2001). The source remains unidentified, but evidently contains a non-thermal component. Super-position of the sources ATCA-3a and ATCA-3b in our observations and the PMN radio catalogue mean it is impossible to determine the spectral slope of the emission. We are therefore unable to discern whether ATCA-3b is a Galactic point source or an AGN.

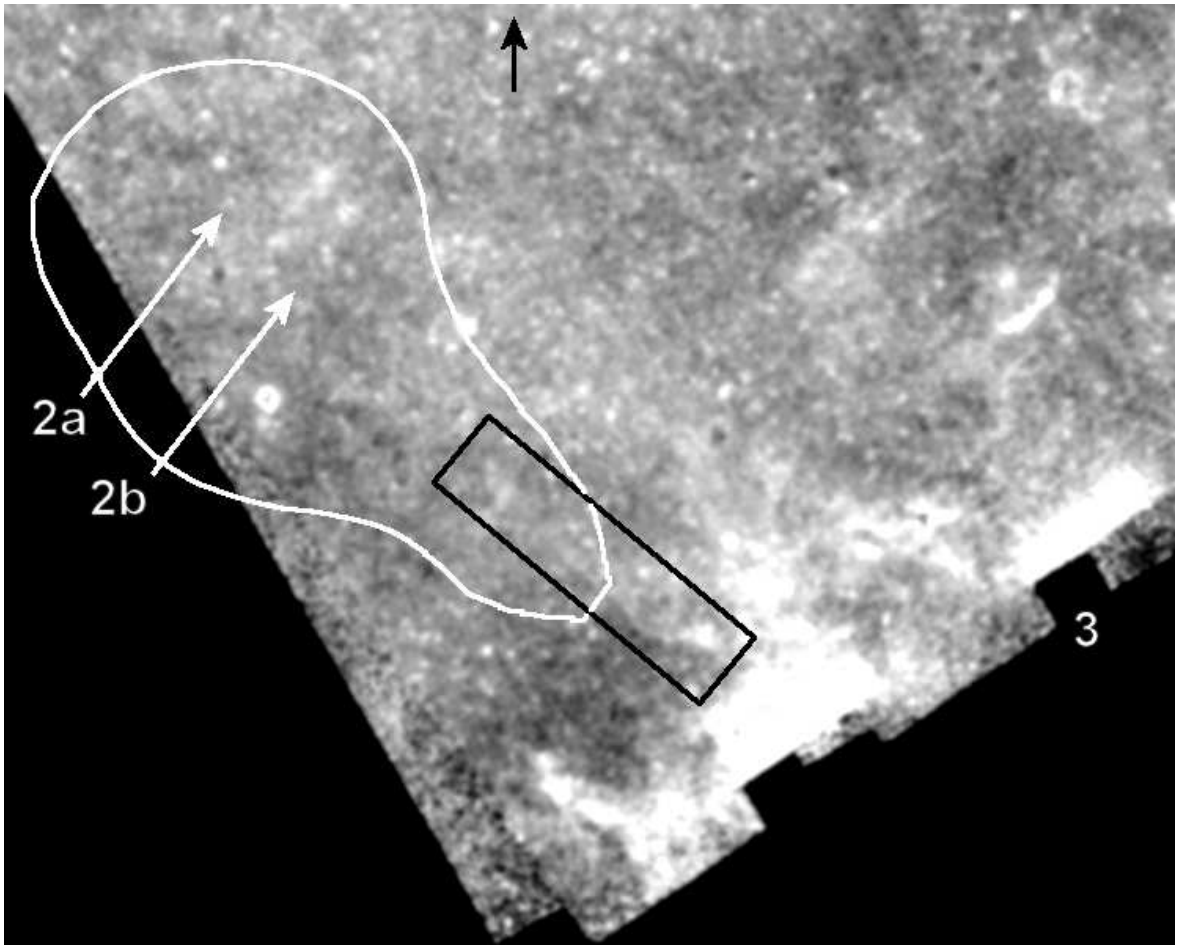

Figure 6.4: *Spitzer* 24-μm emission maps from Boyer et al. (2008). The white contour shows the approximate location of the HVC. The black box outlines a dust filament possibly associated with it. The black arrow points toward the cluster centre. The other labels refer to the position of the SUMSS sources associated with our continuum sources ATCA-2 (a, b) and ATCA-3.

6.3.1.5 ATCA-4

ATCA-4 appears on the edge of our maps. It is identifiable with a single SUMSS source, but with no optical/infrared counterpart. This may be another background galaxy, but without more complete wavelength coverage it is difficult to tell.

6.3.2 The high-velocity cloud

Line emission is present throughout the ATCA maps. Most of it is concentrated around the local rest velocity, with $v_{\rm LSR} = -20 \pm 40$ km s^{-1} (see §6.3.3). The only other clear line emission comes from the high velocity cloud, centred at ∼190 km s^{-1}. Disentangling the HVC from the continuum sources, we can see that it has a clear head-tail structure, with the head at its north-eastern extremity, and the tail extending south-west to around 20′ in length. In the absence of the cluster, the most likely scenario would therefore be that the head is an isolated pocket of neutral hydrogen (*i.e.* a normal HVC) which is being moulded by ram-pressure stripping by hot Halo gas. This has been observed in other halo HVCs without any known associations to other objects (Quilis & Moore 2001).

Alternatively, this HVC may be material swept from ω Cen. The material would be similarly shocked by ram-pressure stripping by Halo gas. This is a more radical solution, but has two key facts in its favour. Firstly, the radial velocity of the HVC (∼191 km s^{-1}) is similar to the 232 km s^{-1} radial velocity of the cluster (van de Ven et al. 2006). The difference is comparable to the cluster's ∼27 km s^{-1} central velocity dispersion (van Leeuwen et al. 2000), and within the 58 km s^{-1} escape velocity from the half-mass radius (Harris 1996; van de Ven et al. 2006). Secondly, the tangential space motion of the cluster is in the direction of the HVC (Okada et al. 2007): if ICM is escaping symmetrically from the cluster, it will be shocked most strongly in this direction. Okada et al. calculate the space motion is small (69.1 ± 5.6 km s^{-1}), suggesting such bow-shocking would be weak. Their *Chandra* observations do not show any evidence of diffuse X-ray emission, though they do not cover a sufficient distance from the cluster to include the HVC.

Their calculated space motion assumes a stationary Halo, but the cluster's proximity to the Galactic Plane (Z = 1400 pc; Harris 1996) means that the local Halo gas may be partly coupled to the 220 km s^{-1} rotation of the Galactic Disc (van Loon et al., accepted MNRAS, hereafter vL+09). At ω Cen's position, this is directed almost

exactly toward us at $v_{\rm LSR} \approx -40$ km s^{-1}, so this could add up to 260 km s^{-1} to ω Cen's space motion (relative to the ambient extra-planar medium), in the radial direction. For reference, Okada et al. find that $\sim$200 km s^{-1} relative motion is needed to generate observable X-ray emission from such tidal shocking.

There is also, however, evidence against the cluster's association with the HVC. Notably, a substantial amount of the HVC's motion (if it is excreted from ω Cen) must be in the radial direction: the radial velocity difference between the two — $\sim$41 km s^{-1} — is a substantial fraction of the cluster's space motion. In a typical bow-shock, one would therefore expect a more 2-D sheath of emission appearing over part of the cluster, which would tend to a progressively more arc-like if the cluster's motion with respect to the Halo gas were more tangential than radial to our line of sight. The HVC appears here as a linear, 1-D structure. Furthermore, the tail of the cloud points directly back (within reasonable error) toward the Large Magellanic Cloud. This agrees with the model of Bland-Hawthorn et al. (2007), which predicts head-tail structure in this direction for clouds in the Magellanic Clouds' kinematic system. Here, HVCs in the Leading Arm and Magellanic Stream are co-moving with the Magellanic Clouds, but being slowly perturbed away from them by Galactic tidal forces. These HVCs then impact hot Halo gas mixed with ablated material from clouds further upstream, creating shock fronts around their leading edges. Though theorised, this has never been previously observed in the Stream (Joss Bland-Hawthorn, private communication).

Even having now partially resolved the HVC, and with better identification of the radio sources in the same line-of-sight, it is difficult to clarify the nature of the HVC's association with ω Cen. It appears that the continuum sources identified have nothing obvious to do with the HVC, especially since the two sources at the north-eastern extremity of the HVC (ATCA-2a and -2b) are most likely background galaxies.

Also notable is the lack of infra-red emission from the cloud. In the case of M15, we clearly see warm (70 K) dust in the *Spitzer* data (Boyer et al. 2006). If the HVC is in such close proximity to the cluster, or has recently left the cluster through whatever

mechanism, we might expect to see evidence of warm dust within the HVC in either *Spitzer* or *IRAS* imaging. Both *IRAS* and *Spitzer* 24-μm maps show faint filamentary structure a few arcminutes to the west of the HVC tail, this appears to be associated with Galactic cirrus (§6.3.3). A second, even fainter filament, much sharper than those identifiable with Galactic foreground ISM, is visible in our *Spitzer* maps and is highlighted in Fig. 6.4. This may be spatially co-incident with the HVC tail, though higher-resolution 21-cm observations are required to determine whether or not the features are truly co-incident. If confirmed, this dust detection could be an important tool for measuring the temperature and metallicity of the HVC.

Kinematically, the cloud appears warm. The half-width half-maximum velocity spread of the cloud is $\sim$10 km s^{-1} over its entire length. For hydrogen, this equates to a temperature of $\sim$4000 K, given $T = mv^2/(3k)$. This would appear to rule out the presence of dust. However, the velocity profile is non-Gaussian. This suggests either that part of the velocity spread is due to the cloud changing shape, probably via interaction with the Halo, or that the cloud is a multi-phase medium. In this latter scenario, the hot, shocked gas on the cloud's leading edge gives rise to much broader emission than the rest of the cloud, which can be cool and contain dust. Unfortunately, the resolution of our observations is insufficient to probe different parts of the cloud accurately, and thus determine the different phases that are present.

On the basis of the above information, while we cannot rule out the association of the cloud with the cluster, it would appear that such a relationship is unlikely. The head-tail structure provides good evidence for shocking of an isolated cloud in the Magellanic Stream by hot Halo gas. Higher-resolution imaging may be able to confirm this, and thus allow an estimate of physical parameters of the Halo gas in that location to be estimated, such as temperature, density and velocity.

While higher-resolution imaging in H I could reveal the cloud's true nature, the deciding factor could also be made by a distance determination to the cloud. Direct distance measurements to H I clouds have historically proved difficult, but limits can

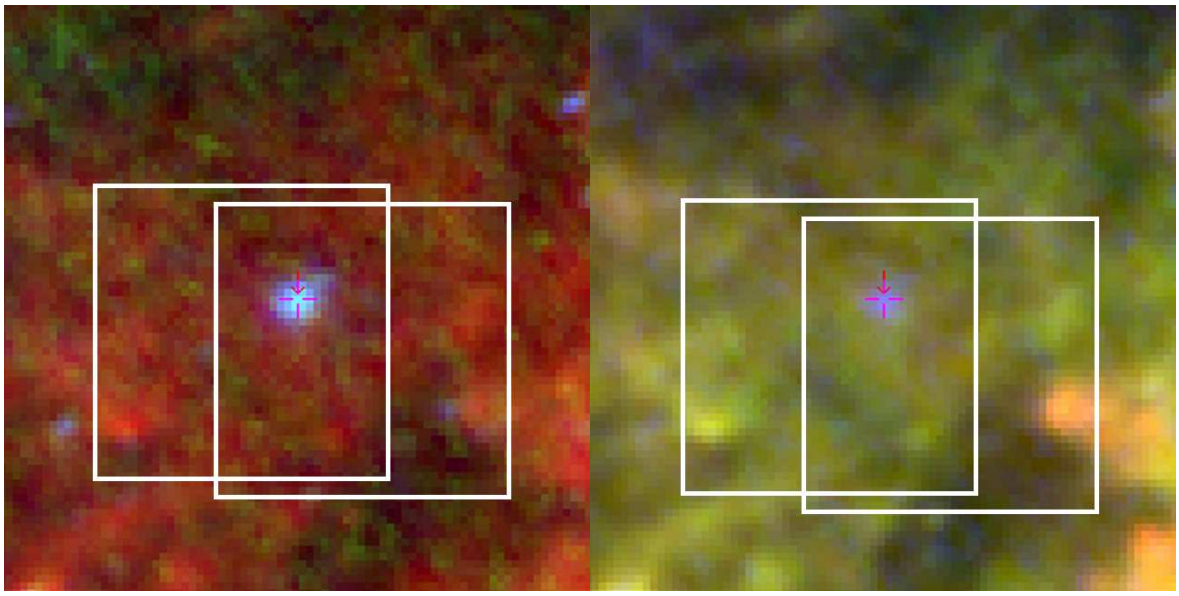

Figure 6.5: *IRAS* maps of the areas covered by the ATCA maps in Fig. 6.1. Left panel: blue, green and red are 12, 25 and 60 μm data, respectively. Right panel: likewise for 25, 60 and 100 μm data. The ATCA map footprints are shown by the white boxes. The magenta cross indicates the cluster centre. The field is 2.5° × 2.5°, north is up.

be set by observing interstellar absorption lines (or lack thereof) at the HVC velocity in stars in the same line of sight.

6.3.3 Galactic foreground

As the Galactic foreground ISM is not directly associated with mass loss in globular clusters, we here only make a brief comparison between our H I maps and the work of other surveys.

6.3.3.1 Comparison with *IRAS* maps

The Galactic ISM is visible as low-level emission in Figs. 6.1 & 6.3. Though at first appearing like pure noise, several of the features in the radio maps are associated with dust features in the Galactic foreground, particularly *Spitzer* Cloud A. Cloud C also appears associated with a region of excess Galactic-velocity emission near source ATCA-3, and Cloud D similarly near ATCA-1. Cloud B appears to have no obvious

radio counterpart.

Data from the longer-wavelength data from the *IRAS* satellite (IRAS catalogs and atlases, Volume 5 1988) mirror the structure found in the *Spitzer* data. The majority of the emission in the region appears to have a peak wavelength between 25 and 60 μm (see Fig. 6.5), which would correspond to a blackbody temperature of $\sim$50–120 K. The cluster itself is bright at shorter wavelengths. While Origlia, Ferraro & Fusi Pecci (1995) have suggested this source corresponds to the Long Period Variable (LPV) V42, it would appear from the *Spitzer* data that mid-infrared emission is present throughout the cluster (Boyer et al. 2008; McDonald et al. 2009).

Towards the right of our westerly pointing, the 100-μm-bright source IRAS 13204–4738/–4740 and an unlisted 60-μm-bright source at $\alpha_{2000} = 13^{\rm h}\,23.2^{\rm m}, \delta_{2000} = -47^\circ\,35'$ appear to be discernible above the background noise (if only just) as identifiable ISM clouds in Fig. 6.1 & 6.3.

6.3.3.2 Comparison between dust and gas emission

By comparing the ATCA H I column densities and velocities with *Spitzer* 24-μm dust maps, we can link the dust and gas components of the ISM visible in the maps. Fig. 6.6 shows the 24-μm dust emission and the H I velocities of neutral gas associated with that dust. It can be clearly seen that the stronger dusty emission corresponds ubiquitously to H I radio velocities between $v_{\rm LSR} = -20$ and 0 km s^{-1}. Emission centred around –13 km s^{-1} appears throughout the radio images, including on the locations of all four *Spitzer* clouds. Some pockets of weaker emission also appear present at velocities of $\sim$–40 km s^{-1}. A few small holes with very little Galactic-velocity emission also appear to correspond to holes in our dust map, one of which lies above the proposed HVC tail.

The small pocket of emission near +40 km s^{-1} is unexplained — one would not expect gas at significantly positive velocities at this Galactic longitude. It seems most likely that this is a residual artefact associated with the bright source ATCA-3. Alternating dark and light bands appear around the source, suggesting that the beam used

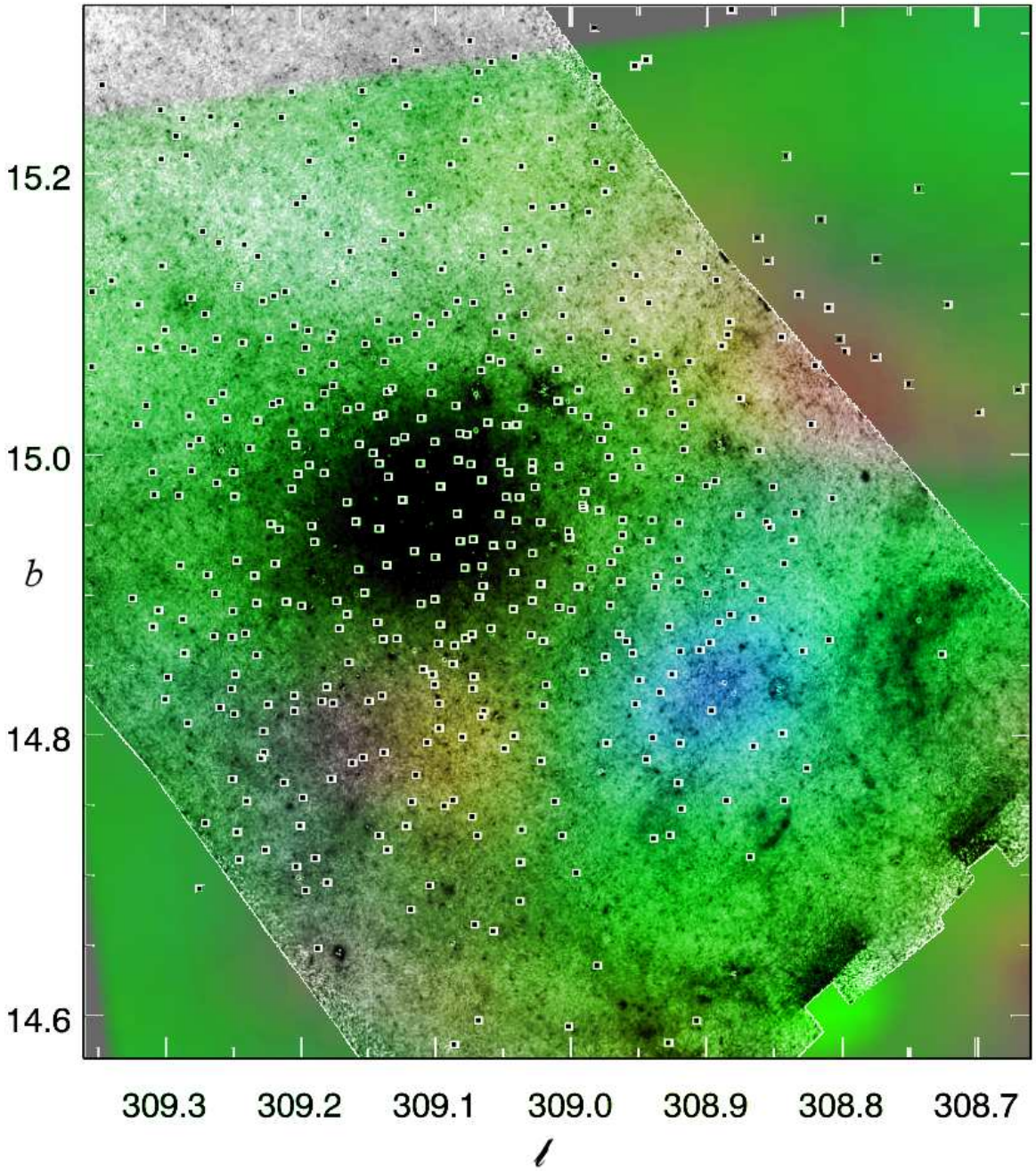

Figure 6.6: *Spitzer* 24-μm emission maps from Boyer et al. (2008) (greyscale). Overlaid in colour are gas velocities from ATCA 21cm maps. Velocities are shown from –60 (red) through –10 (green) to +40 (blue) km s^{-1}. More-saturated (stronger) colours represent brighter 21 cm emission. The small squares locate the horizontal branch stars used in Figs. 6.7 & 6.8.

to clean the data was imperfectly-shaped. The strength of this effect is small: only a few percent of the strength of the source ATCA-3.

We observe most of the cluster through the Scutum-Crux spiral arm (Taylor & Cordes 1993). Velocities of –13 km s^{-1} correspond to gas near the Local Bubble, at distances of around 1300 kpc, while velocities of –40 km s^{-1} are more consistent with extra-planar gas at distances of 4–8 kpc (Wood & Bates 1994; vL+09). Determining more precise distances at this Galactic longitude is difficult, as it is close to the so-called Centaurus tangent.

6.3.3.3 Comparison with absorption line studies

A final brief comparison can be made between the dust and gas maps, and absorption-line maps from vL+09, reproduced in Figs. 6.7 & 6.8. The maps were created from interstellar absorption features in the spectra of hot horizontal-branch stars within ω Cen (vL+09). These stars are relatively free of spectral lines, allowing interstellar absorption lines to become visible due to nebular absorption between the stars and the Earth. Specifically, vL+09 map the Na I D_2 and Ca II K transitions, as well as the strong but unidentified diffuse interstellar bands (DIBs) at 5780 & 5797 Å. By measuring the equivalent widths (EWs) of lines, the column densities of these species can be inferred along lines of sight towards horizontal branch stars in the globular cluster. As the resolution of these spectra is only $\sim$40 km s^{-1}, separating interstellar absorption in front of the cluster at the velocity of the HVC from the photospheric lines of the stars themselves is difficult, as the difference is almost exactly one spectral bin. No obvious HVC signature was visible in the absorption line spectra. This would suggest that the HVC is behind ω Centauri, though the difficulty in extracting any signature means we cannot say this for certain.

More generally, correlations between the dust and H I maps (Fig. 6.6) and absorption-line maps (Figs. 6.7 & 6.8) are difficult to determine, due to the poor sampling in both H I and the absorption-line maps. A possible correlation exists between patches of

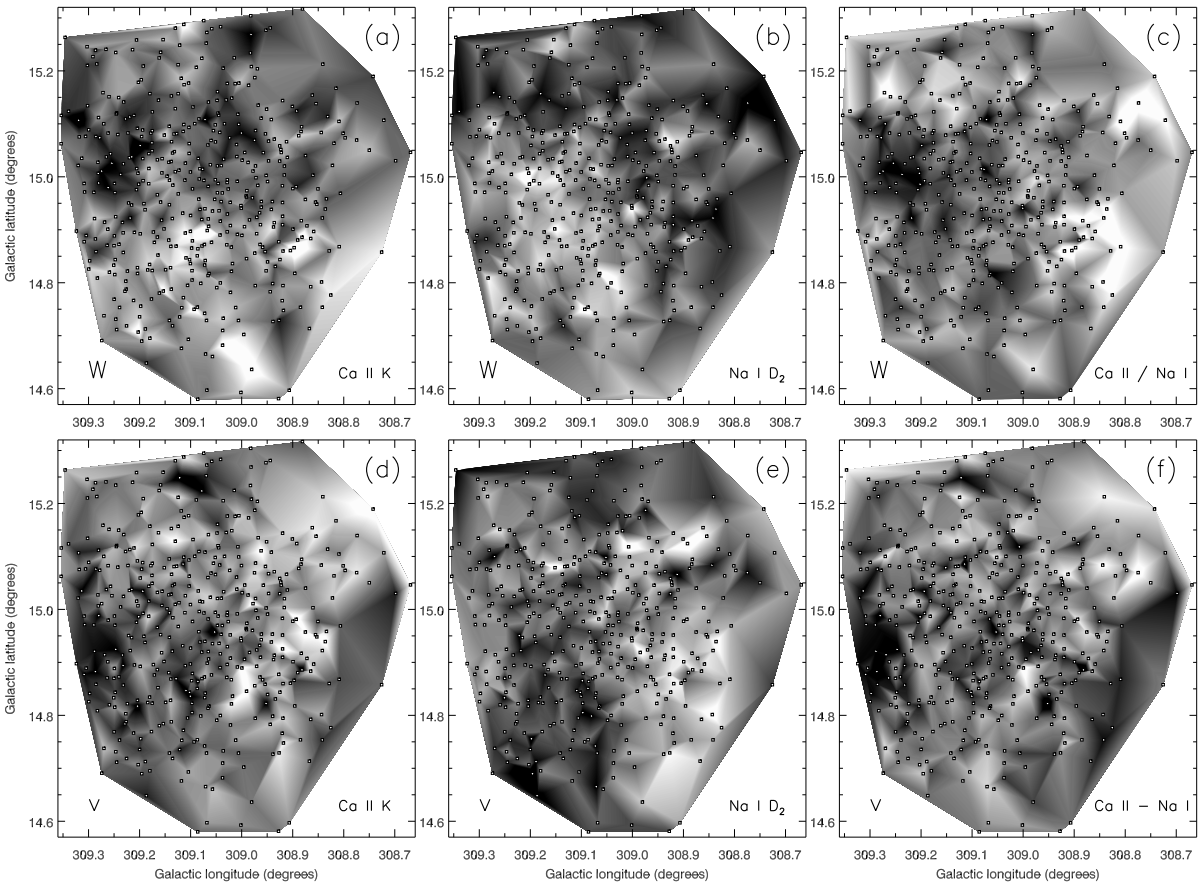

Figure 6.7: Maps of the structure in the foreground ISM as determined from absorption line equivalent widths (W) and velocities (v) in Ca II and Na I D, from vL+09. The colour ranges (black-to-white) span ±2 standard deviations from the median values (high column densities/velocities are white): Ca II spans –43.7 to –29.7 km s^{-1}, Na I spans –27.7 to –20.1 km s^{-1} and (Ca II – Na I) spans –19.0 to –4.3 km s^{-1}.

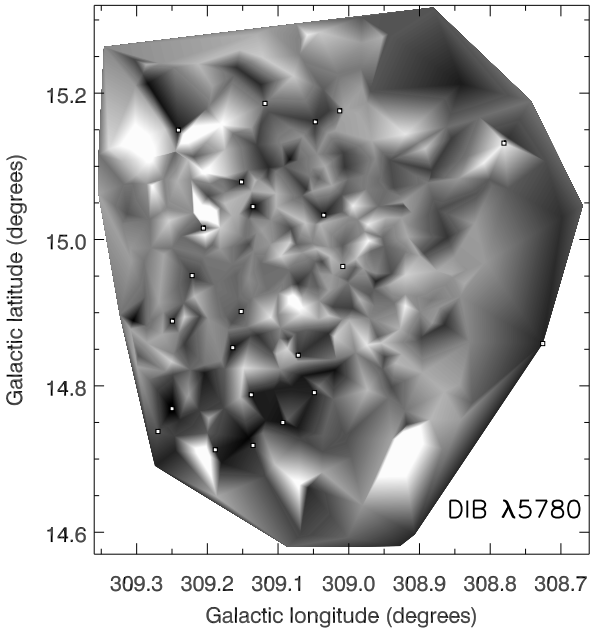

Figure 6.8: Map of the structure in the foreground ISM as determined from absorption line equivalent widths of diffuse interstellar bands, from vL+09. The colour range (black-to-white) span ±2 standard deviations from the median value (high column density/velocity is white). White squares show stars with a large ratio of 5797 Å to 5780 Å absorption.

dust emission and Ca II absorption features, though it is very weak. At first, this seems counter-intuitive, as Ca II should trace generally warmer (mildly ionised) medium. The extent and reasons behind this correlation remain unclear, however Ca II strength may also be correlated with gas (and by inference dust) column density (vL+09). Depletion of Ca II onto dust is found in vL+09, but not enough to reverse the correlation with gas column density.

No obvious correlation exists between Na I absorption maps and either the dust or gas maps. Similarly, no obvious links can be found between DIB strength and dust or gas density. This is surprising, given the good correlation seen in vL+09 between Na I and E(B–V) maps from IRAS/DIRBE, and between these maps and our *Spitzer* dust maps (Fig. 6.6). It may be that the correlation seen on large ($\gtrsim 6'$) scales is not reproduced on smaller ($\lesssim 1'$) scales.

6.4 Conclusions

We have conducted moderate-resolution observations at 21cm of the high-velocity H I cloud near ω Centauri. The cloud has been resolved into a head-tail structure with the head pointing away from the LMC. This suggests a common origin with the LMC, and shaping of the cloud by interaction with surrounding hot Halo gas.

Several continuum sources, probably unassociated with the HVC, are also seen. Some have been identified with other radio and/or infra-red and/or optical sources.

We cannot conclusively state whether the HIPASS cloud has any association with ω Cen. However, the weight of evidence is in favour of the cloud being unassociated. It is likely part of the Magellanic Stream and merely shares a similar line-of-sight to ω Cen. We have also crudely mapped the dust and hydrogen gas in the intervening Galactic ISM and find it to be highly structured on all observable scales. Higher-resolution imaging and limits on the cloud's distance would help determine conditions in the Halo in the cloud's vicinity. As these conditions determine the Magellanic Clouds' interaction with the Halo, and how gas infall from HVCs, etc., impact the Milky Way's ecology, further observations are encouraged of this object.

Table 6.1: Identification of ATCA continuum sources with SUMSS sources. Bracketed figures indicate errors. Fluxes are in mJy beam^{-1}.

ATCA source	RA (J2000)	Dec (J2000)	F_{1384}	SUMSS RA (J2000)	SUMSS Dec (J2000)	F_{843}
ATCA-1	13 28 43.9(.9)	–47 27 40(4)	54	13 28 40.78(.15)	–47 27 48.4(1.7)	123.6(3.8)
ATCA-2a	13 27 29.8(.8)	–47 41 15(5)	95	13 27 32.02(.15)	–47 40 58.0(1.7)	145.0(4.5)
ATCA-2b				13 27 21.37(.18)	–47 43 03.7(2.0)	33.0(1.4)
ATCA-3a	13 25 20.9(1.5)	–47 51 49(3)	360	13 25 21.57(.15)	–47 52 07.3(1.7)	470.9(14.2)
ATCA-3b				13 25 17.68(.15)	–47 50 55.3(1.7)	137.6(4.3)
ATCA-4	13 24 51.0(1.5)	–48 08 05(11)	88	13 24 51.49(.15)	–48 08 19.3(1.7)	178.3(5.4)

Table 6.2: Cross-identification of ATCA continuum sources with PMN counterparts. Bracketed figures indicate errors.

ATCA source	PMN RA (J2000)	PMN Dec (J2000)	Flux at 4.85 GHz (mJy)
ATCA-1	13 28 42.6 (2.5)	–47 28 13 (25)	58 (10)
ATCA-3	13 25 20.2 (1.4)	–47 51 44 (14)	111 (11)

Table 6.3: Identification of ATCA continuum sources with *Spitzer* sources from Boyer et al. (2008). Bracketed figures indicate errors.

ATCA source	Spitzer source (SSTOCEN)	Magnitude 3.6μm	4.5μm	5.8μm	8.0μm	24μm	Notes
ATCA-1	J132840.60–472749.19	13.63(4)		12.64(5)		9.18(7)	1
ATCA-2a	J132731.86–474058.21	16.54(7)	16.14(11)		15.47(20)		
ATCA-2b	J132721.22–474305.11	16.78(8)	16.65(16)				2
	J132721.57–474304.12	16.78(9)	16.82(21)				2
	J132721.97–474305.79	17.01(11)	17.33(31)		15.74(27)		1,2

[1]Galaxy Candidate; [2]sources resolved by *Spitzer*/IRAC

Table 6.4: Possible cross-identification of ATCA continuum sources with optical counterparts. Bracketed figures indicate errors.

ATCA	Catalogue	Magnitude			
source	Source	B^*	V	$R^\dagger$	$I^\ddagger$
ATCA-1	USNO-B1.0 0425-0422681	18.23		16.80	
	GSC 2.3.2 S99R051114	17.67		18.53	18.62
	2MASS 13284063-4727496	[a]			
	OGLE 132840.56-472750.1		19.49(3)		18.19(5)
ATCA-2a	OGLE 132731.69-474058.3 (i)		20.73(8)		19.59(11)
	OGLE 132731.87-471000.5 (ii)		21.07(11)		19.85(16)
	OGLE 132731.58-471001.3 (iii)		18.53(6)		17.61(3)
	OGLE 132731.65-471003.2 (iv)		18.40(2)		17.52(3)
	USNO-B1.0 0423-0431417 (iii)	17.17		16.80	
	USNO-B1.0 0423-0431420 (iv)	16.98	16.64		16.77
	GSC 2.3.2 S99R026299 (iii/iv)	18.14	17.36		16.85
ATCA-2b	USNO-B1.0 0422-0429719	18.00		17.92	
	GSC 2.3.2 S99R023235	18.86		18.85	18.34
	OGLE 132721.45-474304.3		18.77(3)		17.91(5)
ATCA-3b	USNO-B1.0 0421-0403784	19.05		18.33	18.33
	GSC 2.3.2 S99R014332	19.13		18.44	18.24
	DENIS J132517.8-475055	18.5		17.4	18.38(23)

*Or photographic $B_{\rm j}$ magnitude
†Or photographic F magnitude
‡Or photographic N magnitude
[a] $J = 16.52(13)$, $H = 15.52(13)$, $K = 15.04(15)$

7 Discussion

"New opinions are always suspected, and usually opposed, without any other reason but because they are not already common."

— John Locke (1632–1704), *"An essay concerning human understanding"*

To summarise the new works contained in the preceding chapters, we can turn again to the questions raised in our introduction (§1.6.1). As noted, it is beyond the scope of a single PhD thesis to properly address more than a few of these questions and we therefore do not discuss them all in depth here. We can nevertheless make many new and interesting conclusions.

7.1 How much mass are stars of a given metallicity losing per unit time and at what speed?

The ultimate goal of an empirical mass-loss relation for giant-branch stars would be a relation for mass loss based on only the stellar metallicity and initial mass. It would seem that this is perhaps a simplistic view: even within a cluster of stars with near-identical metallicity and initial mass (such as the bulk of ω Cen, §5.4.3) the zero-age horizontal branch stars show a significant spread in mantle mass (the so-called 'second parameter'), pointing to an unexplained variation in RGB mass-loss rates.

In the above works, my colleagues and I have attempted to measure both dust and gas mass-loss rates in a variety of different stars at a range of different metallicities.

7.2 What precise mechanisms drive mass loss in evolved, oxygen-rich, low-mass stars?

The driving mechanisms behind low-mass-star mass loss are still relatively poorly understood and are discussed in the next section. What is generally accepted is that chromospheric mass loss (*e.g.* Dupree, Hartmann & Avrett 1984) gives way at some point to pulsation- and/or radiation-driven, dusty winds (*e.g.* Chapter §5).

Among the key results of this thesis is the identification, at different metallicities, of several different key transitions which stars undergo: namely, we have identified the transition from a chromospherically-driven wind to a pulsation-driven wind; and the transition from predominantly gaseous, chromospheric mass loss to dusty, radiation-driven mass loss. These transitions are summarised in Table 7.1 and Figs. 7.1 & 7.2. In the interests of homogeneity, new temperatures and luminosities have been derived for stars listed in Chapter 3 except for NGC 6388, where there was insufficient photometry available for an accurate determination.

A general trend exists, moving the transition region to warmer temperatures at lower metallicity. Note that age (and hence initial mass) has a very significant effect on the location of a star in both temperature and luminosity at a particular point in its evolution. This may explain the discordant temperatures found in the Milky Way and NGC 6791.

Fig. 7.2 contains only the clusters with similar ages. We can now see that, not only is there a luminosity and temperature dependence of the transition, but also a clear sequence of events through which the stars evolve. We see that chromospheric mass-loss can continue after the onset of dust production, but that stellar pulsation (seen as the onset of variability) can soon overpower the chromosphere's influence. Crucially, this means that the presence of an active chromosphere does not prevent dust formation,

Table 7.1: The transition regions between chromospherically-dominated mass-loss and the onset of pulsation and radiatively-driven dusty winds at a range of metallicities. Colons denote estimated or approximate values. For the Hα transitions, the following stars were used: 47 Tuc V18, NGC 362 o06, NGC 6388 x03 and M15 x01.

Cluster	[Z/H]	Transition region		Method[1]	Source
		Temperature (K)	Luminosity ($L_\odot$)		
NGC 6791	+0.39	3880:[4]		Dust:	§D.2
MWG	0.00	3000:[5]		Mom	JS91
NGC 6388	–0.60	3200	1340	Hα	§3
47 Tuc	–0.76	3700	1280	Hα	§3
NGC 362	–1.16	3950	1800	Hα	§3
ω Cen	–1.62[2]	>3300	<2100	Hα	§3
	–1.62	3977	975	Dust	§5
M15	–2.30	<4550	>920	Hα	§3
	–2.30[3]	4275	2130	Var	M+ip
	–2.30	4770	550	Dust	BWvL+06

[1] Abbreviations: dust — first presence of dust (hence infrared flux excess), mom — estimated comparison of radiation & wind momemtum, Hα — loss of chromospheric emission in Hα lines, var — onset of variability due to pulsation and/or dust production; [2]based on V42, which has no metallicity determination; [3]values taken for K757 or K825, whichever is less evolved; [4]the magnitude of the 14th-brightest star — there are ~ 14 dusty stars in the cluster — temperature derived using $(J-K)$-derived temperature from Alonso, Arribas & Martínez-Roger (1999); [5]defined when $F_{\rm R} > F_{\rm W}$ in Judge & Stencel (1991).

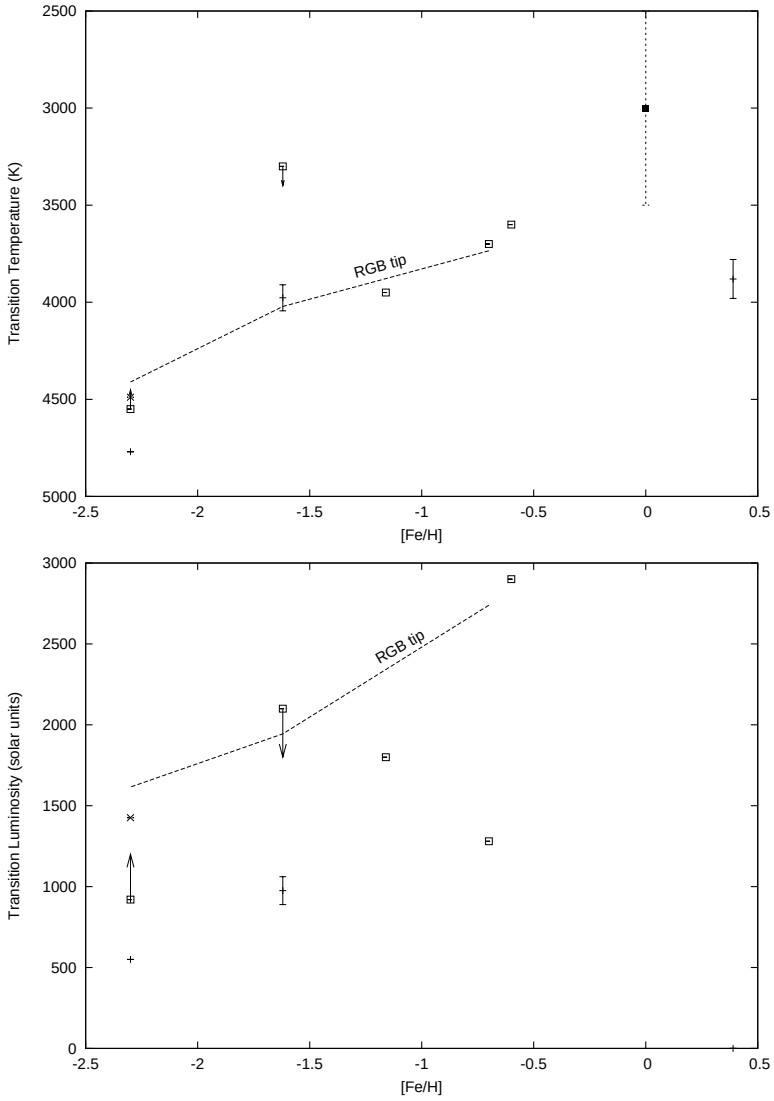

Figure 7.1: The transition region from chromospherically-driven mass-loss to pulsation- and dust-driven mass loss, using data from Table 7.1. Different symbols denote the method used to determine the transition: plus-signs — first presence of dust; hollow squares — disappearance of chromospheric emission at Hα; crosses — onset of variability; filled squares — momentum comparison.

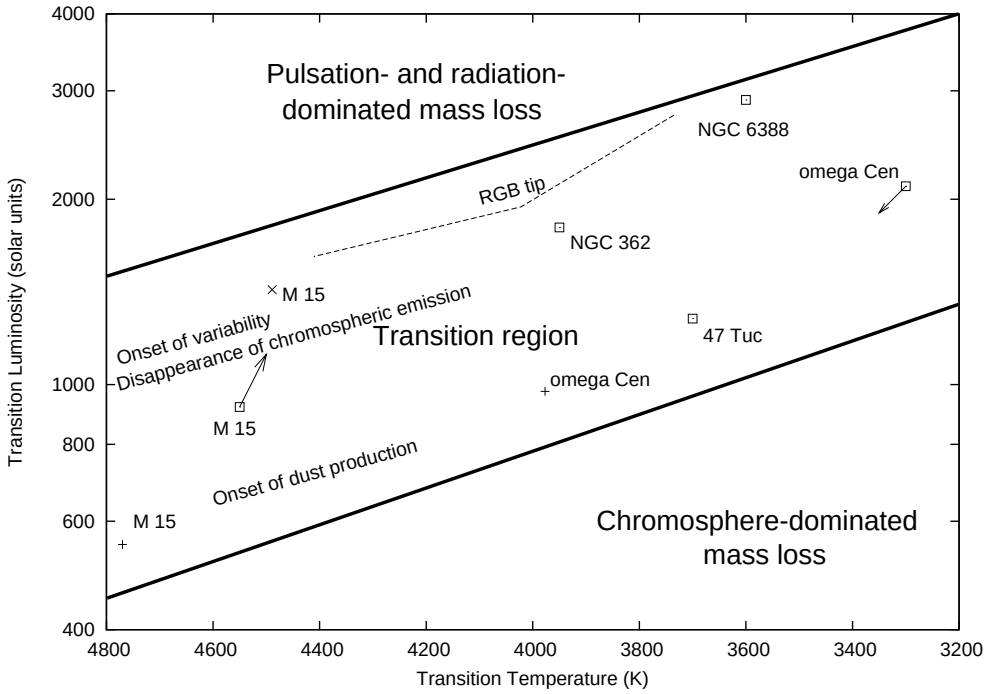

Figure 7.2: The transition from Fig. 7.1 and Table 7.1, displayed on a Hertzsprung-Russell diagram. Symbols are as in Fig. 7.1.

and that a star can lose mass through both line- and continuum-driving of the wind (as well as magnetic effects) at the same time. This dual mass loss may help explain substantial mass loss in stars with silicate-rich dust, if the chromosphere is able to drive a strong enough wind.

The position of the RGB tip in these diagrams is interesting. The transition between the two main types of wind occurs below the RGB tip. From this, we can conclude:

- RGB-tip stars pulsate at all observed metallicities;
- shocks driven by pulsation overpower chromospheric heating at all observed metallicities, however these probably are not very strong in RGB-tip stars at [Fe/H] $\lesssim -2$ (Fig. 7.2; Mészáros, Dupree & Szentgyörgyi 2008);
- dust production is prevalent in RGB stars at all metallicities.

7.3 How do metal-poor stars produce dust and is dust-gas coupling affected?

In the absence of a sufficiently strong chromosphere, conventional wisdom (§1.3.2.1) states that carbon-rich dust must be present to drive a radiation-driven wind, due to its much larger effective cross-section for absorption of radiation. However, as is seen throughout this thesis (in particular §2.3.1 & 5.5.1) there are clear examples of strong silicate-rich outflows.

The debate is as to where the energy to drive the silicates away from the star comes from. To add to this debate, we have shown that ω Cen V42 (§5.5.2.2), although it is ostensibly an oxygen-rich star (C/O $<$ 1), probably harbours carbon-rich dust. Conditions in the wind may therefore only be conducive to producing it at particular times during the pulsation cycle. If V42's wind is driven predominantly by radiation pressure on dust grains, it may be that it is pressure on this carbon-rich dust — not the silicate-rich dust — that is driving the wind, following the model of Höfner & Andersen (2007) (see §1.3.2.2).

Even if we can claim to have solved this problem, the issue of how the wind is driven at very low metallicities remains. M15, with 200-times less dust than Galactic variables, may have insufficient dust to effectively collisionally couple with the escaping gas and thus drive the gas away from the star also. This was encountered in particular in §5.6.3.3, which would suggest that some stars have winds with velocities of $<$ 1 km s^{-1} — less than the turbulent velocity in the wind. It is still difficult to imagine how gas-to-dust coupling can work in this environment, and the real solution may be beyond the reach of our current capabilities.

7.4 How much mass do low-mass stars lose over the course of their evolution and in what stages?

The total mass lost by a low-mass star over its evolution can be well-constrained from white dwarf masses. We have shown in §D.2 that in super-solar-metallicity mass-loss environments there is no preference for larger amounts of mass loss. Furthermore, other studies have shown that the mass of white dwarfs even in the metal-poor M15 does not depart significantly from the canonical 0.5 $M_\odot$ expected from a star that has completely lost its stellar mantle (de Marchi & Paresce 1994).

The key question then becomes in which evolutionary stages do the stars lose mass. This has already been well-constrained by examinations of the horizontal branch of clusters. One typically finds that a 0.80–0.85 $M_\odot$ star must lose $\sim$0.2 $M_\odot$ on the RGB and $\sim$0.10–0.15 $M_\odot$ on the AGB (§1.3.4.10). We corroborate this in the case of ω Centauri, showing that a typical 0.85 $M_\odot$ cluster star loses 0.20–0.25 $M_\odot$ on the RGB and the rest of its mantle mass on the AGB, possibly leaving the AGB before the canonical AGB tip.

Importantly, we find no conclusive evidence for differences between RGB and AGB mass loss for a given set of stellar parameters. Specifically, we find that dust production *must* be occurring on the RGB in the case of ω Cen (§5.5.3.2).

In terms of how evolved a star has to be to lose mass, in addition to finding that there is a relatively clear point at which dust production begins (§5.6.3, §7.2), we find that the mass loss is much more concentrated toward the tip of the RGB and AGB than previous studies have suggested (*e.g.* Origlia et al. 2002).

As the total mass lost appears largely independent of metallicity between $-2.3 \lesssim$ [Fe/H] $\lesssim +0.4$, we can further suggest that the dominating mass-loss mechanism over the star's evolution is likely also independent of metallicity. This is difficult to achieve for a purely radiatively-driven wind, as the sustainable wind speed at low metallicity is much smaller than both the turbulent motion in the wind and the velocity of

stellar pulsation. This would then suggest that highly-evolved stars gain a significant proportion of their wind momentum from stellar pulsations.

7.5 How does mass loss vary with pulsation cycle and length?

Determining how mass-loss varies within a pulsation cycle is very difficult, as we do not have a coherent, self-consistent mass-loss estimator that sufficiently covers the entire pulsation period of any given star. We have seen, in §5.5.2.2 that substantial variation in calculated mass-loss rate can occur over time, though whether this would continue to be the case if further, better data coverage is taken remains to be seen.

To determine any link between mass-loss rates and pulsation period, we have listed in Table 7.2 some mass-loss rates and pulsation periods from this work and from the literature. We can approach this in the knowledge that, on a given period-luminosity sequence (§1.3.4.8), mass loss should increase with increasing pulsation period, as the star evolves.

Examining Table 7.2, there is no obvious correlation between either pulsation period or luminosity, either globally or for a particular metallicity. This can likely be attributed in part to measurement discrepancies among the various methods used to determine mass-loss rates, coupled with the fact that many pulsation periods are either irregular or uncertain (this accounts for most of the stars lying between sequences C & C′). We therefore cannot make any concrete conclusions on the nature of relationships among the various parameters explored here.

Table 7.2: Values for pulsation periods and mass-loss rates. Colons denote uncertain values.

Star	[Z/H]	Period (days)	K^1 (mag)	P-L sequence	Mass-loss rate ($M_\odot$ yr^{-1})	Method[2]	Sources
47 Tuc V1	–0.76	221	–7.16	C	1.0×10^{-6}	Spec	§2.3.1
47 Tuc LW10	–0.76	121:	–6.97	C′/C	2.5×10^{-7}	Dust	§2, O+02
47 Tuc V26	–0.76	65:	–6.82	B+	3.4×10^{-7}	Dust	§2, O+02
47 Tuc V8	–0.76	155	–6.67	C	4.8×10^{-7}	Dust	§2, O+02
47 Tuc V18	–0.76	83:	–5.90	C	2.0×10^{-7}	Spec	§2.3.2
47 Tuc LW8	–0.76	27	–5.97	A–	1.1×10^{-6}	Hα	§3
47 Tuc LW19	–0.76	40	–6.56	A–	2.1×10^{-7}	Hα	§3
47 Tuc V18	–0.76	83:	–5.90	C	7.2×10^{-6}	Hα	§3
ω Cen V6	–1.16	110:	–6.90	C′/C	1.1×10^{-6}	Spec	§5
ω Cen V42	–1.62[3]	149	–5.97	C/D	2.5×10^{-6}	Spec	§5
ω Cen V6	–1.16	110:	–6.90	C′/C	7.3×10^{-6}	Dust	§5
ω Cen V42	–1.62[3]	149	–5.97	C/D	5.9×10^{-6}	Dust	§5
ω Cen V1	–1.77[4]	29	–4.75	C′/C	5.9×10^{-7}	Dust	§5
ω Cen V17	–1.62	65:	–6.38	C′	2.9×10^{-7}	Dust	§5
ω Cen V138	–1.62	75:	–6.06	C′/C	1.9×10^{-7}	Dust	§5
ω Cen V152	–1.62	124:	–6.48	C	1.5×10^{-7}	Dust	§5
ω Cen V148	–1.29	90:	–6.08	C	1.5×10^{-7}	Dust	§5

[1]Absolute K-band magnitudes calculated from 2MASS photometry with distance moduli from Harris (1996); [2]spec — determined from infra-red spectra, dust — from infra-red photometry of dust emission, Hα — from Hα line modelling; [3] metallicity uncertain, mass-loss rates based on [Fe/H] = –1.62 and an amorphous carbon wind; [4]post-AGB star.

7.6 How much of this lost mass is present in the cluster and where has the remainder gone?

We have shown that mass loss within clusters is sufficient to produce observable quantities of dust, in the absence of any clearing mechanisms (§5.6.2). We have further shown that both the lost dust and gas are not there (§4.3.4, §6), meaning that some clearing mechanism must be taking place. This mechanism must be very efficient, with clearing timescales of $\lesssim$ 300 000 years for gas and $\lesssim$ 100 000 years for dust in ω Centauri (§5.6.5.2), which has a comparatively-high escape velocity. This confirms literature results showing that intra-cluster material is either not present at detectable levels or, in the case of 47 Tuc and M15, only present in very small quantities (Freire et al. 2001; van Loon et al. 2006b; Boyer et al. 2006; Barmby et al. 2009).

In terms of the fate of the cleaned gas, it would seem likely that it is being removed from the cluster entirely. However, our efforts to locate it in the act of escape have proved at best inconclusive thus far (§4.3.4, §6). The origins of high-velocity clouds near globular clusters are still unresolved (§6; van Loon et al. 2009).

7.7 How have gas and dust that have been cleaned from the cluster escaped?

The leading contender for removal of both gas and dust remains bow shocking by hot Halo gas. This has now been observed in several clusters (Okada et al. 2007), though still has difficulty in explaining the very short timescales of clearing and large accelerations required to clean the likes of ω Cen over the required timescale (§5.6.5.2). However, the break-up of dust grains by the high temperatures induced in the shock may alleviate this problem to some extent.

7.8 Suggestions for future work

We can still ask a great deal of questions regarding stellar mass loss in globular clusters. In order to understand this important process, we will need to address these questions.

7.8.1 Stellar evolution

- What conditions are required to first initiate dust production?

- What processes govern the end of chromospherically-dominated mass-loss?

To address these questions, we must examine the temperatures, densities and velocities in both the wind (near the condensation radius), in the chromosphere, and in the stellar photosphere itself. In principle, these can all come from both modelling of the stellar infrared excess and from detailed analysis of individual spectral lines. As we have seen, however, this is a difficult process, fraught with uncertainty and a surfeit of parameters. Further efforts to examine this parameter space through high-resolution, high-signal-to-noise spectra and spectro-photometry may reveal enough of the underlying physics to piece together an understanding in the near future, though it may require more sophisticated models to determine the line outflow physics than are currently employed.

At present, high-resolution VLT/CRIRES K-band spectra have been taken in April 2009 (JvL) of giants in ω Cen; further observations are scheduled in 47 Tucanae. This should allow the $^{13}C/^{12}C$ ratio to be determined, providing evidence for the amount of dredge-up that has taken place. Dredge-up is related to evolutionary phase, so we can link this to the stage of evolution these stars are in, and the carbon enhancement which they have undergone. Evidence of outflow (*c.f.* §3) has already been seen in the raw spectra, which may allow us to determine the outflow velocity of the wind.

7.8.2 Wind driving

- Does an oxygen-rich wind require the presence of carbon-rich dust?
- Does dust type change over the pulsation cycle?
- Does mass-loss rate change over the pulsation cycle?

The answers to all these questions can come from continuous infra-red observations of a small sample of carefully-selected stars at different metallicities and/or evolutionary phases. V42 in ω Cen would be a very good candidate for this kind of work. The observations would have to have sufficient wavelength coverage to distinguish both dust type and dust temperature in any one epoch. As we have seen (§5.5.2.2), this is not easy with limited data, and would probably require multi-epoch spectroscopy over a wide wavelength baseline. Unfortunately, this requires a significant amount of telescope time at a world-leading infra-red observatory, which tends to be in short supply.

Mid-infrared spectra have been taken in April 2009 with *Spitzer* IRS of 15 of the dusty giants mentioned in Chapter 5, including V6, V42, V152, the post-AGB stars V1 and Fehrenbach's star, and the carbon star LEID 52030. With these, we should be able to determine the dust species in the wind, and better estimate the mass-loss rate. These observations include V6 and V42, which means we now have mid-infrared spectra at different pulsation phases for these two stars.

An upcoming analysis in conjunction with MLB and JvL of NGC 362, using the same methodology used in Chapter 5, will allow us to better estimate which stars are dust-producing, and the conditions required for dust production to begin.

7.8.3 Removal of the ICM

- Is ω Cen representative of the timescales required to remove dust?
- Is ionisation or ice-coating of dust grains important?
- Why has ICM only been detected in M 15 and 47 Tuc?

- Is bow shocking the leading cause of ICM removal?
- Does dust escape the cluster intact?

Addressing this may be beyond the reasonable capability of current technology, as we are looking for emission from either gas or dust at lower levels than has so far been observed. Deeper imaging would be required in Hα, H I, mid-infrared broadband wavelengths and perhaps other wavelengths where dust emission to reveal any lost mass present in the cluster. The problem then becomes determining what belongs to the cluster and what belongs to the veil of Galactic ISM through which we see it (*e.g.* van Loon et al. 2009). Velocity maps such as those in §6 may help in this and a proposal is planned to obtain higher-resolution maps of this high-velocity cloud with ATCA.

Continuing work to find pulsars in globular clusters may lead to further studies such as those by Freire et al. (2001), though the current statistics for pulsars in globular clusters suggest that there may be insufficient pulsars for us to use. The one notable exception is Terzan 5, though here the problem again becomes one of determining what is ICM and what are variations in the (considerable) intervening Galactic ISM. Further, deeper X-ray studies may also shed light on ram-pressure stripping of ICM, as observed by Okada et al. (2007), however the time required to do any deeper observations is becoming prohibitively large.

The solution may have to wait for future technology, primarily through increases in collecting area from telescopes such as the *James Webb* Space Telescope for near-infrared observations, the *Herschel* Space Telescope for far-infrared observations and the Square Kilometre Array for radio studies. In particular, the SKA should have the ability to probe ICM masses down to $M_{\rm H} \sim 10^{-2}$ M$_\odot$ or lower, while spaceborne observatories may be able to manage a comparable $M_{\rm dust} \sim 10^{-4}$ to 10^{-5} M$_\odot$.

8 Conclusions

"To command the professors of astronomy to confute their own observations is to enjoin an impossibility, for it is to command them to not see what they do see, and not to understand what they do understand, and to find what they do not discover."

— Galileo Galilei (1546–1642)

In this thesis, I expand the boundaries of our knowledge of stellar mass loss in globular clusters. I report on several different types of observations, showing and quantifying mass loss in dozens of stars.

Bringing together the works herein, we can build up a picture of how low-mass stars lose mass as they evolve. It appears that mass loss first progresses through a solar-type wind, dominated by outflows from a stellar chromosphere, which drives low-to-moderate velocity winds. Upon reaching a critical, metallicity-dependant point, the star then begins to produce dust. This is likely silicate-rich dust at first, condensing around Al_2O_3 grains. Following this, the effect of the chromosphere diminishes, and its characteristic signature in spectral lines is lost. The star simultaneously begins to pulsate. From this point, the momentum provided by pulsation may assist the levitation of material from the stellar surface, increasing mass loss. The increased luminosity of the star can now effectively drive a radiatively-driven wind. It remains unknown how a silicate-rich wind may be driven in such a way, due to the dust's low cross-section for absorption of radiation; however, we now have some evidence that out-of-equilibrium effects may allow the formation of carbon-rich dust at some points during the pulsation cycle. Mass loss increases with luminosity until, for all metallicities, the stellar mantle is effectively completely removed, creating a post-AGB star.

Among the measurements herein, mass-loss rates are found for stars just starting to produce copious dust (10^{-7} $M_\odot$ yr^{-1}). These rise to above 10^{-6} $M_\odot$ yr^{-1} in the most evolved stars, increasing roughly as a power-law with luminosity. Stellar chromospheres

may drive similarly-large mass-loss rates, though there is a greater deal of uncertainty on those measurements. In very-metal-poor stars which have dust-dominated mass loss, wind velocities should be very slow. I present no evidence that this is not the case, though at speeds of $\ll 1$ km s^{-1}, this provides problems for removing a turbulent wind from the stellar system.

Based on multi-wavelength observations, we have for the first time an accurate measure of mass loss from an individual globular cluster: ω Centauri, which is losing mass in the form of gas and dust at a rate of 1.2×10^{-5} M$_{\odot}$ yr^{-1}. Although my colleagues (where noted) and I have made a comprehensive search for the gas and dust in this cluster, we have found none: it appears as though the high velocity cloud near the cluster is probably unrelated. This leaves us with what appears to be the shortest estimate for the clearing of a globular cluster to date: $\lesssim 300\,000$ years for the removal of gas and $\lesssim 100\,000$ years for the removal or destruction of dust. The removal mechanism is not obvious — bow shocking remains the best theory to date, though the timescales involved make even this difficult to employ.

Both dusty and chromospherically-driven mass loss are ubiquitous in Galactic globular clusters over all metallicities. We await new observations and new observatories, such as *Herschel*, ALMA, and the *JWST* to further our understanding.

> *"I do not know what I seem to the world, but to myself I appear to have been like a boy playing upon the seashore and diverting myself by now and then finding a smoother pebble or prettier shell than ordinary, while the great ocean of truth lay before me all undiscovered."*
>
> — Sir Isaac Newton (1727).

A Abbreviations and Glossary

"Equipped with his five senses, man explores the universe around him and calls the adventure Science."

— Edwin Powell Hubble (1889–1953).

The conventional abbreviations for SI units and astronomical quantities and constellations are used.

The following abbreviations are used for the names of collaborators in denoting the parts of this research to which they contributed:

IM — Iain McDonald (the author)
JvL — Jacco Th. van Loon
MLB — Martha L. Boyer
AKD — Andrea K. Dupree

The following abbreviations and terms have been used in this thesis:

α elements — elements with an even number of protons and Z > 22, synethesised by α-particle capture in Type II SNe, i.e. Ne, Mg, Si, S, Ar, Ca, Ti, ... Silicon and calcium are pure α elements.

AAS — American Astronomical Society.

ACS — Advanced Camera of Surveys, aboard the *Hubble Space Telescope*.

ADC — analogue-to-digital converter.

ADU — analogue-to-digital units (equal to number of photons received / gain of the CCD).

AGB — asymptotic giant branch.

AGB manqué — a star that 'falls off' the horizontal or giant branch before the AGB-tip due to excessive mass loss. Observationally the star traverses the Hertzsprung-Russell diagram to the white dwarf cooling track.

ALMA — Atacama Large Millimetre Array.

ATCA — Australia Telescope Compact Array.

BHB — Blue Horizontal Branch stars, thought to be evolutionarily different from normal HB stars due to their increased RGB mass loss.

blueshift — as is now conventional, this describes an *decrease* in wavelength due to either a Doppler shift or Hubble expansion, which does not necessarily bring the wavelength of light closer to the colour blue.

BY Dra stars — a type of variable star, exhibiting variability of $\lesssim 0.5$ magnitudes, on a period of days to weeks (once per rotation) due to starspots. Also chromospherically active.

carbon star — a red giant (or dwarf) star in which the atmosphere contains more carbon than oxygen. They are variable, surrounded by carbon-rich dust. This is very opaque at visible wavelengths, making the star very red.

CCD — charge-coupled device.

chopping — the process in (typically) infrared photometry or spectroscopy of moving the telescope's secondary mirror in a square-wave fashion to move the detector 'on' and 'off' the source. This is typically done several times a second. The difference between two identical integrations (on- and off-source) should remove the sky background, leaving only the flux from the target.

CMD — colour-magnitude diagram.

CO — carbon monoxide.

COBE — Cosmic Background Explorer.

C-rich star — see *carbon star*.

CRIRES — CRyogenic high-resolution InfraRed Echelle Spectrograph (mounted on the VLT).

CV — cataclysmic variable — WD/MS binary where the WD is accreting.

δ Scu stars — AO-F5 sub-giants on the instability strip, characterised by very short period pulsations of 0.01 – 0.2 days, with typical magnitude ranges of $0.003 \sim 0.1$ magnitudes (Němec & Mateo 1990). See also SX Phe stars.

DENIS — DEep Near-Infrared Survey.

De Vaucouleurs's Law — Surface brightness profile from de Vaucouleurs (1953): $I(r) = I_0 \exp(-kR^{0.25})$.

DM — dark matter.

dSph galaxies — Dwarf Spheroidal Galaxies, typically referring to the Galactic satellites in this work, including the SagDEG, Sculptor and Ursa Minor Dwarf Spheroidals.

EA — eclipsing Algol — an eclipsing variable star, exhibiting one deep eclipse and one shallow eclipse, composed of pair of unequally-hot stars.

E-AGB — Early Asymptotic Giant Branch.

EHB — Extreme Horizontal Branch.

ESO — European Southern Observatory.

[Fe/H] — a measure of the fractional iron content of the star, related to metallicity, and given by $\log\left(\frac{Fe_*}{Fe_\odot}/\frac{H_*}{H_\odot}\right)$, where $*$ and $\odot$ denote stellar and solar quantities, respectively. Note that some literature sources also use [Fe/H] as a substitution for [Z/H]. Similarly [O/Fe] is oxygen-to-iron ratio, etc.

flash manqué — a star with insufficient mantle mass to undergo a helium flash at the end of the RGB (due to excessive RGB mass loss, unless $t \gg t_{\rm Hubble}$). The star leaves the RGB prematurely and becomes an under-massive, helium-rich white dwarf.

FK Com — single (sub-)giant stars showing strong rotation ($v_{rot} = 50 - 200$ km s^{-1}), thought to be recently coalesed stars.

FUV — Far UltraViolet.

Hα — Hydrogen-alpha (Balmer alpha) transition at 6562.817 Å.

HB — Horizontal Branch.

HBB — Hot Bottom Burning - fusion at the base of the convective envelope.

HD — Prefix used for stars in the Henry Draper Catalogue (Cannon & Pickering 1924).

HI — Hydrogen I: the radio emission feature at 21 cm caused by the relaxation of spin vector of electrons in hydrogen atoms.

HST — Hubble Space Telescope.

Hubble time — The theoretical age of the Universe, as derived from the current rate of expansion.

IC — Index Catalogue: Dreyer (1895) and Dreyer (1908).

ICM — Intra-Cluster Medium.

IGM — Intergalactic Medium.

IMF — Initial Mass Function.

IOTA — Infrared-Optical Telescope Array.

IRAC — Infra-Red Array Camera (Spitzer).

IRAS — Infra-Red Astronomical Satellite.

IRS — Infra-Red Spectrometer (Spitzer).

IRTS — Infra-Red Telescope in Space.

ISM — Interstellar Medium.

ISO — Infra-red Space Observatory.

IUE — International Ultraviolet Explorer.

IVC — Intermediate-Velocity Cloud (see also LVC). A (gas) cloud with velocity between that of the Galaxy and halo (50∼100 km s^{-1}).

Jeans' Law — Density profile from Jeans (1916): $\rho \propto r^{-4}$.

JCMT — James Clark Maxwell Telescope.

JWST — James Webb Space Telescope.

KAO — Kuiper Airborne Observatory.

King profile — Density profile from King (1962): $\rho(r) = \rho_0 \frac{1}{(1+(r/r_c)^2)^{1.5}}$, a revision of Jeans' Law (Jeans 1916).

LEID — LEiden IDentifier, used for stars in ω Centauri, from Martin (1938a).

LMC — Large Magellanic Cloud.

LSP — Long Secondary Period — photometric variability observed in AGB stars on timescales of years.

LSR — Local Standard of Rest.

LPV — Long-Period Variables. Often used for suspected (or known) Mira-like stars.

LTE — Local Thermodynamic Equilibrium.

LVC — Low-Velocity Cloud (see also IVC). A cloud with velocities comparable to that of the Galaxy.

Magellanic Stream — a set of high-velocity clouds, tracing a Great Circle in the sky, connected with the tidal merger of the Magellanic Clouds with our Galaxy.

MIDAS — Munich Image Data Analysis System.

MIPS — Multiband Imaging Photometer for Spitzer.

Mira stars — TP-AGB stars, exhibiting photometric pulsations on timescales of months to years.

MWG — Milky Way Galaxy.

$M_\odot$ — solar mass (approx. 2×10^{30} kg).

M31 — also known as the Andromeda Galaxy, a Local Group spiral galaxy, 2–3-times more massive than the Milky Way.

MOND — MOdified Newtonian Dynamics, a modification to Newton's inverse-square law of gravity, which becomes appreciable over large baselines.

MS — Main Sequence.

MSTO — Main Sequence Turn-Off.

MSX — Midcourse Space Experiment.

NICMOS — Near Infra-red Camera and Multi-Object Spectrometer (HST).

NGC — (Revised) New General Catalogue: Dreyer (1888) and revisions.

nodding — the process in infra-red photometry or spectroscopy of moving the optical axis of the telescope to correct for the slight difference between the sky brightnesses of the 'on' and 'off' chopping cycles.

NRAO — (United States) National Radio Astronomy Observatory.

NUV — Near-Ultra-Violet.

O-rich star — a red giant (or dwarf) star in which the atmosphere contains more oxygen than carbon (*c.f. carbon star*).

Oosterhoff group — an empirical grouping of Galactic globular clusters into two groups, based on the mean periods and relative proportions of their RR*ab* and RR*c* stars, after Oosterhoff (1939).

PAH — polycyclic aromatic hydrocarbon — a complex molecule based on polymerisation of benzene.

PN, PNe — Planetary Nebula(e).

Population I/II stars — young/old stars, found in the galactic bulge and halo, and galactic disc, respectively.

Population III stars — hypothetical 'first stars', entirely devoid of metals.

PSF — point-spread function — the shape a point source (*e.g.* a star) appears on an image.

r-process — a nucleosynthesis reaction process that takes place in core-collapse supernovae where there are large neutron densities. See also *s*-process.

redshift — as is now conventional, this describes an *increase* in wavelength due to either a Doppler shift or Hubble expansion, which does not necessarily bring the wavelength of light closer to the colour red.

RGB — Red Giant Branch.

RGO — Royal Greenwich Observatory.

RLOF — Roche Lobe overflow.

RS CVn stars — a class of detached binary stars, including a chromospherically-active G or K star, with orbits of a few $\sim$ 20 days. Prone to flaring, magnetically active, variability due to photospheric spots.

RRab stars — RR Lyraes, pulsating in the fundamental mode.

RRc stars — RR Lyraes, pulsating in the first overtone.

RRd stars — RR Lyraes with double-mode puslation.

RR Lyr(ae) stars — Population II stars with short (0.2−2 day) periods, moderate (0.3−2 magnitude) amplitudes and early (A2−F6) spectral types. A period-luminosity relationship can be used to derive their distances.

RV Tau stars — a type of variable star, exhibiting variability on a period of about a month or two due to pulsation. Analytically, they form a bridge between classical Cepheids and Mira variables.

s-process — a nucleosynthesis reaction process that takes place in comparatively neutron-poor environments, such as AGB star cores. See also *r*-process.

SagDEG — Sagitarrius Dwarf Elliptical (or Spheroidal) Galaxy, also Sgr dSph.

SED — spectral energy distribution.

SMC — Small Magellanic Cloud.

S/N — signal/noise ratio, also *SNR*.

SN — supernova, also supernovae: *SNe*.

SPIREX — South Pole Infra-Red EXplorer.

SRa–d, SRV — semi-regular variables: SRa — late spectra type (M,C,S)[e], δV $<$ 2.5 mag, P = 35$\sim$1200 days, e.g. Z Aqr; SRb — late spectral type (M,C,S)[e], but with less regular changes (P = 20$\sim$2000 days), e.g. RR CrB, AF Cyg; SRc — late spectral type (M,C,S)[e] I, δV $\sim$ 1 mag, P $\gtrsim$ 30 days, e.g. μ Cep; SRd — earlier spectral type (F,G,K)[e] I–III, δV = 0.1$\sim$4 mag, P = 30$\sim$ 1100, e.g. SX Her, SV UMa.

stacking — when referring to photometric images, the summation of a series of exposures where each exposure is re-aligned of a to a reference image through translation and rotation.

SX Phe — Short period (1–2 hours) variables, similar to δ Scutii variables, but with higher amplitudes and metal-paucity. They possess A2–F5 spectral types, varying by $\sim$0.7 magnitudes. Mainly found in globulars, previously known as USPCs (Ultra-Short Period Cepheids). See Němec & Mateo (1990).

TIMMI2 — Thermal Infrared MultiMode Instrument (2) (ESO 3.6m).

TP-AGB — Thermally-Pulsating Asymptotic Giant Branch.

UIT — Ultraviolet Imaging Telescope.

UT — Universal Time.

VLA — Very Large Array (New Mexico, US).

VLT — Very Large Telescope (Paranal, Chile).

W Vir stars — aka. Type II Cepheids.

WD — White Dwarf.

Wolf-Rayet stars — very massive stars ($\gtrsim$ 20 $M_\odot$) that exhibit high mass-loss rates in stellar winds.

[Z/H] — a measure of the fractional metal content of the star, where a metal is any element heavier than helium. This is also termed the *metallicity*. Given by $\log\left(\frac{Z_*}{Z_\odot}/\frac{H_*}{H_\odot}\right)$, where $*$ and $\odot$ denote stellar and solar quantities, respectively.

B General Data

B.1 Astronomical Bands

The following table contains the photometric passband systems in use throughout this work. In the case of the infrared system, each observatory tends to have slightly different filters. Where this information is available, it is listed.

Table B.1: Observational bands and their wavelengths in the Johnson-Morgan, Cousins, Strömgren and infra-red system. Typical observatory filters tend to be slightly different according to the individual observatory.

Band	Wavelength (μm)	FWHM (μm)	Zero point (Jy)
Johnson-Morgan system			
U	0.365	0.068	1884
B	0.460	0.098	4646
V	0.550	0.089	3953
R	0.700	0.220	2875
I	0.880	0.240	2241
Cousins system			
R_c	0.594	0.140	
I_c	0.790	0.330	
Strömgren system			
u	0.350	0.034	
b	0.410	0.020	
v	0.467	0.016	
y	0.547	0.024	
Sloan system			
u'	0.3543	0.0567	
g'	0.4770	0.1387	
r'	0.6231	0.1373	
i'	0.7625	0.1526	
z'	0.9134	0.0950	
JHKLL'MN system			
J	1.25	0.38	1602
H	1.65	0.48	1010
K	2.20	0.70	630
L	3.50	1.20	278
L'	3.80	0.60	
M	4.80	5.70	153
N	10.6		36.3

Table B.2: Filter bandpasses and zero points for the Spitzer Space Telescope bands. Note that a multiplicative factor of 1.015 has been suggested for IRAC 4 (8 μm) following the publication of Rieke et al. (2008).

Channel	Wavelength (μm)	Zero point (Jy)
IRAC 1	3.6	280.9 ± 4.1
IRAC 2	4.5	179.7 ± 2.6
IRAC 3	5.8	115.0 ± 1.7
IRAC 4	8.0	64.13 ± 0.94
MIPS 24	23.68	7.14 ± 0.08
MIPS 70	71.42	0.775 ± 0.009
MIPS 160	155.9	0.159 ± 0.002

B.2 References used in Tables

Table B.3: Abbreviated references to tables C.3, C.1, C.2, C

Abbreviation	Reference
(A81)	Alcaíno (1981)
(AL86)	Alcaíno & Liller (1986)
(AL87)	Alcaíno & Liller (1987)
(AM88)	Allen & Martos (1988)
(AZ88)	Armandroff & Zinn (1988)
(B+84)	Bell et al. (1984)
(BGD+91)	Brosche et al. (1991)
(BMH05)	Baumgardt, Makino & Hut (2005)
(BP83)	Bica & Pastoriza (1983)
(BPB+08)	Bellini et al. (2009)
(BVS73)	Böhm-Vitense & Szkody (1973)
(BWvL+06)	Boyer et al. (2006)
(CBG+07)	Carretta et al. (2007)
(CG97)	Carretta & Gratton (1997)
(CGC+00)	Carretta et al. (2000)
(C75)	Cudworth (1976)
(CK02)	Chaboyer & Krauss (2002)
(CSD92)	Chaboyer, Sarajedini & Demarque (1992)[1]
(CSF06)	Cacciari, Sollima & Ferraro (2006)
(CdIM02)	Castellani, degl'Innocenti & Marconi (2002)
(D93)	Djorgovski (1993)
(DGvA99)	Dinescu, Girard & van Altena (1999)
(DH93a)	Durrell & Harris (1993b)
(DH93b)	Durrell & Harris (1993a)
(DCL+97)	Dull et al. (1997)

(DM93) Djorgovski & Meylan (1993)
(dPPS+06) del Principe et al. (2006)
(DSC+98) Drukier et al. (1998)
(FWMC93) Fischer et al. (1993)
(FRV85) Fahlman, Richer & VandenBerg (1985)
(G67) Geyer (1967)
(GBC+03) Gratton et al. (2003)
(GF95) Gebhardt & Fischer (1995)
(GHGK02) Geffert et al. (2002)
(H84) Hamuy (1984)
(H96) Harris (1996)
(H+04) Hughes et al. (2004)
(HBCH85) Hesser et al. (1985)
(HHV+87) Hesser et al. (1987)
(HKRW04) Hilker et al. (2004)
(HR00a) Hilker & Richtler (2000a)
(HR00b) Hilker & Richtler (2000b)
(HW00) Hughes & Wallerstein (2000)
(I75) Illingworth (1975)
(I+00) Ivanov et al. (2000)
(IR70) Iben & Rood (1970)
(JS91) Judge & Stencel (1991)
(K65) Köhler (1965)
(K77) Kolkhidashvili (1977)
(K02) Kovács (2002)
(KHRW06) Kayser et al. (2006)
(KL84) Kielkopf & Lattis (1984)
(KTK+02) Kałużny, J. and Thompson, I. and Krzemiński, W. and Olech, A. and Pych, W.
(KTR+07) Kałużny, J. and Thompson, I. B. and Rucinski, S. M. and Pych, W. and Stachov
(L77) Lee (1977)
(LJS+99) Lee et al. (1999)
(LRR+02) Lee et al. (2002)
(LS97) Lehmann & Scholz (1997)
(M87) Meylan (1987)
(M88) Mukherjee (1988)
(MHB04) McNamara, Harrison & Baumgardt (2004)
(MM85) Meylan & Mayor (1985)
(MM86) Meylan & Mayor (1986)
(MMM97) Merritt, Meylan & Mayor (1997)
(M+95) Meylan et al. (1995)
(M+ip) McDonald et al. (in prep.)
(MPA+08) Moretti et al. (2009)
(MSS91) Mandushev, Staneva & Spasova (1991)
(NB75) Norris & Bessell (1975)
(NDCN76) Newell, da Costa & Norris (1976)
(NZ77) Norris & Zinn (1977)

(O+02)	Origlia et al. (2002)
(ONO76)	Ogorodnikov, Nezhinskii & Osipkov (1976)
(P87)	Peterson (1987)
(P93)	Peterson (1993)
(PA75)	Poveda & Allen (1975)
(PG92)	Paturel & Garnier (1992)
(PM93)	Pryor & Meylan (1993)
(PSC89)	Peterson, Seitzer & Cudworth (1989)
(P03)	Pancino (2003)
(P+02)	Pritzl et al. (2002)
(P+04)	Pasquali et al. (2004)
(PWH+03)	Platais et al. (2003)
(RFB+91)	Richer et al. (1991)
(RHS88)	Reed, Hesser & Shawl (1988)
(RJS+02)	Rey et al. (2002)
(S69)	Sandage (1969)
(S70)	Sandage (1970)
(S82)	Scaria (1982)
(S83a)	Sandage (1983)
(S83b)	Seitzer (1983)
(S88)	Sinnott (1988)
(S+04)	Stanford et al. (2004)
(S+06)	Stanford et al. (2006a)
(SDM+07)	Siegel et al. (2007)
(SJK+00)	Sneden et al. (2000)
(SK96)	Suntzeff & Kraft (1996)
(SK97)	Sosin & King (1997)
(SKS+07)	Székely et al. (2007b)
(SPB+99)	Soderberg et al. (1999)
(SR75)	Scott & Rose (1975)
(T92)	Tucholke (1992)
(TKP+01)	Thompson & Kałużny, J. and Pych, W. and Burley, G. and Krzemiński, W. and
(vdV+06)	van de Ven et al. (2006)
(vL+00)	van Leeuwen et al. (2000)
(VPK+07)	Villanova et al. (2007)
(W85)	Webbink (1985)
(WSB07)	Weldrake, Sackett & Bridges (2007)
(Z85)	Zinn (1985)
(ZW84)	Zinn & West (1984)

[1] Standard model

C Background to the main clusters in this work

This appendix describes the individual clusters studied in this thesis. Though chosen for various reasons, these clusters are all relatively massive (hence have a large number of mass-losing stars) and span metallicities from [Fe/H] $\approx$ –0.7 to –2.3. All the clusters are very well studied in the literature, each with its own peculiarities: 47 Tuc is relatively metal-rich and contains several AGB stars with strong mass loss, M 15 is very metal-poor, ω Cen is very populous and has an unusual spread in metallicity, which allows us to make comparisons over a relatively-large range of parameter space.

C.1 NGC 6388

NGC 6388 was discovered by James Dunlop in 1826 using a nine-inch refractor, who describes it as a 'beautiful round nebula' (Dunlop 1828). The New General Catalogue from which it takes its most common name lists it as a very bright, large, round globular cluster that is well resolved (Dreyer 1888). Historically, it has formed part of Shapley's analysis of the scale of the Universe and subsequent efforts to assess the distance to the Galactic Centre (*e.g.* Fernie 1962; Harris 1980).

NGC 6388 forms part of the metal-rich thick disk of globular clusters (Zinn 1985), though literature values for its metallicity vary significantly (Silbermann et al. 1994; Table C.1). Observationally, it lies near the Milky Way, quite close to the Galactic Centre, and thus the flux we receive is subject to considerable extinction on its way through the Galactic Disc. Compared to the other clusters studied in this work, NGC 6388 is also relatively small (Alcaíno 1981; Harris 1996) but has a high escape velocity

Table C.1: Selected data on NGC 6388. Colons denote uncertain values, bracketed figures are uncertainties. References can be found in Appendix B.2.

Property		Value	References
Names		NGC 6388, GCL 70, ESO 279-SC2	S88
Position (J2000.0)		17 36 17.0 –44 44 06	S88
Distance from Sun		10000, 11600±2300 pc	H96, I75, A81
		12600, 9650±650 pc	A81, P+02
Distance from Gal. Cen.		3200, 4700 pc	H96, A81
Galactic co-ords.	(l, b)	345.56°, –6.74°	H96
	(XYZ)	(9600, –2500, –1200) pc	H96
Distance modulus	(V)	16.14, 15.33 mag	H96, MPA+08
HB Mag.	(V)	16.85 mag	H96
Integrated V-band mag.		6.72 mag	H96
E(B–V)		0.37, 0.38, 0.40(3) mag	H96, A81, P+02
		0.38 mag	MPA+08
Abs. Mag	(V)	–9.42 mag	H96
Integrated colour	(U–B)	0.66 mag	H96
	(B–V)	1.17 mag	H96
	(V–R)	0.71 mag	H96
	(V–I)	1.47 mag	H96
Spectral type		G2, G3	H96, A81
Core surface brightness (V)		14.55 mag arcsec^{-2}	H96
Core Flux density		5.34 $L_\odot$ pc^{-3}	H96
Metallicity (log [Fe/H])		–0.60, –0.74(.15)	H96, ZW84
		–0.45(.15), –0.42(.15)	AZ88, BP83
		–0.44(.03)	CBG+07
Radial velocity ($v_{\rm LSR}$)		81.2(1.2), 82.0 km s^{-1}	H96, ZW84
Ellipticity		$(1 - b/a) = 0.01$	H96
Relaxation time	Core	55 Myr	H96
	Half-mass	1.2 Gyr	H96
Radius	Core	$0.12' = 0.34$ pc	H96
	Half-mass	$0.67' = 1.95$ pc	H96
	Tidal	$6.21' = 18.1$ pc	H96
Condensation	$(\log(\frac{r_{\rm tidal}}{r_{\rm core}}))$	1.70	H96
Mass		1.3 $\times 10^6$ $M_\odot$	SR75
		1.12 (.26) $\times 10^6$ $M_\odot$	I75
Escape velocity		78.2 km s^{-1}	W85
Absolute age		11.5 (1.5) Gyr	MPA+08

(Webbink 1985). Its surface brightness profile is well-fit by a King profile (Lugger et al. 1987) and has been found to be particularly round (White & Shawl 1987).

As with most metal-rich clusters, NGC 6388 hosts several Mira and other long period variables (LPVs), mainly discovered by Lloyd Evans & Menzies (1973, 1977). V1, V2 and V4 are Miras; V11–13 and V25 appear to be LPVs too (Hazen & Hesser 1986; Clement et al. 2001). A period-luminosity relation has been established (Matsunaga 2007); while Wallerstein, Kovtyukh & Andrievsky (2007) and Carretta et al. (2007) have measured chemical compositions of giants (though not the stars in §3).

NGC 6388 was suggested to contain significant amounts of intra-cluster medium (ICM) (Scott & Rose 1975; Forte & Mendéz 1988). However, no solid detections have been made (Faulkner & Freeman 1977). A maximum content of 3.8 $M_\odot$ of hydrogen and (from 60$-\mu$m imaging) 0.015 $M_\odot$ of dust have been reported (Lynch, Bowers & Whiteoak 1989; Lynch & Rossano 1990, respectively). If our later results (Chapter 5) are representative, this implies that ICM is cleared within $\sim$700 kyr. A debatable residual colour gradient has been found (*e.g.* Forte & Mendéz 1984; Pastoriza et al. 1986), though differential reddening has also been detected at both optical (Pritzl et al. 2002) and infrared (Law et al. 2003) wavelengths. It has further been suggested that this could be the cause of the apparent metallicity spread in the cluster, which is inferred from an over-wide RGB (Hughes et al. 2006).

The morphology of the cluster's blue horizontal-branch extension, which has a bimodality, blue hook and tilt (Busso, Piotto & Cassisi 2004), has been theorised to be due to helium-enrichment by primordial, intermediate-mass HBB-AGB stars or other non-canonical phenomena (d'Antona 2004; Moehler & Sweigart 2006; Busso et al. 2007). The cluster's α-enhancement and peculiar abundances suggest this self-pollution primarily comes from stars in the 4–8 $M_\odot$ mass range (Carretta et al. 2007), though this evidence is not conclusive (Choi & Yi 2008).

Other features include its unexpectedly-long-period RR Lyrae stars (Pritzl et al. 2000), and its record as the most metal-rich cluster containing Population II Cepheids

(Corwin et al. 2006b). It has been suggested that it may be older than other metal-rich globulars (Rich et al. 1997), though colour-magnitude diagrams show it and 47 Tuc to be fairly similar in age (Catelan et al. 2006). This may be important in understanding the second parameter effect, as the metallicity pair NGC 6388 and 6441 have been used as theoretical test grounds (*e.g.* Pritzl et al. 1999; Moehler, Sweigart & Catelan 1999). These two clusters have also raised calls for a new Oosterhoff group, being significantly more metal-rich and with longer RR-Lyrae periods than the two classical Oosterhoff groups (Pritzl et al. 2000). NGC 6388 is also a candidate for containing an intermediate-mass black hole (Lanzoni et al. 2007), which may have been observed with *XMM*-Newton and *Chandra* (Nucita et al. 2008).

The only significant study of mass loss in NGC 6388 is that of Origlia et al. (2002). This study, using the *ISO* satellite, found infra-red excess at 12 μm around six stars. We investigate these stars, and discuss the paper and its findings in Chapter 3.

C.2 NGC 362

Another of James Dunlop's discoveries (Dunlop 1828), NGC 362 is situated in the constellation of Tucanae, on the opposite side of the SMC to 47 Tuc. It suffers some background contamination from the SMC, but this is generally insignificant. Its radial velocity, though similar to the SMC, is very different from Galactic stars, allowing relatively-easy confirmation of cluster membership. Its moderate distance, in the more-metal-poor halo, makes NGC 362 moderately faint. It suffers little extinction as it lies well away from the Galactic Plane. It is a very round, core-collapsed cluster, with a fairly strong central condensation. Next to M15, it has the lowest escape velocity of the clusters we study here (Harris 1996). Its orbit has a very small perigalactic distance ($\lesssim$ 1000 pc — Tucholke 1992), thus at times it must suffer considerable tidal stress.

Table C.2: Selected data on NGC 362. Colons denote uncertain values, bracketed figures are uncertainties. References can be found in Appendix B.2.

Property		Value	References
Names		NGC 362, GCL 3,	S88
		ESO 51-SC13, C 104	
Position (J2000.0)		01 03 14.3 –70 50 54	S88
Distance from Sun		8500 pc	H96
Distance from Gal. Cen.		9400 pc	H96
Galactic co-ords.	(l, b)	301.53°, –46.25°	H96
	(XYZ)	(3100, –5000, –6200) pc	H96
Distance modulus	(V)	14.81 mag	H96
HB Mag.	(V)	14.0 mag	H96
Integrated V-band mag.		6.40 mag	H96
E(B–V)		0.05 mag	H96
Abs. Mag	(V)	–8.41 mag	H96
Integrated colour	(U–B)	0.16 mag	H96
	(B–V)	0.77 mag	H96
	(V–R)	0.49 mag	H96
	(V–I)	1.01 mag	H96
Spectral type		F9	H96
Core surface brightness (V)		14.88 mag arcsec^{-2}	H96
Core flux density		4.70 L$_\odot$ pc^{-3}	H96
Metallicity (log [Fe/H])		–1.16, –1.27	H96, Z85
Radial velocity ($v_{\rm LSR}$)		223.5(5) km s^{-1}	H96
Ellipticity		$(1 - b/a) = 0.01$	H96
Relaxation time	Core	59 Myr	H96
	Half-mass	0.85 Gyr	H96
Radius	Core	$0.19' = 0.47$ pc	H96
	Half-mass	$0.81' = 2.00$ pc	H96
	Tidal	$16.11' = 39.8$ pc	H96
Condensation	$(\log(\frac{r_{\rm tidal}}{r_{\rm core}}))$	1.94	H96
Mass		1.6 (0.4) $\times 10^5$ M$_\odot$	MSS91
		3.0 (0.5) $\times 10^5$ M$_\odot$	FWMC93
Escape velocity		41.8 km s^{-1}	W85
Orbital period		166 ± 15 Myr	BGD+91
Space motion		$\mu_\alpha = 3.5$ (0.8) $\mu_\delta = -2.6$ (0.8) mas yr^{-1}	T92
Est. absolute age		12.1 (1.7), 15.0(2.5) Gyr	DH93a

The cluster contains an anomalous red horizontal branch (McClure & Norris 1974; Harris 1982), dragging it into the second parameter debate. In contrast with the more metal-rich clusters, it has a deficit of bluer stars and a lack of blue UV emission (Caloi et al. 1981), which can ionise or fragment cluster ICM. Dorman et al. (1997) have, however, detected FUV emission from 84 blue HB stars, which are thought to be created by excess mass loss on the RGB. Of these, 34 are confirmed members.

The cluster may have a metallicity spread, which correlates with cyanogen band strengths as seen from the giant branches (McClure & Norris 1974; Smith 1983). The cyanogen band strengths in turn anti-correlate with infrared colours (Smith 1984). This may be due to evolutionary mixing, since the cluster appears to have a very chemically-homogenous main sequence (Bolte 1987). Relative measurements have compared its age with the cluster NGC 288, which has similar metallicity, and it has been found to be $\sim 2-6$ Gyr younger (Lee, Demarque & Zinn 1988; Demarque et al. 1988; Lee 1989; Bolte 1989; Green & Norris 1990; Dickens et al. 1991). It has been suggested that this age difference can provide a second parameter to describe these two clusters (Bellazzini et al. 2001), though there are likely other competing parameters (Catelan et al. 2001).

Clement et al. (2001) note 16 known variables in the cluster. Recent discoveries have increased this number to 95 (Székely et al. 2006; 2007a), though this second figure contains projected field and SMC variables. Most of these are RR Lyrae stars. However, V2 and V16 are LPVs, though the latter may not be a member. Székely et al. (2006) also suggest that a number of stars show evidence for 10–50-day variations, which they have suggested are due to RGB pulsations (Kiss & Bedding 2003). These stars include V17 (49 days), V19 and V51 (135 days).

No solid detection of intra-cluster medium has been made in NGC 362. An upper limit of $\sim$3.1 $M_\odot$ has been made for H^+ (Hesser & Shawl 1977). Dust concentrations of up to 0.1 $M_\odot$ have been claimed from 'dark clouds' (Mendéz, Orsatti & Forte 1989). However, Barmby et al. (2009) have imaged the cluster in the mid-infrared with *Spitzer* and give a very stringent upper limit of 6.3×10^{-5} $M_\odot$ yr^{-1} on the mass of intra-cluster

dust. *Circum*stellar dust, however, is detected — three mid-infrared-excessive objects were discovered by Origlia et al. (2002) at 12μm; and *AKARI* observations (Ita et al. 2007) find 24-μm excess around eight objects.

C.3 47 Tucanae

Visible on the outskirts of the Small Magellanic Cloud (SMC), though lying in front of it, records of 47 Tucanae do not begin until it was christened as such in Flamsteed's stellar catalogue (Flamsteed 1712; Flamsteed 1725). Its southerly declination meant that it was not catalogued by any of the ancient Northern Hemisphere astronomers, despite its comparatively high brightness. Its 'nebulous' character was revealed by de Lacaille (1763). Dunlop (1828) resolved this *"beautiful large round nebula"* into component stars and noted the gradual condensation toward its centre. It also made its way into the New General Catalogue (Herschel 1786, 1789; 1802) as NGC 104. Selected properties of the cluster can be found in Table C.3.

The *Catalogue of Variable Stars in Globular Clusters* (Sawyer Hogg 1973; Clement 1997) lists 56 variable stars in the cluster, 15 of which have measured periods of ≥ 38 days. This does not include the 115 objects found using the *HST* (Albrow et al. 2001), most of which have starspots (BY Dra-like stars) or are short-period variables.

Glass & Feast (1973) performed the first major infra-red study of 47 Tuc and found H-band excesses in all giants except V1–V3, and a slight excess in V3 in the L-band. Following this, Lloyd Evans (1974) covered 47 Tuc in one of his series of near-infrared photometry papers. In this, he notes the AGB is well-defined and begins at $I = 12.5$, he confirms Sandage's gap at $I \sim 12.0$ and suggests possible gaps exist further up the AGB. He also states that there are no visible carbon stars. Gaps exist on the RGB too (Hesser & Hartwick 1977; Lee 1977): the corresponding 'clumps' of stars, also seen in

Table C.3: Selected data on 47 Tuc. Colons denote uncertain values, bracketed figures are uncertainties. References can be found in Appendix B.2.

Property		Value	References
Names		47 Tuc, NGC 104, GCL 1	S88
		ESO 50-SC9, C 106	
Position (J2000.0)		00 24 05.2 –72 04 51	S88
Distance from Sun		4500 pc	H96
Distance from Gal. Cen.		7400 pc	H96
Galactic co-ords.	(l, b)	$l = 305.90°$, $b = -44.89°$	H96
	(XYZ)	(1900, –2600, –3200) pc	H96
Distance modulus	(V)	13.37, 13.50 (8),	H96, GBC+03,
		13.27 (14), 13.71 (11) mag	ZRO+01, GSA02
HB Mag.	(V)	14.06, 14.13 (10),	H96, GBC+03,
		14.06 (12), 14.0 mag	L77, HHV+87
Integrated V-band mag.		3.95 mag	H96
E(B–V)		0.05 mag	H96
Abs. Mag	(V)	–9.42 mag	H96
Integrated colour	(U–B)	0.37 mag	H96
	(B–V)	0.88 mag	H96
	(V–R)	0.53 mag	H96
	(V–I)	1.14 mag	H96
Spectral type		G4	H96
Core surface brightness (V)		14.43 mag arcsec^{-2}	H96
Core flux density		4.81 $L_\odot$ pc^{-3}	H96
Metallicity (log [Fe/H])		–0.76, –0.66 (4), –0.71 (8)	H96, CG97, GCG+00
Radial velocity		–18.7(2), –16.1 km s^{-1}	H96, SKS+07
Velocity dispersion		11.5 km s^{-1}	PG92
Projected $v_{\rm rot}$		6.60(7) km s^{-1}	SKS+07
Ellipticity		$(1 - b/a) = 0.09$	H96
Relaxation time	Core	91 Myr	H96
	Half-mass	3.0 Gyr	H96
Radius	Core	$0.40' = 0.52$ pc	H96
	Half-mass	$2.79' = 3.65$ pc	H96
	Tidal	$42.86' = 56.1$ pc	H96
Condensation	$(\log(\frac{r_{\rm tidal}}{r_{\rm core}}))$	2.03	H96
Mass		6.3 $\times 10^5$ $M_\odot$	SR75
		6.0 (1.5) $\times 10^5$ $M_\odot$	MSS91
		9.1 $\times 10^5$ $M_\odot$	MM85
Escape velocity		56.8 km s^{-1}	W85
Central density		$\sim$50 000 $M_\odot$ pc^{-3}	GF95
Est. absolute age		11.2 (1.1), 12.5,	GBC+03, GCG+00
		13.0 (2.5), <14,	ZRO+01, GSA02
		12.0:, 14.0 (2.8) Gyr	KTR+07, CSD92

other clusters (§1.3.4.3), are theorised to be due to a "standstill" in stellar evolution (Hesser, Harris & VandenBerg 1987a; Hesser, Harris & VandenBerg 1987b).

Lee (1977) notes a smaller UV excess in the AGB stars than the RGB stars, and that the UV excess decreases further as evolution progresses. It is possible that this is due to decreasing chromospheric activity (see also §3). Short-period U-band variability has also been suggested in the AGB population, with periods of only a few days and amplitudes of a few percent (Edmonds & Gilliland 1995, 1996).

As a large cluster, 47 Tuc has been well-investigated for ICM. As mentioned (§1.5.1), Freire et al. (2001) report around 0.2 $M_\odot$ of ionised hydrogen in its core. Upper limits on dust mass have been placed at 1.5 $\times 10^{-4}$ $M_\odot$ in the entire cluster, and 1.2 $\times 10^{-5}$ $M_\odot$ in the cluster core. Smith et al. (1990) have placed an upper limit of 3.7 $M_\odot$ of H I in the cluster. These results mean that not only is the ICM $> 5\%$ ionised, but also that the gas-to-dust ratio in the ICM exceeds 16 000, compared to the value of $\sim$1000 we would expect when it leaves the star (Nenkova, Ivezić & Elitzur 1999). Circumstellar dust has also been recently found by Ramdani & Jorissen (2001), Origlia et al. (2002), van Loon et al. (2006a), Lebzelter et al. (2006), Origlia et al. (2007) and Ita et al. (2007), all of which are discussed in Chapter 2.

C.4 M 15

C.4.1 Discovery and structure

The discovery of M15 is accredited to Jean-Dominique Maraldi (1746), who found the 'nebulous star' while searching for de Chéseaux' comet, and described it as 'fairly bright and composed of many stars'. It was not resolved by Messier or Bode, though Herschel succeeded while creating the NGC. It has long been known to have a particularly dense core and as such has been classified as 'core collapsed'. It may represent the densest core of all Galactic globulars (Harris 1996). The cluster shows an apparent colour gradient in the core region due to preferential mass segregation of heavier objects (*e.g.* Bailyn

et al. 1989; Cederbloom et al. 1992), which may also have created a faint tidal tail (Lehmann & Scholz 1997). Perhaps most notable, however, is its very low metallicity, of [Fe/H] ~ -2.3 (Harris 1996). Correspondingly, the age of M15 is greater than most other globulars, and indeed most objects in the Universe (see Table C.4).

The first substantial colour-magnitude diagrams of the cluster were produced by Brown (1951) and Johnson & Schwarzschild (1951), reaching $V = 15$ and 17 mag, respectively (*c.f.* the horizontal branch, $V_{\rm HB} = 15.81$ mag; Harris 1996). This was followed by Arp (1955), who provides some of the common identifiers, though avoids the dense inner arcminute or so of the cluster. An earlier astrometric work by Kustner (1921) provides other common identifiers. Deeper studies by Sandage & Katem (1977), Fahlman, Richer & VandenBerg (1985), and Durrell & Harris (1993b) later resolved successively further down the cluster's main sequence. *HST* data also provided a deeper look at the cluster, particularly the core, identifying a population of blue stragglers (Guhathakurta et al. 1993; Ferraro & Paresce 1993), and a separate population of unusual, very blue stars (de Marchi & Paresce 1994), theorised to be helium-core-burning merged white-dwarfs (d'Antona, Vietri & Pesce 1995). Further spectroscopic analysis suggests the stars F1-1 and F2-2 are very extreme HB stars that have lost almost all of their hydrogen envelopes (Moehler, Heber & Durell 1997). Böhm-Vitense & Szkody (1973) find the average giant star mass to be 0.81 $M_\odot$.

Gaps were found in the RGB by Sandage, Katem & Kristian (1968) in their colour-magnitude diagram at $V = 14.9$, 15.5 and 16.1 mag, along with a small (2%) variation in the radii of the giant branch stars[1]. Demarque, Mengel & Sweigart (1972) theorised that this was due to the hydrogen-burning shell traversing a strong temperature gradient between the fast-rotating stellar core and non-rotating envelope.

M15 has a comparatively circular orbit (Ninković 1983), with a variable orbital period of 285 ± 25 Myr, giving ~ 90 plane crossings since its formation (Scholz et al.

[1]These are not to be confused with the gaps in luminosity function due to the starts and ends of the HB (see, *e.g.* Cho & Lee 2007).

1996). Despite its core-collapse, there is evidence that the cluster is being kinematically heated, probably by tidal friction with the Galaxy (Drukier et al. 1998).

C.4.2 Variable and unusual objects

M15 has a diverse collection of non-stellar objects: it contains eight known pulsars, including PSR B2127+11 C — a neutron star binary (Anderson et al. 1990; Prince et al. 1991). It was also the first cluster to have a planetary nebula identified within it (Pease 1928): Pease 1 (K648).

Pease 1 exhibits several spectroscopic peculiarities: it is weak in [O III] and carbon-rich, with a He:H ratio of 2:1 by number (O'Dell, Peimbert & Kinman 1964; Heber, Dreizler & Werner 1993). *HST* data have revealed various key statistics: $M_* = 0.60 \pm 0.02$ M$_\odot$, $R_* = 1.9$ R$_\odot$, $L_* = 4680$ L$_\odot$, $v_{\rm wind\ edge} = -1630$ km s^{-1}, $T_* = 40000 \pm 3000$ K and $M_{\rm nebula} = 0.07 \pm 0.02$ M$_\odot$ (Bianchi et al. 1995; Alves, Bond & Livio 2000). The comparatively high mass may be due to either mass augmentation earlier in the progenitor's history, or decreased mass loss in this metal-poor environment. VLA radio maps show Pease 1 to be 2.5 $\times 10^{-2}$ pc in diameter (Gathier, Pottasch & Goss 1983), with an relatively-young age of $\gtrsim$4270 years old (Bianchi et al. 2001). *IUE* data indicate that it is still losing mass at a rate of $\dot{M} \sim 2 \times 10^{-10}$ M$_\odot$ yr^{-1}.

Like several of the other Galactic globulars, variables were first discovered in M15 by Pickering & Bailey (1897, 1898), and by Pickering et al. (1898). However, excepting the Type II Cepheid V1, they were all RR Lyraes (Clement et al. 2001). Many more variables were later discovered (*e.g.* Bailey et al. 1919; Rosino 1950; Izsak 1951; Rosino 1969; Chu 1976; Kadla et al. 1984; Guhathakurta et al. 1992; Paresce & Ferraro 1992; Ferraro & Paresce 1993; Butler et al. 1998; Corwin et al. 2008).

The more interesting among these include Chu's discovery of variability in K1082 (=V122). This star pulsates on a two-hour timescale, though it does not lie in the δ Scuti region of the colour-magnitude diagram (CMD). A later re-analysis of data for V99 by Barlai & Szeidl (1995) shows that its pulsation amplitude and period have

been erratic over the past century. Other variables not listed in Clement (1997) include a very-short period variable (SX Phe) star and four contact binaries (Jeon et al. 2001a; 2001b; Saad 2005), as well as several other confirmed and unconfirmed variable candidates (Zheleznyak & Kravtsov 2003; Tuairisg et al. 2003; Corwin et al. 2006a). Charles, Clarkson & van Zyl (2002) may have identified a dwarf nova lying at the very heart of the cluster[2], a theory supported in work by Shara et al. (2004). Near the cluster core, *HST* ACS FUV/NUV photometry has found several candidate variables, including another dwarf nova candidate (Dieball et al. 2007).

Giant branch mass-loss in this cluster has been investigated by Origlia et al. (2002), hereafter OFFR02, which is relied on heavily in this work, and is discussed in Chapters 3 & 5. Hα imaging of several M15 giants was reported by Cargile et al. (2003) at the American Astronomical Society Meeting #52, but apparently no more work has been published on these data. Mészáros, Dupree & Szentgyörgyi (2008) also provide a comprehensive analysis of chromospherically-driven outflows in 110 giant stars in the cluster, suggesting mass loss from these stars is episodic.

M15 does not appear to harbour any high-amplitude long-period variables, in contrast to more metal-rich globulars. Mosley & White (1975) conducted a search for variability among M15's giant population, and found seven stars that were suspect variables. Cudworth (1976) derived proper motions for these candidate variables to confirm their membership. A 40 mmag variation on a timescale of 0.18 days has also been given by Bao-An (1990) for K1040, which is near the giant branch tip. This was confirmed by Yao et al. (1993). Hughes & Wallerstein (1997) report that their object 37 (2MASS 322.507506+12.112302, not in Arp or Küstner, hereafter HW37) may be a post-AGB star, though it is not known to be variable. The star K559 (ZNG-1) is known to be a post-AGB star (Zinn, Newell & Gibson 1972), and abundances have been measured by Mooney et al. (2004).

[2]They label this object V1, though it is a different object to that discovered by Pickering & Bailey and listed in Clement et al. (2001). We will hence refer to this as CV1

C.4.3 The cluster core

The first attempt at resolving the dense cluster centre was by Leroy, Aurière & Laques (1976), who found the centre to contain a 'peculiar' object, which could correspond to the 10 μm emission found by MacGregor, Phillips & Selby (1973). Caloi & Panagia (1974), and Peterson (1976) suggest that this central object is a (proto-) planetary nebula, though with no observed [O III] and Hα emission (Aurière, Laques & Leroy 1978; Phillips, Reay & Worswick 1978). Work at resolving the stellar population in the core has dispelled this theory (*e.g.* Aurière & Cordoni 1981; Spasova 1983) and the Hα emission is more likely to be associated with AC5 (=V86) (Naylor 1987). Ca II H & K emission from the core has been theorised to be due to stellar binaries or merged stars (Murphy et al. 1991), but spectra have suggested that this is due to hydrodynamically-generated chromospheres of red giant stars (Dupree & Whitney 1991). The centre of the cluster also appears bright at shorter wavelengths, which is important as high-frequency emissions are capable of being powerful ionisers of any ICM.

C.4.4 A possible central black hole

The X-ray source 3U 2131+11 (=X2127+11), originally thought to be a black hole, appears to be associated with the interacting binary AC211 (Clark, Markert & Li 1975; Newell, da Costa & Norris 1976; Aurière, Cordoni & Koch-Miramond 1985; Charles, Jones & Naylor 1986; Callanan et al. 1987; Hertz 1987; Ilovaisky et al. 1987). A second source, M15-X2, was discovered by *Chandra*, along with X-ray emission from K648 (White & Angelini 2001). M15-X2 is associated with a 110 ms pulsar in a binary (P = 22.6 minutes) with a white dwarf secondary, and is accelerating towards the cluster centre (Wolszczan et al. 1988; Dieball et al. 2005). A very energetic X-ray burst was reported in 1988 (Dotani et al. 1990) and again in 2000 (Smale 2001), caused by an expansion of the neutron star photosphere. It is unclear which X-ray object was the

source of the burst, though it is likely to be M15-X2 (Hannikainen, Charles & van Zyl 2001). The cluster shows a 37-day modulation in X-rays, though again it is not known which object is varying (Corbet, Peele & Smith 1997).

Velocity dispersion measurements of the cluster centre point do not require the presence of an intermediate-mass black hole (*e.g.* Dubath, Meylan & Mayor 1994, Dubath & Meylan 1994; Baumgardt et al. 2003; McNamara, Harrison & Anderson 2003). Such an object has not been ruled out, however, and M15 still remains the globular cluster with the best evidence for containing a central black hole (Gebhardt et al. 2000). The comparatively strong acceleration of PSR 2127+11A, along with the ejection from the cluster of the pulsar binary PSR 2127+11C, suggests a $\sim$ 700 $M_\odot$ black hole may be present (Wolszczan et al. 1989; Phinney & Sigurdsson 1991; Prince et al. 1991; Postnov, Prokhorov & Shakura 1991). A maximum mass of $\sim$2000 $M_\odot$ has been derived from stellar radial velocity measurements (van der Marel 2001), or up to 3900 ± 2200 $M_\odot$ as derived from spectroscopic mapping (Gerssen et al. 2002). The accretion luminosity of such a black hole must be small ($L_{\rm bol}/L_{\rm Edd} \lesssim 3 \times 10^{-8}$; Ho, Terashima & Okajima 2003).

If a more massive black hole is not present, 85% of the cluster's core may be comprised of stellar remnants of various forms: $\sim$44% being stellar-mass black holes along with $\gtrsim$100–1000 neutron stars (Gebhardt et al. 1997; Dull et al. 1997; Murphy et al. 2003; Pasquali et al. 2004). As an alternative theory, Lauer et al. (1991) have also suggested that diffuse dark matter could pervade the cluster centre.

A central density of 7.4–8.6 $\times 10^6$ $M_\odot$ pc^{-3} has been measured via several methods, including radial velocity dispersions and pulsar accelerations. It implies a considerable gravity field in the central region (assuming spherical symmetry, $g = 0.18$ N kg^{-1} at a radius of 0.05 pc), which shows a very high central velocity dispersion (Peterson, Seitzer & Cudworth 1989; Dubath, Mayor & Meylan 1993; Gebhardt et al. 1993; Guhathakurta et al. 1996; van den Bosch et al. 2006). The inner 10″ also rotates with a different rotational axis with a velocity spread comparable to its 10 km s^{-1} rotational

velocity (Gebhardt et al. 2000).

Other stars are also bright at shorter wavelengths: de Boer (1985) found the stars K559, K648 (Pease 1) and K998 to be UV-bright, contributing 50% of the 1200Å flux of the cluster. The cluster itself is comparatively UV-faint (Cháves, Holberg & Landsman 1999), which may mean that dust can survive in the cluster without being subject to too much ionising radiation.

C.4.5 Foreground absorption and the intra-cluster medium

The foreground absorption to the cluster, $E(B-V) \sim 0.12$ mag, is relatively small (Harris 1996). This includes a number of clumpy, intermediate-velocity clouds (IVCs) with recession velocities of +40∼90 km s^{-1}. These appear in both 21 cm H I emission, and as satellite lines in the Na I D, K I, Ca II H & K lines of stellar spectra (Kennedy 1997; Kennedy et al. 1998; Lehner et al. 1999; Smoker et al. 1999). The H I and Na I D clouds in both the Galaxy and the IVC have been crudely mapped, with both found to be quite clumpy. Kinetically, the IVCs are found to be warmer than the Galactic foreground ISM (Meyer & Lauroesch 1999; Smoker et al. 2001; Smoker et al. 2002).

The cluster itself has been a subject of regular study as a candidate for intra-cluster material, as it is expected to accumulate ∼7.8 $\times 10^{-7}$ M$_\odot$ yr^{-1} (Smith, Woodsworth & Hesser 1995). Infrared detections of the cluster were made at 2.3, 4.7 and 10.2 μm, requiring $\sim 10^{-5}$ M$_\odot$ of dust at ∼300 K (MacGregor, Phillips & Selby 1973; Hansen & Hesser 1975). Findings of optical extinction variations and a possible detection of polarisation suggested the presence of ∼0.001 M$_\odot$ of dust (Kanagy 1977; Kanagy & Wyatt 1978; Martin & Shawl 1981), though the results can be accounted for by under-densities in the star distribution (Aurière & Leroy 1990).

Early upper limits on the mass of various ICM components were placed at 0.8 M$_\odot$ for H I, 0.7 M$_\odot$ for H II, 0.1 M$_\odot$ for warm dust grains and 0.4 M$_\odot$ for the total molecular content (Conklin & Kimble 1974; Hesser & Shawl 1977; Lynch & Rossano 1990; Smith, Woodsworth & Hesser 1995, respectively).

The detection of dust in the cluster using far-infrared *ISO* data was made by Evans et al. (2003), making M15 the first and hitherto only globular cluster to contain any direct evidence of ICM. A dust mass of $(4.8 \pm 1.6) \times 10^{-4}$ $M_\odot$ was detected, based on a 0.1 μm grain size, with a temperature of around 50 K. Further observations by van Loon et al. (2006b) then determined that a cloud of H I gas exists in M15 at a velocity matching that of M15 ($v_{\rm LSR,M15} = -94.8$ km s^{-1}) and not associated with the planetary nebula. The mass of H I in this cloud is estimated at $M_{\rm H} \approx 0.3$ $M_\odot$. Kinematically, it is also well-separated from the IVCs in front of the cluster.

Associated dust was confirmed in *Spitzer* data by Boyer et al. (2006). The cloud size is estimated at $(9 \pm 2) \times 10^{-4}$ $M_\odot$, suggesting a 10^6 year dispersion time for the ICM. This dust cloud, emitting at 70 ± 2 K, is approximately $17''$ west of the cluster centre and is roughly coincident with an unresolved radio source detected in the NRAO VLA sky survey (Condon et al. 1998).

C.5 M 54

M54 was discovered by Charles Messier in 1778 (Messier 1780). Although conspicuous, it is difficult to resolve in small telescopes. It is well established that the cluster is part of the Sagittarius Dwarf Elliptic Galaxy (SagDEG), as it co-incides with one of its major concentrations and has a similar radial velocity. It has further been suggested that M54 is, or is associated with, the dwarf galaxy's core, but may not have always been so (Bassino & Muzzio 1995; Bellazzini et al. 2008).

Its distance belies the fact that it is one of the most luminous globular clusters in our Galaxy. It also contains a large number of known variable stars. We do not devote a large amount of time to M54 as the only target we have observed in it appears not to be related to the cluster.

Table C.4: Selected data on M 15. Colons denote uncertain values, bracketed figures are uncertainties. References can be found in Appendix B.2.

Property		Value	References
Names		M 15, NGC 362, GCL 120	S88
Position (J2000.0)		21 29 58.3 +12 10 01	S88
Distance from Sun		10300, 9980 (470) pc	H96, MHB04
Distance from Gal. Cen.		10400 pc	H96
Galactic co-ords.	(l, b)	65.01°, –27.31°	H96
	(XYZ)	(3900, 8300, –4700) pc	H96
Distance modulus	(V)	15.37, 14.93, 14.32(30) mag	H96, S70, I+00
HB Mag.	(V)	15.83 mag	H96
Integrated V-band mag.		6.20 mag	H96
E(B–V)		0.10, 0.12, 0.10(1) mag	H96, S69, DH93b
Abs. Mag	(V)	–9.17 mag	H96
Integrated colour	(U–B)	0.06 mag	H96
	(B–V)	0.68 mag	H96
	(V–I)	0.85 mag	H96
Spectral type		F3–4	H96
Core surface brightness	(V)	14.21 mag arcsec^{-2}	H96
Core flux density		5.38 $L_\odot$ pc^{-3}	H96
Metallicity (log [Fe/H])		–2.26, –2.15(.08), –2.19(.09)	H96, ZW84, NZ77
Radial velocity ($v_{\rm LSR}$)		–107.0(.2), –106.9(.3)	H96, DSC+98
		–106.2(.3) km s^{-1}	SPB+99
Velocity Dispersion		10, 17.4(4.6), 9.0(.6) km s^{-1}	C76, KL84, PSC89
Ellipticity		$(1 - b/a) = 0.05$	H96
Relaxation time	Core	10 Myr	H96
	Half-mass	2.2 Gyr	H96
Radius	Core	$0.07' = 0.21$ pc	H96
		$0.003' = 0.01$ pc†	LS97
	Half-mass	$1.06' = 3.18$ pc	H96
	Tidal	$21.50' = 64.4$ pc	H96
		$27.05'$ $(.95') = 81.0$ pc*	SK97
		$20' = 60.0$ pc†	LS97
Condensation	$(\log(\frac{r_{\rm tidal}}{r_{\rm core}}))$	2.50	H96
Mass		5.9, 4.7 $\times 10^5$ $M_\odot$	SR75, NDCN76
		3.42*, 4.9† $\times 10^5$ $M_\odot$	SK97, DCL+97
		4.5, 5.4 $\times 10^5$ $M_\odot$	MHB04, P+04
Population		$\sim$700 000, 949 000*	K77, SK97
Escape velocity		40.9 km s^{-1}	W85
Central density		25000 $M_\odot$ pc^{-3}	GF95
Est. absolute age		15.1 (2.4), 12(1), 14.1(.1)	CSD92, IR70, BVS73
		15.6(3.1), 18(2), 16(3)	SKS81, S83a, FRV85
		14(3)**, 13.2 Gyr	SJK+00, MHB04

*King-model parameters.
†Fokker-Planck-model parameters.
**Determined spectroscopically.

C.6 ω Centauri

C.6.1 Discovery & early history

Omega Centauri is the most massive and most populous Galactic globular cluster. It is also one of the nearest. First catalogued by Ptolemy (170) as "*Quae est in principio scapulae*" ([the star] in the beginning of the shoulder blade [of the Centaur]), it was later given its usual designation in Bayer's *Uranometria* (Bayer & Mair 1603). Historically regarded as a star, it remained unresolved until the invention of the telescope: Edmond Halley (1678) describes it in his *Catalogus stellarum Australium* as "*in dorso Equino Nebulus*" (nebula on the back of the horse). This makes it the second globular discovered, after M 22.

Despite appearing in Halley and de Lacaille's later catalogues of nebulae (Halley 1716; de Lacaille 1755), it was not included in Messier's catalogue due to its southerly position. It was later recorded in Dreyer's *New General Catalogue* (Dreyer 1888). Like the other clusters described herein, it was used to help Shapley and his successors affirm our place in the Galaxy (*e.g.* Shapley 1918a; Fernie 1962).

C.6.2 Physical structure

One of the many peculiarities of ω Centauri is its profound ellipticity, exceeded only by a few Galactic globulars (*e.g.* NGC 6144 and 6273). Documented by Shapley (1918b) from star counts (later also Dickens & Woolley 1967), it was confirmed by Schilt (1928) using out-of-focus photography. Theory at the time suggested this was due to tidal forces. Sisteró & Fourcade (1970) later found that the cluster's ellipticity is radially dependant, with ellipticity increasing with radius and position angle rotating slightly.

The cluster's rotation was first found through the Royal Greenwich Observatory survey[3], collectively published as Woolley (1964). They observed this rotation rate to

[3]This survey was published in the following Royal Greenwich Observatory Bulletins: 87, 99–101, 128 and 129; and under the following authors: Dickens, Woolley & Carey (1966); Harding (1965);

be compatible with the cluster's ellipticity. Such rotation may expedite cluster core collapse (Boily 2000). The inclination angle for ω Cen's rotation axis has been estimated to be $50^\circ \pm 4^\circ$ by van de Ven et al. (2006), who also find a disk-like component in the inner $3'$. Additionally, the cluster's velocity dispersion may be anisotropic (Meylan 1987; Merritt, Meylan & Mayor 1997; Jurcsik 1998), though the methods of evaluation of this anisotropy have been questioned (Seitzer 1983; van Leeuwen et al. 2000; King & Anderson 2002; Ashurov & van Leeuwen 2002).

A radial colour gradient exists, being bluest in the 2–$4'$ from the cluster core; the core is red in (R–I) and blue in (U–B), arguably due to mass-segregation effects (Scaria & Bappu 1981; Scaria 1982). Radial chemical gradients have also been suggested, particularly in cyanogen (*e.g.* Freeman 1985), though evidence shows the colour gradients cannot be purely chemical (Pastoriza et al. 1986). A correlation between radial velocity and calcium gradient has also been reported (Norris et al. 1997).

Though models of the cluster's formation suggest a dark matter halo may exist (Carraro & Lia 2000), searches for massive dark matter objects (MACHOs/WIMPs) have been unsuccessful (Mighell et al. 1992). More recent results suggest that there is no need to invoke modified Newtonian gravity either (McLaughlin & Meylan 2003).

Like many other clusters, ω Cen's age was originally overstated due to poorly-constrained evolutionary models (Table C.6). It is now reckoned to be close to the age of the Universe, but with considerable age difference among the populations (§C.6.4).

The small apogalactic distance of ω Cen's orbit means that it must undergo considerable stress as it passes through the Galactic plane. Leon, Meylan & Combes (2000) used star counts to suggest two tidal tails in a roughly north-south alignment with respect to the cluster, and extending nearly two degrees in both directions. More recently, however, da Costa & Coleman (2008) suggest that these apparent tails are merely tracers of Galactic foreground extinction, traceable in mid-infrared maps near

Murray, Candy & Jones (1965); Dickens & Saunders (1965); Dickens & Woolley (1967); Dickens & Carey (1967).

the cluster. They estimate that $< 0.7 \pm 0.2\%$ of the cluster's mass lies in the range of 1–2 $r_{\rm tidal}$ meaning that, if the cluster is the stripped core of a larger body (§C.6.6), its stripping largely occurred early on in its history. Dinescu (2002) also find putative evidence of tidally-stripped stars from the cluster, which may trace its past orbit. Meza et al. (2005) also claim to have identified candidates in the solar neighbourhood that could be stars stripped from ω Cen, on the basis of their orbital angular momenta.

C.6.3 The cluster population

Models of stellar and dynamic evolution estimate that 7–9% of the mass of the cluster exists as heavy remnants (neutron stars or black holes), 32–40% as white dwarfs, with the remaining 51–61% as nuclear-burning stars (Meylan & Mayor 1986; Meylan 1987). Other models, however, suggest a larger $\sim$55% of the mass is in heavy remnants (Giersz & Heggie 2003). *HST* observations have shown over 2000 white dwarf candidates in the cluster (Monelli et al. 2005), and Calimada et al. (2008a,2008b) have presented tentative evidence that young white dwarfs ($\lesssim$600 Myr) may be more centrally condensed than the rest of the stellar population. There is also some evidence that the cluster core harbours a black hole of some $3 - 5 \times 10^4$ M$_\odot$ (Noyola, Gebhardt & Bergmann 2006, 2008). Despite significant numbers of heavy remnants, the cluster is also comparatively X-ray faint, suggesting a lack of ionising radiation (Hartwick, Grindlay & Cowley 1982). Presently, the mass function of the cluster's stars varies roughly as $N(M) \propto M^{-1}$ down to at least $\sim$0.15 M$_\odot$, though with a Kroupa-like IMF dominating at $M > 0.5$ M$_\odot$ (Pulone et al. 1998; Sollima, Ferraro & Bellazzini 2007).

Radial velocity studies on cluster members were performed by Mayor et al. (1997) (giants); Suntzeff & Kraft (1996) (upper & lower RGB); and Reijns et al. (2006); though the most extensive has been by van Loon et al. (2007), which we use extensively throughout this work (hereafter vL+07). Numerous proper motion studies have also been carried out (see references in Table C.6), though we base membership analysis on van Leeuwen et al. (2000) (hereafter vL+00).

Van Leeuwen's study identified several key features. Firstly, there is a paucity of HB stars near the cluster centre compared to outside the half-mass radius, again probably linked to mass segregation. The cluster rotation appears to peak at ∼7 km s^{-1} and the three-dimensional velocity dispersion increases to nearly 30 km s^{-1} in the cluster core. Freeman (2001) corroborates the rotation speed, which also agrees with an earlier radial velocity value of 7.7 km s^{-1} from Seitzer (1983). Both Seitzer and Freeman, however, find the (two-dimensional) velocity dispersion to be around 16 km s^{-1}, suggesting the 3D dispersion is marginally less. Other radial velocity studies suggest a higher central dispersion (*e.g.* Meylan 1987; Meylan et al. 1995).

C.6.4 Colour-magnitude diagrams and the metallicity spread

The first substantial colour-magnitude diagrams to resolve below the HB were compiled by Belserene (1956a, 1959), with the MSTO found by Conklin & Kimble (1974).

The first hints of a metallicity spread came with the RGO survey, in which Dickens & Woolley (1967) noted the large spread of magnitudes in the cluster's giant branch. This was confirmed by *UBV* and near-IR photometry (Geyer 1967; Lloyd Evans 1977). A handful of stars (LEID 15023, 42116, 44021 and 50014) were put forward as candidate members of a metal-poor population by Hesser, Hartwick & McClure (1977).

The stars on the cooler edge of the giant branch were found to be barium- and CN-enhanced (Mallia 1976; Dickens & Bell 1976; Bessell & Norris 1976; vL+07). An overabundance of *s*-process elements in the cool giant-branch star ROA 371 and nitrogen in the warm giant ROA 371 were also found by Dickens & Bell. Hypothesis at the time was that this was due to AGB mixing variations (Dickens & Powell 1973; Schmidt & van den Bergh 1974; Freeman & Rodgers 1975; Norris & Bessell 1975; Mallia 1976). Soon after, however, varying helium and calcium abundances were found in the cluster's RR Lyrae stars (Caputo & Castellani 1975; Freeman & Rodgers 1975; Bell & Manduca 1977; Manduca & Bell 1978; Caputo 1979; Caputo 1981), meaning these abundance variations were introduced before the AGB stage.

Star-to-star variations were also found in the relative abundances of CO, oxygen, calcium and other elements (Persson et al. 1980; Mallia & Pagel 1981; Cohen 1981; Gratton 1982). The correlation of CO abundance with *s*-process enhancement suggested that subsequent giant-branch mixing still plays at least some rôle in the abundance variations (Carbon et al. 1982; Norris 1987; Norris 1988; François, Spite & Spite 1988). The relative amount of mixing, between the hydrogen-burning shell and convective envelope, may be determined by the angular velocity at the base of the convective zone. This may explain the [O/Fe] / [Na/Fe] anticorrelation, $^{17}O/^{16}O$ and $^{18}O/^{16}O$ ratios, and CN bimodality in many globulars, plus the anomalous Al and [Mg/Al] values in ω Cen (Brown et al. 1991; Denissenkov & Weiss 1996; Denissenkov & Tout 2000). Mixing deeper in the atmosphere may explain the low $^{13}C/^{12}C$ ratio and its lack of correlation with metallicity (Smith, Terndrup & Suntzeff 2002).

A primordial abundance spread had been suggested in earlier works, particularly John Norris's 'occasional' series of papers (Bessell & Norris 1976; Norris & Bessell 1977; Norris 1978; Paltoglou & Norris 1989; Norris & da Costa 1995; and Norris, Freeman & Mighell 1996), however it wasn't until the 1980s that evidence for a photometric spread either side of the MSTO was found (Cannon 1980b; Rodgers et al. 1980; Cannon & Stewart 1981; Bell et al. 1981; Rodgers & Harding 1983; Hesser et al. 1985), which continues down the main sequence (Alcaíno & Liller 1987; Ortolani 1988; Noble et al. 1988). Later *HST* data showed the main sequence to clearly bifurcate into two distinct chemical groups (Anderson 2002; Bedin et al. 2004).

The situation was further complicated by the discovery of a third, even more anomalous RGB branch, or 'RGB-a', by Pancino et al. (2000). The RGB-a is a population of stars forming a parallel giant branch at much cooler temperatures and lower optical brightnesses than that of the main RGB (see Fig. 1.2). The cooler temperatures are a result of a much higher metallicity, found to be $[Fe/H]_{RGB-a} = -0.55$ to -0.62 (Pancino 2004; Rey et al. 2004). This anomalous branch has now been traced down to the sub-giant branch, or SGB-a (Villanova et al. 2007).

Recent spectroscopic observations have been carried out using multi-fibre spectrographs, allowing chemical abundances to be measured for hundreds or thousands of stars in one programme. These have yet to be fully digested by the modelling community. They include the main-sequence survey using AAT/2dF by da Costa et al. (2005); the 429 stars covered with VLT/FORS2/MXU by Kayser et al. (2006); and the post-main-sequence 2dF survey by vL+07; as well as smaller, conventional spectroscopic surveys, including the aforementioned FLAMES surveys (Gratton et al. 2005; Piotto et al. 2005; Sollima et al. 2005b); the GIRAFFE survey by Villanova et al. (2007); and the on-going main-sequence survey by Stanford et al (2004, 2006a, 2006b, 2007). Additionally, Willemsen et al. (2005) and Johnson et al. (2008) have automatically calculated the metallicities of several hundred stars.

The MS 2dF survey found that carbon-enhanced stars (stars with strong CH G-bands, with δ[C/Fe] = 0.5–1.0) are observed at all metallicities, making up ∼5% of their sample; that the CN-rich, nitrogen-enhanced stars account for ∼40% of the cluster, at least above [Fe/H] ∼ –1.3; and that strontium (an *s*-process element) is also strongly enhanced in many cluster stars. Kayser et al. (2006) find the α-enhancement is small over the majority of their observations.

Interestingly, the 2dF spectral atlas of vL+07 suggests that third dredge-up does occur among AGB stars, and that barium enhancement may serve to distinguish RGB and AGB stars where this is otherwise not possible. We return to this in §5.6.4.

C.6.5 Origins of the metallicity spread

A primordial metallicity spread can be generated by two scenarios: a merger of two or more objects, or a direct enrichment by high-mass stars during cluster formation.

A merger scenario was proposed by Icke & Alcaíno (1988). This would explain the clumpy [Fe/H] spread, the flattening and its large mass; its unusual orbit (almost co-planar with the Galaxy Disc, and retrograde with a small apogalactic distance) (Majewski et al. 2000). It would also explain the large age spread and chemical gradients

within the cluster (Ferraro 2000; Ferraro, Bellazzini & Pancino 2002; Pancino 2003). However, the existence of more than two populations of stars means that the merger would have to involve several (presumably independent) objects, and the current distribution of the Galaxy's globular system means that appears dynamically unlikely (Thurl & Johnston 2002). Radial velocities recently obtained from FLAMES (Pancino et al. 2007) show the different populations rotate homogenously, suggesting the merger scenario is unlikely. In a similar vein, Fellhauer (2004) suggest that ω Cen formed in a 'super-cluster', such as the knots seen in interacting galaxies (*e.g.* Knierman et al. 2003). This has the same advantages of the merger scenario in producing multiple populations of stars, but involves the formation of a super-cluster during the collision of a dwarf galaxy with the Milky Way. During this scenario, unrelated stars from the super-cluster become tidally bound to the stripped core of the dwarf galaxy, giving rise to a sub-population with a different metallicity.

In the enrichment model, supernovae and high-mass AGB stars provide heavy elements which can enrich a second generation of stars. The deaths of these stars may trigger the formation of this second generation (Dopita & Smith 1986; Smith 1987 [review]; Caldwell & Dickens 1988). The minimum mass of the original stellar cluster required for this method has been variously estimated between $> 10^{4.6}$ and $10^{8.9}$ $M_{\odot}$ (Dopita & Smith 1986; Morgan & Lake 1989; Giersz & Heggie 2003; Tsuchiya, Dinescu & Korchagin 2003): the difficulty here is that the ICM must remain within the cluster during the enrichment phase, suggesting ω Cen was originally a much more massive object (Hughes & Wallerstein 2000). A further difficulty with this model is that it must occur over the entire lifetime of star formation (several Gyr — see Table C.6).

More outlandishly, Bedin et al. (2004) suggest that ω Cen's anomalous population is a completely separate object, located $\sim$1.6 kpc *behind* ω Cen. This is a better fit to the theoretical isochrones than having the anomalous population as a helium-enriched part of the cluster. Freyhammer et al. (2005) advocate this hypothesis, but reduce the distance between the two clusters to $\sim$500 pc. They also suggest that there is likely a

substantial amount of interstellar reddening between the two clusters. This scenario, however, would not only rely on quite a feat of chance, but also counter the observations by Norris (2004), Piotto et al. (2005) and others that the metal-intermediate population *is* helium-enriched by around 12–14%, and that the bifurcated main sequence is due to helium- and metal-enrichment. On the basis of their FLAMES survey, Gratton et al. (2005) and Pancino et al. (2007) find the radial velocity and rotation of ω Cen's different populations to be identical, thus making the superimposition theory even less likely.

Other alternatives scenario for the observed abundance spreads include radial segregation of dust during the proto-globular collapse (Bhatt 1988), which could also explain the existence of radial chemical gradients in globulars (see, *e.g.*, above references by Norris). Alternatively, (post-)main-sequence binary mergers could lead to CN-enhancements (Campbell 1986), though this seems unlikely for producing anything except the 'blue straggler' population (see, *e.g.* Bailyn et al. 1992 for this case).

C.6.6 The dwarf galaxy disruption model

The prevaling theory for ω Cen's formation combines several of the above ideas. It stems from the fact that metallicity spread itself, along with the size of ω Centauri, makes it more akin to dwarf spheroidal (dSph) galaxies (Norris & Bessell 1978; Demers, Kunkel & Hardy 1979; Meylan 1987). This suggests that ω Cen may either be a 'bridging' object between the two classes, or the stripped core of a dwarf spheroidal. It now appears that many other clusters and dwarf galaxies[4] may share a lesser primordial metallicity spread, suggesting this is quite normal. Separate evidence suggests that other clusters[5] may also have originally been dwarf galaxy cores. This theory has also been accredited by the recent discovery of faint dwarf galaxies in our own halo,

[4] M 22 (Hesser & Harris 1979; Cohen 1981); 47 Tuc (Norris & Freeman 1979); M 5 and M 13 (Peterson 1980); NGC 2808 (Piotto et al. 2007); and NGC 1851 (Milone et al. 2008); and the extragalactic M 31 G1, G78, G213 and G280 (Meylan et al. 2001b; Meylan 2002; Fuentes-Carrera et al. 2008); SagDEG (McWilliam & Smecker-Hane 2005).

[5] M 54 — (Sarajedini & Layden 1995); NGC 2419 — (van den Bergh & Mackey 2004; Ripepi et al. 2007); M 31 037-B327 — (Ma et al. 2006a).

e.g. SDSS J1257+3419, that appears to be on the dwarf galaxy side of this nebulous transition (Kamaya 2007).

The dwarf-disruption scenario has the advantages of the cluster originating as a body of sufficient mass to retain hold of its ISM, while having a sufficient ISM reservoir to fuel continuing star formation. The metal-rich populations are created through self-pollution of the cluster gas by massive stars during a relatively slow, discontinuous period of star formation of up to 6 Gyr (Hilker & Richtler 2000b). Bekki & Freeman (2003) suggest that the multiple populations could have formed due to gas inflow to the cluster core as the proto-cluster was tidally shocked during its first few passages through the Galactic Plane. Relative abundances of heavy elements suggest that type II supernovae and massive AGB stars created the majority of the observed abundance oddities, including α-enhancement and richness of s-process elements found (Brown & Wallerstein 1993; Norris & da Costa 1995; Smith, Cunha & Lambert 1995; Smith & Kraft 1996; Parmentier et al. 1999; Smith et al. 2000; Vanture, Wallerstein & Suntzeff 2002; Kayser et al. 2006; Marcolini et al. 2007; Stanford et al. 2007). Type I supernovae, from binary systems with a degenerate primary, and Wolf-Rayet stars in OB associations have also played a lesser rôle in shaping the chemical abundances of the cluster, particularly nitrogen (Pancino 2002; Cunha et al. 2002; Smith 2006). Gravitational dynamics appear to make it difficult to create ω Cen in its present orbit unless it is created near the Galactic Disc (Zhao 2002; Tsuchiya, Dinescu & Korchagin 2003), suggesting that ω Cen formed as part of hierarchical merging of the proto-Milky Way (Gnedin et al. 2002). The possibility of an overlapping age spread in both the metal-rich and metal-poor populations suggests that the original dwarf galaxy had a composite nature (Villanova et al. 2007).

The main drawback with this version of ω Cen's formation is the large helium-enrichment needed to explain the colour-magnitude diagram ($\gtrsim$14% of the HB contains helium-enhanced stars (Moehler et al. 2007)). The required enrichment, however, is less than what was once thought necessary (Marcolini et al. 2007). A photometric study

carried out by Sollima et al. (2007) using the VLT/FORS1, found the blue-MS to be more centrally condensed than the red-MS, suggesting that the helium over-abundance could have been present as far back as the proto-stellar clouds from which the cluster formed. Furthermore, similar multiple populations have been found in intermediate-age Magellanic Cloud clusters that are not thought to be dwarf galaxy remnants in themselves (Mackey et al. 2008).

The solution to the ω Cen metallicity conundrum therefore seems to be (as is often the case) a combination of factors. Observationally, there appear to be at least three distinct metallicity populations (*e.g.* Hilker & Richtler 2002; Smith 2002; Frinchaboy et al. 2002) with considerable abundance spreads both between and within them. Historically, it appears the cluster may have undergone a merger at some point in its existence; and further spread in the chemical abundances is likely due to a combination of primordial enrichment via supernovae and intermediate-mass AGB star winds, and internal atmospheric mixing on the giant branch. Its enrichment history thus far appears unique among Galactic globulars (Cannon et al. 2002) and it may be close to the upper limit of what we can realistically call a globular cluster.

C.6.7 Variable stars (general)

As with M15 and other clusters, an extensive list of variable stars had been identified by Pickering & Bailey (1895, 1897, 1898), and by Pickering et al. (1898). Bailey & Pickering (1902) present an exhaustive investigation of the first 128 variables discovered. These include four LPVs (V1, V2[6], V6 and V42), two irregular variables with timescales of over a month (V17 and V53), one Type II Cepheid (V29) (see Thackeray 1960), and the then shortest-known period variable, the SX Phe star V65 (see Hertzsprung 1933). Later, Martin (1938a) published photometry on 155 variables, including the irregular variables V138, V148 and V152. The remainder are mostly RR

[6]Identified as a field star by Feast (1965).

Lyrae. Despite this large number of variables, ω Centauri has been accused of being variable-poor, on the basis that although it has more variables than other clusters, it also has a far larger population as a whole (Belserene 1956b). Martin's original photometry and Leiden identifiers (LEIDs) were used by vL+00 for a proper motion membership survey of the cluster, which we use in Chapters 4, 5 & 6.

Further RR Lyrae were discovered by Wilkens (1964). Geyer & Szeidl (1970) note that the RR Lyrae variables span the range $<(B-V)> = 0.15 \sim 0.42$ mag with $<V> \sim 14.5$ mag, extending significantly bluer than their comparison, M 3. Further to this, variability appears to start on the RGB/AGB at around $(B-V) \approx 1.5$ mag (Cannon & Stobie 1973). Period changes have been found in the RR Lyrae stars, showing possible evidence of stellar evolution in progress (Martin 1938a; Wright 1940; Belserene 1961, 1964; Wilkens 1967; Jurcsik 2000).

Kałużny et al. (2004) provide more short-period variables from the CASE catalogue, but also include a few variables with periods of 30–60 days[7] and three others showing probable variations on longer timescales. The cluster's SX Phe stars were revisited by Olech et al. (2005), who find masses of 0.9–1.15 $M_\odot$ and rotation speeds exceeding 100 km s^{-1} for some stars, suggesting these are merged binaries.

C.6.8 Long-period variables

The lightcurve of the optically brightest variable, V1 (LEID 32029, ROA 5701), was improved through measurements by Sawyer (1931) and Martin (1938b). Fourier analysis shows it pulsates irregularly in several overtones of its 220-day period, the dominant mode being identified as 29.34891 or 31.897(2) days, as well as having a secondary period of 176 days (Jones 1968; van Leeuwen et al. 2000). Its spectral type has been identified separately as F0 Ib and F6, its mass estimated at 0.51 $M_\odot$, and its radial

[7]Kałużny, J. and Olech, A. and Thompson, I. B. and Pych, W. and Krzemiński, W. and Schwarzenberg-Czerny, A. () also list new V395 as having a period of 149 days, however this object is co-incident with V42.

velocity amplitude at 25 km s^{-1} (Joy 1949; Jones 1968; González 1994). Chemical models also suggest that ∼0.1% of its atmosphere (and that of ROA 24) is comprised of material mixed from the *s*-processed region (González & Wallerstein 1994).

A further interesting turn was taken when Moehler et al. (1998) announced that this star was a post-AGB object. Surprisingly, they found it to be iron-depleted, which they theorise is due to gas-dust separation in its atmosphere while it was producing a dust-driven wind (*c.f.* van Winckel, Mathis & Waelkens 1992). Recently, Thompson et al. (2006) have performed an abundance analysis with AAT/UCLES. They find a temperature of 25 000 K, $\log g = 3.2 \pm 0.2$ and a microturbulence of $\xi < 10$ km s^{-1}. Moelher et al. suggest V1 has undergone gas-dust separation, whereby radiation pressure forces dust particles away from the star in a circumstellar shell, while the 'cleaned' gas is re-accreted onto the star. Thompson et al. (2006), however, do not find the chemical signatures of this (*e.g.* depleted Fe, Mg and Si, but not S). They suggest *s*-processing may account for the low [Fe/H] ratio (–2.6) derived by Moelher et al. They also suggest that it has not undergone third dredge-up due to its under-abundance of carbon, thus it could be a 'post-early-AGB star' (see, *e.g.* Conlon, Dufton & Keenan 1994; Jasniewicz et al. 2004). Thompson et al. (2007) later confirm Moelher et al.'s iron ratio, citing [Fe/H] = –2.4, and re-derive $T = 25000 \pm 1000$ K, $\log g = 3.3 \pm 0.1$, $\xi = 1^{+2}_{-1}$ km s^{-1} and $v_{\rm rot} = 3$ km s^{-1}.

The variables V6 (LEID 33062) and V42 (LEID 44262, ROA 90) are the cluster's two brightest stars in the infrared. V6's period is irregular: it is listed as 73.513 days in Sawyer Hogg (1973) but 100–120 days in Dickens, Feast & Lloyd Evans (1972). Glass & Feast (1973, 1977) show excess and variability in the L-band. Classified as a M4–5 or S3/1 emission line variable, its radial velocity varies by 36 ± 19 km s^{-1} (Dickens, Feast & Lloyd Evans 1972; Webbink 1981; Vanture, Wallerstein & Suntzeff 2002). It is also known to be a TiO variable and probably shows variable hydrogen emission (Lloyd Evans 1983d, 1983a, 1986). Its temperature has been estimated at 3300–3600 K and its gravity at $\log(g)$ of 0.0 (assuming $M = 0.8$ $M_\odot$; Persson et al. 1980; Frogel 1983). V6

appears to belong to one of the more metal-rich sub-populations ([Fe/H] = –1.22, (Zinn & West 1984); –1.26, (Norris & da Costa 1995); –1.08 ± 0.22, (Vanture, Wallerstein & Suntzeff 2002)), and is mildly *s*-process enhanced. It also shows enhancements of CN, NH and H_2O (Frogel 1983; Cohen & Bell 1986).

V42 has been classified as an M1–2.5 emission line variable, exhibiting possible radial velocity variations between +253 and +272 km s^{-1}. It has been suggested that the star bridges the gap between SRd variables and emission-line LPVs (Feast 1965; Dickens, Feast & Lloyd Evans 1972). Its 148.64(3)-day period is the longest of the cluster members and among the longest-period variables in globulars as a whole (Clement 1997; van Leeuwen et al. 2000). Dickens et al. also report that the TiO bands weaken and hydrogen emission lines are present only at the bluer end of the star's cycle (see also Lloyd Evans 1983a, 1983b), suggesting an additional opacity source. Cacciari & Freeman (1983) estimate $\log(g) = 0.5$ and $T = 3950$ K. Menzies & Whitelock (1985) calculate a much lower temperature of 2818 K, based on infra-red data, and show V42 undergoes substantial variability even in the L-band. It also appears to be enhanced in CN and NH (Cohen & Bell 1986).

V29 (LEID 43105) was classified as a W Vir (Cepheid) variable by Thackeray (1960), later as a post-AGB star by González & Wallerstein (1994), showing temperature variations of around 600 K and a low metallicity of [Fe/H] $= -1.99 \pm 0.14$ (see also González 1994). V43 (LEID 39156), V48 (LEID 46162) and V92 (LEID 26026) were also suggested to be post-AGB objects in the latter two papers.

Although ω Cen has many classified variables, there is considerable evidence that Hα variability (including line core shifts), exists in many more stars (*e.g.* Bates, Kemp & Montgomery 1993). This is likely related to pulsation and thus (probably) varying outflow conditions. Table C.5 lists the known long-period variable stars in ω Cen.

Table C.5: Long-period variable stars and candidate LPVs with periods >20 days in ω Centauri. Colons denote irregular periods/amplitudes.

Number	Period (days)	Amplitude[a] $\Delta(V+R)$	References & Notes
V2	235.74	4.11:	2,2,b,f
V6	110:	1.4	2,2
V16	23.79	0.09	1,1,c
V27	20.3	0.09	1,1,c
V31	23.25	0.05	1,1,c
V42	146.5972	2.4	2,2,b,d
V87	24.39	0.50	1,1,c
V98	21.81	0.02	1,1,c
V123	23.35	0.07	1,1,c,d
V126	23.32	0.03	1,1,c
V157	22.3	$\geq$0.65	1,1,c
V159	23.82	0.80	1,1,c
V160	25.11	0.90	1,1,c
V162	70	0.5	2,2,b
V164	37:	0.3	2,2,b
V223	23.695	0.27	2,2
V224	37.886	0.04	2,2
V269	145	0.83	2,2
V292	46.6		2
V293	98.8		2
V391	60:		2
V392	56.1		2

[a]Sources from Kałużny et al. (2004) have only V-band amplitudes.
[b]Identified as a short-period variable by Weldrake et al.
[c]Identified as a short-period variable by Kałużny et al.
[d]Identical to Kałużny et al.'s V395 (P = 149 days).
[e]Identical to Kałużny et al.'s V216 (P = 23.737 days, ΔV = 0.07).
[f]Field star.
References: 1 — Weldrake, Sackett & Bridges (2007),
2 — Kałużny et al. (2004).

C.6.9 Other stellar curios

The RGO's spectroscopic survey of bright stars in the cluster revealed the first CH star observed in a globular: ROA 55 (Harding 1962 — Harding refers to it as #11051), also known as LEID 52030. Further carbon stars, ROA 70 (Dickens 1972) and ROA 153 (Stock & Wing 1972) were also found. The latter has since been recognised as a non-member (Smith & Wing 1973). Wing & Stock (1973) performed crude spectrophotometry and abundance calculations. Later, ROA 279, ROA 577 (LEID 41071), ROA 134 (LEID 32059), LEID 14043 and LEID 53019 were also identified as carbon stars (Bond 1975; Cowley & Crampton 1985; van Loon et al. 2007).

Fehrenbach & Duflot (1962) uncovered the post-AGB star HD 116745 (LEID 16018, ROA 24, TYC-8252-2789-1), now commonly known as 'Fehrenbach's star'. Van Leeuwen's (2000) proper motion study gave it only an 18% probability of membership, though the RGO spectroscopic analysis and vL+07 show it to have a velocity similar to the cluster. It therefore appears likely that it is a member of the cluster. With its F5 spectral type, it lies well away from the giant branch and has unusual colours for an F-type star (Jones 1973b, 1973a). Glass & Feast (1977) also record its infra-red colours, but do not identify any near-infra-red excess. Abundance analyses of Fehrenbach's star were performed by Dickens & Powell (1973), and González & Wallerstein (1992). It has an estimated [Fe/H] of -1.2 ± 0.3. There appears to be up to a dex difference in relative [metal/Fe] abundances compared to solar values, implying substantial mass loss and mixing. The star ROA 5701 (LEID 30120), with a temperature of $\sim$23 000 K and a heavily-depleted iron and carbon content ([Fe/H] ~ -2.7, [C/H] < -2.7) was later also found to be a post-AGB object by Moehler et al. (1998).

C.6.10 X-ray sources

During the *Einstein* globular cluster observations by Hertz & Grindlay (1983), five point sources (A–E) were discovered in the vicinity of the cluster. The *Einstein* satellite

also reputedly observed diffuse X-ray emission from the cluster, which is described in §C.6.13. *ROSAT* detected all five sources again, and provided a few other detections including HD 116993 (LEID 53208, member), HD 116649 (LEID 88015, non-member) and HD 117193 (Verbunt et al. 1993; Johnston, Verbunt & Hasinger 1994).

The search for optical counterparts to the suspected X-ray cataclysmic variables was at first unsuccessful (Margon & Bolte 1987). The first white dwarf candidates were found in the survey by Ortolani & Rosino (1987). More recently, Carson, Cool & Grindlay (2000) suggest possible CV counterparts for the three sources contained within the *Einstein* C source (the cluster core). Refined positions for the X-ray sources in the core are given by Verbunt & Johnston (2000). Davies (2002) notes that the relative lack of observed X-ray binaries can be explained since the most likely timescales for mass transfer onto a compact object appears to be about 5–10 Gyr ago.

Cool, Haggard & Carlin (2002) report 140 X-ray sources detected in deep *Chandra* data for ω Cen. They estimate that $\sim$30 of these are cluster sources, with the remainder being background objects. They also report OGLE-GC-22 and OGLE-GC-15 as RS CVn and EA variables, respectively. Rutledge et al. (2002) identify one source, CXOU 132619.7–472910.8, with a possible quiescently accreting neutron star in the cluster — unusual in a cluster with no known pulsars — whose companion is estimated to be $\lesssim$ 0.14 $M_\odot$ (Haggard et al. 2004). A radius of $\sim$14 km was assigned to the neutron star, assuming a distance of 5300 pc (Gendre, Barret & Webb 2003).

C.6.11 Stellar mass loss

There are few measurements of mass-loss rates in the literature. Mallia & Pagel (1978) carried out detailed mass-loss estimations on individual stars, finding $\sim$3.5 $\times 10^{-8}$ $M_\odot$ yr^{-1} for ROA 44 & 65 (LEID 38049 & 36036) using a then-novel method to estimate outflow from blueshifted Hα line cores and absorption widths, similar to that used in Chapter 3. Peterson (1981) suggests that mass loss is occurring in ROA 48 & 55 (LEID 32138 & 52030), but declines to estimate a rate due to the uncertainties involved.

Origlia, Ferraro & Fusi Pecci (1995) use the co-incidence between the *IRAS* point source and V42 to estimate the dust mass surrounding the star. Their results suggest that V42 is accountable for a significant fraction of the 12-μm emission for that region of the cluster and is surrounded by a considerable amount of warm dust, ejected at sometime around 1925, and possibly linked to a thermal pulse event. They derive a mass-loss rate of 10^{-6} $M_\odot$ yr^{-1} and a dust temperature of 190 K. Later, the same team (OFFR02) re-derive the mass-loss rate on the basis of ISOCAM data, finding 7.1×10^{-7} $M_\odot$ yr^{-1}, with a 347 K dust envelope.

Finally, Montgomery, Bates & Kemp (1995) show outward motion occurring in ROA 213, but do not comment on the subject of mass loss explicitly. They do suggest that the Na D lines can also be used to estimate mass loss using the same method.

C.6.12 Foreground absorption

The first reference to 'absorbing matter' in ω Centauri comes from Lindsay (1953), who noticed a dark patch on one side of the cluster — *i.e.* a deficit of stars. Fitzgerald (1955), who took the original plate, notes that there are 'lanes' present in the photograph (in particular the 'serpentine "lane" on the western side running from north-west to south-east' and the 'thin dark "lanes"', discernible on the eastern side of the cluster), which are unlikely to be due to patterns in a random distribution of stars. Fitzgerald suggests the extinction comes from filaments in front of the cluster. In a later publication, Lindsay (1956) found that the stellar density on one side of the cluster is less than the other, corresponding to around 0.25 mag difference.

Arp's 1958 study showed little extinction in a region around $30'$ from the cluster centre, with $E(B-V) = 0.03 \pm 0.02$ mag, in agreement with Belserene (1956a). Norris & Bessell (1975) calculated $\Delta E(B-V)$ across the cluster to be 0.04 mag. $E(B-V)$ for the cluster itself is estimated (from Harris 1996; Lub 2002) to be around 0.11∼0.12 mag. Estimates from the foreground Sco-Cen association of stars can be used to set a lower limit of $E(B-V) > 0.07$–0.08 mag for the cluster and a tentative upper limit

from *COBE* CMB data to be E(B–V) < 0.14 mag[8].

The first evidence from spectroscopic observations of foreground absorption is in Jones (1968), who found an interstellar Ca II K line at a velocity of $v_{\rm LSR}$ of +30 km s^{-1} in the spectrum of V1. Bates et al. (1992) also measure the interstellar absorption in the Na D lines and, critically, find the absorption varies significantly on scales of under an arcminute (see also Wood & Bates 1994). Later studies using hot-HB stars confirm this (Calamida et al. 2005, 2006). vL+07 crudely map the foreground ISM using HB stars, finding it denser on the eastern half of the cluster.

Imaging of the Galactic ISM was performed by Danziger, Dennefeld & Schuster (1976), who observed reflection nebulae and patchy obscuration to the south and east of the cluster using long-exposure photography with narrow-band nebulae filters, a feat repeated more clearly in wide-band imaging by Cannon (1980a).

C.6.13 Intra-cluster medium & the high-velocity cloud

Constraints, albeit large ones, were put on the total H II in ω Cen by Hesser & Shawl (1977), though these were of order the expected gas production over a Galactic orbit anyway. To date, no significant detections of H I in ω Cen have been made.

Diffuse X-ray emission, possibly emission from shocks caused by the interaction between the cluster and the halo, was observed by Hartwick, Grindlay & Cowley (1982) using *Einstein*. The morphology they find is consistent with the space motion of the cluster. Assuming that it was shocked material originating from the cluster, moving at 300 km s^{-1} with respect to the ambient medium, Grindlay (1985) calculates a temperature of $\sim 1.4 \times 10^6$ K, and a mass of ~ 12 M$_\odot$ which is replenished at 4×10^{-7} M$_\odot$ yr^{-1}. However, work by Faulkner & Smith (1991a) makes the claim of association less likely on the basis of energetics and further observations by the *UIT* satellite have failed to identify this cloud altogether (Whitney et al. 1994).

[8]This value from Lub (2002) comes with a possible zero-point offset and multiplicative deviation.

H I (21cm) observations were taken from Parkes by Smith et al. (1990). The authors found a high-velocity cloud in the vicinity of ω Cen, blue-shifted from the cluster centre by $\sim$40 km s^{-1} and with a width of $\sim$50 km s^{-1}. It was suggested at the time that this cloud could be part of the Magellanic Stream, or that the gas could represent material in the process of being lost from the cluster. Based on the *Einstein* results, they suggest that gas accumulated within ω Cen could be in a hot, ionised state. They obtain an upper limit for neutral hydrogen within the cluster of 2.8 $M_{\odot}$. We will return to this cloud in Chapter 6.

Origlia et al. (1997) also crudely mapped the cluster in the CO(1-0) transition. They successfully observed a high velocity molecular cloud, which extends across the face of the cluster, with a velocity of around 190$\sim$200 km s^{-1} and brightest near V42. They make an attempt to associate the two objects. We now know that the cloud would have to be at a radial velocity some 60 km s^{-1} different to the star, making such a situation unlikely. Their alternative explanation, that the CO emission traces a high-velocity component of the Magellanic Stream, would appear more likely, though it is not entirely spacially co-incident with the H I detection.

Upper limits on dust measurements in ω Cen lagged behind gas measurements in their relative sensitivities, largely due to the high gas-to-dust ratio, and the need for orbiting observatories for sensitive infrared observation. The first significant limits were placed by Lynch & Rossano (1990), who estimate no more than 7.1×10^{-3} $M_{\odot}$ of warm dust can be present based on 60-μm observations, though this value has a high temperature dependence. We review this figure in Chapters 4 & 5.

Table C.6: Selected data on ω Centauri. Colons denote uncertain values, bracketed figures are uncertainties. References can be found in Appendix B.2.

Property	Value	References
Names	NGC 5139, GCL 24, ESO 270-SC11, C80, Lacaille I.5, Dunlop 440,	S88

Continued on next page

Table C.6 – continued from previous page

Property		Value	References
		Bennett 61, De Cheseaux 18	
Position (J2000.0)		13 26 47.0 –47 28 53	S88
		13 26 45.89 –47 28 36.7	DM93
Distance from Sun		5300, 5360(300), 4900 pc	H96, TKP+01, P93
		4500, 5520(130)	vL+00, dPPS+06
		4800(300) pc	vdV+06
Distance from Gal. Cen.		6400, 6300 pc	H96, D93
Galactic co-ords.	(l, b)	309.10°, –14.97°	H96
	(XYZ)	(3200, –3900, 1400) pc	H96
Dist. mod.	(V mag)	13.97, 13.86, 14.09(4),	H96, G67, KTK+02
		13.83(.10), 14.05(15), 13.92,	K02, CdIM02, D93
		13.27, 14.05(11), 13.70,	vL+00, TKP+01, CSF06
		13.71(5), 13.75(.13)	dPPS+06, vdV+06
		13.68(.27) mag	WSB07
HB Mag.	(V mag)	14.53, 14.52 mag	H96, P93
Turnoff Mag.	(V mag)	18.3 mag	AL87
Integrated V-band mag.		3.68, 3.85, 3.55, 3.53 mag	H96, S82, M87, D93
E(B–V)		0.15, 0.12, 0.11, 0.09(3) mag	D93, H96, RHS88, K02
Δ E(B–V)		$\lesssim$0.04 mag	NB75
Visual abosrption (A_V)		0.47 mag	D93
Abs. Mag	(V)	–10.29, –10.07 mag	H96, D93
Integrated colour	(U–B)	0.19, 0.28, 0.16, 0.10 mag	H96, S82, H84, RHS88
	(B–V)	0.78, 0.62, 0.81, 0.78, 0.67 mag	H96, S82, H84, RHS88
		0.62 mag	K65
	(V–R)	0.51, 1.03, 0.50, 0.44 mag	H96, S82, H84, RHS88
	(V–I)	1.05, 1.29, 1.06, 0.92 mag	H96, S82, H84, RHS88
Spectral type		F5	H96
Core surf. brightness (V)		16.77 mag arcsec^{-2}	H96
Core flux density		3.37 $L_\odot$ pc^{-3}	H96
Metallicity (log [Fe/H])*		–1.62, –1.59(.20), –1.70(7)[a]	H96, ZW84, SK96
Radial velocity (v_{LSR})		232.3(.5), 232.2(.8) km s^{-1}	H96, MM86
		232.02(3) km s^{-1}	vdV+06
Proper motion (μ_x,μ_y)		–3.6, –6.0	RGO1[b]
		–5.1, –3.6 mas yr^{-1}	DGvA99
		–4.0, –4.4 mas yr^{-1}	vL+00
		–4.2, –5.1 mas yr^{-1}	GHGK02
		–3.67, –5.12 mas yr^{-1}	BPB+08
Central density		2679, 3162, 2110 $M_\odot$ pc^{-3}	RFB+91, PM93, MMM97
Ellipticity		$(1 - b/a) = 0.17, 0.12$[e]	H96, GNH83
Inclination		50°(4°)	vdV+06
Relaxation time	Core	1122, 400–2700 Myr	H96, M87
	$\frac{1}{2}$-mass	10, 16–46 Gyr	H96, M87
Radius	Core	$1.40' = 2.15$ pc	H96

Continued on next page

Table C.6 – continued from previous page

Property	Value	References
$\frac{1}{2}$-mass	$4.18' = 6.44$ pc	H96
Tidal	$57.03' = 87.9$ pc	H96
Condensation ($\log(\frac{r_{\rm tidal}}{r_{\rm core}})$)	1.61	(H96 vL+00)
	1.24, 1.15	TKD95, W85
Mass	24.9, >3.24, 10 $\times 10^6$ $M_\odot$	SR75, PA75, ONO76
	3, 3.2(.5), 2.9 $\times 10^6$ $M_\odot$	S83b, MM85, MM86
	3.9, 2.4, 5.1 $\times 10^6$ $M_\odot$	M87, MSS91, M+95
	4.0, 2.9 $\times 10^6$ $M_\odot$	PM95, MMM97
	2.5(.3) $\times 10^6$ $M_\odot$	vdV+06
Escape velocity	51.2 km s^{-1}	W85
Max. rot. vel. $\times \sin(i)$	8.0 $\pm$ 0.7 km s^{-1} at 11.6 pc	MM86
	7.7, 7.9, 8 km s^{-1}	S83b, MMM97, vdV+06
Core velocity dispersion	19.6(2.3), 25$\sim$29 km s^{-1}	MM86, vL+00
Perigalactic distance	2.03 kpc	AM88
Apogalactic distance	7.32 kpc	AM88
Orbital period	1.02 $\times 10^8$ yr	AM88
Est. absolute age (Gyr)	18, 17(1.5), 19[d],	B+84, AL86, P87
	11.8(.6), 11.10(.67),	KTK+02[c], CK02[c]
	(9.1–16.7 & 12.9–18.5),	TKP+01[c], P03
	12–14	TKP+01[c], P03
	$Z_{\rm mp,mi,mr}$ = 12, 10.8, 8	PWH+03*
	$Z_{\rm mp,mi,mr}$ =	
	12.1(1.4), 10.5(1.7), 9.4(0.9)	HKRW04*
Est. age spread† (Gyr)	1.8, 2, 2,	HBCH85, M88, LJS+99
	3, 3, 6,	HR00a, HW00, HR00b
	3–6, 4, 4,	HR02, RJS+02, LRR+02
	4–5, 4, $\geq$4,	P03, PWH+03, S+04
	$\sim$4, 3–5, 3,	RLR04, H+04, HKRW04
	2, 2–4, >3,	SPF+05, S+06, KHRW06
	4–5	VPK+07
Est. [Z/H] spread†	0.5–0.6, 0.4 dex	M88, P03

*ω Cen is known to contain multiple populations at different metallicities, peaking at roughly [Fe/H] $\sim$–1.6, $\sim$–1.2 and –0.9$\sim$–0.5 (Origlia et al. 2003). These are denoted respectively here as *mp* = metal-poor, *mi* = metal-intermediate, *mr* = metal-rich.
†Required age/metallicity spread to explain the dispersion of the giant branch.
[a]Modal value.
[b]Corrected using modern absolute references from Tycho2 data.
[c]For the metal-poor binary OGLE GC-17.
[d]Note that these values are all greater than a Hubble time.
[e]Average value.

D Other works

"The earth was made so various, that the mind
Of desultory man, studious of change
And pleased with novelty, might be indulged."

— William Cowper (1731–1800), *The Task*

This appendix contains other associated works with which I have been involved during my PhD which either do not warrant full discussion in themselves, or in which I only played a small rôle. Their summaries are included as they have implications for the rest of the works herein.

D.1 A spectral atlas of post-main-sequence stars in ω Centauri

Published as van Loon, van Leeuwen, Smalley, et al., 2007, MNRAS, 382, 1353.

This survey obtained spectra for over 1500 stars with proper motions suggesting membership of ω Centauri, confirming membership through radial velocities. By comparison to Kurucz model atmospheres (*c.f.* Chapter 3), first-order estimates of temperatures, gravities and metallicities were automatically generated for these stars.

While numerous conclusions were drawn from this study, the most relevant were the finding of numerous carbon stars, post-AGB stars and other UV-bright stars within the cluster. Several stars were also shown to exhibit hydrogen line emission (*c.f.* Chapter 3).

The radial velocity was used in Chapter 5 as part of membership selection. We also test the association of Ba-rich stars with the anomalous (metal-rich) RGB in §5.6.4.

D.2 NGC 6791: no super mass loss at super-solar metallicity

Published as van Loon, Boyer & McDonald, 2008, ApJ, 680, L49.

D.2.1 Introduction

NGC 6791 is a peculiar open cluster that shares many characteristics with globular clusters. The most important of these is its large age — around 8 Gyr. It is also very metal rich at [Z/H] = 0.39 ± 0.05. These, along with its eccentric and inclined orbit and chemical peculiarities, lead Carraro et al. (2006) to suggest that it is an ω-Cen-like remnant of a disrupted dwarf galaxy, though it does not share ω Cen's metallicity spread.

Arguments exist for larger mass-loss rates in this high-metallicity environment, suggesting that the stars may lose more mass on the RGB, becoming flash-manqué stars and leaving under-massive helium white dwarfs (Castellani & Castellani 1993; Hansen 2005; Kalirai et al. 2007). This would dramatically change the white dwarf populations assumed in such metal-rich systems. By comparing the luminosity functions on the giant branches with models and by observing current mass-loss rates, we can determine whether stars are losing excess mass on the giant branch or not.

D.2.2 Observations

Photometry was extracted from *Spitzer* Space Telescope observations, covering $20' \times 15'$ in the four IRAC bands, offset slightly from the cluster centre. Membership was determined from proper motion observations in the USNO-B and UCAC2 catalogues (Monet et al. 2003; Zacharias et al. 2004) and in Dias et al. (2006). A cut was placed, limiting our analysis to within $6'$ of the cluster centre.

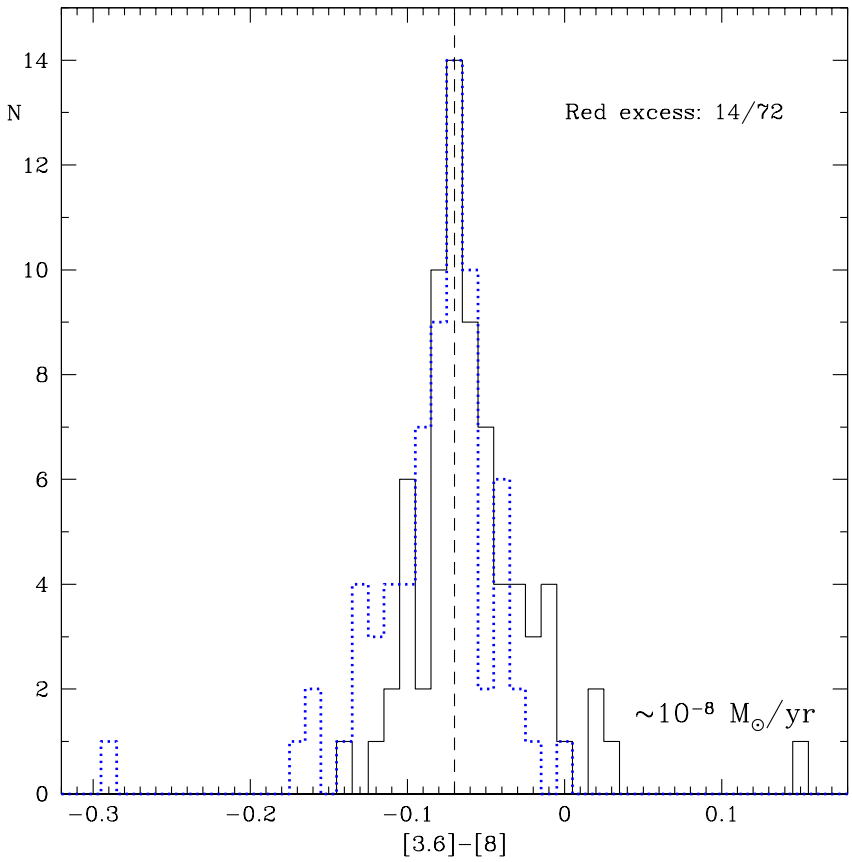

Figure D.1: Distribution of [3.6] − [8] colour in *Spitzer* IRAC data of NGC 6791. The dotted line shows the same histogram, mirrored around the peak, showing an asymmetric distribution indicative of circumstellar dust.

D.2.3 Circumstellar dust

Dust can be inferred by a more positive [3.6] − [8] colour than the bulk of the giant population. A histogram of colour distribution, shown in Fig. D.1, reveals that a small fraction of stars (19%) do show a small colour excess.

A reddening of $\Delta([3.6]-[8]) = 0.1$ mag corresponds to $\dot{M} \sim 1-2\times10^{-8}$ $M_\odot$ yr^{-1}, assuming an M-type star with Al_2O_3 or silicate dust, a luminosity of $L = 3000$ $L_\odot$, a wind speed of $v = 10$ km s^{-1}, and a gas-to-dust ratio of $\psi = 200$ (Groenewegen 2006). In the more metal-rich NGC 6791, we expect $\psi \sim 80$ and $v \sim 16$ km s^{-1} (Marshall et al. 2004). As we also expect $\dot{M} \propto v\sqrt{L}\psi$ (van Loon 2000b), we find that

the actual mass-loss rate is likely to be ~ 5 times lower, *i.e.* $\dot{M} \sim 2 - 4 \times 10^{-9}$ $M_\odot$ yr^{-1}. Higher velocities in chromospherically-driven winds (§3 and references therein) may increase this, but we can conservatively estimate that $\dot{M} \lesssim 10^{-8}$ $M_\odot$ yr^{-1} in these cases. This compares favourably with estimates from Reimers (1975) and Schröder & Cuntz (2005).

The cluster's RGB stars have an initial mass of 1.1 $M_\odot$, thus require 0.7 $M_\odot$ of mass loss to produce the white dwarf masses seen by Kalirai et al. (2007). If mass loss of $\lesssim 10^{-8}$ $M_\odot$ yr^{-1} occurs over 19% of the RGB ($\sim 19\% \times 8 \times 10^7$ yr; Marigo et al. 2008), then total RGB mass loss is still $\lesssim 0.2$ $M_\odot$ — insufficient to produce flash-manqué stars. The fraction of dusty stars also implies that at most $19 \pm 5\%$ of stars can produce flash-manqué stars, and this requires $\dot{M} \sim 10^{-8}$ $M_\odot$ yr^{-1} over the *whole* RGB, in contrast to expectations (§5.6.3.1). A 'super-wind' phase of extreme mass loss ($\sim 10^{-6}$ $M_\odot$ yr^{-1}) may occur near the RGB-tip, as seen in ω Centauri (§5.6.3.4), but this would produce a flash-manqué star with a core mass near-identical to that of a normal CO core that had followed the AGB.

D.2.4 The RGB luminosity function

White dwarf masses 0.1 $M_\odot$ less than the core mass of an RGB-tip star would require a depletion over 0.6 dex in $\log(L)$, or 1.5 magnitudes (Castellani & Castellani 1993, Table 2). To demonstrate this is not the case, luminosity functions were constructed, which are shown in Fig. D.2. These closely match Padova models (Marigo et al. 2008) for an age of 8 Gyr and distance modulus of 13.0 mag, which do not include any RGB mass loss. We do find that the luminosity function *is* depleted toward the upper-RGB, however the early truncation in the infrared can be attributed purely to the stochastic effect of having a small sample of stars in the upper RGB. The early truncation of the V-band data can be expected due to the lack of models matching the metallicity of the cluster ($Z \sim 0.05$), which can be expected from Fig. D.2 to truncate at $\sim 11^{th}$ magnitude, as do the data. Additionally, the size of the red clump in the luminosity

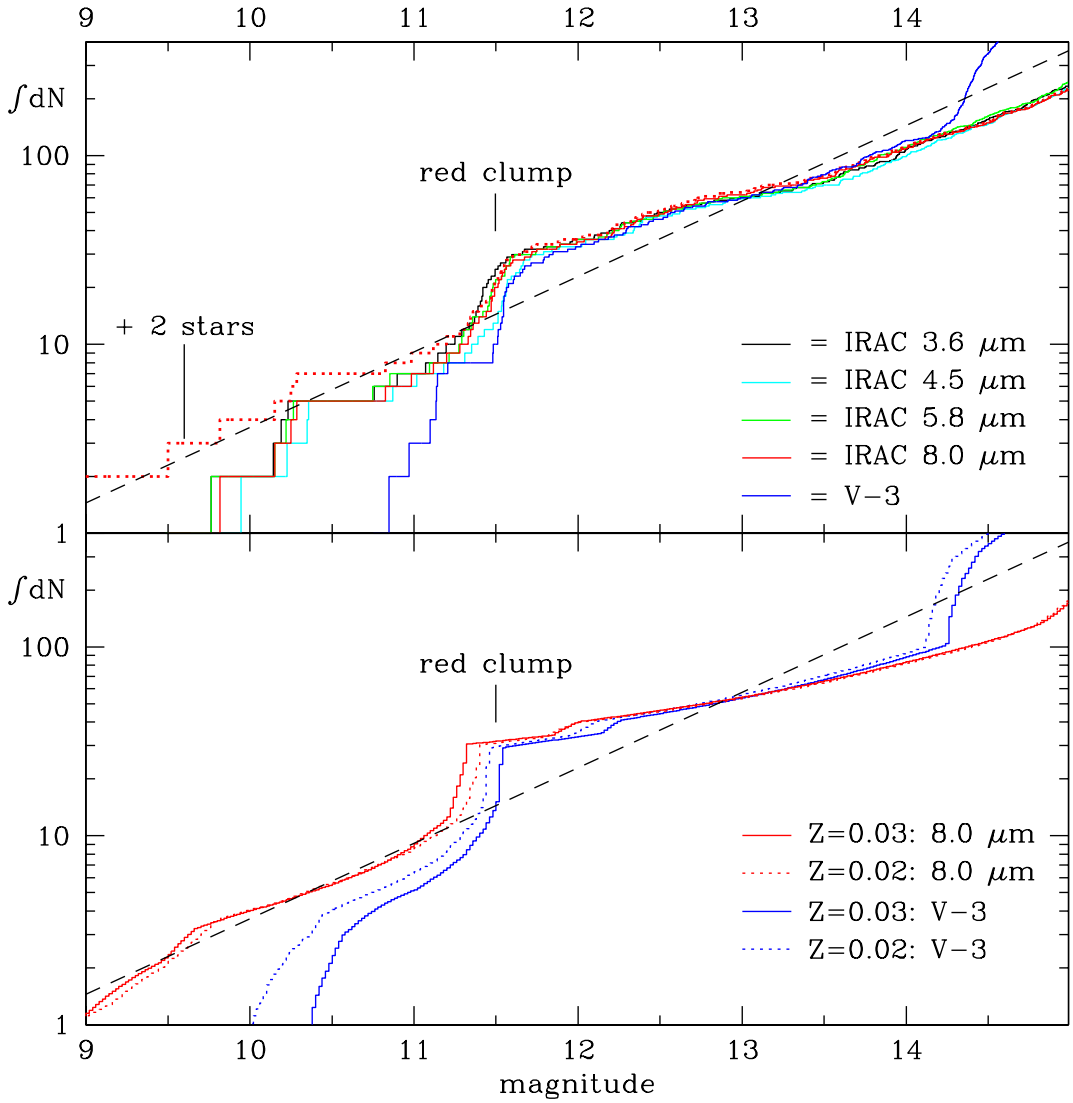

Figure D.2: Cumulative luminosity histograms of NGC 6791 in the four *Spitzer* IRAC bands and V-band (Stetson, Bruntt & Grundahl 2003). The latter is shifted by 3 mag to align the red clump (mag. 11.5). The dash-dotted line shows the 8-μm function with two extra stars, demonstrating that the discrepancy with the corresponding 8-Gyr Padua models (Marigo et al. 2008, lower panel) is merely due to Poissonian noise.

functions also agrees well with the models, confirming that most RGB stars do indeed undergo a helium flash.

D.2.5 Conclusions

Little circumstellar dust is found around stars in NGC 6791, suggesting abnormal RGB mass loss in not occurring. Good agreement is found when comparing the optical and infrared luminosity functions with models, suggesting the vast majority of RGB stars proceed to the red clump and AGB. This suggests that there are few flash-manqué stars to produce the low-mass helium white dwarfs suggested in the literature.

D.3 Detailed maps of interstellar clouds in front of ω Centauri

Accepted for publication as van Loon, Smith, McDonald, et al., 2009, MNRAS.

This study obtained medium-resolution spectra of 452 horizontal-branch stars in ω Centauri. Absorption from the intervening Galactic ISM is clearly present in these spectra, notably around the Ca II K and Na I D_2 lines, but also weakly in the 5780 and 5797 Å diffuse interstellar bands (DIBs).

Spatial maps of the strengths and velocities of these lines were created, and are shown in Figs. 6.7 & 6.8, where we compare these maps to the observed H I emission. From analysis of these maps, and comparison to existing data, it is found that these lines trace neutral and weakly-ionised media in the interface between the Galactic Disc and Halo. The neutral medium is found to be at a likely distance of $1 - 2$ kpc, with the ionised medium at roughly $2 - 4$ kpc. The unidentified DIBs at 5780 and 5797 Å appear to be associated with the extra-planar gas, being associated with ionised and neutral molecules, respectively, based on their location within the clouds. Both the neutral and ionised ISM phases are found to be highly structured down to the level of

$\lesssim$1 pc, even outside the Galactic plane, at large distances from any structure-producing supernovae.

D.4 Other publications

Publications I have been involved in, but not directly related to Galactic globular clusters:

van Loon, Cohen, Oliveira, et al., 2008, A&A, 487, 1055
Molecules and dust production in the Magellanic Clouds

Pollacco, Skillen, Collier Cameron, et al., 2008, MNRAS, 385, 1576
WASP-3b: a strongly-irradiated transiting gas-giant planet

Joshi, Pollacco, Collier Cameron, et al., 2009, MNRAS, 392, 1532
WASP-14b: A 7.7 Jupiter mass transiting exoplanet in an eccentric orbit

Christian, Gibson, Simpson, et al., 2009, MNRAS, 392, 1585
WASP-10b: A 3 Jupiter mass, eccentric transiting gas-giant planet

Hebb, Cameron, Loeillet, et al., 2009, ApJ, 693, 1920
WASP-12b: The hottest transiting planet yet discovered

West, Cameron, Hebb, et al., submitted A&A
The sub-Jupiter mass transiting exoplanet WASP-11b

Bibliography

Adams W. S., MacCormack E., 1935, ApJ, 81, 119

Adelman-McCarthy J. K., Agüeros M. A., Allam S. S., Allende Prieto C., Anderson K. S. J., Anderson S. F., Annis J., Bahcall N. A., Bailer-Jones C. A. L., Baldry I. K., Barentine J. C., Bassett B. A., et al., 2008, ApJS, 175, 297

Agúndez M., Cernicharo J., Pardo J. R., Fonfría Expósito J. P., Guélin M., Tenenbaum E. D., Ziurys L. M., Apponi A. J., 2008, Ap&SS, 313, 229

Albrow M. D., Gilliland R. L., Brown T. M., Edmonds P. D., Guhathakurta P., Sarajedini A., 2001, ApJ, 559, 1060

Alcaíno G., Liller W., 1986, MmSAI, 57, 321

Alcaíno G., Liller W., 1987, AJ, 94, 1585

Alcaíno G., 1981, A&AS, 44, 33

Allen C., Martos M. A., 1988, Revista Mexicana de Astronomia y Astrofisica, 16, 25

Alonso A., Arribas S., Martínez-Roger C., 1999, A&AS, 140, 261

Alves D. R., Bond H. E., Livio M., 2000, AJ, 120, 2044

Anderson J., 2002, in van Leeuwen F., Hughes J. D., Piotto G., eds, Omega Centauri, A Unique Window into Astrophysics, 87

Anderson S. B., Gorham P. W., Kulkarni S. R., Prince T. A., Wolszczan A., 1990, Nature, 346, 42

Anderson J., King I. R., Meylan G., 1998, Bull. Amer. Astron. Soc., 30, 1347

Armandroff T. E., Demarque P., 1984, A&A, 139, 305

Armandroff T. E., Zinn R., 1988, AJ, 96, 92

Arp H. C., 1955, AJ, 60, 317

Arp H. C., 1958, AJ, 63, 118

Ashman K. M., Zeph S. E., 1998, Globular Cluster Systems, Cambridge University Press

Ashurov A. E., van Leeuwen F., 2002, in van Leeuwen F., Hughes J. D., Piotto G., eds, Omega Centauri, A Unique Window into Astrophysics, 51

Asida S. M., Tuchman Y., 1995, ApJ, 455, 286

Aurière M., Cordoni J.-P., 1981, A&AS, 46, 347

Aurière M., Leroy J. L., 1990, A&A, 234, 164

Aurière M., Cordoni J. P., Koch-Miramond L., 1985, IAUC, 4101, 1

Aurière M., Laques P., Leroy J. L., 1978, A&A, 63, 341

Avrett E. H., Löser R., 1992, in Giampapa M. S., Bookbinder J. A., eds, ASP Conf. Ser. 26: Cool Stars, Stellar Systems, and the Sun, 489

Baade W., 1944, ApJ, 100, 137

Bahcall J., 2004, Dark Matter in the Universe, World Scientific

Bailey S. I., Pickering E. C., 1902, Annals of Harvard College Observatory, 38, 1

Bailey S. I., Leland E. F., Woods I. E., Pickering E. C., 1919, Annals of Harvard College Observatory, 78, 195

Bailyn C. D., Grindlay J. E., Cohn H., Lugger P. M., Stetson P. B., Hesser J. E., 1989, AJ, 98, 882

Bailyn C. D., Sarajedini A., Cohn H., Lugger P. M., Grindlay J. E., 1992, AJ, 103, 1564

Bao-An Y., 1990, IBVS, 3431, 1

Barbier M., Petit H., Mayor M., Mennessier M. O., 1988, A&AS, 72, 463

Barlai K., Szeidl B., 1995, IBVS, 4171, 1

Barmby P., Boyer M. L., Woodward C. E., Gehrz R. D., van Loon J. T., Fazio G. G., Marengo M., Polomski E., 2009, AJ, 137, 207

Barnard E. E., 1919, ApJ, 49, 1

Barnard E. E., 1931, Publications of the Yerkes Observatory, 6, 1

Barnes D. G., Staveley-Smith L., de Blok W. J. G., Oosterloo T., Stewart I. M., Wright A. E., Banks G. D., Bhathal R., Boyce P. J., Calabretta M. R., Disney M. J., Drinkwater M. J., et al., 2001, MNRAS, 322, 486

Bassino L. P., Muzzio J. C., 1995, The Observatory, 115, 256

Bates B., Wood K. D., Catney M. G., Gilheany S., 1992, MNRAS, 254, 221

Bates B., Kemp S. N., Montgomery A. S., 1993, A&AS, 97, 937

Baumgardt H., Hut P., Makino J., McMillan S., Portegies Zwart S., 2003, ApJL, 582, 21

Baumgardt H., Makino J., Hut P., 2005, ApJ, 620, 238

Bayer J., Mair A., 1603, Ioannis Bayeri Rhainani I.C. Uranometria: omnium asterismorum continens schemata, no a methodo delineata, aereis laminis expressa, Augustae Vindelicorum: Excudit Christophorus Mangus

Beck H. K. B., Gail H.-P., Henkel R., Sedlmayr E., 1992, A&A, 265, 626

Bedin L. R., Piotto G., Anderson J., Cassisi S., King I. R., Momany Y., Carraro G., 2004, ApJL, 605, 125

Behr B. B., Djorgovski S. G., Cohen J. G., McCarthy J. K., Côté P., Piotto G., Zoccali M., 2000, ApJ, 528, 849

Beichmann C. A., Helou G., Walker D. W., 1988, Infrared astronomical satellite (IRAS). Catalogs and atlases, NASA RP (Reference Publication). NASA, Washington.

Beintema D. A., van den Ancker M. E., Molster F. J., Waters L. B. F. M., Tielens A. G. G. M., Waelkens C., de Jong T., de Graauw T., Justtanont K., Yamamura I., Heras A., Lahuis F., Salama A., 1996, A&A, 315, 369

Bekki K., Freeman K. C., 2003, MNRAS, 346, 11

Bell R. A., Manduca A., 1977, Bull. Amer. Astron. Soc., 602

Bell R. A., Cannon R. D., Harris G. L. H., Hesser J. E., 1981, ApJ, 249, 637

Bell R. A., Cannon R. D., Harris G. L. H., Hesser J. E., 1984, Bull. Amer. Astron. Soc., 734

Bellazzini M., Pecci F. F., Ferraro F. R., Galleti S., Catelan M., Landsman W. B., 2001, AJ, 122, 2569

Bellazzini M., Ferraro F. R., Sollima A., Pancino E., Origlia L., 2004, A&A, 424, 199

Bellazzini M., Ibata R. A., Chapman S. C., Mackey A. D., Monaco L., Irwin M. J., Martin N. F., Lewis G. F., Dalessandro E., 2008, AJ, 136, 1147

Bellini A., Piotto G., Bedin L. R., Anderson J., Platais I., Momany Y., Moretti A., Milone A. P., Ortolani S., 2009, A&A, 493, 959

Belokurov V., Evans N. W., Irwin M. J., Hewett P. C., Wilkinson M. I., 2006, ApJL, 637, 29

Belserene E. P., 1956a, Contributions from the Rutherford Observatory of Columbia University New York, 33, 1

Belserene E. P., 1956b, Contributions from the Rutherford Observatory of Columbia University New York, 33, 13

Belserene E. P., 1959, AJ, 64, 58

Belserene E. P., 1961, AJ, 66, 38

Belserene E. P., 1964, AJ, 69, 475

Benacquista M., 2002, Living Reviews in Relativity, 5, 2

Bessell M. S., Norris J., 1976, ApJ, 208, 369

Bhatt H. C., 1988, MNRAS, 233, 867

Bianchi L., Ford H., Bohlin R., Paresce F., de Marchi G., 1995, A&A, 301, 537

Bianchi L., Bohlin R., Catanzaro G., Ford H., Manchado A., 2001, AJ, 122, 1538

Bica E. L. D., Pastoriza M. G., 1983, Ap&SS, 91, 99

Bica E., Dottori H., Pastoriza M., 1986, A&A, 156, 261

Biermann L., 1951, Zeitschrift fur Astrophysik, 29, 274

Binney J., Tremaine S., 1988, Galactic Dynamics, Princeton University Press

Bittner J. D., Howard J. B., 1981, Pittsburgh: The Combustion Institute: 18th Symp. (International) on Combustion, 313

Bland-Hawthorn J., Sutherland R., Agertz O., Moore B., 2007, ApJL, 670, 109

Blöcker T., 2001, Ap&SS, 275, 1

Böhm-Vitense E., Szkody P., 1973, ApJ, 184, 211

Boily C. M., 2000, in Lançon A., Boily C. M., eds, Massive Stellar Clusters, 190

Bolte M., 1987, ApJ, 315, 469

Bolte M., 1989, AJ, 97, 1688

Bonačić Marinović A., Izzard R. G., Lugaro M., Pols O. R., 2007, A&A, 469, 1013

Bond H. E., 1975, ApJL, 202, 47

Bonnell I. A., Davies M. B., 1998, MNRAS, 295, 691

Bono G., Caputo F., Marconi M., 1995, AJ, 110, 2365

Bono G., Fulle M., Pulone L., 1990, in Vangioni-Flam E., Audouze J., Casse M., Tran Thanh van J., eds, Proceedings of the Fifth IAP Workshop, Astrophysical Ages and Dating Methods, June 26-30, 1989. Editions Frontieres, Gif sur Yvette, France., 283

Bowen G. H., 1988a, in Stalio R., Willson L. A., eds, ASSL Vol. 148: Pulsation and Mass Loss in Stars, 3

Bowen G. H., 1988, ApJ, 329, 299

Boyer M. L., Woodward C. E., van Loon J. T., Gordon K. D., Evans A., Gehrz R. D., Helton L. A., Polomski E. F., 2006, AJ, 132, 1415

Boyer M. L., McDonald I., van Loon J. T., Woodward C. E., Gehrz R. D., Evans A., Dupree A. K., 2008, AJ, 135, 1395

Brahe T., 1603a, Astronomiae Instauratae Progymnasmata, in Opera omnia 2, 307, [reprinted] Swets and Zeitlinger, Amsterdam, 1972

Brahe T., 1603b, Astronomiae Instauratae Progymnasmata, in Opera omnia 3, 81, [reprinted] Swets and Zeitlinger, Amsterdam, 1972

Brandt J. C., 1970, Introduction to the solar wind, Series of Books in Astronomy and Astrophysics, San Francisco: Freeman

Bressan A., Granato G. L., Silva L., 1998, A&A, 332, 135

Brosche P., Geffert M., Dörenkamp P., Tucholke H.-J., Klemola A. R., Ninković S., 1991, AJ, 102, 2022

Brown J. A., Wallerstein G., 1993, AJ, 106, 133

Brown A., 1951, ApJ, 113, 344

Brown J. A., Wallerstein G., Cunha K., Smith V. V., 1991, A&A, 249, 13

Brüns C., Kerp J., Staveley-Smith L., Mebold U., Putman M. E., Haynes R. F., Kalberla P. M. W., Muller E., Filipović M. D., 2005, A&A, 432, 45

Buonanno R., Corsi C. E., Fusi Pecci F., 1985, A&A, 145, 97

Busso G., Cassisi S., Piotto G., Castellani M., Romaniello M., Catelan M., Djorgovski S. G., Recio Blanco A., Renzini A., Rich M. R., Sweigart A. V., Zoccali M., 2007, A&A, 474, 105

Busso G., Piotto G., Cassisi S., 2004, MmSAI, 75, 46

Butler R. F., Shearer A., Redfern R. M., Colhoun M., O'Kane P., Penny A. J., Morris P. W., Griffiths W. K., Cullum M., 1998, MNRAS, 296, 379

Cacciari C., Freeman K. C., 1983, ApJ, 268, 185

Cacciari C., Bragaglia A., Rossetti E., Fusi Pecci F., Mulas G., Carretta E., Gratton R. G., Momany Y., Pasquini L., 2004, A&A, 413, 343

Cacciari C., Sollima A., Ferraro F. R., 2006, MmSAI, 77, 245

Cahn J. H., Wyatt S. P., 1978, ApJL, 224, 79

Calamida A., Stetson P. B., Bono G., Freyhammer L. M., Grundahl F., Hilker M., Andersen M. I., Buonanno R., Cassisi S., Corsi C. E., Dall'Ora M., del Principe M., et al., 2005, ApJL, 634, 69

Calamida A., Stetson P. B., Bono G., Freyhammer L. M., Grundahl F., Hilker M., Buonanno R., Corsi C. E., del Principe M., Piersimoni A. M., 2006, MmSAI, 77, 324

Calamida A., Corsi C. E., Bono G., Stetson P. B., Prada Moroni P., Degl'Innocenti S., Ferraro I., Iannicola G., Koester D., Pulone L., Monelli M., Amico P., Buonanno R., Caputo F., D'Odorico S., Freyhammer L. M., Marchetti E., Nonino M., Romaniello M., 2008, ApJL, 673, 29

Calamida A., Corsi C. E., Bono G., Stetson P. B., Prada Moroni P. G., Degl'Innocenti S., Ferraro I., Iannicola G., Koester D., Pulone L., Monelli M., Amico P., Buonanno R., Freyhammer L. M., Marchetti E., Nonino M., Romaniello M., 2008b, MmSAI, 79, 347

Caldwell S. P., Dickens R. J., 1988, MNRAS, 233, 367

Callanan P. J., Fabian A. C., Tennant A. F., Redfern R. M., Shafer R. A., 1987, MNRAS, 224, 781

Caloi V., Panagia N., 1974, A&A, 36, 139

Caloi V., Castellani A., Castellani V., Macchetto F., Melnick J., 1981, A&A, 103, 386

Campbell W. W., 1892, A&A, 11, 799

Campbell B., 1986, ApJ, 307, 750

Cannon A. J., Pickering E. C., 1924, Henry Draper (HD) catalog and HD extension, Annals of the Astronomical Observatory, Cambridge: Harvard College, Astronomical Observatory, 1924

Cannon R. D., Stewart N. J., 1981, MNRAS, 195, 15

Cannon R. D., Stobie R. S., 1973, MNRAS, 162, 227

Cannon R. D., 1980, A&A, 81, 379

Cannon R. D., 1980b, in Hesser J. E., ed., Star Formation, 429

Cannon R. D., Croke B. F. W., da Costa G. S., Norris J. E., 2002, in van Leeuwen F., Hughes J. D., Piotto G., eds, Omega Centauri, A Unique Window into Astrophysics, 119

Caputo F., Castellani V., 1975, Ap&SS, 38, 39

Caputo F., 1979, MmSAI, 50, 113

Caputo F., 1981, Ap&SS, 76, 329

Carbon D. F., Romanishin W., Langer G. E., Butler D., Kemper E., Trefzger C. F., Kraft R. P., Suntzeff N. B., 1982, ApJS, 49, 207

Carciofi A. C., Bjorkman J. E., Magalhães A. M., 2004, ApJ, 604, 238

Cargile P., Gebhardt K., Sneden C., Pilachowski C. A., 2003, Bull. Amer. Astron. Soc., 1291

Cariulo P., Castellani V., degl'Innocenti S., 2004, VizieR Online Data Catalog, 6113

Carraro G., Lia C., 2000, A&A, 357, 977

Carraro G., Villanova S., Demarque P., McSwain M. V., Piotto G., Bedin L. R., 2006, ApJ, 643, 1151

Carretta E., Gratton R. G., 1997, A&AS, 121, 95

Carretta E., Gratton R. G., Clementini G., Fusi Pecci F., 2000, ApJ, 533, 215

Carretta E., Bragaglia A., Gratton R. G., Momany Y., Recio-Blanco A., Cassisi S., François P., James G., Lucatello S., Moehler S., 2007, A&A, 464, 967

Carson J. E., Cool A. M., Grindlay J. E., 2000, ApJ, 532, 461

Castellani M., Castellani V., 1993, ApJ, 407, 649

Castellani V., degl'Innocenti S., Marconi M., 2002, in van Leeuwen F., Hughes J. D., Piotto G., eds, Omega Centauri, A Unique Window into Astrophysics, 193

Castellani V., Chieffi A., Tornambe A., Pulone L., 1985, ApJ, 296, 204

Castellani V., Degl'Innocenti S., Marconi M., Prada Moroni P. G., Sestito P., 2003, A&A, 404, 645

Castellani V., Giannone P., Renzini A., 1970, Ap&SS, 9, 418

Castellani V., Maceroni C., Tosi M., 1983, A&A, 128, 64

Castor J. I., 1970, MNRAS, 149, 111

Catelan M., 2000, in Noels A., Magain P., Caro D., Jehin E., Parmentier G., Thoul A. A., eds, Liège Int. Astroph. Colloq., 485

Catelan M., Borissova J., Sweigart A. V., Spassova N., 1998, ApJ, 494, 265

Catelan M., Bellazzini M., Landsman W. B., Ferraro F. R., Fusi Pecci F., Galleti S., 2001, AJ, 122, 3171

Catelan M., Bellazzini M., Ferraro F. R., Fusi Pecci F., Galleti S., Landsman W. B., 2002, in Geisler D. P., Grebel E. K., Minniti D., eds, Extragalactic Star Clusters, 116

Catelan M., Stetson P. B., Pritzl B. J., Smith H. A., Kinemuchi K., Layden A. C., Sweigart A. V., Rich R. M., 2006, ApJL, 651, 133

Catelan M., Rood R. T., Ferraro F. R., 2002, in Geisler D. P., Grebel E. K., Minniti D., eds, Extragalactic Star Clusters, 113

Cayrel de Strobel G., Soubiran C., Ralite N., 2001, A&A, 373, 159

Cederbloom S. E., Moss M. J., Cohn H. N., Lugger P. M., Bailyn C. D., Grindlay J. E., McClure R. D., 1992, AJ, 103, 480

Chaboyer B., Krauss L. M., 2002, ApJL, 567, 45

Chaboyer B., Sarajedini A., Demarque P., 1992, ApJ, 394, 515

Chabrier G., 2001, ApJ, 554, 1274

Charles P. A., Clarkson W. I., van Zyl L., 2002, New Astronomy, 7, 21

Charles P. A., Jones D. C., Naylor T., 1986, Nature, 323, 417

Cháves M., Holberg J. B., Landsman W. B., 1999, AJ, 117, 962

Chernoff D., 1993, ASP Conference Series, 50, 243

Chiosi C., 1998, in Aparicio A., Herrero A., Sánchez F., eds, Stellar astrophysics for the local group: VIII Canary Islands Winter School of Astrophysics, 1

Cho D.-H., Lee S.-G., 2007, AJ, 133, 2163

Choi E., Yi S. K., 2008, MNRAS, 386, 1332

Christensen-Dalsgaard J., Kjeldsen H., Mattei J. A., 2001, ApJL, 562, 141

Chu Y.-H., 1976, Acta Astronomica Sinica, 17, 157

Cioni M.-R. L., Girardi L., Marigo P., Habing H. J., 2006, A&A, 448, 77

Cioni M.-R. L., Girardi L., Marigo P., Habing H. J., 2006, A&A, 452, 195

Cioni M.-R. L., Girardi L., Marigo P., Habing H. J., 2006, A&A, 456, 967

Clark G. W., Markert T. H., Li F. K., 1975, ApJL, 199, 93

Clement C., 1997, VizieR Online Data Catalog, 5097

Clement C. M., Muzzin A., Dufton Q., Ponnampalam T., Wang J., Burford J., Richardson A., Rosebery T., Rowe J., Hogg H. S., 2001, AJ, 122, 2587

Cohen J. G., Bell R. A., 1986, ApJ, 305, 698

Cohen J. G., 1976, ApJL, 203, 127

Cohen J. G., 1981, ApJ, 247, 869

Cohen M., Walker R. G., Carter B., Hammersley P., Kidger M., Noguchi K., 1999, AJ, 117, 1864

Condon J. J., Cotton W. D., Greisen E. W., Yin Q. F., Perley R. A., Taylor G. B., Broderick J. J., 1998, AJ, 115, 1693

Conklin I. K., Kimble R. A., 1974, Bull. Amer. Astron. Soc., 468

Conlon E. S., Dufton P. L., Keenan F. P., 1994, A&A, 290, 897

Cool A. M., Haggard D., Carlin J. L., 2002, in van Leeuwen F., Hughes J. D., Piotto G., eds, Omega Centauri, A Unique Window into Astrophysics, 277

Corbet R., Peele A., Smith D. A., 1997, IAUC, 6632, 3

Corwin T. M., Borissova J., Catelan M., Smith H. A., Kurtev R., 2006a, MmSAI, 77, 107

Corwin T. M., Sumerel A. N., Pritzl B. J., Smith H. A., Catelan M., Sweigart A. V., Stetson P. B., 2006, AJ, 132, 1014

Corwin T. M., Borissova J., Stetson P. B., Catelan M., Smith H. A., Kurtev R., Stephens A. W., 2008, AJ, 135, 1459

Cowley A. P., Crampton D., 1985, PASP, 97, 835

Cudworth K. M., 1976, AJ, 81, 519

Cunha K., Smith V. V., Suntzeff N. B., Norris J. E., da Costa G. S., 2002, in van Leeuwen F., Hughes J. D., Piotto G., eds, Omega Centauri, A Unique Window into Astrophysics, 117

Cuntz M., Ulmschneider P., 1994, in Caillault J.-P., ed., ASP Conf. Ser. 64: Cool Stars, Stellar Systems, and the Sun, 368

Cuntz M., 1992, in Giampapa M. S., Bookbinder J. A., eds, ASP Conf. Ser. 26: Cool Stars, Stellar Systems, and the Sun, 383

Cuntz M., 1997, A&A, 325, 709

Cuntz M., Harper G. M., Bennett P. D., 2001, A&A, 376, 154

Curtis H., 1921a, BNRC, 2, 171

Curtis H., 1921b, BNRC, 2, 194

Cutri R. M., Nelson B. O., Kirkpatrick J. D., Huchra J. P., Smith P. S., 2001, in Clowes R., Adamson A., Bromage G., eds, The New Era of Wide Field Astronomy, 78

Cutri R. M., Skrutskie M. F., van Dyk S., Beichman C. A., Carpenter J. M., Chester T., Cambrésy L., Evans T., Fowler J., Gizis J., Howard E., Huchra J., et al., 2003, 2MASS All Sky Catalog of point sources., The IRSA 2MASS All-Sky Point Source Catalog, NASA/IPAC Infrared Science Archive.

da Costa G. S., Armandroff T. E., 1995, AJ, 109, 2533

da Costa G. S., Coleman M. G., 2008, AJ, 136, 506

da Costa G. S., Stanford L. M., Norris J. E., Cannon R. D., 2005, in Hill V., François P., Primas F., eds, From Lithium to Uranium: Elemental Tracers of Early Cosmic Evolution, 369

Danchi W. C., Bester M., Degiacomi C. G., Greenhill L. J., Townes C. H., 1994, AJ, 107, 1469

d'Antona F., 2004, MmSAI, 75, 377

d'Antona F., Vietri M., Pesce E., 1995, MNRAS, 272, 730

Danziger I. J., Dennefeld M., Schuster H. E., 1976, A&A, 48, 479

Davies M. B., 2002, in van Leeuwen F., Hughes J. D., Piotto G., eds, Omega Centauri, A Unique Window into Astrophysics, 215

Davis D. S., Richer H. B., Anderson J., Brewer J., Hurley J., Kalirai J. S., Rich R. M., Stetson P. B., 2008, AJ, 135, 2155

d'Cruz N., Dorman B., Rood R., O'Connell R., 1995, Bull. Amer. Astron. Soc., 840

d'Cruz N. L., Dorman B., Rood R. T., O'Connell R. W., 1996, ApJ, 466, 359

de Angeli F., Piotto G., Cassisi S., Busso G., Recio-Blanco A., Salaris M., Aparicio A., Rosenberg A., 2005, AJ, 130, 116

de Boer K. S., 1985, A&A, 142, 321

de Buizer J., Fisher R., 2005, in Käufl H. U., Siebenmorgen R., Moorwood A., eds, High Resolution Infrared Spectroscopy in Astronomy, 84

de Lacaille N. L., 1755, Mem. Roy. Acad. Paris, 1, 194

de Lacaille N. L., 1763, Coelum Australe Stelliferum, Paris: Sumptibus Hipp. Lud. Guerin & Lud. Fr. Delatour, ed. J. D. Maraldi

de Laverny P., Mennessier M. O., Mignard F., Mattei J. A., 1998, A&A, 330, 169

de Marchi G., Paresce F., 1994, ApJ, 422, 597

de Marchi G., Pulone L., Paresce F., Tidal Disruption and the Tale of Three Clusters, 419, 2009

de Vaucouleurs G., 1953, MNRAS, 113, 134

Decin L., Eriksson K., 2007, A&A, 472, 1041

Decin L., Cherchneff I., Hony S., Dehaes S., de Breuck C., Menten K. M., 2008, A&A, 480, 431

Dehaes S., Groenewegen M. A. T., Decin L., Hony S., Raskin G., Blommaert J. A. D. L., 2007, MNRAS, , 257

del Principe M., Piersimoni A. M., Storm J., Bono G., Caputo F., Cassisi S., Freyhammer L. M., Marconi M., Stetson P. B., 2006, MmSAI, 77, 330

Demarque P., Armandroff T. E., 1984, Bull. American Astron. Soc., 16, 526

Demarque P., Lee Y. W., Zinn R., Green E. M., 1988, in Cayrel de Strobel G., Spite M., Lloyd Evans T., eds, The Abundance Spread within Globular Clusters: Spectroscopy of Individual Stars JCM 5 and CM 37/3, 97

Demarque P., Mengel J. G., Sweigart A. V., 1972, ApJL, 173, 27

Demers S., Kunkel W. E., Hardy E., 1979, ApJ, 232, 84

Denissenkov P. A., Tout C. A., 2000, MNRAS, 316, 395

Denissenkov P. A., Weiss A., 1996, A&A, 308, 773

Derekas A., Kiss L. L., Bedding T. R., Kjeldsen H., Lah P., Szabó G. M., 2006, ApJL, 650, 55

Deutsch A. J., 1956, ApJ, 123, 210

Deutsch A. J., 1967, PASP, 79, 431

Deutsch A. J., 1970, in Houziaux L., Butler H. E., eds, IAU Symp. 36: Ultraviolet Stellar Spectra and Related Ground-Based Observations, 199

Dias W. S., Assafin M., Flório V., Alessi B. S., Líbero V., 2006, A&A, 446, 949

Dickens R. J., Bell R. A., 1976, ApJ, 207, 506

Dickens R. J., Carey J. V., 1967, Royal Greenwich Observatory Bulletin, 129, 335

Dickens R. J., Powell A. L. T., 1973, MNRAS, 161, 249

Dickens R. J., Saunders J., 1965, Royal Greenwich Observatory Bulletin, 101, 101

Dickens R. J., Woolley R. v. d. R., 1967, Royal Greenwich Observatory Bulletin, 128, 255

Dickens R. J., 1972, MNRAS, 159, 7P

Dickens R. J., Croke B. F. W., Cannon R. D., Bell R. A., 1991, Nature, 351, 212

Dickens R. J., Feast M. W., Lloyd Evans T., 1972, MNRAS, 159, 337

Dickens R. J., Woolley R. v. d. R., Carey J. V., 1966, Royal Observatory Annals, 2, 1

Dieball A., Knigge C., Zurek D. R., Shara M. M., Long K. S., Charles P. A., Hannikainen D. C., van Zyl L., 2005, ApJL, 634, 105

Dieball A., Knigge C., Zurek D. R., Shara M. M., Long K. S., Charles P. A., Hannikainen D., 2007, ApJ, 670, 379

Dijkstra C., Speck A. K., Reid R. B., Abraham P., 2005, ApJL, 633, 133

Dinescu D. I., 2002, in van Leeuwen F., Hughes J. D., Piotto G., eds, Omega Centauri, A Unique Window into Astrophysics, 365

Dinescu D. I., Majewski S. R., Girard T. M., Cudworth K. M., 2000, AJ, 120, 1892

Dinescu D. I., Girard T. M., van Altena W. F., 1999, AJ, 117, 1792

Djorgovski S., Meylan G., 1993, in Djorgovski S. G., Meylan G., eds, Structure and Dynamics of Globular Clusters, 325

Djorgovski S., 1993, in Djorgovski S. G., Meylan G., eds, Structure and Dynamics of Globular Clusters, 373

Dopita M. A., Smith G. H., 1986, ApJ, 304, 283

Dorfi E. A., Höfner S., 1996, A&A, 313, 605

Dorman B., Shah R. Y., O'Connell R. W., Landsman W. B., Rood R. T., Bohlin R. C., Neff S. G., Roberts M. S., Smith A. M., Stecher T. P., 1997, ApJL, 480, 31

Dotani T., Inoue H., Murakami T., Nagase F., Tanaka Y., 1990, Nature, 347, 534

Dotter A., 2008, ApJL, 687, 21

Dotter A., Chaboyer B., Jevremović D., Kostov V., Baron E., Ferguson J. W., 2008, ApJS, 178, 89

Draine B. T., Lee H. M., 1984, ApJ, 285, 89

Draine B. T., Salpeter E. E., 1979, ApJ, 231, 77

Draine B. T., 1981, in Iben, Jr. I., Renzini A., eds, Physical Processes in Red Giants, 317

Draine B. T., 1989, in Böhm-Vitense E., ed., Infrared Spectroscopy in Astronomy, 93

Dreyer J. L. E., 1888, MRAS, 49, 1

Dreyer J. L. E., 1895, MRAS, 51, 185

Dreyer J. L. E., 1898, Trans. Royal Irish Acad., 26, 397

Dreyer J. L. E., 1908, MRAS, 59, 105

Drukier G. A., Slavin S. D., Cohn H. N., Lugger P. M., Berrington R. C., Murphy B. W., Seitzer P. O., 1998, AJ, 115, 708

Dubath P., Meylan G., 1994, A&A, 290, 104

Dubath P., Mayor M., Meylan G., 1993, in Djorgovski S. G., Meylan G., eds, Structure and Dynamics of Globular Clusters, 69

Dubath P., Meylan G., Mayor M., 1991, The Messenger, 64, 35

Dubath P., Meylan G., Mayor M., 1994, ApJ, 426, 192

Duley W. W., Williams D. A., 1981, MNRAS, 196, 269

Dull J. D., Cohn H. N., Lugger P. M., Murphy B. W., Seitzer P. O., Callanan P. J., Rutten R. G. M., Charles P. A., 1997, ApJ, 481, 267

Dunlop J., 1828, Philosophical Transactions Series I, 118, 113

Dupree A. K., Whitney B. A., 1991, Nature, 354, 284

Dupree A. K., Hartmann L., Smith G. H., Rodgers A. W., Roberts W. H., Zucker D. B., 1994, ApJ, 421, 542

Dupree A. K., Hartmann L., Avrett E. H., 1984, ApJL, 281, 37

Dupree A. K., Hartmann L., Smith G. H., 1990, in Wallerstein G., ed., ASP Conf. Ser. 9: Cool Stars, Stellar Systems, and the Sun, 408

Dupree A. K., Sasselov D. D., Lester J. B., 1992, ApJL, 387, 85

Durrell P. R., Harris W. E., 1993, AJ, 105, 1420

Durrell P. R., Harris W. E., 1993, in Smith G. H., Brodie J. P., eds, The Globular Cluster-Galaxy Connection, 91

Dyck H. M., Johnson H. R., 1969, ApJ, 156, 389

Eaton J. A., Johnson H. R., Cadmus, Jr. R. R., 1990, ApJ, 364, 259

Edmonds P. D., Gilliland R. L., 1995, Bull. Amer. Astron. Soc., 1429

Edmonds P. D., Gilliland R. L., 1996, ApJL, 464, 157

Eggen O. J., Lynden-Bell D., Sandage A. R., 1962, ApJ, 136, 748

Elvey C. T., 1928, ApJ, 68, 416

Engelbracht C. W., Gordon K. D., Rieke G. H., Werner M. W., Dale D. A., Latter W. B., 2005, ApJL, 628, 29

Engelke C. W., 1992, AJ, 104, 1248

Evans A., Geballe T. R., Smalley B., Tyne V. H., Eyres S. P. S., 2002, A&A, 394, 971

Evans A., Stickel M., van Loon J. T., Eyres S. P. S., Hopwood M. E. L., Penny A. J., 2003, A&A, 408, 9

Fahlman G. G., Richer H. B., VandenBerg D. A., 1985, ApJS, 58, 225

Falceta-Gonçalves D., Vidotto A. A., Jatenco-Pereira V., 2006, MNRAS, 368, 1145

Faulkner D. J., Coleman C. S., 1984, MNRAS, 206, 121

Faulkner D. J., Freeman K. C., 1977, ApJ, 211, 77

Faulkner D. J., Smith G. H., 1991a, ApJ, 380, 441

Faulkner D. J., Smith G. H., 1991b, Proc. Astron. Soc. Australia, 9, 132

Faulkner D. J., 1984, MNRAS, 206, 109

Faulkner D. J., Scott T. R., Wood P. R., Wright A. E., 1991, ApJL, 374, 45

Fazio G. G., Hora J. L., Allen L. E., Ashby M. L. N., Barmby P., Deutsch L. K., Huang J.-S., Kleiner S., Marengo M., Megeath S. T., Melnick G. J., Pahre M. A., et al., 2004, ApJS, 154, 10

Feast M. W., 1965, The Observatory, 85, 16

Feast M., Whitelock P., Menzies J., 2002, MNRAS, 329, 7

Fehrenbach C., Duflot R., 1962, Academie des Science Paris Comptes Rendus Serie B Sciences Physiques, 255, 1291

Fekel F. C., Balachandran S., 1994, in Caillault J.-P., ed., ASP Conf. Ser. 64: Cool Stars, Stellar Systems, and the Sun, 279

Fellhauer M., 2004, in Schielicke R. E., ed., Reviews in Modern Astronomy, 209

Fernie J. D., 1962, AJ, 67, 769

Ferraro F. R., Paresce F., 1993, AJ, 106, 154

Ferraro F. R., 2000, in Schielicke R. E., ed., Astronomische Gesellschaft Meeting Abstracts, 38

Ferraro F. R., Bellazzini M., Pancino E., 2002, ApJL, 573, 95

Fischer P., Welch D. L., Mateo M., Cote P., 1993, AJ, 106, 1508

Fitzgerald A. P., 1955, Irish AJ, 3, 204

Flamsteed J., 1712, HISTORIA Coelestis libri DUO quorum prior exhibet Catalogum Stellarum Fixarum Britannicum et Planetarum omnium Observationibus ; posterior Transitus Syderum (...) 1676-1705, London : J. Matthews; VI; in folio; DCC.f.6

Flamsteed J., 1725, HISTORIA Coelestis Britannicae, tribus Voluminibus contenta (1675-1689), (1689-1720), vol. 1, 2, 3, London : H. Meere; in folio; DCC.f.9, DCC.f.10, DCC.f.11

Fluks M. A., Plez B., The P. S., de Winter D., Westerlund B. E., Steenman H. C., 1994, A&AS, 105, 311

Forte J. C., Mendéz M., 1984, AJ, 89, 648

Forte J. C., Mendéz M., 1988, AJ, 95, 500

Forte J. C., Mendéz M., 1989, ApJ, 345, 222

Forte J. C., Bassino L. P., Vega E. I., Pellizza González L. J., Cellone S. A., Méndez M. R., 2002, AJ, 123, 3263

Fouqué P., Chevallier L., Cohen M., Galliano E., Loup C., Alard C., de Batz B., Bertin E., Borsenberger J., Cioni M. R., Copet E., Dennefeld M., et al., 2000, A&AS, 141, 313

Fox M. W., 1982, MNRAS, 199, 715

François P., Spite M., Spite F., 1988, A&A, 191, 267

Frank J., Gisler G., 1976, MNRAS, 176, 533

Fraser O. J., Hawley S. L., Cook K. H., Keller S. C., 2005, AJ, 129, 768

Freeman K. C., Rodgers A. W., 1975, ApJL, 201, 71

Freeman K. C., 1985, in Goodman J., Hut P., eds, Dynamics of Star Clusters, 33

Freeman K. C., 2001, in Deiters S., Fuchs B., Just A., Spurzem R., Wielen R., eds, Dynamics of Star Clusters and the Milky Way, 43

Freire P. C., Kramer M., Lyne A. G., Camilo F., Manchester R. N., d'Amico N., 2001, ApJL, 557, 105

Frenklach M., Clary D. W., Gardiner W. C., Stein S. E., 1984, Pittsburgh: The Combustion Institute: 20th Symp. (International) on Combustion, 887

Freyhammer L. M., Monelli M., Bono G., Cunti P., Ferraro I., Calamida A., Degl'Innocenti S., Prada Moroni P. G., del Principe M., Piersimoni A., Iannicola G., Stetson P. B., et al., 2005, ApJ, 623, 860

Frinchaboy P. M., Rhee J., Ostheimer J. C., Majewski S. R., Patterson R. J., Johnson W. Y., Dinescu D. I., Palma C., Westfall K. B., 2002, in van Leeuwen F., Hughes J. D., Piotto G., eds, Omega Centauri, A Unique Window into Astrophysics, 143

Frogel J. A., Elias J. H., 1988, ApJ, 324, 823

Frogel J. A., 1983, ApJ, 272, 167

Fuentes-Carrera I., Jablonka P., Sarajedini A., Bridges T., Djorgovski G., Meylan G., 2008, A&A, 483, 769

Fusi Pecci F., Bellazzini M., 1997, in Philip A. G. D., Liebert J., Saffer R., Hayes D. S., eds, The Third Conference on Faint Blue Stars, 255

Fusi Pecci F., Cacciari C., Federici L., Pasquali A., 1993, in Smith G. H., Brodie J. P., eds, The Globular Cluster-Galaxy Connection, 410

Gathier R., Pottasch S. R., Goss W. M., 1983, A&A, 127, 320

Gauba G., Parthasarathy M., 2004, A&A, 417, 201

Gebhardt K., Fischer P., 1995, AJ, 109, 209

Gebhardt K., Pryor C., Williams T. B., Hesser J. E., 1993, in Djorgovski S. G., Meylan G., eds, Structure and Dynamics of Globular Clusters, 77

Gebhardt K., Pryor C., Williams T. B., Hesser J. E., Stetson P. B., 1997, AJ, 113, 1026

Gebhardt K., Pryor C., O'Connell R. D., Williams T. B., Hesser J. E., 2000, AJ, 119, 1268

Gebhardt K., Rich R. M., Ho L. C., 2002, ApJL, 578, 41

Gebhardt K., Rich R. M., Ho L. C., 2005, ApJ, 634, 1093

Geffert M., Hilker M., Geyer E. H., Krämer G.-H., 2002, in van Leeuwen F., Hughes J. D., Piotto G., eds, Omega Centauri, A Unique Window into Astrophysics, 399

Gehrz R. D., Woolf N. J., 1971, ApJ, 165, 285

Gehrz R., 1989, in Allamandola L. J., Tielens A. G. G. M., eds, Interstellar Dust, 445

Gendre B., Barret D., Webb N. A., 2003, A&A, 400, 521

Gerssen J., van der Marel R. P., Gebhardt K., Guhathakurta P., Peterson R. C., Pryor C., 2002, AJ, 124, 3270

Geyer E. H., Szeidl B., 1970, A&A, 4, 40

Geyer E. H., 1967, Zeitschrift fur Astrophysik, 66, 16

Giersz M., Heggie D. C., 2003, MNRAS, 339, 486

Gillett F. C., Jacoby G. H., Joyce R. R., Cohen J. G., Neugebauer G., Soifer B. T., Nakajima T., Matthews K., 1989, ApJ, 338, 862

Glass I. S., Feast M. W., 1973, MNRAS, 163, 245

Glass I. S., Feast M. W., 1977, MNRAS, 181, 509

Gnedin O. Y., Zhao H., Pringle J. E., Fall S. M., Livio M., Meylan G., 2002, ApJL, 568, 23

Goldstein B. R., Peng Yoke H., 1965, AJ, 70, 748

González G., Wallerstein G., 1992, MNRAS, 254, 343

González G., Wallerstein G., 1994, AJ, 108, 1325

González G., 1994, AJ, 108, 1312

Gratton R. G., 1982, A&A, 115, 336

Gratton R. G., 1983, ApJ, 264, 223

Gratton R. G., Bragaglia A., Carretta E., Clementini G., Desidera S., Grundahl F., Lucatello S., 2003, A&A, 408, 529

Gratton R., Bragaglia A., Carretta E., Lucatello S., Bedin L. R., Piotto G., Villanova S., 2005, in Hill V., François P., Primas F., eds, From Lithium to Uranium: Elemental Tracers of Early Cosmic Evolution, 357

Gratton R. G., Pilachowski C. A., Sneden C., 1984, A&A, 132, 11

Gray D. F., 1983, PASP, 95, 181

Gray D. F., 1992, The Observation and Analysis of Stellar Photospheres, The Observation and Analysis of Stellar Photospheres. Cambridge University Press, UK.

Green E. M., Norris J. E., 1990, ApJL, 353, 17

Gregory P. C., Vavasour J. D., Scott W. K., Condon J. J., 1994, ApJS, 90, 173

Grillmair C. J., Johnson R., 2006, ApJL, 639, 17

Grindlay J. E., 1985, in Goodman J., Hut P., eds, Dynamics of Star Clusters, 43

Grocholski A. J., Cole A. A., Sarajedini A., Geisler D., Smith V. V., 2006, AJ, 132, 1630

Groenewegen M. A. T., 2006, A&A, 448, 181

Guhathakurta P., Yanny B., Schneider D. P., Bahcall J. N., 1992, Bull. Amer. Astron. Soc., 1188

Guhathakurta P., Yanny B., Schneider D. P., Bahcall J. N., 1993, in Saffer R. A., ed., Blue Stragglers, 60

Guhathakurta P., Yanny B., Schneider D. P., Bahcall J. N., 1996, AJ, 111, 267

Guhathakurta P., Webster Z. T., Yanny B., Schneider D. P., Bahcall J. N., 1998, AJ, 116, 1757

Gustafsson B., Bell R. A., Eriksson K., Nordlund A., 1975, A&A, 42, 407

Gustafsson B., Edvardsson B., Eriksson K., Jørgensen U. G., Nordlund Å., Plez B., 2008, A&A, 486, 951

Habing H. J., Olofsson H., 2003, Asymptotic giant branch stars, Astronomy and astrophysics library, New York, Berlin: Springer, 2003

Habing H. J., 1996, 7, 97

Hagen W., 1978, ApJS, 38, 1

Hagen W., Stencel R. E., Dickinson D. F., 1983, ApJ, 274, 286

Haggard D., Cool A. M., Anderson J., Edmonds P. D., Callanan P. J., Heinke C. O., Grindlay J. E., Bailyn C. D., 2004, ApJ, 613, 512

Halley E., 1678, Catalogus stellarum Australium, Harford, London

Halley E., 1714, Phil. Trans. Roy. Soc. London, 29, 390

Halley E., 1716, Philosophical Transactions Series I, 29, 390

Hamuy M., 1984, A&AS, 57, 91

Han Z., Podsiadlowski P., Eggleton P. P., 1995, Asymmetrical Planetary Nebulae, 66

Hanner M., 1988, Technical Report

Hannikainen D., Charles P., van Zyl L., 2001, Two Years of Science with Chandra, Abstracts from the Symposium held in Washington, DC.

Hansen O. L., Hesser J. E., 1975, Nature, 257, 568

Hansen B. M. S., 2005, ApJ, 635, 522

Harding G. A., 1962, The Observatory, 82, 205

Harding G. A., 1965, Royal Greenwich Observatory Bulletin, 99, 65

Harris W. E., Canterna R., 1979, ApJL, 231, 19

Harris W. E., 1980, IAU Symp. 85: Star Formation, 81

Harris W. E., 1982, ApJS, 50, 573

Harris W. E., 1996, ApJ, 112, 1487

Hartwick F. D. A., Grindlay J. E., Cowley A. P., 1982, ApJL, 254, 11

Hauschildt P. H., Baron E., 1999, J. Comp. Appl. Math, 102, 41

Hazen M. L., Hesser B. H., 1986, AJ, 92, 1094

Heasley J. N., Milkey R. W., 1976, ApJL, 205, 43

Hebden J. C., Eckart A., Hege E. K., 1987, ApJ, 314, 690

Heber U., Dreizler S., Werner K., 1993, Acta Astronomica, 43, 337

Heras A. M., Hony S., 2005, A&A, 439, 171

Herschel W., 1786, Phil. Trans. Roy. Soc. London, 76, 457

Herschel W., 1789, Phil. Trans. Roy. Soc. London, 79, 212

Herschel W., 1802, Phil. Trans. Roy. Soc. London, 92, 477

Hertz P., Grindlay J. E., 1983, ApJ, 275, 105

Hertz P., 1987, ApJL, 315, 119

Hertzsprung E., 1933, BAIN, 7, 83

Hessels J. W. T., Ransom S. M., Stairs I. H., Kaspi V. M., Freire P. C. C., Backer D. C., Lorimer D. R., 2004, in Camilo F., Gaensler B. M., eds, IAU Symposium, 131

Hesser J. E., Harris G. L. H., 1979, ApJ, 234, 513

Hesser J. E., Hartwick F. D. A., 1977, ApJS, 33, 361

Hesser J. E., Shawl S. J., 1977, ApJL, 217, 143

Hesser J. E., Bell R. A., Cannon R. D., Harris G. L. H., 1985, ApJ, 295, 437

Hesser J. E., Harris W. E., VandenBerg D. A., Allwright J. W. B., Shott P., Stetson P. B., 1987, PASP, 99, 739

Hesser J. E., Harris W. E., VandenBerg D. A., 1987, Bull. American Astron. Soc., 19, 676

Hesser J. E., Harris W. E., VandenBerg D. A., 1987, PASP, 99, 1148

Hesser J. E., Hartwick F. D. A., McClure R. D., 1977, ApJS, 33, 471

Hevelius J., 1662, Historiola Mirae Stellae, (Danzig) 1662

Hilditch R. W., 2001, An Introduction to Close Binary Stars, Cambridge, UK: Cambridge University Press, March 2001.

Hilker M., Richtler T., 2000a, in Noels A., Magain P., Caro D., Jehin E., Parmentier G., Thoul A. A., eds, Liège Int. Astroph. Colloq., 509

Hilker M., Richtler T., 2000, A&A, 362, 895

Hilker M., Richtler T., 2002, in van Leeuwen F., Hughes J. D., Piotto G., eds, Omega Centauri, A Unique Window into Astrophysics, 59

Hilker M., Kayser A., Richtler T., Willemsen P., 2004, A&A, 422, 9

Hinkle K. H., Lebzelter T., Joyce R. R., Fekel F. C., 2002, AJ, 123, 1002

Hinshaw G., Weiland J. L., Hill R. S., Odegard N., Larson D., Bennett C. L., Dunkley J., Gold B., Greason M. R., Jarosik N., Komatsu E., Nolta M. R., et al., 2009, ApJS, 180, 225

Ho L. C., Terashima Y., Okajima T., 2003, ApJL, 587, 35

Höfner S., Andersen A. C., 2007, A&A, 465, 39

Höfner S., 2007, in Kerschbaum F., Charbonnel C., Wing R. F., eds, Why Galaxies Care About AGB Stars: Their Importance as Actors and Probes, 145

Högbom J. A., 1974, A&AS, 15, 417

Holden E. S., 1891, PASP, 3, 375

Hony S., 2002, Ph.D. Thesis

Houdashelt M. L., Bell R. A., Sweigart A. V., 2000, AJ, 119, 1448

Hoyle F., Wickramasinghe N. C., 1969, Nature, 223, 459

Hubble E. P., 1926, ApJ, 64, 321

Hubble E. P., 1929, ApJ, 69, 103

Hubble E., 1934, ApJ, 79, 8

Huggins W., 1868, Phil. Trans. Roy. Soc. London, 158, 529

Hughes J., Wallerstein G., 1997, PASP, 109, 274

Hughes J., Wallerstein G., 2000, AJ, 119, 1225

Hughes J., Wallerstein G., van Leeuwen F., Hilker M., 2004, AJ, 127, 980

Hughes J. D., Wallerstein G., Covarrubias R., Hays N., 2006, Bull. Amer. Astron. Soc., 144

Ibata R. A., Wyse R. F. G., Gilmore G., Irwin M. J., Suntzeff N. B., 1997, AJ, 113, 634

Ibata R. A., Gilmore G., Irwin M. J., 1994, Nature, 370, 194

Iben I. J., Rood R. T., 1970, ApJ, 161, 587

Iben, Jr. I., Truran J. W., 1978, ApJ, 220, 980

Icke V., Alcaíno G., 1988, A&A, 204, 115

Icke V., Frank A., Heske A., 1992, A&A, 258, 341

Illingworth G., 1975, in Oppenheim A. V., Schafer R. W., eds, Dynamics of the Solar Systems, 151

Ilovaisky S. A., Aurière M., Chevalier C., Koch-Miramond L., Cordoni J.-P., Angebault L. P., 1987, A&A, 179, 1

IRAS catalogs and atlases, Volume 5, 1988

Ita Y., Tanabé T., Matsunaga N., Nakajima Y., Nagashima C., Nagayama T., Kato D., Kurita M., Nagata T., Sato S., Tamura M., Nakaya H., Nakada Y., 2004, MNRAS, 347, 720

Ita Y., Tanabé T., Matsunaga N., Nakada Y., Matsuura M., Onaka T., Matsuhara H., Wada T., Fujishiro N., Ishihara D., Kataza H., Kim W., et al., 2007, PASJ, 59, 437

Ivanov V. D., Borissova J., Alonso-Herrero A., Russeva T., 2000, AJ, 119, 2274

Ivezić Ž., Elitzur M., 1995, ApJ, 445, 415

Ivezić Ž., 2007, in Kerschbaum F., Charbonnel C., Wing R. F., eds, Why Galaxies Care About AGB Stars: Their Importance as Actors and Probes, 485

Izsak I., 1951, Commmunications of the Konkoly Observatory Hungary, 28, 1

Jacoby G. H., Morse J. A., Fullton L. K., Kwitter K. B., Henry R. B. C., 1997, AJ, 114, 2611

Jäger C., Mutschke H., Begemann B., Dorschner J., Henning T., 1994, A&A, 292, 641

Jasniewicz G., de Laverny P., Parthasarathy M., Lèbre A., Thévenin F., 2004, A&A, 423, 353

Jeans J. H., 1916, MNRAS, 76, 567

Jeon Y.-B., Kim S.-L., Lee H., Lee M. G., 2001, AJ, 121, 2769

Jeon Y.-B., Lee H., Kim S.-L., Lee M. G., 2001, IBVS, 5189, 1

Jiménez R., 1998, Proc. Nat. Acad. Sci., 95, 13

Johnson H. L., Schwarzschild M., 1951, ApJ, 113, 630

Johnson C. I., Pilachowski C. A., Simmerer J., Schwenk D., 2008, ApJ, 681, 1505

Johnson H. R., Luttermoser D. G., Eaton J., Chromospheres in Red Giants, 1994, in Wamsteker W., Longair M. S., Kondo Y., eds, ASSL Vol. 187: Frontiers of Space and Ground-Based Astronomy, 593

Johnston H. M., Verbunt F., Hasinger G., 1994, A&A, 289, 763

Jones D. H. P., 1968, MNRAS, 140, 265

Jones D. H. P., 1973, ApJS, 25, 487

Jones D. H. P., 1973b, IAU Colloq. 21: Variable Stars in Globular Clusters and in Related Systems, 84

Jones K. J., 1991, Messier's Nebulae and Star Clusters, Cambridge University Press, 2nd edition

Joy A. H., 1949, ApJ, 110, 105

Judge P. G., Stencel R. E., 1991, ApJ, 371, 357

Judge P. G., Luttermoser D. G., Neff D. H., Cuntz M., Stencel R. E., 1993, AJ, 105, 1973

Jura M., Kleinmann S. G., 1992, ApJS, 79, 105

Jura M., Chen C., Plavchan P., 2002, ApJ, 569, 964

Jurcsik J., 1998, ApJL, 506, 113

Jurcsik J., 2000, in Szabados L., Kurtz D., eds, IAU Colloq. 176: The Impact of Large-Scale Surveys on Pulsating Star Research, 254

Kadla Z. I., Gerashchenko A. N., Yablokova N. V., Spasova N., 1984, Astronomicheskij Tsirkulyar, 1314, 1

Kalirai J. S., Bergeron P., Hansen B. M. S., Kelson D. D., Reitzel D. B., Rich R. M., Richer H. B., 2007, ApJ, 671, 748

Kalirai J. S., Hansen B. M. S., Kelson D. D., Reitzel D. B., Rich R. M., Richer H. B., 2008, ApJ, 676, 594

Kałużny, J. and Kubiak, M. and Szymański, M. and Udalski, A. and Krzemiński, W. and Mateo, M., 1996, A&AS, 120, 139

Kałużny, J. and Olech, A. and Thompson, I. B. and Pych, W. and Krzemiński, W. and Schwarzenberg-Czerny, A., 2004, A&A, 424, 1101

p. Kałużny, J. and Thompson, I. and Krzemiński, W. and Olech, A. and Pych, W. and Mochejska, B., 2002, in van Leeuwen F., Hughes J. D., Piotto G., eds, ASP Conf. Ser. 265: Omega Centauri, A Unique Window into Astrophysics, 155

Kałużny, J. and Thompson, I. B. and Rucinski, S. M. and Pych, W. and Stachowski, G. and Krzemiński, W. and Burley, G. S. , 2007, AJ, 134, 541

Kamaya H., 2007, A&A, 471, 805

Kanagy S. P., Wyatt S. P., 1978, AJ, 83, 779

Kanagy, II S. P., 1977, PhD thesis, Illinois Univ., Urbana-Champaign.

Kawakatu N., Umemura M., 2005, ApJ, 628, 721

Kayser A., Hilker M., Richtler T., Willemsen P. G., 2006, A&A, 458, 777

Keady J. J., 1982, PhD Thesis, State University of New Mexico

Kemper F., Stark R., Justtanont K., de Koter A., Tielens A. G. G. M., Waters L. B. F. M., Cami J., Dijkstra C., 2003, A&A, 407, 609

Kennedy D. C., 1997, Irish AJ, 24, 39

Kennedy D. C., Bates B., Keenan F. P., Kemp S. N., Ryans R. S. I., Davies R. D., Sembach K. R., 1998, MNRAS, 297, 849

Kepler J., 1606, De stella nova in pede serpentarii, Typis Pauli Sessii; impensis authoris

Kepler J., 1614, De vero anno quo aeternus Dei Filius humanam naturam in utero benedictae Virginis Mariae assumpsit, (Frankfurt) 1614

Khalisi E., Amaro-Seoane P., Spurzem R., 2007, MNRAS, 374, 703

Kielkopf J. F., Lattis J. M., 1984, Bull. Amer. Astron. Soc., 967

King I. R., Anderson J., 2002, in da Costa G. S., Jerjen H., eds, ASP Conf. Ser. 273: The Dynamics, Structure & History of Galaxies: A Workshop in Honour of Professor Ken Freeman, 167

King I., 1962, AJ, 67, 471

Kiss L. L., Bedding T. R., 2003, MNRAS, 343, 79

Knierman K. A., Gallagher S. C., Charlton J. C., Hunsberger S. D., Whitmore B., Kundu A., Hibbard J. E., Zaritsky D., 2003, AJ, 126, 1227

Koch A., Grebel E. K., Odenkirchen M., Martínez-Delgado D., Caldwell J. A. R., 2004, AJ, 128, 2274

Köhler J. A., 1965, The Observatory, 85, 197

Kolkhidashvili M. G., 1977, Abastumanskaia Astrofizicheskaia Observatoriia Biulleten, 48, 141

Koninx J.-P. M., Pijpers F. P., 1992, A&A, 265, 183

Konstantinova-Antova R. K., 2001, in Schielicke E. R., ed., Astronomische Gesellschaft Meeting Abstracts, 88

Koopmann R. A., Lee Y.-W., Demarque P., Howard J. M., 1994, ApJ, 423, 380

Kovács G., 2002, in van Leeuwen F., Hughes J. D., Piotto G., eds, Omega Centauri, A Unique Window into Astrophysics, 163

Kozasa T., Hasegawa H., Seki J., 1984, Ap&SS, 98, 61

Krockenberger M., Grindlay J. E., 1995, ApJ, 451, 200

Kurucz R., 1993, SYNTHE Spectrum Synthesis Programs and Line Data. Kurucz CD-ROM No. 18. Cambridge, Mass.: Smithsonian Astrophysical Observatory, 1993., 18

Kurucz R., 1999, 1999 TiO linelist from Schwenke (1998). Kurucz CD-ROM No. 24. Cambridge, Mass.: Smithsonian Astrophysical Observatory, 1999., 24

Kustner F., 1921, Veroeffentlichungen des Astronomisches Institute der Universitaet Bonn, 15, 1

Lambert D. L., Snell R. L., 1975, MNRAS, 172, 277

Lamers H. J. G. L. M., Cassinelli J. P., 1999, Introduction to Stellar Winds, Cambridge University Press

Lamers H. J. G. L. M., Cerruti-Sola M., Perinotto M., 1987, ApJ, 314, 726

Lanzoni B., Dalessandro E., Ferraro F. R., Mancini C., Beccari G., Rood R. T., Mapelli M., Sigurdsson S., 2007, ApJ, 663, 267

Lauer T. R., Holtzman J. A., Faber S. M., Baum W. A., Currie D. G., Ewald S. P., Groth E. J., Hester J. J., Kelsall T., Light R. M., Lynds C. R., O'Neil, Jr. E. J., et al., 1991, ApJL, 369, 45

Law D. R., Majewski S. R., Skrutskie M. F., Carpenter J. M., Ayub H. F., 2003, AJ, 126, 1871

le Bertre T., 1993, A&AS, 97, 729

Lebzelter T., Wood P. R., 2005, A&A, 441, 1117

Lebzelter T., 1999, A&A, 351, 644

Lebzelter T., Nowotny W., Horn J., Hinkle K., Höfner S., Aringer B., Gautschy R., 2002, Hvar Observatory Bulletin, 26, 25

Lebzelter T., Wood P. R., Hinkle K. H., Joyce R. R., Fekel F. C., 2005, A&A, 432, 207

Lebzelter T., Posch T., Hinkle K., Wood P. R., Bouwman J., 2006, ApJL, 653, 145

Ledent G., 2000, M.Sc. Thesis

Lee J.-W., Carney B. W., 1999, AJ, 118, 1373

Lee S. W., 1977, A&AS, 27, 381

Lee Y.-W., 1989, PhD thesis, Yale Univ., New Haven, CT.

Lee Y. W., Demarque P., Zinn R., 1988, in Philip A. G. D., ed., Calibration of Stellar ages, 149

Lee Y.-W., Joo J.-M., Sohn Y.-J., Rey S.-C., Lee H.-C., Walker A. R., 1999, Nature, 402, 55

Lee Y.-W., Rey S.-C., Ree C. H., Joo J.-M., Sohn Y.-J., Yoon S.-J., 2002, in van Leeuwen F., Hughes J. D., Piotto G., eds, Omega Centauri, A Unique Window into Astrophysics, 305

Lee Y.-W., Gim H. B., Dinescu D. I., 2007, ApJL, 661, 49

Lehmann I., Scholz R.-D., 1997, A&A, 320, 776

Lehner N., Rolleston W. R. J., Ryans R. S. I., Keenan F. P., Bates B., Pollacco D. L., Sembach K. R., 1999, A&AS, 134, 257

Leon S., Meylan G., Combes F., 2000, A&A, 359, 907

Leroy J. L., Aurière M., Laques P., 1976, A&A, 53, 227

Levesque E. M., Massey P., Olsen K. A. G., Plez B., Josselin E., Maeder A., Meynet G., 2005, ApJ, 628, 973

Levesque E. M., Massey P., Olsen K. A. G., Plez B., Meynet G., Maeder A., 2006, ApJ, 645, 1102

Lewis B. M., 1989, AJ, 98, 1814

Liller W., Alcaíno G., 1987, in Appenzeller I., Jordan C., eds, IAU Symp. 122: Circumstellar Matter, 357

Lindsay E. M., 1953, Irish AJ, 2, 140

Lindsay E. M., 1956, Vistas in Astronomy, 2, 1057

Linsky J. L., Haisch B. M., 1979, ApJL, 229, 27

Lloyd Evans T., Menzies J. W., 1973, in Fernie J. D., ed., ASSL Vol. 36: IAU Colloq. 21: Variable Stars in Globular Clusters and in Related Systems, 151

Lloyd Evans T., Menzies J. W., 1977, MNRAS, 178, 163

Lloyd Evans T., 1974, MNRAS, 167, 393

Lloyd Evans T., 1977, MNRAS, 178, 345

Lloyd Evans T., 1983, MNRAS, 204, 961

Lloyd Evans T., 1983, MNRAS, 204, 975

Lloyd Evans T., 1983c, South African Astronomical Observatory Circular, 7, 86

Lloyd Evans T., 1983d, South African Astronomical Observatory Circular, 7, 96

Lloyd Evans T., 1984, MNRAS, 209, 825

Lloyd Evans T., 1986, South African Astronomical Observatory Circular, 10, 1

Lombardi, Jr. J. C., Rasio F. A., Shapiro S. L., 1996, ApJ, 468, 797

Lub J., 2002, in van Leeuwen F., Hughes J. D., Piotto G., eds, Omega Centauri, A Unique Window into Astrophysics, 95

Lugger P. M., Cohn H., Grindlay J. E., Bailyn C. D., Hertz P., 1987, ApJ, 320, 482

Lynch D. K., Rossano G. S., 1990, AJ, 100, 719

Lynch D. K., Bowers P. F., Whiteoak J. B., 1989, AJ, 97, 1708

Ma J., van den Bergh S., Wu H., Yang Y., Zhou X., Chen J., Wu Z., Jiang Z., Wu J., 2006, ApJL, 636, 93

Ma J., Zhou X., Burstein D., Chen J., Jiang Z., Wu Z., Wu J., 2006, PASP, 118, 98

Ma J., Zhou X., Burstein D., Yang Y., Fan Z., Chen J., Jiang Z., Wu Z., Wu J., Zhang T., 2006, A&A, 449, 143

Maccarone T., Knigge C., 2007, Astronomy and Geophysics, 48, 12

Maccarone T. J., Kundu A., Zepf S. E., Rhode K. L., 2007, Nature, 445, 183

MacGregor A. D., Phillips J. P., Selby M. J., 1973, MNRAS, 164, 31P

Mackey A. D., Broby Nielsen P., Ferguson A. M. N., Richardson J. C., 2008, ApJL, 681, 17

Majewski S. R., Patterson R. J., Dinescu D. I., Johnson W. Y., Ostheimer J. C., Kunkel W. E., Palma C., 2000, in Noels A., Magain P., Caro D., Jehin E., Parmentier G., Thoul A. A., eds, Liège Int. Astroph. Colloq., 619

Mallia E. A., Pagel B. E. J., 1978, MNRAS, 184, 55P

Mallia E. A., Pagel B. E. J., 1981, MNRAS, 194, 421

Mallia E. A., 1976, A&A, 48, 129

Manduca A., Bell R. A., 1978, ApJ, 225, 908

Mandushev G., Staneva A., Spasova N., 1991, A&A, 252, 94

Maraldi G., 1746, Mémoires de la Académie des Sciences, 1746, 58

Marcolini A., Sollima A., d'Ercole A., Gibson B. K., Ferraro F. R., 2007, MNRAS, 382, 443

Marengo M., 2000, PhD Thesis, Int. School for Advanced Studies (SISSA/ISAS), Trieste

Margon B., Bolte M., 1987, ApJL, 321, 61

Marigo P., Girardi L., Bressan A., Groenewegen M. A. T., Silva L., Granato G. L., 2008, A&A, 482, 883

Marshall J. R., van Loon J. T., Matsuura M., Wood P. R., Zijlstra A. A., Whitelock P. A., 2004, MNRAS, 355, 1348

Martin P. G., Shawl S. J., 1981, ApJ, 251, 108

Martin W. C., 1938a, Annalen van de Sterrewacht te Leiden, 17, 1

Martin W. C., 1938, BAIN, 8, 290

Martin N. F., Ibata R. A., Bellazzini M., Irwin M. J., Lewis G. F., Dehnen W., 2004, MNRAS, 348, 12

Mathis J. S., Rumpl W., Nordsieck K. H., 1977, ApJ, 217, 425

Matsunaga N., 2007, in Kerschbaum F., Charbonnel C., Wing R. F., eds, Why Galaxies Care About AGB Stars: Their Importance as Actors and Probes, 86

Matsunaga N., Mito H., Nakada Y., Fukushi H., Tanabé T., Ita Y., Izumiura H., Matsuura M., Ueta T., Yamamura I., 2008, PASJ, 60, 415

Mattsson L., Wahlin R., Höfner S., Eriksson K., 2008, A&A, 484, 5

Mauas P. J. D., Cacciari C., Pasquini L., 2006, A&A, 454, 609

Mauch T., Murphy T., Buttery H. J., Curran J., Hunstead R. W., Piestrzynski B., Robertson J. G., Sadler E. M., 2003, MNRAS, 342, 1117

Mauron N., Huggins P. J., 1999, A&A, 349, 203

Mauron N., 2008, A&A, 482, 151

Mayall N. U., 1946, ApJ, 104, 290

Mayor M., Meylan G., Udry S., Duquennoy A., Andersen J., Nordström B., Imbert M., Maurice E., Prevot L., Ardeberg A., Lindgren H., 1997, AJ, 114, 1087

McClure R. D., Norris J., 1974, ApJ, 193, 139

McDonald I., van Loon J. T., 2007, A&A, 476, 1261

McDonald I., van Loon J. T., Decin L., Boyer M. L., Dupree A. K., Evans A., Gehrz R. D., Woodward C. E., 2009, MNRAS, 394, 831

McLaughlin D. E., Fall S. M., 2008, ApJ, 679, 1272

McLaughlin D. E., Meylan G., 2003, in Piotto G., Meylan G., Djorgovski S. G., Riello M., eds, New Horizons in Globular Cluster Astronomy, 153

McLaughlin D. E., van der Marel R. P., 2005, ApJS, 161, 304

McNamara B. J., Harrison T. E., Anderson J., 2003, ApJ, 595, 187

McNamara B. J., Harrison T. E., Baumgardt H., 2004, ApJ, 602, 264

McWilliam A., Smecker-Hane T. A., 2005, ApJL, 622, 29

Mendéz M., Orsatti A. M., Forte J. C., 1989, ApJ, 338, 136

Menzel D. H., Pekeris C. L., 1935, MNRAS, 96, 77

Menzies J. W., Whitelock P. A., 1985, MNRAS, 212, 783

Merritt D., Meylan G., Mayor M., 1997, AJ, 114, 1074

Messier C., 1774, Tables des Nebuleuses, ainsi que des amas d'Etoiles, que l'on decouvre parmi les Etoiles fixes sur l'horizon de Paris; observes a l'Observatoire de la Marine., Memoires de l'Academie des Sciences (1771)

Messier C., 1780, Catalogue des Nebuleuses & des amas d'Etoiles, Connoissance des Temps (1783)

Messier C., 1781, Catalogue des Nebuleuses & des amas d'Etoiles, Connoissance des Temps (1784)

Mészáros S., Dupree A. K., Szalai T., 2009, aj, 137, 4282

Mészáros S., Dupree A. K., Szentgyörgyi A., 2008, AJ, 135, 1117

Meyer D. M., Lauroesch J. T., 1999, ApJL, 520, 103

Meylan G., Mayor M., 1985, Bull. Amer. Astron. Soc., 882

Meylan G., Mayor M., 1986, A&A, 166, 122

Meylan G., 1987, A&A, 184, 144

Meylan G., 1988, A&A, 191, 215

Meylan G., 2002, in van Leeuwen F., Hughes J. D., Piotto G., eds, Omega Centauri, A Unique Window into Astrophysics, 3

Meylan G., Dubath P., Mayor M., 1991, ApJ, 383, 587

Meylan G., Mayor M., Duquennoy A., Dubath P., 1995, A&A, 303, 761

Meylan G., Sarajedini A., Jablonka P., Djorgovski S. G., Bridges T., Rich R. M., 2001, AJ, 122, 830

Meza A., Navarro J. F., Abadi M. G., Steinmetz M., 2005, MNRAS, 359, 93

Mighell K. J., Freeman K. C., Silk J. I., VandenBerg D. A., 1992, Bull. Amer. Astron. Soc., 1187

Miller B. W., Whitmore B. C., Schweizer F., Fall S. M., 1997, AJ, 114, 2381

Milone A. P., Bedin L. R., Piotto G., Anderson J., King I. R., Sarajedini A., Dotter A., Chaboyer B., Marín-Franch A., Majewski S., Aparicio A., Hempel M., et al., 2008, ApJ, 673, 241

Mochejska B. J., Kałużny, J. and Krockenberger, M. and Sasselov, D. D. and Stanek, K. Z., 1998, Acta Astronomica, 48, 455

Moehler S., Sweigart A. V., 2006, A&A, 455, 943

Moehler S., 2001, PASP, 113, 1162

Moehler S., Heber U., Lemke M., Napiwotzki R., 1998, A&A, 339, 537

Moehler S., Koester D., Zoccali M., Ferraro F. R., Heber U., Napiwotzki R., Renzini A., 2004, A&A, 420, 515

Moehler S., Dreizler S., Lanz T., Bono G., Sweigart A. V., Calamida A., Monelli M., Nonino M., 2007, A&A, 475, 5

Moehler S., Heber U., Durell P. R., 1997, A&A, 317, 83

Moehler S., Sweigart A. V., Catelan M., 1999, A&A, 351, 519

Monelli M., Corsi C. E., Castellani V., Ferraro I., Iannicola G., Prada Moroni P. G., Bono G., Buonanno R., Calamida A., Freyhammer L. M., Pulone L., Stetson P. B., 2005, ApJL, 621, 117

Monet D. G., Levine S. E., Canzian B., Ables H. D., Bird A. R., Dahn C. C., Guetter H. H., Harris H. C., Henden A. A., Leggett S. K., Levison H. F., Luginbuhl C. B., et al., 2003, AJ, 125, 984

Montegriffo P., Ferraro F. R., Fusi Pecci F., Origlia L., 1995, MNRAS, 276, 739

Montegriffo P., Ferraro F. R., Origlia L., Fusi Pecci F., 1998, MNRAS, 297, 872

Montgomery A. S., Bates B., Kemp S. N., 1995, Irish AJ, 22, 186

Mooney C. J., Rolleston W. R. J., Keenan F. P., Dufton P. L., Smoker J. V., Ryans R. S. I., Aller L. H., Trundle C., 2004, A&A, 419, 1123

Moretti A., Piotto G., Arcidiacono C., Milone A. P., Ragazzoni R., Falomo R., Farinato J., Bedin L. R., Anderson J., Sarajedini A., Baruffolo A., Diolaiti E., et al., 2009, A&A, 493, 539

Morgan S., Lake G., 1989, ApJ, 339, 171

Mosley D. R., White R. E., 1975, Bull. Amer. Astron. Soc., 535

Mukherjee K., 1988, Bull. Amer. Astron. Soc., 717

Muller G., Hartwig E., 1918, Geschichte und Literatur des Lichtwechsels der bis Ende 1915 ALS sicher veranderlich anerkannten Sterne : nebst einem Katalog der Elemente ihres Lichtwechsels, Leipzig : In Kommission bei Poeschel & Trepte, 1918-1922.

Munari U., Siviero A., Ochner P., Dallaporta S., Simoncelli C., 2008, Baltic Astronomy, 17, 223

Murphy B. W., Rutten R. G. M., Callanan P. J., Seitzer P., Charles P. A., 1991, Nature, 351, 130

Murphy B. W., Cohn H. N., Lugger P. M., Drukier G. A., 2003, Bull. Amer. Astron. Soc., 735

Murray C. A., Candy M. P., Jones D. H. P., 1965, Royal Greenwich Observatory Bulletin, 100, 81

Naylor T., 1987, PhD thesis, Oxford Univ.

Nenkova M., Ivezić Ž., Elitzur M., 1999, LPI Contributions, 969, 20

Neugebauer M., Snyder C. W., 1962, Science, 138, 1095

Neugebauer G., Habing H. J., van Duinen R., Aumann H. H., Baud B., Beichman C. A., Beintema D. A., Boggess N., Clegg P. E., de Jong T., Emerson J. P., Gautier T. N., et al., 1984, ApJL, 278, 1

Newell B., Graham J. A., 1976, ApJ, 204, 804

Newell R. T., Hjellming R. M., 1982, ApJL, 263, 85

Newell B., da Costa G. S., Norris J., 1976, ApJL, 208, 55

Nieuwenhuijzen H., de Jager C., 1990, A&A, 231, 134

Ninković S., 1983, Astronomische Nachrichten, 304, 305

Noble R. G., Buttress J., Griffiths W. K., Penny A. J., Dickens R. J., Cannon R. D., 1988, in Grindlay J. E., Philip A. G. D., eds, The Harlow-Shapley Symposium on Globular Cluster Systems in Galaxies, 631

Nordhaus J., Busso M., Wasserburg G. J., Blackman E. G., Palmerini S., 2008, ApJL, 684, 29

Norris J., Bessell M. S., 1975, ApJL, 201, 75

Norris J., Bessell M. S., 1977, ApJL, 211, 91

Norris J., Bessell M. S., 1978, ApJL, 225, 49

Norris J. E., da Costa G. S., 1995, ApJ, 447, 680

Norris J., Freeman K. C., 1979, ApJL, 230, 179

Norris J., Zinn R., 1977, ApJ, 215, 74

Norris J., 1978, in Philip A. G. D., Hayes D. S., eds, The HR Diagram - The 100th Anniversary of Henry Norris Russell, 195

Norris J., 1987, ApJL, 313, 65

Norris J., 1988, in Grindlay J. E., Philip A. G. D., eds, The Harlow-Shapley Symposium on Globular Cluster Systems in Galaxies, 93

Norris J. E., 2004, ApJL, 612, 25

Norris J. E., Freeman K. C., Mayor M., Seitzer P., 1997, ApJL, 487, 187

Norris J. E., Freeman K. C., Mighell K. J., 1996, ApJ, 462, 241

Noyola E., Gebhardt K., Bergmann M., 2006, in Kannappan S. J., Redfield S., Kessler-Silacci J. E., Landriau M., Drory N., eds, New Horizons in Astronomy: Frank N. Bash Symposium, 269

Noyola E., Gebhardt K., Bergmann M., 2008, ApJ, 676, 1008

Nucita A. A., de Paolis F., Ingrosso G., Carpano S., Guainazzi M., 2008, A&A, 478, 763

Nuth, III J. A., Ferguson F. T., 2006, ApJ, 649, 1178

Němec J., Mateo M., 1990, in Cacciari C., Clementini G., eds, Confrontation Between Stellar Pulsation and Evolution, 64

O'Connell R. W., 1999, ARAA, 37, 603

O'Dell C. R., Peimbert M., Kinman T. D., 1964, ApJ, 140, 119

Odenkirchen M., Grebel E. K., Dehnen W., Ibata R., Rix H.-W., Stolte A., Wolf C., Rockosi C. M., The SDSS Collaboration, 2000, in Schielicke R. E., ed., Astronomische Gesellschaft Meeting Abstracts, 58

Ogorodnikov K. F., Nezhinskii E. M., Osipkov L. P., 1976, Pis ma Astronomicheskii Zhurnal, 2, 146

Ohnaka K., Driebe T., Weigelt G., Wittkowski M., 2007, A&A, 466, 1099

Okada Y., Kokubun M., Yuasa T., Makishima K., 2007, PASJ, 59, 727

Olech A., Dziembowski W. A., Pamyatnykh A. A., Kałużny, J. and Pych, W. and Schwarzenberg-Czerny, A. and Thompson, I. B., 2005, MNRAS, 363, 40

Oosterhoff P. T., 1939, The Observatory, 62, 104

Origlia L., Gredel R., Ferraro F. R., Fusi Pecci F., 1997, MNRAS, 289, 948

Origlia L., Ferraro F. R., Fusi Pecci F., Rood R. T., 2002, ApJ, 571, 458

Origlia L., Ferraro F. R., Bellazzini M., Pancino E., 2003, ApJ, 591, 916

Origlia L., Rood R. T., Fabbri S., Ferraro F. R., Fusi Pecci F., Rich R. M., 2007, ApJL, 667, 85

Origlia L., Ferraro F. R., Fusi Pecci F., 1995, MNRAS, 277, 1125

Ortolani S., Rosino L., 1987, A&A, 185, 102

Ortolani S., 1988, in Grindlay J. E., Philip A. G. D., eds, The Harlow-Shapley Symposium on Globular Cluster Systems in Galaxies, 629

Paltoglou G., Norris J. E., 1989, ApJ, 336, 185

Pancino E., 2002, in van Leeuwen F., Hughes J. D., Piotto G., eds, Omega Centauri, A Unique Window into Astrophysics, 313

Pancino E., 2003, PhD thesis, INAF, Bologna Observatory

Pancino E., 2004, in McWilliam A., Rauch M., eds, Origin and Evolution of the Elements, 45

Pancino E., Ferraro F. R., Bellazzini M., Piotto G., Zoccali M., 2000, ApJL, 534, 83

Pancino E., Galfo A., Ferraro F. R., Bellazzini M., 2007, ApJL, 661, 155

Papoular R., Pégourié B., 1983, A&A, 128, 335

Paresce F., Ferraro F. R., 1992, Bull. Amer. Astron. Soc., 1188

Parmentier G., Jehin E., Magain P., Neuforge C., Noels A., Thoul A. A., 1999, A&A, 352, 138

Pasquali A., de Marchi G., Pulone L., Brigas M. S., 2004, A&A, 428, 469

Pasquini L., Brocato E., 1992, A&A, 266, 340

Pasquini L., Brocato E., Pallavicini R., 1990, A&A, 234, 277

Pastoriza M. G., Bica E. L. D., Copetti M. V. F., Dottori H. A., 1986, Ap&SS, 119, 279

Paturel G., Garnier R., 1992, A&A, 254, 93

Patzer A. B. C., Köhler T. M., Sedlmayr E., 1995, Planetary and Space Science, 43, 1233

Pease F. G., 1928, PASP, 40, 342

Perez J., Roy F., 2003, in Piotto G., Meylan G., Djorgovski S. G., Riello M., eds, New Horizons in Globular Cluster Astronomy, 503

Perrin G., Ridgway S. T., Coudé du Foresto V., Mennesson B., Traub W. A., Lacasse M. G., 2004, A&A, 418, 675

Persson S. E., Cohen J. G., Matthews K., Frogel J. A., Aaronson M., 1980, ApJ, 235, 452

Peterson A. W., 1976, A&A, 53, 441

Peterson R. C., 1980, in Hesser J. E., ed., Star Formation, 461

Peterson R. C., 1981, ApJL, 248, 31

Peterson C. J., 1987, PASP, 99, 1153

Peterson C. J., 1993, in Djorgovski S. G., Meylan G., eds, Structure and Dynamics of Globular Clusters, 337

Peterson R. C., Seitzer P., Cudworth K. M., 1989, ApJ, 347, 251

Peytremann E., 1974, A&A, 33, 203

Phillips J. P., Reay N. K., Worswick S. P., 1978, A&A, 70, 625

Phinney E. S., Sigurdsson S., 1991, Nature, 349, 220

Pickering E. C., Bailey S. I., 1895, ApJ, 2, 321

Pickering E. C., Bailey S. I., 1897, ApJ, 6, 258

Pickering E. C., Bailey S. I., 1898, ApJ, 8, 257

Pickering E. C., 1894, Astronomische Nachrichten, 135, 129

Pickering E. C., Bailey S. I., Fleming W. P., Leland E. F., Wells L. D., 1898, ApJ, 7, 208

Pickles A. J., 1998, PASP, 110, 863

Pietrinferni A., Cassisi S., Salaris M., Castelli F., 2006, ApJ, 642, 797

Pijpers F. P., Hearn A. G., 1989, A&A, 209, 198

Pijpers F. P., 1993, A&A, 267, 471

Pilachowski C. A., 1984, ApJ, 281, 614

Piotto G., Villanova S., Bedin L. R., Gratton R., Cassisi S., Momany Y., Recio-Blanco A., Lucatello S., Anderson J., King I. R., Pietrinferni A., Carraro G., 2005, ApJ, 621, 777

Piotto G., Bedin L. R., Anderson J., King I. R., Cassisi S., Milone A. P., Villanova S., Pietrinferni A., Renzini A., 2007, ApJL, 661, 53

Platais I., Wyse R. F. G., Hebb L., Lee Y.-W., Rey S.-C., 2003, ApJL, 591, 127

Postnov K. A., Prokhorov M. E., Shakura N. I., 1991, in Lewin W. H. G., Clark G. W., Sunyaev R. A., Trivers K. K., Abramson D. M., eds, High-Energy Astrophysics: American and Soviet Perspectives, 316

Poveda A., Allen C., 1975, ApJ, 197, 155

Prince T. A., Anderson S. B., Kulkarni S. R., Wolszczan A., 1991, ApJL, 374, 41

Pritzl B. J., Smith H. A., Catelan M., Sweigart A. V., 1999, Bull. Amer. Astron. Soc., 907

Pritzl B., Smith H. A., Catelan M., Sweigart A. V., 2000, ApJL, 530, 41

Pritzl B. J., Smith H. A., Catelan M., Sweigart A. V., 2002, AJ, 124, 949

Pryor C., Meylan G., 1993, in Djorgovski S. G., Meylan G., eds, Structure and Dynamics of Globular Clusters, 357

Ptolemy C., 170, Mathematical Syntaxis (Al Magest), Books VII & VIII

Pulone L., de Marchi G., Paresce F., Allard F., 1998, ApJL, 492, 41

Putman M. E., de Heij V., Staveley-Smith L., Braun R., Freeman K. C., Gibson B. K., Burton W. B., Barnes D. G., Banks G. D., Bhathal R., de Blok W. J. G., Boyce P. J., et al., 2002, AJ, 123, 873

Puzia T. H., Zepf S. E., Kissler-Patig M., Hilker M., Minniti D., Goudfrooij P., 2002, A&A, 391, 453

Quilis V., Moore B., 2001, ApJL, 555, 95

Ragland S., Traub W. A., Berger J.-P., Danchi W. C., Monnier J. D., Willson L. A., Carleton N. P., Lacasse M. G., Millan-Gabet R., Pedretti E., Schloerb F. P., Cotton W. D., et al., 2006, ApJ, 652, 650

Ramdani A., Jorissen A., 2001, A&A, 372, 85

Ramstedt S., Schöier F. L., Olofsson H., Lundgren A. A., 2008, A&A, 487, 645

Rasio F. A., Shapiro S. L., 1991, ApJ, 377, 559

Reed B. C., Hesser J. E., Shawl S. J., 1988, PASP, 100, 545

Reid M. J., 1993, ARAA, 31, 345

Reijns R. A., Seitzer P., Arnold R., Freeman K. C., Ingerson T., van den Bosch R. C. E., van de Ven G., de Zeeuw P. T., 2006, A&A, 445, 503

Reimers D., 1975, Memoires of the Société Royale des Sciences de Liège, 8, 369

Rey S.-C., Joo J.-M., Sohn Y.-J., Ree C. H., Lee Y.-W., 2002, in van Leeuwen F., Hughes J. D., Piotto G., eds, Omega Centauri, A Unique Window into Astrophysics, 177

Rey S.-C., Lee Y.-W., Ree C. H., Joo J.-M., Sohn Y.-J., Walker A. R., 2004, AJ, 127, 958

Rich R. M., Sosin C., Djorgovski S. G., Piotto G., King I. R., Renzini A., Phinney E. S., Dorman B., Liebert J., Meylan G., 1997, ApJL, 484, 25

Richer H. B., 1978, ApJL, 224, 9

Richer H. B., Fahlman G. G., Buonanno R., Fusi Pecci F., Searle L., Thompson I. B., 1991, ApJ, 381, 147

Richer H. B., Harris W. E., Fahlman G. G., Bell R. A., Bond H. E., Hesser J. E., Holland S., Pryor C., Stetson P. B., VandenBerg D. A., van den Bergh S., 1996, ApJ, 463, 602

Rieke G. H., Young E. T., Engelbracht C. W., Kelly D. M., Low F. J., Haller E. E., Beeman J. W., Gordon K. D., Stansberry J. A., Misselt K. A., Cadien J., Morrison J. E., et al., 2004, ApJS, 154, 25

Rieke G. H., Blaylock M., Decin L., Engelbracht C., Ogle P., Avrett E., Carpenter J., Cutri R. M., Armus L., Gordon K., Gray R. O., Hinz J., et al., 2008, AJ, 135, 2245

Ripepi V., Clementini G., di Criscienzo M., Greco C., Dall'Ora M., Federici L., di Fabrizio L., Musella I., Marconi M., Baldacci L., Maio M., 2007, ApJL, 667, 61

Roberts M. S., 1960, AJ, 65, 457

Roberts M. S., 1986, IAU Symposium, 126, 411

Roberts M. S., 1988, in Grindlay J. E., Philip A. G. D., eds, IAU Symp. 126: The Harlow-Shapley Symposium on Globular Cluster Systems in Galaxies, 411

Robinson R. D., Carpenter K. G., Brown A., 1998, ApJ, 503, 396

Rodgers A. W., Harding P., 1983, PASP, 95, 979

Rodgers A. W., Newell E. B., Stapinski T., Harding P., Norris J., 1980, PASP, 92, 288

Rosino L., 1950, ApJ, 112, 221

Rosino L., 1969, IBVS, 327, 1

Rosse E. O., 1861, Phil. Trans. Roy. Soc. London, 151, 681

Russell S. C., Dopita M. A., 1990, ApJS, 74, 93

Rutledge R. E., Bildsten L., Brown E. F., Pavlov G. G., Zavlin V. E., 2002, ApJ, 578, 405

Rutten R. G. M., Pylyser E., 1988, A&A, 191, 227

Rybicki G. B., Hummer D. G., 1978, ApJ, 219, 654

Saad S. M., 2005, Ap&SS, 296, 301

Sahai R., Trauger J. T., Watson A. M., Stapelfeldt K. R., Hester J. J., Burrows C. J., Ballister G. E., Clarke J. T., Crisp D., Evans R. W., Gallagher, III J. S., Griffiths R. E., et al., 1998, ApJ, 493, 301

Salpeter E. E., 1977, ARAA, 15, 267

Sandage A., Katem B., 1977, ApJ, 215, 62

Sandage A., 1969, ApJ, 157, 515

Sandage A., 1970, ApJ, 162, 841

Sandage A. R., 1971, Carnegie Inst. Year Book, 70, 411

Sandage A., 1983, AJ, 88, 1159

Sandage A., Katem B., Kristian J., 1968, ApJL, 153, 129

Santos, Jr. J. F. C., Bica E., Clariá J. J., Piatti A. E., Girardi L. A., Dottori H., 1995, MNRAS, 276, 1155

Sarajedini A., Layden A. C., 1995, AJ, 109, 1086

Sawyer H. B., 1931, Harvard College Observatory Circular, 366, 1

Sawyer Hogg H., 1939, Publications of the David Dunlap Observatory, 1, 1

Sawyer Hogg H., 1949, JRAS Canada, 43, 45

Sawyer Hogg H., 1973, Publications of the David Dunlap Observatory, 3, 6

Scaria K. K., Bappu M. K. V., 1981, Journal of Astrophysics and Astronomy, 2, 215

Scaria K. K., 1982, Bulletin of the Astronomical Society of India, 10, 340

Scarpa R., Marconi G., Gilmozzi R., Carraro G., 2007, A&A, 462, 9

Schatzman E. L., Praderie F., King A. R., 1993, The Stars, The Stars, XV, 402 pp. 143 figs.. Springer-Verlag Berlin Heidelberg New York. Also Astronomy and Astrophysics Library

Schilt J., 1928, Popular Astronomy, 36, 296

Schmidt K.-H., van den Bergh S., 1974, Astronomische Nachrichten, 295, 101

Schöier F. L., Olofsson H., Wong T., Lindqvist M., Kerschbaum F., 2004, A&A, 422, 651

Scholz R.-D., Odenkirchen M., Hirte S., Irwin M. J., Börngen F., Ziener R., 1996, MNRAS, 278, 251

Schröder K.-P., Cuntz M., 2005, ApJL, 630, 73

Schröder K.-P., Cuntz M., 2007, A&A, 465, 593

Schröder L. L., Brodie J. P., Kissler-Patig M., Huchra J. P., Phillips A. C., 2002, AJ, 123, 2473

Schröder K.-P., Winters J. M., Sedlmayr E., 1999, A&A, 349, 898

Schultz H., 1866, AN, 67, 1

Schütz O., Meeus G., Sterzik M. F., 2005, A&A, 431, 165

Schwarzmeier J., 2007, How to start with galaxy dynamics computer simulations, University of West Bohemia in Pilsen Press, 1st edition

Schwarzschild M., Härm R., 1965, ApJ, 142, 855

Schweizer F., Miller B. W., Whitmore B. C., Fall S. M., 1996, AJ, 112, 1839

Scott E. H., Durisen R. H., 1978, ApJ, 222, 612

Scott E. H., Rose W. K., 1975, ApJ, 197, 147

Searle L., Zinn R., 1978, ApJ, 225, 357

Sedlmayr E., 1994, in Gråe Jørgensen U., ed., LNP Vol. 428: IAU Colloq. 146: Molecules in the Stellar Environment, 163

Seeds M. A., 2004, Stars and Galaxies, Thomson Brooks/Cole

Seitzer P. O., 1983, PhD thesis, Virginia Univ., Charlottesville

Shapley H., 1918a, PASP, 30, 142

Shapley H., 1918b, ApJ, 48, 154

Shapley H., 1919a, PASP, 31, 261

Shapley H., 1919b, ApJ, 49, 311

Shara M. M., Hinkley S., Zurek D. R., Knigge C., Bond H. E., 2004, AJ, 128, 2847

Shih I. C., Maccarone T. J., Kundu A., Zepf S. E., 2008, MNRAS, , 481

Shu C., et al., 1044, Ch'ing Li Kuo Chao Hui Yao, Astronomical Bureau, Kaifêng

Siegel M. H., Dotter A., Majewski S. R., Sarajedini A., Chaboyer B., Nidever D. L., Anderson J., Marín-Franch A., Rosenberg A., Bedin L. R., Aparicio A., King I., et al., 2007, ApJL, 667, 57

Silbermann N. A., Smith H. A., Bolte M., Hazen M. L., 1994, AJ, 107, 1764

Simis Y. J. W., Icke V., Dominik C., 2001, A&A, 371, 205

Simoda M., Tanikawa K., 1970, PASJ, 22, 143

Simon T., Drake S. A., 1989, ApJ, 346, 303

Sinnott R. W., 1988, The complete new general catalogue and index catalogues of nebulae and star clusters by J. L. E. Dreyer, Cambridge: Sky Publishing Corporation and Cambridge University Press.

Sisteró R. F., Fourcade C. R., 1970, AJ, 75, 34

Skrutskie M. F., Cutri R. M., Stiening R., Weinberg M. D., Schneider S., Carpenter J. M., Beichman C., Capps R., Chester T., Elias J., Huchra J., Liebert J., et al., 2006, AJ, 131, 1163

Slipher V. M., 1918, Popular Astronomy, 26, 8

Slipher V. M., 1922, Popular Astronomy, 30, 11

Slipher V. M., 1924, Popular Astronomy, 32, 622

Smale A. P., 2001, ApJ, 562, 957

Smith G. H., Dupree A. K., 1988, AJ, 95, 1547

Smith G. H., Kraft R. P., 1996, PASP, 108, 344

Smith M. G., Wing R. F., 1973, PASP, 85, 659

Smith G. H., 1983, AJ, 88, 410

Smith G. H., 1984, AJ, 89, 1545

Smith G. H., 1987, PASP, 99, 67

Smith G., 1996, PASP, 108, 176

Smith G. H., 1999, PASP, 111, 980

Smith V. V., 2002, in van Leeuwen F., Hughes J. D., Piotto G., eds, Omega Centauri, A Unique Window into Astrophysics, 109

Smith G. H., 2006, Bulletin of the Astronomical Society of India, 34, 235

Smith V. V., Cunha K., Lambert D. L., 1995, AJ, 110, 2827

Smith G. H., Dupree A. K., Strader J., 2004, PASP, 116, 819

Smith G. H., Wood P. R., Faulkner D. J., Wright A. E., 1990, ApJ, 353, 168

Smith V. V., Suntzeff N. B., Cunha K., Gallino R., Busso M., Lambert D. L., Straniero O., 2000, AJ, 119, 1239

Smith V. V., Terndrup D. M., Suntzeff N. B., 2002, ApJ, 579, 832

Smith G. H., Woodsworth A. W., Hesser J. E., 1995, MNRAS, 273, 632

Smoker J. V., Lehner N., Keenan F. P., Totten E. J., 1999, Irish AJ, 26, 105

Smoker J. V., Lehner N., Keenan F. P., Totten E. J., Murphy E., Sembach K. R., Davies R. D., Bates B., 2001, MNRAS, 322, 13

Smoker J. V., Haffner L. M., Keenan F. P., Davies R. D., Pollacco D., 2002, MNRAS, 337, 385

Sneden C., Johnson J., Kraft R. P., Smith G. H., Cowan J. J., Bolte M. S., 2000, ApJL, 536, 85

Sneden C., Johnson H. R., Krupp B. M., 1976, ApJ, 204, 281

Sobolev V. V., 1960, Moving envelopes of stars, Cambridge: Harvard University Press, 1960

Soderberg A. M., Pilachowski C. A., Barden S. C., Willmarth D., Sneden C., 1999, PASP, 111, 1233

Soker N., Catelan M., Rood R. T., Harpaz A., 2001, ApJL, 563, 69

Sollima A., Ferraro F. R., Origlia L., Pancino E., Bellazzini M., 2004, A&A, 420, 173

Sollima A., Ferraro F. R., Pancino E., Bellazzini M., 2005, MNRAS, 357, 265

Sollima A., Pancino E., Ferraro F. R., Bellazzini M., Straniero O., Pasquini L., 2005, ApJ, 634, 332

Sollima A., Ferraro F. R., Bellazzini M., Origlia L., Straniero O., Pancino E., 2007, ApJ, 654, 915

Sollima A., Lanzoni B., Beccari G., Ferraro F. R., Fusi Pecci F., 2008, A&A, 481, 701

Sollima A., Ferraro F. R., Bellazzini M., 2007, MNRAS, 381, 1575

Sosin C., King I. R., 1997, AJ, 113, 1328

Soszyński I., 2007, ApJ, 660, 1486

Soszyński I., 2009, in van Loon J. T., Oliveira J. M., eds, IAU Symposium, 30

Soszyński I., Udalski A., Kubiak M., Szymański M., Pietrzyński G., Zebrun K., Szewczyk O., Wyrzykowski Ł., 2004, Acta Astronomica, 54, 129

Space Telescope Science Institute, Osservatorio Astronomico di Torino, 2007, VizieR Online Data Catalog, 1305

Spasova N. M., 1983, Bolgarska Akademiia Nauk Doklady, 36, 705

Speck A. K., Barlow M. J., Sylvester R. J., Hofmeister A. M., 2000, A&AS, 146, 437

Spergel D. N., 1991, Nature, 352, 221

Spitzer L. J., 1939, ApJ, 90, 494

Spitzer L., 1987, Dynamical evolution of globular clusters, Princeton, NJ, Princeton University Press, 1987

Spruit H. C., 1992, A&A, 253, 131

Stancliffe R. J., Jeffery C. S., 2007, MNRAS, 375, 1280

Stanford L. M., da Costa G. S., Norris J. E., Cannon R. D., 2004, MmSAI, 75, 290

Stanford L. M., da Costa G. S., Norris J. E., Cannon R. D., 2006, ApJ, 647, 1075

Stanford L. M., da Costa G. S., Norris J. E., Cannon R. D., 2006, ApJL, 653, 117

Stanford L. M., da Costa G. S., Norris J. E., Cannon R. D., 2007, ApJ, 667, 911

Steiman-Cameron T. Y., Johnson H. R., Honeycutt R. K., 1985, ApJL, 291, 51

Stencel R. E., 1981, SAO Special Report, 392, 137

Stetson P. B., Bruntt H., Grundahl F., 2003, PASP, 115, 413

Stetson P. B., VandenBerg D. A., Bolte M., 1996, PASP, 108, 560

Stock J., Wing R. F., 1972, Bull. Amer. Astron. Soc., 324

Strader J., Beasley M. A., Brodie J. P., 2007, AJ, 133, 2015

Straniero O., Chieffi A., Limongi M., Busso M., Gallino R., Arlandini C., 1997, ApJ, 478, 332

Straniero O., Gallino R., Cristallo S., 2006, Nuclear Physics A, 777, 311

Suh K.-W., 1999, MNRAS, 304, 389

Suntzeff N. B., Kraft R. P., 1996, AJ, 111, 1913

Sweigart A. V., Demarque P., 1972, A&A, 20, 445

Sweigart A. V., Demarque P., 1973, in Fernie J. D., ed., ASSL Vol. 36: IAU Colloq. 21: Variable Stars in Globular Clusters and in Related Systems, 221

Sweigart A. V., 1990, in Cacciari C., Clementini G., eds, ASP Conf. Ser. 11: Confrontation Between Stellar Pulsation and Evolution, 1

Sweigart A. V., 1994, in Adelman S. J., Upgren A. R., Adelman C. J., eds, Hot Stars in the Galactic Halo, 17

Székely P., Kiss L. L., Csák B., Derekas A., Bedding T. R., Szatmáry K., 2006, MmSAI, 77, 346

Székely P., Kiss L. L., Jackson R., Derekas A., Csák B., Szatmáry K., 2007, A&A, 463, 589

Székely P., Kiss L. L., Szatmáry K., Csák B., Bakos G. Á., Bedding T. R., 2007, Astronomische Nachrichten, 328, 879

Tanabé T., Nishida S., Matsumoto S., Onaka T., Nakada Y., Soyano T., Ono T., Sekiguchi K., Glass I. S., 1997, Nature, 385, 509

Tayler R. J., Wood P. R., 1975, MNRAS, 171, 467

Taylor J. H., Cordes J. M., 1993, ApJ, 411, 674

Thackeray A. D., 1960, The Observatory, 80, 226

Thomas R. N., 1957, ApJ, 125, 260

Thompson I. B., Kałużny, J. and Pych, W. and Burley, G. and Krzemiński, W. and Paczyński, B. and Persson, S. E. and Preston, G. W., 2001, AJ, 121, 3089

Thompson H. M. A., Keenan F. P., Dufton P. L., Ryans R. S. I., Smoker J. V., 2006, MNRAS, 368, 1749

Thompson H. M. A., Keenan F. P., Dufton P. L., Ryans R. S. I., Smoker J. V., Lambert D. L., Zijlstra A. A., 2007, MNRAS, 378, 1619

Thoul A., Jorissen A., Goriely S., Jehin E., Magain P., Noels A., Parmentier G., 2000, MmSAI, 71, 791

Thoul A., Jehin E., Magain P., Noels A., Parmentier G., 2001, in Deiters S., Fuchs B., Just A., Spurzem R., Wielen R., eds, ASP Conf. Ser. 228: Dynamics of Star Clusters and the Milky Way, 571

Thurl C., Johnston K. V., 2002, in van Leeuwen F., Hughes J. D., Piotto G., eds, Omega Centauri, A Unique Window into Astrophysics, 337

Tielens A. G. G. M., 1990, in Mennessier M. O., Omont A., eds, From Miras to Planetary Nebulae: Which Path for Stellar Evolution?, 186

Townsend R., 2007, in Stancliffe R. J., Dewi J., Houdek G., Martin, Tout C. A. R. G., eds, Unsolved Problems in Stellar Physics: A Conference in Honor of Douglas Gough, 345

Trager S. C., King I. R., Djorgovski S., 1995, AJ, 109, 218

Trumpler R. J., 1940, ApJ, 91, 186

Tsuchiya T., Dinescu D. I., Korchagin V. I., 2003, ApJL, 589, 29

Tuairisg S. Ó., Butler R. F., Shearer A., Redfern R. M., Butler D., Penny A., 2003, MNRAS, 345, 960

Tucholke H. J., 1992, A&AS, 93, 311

Tuthill P. G., Danchi W. C., Hale D. S., Monnier J. D., Townes C. H., 2000, ApJ, 534, 907

Tuthill P. G., Monnier J. D., Danchi W. C., 1999, in le Bertre T., Lebre A., Waelkens C., eds, Asymptotic Giant Branch Stars, 331

Ulmschneider P., 1998, Highlights of Astronomy, 11, 831

Ulvestad J. S., Greene J. E., Ho L. C., 2007, ApJL, 661, 151

Umbreit S., Chatterjee S., Rasio F. A., 2008, ApJL, 680, 113

Valenti E., Ferraro F. R., Origlia L., 2004, MNRAS, 351, 1204

van de Ven G., van den Bosch R. C. E., Verolme E. K., de Zeeuw P. T., 2006, A&A, 445, 513

van den Bergh S., Mackey A. D., 2004, MNRAS, 354, 713

van den Bosch R., de Zeeuw T., Gebhardt K., Noyola E., van de Ven G., 2006, ApJ, 641, 852

van der Bliek N. S., Manfroid J., Bouchet P., 1996, A&AS, 119, 547

van der Marel R. P., 2001, in Kaper L., van den Heuvel E. P. J., Woudt P. A., eds, Black Holes in Binaries and Galactic Nuclei, 246

van Leeuwen F., le Poole R. S., Reijns R. A., Freeman K. C., de Zeeuw P. T., 2000, A&A, 360, 472

van Loon J. T., 2000, A&A, 354, 125

van Loon J. T., 2000, A&A, 354, 125

van Loon J. T., 2006, in Lamers H. J. G. L. M., Langer N., Nugis T., Annuk K., eds, Stellar Evolution at Low Metallicity: Mass Loss, Explosions, Cosmology, 211

van Loon J. T., to appear in AIP proceedings of the IXth Torino Workshop on Evolution and Nucleosynthesis in AGB stars (ArXiv e-prints 0801.0557)

van Loon J. T., Boyer M. L., McDonald I., 2008, ApJL, 680, 49

van Loon J. T., Groenewegen M. A. T., de Koter A., Trams N. R., Waters L. B. F. M., Zijlstra A. A., Whitelock P. A., Loup C., 1999, A&A, 351, 559

van Loon J. T., McDonald I., Oliveira J. M., Evans A., Boyer M. L., Gehrz R. D., Polomski E., Woodward C. E., 2006, A&A, 450, 339

van Loon J. T., Stanimirović S., Evans A., Muller E., 2006, MNRAS, 365, 1277

van Loon J. T., van Leeuwen F., Smalley B., Smith A. W., Lyons N. A., McDonald I., Boyer M. L., 2007, MNRAS, 382, 1353

van Loon J. T., Cohen M., Oliveira J. M., Matsuura M., McDonald I., Sloan G. C., Wood P. R., Zijlstra A. A., 2008, A&A, 487, 1055

van Loon J. T., Stanimirović S., Putman M. E., Peek J. E. G., Gibson S. J., Douglas K. A., Korpela E. J., 2009, MNRAS, 396, 1096

van Loon J. T., Marshall J. R., Zijlstra A. A., 2005, A&A, 442, 597

van Winckel H., Mathis J. S., Waelkens C., 1992, Nature, 356, 500

VandenBerg D. A., Bergbusch P. A., Dowler P. D., 2006, ApJS, 162, 375

VandenBerg D. A., Stetson P. B., Bolte M., 1996, ARAA, 34, 461

Vanture A. D., Wallerstein G., Suntzeff N. B., 2002, ApJ, 569, 984

Verbunt F., Johnston H. M., 2000, A&A, 358, 910

Verbunt F., Hasinger G., Johnston H. M., Bunk W., 1993, Advances in Space Research, 13, 151

Villanova S., Piotto G., King I. R., Anderson J., Bedin L. R., Gratton R. G., Cassisi S., Momany Y., Bellini A., Cool A. M., Recio-Blanco A., Renzini A., 2007, ApJ, 663, 296

Vlemmings W., Diamond P., Langevelde H. J. V., 2005, ASP Conf. Ser. 340: Future Directions in High Resolution Astronomy, 394

Voshchinnikov N. V., Henning T., 2008, A&A, 483, 9

Wachter A., Schröder K.-P., Winters J. M., Arndt T. U., Sedlmayr E., 2002, A&A, 384, 452

Wachter A., Winters J. M., Schröder K.-P., Sedlmayr E., 2008, A&A, 486, 497

Wallerstein G., Kovtyukh V. V., Andrievsky S. M., 2007, AJ, 133, 1373

Webbink R. F., 1981, ApJS, 45, 259

Webbink R. F., 1985, in Goodman J., Hut P., eds, IAU Symp. 113: Dynamics of Star Clusters, 541

Weigert A., 1965, Mitteilungen der Astronomischen Gesellschaft Hamburg, 19, 61

Weldrake D. T. F., Sackett P. D., Bridges T. J., 2007, AJ, 133, 1447

White N. E., Angelini L., 2001, ApJL, 561, 101

White R. E., Shawl S. J., 1987, ApJ, 317, 246

White S. D. M., 1977, MNRAS, 179, 33

Whitelock P. A., Feast M. W., van Leeuwen F., 2008, MNRAS, 386, 313

Whitmore B. C., Miller B. W., Schweizer F., Fall S. M., 1997, AJ, 114, 1797

Whitmore B. C., Zhang Q., Leitherer C., Fall S. M., Schweizer F., Miller B. W., 1999, AJ, 118, 1551

Whitney J. H., O'Connell R. W., Rood R. T., Dorman B., Landsman W. B., Cheng K.-P., Bohlin R. C., Hintzen P. M. N., Roberts M. S., Smith A. M., Smith E. P., Stecher T. P., 1994, AJ, 108, 1350

Whittet D. C. B., 1992, Dust in the galactic environment, Institute of Physics Publishing.

Wilkens H., 1964, Boletin de la Asociacion Argentina de Astronomia La Plata Argentina, 8, 9

Wilkens H., 1967, Zentralinstitut fuer Astrophysik Sternwarte Sonneberg Mitteilungen ueber Veraenderliche Sterne, 4, 93

Willemsen P. G., Hilker M., Kayser A., Bailer-Jones C. A. L., 2005, A&A, 436, 379

Willson L. A., 2000, ARAA, 38, 573

Willson L. A., 2007, 378, 211

Wing R. F., Stock J., 1973, ApJ, 186, 979

Winters J. M., le Bertre T., Jeong K. S., Helling C., Sedlmayr E., 2000, A&A, 361, 641

Winters J. M., le Bertre T., Pety J., Neri R., 2007, A&A, 475, 559

Woitke P., 2006, A&A, 452, 537

Woitke P., 2006, A&A, 460, 9

Wolf M., Rayet G., 1867, Compte Rendu, 65, 291

Wolszczan A., Middleditch J., Kulkarni S. R., Backer D. C., Fruchter A. S., 1988, IAUC, 4552

Wolszczan A., Kulkarni S. R., Middleditch J., Backer D. C., Fruchter A. S., Dewey R. J., 1989, Nature, 337, 531

Wood K. D., Bates B., 1994, MNRAS, 267, 660

Wood P. R., 1990, in Mennessier M. O., Omont A., eds, From Miras to Planetary Nebulae: Which Path for Stellar Evolution?, 67

Wood P. R., 2000, PASA, 17, 18

Wood B. E., 2004, Living Reviews in Solar Physics, 1, 2

Wood P. R., Bessell M. S., Fox M. W., 1983, ApJ, 272, 99

Wood P. R., Whiteoak J. B., Hughes S. M. G., Bessell M. S., Gardner F. F., Hyland A. R., 1992, ApJ, 397, 552

Wood P. R., Alcock C., Allsman R. A., Alves D., Axelrod T. S., Becker A. C., Bennett D. P., Cook K. H., Drake A. J., Freeman K. C., Griest K., King L. J., et al., 1999, in le Bertre T., Lebre A., Waelkens C., eds, IAU Symp. 191: Asymptotic Giant Branch Stars, 151

Wood P. R., Olivier E. A., Kawaler S. D., 2004, ApJ, 604, 800

Woolley R. V. D. R., 1964, Nature, 203, 961

Wright F. W., 1940, Harvard College Observatory Bulletin, 912, 8

Yamada S., Okazaki A. T., Fujimoto M. Y., 2008, ApJ, 678, 922

Yao B.-A., Zhang C.-S., Qin D., Tong J.-H., 1993, Ap&SS, 210, 163

Yokoo T., Fukue J., 1992, PASJ, 44, 253

Yoon S.-J., Lee Y.-W., 2003, in Piotto G., Meylan G., Djorgovski S. G., Riello M., eds, New Horizons in Globular Cluster Astronomy, 513

Yoon S.-J., Joo S.-J., Ree C. H., Han S.-I., Kim D.-G., Lee Y.-W., 2008, ApJ, 677, 1080

Zacharias N., Urban S. E., Zacharias M. I., Wycoff G. L., Hall D. M., Monet D. G., Rafferty T. J., 2004, AJ, 127, 3043

Zhao H. S., 2002, in van Leeuwen F., Hughes J. D., Piotto G., eds, Omega Centauri, A Unique Window into Astrophysics, 391

Zheleznyak A. P., Kravtsov V. V., 2003, Astronomy Letters, 29, 599

Zinn R., West M. J., 1984, ApJS, 55, 45

Zinn R., 1985, ApJ, 293, 424

Zinn R. J., Newell E. B., Gibson J. B., 1972, A&A, 18, 390

Zoccali M., Renzini A., Ortolani S., Bica E., Barbuy B., 2001, AJ, 121, 2638